ASME
SETTING THE STANDARD

Journal of Engineering for Gas Turbines and Power

Published Bimonthly by ASME

VOLUME 131 • NUMBER 1 • JANUARY 2009

Editor
D. R. BALLAL (2011)
Assistant to the Editor
S. D. BALLAL
Associate Editors
Gas Turbine (Review Chairs)
K. BRUN (2009)
T. SATTELMAYER (2009)
Coal, Biomass & Alternative Fuels
K. ANNAMALAI (2010)
Combustion & Fuels
N. K. RIZK (2009)
T. SATTELMAYER (2009)
Controls, Diagnostics, & Instrumentation
A. VOLPONI (2010)
Cycle Innovation
P. PILIDIS (2010)
Electric Power
P. CHIESA (2011)
Structures and Dynamics
P. S. KEOGH (2010)
J. SZWEDOWICZ (2009)
D. P. WALLS (2009)
Advanced Energy Systems
J. KAPAT (2010)
Internal Combustion Engines
C. RUTLAND (2009)
T. RYAN III (2009)
J. WALLACE (2011)
M. WOOLDRIDGE (2011)
Nuclear Engineering
J. KUNZE (2011)
I. PIORO (2011)

PUBLICATIONS COMMITTEE
Chair, B. RAVANI

OFFICERS OF THE ASME
President, T. M. BARLOW
Executive Director,
T. G. LOUGHLIN
Treasurer,
T. D. PESTORIUS

PUBLISHING STAFF
Managing Director, Publishing
P. DI VIETRO
Manager, Journals
C. MCATEER
Production Coordinator
J. SIERANT

Transactions of the ASME, Journal of Engineering for Gas Turbines and Power (ISSN 0742-4795) is published bimonthly (Jan., Mar., May, July, Sep, Nov.) by The American Society of Mechanical Engineers, Three Park Avenue, New York, NY 10016. Periodicals postage paid at New York, NY and additional mailing offices. POSTMASTER: Send address changes to Transactions of the ASME, Journal of Engineering for Gas Turbines and Power, c/o THE AMERICAN SOCIETY OF MECHANICAL ENGINEERS, 22 Law Drive, Box 2300, Fairfield, NJ 07007-2300.
CHANGES OF ADDRESS must be received at Society headquarters seven weeks before they are to be effective. Please send old label and new address.
STATEMENT from By-Laws. The Society shall not be responsible for statements or opinions advanced in papers or ... printed in its publications (B7.1, par. 3).
COPYRIGHT © 2009 by the American Society of Mechanical Engineers. For authorization to photocopy material for internal or personal use under circumstances not falling within the fair use provisions of the Copyright Act, contact the Copyright Clearance Center (CCC), 222 Rosewood Drive, Danvers, MA 01923, Tel: 978-750-8400, www.copyright.com.
Canadian Goods & Services Tax Registration #126148048

EDITORIAL

010201 Journal of Engineering for Gas Turbines and Power Welcomes ASME Nuclear Engineering Division Participation!
Dilip R. Ballal

RESEARCH PAPERS

Gas Turbines: Aircraft Engine

011201 Optimal Mission Analysis Accounting for Engine Aging and Emissions
M. Kelaidis, N. Aretakis, A. Tsalavoutas, and K. Mathioudakis

Gas Turbines: Ceramics

011301 High Temperature Radiation Heat Transfer Performance of Thermal Barrier Coatings With Multiple Layered Structures
Xiao Huang

Gas Turbines: Combustion, Fuels, and Emissions

011501 Radiation Benchmarking in a Model Combustor
Lei-Yong Jiang and Ian Campbell

011502 Comparison of Unsteady Reynolds Averaged Navier–Stokes and Large Eddy Simulation Computational Fluid Dynamics Methodologies for Air Swirl Fuel Injectors
David Dunham, Adrian Spencer, James J. McGuirk, and Mehriar Dianat

Gas Turbines: Controls, Diagnostics, and Instrumentation

011601 A Generalized Likelihood Ratio Test for Adaptive Gas Turbine Performance Monitoring
S. Borguet and O. Léonard

Gas Turbines: Electric Power

011801 Cyclic Carbonation Calcination Studies of Limestone and Dolomite for CO_2 Separation From Combustion Flue Gases
Sivalingam Senthoorselvan, Stephan Gleis, Spliethoff Hartmut, Patrik Yrjas, and Mikko Hupa

Gas Turbines: Manufacturing, Materials, and Metallurgy

012101 Wide Gap Braze Repair Using Vertically Laminated Repair Scheme
Doug Nagy and Xiao Huang

Gas Turbines: Marine

012201 The Performance Evaluation With Diffuser Geometry Variations of the Centrifugal Compressor in a Marine Engine (70 MW) Turbocharger
Hong-Won Kim, Jong-Il Park, Seung-Hyup Ryu, Seong-Wook Choi, and Sang-Hak Ghal

Gas Turbines: Microturbines and Small Turbomachinery

012301 Design, Fabrication, and Performance of Foil Gas Thrust Bearings for Microturbomachinery Applications
Brian Dykas, Robert Bruckner, Christopher DellaCorte, Brian Edmonds, and Joseph Prahl

(Contents continued on inside back cover)

This journal is printed on acid-free paper, which exceeds the ANSI Z39.48-1992 specification for permanence of paper and library materials. ♾™
♻ 85% recycled content, including 10% post-consumer fibers.

Downloaded 03 Jun 2010 to 171.66.16.160. Redistribution subject to ASME license or copyright; see http://www.asme.org/terms/Terms_Use.cfm

(Contents continued)

Journal of Engineering for Gas Turbines and Power JANUARY 2009

Volume 131, Number 1

012302 Design and Performance Evaluation of a Trigeneration System Incorporating Hydraulic Storage and an Inverted Brayton Cycle
Matthew Blieske, J. E. D. Gauthier, and X. Huang

012303 Ten Years of Experience With a Small Jet Engine as a Support for Education
O. Léonard, J. P. Thomas, and S. Borguet

Gas Turbines: Structures and Dynamics

012501 Effect of Side Feed Pressurization on the Dynamic Performance of Gas Foil Bearings: A Model Anchored to Test Data
Tae Ho Kim and Luis San Andrés

012502 Reduction of Multistage Disk Models: Application to an Industrial Rotor
Arnaud Sternchüss, Etienne Balmès, Pierrick Jean, and Jean-Pierre Lombard

012503 Nonlinear Numerical Prediction of Gas Foil Bearing Stability and Unbalanced Response
Sébastien Le Lez, Mihaï Arghir, and Jean Frêne

012504 Damping Ratio Estimation Techniques for Rotordynamic Stability Measurements
C. Hunter Cloud, Eric H. Maslen, and Lloyd E. Barrett

012505 Measurements of Leakage and Power Loss in a Hybrid Brush Seal
Luis San Andrés, José Baker, and Adolfo Delgado

012506 Nonlinear Stochastic Dynamics, Chaos, and Reliability Analysis for a Single Degree of Freedom Model of a Rotor Blade
Pankaj Kumar and S. Narayanan

012507 Measurements Versus Predictions for the Rotordynamic Characteristics of a Five-Pad Rocker-Pivot Tilting-Pad Bearing in Load-Between-Pad Configuration
Clint R Carter and Dara W. Childs

012508 Relationship of Influence Coefficients Between Static-Couple and Multiplane Methods on Two-Plane Balancing
John J. Yu

Internal Combustion Engines

012801 The Lean Mixture Operational Limits of a Spark Ignition Engine When Operated on Fuel Mixtures
Hailin Li, Ghazi A. Karim, and A. Sohrabi

012802 Three–Dimensional Transient Elastic Thermal Stress Field During Diesel Particulate Filter Regeneration
Zhenhua Guo, Zhaoyan Zhang, Biqing Sheng, and Wen Peng

012803 Effects of Key Factors on the Engine Combustion Mode Switching Between HCCI and SI
Tian Guohong, Wang Zhi, Wang Jianxin, Hongming Xu, and Shuai Shijin

012804 Three-Dimensional Computational Fluid Simulation of Diesel and Dual Fuel Engine Combustion
Chengke Liu and G. A. Karim

Nuclear Power

012901 Thermal-Design Options for Pressure-Channel SCWRS With Cogeneration of Hydrogen
Maria Naidin, Sarah Mokry, Farina Baig, Yevgeniy Gospodinov, Udo Zirn, Igor Pioro, and Greg Naterer

012902 Effect of Hydrated Salt Additives on Film Boiling Behavior at Vapor Film Collapse
Takahiro Arai and Masahiro Furuya

012903 Effects of Surface Tension on Two-Phase Void Drift Between Triangle Tight Lattice Subchannels
Akimaro Kawahara, Michio Sadatomi, and Tatsuya Higuchi

012904 On the Pressure Dependency of Physical Parameters in Case of Heat Transfer Problems of Supercritical Water
Gabor Hazi and Istvan Farkas

012905 Computational Fluid Dynamics Assessment of the Local Hot Core Temperature in a Pebble-Bed Type Very High Temperature Reactor
Min-Hwan Kim, Hong-Sik Lim, and Won Jae Lee

012906 Experimental and Numerical Modeling of Transition Matrix From Momentum to Buoyancy-Driven Flow in a Pressurized Water Reactor
Thomas Höhne, Sören Kliem, and Roman Vaibar

012907 Inert Matrix Fuel Analysis by Means of the TRANSURANUS Code: The Halden IFA-652 In-Pile Test
R. Calabrese, F. Vettraino, and T. Tverberg

012908 Development of a Hybrid Turbulent Particle Dispersion Model and Implementation in the Gasflow Code
Zhanjie Xu, John R. Travis, and Wolfgang Breitung

(Contents continued on facing page)

Downloaded 03 Jun 2010 to 171.66.16.160. Redistribution subject to ASME license or copyright; see http://www.asme.org/terms/Terms_Use.cfm

Journal of Engineering for Gas Turbines and Power JANUARY 2009

Volume 131, Number 1

TECHNICAL BRIEFS

014501 Preliminary Design Analysis of Hot Gas Ducts for the Nuclear Hydrogen System
Kee-nam Song and Yong-wan Kim

The ASME Journal of Engineering for Gas Turbines and Power is abstracted and indexed in the following:

AESIS (Australia's Geoscience, Minerals, & Petroleum Database), Applied Science & Technology Index, Aquatic Sciences and Fisheries Abstracts, Civil Engineering Abstracts, Compendex (The electronic equivalent of Engineering Index), Computer & Information Systems Abstracts, Corrosion Abstracts, Current Contents, Engineered Materials Abstracts, Engineering Index, Enviroline (The electronic equivalent of Environment Abstracts), Environment Abstracts, Environmental Science and Pollution Management, Fluidex, INSPEC, Mechanical & Transportation Engineering Abstracts, Mechanical Engineering Abstracts, METADEX (The electronic equivalent of Metals Abstracts and Alloys Index), Pollution Abstracts, Referativnyi Zhurnal, Science Citation Index, SciSearch (The electronic equivalent of Science Citation Index), Shock and Vibration Digest

Downloaded 03 Jun 2010 to 171.66.16.160. Redistribution subject to ASME license or copyright; see http://www.asme.org/terms/Terms_Use.cfm

Journal of Engineering for Gas Turbines and Power

Editorial

Journal of Engineering for Gas Turbines and Power Welcomes ASME Nuclear Engineering Division Participation!

A happy new year to all of you! I am pleased to announce that in April 2008, ASME's Nuclear Engineering Division (NED) selected this journal for the publication of nuclear power engineering papers. This is an important strategic step forward for both NED and JEGTP. As an editor, I welcome all authors who contribute to ASME NED conferences and promise them rapid and fair paper reviews. The publication of 50 or more nuclear engineering papers annually will significantly contribute to my own vision and aspiration for JEGTP, which is to make it a *top* journal in the broad area of power and energy.

Last year, two major changes were put into place that affected the world of ASME publishing. First, ASME introduced e-First, a novel online paper publication process, and launched the ASME Digital Library (http://www.asmedl.org). This Digital Library is ASME's primary repository of current and archival literature featuring ASME Transaction Journals from 1990 to the present, among other publications. As the ASME Digital Library continues to expand, it ultimately will include the complete archive of ASME's Transactions Journals dating back to 1880. This represents a significant milestone in the world of scientific publishing!

Second, JEGTP made a giant leap forward with a bimonthly publication schedule with a total of 1616 printed pages (=183 papers in CY2008), a new record! Moreover, the e-First publication process is regularly producing completed JEGTP issues two months ahead of the printed issues.

Last year, JEGTP secured four new outstanding individuals as associate editors. They are: Jim Wallace (University of Toronto, Canada) and Margaret Wooldridge (University of Michigan, Ann Arbor serving a second term), covering internal combustion engines, and Jay Kunze (Idaho State University, Pocatello, ID) and Igor Pioro (University of Ontario Institute of Technology, Ontario, Canada), covering nuclear engineering. My congratulations to these individuals for their appointments and work on behalf of the journal. Also, I thank the outgoing associate editor, Jim Cowart (U.S. Naval Academy, Annapolis, MD) and Ashok Rao (University of California, Irvine, CA), for their many years of valuable service to the journal.

Summarizing, because of the events that unfolded and the improvements made during 2008, the journal has grown to cover an even broader range of topics in gas turbines, nuclear engineering, internal combustion engines, fossil power generation, and advanced energy systems. JEGTP remains the number one ranked journal in the world in the area of gas turbine engineering and power and your continuing research contributions will keep it there!

Dilip R. Ballal
University of Dayton,
KL-503 300, College Park,
Dayton, OH 45469-0140

Copyright © 2009 by ASME

Downloaded 02 Jun 2010 to 171.66.16.109. Redistribution subject to ASME license or copyright; see http://www.asme.org/terms/Terms_Use.cfm

Optimal Mission Analysis Accounting for Engine Aging and Emissions

M. Kelaidis
Research Assistant
e-mail: manousos@gmail.com

N. Aretakis
Research Associate
e-mail: naret@central.ntua.gr

A. Tsalavoutas
Research Associate
e-mail: ttsal@ltt.ntua.gr

K. Mathioudakis
Professor
e-mail: kmathiou@central.ntua.gr

Laboratory of Thermal Turbomachines,
National Technical University of Athens,
Iroon Polytechniou 9,
Zografou, Athens 15780, Greece

An aircraft mission analysis procedure, accounting for engine aging deterioration and incorporating emission estimation capability, is presented. It consists of three main modules: a flight simulation module, an engine performance simulation module, and an optimizer. A key feature of the approach is the incorporation of engine deterioration modeling. This extends the procedure's ability to estimate onboard performance of an engine as it ages through time and usage. Additionally, the possibility to investigate environmental impact is offered through pollutant emission semi-empirical correlations, which are coupled to the engine performance calculations. The adaptive character of the models employed allows for accurate performance and emission estimations once an initial set of data is available for the engine. The proposed procedure allows the optimization of a flight scenario for a variety of aircrafts, missions, and engine condition combinations in order to meet predefined criteria. Mission profile characteristics (e.g., cruise, altitude, and speed) providing optimum overall performance in terms of fuel conservation, time related costs, or pollutant production are studied.
[DOI: 10.1115/1.2969095]

1 Introduction

Global air traffic is forecast to grow at an average annual rate of around 5% in the next 20 years. More passengers are becoming financially capable of traveling frequently, more companies are expanding in transnational activities, markets with great potential are emerging (e.g., India and China), and demand for freighters is increasing. At the same time, airframe and engine manufacturers are advancing rapidly in the design and production processes, delivering aircrafts with improved fuel efficiency, lower maintenance costs, and reduced environmental impact.

Air transport has to deal with three main issues: high oil prices, air traffic congestion over Europe and U.S., and growing public sensitivity for environmental issues. Both manufacturers and operators (airlines) are thus obliged to find a solution to these problems by developing new methods and tools, which allow the operation of aircrafts in a globally more efficient way.

The present study couples conventional mission analysis techniques to modern numerical methods, taking advantage of current computational power, in order to answer to such issues through virtually costless simulation and optimization. Novel elements introduced here are the capability of handling engine deterioration as well as pollutant emissions over the entire mission and their incorporation in optimization studies.

The techniques introduced are incorporated under a software tool, which features characteristics found in well established commercial applications (e.g., PIANO, Lissys [1] and PACELAB MISSION [2]), such as full mission analysis and optimization for a large variety of flight profiles. It gives, however, additional capabilities by allowing the investigation of engine deterioration effects through the use of a detailed engine monitoring module, which is further supplemented with emission estimation capability.

Compared with other approaches to the problem of performance analysis and emission production (e.g., Döpelheuer [3], Avellán and Grönstedt [4], Visser and Kluiters [5], and Shakariyants et al. [6,7]), the method described here offers the advantage of integrating all different aspects (materialized by a complete software package), allowing for a wide range of investigations rather than studying limited test cases.

2 Mission Analysis Model

The numerical model developed for aircraft mission analysis covers all segments of a modern commercial aircraft's typical flight: taxi, take-off, climb, cruise, descent, and final approach.[1] The aircraft trajectory (in the *X*-*Z* plane) is analyzed by using the basic equations of flight mechanics. At the same time, engine operation is monitored along the specified flight profile.

The proposed model allows the analysis of a variety of possible missions within the limits of safety and traffic regulations. In each case, the required input data are mission length, payload and fuel, cruise altitude and velocity, desired climb and descent trajectories, and finally, a representation of engine condition during the flight (engine degradation level). Aircraft kinematics is calculated by combining the aerodynamic requirements for flight and the potential of the propelling jet engines. A computational engine performance simulator is used to generate accurate information about engine performance and condition at any instant of the mission. The model delivers the overall mission results: the exact aircraft trajectory with kinematics information at every instant and all engine performance parameters, including emissions, at every point, as well as burned fuel and flight duration. The principles employed and the modules constituting the calculation package are described in the following.

2.1 Flight Mechanics: Trajectory Calculation. The main longitudinal forces applied to the aircraft during flight are weight, thrust, aerodynamic lift, and drag. The model assumes moment equilibrium and total absence of dynamic effects (zero moments of inertia of punctual mass). The sum of these forces equals the momentum rate of change, according to Newton's second law,

Contributed by the International Gas Turbine Institute of ASME for publication in the JOURNAL OF ENGINEERING FOR GAS TURBINES AND POWER. Manuscript received April 11, 2008; final manuscript received April 14, 2008; published online November 20, 2008. Review conducted by Dilip R. Ballal. Paper presented at the ASME Turbo Expo 2008: Land, Sea and Air (GT2008), Berlin, Germany, June 9–13, 2008.

[1]The package has been given the name CAMACM. (Commercial Aircraft Mission Analysis Computational Model)

Copyright © 2009 by ASME

Downloaded 02 Jun 2010 to 171.66.16.109. Redistribution subject to ASME license or copyright; see http://www.asme.org/terms/Terms_Use.cfm

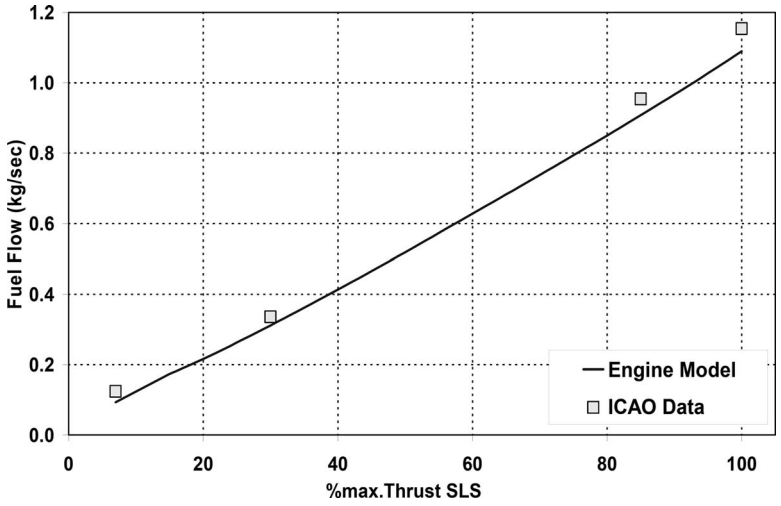


Fig. 1 Comparison of predicted (model) and ICAO published data (fuel consumption versus thrust)

$$\boldsymbol{F}+\boldsymbol{W}+\boldsymbol{L}+\boldsymbol{D}=\frac{d(m\cdot\boldsymbol{U})}{dt} \tag{1}$$

The derivative of the momentum can be developed in two terms since the aircraft mass is variable due to fuel consumption,

$$\Sigma\boldsymbol{F}=\frac{dm}{dt}\boldsymbol{U}+m\frac{d\boldsymbol{U}}{dt} \tag{2}$$

The two equations are coupled and constitute a system of differential equations thus described. Forces and aircraft momentum are analyzed in components along the axes of motion X and Z. The velocity derivative is discretized using the Euler method. Taking the flight path angle (noted as θ here) constant during a calculation time-step, the equations can take the form

$$\begin{bmatrix}|\boldsymbol{F}_i|\cos\theta\\ |\boldsymbol{F}_i|\sin\theta\end{bmatrix}+\begin{bmatrix}0\\ -m_i|\boldsymbol{g}_i|\end{bmatrix}+\begin{bmatrix}-0.5\rho_i\mathrm{SC}_L|\boldsymbol{U}_i|^2\sin\theta\\ 0.5\rho_i\mathrm{SC}_L|\boldsymbol{U}_i|^2\cos\theta\end{bmatrix}+\begin{bmatrix}-0.5\rho_i\mathrm{SC}_D|\boldsymbol{U}_i|^2\cos\theta\\ -0.5\rho_i\mathrm{SC}_D|\boldsymbol{U}_i|^2\sin\theta\end{bmatrix}=-|\dot{W}_f|\cdot\begin{bmatrix}|\boldsymbol{U}_i|\cos\theta\\ |\boldsymbol{U}_i|\sin\theta\end{bmatrix}+\frac{m_i}{\delta t}\cdot\begin{bmatrix}|\boldsymbol{U}_{i+1}|_X-|\boldsymbol{U}_i|\cos\theta\\ |\boldsymbol{U}_{i+1}|_Z-|\boldsymbol{U}_i|\sin\theta\end{bmatrix} \tag{3}$$

The kinematics solver uses the scheduled trajectory (defined in the climb, cruise, and descent envelopes) to determine the required values of thrust and lift coefficients for every point of flight. Climb and descent envelopes are similar to the classic schemes (constant calibrated air speed/constant Mach, see, for example, Eshelby [8] and Mair and Birdsall [9]). However, in this model they are described by a very small number of parameters, which are given as inputs (namely, climb coefficient (CLICO), initial and final angle theta, descent speed, and rate of descent at specific altitudes).

Aerodynamic forces on the aircraft (lift and drag) are estimated by an aerodynamics module, while instantaneous engine thrust and fuel consumption are estimated by the engine module discussed in the next paragraph. Thus, the only unknown is the value of the velocity at point $i+1$, which is calculated in a straightforward manner. An additional control loop makes sure that the prescheduled trajectory is followed with maximum fidelity. A full description of the mission model is given by Kelaidis [10].

2.2 Submodels. The main kinematics solver interacts with the following three submodules: atmosphere, aerodynamics, and engine.

Atmosphere. This provides the ambient conditions during the flight using numerical expressions of the International Standard Atmosphere (ISA) as it is described in the base of aircraft data (BADA) manual (see Byrne [11]).

Aerodynamics. This is an aircraft aerodynamic model that comprises a set of drag polar curves (second degree polynomials of C_D as a function of C_L) for a variety of typical high lift devices (flaps/flaperons and slats and/or droop nose) settings. It also takes into account the flight Mach number and the ground effect. It should be mentioned that the aerodynamic model does not correspond to specific aircraft characteristics but is of a generic structure, allowing the representation of any modern airliner.

Engine. The engine module incorporates a numerical performance model of a modern high bypass turbofan engine, which allows the estimation of the engine cycle at different operating conditions, described by Stamatis et al. [12,13]. A crucial feature of this model is its ability to represent specific engines after an adaptation to available performance data. This adaptation is achieved by tuning appropriate component performance modification factors, so that model predictions match actual engine data. These same factors allow a representation of engine deterioration and are thus used as engine condition parameters (ECPs). For example, compressor and turbine degradation is represented by altering flow capacity and efficiency (Mathioudakis et al. [14]).

The particular engine model used in the examples shown here was adapted to GE-SNECMA CFM56-3C1 using the International Civil Aviation Association (ICAO) databank values of this engine ([15]). The adapted model accuracy can be appreciated in Fig. 1, where the predicted fuel flows at four thrust levels are presented versus the corresponding values of the ICAO data bank. A good agreement between model predictions and measurements is observed.

The operation of the engine performance model is supported by a secondary control module. This module stands between the kinematics solver (where the required thrust is determined) and the main engine model. Its role is to ensure acceptable engine operating conditions by not allowing extreme conditions such as overspeeding, overheating, and subidling.

2.3 Example Analysis. In order to illustrate the capabilities of the developed procedure, the analysis results of two test cases are presented. The missions of two aircrafts that differ only in engine condition are analyzed. Both aircrafts use the same type of engines, the first one with new engines (REF) and the second one with engines that suffer a high degradation level (DEGR). The

Downloaded 02 Jun 2010 to 171.66.16.109. Redistribution subject to ASME license or copyright; see http://www.asme.org/terms/Terms_Use.cfm

Table 1 Test-case main mission parameters

Distance	2000 km (1080 nm)
Flight altitude	35,000 ft (constant)
Cruise speed	$M0.8$(constant)
Payload	12.6 tons (120 pax+5 crew)
Fuel boarded	7 tons (reserves included)

principal mission parameters are given in Table 1, while the overall mission analysis results for these two cases are shown in Table 2.

Both aircrafts are scheduled to follow the same 4D trajectory, meaning the X-Z path and identical evolutions of $X(t)$ and $Z(t)$ functions (except for take-off). As can be noticed from the results, the cruise segment represents 69% of the trip time and 66% of the burned fuel. It can also be observed that 24% of the total fuel is spent during the climb. Thus, this segment constitutes a significant part of the overall mission and thus cannot be neglected in the optimization procedure discussed later.

Table 2 Overall mission analysis results

Segment	Time (min)		Burned fuel (kg)	
	REF	DEGR	REF	DEGR
WT	10.0	10.0	148.2	148.2
TO	0.5	0.6	61.9	64.5
CL	17.0	17.1	1138.5	1186.0
CR	114.3	114.3	3165.8	3280.8
DE	23.7	23.7	262.7	262.4
Total	165.6	165.7	4777	4942

The effects of engine degradation on engine operation are illustrated in Figs. 2–4. Although the two aircrafts follow the same trajectory (same thrust requirements), engine degradation causes an increase in specific fuel consumption (SFC), speed, and turbine inlet temperature (TIT).

The aircraft with degraded engines will need 3.5% more fuel for the same flight compared to the one with intact engines. It is obvious that this fact will significantly affect the direct operating cost (DOC) of the aircraft (see, for example, Ekstrand et al. [16]). Another fact that must be taken into account is that the increased turbine inlet temperatures in conjunction with the higher speeds could lead to an increase in engine fatigue life consumption.

3 Optimization of Flight Trajectory

3.1 Problem Definition. The optimization of flight parameters (such as altitude, cruise, and climb speeds) is a common

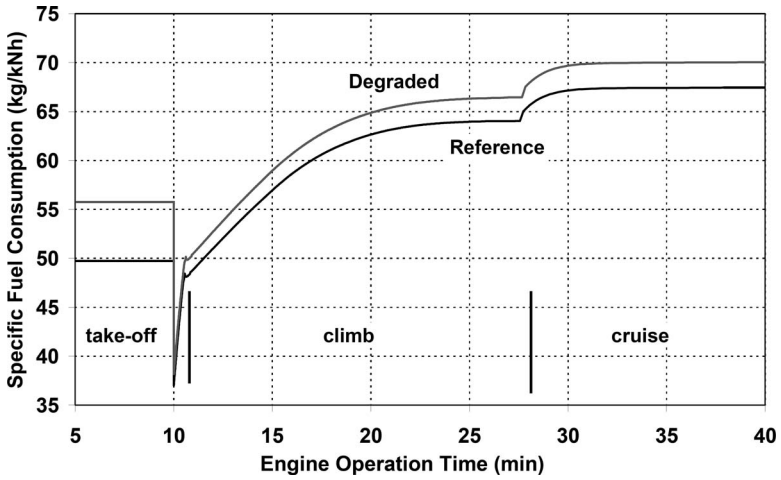


Fig. 2 SFC versus time during take-off, climb, and cruise for two different engine condition cases

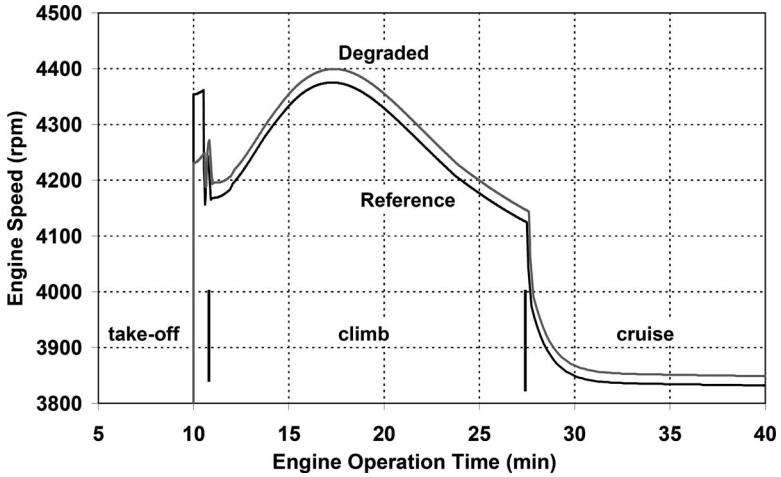


Fig. 3 Engine speed versus time during take-off, climb, and cruise for two different engine condition cases

Downloaded 02 Jun 2010 to 171.66.16.109. Redistribution subject to ASME license or copyright; see http://www.asme.org/terms/Terms_Use.cfm

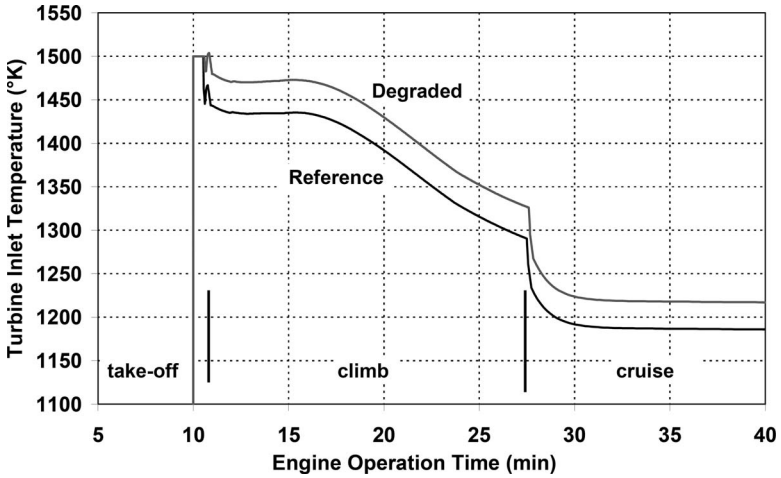


Fig. 4 TIT versus time during take-off, climb, and cruise for two different engine condition cases

practice for airliners, which is automatically performed by the flight management system (FMS), aiming to reduce as much as possible fuel and time costs within the frame imposed by regulations.

From a strictly mathematical point of view, the optimization of a mission is a complex problem, involving contradicting and stochastic (e.g., winds) factors, with no straightforward solution. Traditional methods, using parametric analyses that locate the optimum through derivatives, can provide useful results. However, current computational capability permits more advanced methods to be employed. In this section, a procedure that combines the above described model with an optimization algorithm is demonstrated.

During this procedure, the optimization code calls the mission analysis model, each time with different main flight parameters as inputs. Four major parameters that define the 4D trajectory (and, consequently, engine operation) have been selected as optimization variables: cruise flight level (CRFL), cruise speed (CRSP), and two coefficients related to the climb envelope (CLICO and THETA_0). The four optimization variables have some predefined initial values, and they are restricted in a certain variation area by a set of constraints (Table 3). The flow chart of the flight trajectory optimization procedure is shown in Fig. 5.

3.2 Optimization Method. The values of the previously described optimization variables that correspond to the optimum flight profile are evaluated through the minimization of a cost function. The cost (or objective) function used in the present analysis is given by the following equation:

$$\text{CF} = C_{w_1}\frac{\text{fuel}}{\text{fuel}_{\text{ini}}} + C_{w_2}\frac{\text{time}}{\text{time}_{\text{ini}}} \tag{4}$$

where C_{w_i} are weighting factors. In the presented applications, only the total fuel consumption over a mission was considered, while time related costs were not taken into account due to lack of available data.

The minimization of Eq. (4) is accomplished by using the "simplex downhill method in multidimensions" (Press et al. [17]). This method has been chosen for its robustness and simplicity and because it does not need the evaluation of any derivatives. For all cases inside the search area imposed by the given constraints, it showed good convergence in less than (or about) 100 iterations. An example of a typical convergence history is shown in Fig. 6.

3.3 Optimization Scenarios. In order to investigate the influence of aircraft main performance drivers to the "optimum" flight, a series of optimization scenarios has been analyzed. Here, three of these scenarios are presented, covering the effects of engine deterioration level, mission length, and finally, take-off weight (TOW). It is recalled that in each case the main mission parameters (CRFL, CRSP, CLICO, and THETA_0) are optimized for minimum overall fuel consumption.

3.3.1 Scenario 1: Engine Deterioration Level. Three aircrafts (A, B, and C) are flying at a 1500 km mission with 58.8 ton TOW. Aircraft-A has engines in a reference condition. Aircraft-B has degraded engines by 1% for each component of the turbofan. Aircraft-C has "improved" engines by 1% for each component (regarding the flow capacity and efficiency). Optimization results for each aircraft are given in Table 4.

The corresponding three climb trajectories are shown in Fig. 7. Engine degradation is observed to result to small variations in optimum cruise altitude, while it has a larger impact on climb parameters. Higher degradation levels make the optimum climb trajectory less steep in terms of both flight path angle and speed schedule.

3.3.2 Scenario 2: Mission Length. Three aircrafts (A, B, and C) start with the same TOW (58.8 tons) and ECP (reference) for three different flights, where only the length varies: 500 km (short) for Aircraft-A, 1500 km (medium) for Aircraft-B, and 2500 km (long) for Aircraft-C.

As shown in Table 5, the optimum 4D trajectories for Aircraft-B and Aircraft-C vary only in the climb phase, where for the medium trip a relatively steeper climb is required, as shown in Fig. 8 where the optimized climb trajectories for the three cases are presented. During the cruise both aircrafts fly close to optimum at 35,500–36,000 ft with a flight Mach number equal to 0.82. On the other hand, for the short mission (a typical 1 h flight) the optimum trajectory is quite different, especially at the cruise segment. The optimum short mission demands both lower flight altitude (32,100 ft) and speed ($M=0.805$).

Table 3 Initial values of the mission parameters (free variables) imposed to optimization and constraints

Variable	Initial value	Upper constraint	Lower constraint
THETA_0 (deg)	8	15	5
CLICO	1.10	1.25	1.00
CRFL (ft.)	36,000	37,000	26,000
CRSP (Mach)	0.8	0.82	0.67

Downloaded 02 Jun 2010 to 171.66.16.109. Redistribution subject to ASME license or copyright; see http://www.asme.org/terms/Terms_Use.cfm

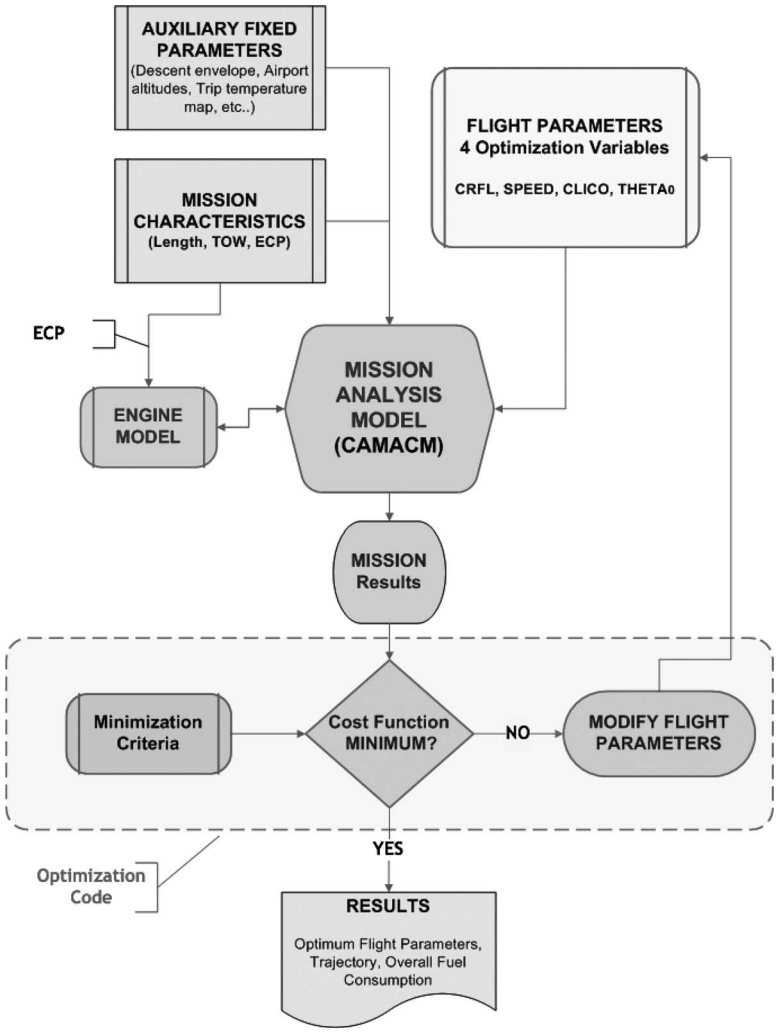


Fig. 5 Flow chart for the optimization procedure

It is noted that the optimization results of the current study are very similar to typical cruise speeds and altitudes for short and medium-short flights. This is a good indication of the overall performance of both the mission analysis model and the optimization procedure.

3.3.3 Scenario 3: Take-Off Weight. In this scenario, two aircrafts (A and B) are scheduled to carry out two missions: a long trip (2500 km) for Aircraft-A, and a short trip (500 km) for Aircraft-B. Each flight is repeated for four different TOWs from

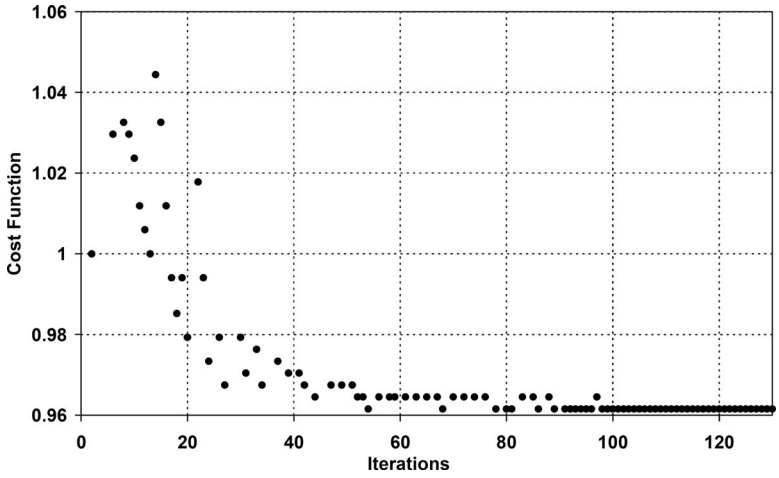


Fig. 6 Convergence history (CF versus Iterations) for a typical optimization case

Downloaded 02 Jun 2010 to 171.66.16.109. Redistribution subject to ASME license or copyright; see http://www.asme.org/terms/Terms_Use.cfm

Table 4 Optimized mission parameters for three engine condition cases

Engines condition	Optimized values CRFL	CRSP	$THETA_0$	CLICO
Degraded	34,000	*M*0.818	7.0 deg	1.244
Reference	35,700	*M*0.819	7.9 deg	1.250
Improved	35,200	*M*0.820	9.4 deg	1.249

Table 5 Optimized mission parameters for different mission length cases

Mission length	Optimized values CRFL	CRSP	$THETA_0$	CLICO
500 km	32,100	*M*0.805	7.8 deg	1.25
1500 km	35,700	*M*0.820	7.8 deg	1.25
2500 km	35,900	*M*0.819	6.5 deg	1.24

52.8 tons to 58.8 tons. All missions go through optimization in order to investigate the TOW effect on the optimum flight trajectories.

In Fig. 9 the optimum cruise speed for different TOWs and for the short and long trip cases is shown. In Figs. 10 and 11 the same information is presented for the optimum cruise altitude and initial flight path angle, respectively.

Regarding the long mission, the optimum cruise speed is not affected by the TOW variation ($M=0.82$ for all cases), while the corresponding flight altitude shows a small dependency on the TOW. This is simple to explain: as the cruise altitude increases, the aircraft burns more fuel during the climb. Another expected result is the optimum $THETA_0$ evolution with TOW, which decreases. One can understand by these facts that the climb segment plays a major role in mission optimization, even for "3 h" flights.

The TOW effect on the optimum short mission is quite different from that on the long one. Here, the climb segment is dominant in terms of fuel consumption (2/3 of the overall mission fuel). Thus, even the optimum cruise characteristics (speed-altitude) are, in fact, determined by their relation with the climb phase. In the same set of graphs, it is also evident that the cruise altitude is independent of the TOW, and the $THETA_0$ follows an expected negative evolution for increasing TOW. On the contrary, optimum cruise Mach increases for a heavier aircraft. Having in mind that higher cruise speeds also induce a faster climb (velocity profile versus altitude), it can be concluded that the optimum short mission derives from a transition from a "steep/slow climb" to a "shallow/fast climb" as the TOW increases. The dependence of climb parameters to cruise speed is introduced in the present model by setting the final climb speed as a large percentage (constant predefined) of the cruise speed (for short cruise accelerations) and the climb envelope (velocity profile) also as a function of the final climb speed.

4 Pollutant Emission Estimation

The rapid growth of air traffic has increased the interest of the community, including airlines and engine manufactures, in the environmental impact of air transport. A number of research programs (see, for example, Ref. [18]) aiming for the study and development of new technologies that will help decrease the level of emitted pollutants and noise have been initiated. At the same time some methods that allow the prediction of emitted pollutants during an aircraft flight have been proposed.

A method proposed by Shakariyants et al. [6] is based on a multireactor combustor model that allows the prediction of four principal pollutants: nitrogen oxide (NO_x), unburned hydrocarbon (UHC), CO, and soot. Flight related data are evaluated by solving aircraft equations of motion assuming a nonslip flight, while engine performance data are provided by a commercial software package (GSP, NLR, Amsterdam; see Visser and Broomhead [19]). Another method proposed by Shakariyants et al. [7] utilizes the Boeing 2 fuel flow methodology that calculates emission indices based on fuel flow and ICAO certification data.

In the present study, emission semi-empirical correlations have been selected for the prediction of emitted pollutants during a flight because of their simplicity and the limited amount of required data. Such correlations can provide predictions with acceptable accuracy once they are adapted to reference emission data, as shown by Tsalavoutas et al. [20]. The implementation of emission correlation to the previously described mission analysis model will be discussed in the following.

4.1 Emission Correlations

4.1.1 NO_x Correlation. In order to predict NO_x emissions, the generic correlation of Eq. (5), based on Sullivan's correlation (see Eq. (6) in Döpelheuer and Lecht [21]), has been formulated and used,

$$NO_x = C_1 \cdot P_3^{C_2 \cdot 0.5} \cdot e^{(T_3/C_3 \cdot 300)} \cdot FAR^{C_4} \tag{5}$$

where fuel to air ratio (FAR) has been added as a factor that carries information about the burner's thermal load. Using the adaptation method described by Tsalavoutas et al. [20] and the ICAO emission data for the simulated engine, the coefficients C_1–C_4 ended up in an optimized set of values, giving a very good

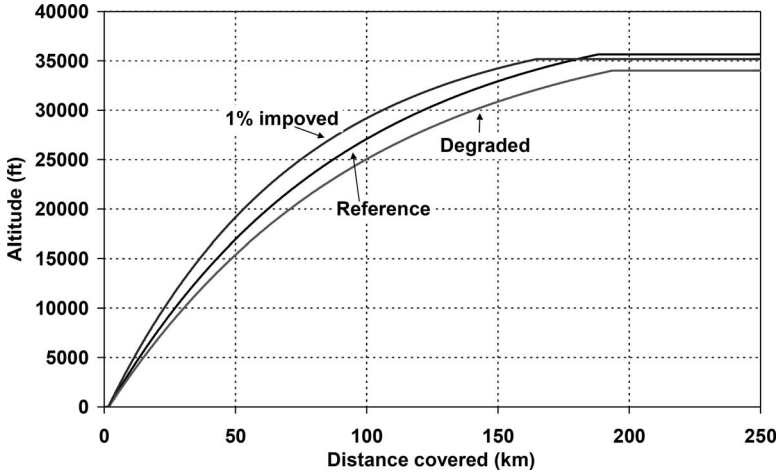


Fig. 7 Optimized climb trajectories

Downloaded 02 Jun 2010 to 171.66.16.109. Redistribution subject to ASME license or copyright; see http://www.asme.org/terms/Terms_Use.cfm

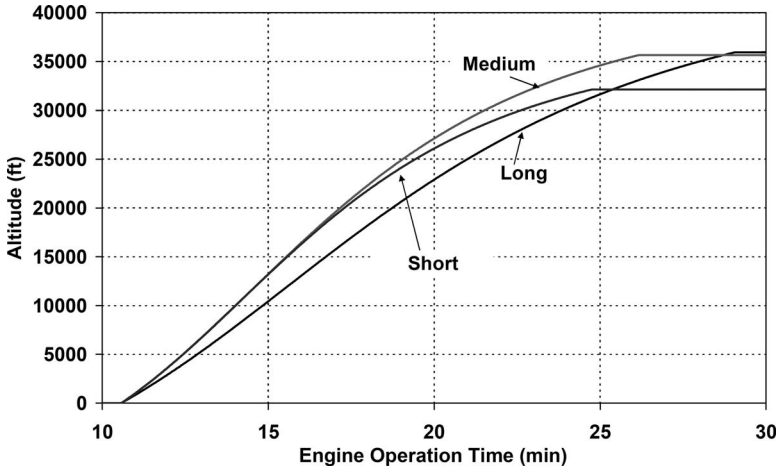


Fig. 8 Optimized climb trajectories for different mission length cases

level of adaptation quality, as shown in Fig. 12. The adapted form of the NO_x correlation has been used in the present investigation that combines the mission analysis model with emission calculation during each phase of flight.

4.1.2 CO and UHC Correlations. Döpelheuer's correlations described in Döpelheuer and Lecht [21] are used for the estimation of CO and UHC emissions,

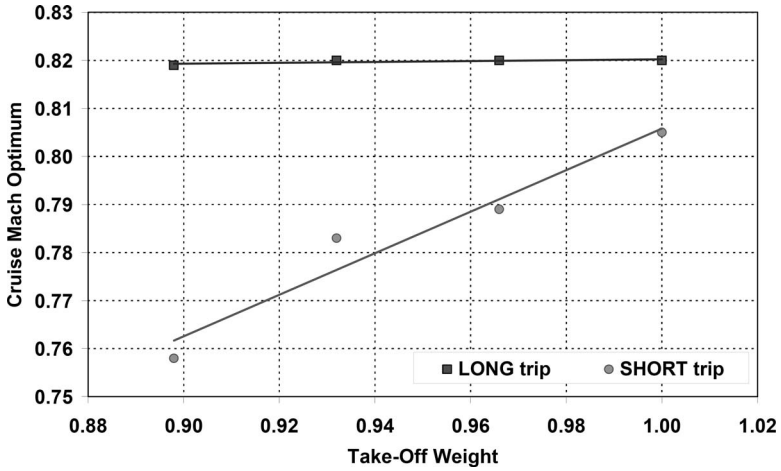


Fig. 9 Evolution of optimum cruise speed with TOW for two different mission length cases

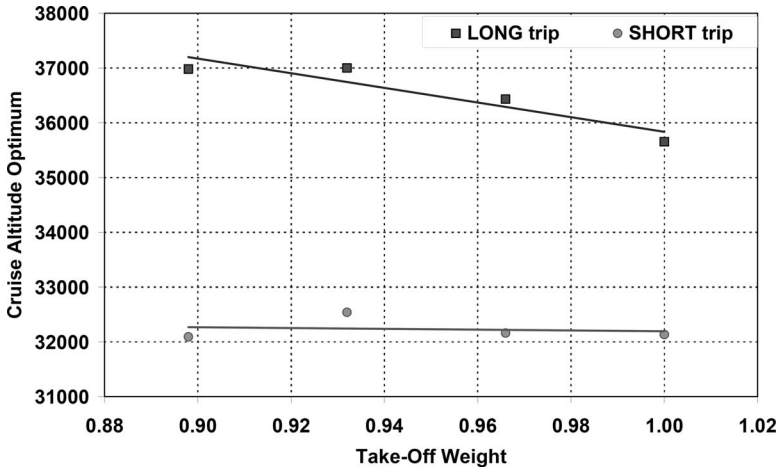


Fig. 10 Evolution of optimum cruise altitude with TOW for two different mission length cases

Downloaded 02 Jun 2010 to 171.66.16.109. Redistribution subject to ASME license or copyright; see http://www.asme.org/terms/Terms_Use.cfm

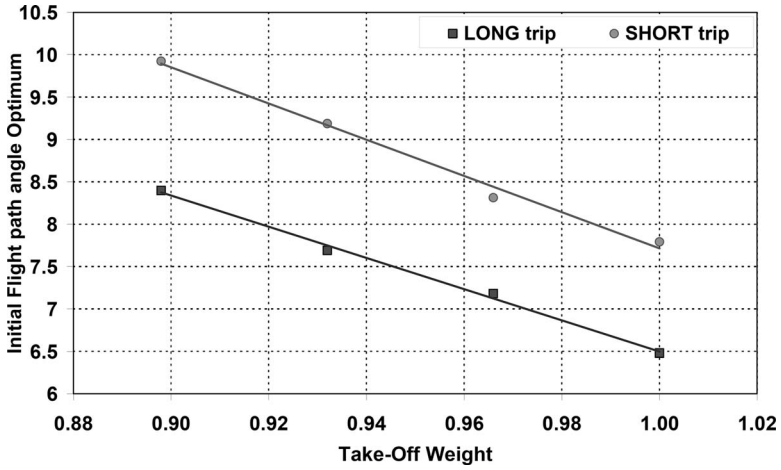


Fig. 11 Evolution of optimum initial flight path angle with TOW for two different mission length cases

$$\mathrm{EICO,EIUHC} = f\left(\frac{m_{\mathrm{air}}}{P_3^{1.8}\cdot e^{(T_3/300)}}\right)\cdot\left\{\frac{T_3}{T_{3,\mathrm{ref}}}\cdot\frac{P_{3,\mathrm{ref}}}{P_3}\right\}^C \quad (6)$$

Equations (5) and (6) evaluate emissions during flight based on the adaptation to ground level emissions (for example, those provided at the ICAO data bank).

4.1.3 Implementation. The above mentioned relations will provide an estimation of emissions if the relevant engine cycle variables are known. The engine performance model provides the values of all such variables at any instant of the flight mission. The emission evaluation module is thus interconnected to the engine module to produce emission data for every point of missions studied.

4.2 Example: Emission Production Rate During Flight. A test case has been analyzed in order to obtain some first results regarding the "emission production rate profile" during a typical flight. A short length mission of a single aisle aircraft has been chosen. The basic mission parameters are presented in Table 6.

The predicted pollutant emissions are presented in Fig. 13. During the warm-up, taxi (first 10 min of engine operation), and descent segments (approximately the last 20 min of mission) the CO/UHC emission production rate is at very high levels. Compared with the emission production rate of CO and UHC during the climb/cruise (low levels), the emitted UHC production rate during warm-up/taxi/descent is about ten times higher. Regarding the CO emission production rate, the above mentioned ratio is around 4.

The NO_x emission production rate is clearly large for higher power settings (40–45 g/s for the take-off and 20–30 g/s for the initial climb), but during the cruise it does not exceed 3 g/s. This distribution of NO_x emissions seems to affect a lot more the departure airport vicinity (considering numerous take-offs per day) and the lower atmosphere (first 5 min of climb) than the high altitude (above 20,000 ft) level, where the cruise takes place.

5 Discussion

The presented mission analysis model is a useful tool able to contribute in scientific and industrial research on aircraft performance, aero-engine onboard operation, and the environmental impact of air transport. A user may take full advantage of the model's potential and carry out a variety of investigations as follows:

- Alter the set of mission parameters (e.g., the climb trajectory control) in order to examine its effect on the aircraft and engine performance.
- Work out an optimization analysis for a given aircraft operation on various mission profiles or compare different aircrafts' best adaptations to the special characteristics of a single mission.

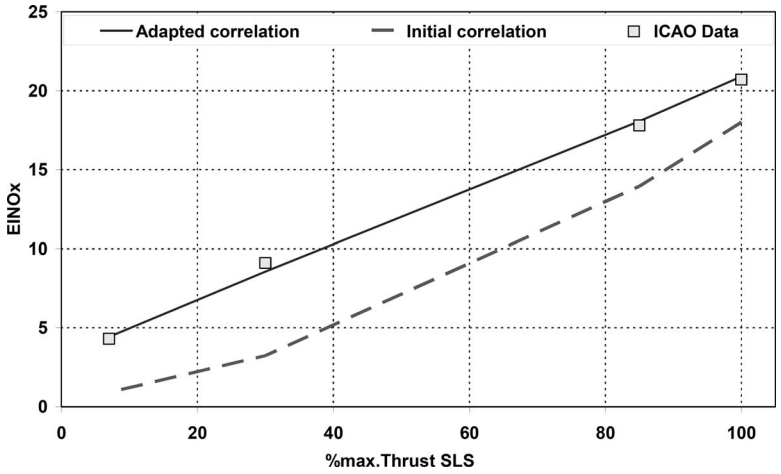


Fig. 12 Comparison of estimated NO_x derived from both the initial and the adapted form of the correlation with the ICAO published data

Downloaded 02 Jun 2010 to 171.66.16.109. Redistribution subject to ASME license or copyright; see http://www.asme.org/terms/Terms_Use.cfm

Table 6 Mission characteristics for the test case of pollutant emission production rate prediction

Distance	1000 km (540 nm)
Flight altitude	30,000 feet (constant)
Cruise speed	M0.78(constant)
Payload	120 pax+5 crew
Fuel boarded	7 tons (reserves included)

- Conduct large scale investigations concerning fuel conservation and civil aviation environmental impact by using the appropriate input data.
- Perform a preliminary fleet management investigation regarding the variation of each individual aircraft engine condition.
- Attain a better understanding of the modern flight mechanics and aero-engine operation through a realistic comprehensible mission simulation.
- Finally, analyze the "Green Flight" scenario; that is, flight trajectory optimization primarily aiming at pollutant emission and CO_2 reduction.

The engine model employed is an independent module that is externally supplied. The flexibility to use any other model thus exists. This way the developed mission analysis software could be used to make studies of future engine technologies. Emission correlations are also implemented as independent modules. Alternative combustion technologies can thus be implemented in the form of different correlations.

A further important feature of the engine model is its ability to adapt to engines of different conditions. The same model can thus be used first for deterioration tracking (by coupling it, for example, with a deterioration tracking algorithm, such as the one proposed by Mathioudakis et al. [14]) and subsequently as a realistic engine simulator supporting the mission analysis. The same comment holds for the emission estimator, which can also be coupled to an adaptation scheme (e.g., Tsalavoutas et al. [20]) for an accurate tuning to a specific engine.

The proposed mission analysis method requires small time-steps and thus a large number of iterations. An extensive sensitivity analysis has been performed in order to define a set of optimum values of time-steps that will be used for the analysis of different flight segments. The following values have been obtained: take-off $\Delta t=0.1$ s, climb and descent $\Delta t=1$ s, and cruise $\Delta t=10$ s.

The computational time can be significantly reduced to a few milliseconds per mission using engine performance data stored in memory (arrays of SFC as a function of thrust, Mach, altitude, and ΔTISA) instead of using the full engine model. The accuracy penalty is less than 0.5%. This is very important in the case of optimization where a large number of missions need to be evaluated. Final refinements of the results can then be performed by employing the full engine model. The modules previously discussed have been integrated in a single software package with a user friendly interface (see Ref. [22]).

6 Conclusions

An integrated approach on transport aircraft performance modeling has been presented. It provides answers about flight trajectory optimization for fuel minimization while taking into account engine deterioration. This is achieved through an advanced numerical model that couples a flight kinematics solver with full engine monitoring and an optimization code. Additionally, the capability to predict pollutant emission production is also implemented in the proposed model in order to quantify the environmental impact of a given mission.

The potential of the discussed method has been demonstrated through a series of examples: engine degradation effect on the overall fuel consumption, optimization of flight trajectories for various test cases (different mission lengths, take-off weights, and ECPs), and major pollutant production throughout a typical short haul flight.

Acknowledgment

The work described in this paper, particularly the work on emissions, has been supported by the project AEROTEST, while the integration aspects have profited from activities in the ECATS Network. Financial support from the European Union Commission is gratefully acknowledged. The assistance of Ph. Kamboukos in the engine model adaptation is also acknowledged.

Nomenclature

- 4D = three space dimensions+time
- C_D = aircraft drag coefficient
- C_L = aircraft lift coefficient
- CL = climb
- CLICO = climb coefficient: the ratio between the preferred climb speed at half of the cruise flight level with the one that results from linear speed variation

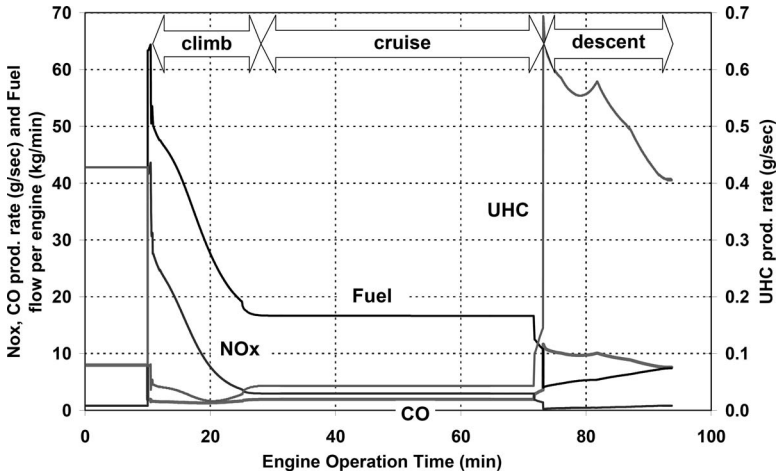


Fig. 13 Predicted pollutant emission production rate during a typical short mission (1.5 h)

Downloaded 02 Jun 2010 to 171.66.16.109. Redistribution subject to ASME license or copyright; see http://www.asme.org/terms/Terms_Use.cfm

CO = carbon monoxide
CR = cruise
D = aerodynamic drag
DE = descent
EI = emission index of pollutant (grams of pollutant produced from 1 kg of burned fuel)
F = net thrust (installed)
G = gravity acceleration
L = aerodynamic lift
M = Mach number
m = aircraft mass
NO_x = nitrogen oxides (NO and NO_2)
P_3 = compressor delivery pressure
S = aircraft reference aerodynamic surface
SLS = sea level static
T = temperature
T_3 = compressor delivery temperature
$THETA_0$ = initial climb gradient value (soon after take-off) that determines the climb trajectory
U = aircraft velocity
W = aircraft weight
Wf = fuel consumption (rate)
WT = warm-up and taxi
ΔTISA = deviation from the standard temperature distribution as described in the ISA model
θ = flight path angle
ρ = ambient air density

References

[1] PIANO, Lissys, http://www.lissys.demon.co.uk/
[2] PACELAB MISSION, http://www.pacelab.com
[3] Döpelheuer, A., 2000, "Aircraft Emission Parameter Modelling," Air & Space Europe, **2**(3), pp. 34–37.
[4] Avellán, R., and Grönstedt, T., "Preliminary Design of Subsonic Transport Aircraft and Engines," Paper No. ISABE-2007-1195.
[5] Visser, W. P. J., and Kluiters, S. C. A., 1999, "Modeling the Effects of Operating Conditions and Alternative Fuels on Gas Turbine Performance and Emissions," *RTO Meeting Proceedings*, Lisbon, Portugal, 12–16 October 1998, Vol. 14.
[6] Shakariyants, S. A., van Buijtenen, J. P., Visser, W. P. J., and Tarasov, A., 2006, "A Multidisciplinary Aero-Engine Exhaust Emission Study," ASME Paper No. GT2006-90749.
[7] Shakariyants, S. A., van Buijtenen, J. P., Visser, W. P. J., and Tarasov, A., 2006, "Generic Airplane and Aero-Engine Simulation Procedures for Exhaust Emission Studies," ASME Paper No. GT2007-27943.
[8] Eshelby, M. E., 2000, *Aircraft Performance: Theory and Practice*, Elsevier Science, New York.
[9] Mair, A., and Birdsall, D. L., 1992, *Aircraft Performance*, Cambridge University Press, Cambridge, England.
[10] Kelaidis, M., 2006, "Aircraft Mission Analysis and Optimization of Flight Parameters," Diploma thesis, National Technical University of Athens, Athens.
[11] Byrne, J., 1995, EUROCONTROL, Revision 2.3, "User Manual for the Base of Aircraft Data (BADA)."
[12] Stamatis, A., Mathioudakis K., Ruiz, J., and Curnock B., "Real Time Engine Model Implementation for Adaptive Control and Performance Monitoring of Large Civil Turbofans," ASME Paper No. 2001-GT-0362.
[13] Stamatis, A., Kamboukos, Ph., Aretakis, N., and Mathioudakis, K.,"On Board Adaptive Models: A General Framework and Implementation Aspects," ASME Paper No. GT-2002-30622.
[14] Mathioudakis, K., Kamboukos, Ph., and Stamatis, A., 2002, "Turbofan Performance Deterioration Tracking Using Non-Linear Models and Optimization Techniques," ASME J. Turbomach., **124**, pp. 580–587.
[15] UK Civil Aviation Authority, 2006, "Aircraft Engine Emissions Individual Datasheets," ICAO Aircraft Engine Emissions Databank at http://www.caa.co.uk/
[16] Ekstrand, H., Avellán, R., and Grönstedt, T., "Minimizing Direct Operating Costs (Doc) for a Small European Airline," Paper No. ISABE-2007-1105.
[17] Press, W. H., Flannery, B. P., Teukolsky, S. A., and Vetterling, W. T., 1986, *Numerical Recipes: The Art of Scientific Computing*, Cambridge University Press, Cambridge, England.
[18] Aeronautics Research 2003–2006 Projects, European Commission, Project Synopses.
[19] Visser, W. P. J., and Broomhead, M. J., 2000, "GSP—A Generic Object-Oriented Gas Turbine Simulation Environment," NLR, Report No. NLR-TP-2000-267.
[20] Tsalavoutas, A., Kelaidis, M., Thoma, N., and Mathioudakis, K., "Correlations Adaptation for Optimal Emissions Prediction," ASME Paper No. GT2007-27060.
[21] Döpelheuer, A., and Lecht, M., 1998, "Influence of Engine Performance on Emissions Characteristics," Symposium of the Applied Vehicle Technology Pane-Gas Turbine Engine Combustion, Emissions and Alternative Fuels, Lisbon, Portugal, Oct. 1998.
[22] CAMACM demo version at http://www.ltt.mech.ntua.gr

Downloaded 02 Jun 2010 to 171.66.16.109. Redistribution subject to ASME license or copyright; see http://www.asme.org/terms/Terms_Use.cfm

High Temperature Radiation Heat Transfer Performance of Thermal Barrier Coatings With Multiple Layered Structures

Xiao Huang
Department of Mechanical and Aerospace Engineering, Carleton University, ON, K1S 5B6, Canada

Meeting the demands for ever increasing operating temperatures in gas turbines requires concurrent development in cooling technologies, new generations of superalloys, and thermal barrier coatings (TBCs) with increased insulation capability. In the case of the latter, considerable research continues to focus on new coating material compositions, the alloying/doping of existing yttria stabilized zirconia ceramics, and the development of improved coating microstructures. The advent of the electron beam physical vapor deposition coating process has made it possible to consider the creation of multiple layered coating structures to meet specific performance requirements. In this paper, the advantages of layered structures are first reviewed in terms of their functions in impeding thermal conduction (via phonons) and thermal radiation (via photons). Subsequently, the design and performance of new multiple layered coating structures based on multiple layered stacks will be detailed. Designed with the primary objective to reduce thermal radiation transport through TBC systems, the multiple layered structures consist of several highly reflective multiple layered stacks, with each stack used to reflect a targeted radiation wavelength range. Two ceramic materials with alternating high and low refractive indices are used in the stacks to provide multiple-beam interference. A broadband reflection of the required wavelength range is obtained using a sufficient number of stacks. In order to achieve an 80% reflectance to thermal radiation in the wavelength range 0.3–5.3 μm, 12 stacks, each containing 12 layers, are needed, resulting in a total thickness of 44.9 μm. Using a one dimensional heat transfer model, the steady state heat transfer through the multiple layered TBC system is computed. Various coating configurations combining multiple layered stacks along with a single layer are evaluated in terms of the temperature profile in the TBC system. When compared with a base line single layered coating structure of the same thickness, it is estimated that the temperature on the metal surface can be reduced by as much as 90°C due to the use of multiple layered coating configurations. This reduction in metal surface temperature, however, diminishes with increasing the scattering coefficient of the coating and the total coating thickness. It is also apparent that using a multiple layered structure throughout the coating thickness may not offer the best thermal insulation; rather, placing multiple layered stacks on top of a single layer can provide a more efficient approach to reducing the heat transport of the TBC system. [DOI: 10.1115/1.2967495]

1 Introduction

Thermal barrier coatings (TBCs) have played an important role in protecting superalloy substrate components in gas turbine engines from reaching excessive temperatures. Further increases in turbine inlet temperatures (TITs) for an improved efficiency of gas turbines requires the continuous development of new superalloys, better cooling schemes, and most importantly, superior thermal barrier coating systems. Typically, the TBC system consists of a ceramic top layer, a metallic bond coat layer situated between the ceramic layer and the superalloy substrate, the superalloy substrate, and a very thin thermally grown oxide (TGO) layer formed at the ceramic/bond coat interface, as shown in Fig. 1. The application of a low thermal conductivity ceramic coating can reduce the metal surface temperature by as much as 150°C. Some of the basic requirements for the ceramic top coating are (1) good thermal insulation (low thermal conductivity and opaque to thermal radiation), (2) high melting point, (3) stable phases at operating temperatures, (4) appropriate thermal expansion coefficient matching that of the superalloy substrate to reduce thermal stress, and (5) thermodynamically compatible with the bond coat [1]. Zirconium oxide, either fully stabilized or partially stabilized by trivalent yttrium oxide (Y_2O_3), is to date the most successfully developed TBC material.

There are two commercial methods for the deposition of TBCs, namely, plasma spraying (PS) and electron beam physical vapor deposition (EB-PVD). PVD is fundamentally a vaporization coating technique in which a vapor phase is generated from a solid material through an externally applied energy. The evaporated material transfers from the source to the substrate, forming a coating. In EB-PVD, the evaporation is obtained with a focused electron beam [2] and a deposition rate of up to 150 μm/min (or 10–15 kg/h) can be achieved. Compared with other coating deposition techniques, the EB-PVD process produces denser and more strain tolerant coatings due to the occurrence of a lamellar structure. Additionally, by varying the coating process parameters or using the co-evaporation of more than one material, coatings comprised of alternating layers of different microstructures or compositions can be made [3]. Due to the versatility of the PVD

Contributed by the International Gas Turbine Institute of ASME for publication in the JOURNAL OF ENGINEERING FOR GAS TURBINES AND POWER. Manuscript received April 1, 2008; final manuscript received April 2, 2008; published online October 10, 2008. Review conducted by Dilip R. Ballal. Paper presented at the ASME Turbo Expo 2008: Land, Sea and Air (GT2008), Berlin, Germany, June 9–13, 2008.

Copyright © 2009 by ASME

Downloaded 02 Jun 2010 to 171.66.16.109. Redistribution subject to ASME license or copyright; see http://www.asme.org/terms/Terms_Use.cfm

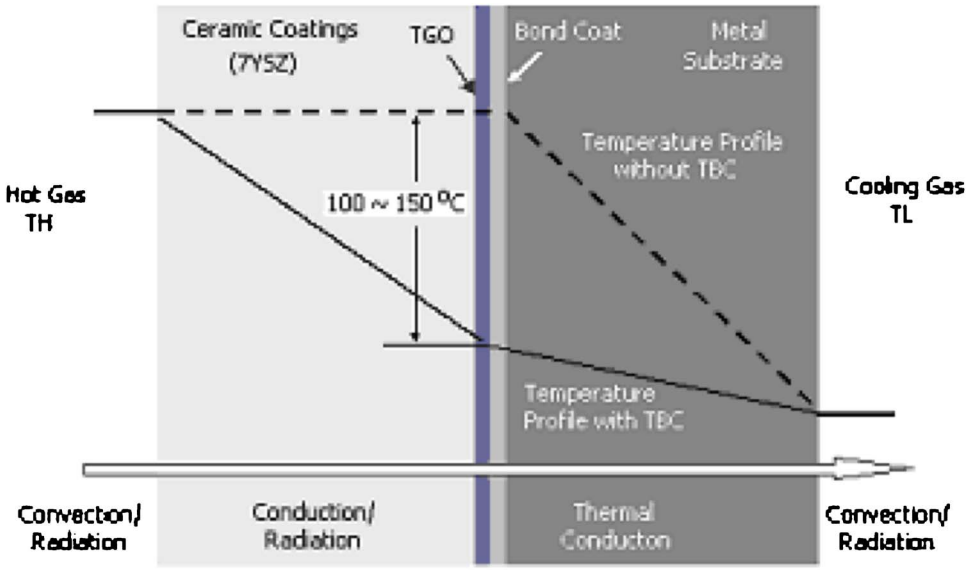


Fig. 1 Typical thermal barrier coating system

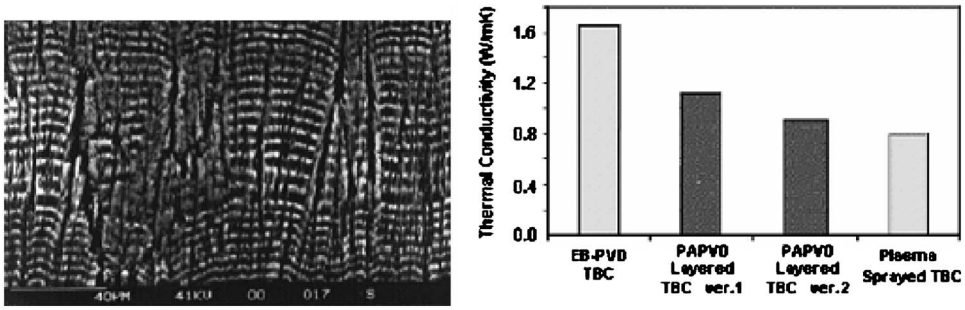
based process, multiple layered coating structures can be fabricated, offering unique properties particularly in enhancing the thermal insulation of TBCs. Sections 1.1, 1.2 and 1.3 review the progress in the advancement of multiple layered TBCs in reducing thermal conductivity and increasing the reflectivity to thermal radiation. Subsequently, the recent development of multiple layered coating structures based on multiple layered stack configuration will be discussed.

1.1 Multiple Layered TBCs in Reducing Thermal Conductivity (Phonon Transport). An effective way to reduce the thermal conduction of TBCs with predetermined compositions is to increase the phonon scattering via pore modification or increasing the number of grain boundaries and layer interfaces [4,5]. Layer interfaces can be introduced into the columnar structure of an EB-PVD coating by modifying the process parameters [6,7]. As seen in Fig. 2, layers with varying densities parallel to the coating surface were obtained by modulating the dc bias applied to the substrate during deposition. These layer interfaces increased the phonon scattering effect and resulted in a reduction in thermal conductivity by up to 45%, as shown in Fig. 2(*b*). This modification enables EB-PVD TBCs with thermal conductivity to approach that of plasma sprayed TBCs, where intersplat and intrasplat pores and microcracks play a role in reducing the thermal conductivity.

Alternatively, a multiple layer coating structure was produced using a "shutter" method during the EB-PVD process, as shown in Fig. 3. The measured thermal conductivity of such a structure is a function of the total number of layers produced by the shutter method. There was an observed 30% reduction in thermal conductivity for coatings with 20 layers [7].

1.2 Multiple Layered TBCs With Reduced Thermal Radiation (Photon Transport). It has been reported that yttria stabilized zirconia (YSZ) based ceramic material exhibits high transmittance (low absorption) in the wavelength range 0.3–5 μm [8]. As such, thermal radiation, if not reflected, will transmit directly through zirconia based TBCs to the metal substrate. Beyond this wavelength range, YSZ shows partial absorption and partial transmission (5–10 μm), i.e., the radiation will be partially transmitted and partially absorbed and re-emitted. At wavelengths greater than 10 μm, the coating is opaque and all the radiation is absorbed and transformed into heat, resulting in a localized temperature increase.

The wavelength range for thermal radiation is strongly dependent on the environmental temperature. With an increase in gas temperature, the radiation emitted from hot gas shifts to a shorter wavelength range. At operating temperatures between 1700 K and 2000 K, about 80% of the radiation flux emitted from the hot gases falls within the 0.3–10 μm wavelength range [9]. Therefore, a significant amount of radiation (photons) may be transmitted directly through the coating resulting in a reduced thermal



(*a*) (*b*)

Fig. 2 (*a*) EB-PVD TBC deposited by plasma assisted physical vapor deposition (PAPVD) process. The periodicities of the layers are between 0.2 μm and 2.0 μm. (*b*) Thermal conductivities of the layered EB-PVD TBC compared with the EB-PVD and thermal sprayed TBCs [6].

Downloaded 02 Jun 2010 to 171.66.16.109. Redistribution subject to ASME license or copyright; see http://www.asme.org/terms/Terms_Use.cfm

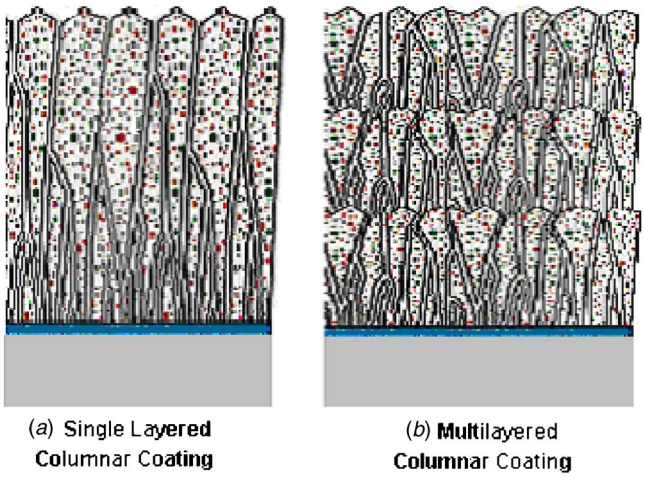


Fig. 3 (*a*) **Typical standard vapor phase columnar structure and** (*b*) **modified columnar microstructure with multiple interfaces** [**6**]

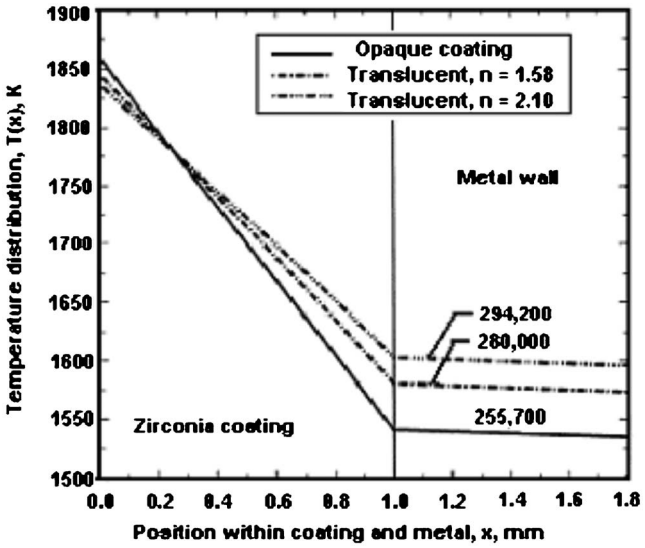


Fig. 4 Temperature distributions calculated in a zirconia thermal barrier coating on the wall of a combustor compared with an opaque thermal barrier coating [**6**]

insulation capability for YSZ based TBCs. In fact, the effect of thermal radiation on the increased thermal conductivity has been observed by several researchers [3,10,11]. According to the thermal conductivity theory, the intrinsic thermal conductivity of ceramic coatings has an inverse dependence on the temperature. However, the measured thermal conductivities for zirconia based ceramic coatings were found to increase with temperature, and this was attributed to the increased thermal radiation transport at higher temperatures.

The temperature increase on a metallic substrate resulting from the thermal radiation transmission through TBCs has been evaluated by Siegel and Spuckler [12] in their numerical analysis. In the study, the radiation transport through TBCs to the metal component was assumed to originate from two sources: (1) the external radiation from hot gases or soot directly incident on the coating surface and transmitted to the substrate and (2) the internal radiation emission within the hot coating itself when heated by convection from combustion gases, conduction within the coating system, or absorption of external and internal radiation. It was found that at a gas temperature of 2000 K, the temperature increase on the metallic substrate resulting from the transmission of radiation through TBCs was as much as 50°C compared with that of an opaque coating, as shown in Fig. 4.

1.3 Multiple Layered TBC With Increased Reflectivity to Thermal Radiation. Given the transparent nature of YSZ based TBC materials, several approaches can be taken to reduce the thermal radiation transport through the system. Specifically, these include increasing the scattering to photons or increasing the reflectivity to photons. Increasing the number of layers in the TBC structure, as well as increasing the number of scattering defects such as microcracks and pores within the coating, was found to reduce thermal radiation [5,7,13]. Furthermore, inserting highly reflective metallic layers within the ceramic coating (Fig. 5(*a*)) was believed to bring about a 24% reduction in the net heat flux (Fig. 5(*b*)) for a ceramic coating containing one single metallic layer as compared to a ceramic coating without a reflective metallic layer [14].

Multiple layered coatings with an increased reflectance to thermal radiation can also be fabricated with two or more layers of ceramic materials. A multiple layered structure with alternating 8YSZ (400 nm) and Al_2O_3 (100 nm), described as variable $8YSZ/Al_2O_3$, is shown in Fig. 6(*a*). The hemispherical reflectance to radiation was increased significantly from the base line single layered 8YSZ, as shown in Fig. 6(*b*). It is to be noted from the figure that the reflectance of these coating structures is highly dependent on the radiation wavelength.

2 Current Research in Designing New Multiple Layered Coating Structures

Based on the brief review given, it is apparent that multiple layered coating structures can be fabricated using the state-of-the-art PVD process, and that these layered structures have great potential to reduce the metal surface temperature by impeding both thermal conduction and thermal radiation. However, the current multiple layered structures do not offer an increased reflectance to a broadband radiation wavelength range, a variable dependent on the gas temperature. To this end, the coating research group at Carleton University has designed a novel highly reflective multiple layered structure that is capable of covering a broadband radiation wavelength range [9,15]. A brief introduction to the design and the resulting improvements are summarized herein, with further details on the design and the mathematical modeling given in Ref. [16].

To achieve a significant reduction in temperature at the substrate caused by radiation, the concept of using multiple layered coatings containing several stacks to effectively reflect radiation within a wavelength range 0.3–5 μm [8] is used in our study. Each stack is specifically designed to reflect a targeted range of wavelength, with a broadband reflection of the required wavelength range being achieved using a sufficient number of appropriately designed stacks. To achieve high reflectance for each wavelength range, each stack contains several layers consisting of materials with alternating high and low refractive indices. The optical thickness of each layer is designed to be a quarter of the targeted wavelength in order to satisfy the condition of multiple-beam interference [17]. Since radiation with shorter wavelengths scatters more than longer wavelengths [18], the stack reflecting the shortest wavelength range is placed close to the incident radiation. Figure 7 shows schematically how the radiation is reflected or transmitted by these multiple layers.

The targeted wavelength range for consideration in this paper is 0.3–5 μm, where the YSZ is transparent. YSZ is selected as the material with a high refractive index and Al_2O_3 is selected as the material with a lower refractive index (it also has a transparent range in the same wavelength range [19]). To achieve greater than 80% hemispherical reflectance, the YSZ/Al_2O_3 multiple layered

Downloaded 02 Jun 2010 to 171.66.16.109. Redistribution subject to ASME license or copyright; see http://www.asme.org/terms/Terms_Use.cfm

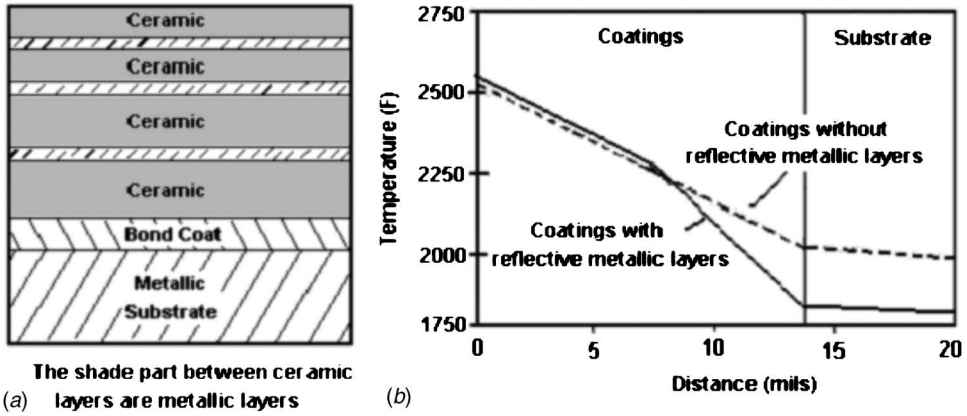


Fig. 5 (*a*) **Sectional view of a ceramic coating having metallic reflective layers and** (*b*) **temperature versus distance for exposed surfaces, illustrating the benefits attained by forming a protective coating** [6]

coating system requires a total of 12 stacks, with 12 layers within each stack. The thicknesses for layers in the first and last stacks in this design are described in Table 1. The total physical thickness for the 12 stacks is 44.9 μm. The theoretical hemispherical reflectance of this particular multiple layered structure was calculated and is shown in Fig. 8. The refractive index of the incident medium was assumed to be 1.0. It can be seen that greater than 80% hemispherical reflectance can be achieved using this 12-stack-design. Once the multiple layered stacks were determined, various configurations consisting of multiple layered stacks with high reflectance and a single layer of ceramic material with low thermal conductivity were considered, as shown in Fig. 9. Configuration *A* is the base line single layer coating structure. Structure *B* consists of a top layer of multiple layered stacks (M) and a single layer (S_1) with low thermal conductivity. In Configuration *C*, the single layer (S_1) (with low thermal conductivity and a low refractive index) is placed on top of the multiple layered stacks (M). In Configuration *D*, two multiple layered stacks (M) are employed with a single layer (S_1) sandwiched in between. In all configurations, a thin 7YSZ based ceramic layer (S_2, 5 μm) is used to provide the interface transaction to the bond coat should materials other than 7YSZ be selected for either the M or S_2 layer. The total coating thickness is kept at 250 μm for all four configurations, with the thickness of the multiple layered stacks being 44.9 μm based on the design described earlier.

For Configurations *B–D*, the function of the single layer S_1 is to reduce the thermal conduction through the coating to the metal substrate. Consequently, selecting materials with low thermal conductivity is the primary design criteria for this single layer. Suitable materials include tertiary YSZ doped with Yb_2O_3 or Sc_2O_3 [16] or zirconates with reportedly low thermal conductivity values. Additionally, the single layer S_1 in Configuration *B* is required to have a high scattering coefficient so that both the transmitted and emitted radiation from the top layer can be scattered; a high refractive index is also desirable for S_1 in order to increase the reflectivity of the multiple layered stacks. In Configuration *C*, on the other hand, it is advantageous for S_1 to have a low scattering coefficient as well as a low refractive index to ensure low internal radiation emitted by the S_1 layer [20] and reduced internal

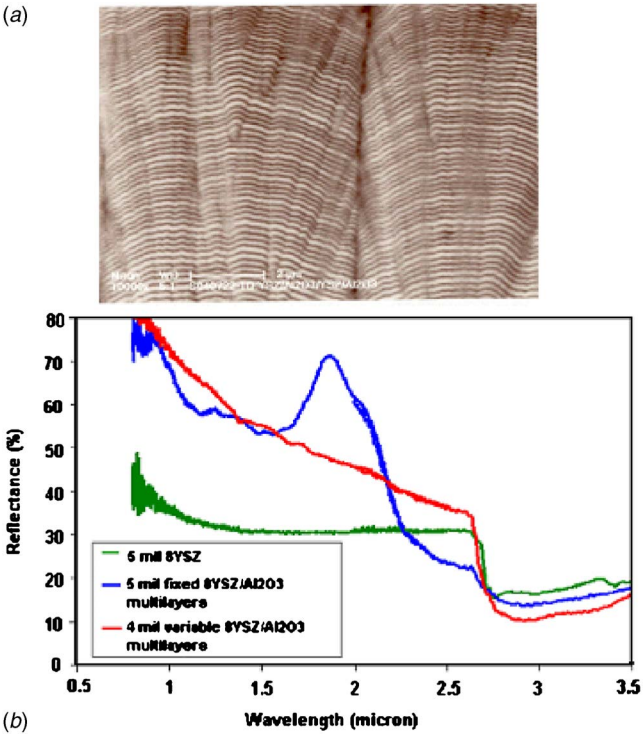


Fig. 6 (*a*) **Multiple layered 8YSZ/Al_2O_3 structure and** (*b*) **increased hemispherical IR reflectance with fixed and variable spacing** [7]

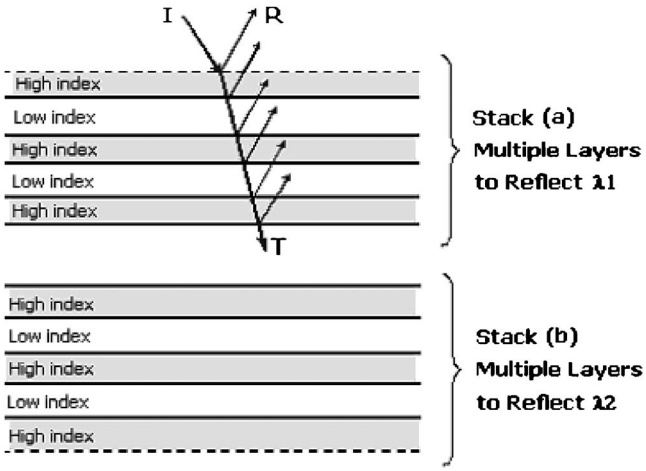


Fig. 7 Schematic of the multiple layered coating structure containing two stacks (*T*=**transmitted,** *R*=**reflected, and** *I*=**incident radiation**)

Downloaded 02 Jun 2010 to 171.66.16.109. Redistribution subject to ASME license or copyright; see http://www.asme.org/terms/Terms_Use.cfm

Table 1 Physical thickness of each layer for the first and last stacks

Stack No.	Targeted wavelength (μm)	No. of layers	Refractive index		Thickness of each layer (μm)	
			High	Low	High index	Low index
1	0.5	12	2.18	1.58	0.0595	0.0823
12	5.57	12	2.18	1.58	0.663	0.928

reflection at the interface between the coating outer surface and the hot gas. Additionally, in this configuration, phase stability is also crucial to the performance of the system since the single layer S_1 is directly exposed to the hot environment. The refractive index of the single layer S_2 material must be as low as possible, and the scattering coefficient should be high, so that the remaining radiation cannot reach the metal substrate directly.

Based on the multiple layered stack design and the configuration selection, mathematical models and associated software were developed to compute the heat flux entering the coating system and the resulting temperature distribution in the steady state condition. Boundary conditions and material properties used for the computation are summarized in Table 2. The effect of scattering on the single layer is considered by assigning two different values. Since the scattering coefficients for 7YSZ and Al_2O_3 at elevated temperatures were not available, two arbitrary values were used to represent extreme scenarios. The scattering effect on the multiple layer M was not considered in this study. Additionally, the effect of increasing the thickness of the single layer S_1 is investigated by changing the total coating thickness from 250 μm to 1000 μm while keeping the thickness of stack M constant. The computation method can be found in Ref. [21].

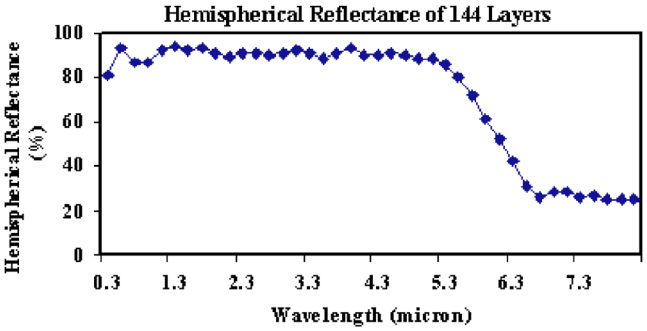


Fig. 8 Hemispherical reflectance of the multiple layered coatings with 12 stacks

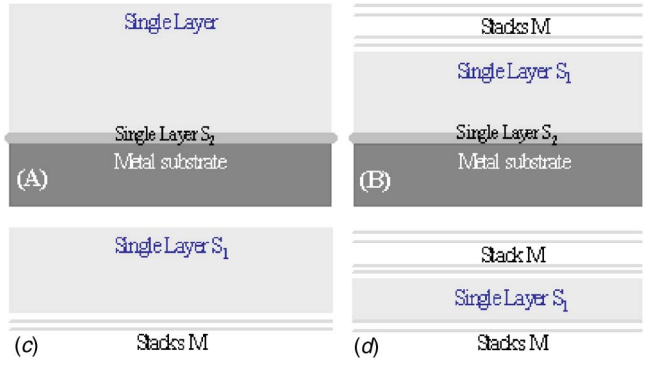


Fig. 9 Multiple layered coating configurations. (*a*) Configuration *A*: base line single layer, (*b*) Configuration *B*: *M* (top) + S_1 + S_2, (*c*) Configuration *C*: S_1 (top) + *M* + S_2, and (d) Configuration *D*: *M* (top) + S_1 + *M* + S_2.

The results obtained for temperatures at both the coating and metal surfaces, as well as the total heat and radiation fluxes, for Configurations *A*, *B*, *C*, and *D* are given in Table 3. The metal and coating surface temperatures for Configurations *A–D* under both low and high scattering conditions are schematically illustrated in Fig. 10. The effect of the total coating thickness on the metal surface temperature differences between Configurations *B* and *C* and Configuration *A* is shown in Fig. 11.

3 Simulation Results

3.1 Metal Surface Temperature Reductions. From Fig. 10, it can be seen that Configurations *B*, *C*, and *D* exhibit considerable temperature reductions in the metal surface when compared with that of Configuration *A* of the same thickness. It is also evident that Configuration *B*, with multiple layered stacks placed on the surface, can realize the most significant temperature reduction (45°C) in the metal substrate under a low scattering condition. In contrast, Configuration *D* with two multiple stacks only achieved a 41°C reduction in metal surface temperature. The radiation flux entering Configuration *D* is, however, lower than that for Configuration *B*. This is perhaps due to the increased overall thermal conductivity of Configuration *D* since more Al_2O_3 (with higher thermal conductivity than 7YSZ) is used in Configuration *D*, resulting in more thermal conduction. If alternate materials

Table 2 Numerical values and boundary conditions used in computational analyses

Parameters	Value	Reference
Hot gas temperature (K)	2000	[6]
Cool side temperature (K)	800	[6]
Convection coefficient ($W/m^2 K^1$)	3000	[20]
Thermal conductivity of metal substrate (W/m K)	33	[6]
Thermal conductivities of single layers S_1 and S_2 (W/m K)	0.8	7YSZ
Thermal conductivity of the layer (7YSZ) with a high refractive index (W/m K)	0.8	7YSZ
Thermal conductivity of the layer (Al_2O_3) with a low refractive index (W/m K)	2.4	Al_2O_3
Total thickness of ceramics (m)	0.00025 0.0005 0.001	By design
Total thickness of high-reflectance multiple layered stacks *M* (m)	0.0000449	By design
Thickness of the metal substrate (m)	0.001	By design
Thickness of the 7YSZ thin layer S_2 (m)	0.000005	By design
Refractive index of hot gas	1.0	[20]
Refractive index of 7YSZ	2.1	[8]
Refractive index of Al_2O_3	1.5	[8]
Scattering coefficient of single layer ceramics (m^{-1})	0 1000 10,000	By design
Absorption coefficient of a single layer ceramic material (m^{-1})	30	[20]
Emissivity of the bond coat	0.5	[20]
Emissivity of the substrate	0.7	[20]

Downloaded 02 Jun 2010 to 171.66.16.109. Redistribution subject to ASME license or copyright; see http://www.asme.org/terms/Terms_Use.cfm

Table 3 Calculated temperatures of the coating and metal surfaces and the total heat and radiation fluxes

		Configuration *A*	Configuration *B*		Configuration *C*		Configuration *D*	
$\sigma_{s\lambda}=1000\ m^{-1}$	Coating surface temperature (K)	1699.6	1665.3	34.3[a]	1669.1	30.5[a]	1655.1	44.5[a]
	Metal surface temperature (K)	1416.5	1371.8	44.7[a]	1379.4	37.1[a]	1375.4	41.1[a]
	Total heat flux (W/m^2)	1,227,190.6	1,091,288.6		1,114,268.3		1,102,389.1	
	Radiation flux (W/m^2)	321,461.3	81,113.1		116,936.4		61,247.2	
$\sigma_{s\lambda}=10{,}000\ m^{-1}$	Coating surface temperature (K)	1688.0	1661.7	26.3[a]	1669.9	18.1[a]	1652.4	35.6[a]
	Metal surface temperature (K)	1394.0	1365.0	29.0[a]	1380.4	13.6[a]	1370.5	23.5[a]
	Total heat flux (W/m^2)	1,158,713.2	1,070,935.9		1,117,473.3		1,087,609.2	
	Radiation flux (W/m^2)	217,850.5	49,874.6		121,283.5		38,278.5	

[a]Temperature differences between Configurations *B*, *C*, and *D*, and Configuration *A*.

with lower refractive indices and thermal conductivities could be found to replace Al_2O_3, Configuration *D* may become the most effective coating configuration.

Configuration *C* with multiple layered stacks *M* placed below the single layer has a lesser effect on the metal surface temperature reduction (37°C) when compared with Configurations *B* and *D*. The utilization of 7YSZ as the top layer S_1 results in reduced reflectance to the multiple layered stacks. Increasing the number of layers in each stack or selecting materials with larger differences in high and low refractive indices could also improve the hemispherical reflectance for Configuration *C* and hence reduce the metal surface temperature further.

Point defect scattering from pores, cracks, or interfaces in the coatings can be substantial. As such, the effect of scattering on heat transport in the four configurations was also investigated by using two scattering coefficient values of 1000 m^{-1} and 10,000 m^{-1}, respectively. As shown in Fig. 10(*a*), Configuration *A* benefits from the increase in scattering, with a 23°C temperature reduction being achieved due to the scattering effect. For Configurations *B* and *D*, where the coating surfaces are composed of multiple layered stacks, the increased scattering coefficient results in a slight reduction in the metal surface temperature (5–7°C). However, in Configuration *C* with a single layer (S_1) at the top surface, an increase in the metal surface temperature was found when the scattering coefficient is varied from 1000 m^{-1} to 10,000 m^{-1}, as shown in Fig. 10(*a*). Since the radiation reflected by the multiple layered stacks is scattered within the top single layer (S_1), some of the radiation may travel back to the multiple layered stacks when the scattering coefficient in the single layer is increased, thereby contributing to the increase in the metal surface temperature.

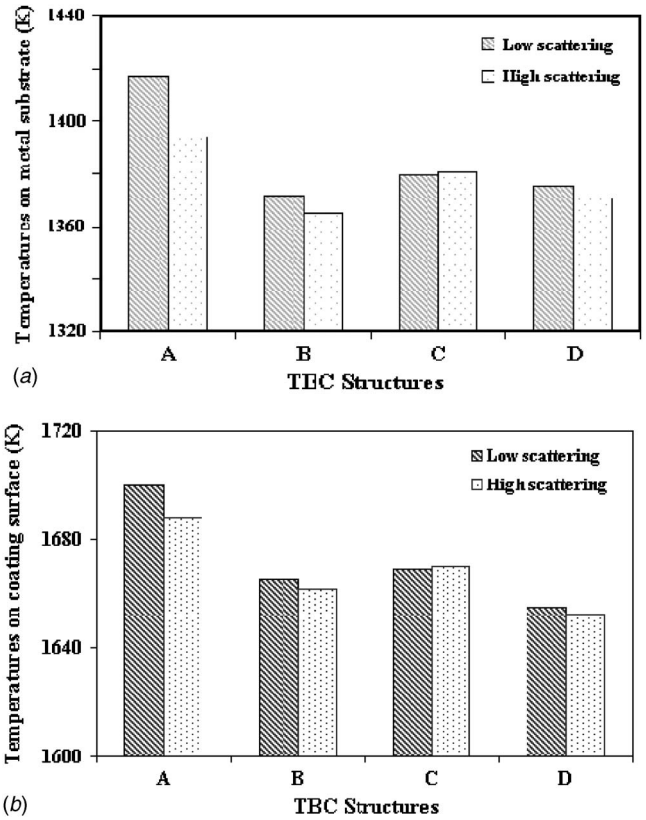


Fig. 10 (*a*) Temperatures on the metal surface, and (*b*) coating surface for Configurations *A*, *B*, *C*, and *D* under low and high scattering conditions

3.2 Coating Surface Temperature Reductions. Comparing the temperature reduction values summarized in Table 3 and Fig. 10(*b*), it can be seen that in addition to the temperature decrease in the metal surface, the temperatures on the coating surface can be significantly reduced as well with the use of the multiple layered coating structure. When multiple layered stacks are present, the radiation flux through the coating is effectively lowered, and as such the coating surface temperature is reduced. In contrast to the coating surface temperature in Configuration *A*, Configurations *B*, *C*, and *D* achieved coating surface temperature reductions of 34°C, 31°C, and 45°C, respectively, under the low scattering condition, and 26°C, 18°C, and 36°C, respectively, under the higher scattering condition. When the scattering coefficient is increased from 1000 m^{-1} to 10,000 m^{-1}, the absolute temperatures on all coating surfaces, with the exception of Structure *C*, were reduced.

3.3 Effect of Total Coating Thickness on Metal Surface Temperature Reduction. The effect of the total coating thickness on the potential temperature reduction realized by the application of multiple layered stacks is clearly seen in Fig. 11. The tempera-

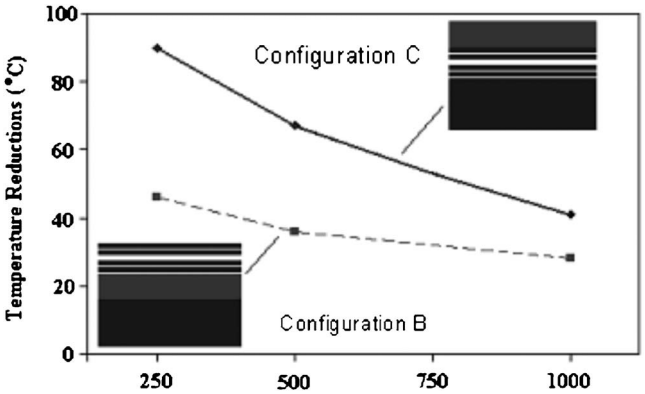


Fig. 11 Metal surface temperature reduction as a function of the total coating thickness

Downloaded 02 Jun 2010 to 171.66.16.109. Redistribution subject to ASME license or copyright; see http://www.asme.org/terms/Terms_Use.cfm

ture reductions in the metal surface for both Configurations *B* and *C* are less pronounced when the total coating thickness (or the thickness for a single layer) is further increased. This indicates that the multiple layered structure is more advantageous where thinner coatings are called for. It is also to be noted that the scattering effect in this analysis was not considered.

4 Conclusions and Future Studies

The EB-PVD process can provide more opportunities for the development of multiple layered TBC structures with varied densities, compositions, and defect distributions. Both the thermal conduction and the radiation transfer can be hindered in multiple layered TBC structures achieving increased thermal insulation to the metal substrate. In anticipation of further increases in gas turbine operating temperature, radiative heat transport needs to be addressed. A multiple layered coating structure with high reflectance to broadband wavelength thermal radiation can be designed and employed to prevent metal surface temperature increases resulting from thermal radiation.

Computational analyses were conducted to determine the metal and coating surface temperatures under various coating configurations. The influence of multiple layered stack placement, coating thickness, and scattering in the single layer was evaluated. It is found that Configuration *B*, with multiple layered stacks placed on the top layer, exhibited the most significant effect in reducing the radiative heat transport into the coating system. It is also apparent that the use of multiple layers throughout the entire coating structure may not provide the best thermal insulation if two or more materials are to be used since the thermal conduction may not be optimized. The presence of multiple layer boundaries in the described structure may further reduce the thermal conduction due to the increased phonon scattering at the layer boundaries. It is anticipated that the high-reflectance multiple layered coating system can potentially reduce both the photon and phonon transports through the TBC system.

References

[1] Clarke, D. R., and Levi, C. G., 2003, "Materials Design for the Next Generation Thermal Barrier Coatings," Annu. Rev. Mater. Res., **33**, pp. 383–417.

[2] Singh, J., and Wolfe, D. E., 2005, "Review: Nano and Macro-Structured Component Fabrication by Electron Beam-Physical Vapor Deposition (EB-PVD)," J. Mater. Sci., **40**, pp. 1–26.

[3] Singh, J., and Wolfe, D. E., 2000, "Electron Beam-Physical Vapor Deposition Technology: Present and Future Applications," Institute for Manufacturing and Sustainment Technologies (iMAST) Quarterly, Penn State University, State College, PA, Vol. 3, pp. 3–6.

[4] Hass, D. D., Slifka, A. J., and Wadley, H. N. G., 2001, "Low Thermal Conductivity Vapor Deposited Zirconia Microstructures," Acta Mater., **49**, pp. 973–983.

[5] Gu, S., Lu, T. J., Hass, D. D., and Wadley, H. N. G., 2001, "Thermal Conductivity of Zirconia Coatings With Zig-Zag Pore Microstructures," Acta Mater., **49**, pp. 2539–2547.

[6] Nicholls, J. R., and Lawson, K. J., 2002, "Methods to Reduce the Thermal Conductivity of EB-PVD TBCs," Surf. Coat. Technol., **151–152**, pp. 383–391.

[7] Wolfe, D. E., Singh, J., Miller, R. A., Eldridge, J. I., and Zhu, D., 2005, "Tailored Microstructure of EB-PVD 8YSZ Thermal Barrier Coatings With Low Thermal Conductivity and High Thermal Reflectivity for Turbine Applications," Surf. Coat. Technol., **19**, pp. 132–149.

[8] Eldridge, J. I., Spuckler, C. M., and Street, K. W., 2002, "Infrared Radiative Properties of Yttria-Stabilized Zirconia Thermal Barrier Coatings," *Proceedings of the 26th Annual Conference of Composites, Advanced Ceramics, Materials and Structures: B*, Cocoa Beach, FL, Jan. 13–18, American Ceramic Society, Westerville, OH, pp. 417–430.

[9] Wang, D., Huang, X., and Patnaik, P. C., 2006, "Design and Modeling of Multiple Layered TBC System With High Reflectance," J. Mater. Sci., **41**(19), pp. 6245–6255.

[10] Wahiduzzaman, S. and Morel, T., 1987, "Effect of Translucence of Engineering Ceramics on Heat Transfer in Diesel Engines," NASA, Report No. ORNL/Sub/86-22042/1.

[11] Zhu, D., Bansal, N. P., and Miller, R. A., 2004, "Thermal Conductivity and Stability of $HfO_2-Y_2O_2$ and $La_2Zr_2O_7$ Evaluated for 1650°C Thermal/Environmental Barrier Coating Applications," Ceram. Trans., **153**, pp. 331–343.

[12] Siegel, R., and Spuckler, C. M., 1998, "Analysis of Thermal Radiation Effects on Temperatures in Turbine Engine Thermal Barrier Coatings," Mater. Sci. Eng., A, **245**, pp. 150–159.

[13] Nicholls, J. R., and Lawson, K. J., 2001, "Low Thermal Conductivity EB-PVD Thermal Barrier Coatings," Mater. Sci. Forum, **369–372**, pp. 595–606.

[14] Allen, W. P., 2003,"Reflective Coatings to Reduce Radiation Heat Transfer," U.S. Patent No. US 0008170 A1.

[15] Wang, D., Huang, X., and Patnaik, P. C., 2004, "Design of a Multilayered Thermal Barrier Coating Structure for Optimized Thermal Properties," *Proceedings of the 43rd Annual Conference of Metallurgists of CIM*, Hamilton, Ontario, Canada, Aug. 22–25, pp. 93–107.

[16] Wang, D., 2006, Ph.D. thesis, Carleton University, ON, Canada.

[17] Macleod, H. A., 1986, *Thin-Film Optical Filters*, 2nd ed., Adam Hiller, New York, pp. 158–186.

[18] Ditchburn, R. W., 1963, *Light*, 2nd ed., Blackie, London, pp. 582–585.

[19] E. D. Palik, ed., 1985, *Handbook of Optical Constants of Solids*, Academic, New York.

[20] Siegel, R., and Howell, J. R., 2001, *Thermal Radiation Heat Transfer*, 4th ed., Taylor & Francis, London.

[21] Huang, X., Wang, D., and Patnaik, P., 2007, "Design and Computational Analysis of Highly Reflective Multiple Layered Thermal Barrier Coating Structure," Mater. Sci. Eng., A, **460–461**, pp. 101–110.

Downloaded 02 Jun 2010 to 171.66.16.109. Redistribution subject to ASME license or copyright; see http://www.asme.org/terms/Terms_Use.cfm

Radiation Benchmarking in a Model Combustor

Lei-Yong Jiang[1]
e-mail: leiyong.jiang@nrc-cnrc.gc.ca

Ian Campbell

Gas Turbine Laboratory,
Institute for Aerospace Research,
National Research Council of Canada,
1200 Montreal Road, M-10,
Ottawa, ON, K1A 0R6, Canada

Radiation heat transfer in a model combustor with interior and exterior conjugate heat transfers has been numerically studied. The previous investigations on turbulence, combustion, and scalar transfer modeling (Reynolds analogy), and comparisons with a comprehensive experimental database provide a reliable base to evaluate the effect of radiation heat transfer on the flow field and NO emission in the combustor. Some of the numerical results with and without radiation are presented and compared with the experimental measurements. It is found that the total radiation heat flux through the combustor wall is about 4.2% of the total energy released from the input fuel. The effect of radiation on the flow field is minor, particularly to the velocity field. In contrast, it has significant effects on the NO field, where the predicted values without radiation are two times higher than those with radiation or the experimental data. A considerable effect of radiation on the combustor wall temperature is also observed. In summary, to provide valuable predictions of NO emission and combustor liner temperature, the radiation heat transfer should be properly taken into account in numerical simulations.
[DOI: 10.1115/1.2966417]

Keywords: radiation heat transfer, discrete ordinate model, combustor simulation, NO_x emission

1 Introduction

To improve accuracy of numerical simulations and to evaluate/develop various physical models, benchmarking on a diffusion flame model combustor has been carried out at the National Research Council of Canada. Many turbulence, combustion, and NO_x models have been studied [1–3] against a comprehensive database obtained from a series of experimental measurements [4]. Advantages and limitations of these physical models have been revealed [1–3]. In addition, the current approach for modeling scalar transfers in turbulent reacting flows, Reynolds analogy, is also assessed [5]. These findings may provide some useful information or guidelines to combustor simulations.

The above studies have shown that the velocity, temperature, and species fields in the combustor as well as the wall temperature profile can be well or reasonably well predicted with proper physical models. As a result, the radiation heat transfer issue in the combustor can be examined with an added degree of confidence.

Various aspects related to radiation modeling in combustion systems have been excellently reviewed by Viskanta and Menguc [6] and the research needs have been identified. Although extensive studies on radiation heat transfer have been carried out in other combustion systems [6], investigations in gas turbine combustors are few. A numerical heat transfer analysis of a single can gas turbine combustor (GE10) was performed by Andreini et al. [7], where a discrete ordinate (DO) radiation model and a simple gray gas property formulation for water vapor and carbon dioxide were employed. The predicted liner cap temperature was in good agreement with the experimental values obtained from three embedded thermocouples. Kutsenko and Onegin described their computational fluid dynamics (CFD)-based analysis capabilities for evaluating low NO_x combustion techniques [8], and a typical gas turbine combustor was chosen as a test model. In their studies, a discrete ordinate radiation model was also employed while the absorption coefficient of gas mixture was obtained from an exponential wide-band model. It was found that the effect of radiation heat transfer on NO emission level was significant. For a natural gas fired case, NO was overpredicted by 75% in comparison with an experimental value if the radiation heat transfer was not taken into account.

In the above examples, no validations were made regarding the velocity and temperature fields inside the combustor as well as the combustor liner temperature distribution due to difficulties in carrying out measurements inside practical gas turbine combustors. It is well known that the radiation heat transfer is directly related to the temperature distribution inside the combustor and along the liner wall. Due to a lack of the flow field information, it is hard to pinpoint actual problems or make reliable conclusions on radiation heat transfer issues.

The objective of the present work is to quantitatively determine the effect of radiation heat transfer on the temperature, velocity, and NO_x fields in the model combustor. Since the model geometry is much simpler than practical combustors and more importantly a comprehensive experimental database is available, the outcome of this work could provide valuable information for radiation modeling in combustors.

2 Numerical Simulations

Axisymmetric, steady, turbulent, reacting flows were considered in the present study, and a commercial software package, FLUENT, was used for all numerical simulations. The computation domain, governing equations, selected physical models, boundary conditions, and solution methods are described in Secs. 2.1–2.6.

2.1 Computational Domain. A schematic diagram of the model combustor is shown in Fig. 1, including the fuel and air inlets, disk flame-holder, combustion chamber, and contracted exhaust section (all dimensions are in millimeters). Air entered the combustion chamber around a bluff body, while fuel was fed through the center of the disk flame-holder. The computational domain in the present study covered the entire combustor flow field from the fuel and air inlets to the exhaust exit, as shown in Fig. 2. The interior and exterior conjugate heat transfers from the combustion mixture to the flame-holder body and steel/insulation

[1]Corresponding author.

Contributed by the International Gas Turbine Institute of ASME for publication in the JOURNAL OF ENGINEERING FOR GAS TURBINES AND POWER. Manuscript received March 28, 2008; final manuscript received March 31, 2008; published online October 6, 2008. Review conducted by Dilip R. Ballal. Paper presented at the 2008 ASME Turbo Expo 2008: Land, Sea and Air (GT2008), Berlin, Germany, June 9–13, 2008.

Copyright © 2009 by ASME

Downloaded 02 Jun 2010 to 171.66.16.109. Redistribution subject to ASME license or copyright; see http://www.asme.org/terms/Terms_Use.cfm

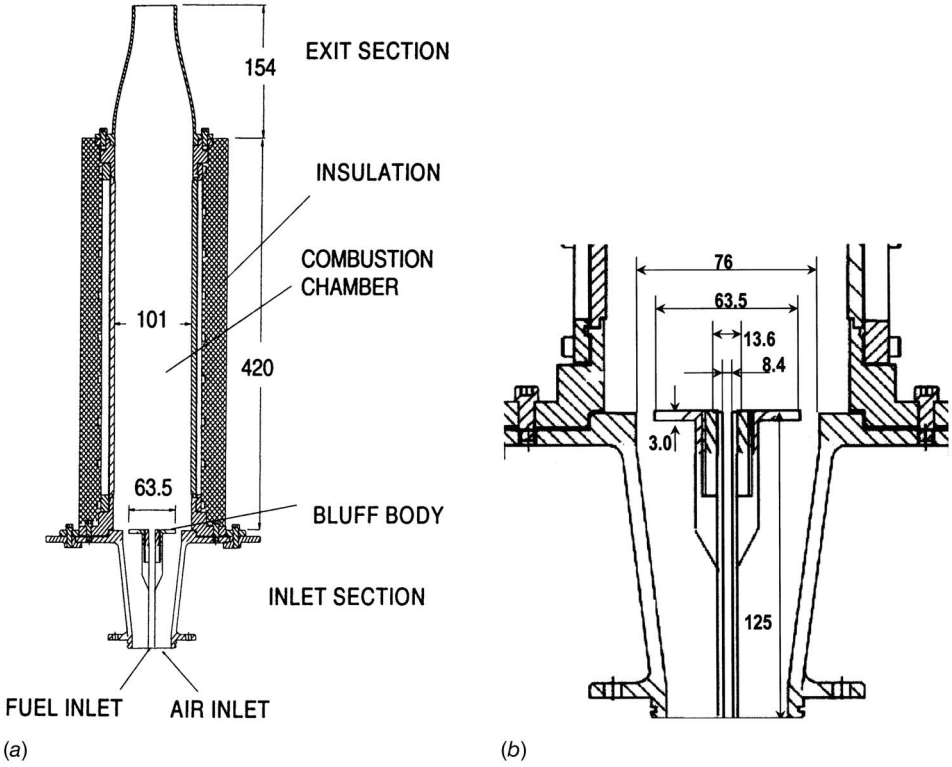


Fig. 1 The model combustor

walls were also modeled.

Since the flow field was axisymmetric, 2D quadrilateral meshes were generated over the flow region and interior and exterior conjugate heat transfer regions. Fine grids were laid behind the flameholder in the combustion chamber in order to resolve the recirculation region. Fine grids were also generated in the shear layers between the recirculation region and fuel and air jets as well as in the gap between the flame-holder edge and the air inlet chamber wall. Coarse grids were used in the solid stainless steel and ceramic regions. A total number of 74,100 elements were used for most of the simulations. The skewness was less than 0.2 in the flow field domain and the aspect ratio was less than 12 for 99.5% elements. Efforts were made to keep the wall parameter, y^+ $(\sqrt{\tau_w/\rho}y/\upsilon)$, in the desired range of 30–60. A number of meshes were tested to ensure the mesh independence of the numerical solutions.

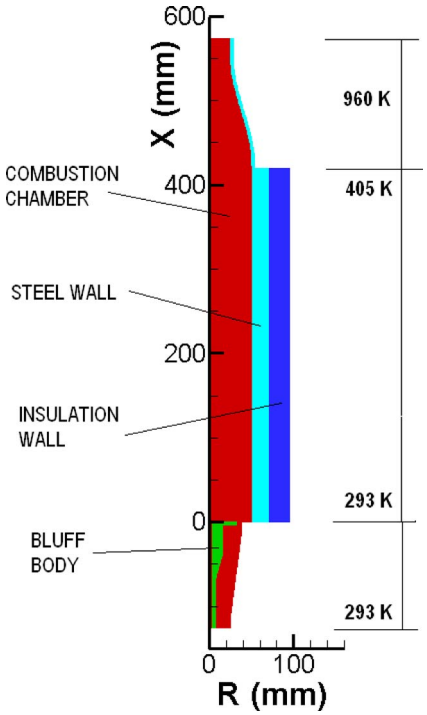


Fig. 2 Computational domain and exterior wall temperature

2.2 Governing Equations and Closure. The Favre-averaged conservation equations for mass, momentum, and total enthalpy can be expressed in a coordinate-free form as [9,10]

$$\nabla \cdot (\bar{\rho}\tilde{\mathbf{V}}) = 0 \tag{1}$$

$$\nabla \cdot (\bar{\rho}\tilde{\mathbf{V}}\tilde{\mathbf{V}}) = -\nabla \bar{p} + \nabla \cdot \mathbf{T} - \nabla \cdot (\overline{\rho \mathbf{v}''\mathbf{v}''}) \tag{2}$$

$$\nabla \cdot (\bar{\rho}\tilde{\mathbf{V}}\tilde{Y}_i) = \nabla \cdot (\rho D_i \nabla \tilde{Y}_i) - \nabla \cdot (\overline{\rho \mathbf{v}''Y_i''}) + \omega_i \tag{3}$$

$$\nabla \cdot (\bar{\rho}\tilde{\mathbf{V}}\tilde{h}) = \nabla \cdot \left(\frac{\mu}{Pr_l}\nabla \tilde{h}\right) - \nabla \cdot (\overline{\rho \mathbf{v}''h''}) + S_h \tag{4}$$

In the above equations, $\bar{\rho}$ is the mean density, $\tilde{\mathbf{V}}$ is the mean velocity vector, $\mathbf{v}''$ stands for fluctuation velocity vector, $\mathbf{T} = \mu[\nabla\tilde{\mathbf{V}} + (\nabla\tilde{\mathbf{V}})^T] - (2/3)\mu\nabla \cdot \tilde{\mathbf{V}}\mathbf{I}$ represents viscous stress tensor with I a unit tensor, $\tilde{Y}_i$ is the mass fraction of the ith species, h denotes total enthalpy, $\rho\mathbf{v}''\mathbf{v}''$ represents Reynolds stresses (or turbulence momentum transfer), $\rho\mathbf{v}''Y''$ and $\rho\mathbf{v}''h''$ are turbulence scalar transfer terms, and D and Pr_l are laminar diffusivity and Prandtl number, respectively.

For closure of the above equations, the turbulence transfer terms and sources have to be properly treated. A benchmarking on turbulence modeling [1] indicates that the Reynolds stress model

Downloaded 02 Jun 2010 to 171.66.16.109. Redistribution subject to ASME license or copyright; see http://www.asme.org/terms/Terms_Use.cfm

(RSM) is superior over three popular two-equation eddy-viscosity models and is able to excellently predict the flow patterns and two recirculation zone lengths in the combustor. It also provides fairly good predictions for all Reynolds stress components and turbulence kinetic energy. Therefore, this model is chosen to model the turbulence momentum transfer term, $\rho\overline{\mathbf{v}''\mathbf{v}''}$, in Eq. (2) in the present work.

Based on the investigation of the Reynolds analogy concept [5], an optimal turbulent Prandtl/Schmidt number, $\mathrm{Pr}_t = \mathrm{Sc}_t = 0.5$, is used to model the turbulence scalar transfer terms, $\rho\overline{\mathbf{v}''Y''}$ and $\rho\overline{\mathbf{v}''h''}$, in Eqs. (3) and (4). As a result, both the velocity and temperature fields in the combustor as well as the combustor wall temperature profile can be reasonably and quantitatively predicted [5].

The species source term, ω_i, in Eq. (3) is obtained from the eddy dissipation combustion model (EDM). A benchmarking study [2] has indicated that the mean temperature field can be fairly well captured by this model. The energy source term, S_H, in Eq. (4) includes viscous heating and radiation heat transfer. The approach used to model radiation heat transfer is given in Sec. 2.3.

2.3 Radiation Modeling. A discrete ordinate radiation model [11] is selected to resolve radiation heat transfer in the combustor. This model has been widely used [6–8,10] since it spans the entire range of optical thicknesses and allows users to solve problems from surface-to-surface radiation to participating radiation in combustion problems, including semitransparent walls.

The radiative heat transfer equation used in the present study for an absorbing and emitting medium at position $\boldsymbol{r}$ in the direction $\boldsymbol{s}$ can be expressed as

$$\frac{dI(\boldsymbol{r},\boldsymbol{s})}{ds} + aI(\boldsymbol{r},\boldsymbol{s}) = a\frac{\sigma T^4}{\pi} \tag{5}$$

where $\boldsymbol{r}$ is the position vector, $\boldsymbol{s}$ stands for direction vector, s is the path length, a denotes absorption coefficient, σ represents Stefan–Boltzmann constant (5.672×10^{-8} W/m^2 K^4), I and T are radiation intensity and local temperature respectively. The first term on the left of Eq. (5) is outgoing radiation, and the second term is absorption loss to medium gas mixture. The right of Eq. (5) represents gas mixture emission. It should be mentioned that since a gaseous fuel (propane) is used in the present study, the scattering from gas mixture is neglected. The above radiation transfer equation is solved along a finite number of discrete solid angles, each associated with a vector direction fixed in the global Cartesian system [11].

The three dimensional nature of radiation heat transfer in this axisymmetrical combustor is modeled although a 2D mesh is used in the flow calculation. Most of the simulations are performed with 32 radiation directions. A sensitive simulation with 128 radiation directions was performed, and the difference in averaged radiation incident heat flux on the combustor chamber interior wall is only 0.4%.

A weighted-sum-of-gray-gases model from Ref. [12] is used to evaluate the total emissivity of the gas mixture from water vapor and carbon dioxide, that is,

$$\varepsilon = \sum_{i=0}^{I} a_{\varepsilon,i}(T)(1 - e^{-k_i ps}) \tag{6}$$

where $a_{\varepsilon,i}$ is the emissivity weighting factor for the ith gray gas, the quantity in parentheses stands for the ith gray gas emissivity, k_i is the absorption coefficient of the ith gray gas, p is the sum of the partial pressures of water vapor and carbon dioxide, and s represents the path length. The values of $a_{\varepsilon,i}$ and k_i depend on gas composition, and $a_{\varepsilon,i}$ are also functions of temperature. These values are estimated by fitting Eq. (6) to an exponential wide-band model, obtained experimentally, and valid in the ranges of $0.001\ \text{atm m} \le \text{ps} \le 10\ \text{atm m}$ and $600\ \text{K} \le T \le 2400\ \text{K}$ [12].

The combustor interior steel walls are opaque. A portion of the incident radiation flux is absorbed by them and the rest is reflected. A complete diffuse reflection is assumed in the present study. As pointed out by Incropera and De Witt [13], this approach is reasonable for most engineering applications.

Since it is difficult to accurately determine the emissivity of the combustor walls, three levels of emissivity are considered in the present work. That is, lightly oxidized, stably oxidized, and blackbody cases, and their emissivity values are calculated by the following expressions, respectively:

$$\varepsilon = -2.03257E-10T^3 + 6.72346E-07T^2 - 4.11082E-04T + 0.3376 \quad (\varepsilon = 0.27-0.46) \tag{7}$$

$$\varepsilon = -3.8794E-07T^2 + 8.0332E-04T + 0.48882 \quad (\varepsilon = 0.70-0.90) \tag{8}$$

$$\varepsilon = 1.0 \tag{9}$$

The temperature dependent polynomials in Eqs. (7) and (8) are obtained or extrapolated from Ref. [13].

2.4 Other Physical Models. Based on the previous study [3], a post-processing approach is employed for NO_x modeling. In all simulations, the thermal and prompt NO are computed, and the partial-equilibrium O and OH as well as turbulence effect are considered. The prompt NO, the NO re-burn mechanism and the third reaction of the extended Zeldovich mechanism are not considered in the study, since they have negligible effects on the overall NO formulation [3].

For conjugate or coupled heat transfer calculation, both fluid and solid regions are solved together. In solid regions, since only heat conduction is involved the energy transport equation becomes much simpler than Eq. (4) used for fluid regions, that is,

$$\nabla \cdot (k \nabla T) = 0 \tag{10}$$

where k is the thermal conductivity of solid material. The flow parameters, such as temperature and heat flux, at the interfacing surfaces between the solid and fluid are determined by the governing equations ((1)–(4) and (10)).

At internal wall boundaries, an enhanced wall boundary treatment is applied. In this approach, a two-layer model is combined with wall functions, and the viscous and fully turbulent regions are smoothly blended [10].

2.5 Boundary Conditions. The fuel (propane) mass flow rate is 16.2 g/s, the airflow rate is 550 g/s, and the corresponding overall equivalence ratio is 0.46. The Reynolds number based on the air entry velocity and flame-holder diameter is 1.9×10^5. An estimated turbulence intensity of 10% and hydraulic diameters are used to estimate Reynolds stress components and turbulence dissipation rate at the fuel and air inlets. A sensitivity study was performed with the inlet turbulence intensities of 5% and 2%, respectively. The difference in computed turbulence kinetic energy along the combustor centerline is observable only in the fuel inlet passage and a small region near $x=80$ mm, and the maximum deviation between the 2% case and the 10% case is only 2.3%. The difference is even smaller for the mean axial velocity and temperature along the combustor centerline. For both air and fuel flows, the inlet temperature is 293 K.

The exterior wall temperatures are defined based on the experimental measurements, as shown in Fig. 2. A room temperature of 293 K is assigned to the walls of the inlet section and the upstream edges of the combustion chamber and ceramic insulation walls. A linear temperature profile from 294 K to 405 K is specified along the outer boundary of the ceramic insulation wall. The temperature of the exterior boundary of the exit section is set to 960 K, as an estimation of the experimental observation. A sensitive study with a value of 823 K was performed; the difference in averaged temperature is only 0.023% at section $x=360$ mm where the last experimental data point is available. Based on the

Downloaded 02 Jun 2010 to 171.66.16.109. Redistribution subject to ASME license or copyright; see http://www.asme.org/terms/Terms_Use.cfm

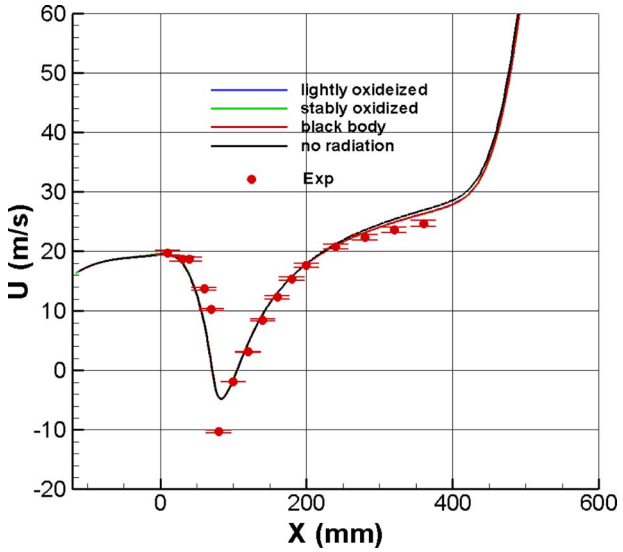


Fig. 3 Axial velocity profiles along the combustor centerline

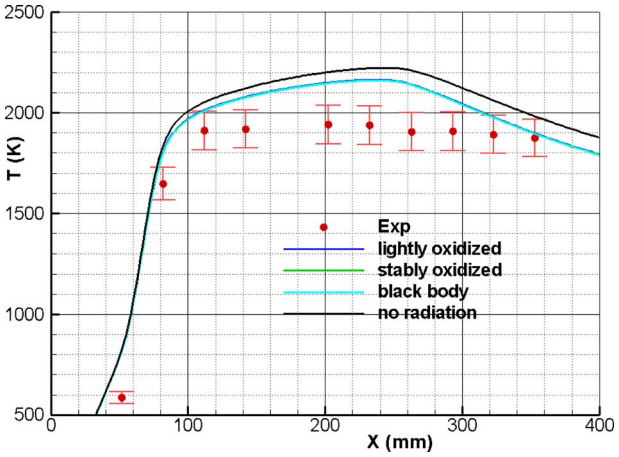


Fig. 4 Temperature profiles along the combustor centerline

thermal resistance and preliminary results, a linear temperature profile from 960 K to 780 K is assigned to the downstream edge of the combustion chamber wall, while another linear profile from 780 K to 405 K is defined at the downstream edge of the insulation wall. Finally, the pressure at the combustor exit is set to the atmospheric value.

Polynomials used to calculate the specific heat of species as a function of temperature are determined from Ref. [14], where the chemical dissociation is considered. For other thermal properties of the mixture such as molecular viscosity and thermal conductivity, the values for air at 900 K are used. The thermal conductivity is 25 W/m K for the stainless steel and 0.1 W/m K for the ceramic insulation.

2.6 Solution Methods. A segregated solver with a second-order accurate scheme was used to resolve the flow field. A node-based method for derivatives was chosen in order to maintain numerical accuracy and stability. At convergence, the normalized residuals of flow variables were less than 10^{-5} in all test cases. The monitored axial velocities at two points in the shear layer downstream of the flame-holder remained unchanged at least for the first four digits. A four-node LINUX cluster, 64 bit, 2.6 GHz, dual CPU, and 8 Gbyte RAM for each node, was used to perform all simulations. It took about 45 min to reach converged results for the DO model with 32 radiation directions.

3 Results and Discussion

Numerical simulations were carried out with three levels of emissivity of the combustor interior walls. For comparison, a simulation without radiation was also performed. Some results are presented and discussed below and the effects of radiation on the axial velocity, temperature, and NO emission fields are illustrated.

3.1 Radiation Effect on Flow Fields. Shown in Fig. 3 are the axial velocity profiles along the combustor centerline for the lightly oxidized, stably oxidized, blackbody, and no-radiation cases. The results are compared with the experimental data with an estimated measurement error of 2%. The results for the three levels of emissivity are almost identical and in good agreement with the experimental data, except that the peak value of negative velocities is underpredicted. The difference between with and without radiation cases is minor and only observable in the downstream region (250–450 mm). This observation is understandable since the total radiation heat flux through the combustor interior walls is only 4.2% of the total energy released by the input fuel.

The effect of radiation heat transfer on the temperature profiles along the combustor centerline is illustrated in Fig. 4. Error bars represent the measurement error of about 5%. Similar to Fig. 3, the numerical results for three levels of emissivity overlap each other. With radiation, the temperature profile along the combustor centerline is reasonably well predicted although the numerical profiles show a peak in the middle portion and the maximum deviation is about 200 K. The anticipated main reason is that the temperature was measured by a 0.25 mm diameter thermocouple [4]. Owing to the radiation and conduction losses from the thermocouple, the measurement error could exceed 100 K over regions where the gas temperature was high and the flow velocity was low [15].

For the case without radiation, the temperature profile is overpredicted, and the maximum difference with and without radiation is about 50 K or 2.5%. In short, the effect of radiation heat transfer on the temperature field is minor.

3.2 Radiation Effect on Combustor Wall Temperature. Figure 5 illustrates the radiation effect on the interior wall temperature of the combustion chamber. Overlapped in the figure are the experimental data with a measurement error of 5%. It is clear that without radiation, the chamber wall temperature is signifi-

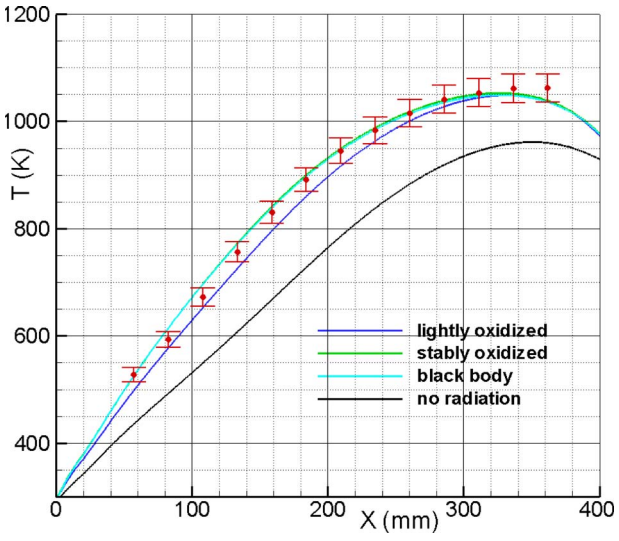


Fig. 5 Temperature profiles along the combustor wall

Downloaded 02 Jun 2010 to 171.66.16.109. Redistribution subject to ASME license or copyright; see http://www.asme.org/terms/Terms_Use.cfm

Table 1 Emissivity level and radiation heat flux

Emissivity level	Lightly oxidized	Stably oxidized	Blackbody
Radiation flux (w/m^2)	87,742	61,641	58,017

cantly underpredicted. The maximum difference reaches 300 K. This suggests that for accurate prediction of combustor liner temperature, the radiation heat transfer should be properly modeled.

With radiation, the results for the lightly oxidized case are almost identical with those from the stably oxidized case. Difference between these two cases and the blackbody case is observable. The maximum deviation is ~50 K or ~5% of the average temperature within the range of measurement errors. These results indicate that the effect of emissivity level on the wall temperature is limited. The anticipated reason may be that as the wall emissivity decreases, the reflected portion of incident radiation will increase (or the absorption portion will decrease), and then the incident radiation will increase. As a result, the final radiation absorption at the wall will not change significantly. Table 1 confirms this expectation, where the area-averaged surface incident radiation fluxes at the combustion chamber interior wall are given for three levels of emissivity considered in the present study.

4 Radiation Effect on NO Emission

The NO contours for the stably oxidized case are shown in Fig. 6 and compared with the experimental measurements. Considering the difficulties in NO modeling [3], the numerical results are really promising in comparison with the experimental data. The predicted maximum NO is 56.5 ppm, very close to the experimental value of 54.3 ppm. The contour plots for the other two emissivity levels are similar to those in Fig. 6 although they are not shown here. The maximum value is 58.9 ppm for the case of the lightly oxidized wall and 56.0 ppm for the blackbody case. In Fig. 6, the predicted NO region is shifted downstream in comparison with the experimental results although the high temperature region is properly predicted (Ref. [5], Fig. 10). The delay of NO formation prediction suggests that the NO formation mechanisms should be further studied in order to improve accuracy.

Figure 7 compares the numerical results without radiation with the experimental measurements. It is obvious that the effect of radiation on the NO prediction is significant. The predicted maximum NO reaches 124 ppm, twice higher than that with radiation

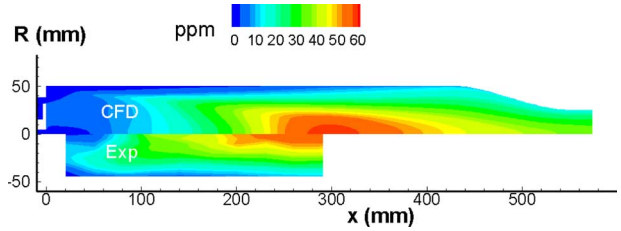


Fig. 6 Comparison between the predicted and measured NO contours with radiation

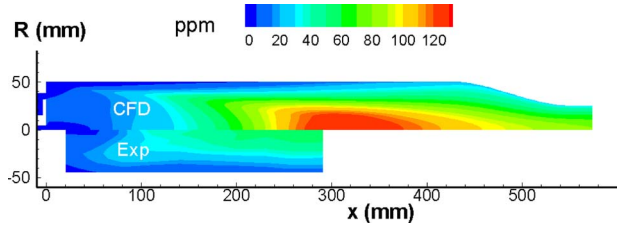


Fig. 7 Comparison between the predicted and measured NO contours without radiation

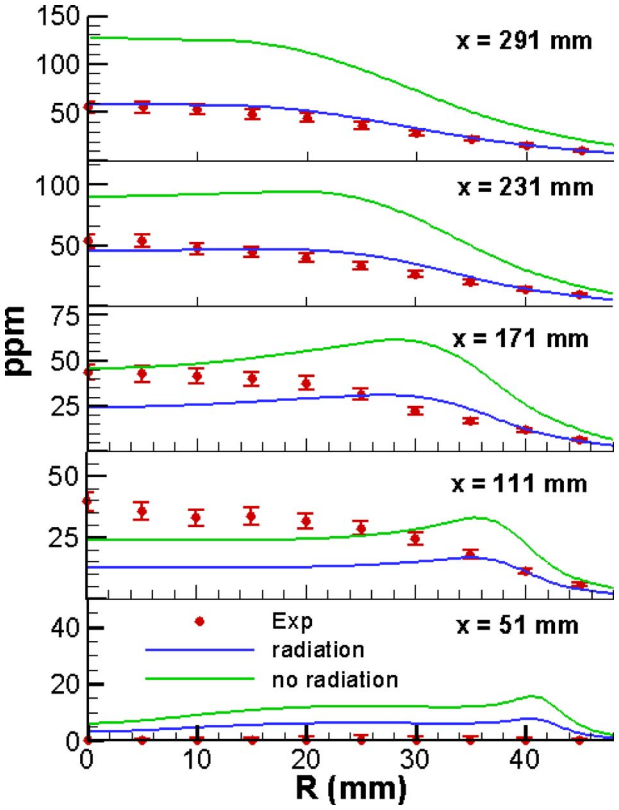


Fig. 8 NO profiles at cross sections, x=51–291 mm

or the experimental value. This is consistent with the observation by Kutsenko and Onegin [8], where 75% overprediction of the overall NO emission is reported.

The NO profiles at five cross sections, x=51 mm to 291 mm, with and without radiation are shown in Fig. 8 and compared with the experimental data. The estimated measurement error is 10%. For the case with radiation, the trends and magnitudes agree well with the measurements at downstream sections. At upstream sections, large deviations are obvious due to the downstream shift of the NO region, as shown in Fig. 6. For the case without radiation, the predicted values are twice higher than measurements or those with radiation at two downstream sections as well as in the local region of the middle section. The above results clearly illustrate that although the radiation energy is only about 4.2% of the energy released by fuel and has limited effect on the flow field its effect on NO emission is significant. This indicates that for NO emission prediction in reacting flows, the radiation heat transfer should be properly modeled.

5 Conclusions

The effects of radiation heat transfer on the flow field, wall temperature, and NO emission of a propane diffusion flame combustor with the interior and exterior conjugate heat transfers have been numerically studied. The previous investigations on turbulence, combustion, and scalar transfer modeling (Reynolds analogy) make the present study more reliable since the radiation heat transfer is directly related to the temperature field inside the combustor and at the combustor wall.

For the present configuration and operating condition, it is found that the total radiation heat flux through the combustor wall is 4.2% of the total energy released by the input fuel. The effect of radiation on the velocity and temperature fields is minor, particularly on the velocity field.

In contrast, it has significant effects on the NO prediction, and the predicted value is two times larger than those with radiation

Downloaded 02 Jun 2010 to 171.66.16.109. Redistribution subject to ASME license or copyright; see http://www.asme.org/terms/Terms_Use.cfm

and the experimental measurements. A considerable effect on the combustor wall temperature prediction is also observed.

In addition, the effect of wall material property, emissivity, velocity, and temperature fields in the combustor is negligibly small, while it shows slight effect on the combustor wall temperature prediction.

Acknowledgment

The authors are grateful to Dr. Bill Wallace for his valuable comments and suggestions during the preparation of this paper.

Nomenclature

a = absorption coefficient
D = molecular diffusivity
h = total enthalpy
I = radiation intensity
p = partial pressure
Pr_t = turbulence Prandtl number
r = radial coordinate
$\boldsymbol{r}$ = position vector
S = energy source term
$\boldsymbol{s}$ = direction vector
Sc_t = turbulence Schmidt number
T = temperature
U = mean axial velocity
$\mathbf{V}$ = velocity vector
$\mathbf{v}1$ = fluctuating velocity vector
x = coordinate along the combustor axis of symmetry
Y = species mass fraction
y^+ = nondimensional parameter, $\sqrt{\tau_w/\rho}\, y / \nu$
y = distance to the wall boundary
ε = emissivity
ω = species source term
ρ = density
σ = Stefan–Boltzmann constant
μ = laminar viscosity

References

[1] Jiang, L. Y., and Campbell, I., 2007, "Turbulence Modeling in a Model Combustor," Can. Aeronautics Space J., **53**(2), pp. 47–57.
[2] Jiang, L. Y., and Campbell, I., 2007, "Combustion Modeling in a Model Combustor," J. Aerosp. Power, **22**(5), pp. 694–703.
[3] Jiang, L. Y., and Campbell, I., 2005, "A Critical Evaluation of NO_x Modeling in a Model Combustor," ASME J. Eng. Gas Turbines Power, **127**(3), pp. 483–491.
[4] Campbell, I., and Logan, D. L., 1997, *An Experimental Study of a Combusting Flow Past a Confined Bluff Body*, Combustion Institute-Canadian Section, Halifax, Canada.
[5] Jiang, L. Y., and Campbell, I., 2008, "Reynolds Analogy in Combustor Modeling," Int. J. Heat Mass Transfer, **51**(5-6), pp. 1251–1263.
[6] Viskanta, R., and Menguc, M. P., 1987, "Radiation Heat Transfer in Combustion Systems," Prog. Energy Combust. Sci., **13**, pp. 97–160.
[7] Andreini, A., Bacci, A., Carcasci, C., Facchini, B., Asti, A., Ceccherini, G., Del Puglia, E., and Modi, R., 2005, "Numerical Heat Transfer Analysis of an Innovative Gas Turbine Combustor: Coupled Study of Radiation and Cooling in the Upper Part of the Liner," ASME Paper No. GT-2005-68365.
[8] Kutsenko, Yu. G., and Onegin, S. F., 2006, "Development and Application of CFD-Based Analysis Methodology to Evaluate Efficiency of Low NO_x Combustion Technologies," *ASME Turbo Expo*, Paper No. GT-2006-90530.
[9] Ferziger, J. H., and Peric, M., 2002, *Computational Methods for Fluid Dynamics*, Springer-Verlag, New York, pp. 1–10.
[10] Fluent Inc., 2006, "Fluent 6.2 Documentation," 10 Cavendish Court, Lebanon, NH 03766.
[11] Raithby, G. D., and Chui, E. H., 1990, "A Finite-Volume Method for Predicting a Radiant Heat Transfer in Enclosures With Participating Media," ASME J. Heat Transfer, **112**, pp. 415–423.
[12] Smith, T. F., Shen, Z. F., and Friedman, J. N., 1982, "Evaluation of Coefficients for the Weighted Sum of Gray Gases Model," ASME J. Heat Transfer, **104**, pp. 602–608.
[13] Incropera, F. P., and De Witt, D. P., 2002, *Fundamentals of Heat and Mass Transfer*, 5th ed., Wiley, New York, pp. 732 and 929.
[14] Rose, J. W., and Cooper, J. R., 1997, *Technical Data on Fuel*, Wiley, New York.
[15] Sislian, J. P., Jiang, L. Y., and Cusworth, R. A., 1988, "Laser Doppler Velocimetry Investigation of the Turbulence Structure of Axisymmetric Diffusion Flames," Prog. Energy Combust. Sci., **14**(2), pp. 99–146.

Downloaded 02 Jun 2010 to 171.66.16.109. Redistribution subject to ASME license or copyright; see http://www.asme.org/terms/Terms_Use.cfm

Comparison of Unsteady Reynolds Averaged Navier–Stokes and Large Eddy Simulation Computational Fluid Dynamics Methodologies for Air Swirl Fuel Injectors

David Dunham

Adrian Spencer
e-mail: a.spencer@lboro.ac.uk

James J. McGuirk

Mehriar Dianat

Department of Aeronautical and Automotive Engineering,
Loughborough University,
Loughborough LE11 3TU, UK

It is well documented that various large-scale quasiperiodic flow structures, such as a precessing vortex core (PVC) and multiple vortex helical instabilities, are present in the swirling flows typical of air swirl fuel injectors. Prediction of these phenomena requires time-resolved computational methods. The focus of the present work was to compare the performance and cost implications of two computational fluid dynamics (CFD) methodologies—unsteady Reynolds averaged Navier–Stokes (URANS) using a k-ε model and large eddy simulation (LES) for such flows. The test case was a single stream radial swirler geometry, which has been the subject of extensive experimental investigation. Both approaches captured the gross (time-mean) features of strongly swirling confined flows in reasonable agreement with experiment. The temporal dynamics of the quadruple vortex pattern emanating from within the swirler and observed experimentally were successfully predicted by LES, but not by URANS. Spectral analysis of two flow configurations (with and without a central jet) revealed various coherent frequencies embedded within the broadband turbulent frequency range. LES reproduced these characteristics, in excellent agreement with experimental data, whereas URANS predicted the presence of coherent motions but at incorrect amplitudes and frequencies. For the no-jet case, LES-predicted spectral data indicated the occurrence of a PVC, which was also observed experimentally for this flow condition; the URANS solution failed to reproduce this measured trend. On the evidence of this study, although k-ε based URANS offers considerable computational savings, its inability to capture the temporal characteristics of the flows studied here sufficiently accurately suggests that only LES-based CFD, which captures the stochastic nature of the turbulence much more faithfully, is to be recommended for fuel injector flows. [DOI: 10.1115/1.2969096]

1 Introduction

Swirling flowfields have been utilized for many decades as part of fuel injector design in gas turbine combustion systems. Their primary purpose is to promote a flame-stabilizing recirculation zone that also encourages rapid mixing between incoming fuel and air and hot burned gases. Comprehensive reviews of swirl flows relevant to combustor applications have been given by Leibovich [1], Gupta et al. [2], and most recently by Lucca-Negro and O'Doherty [3]. These reviews also cover the important phenomenon of vortex breakdown, which was the first instability observed in high swirl flows, Benjamin [4], and its relevance to combustor fuel injectors has been discussed recently by Spencer et al. [5].

Several previous experimental and computational investigations have studied the problem of the highly time-dependent flowfields, dominated by unsteady coherent motions, downstream of air swirl fuel injectors. A comprehensive set of time-resolved measurements for both velocity and scalar mixing under isothermal conditions was performed by Midgley [6] (see also Refs. 7 and 8). These data indicated a clear connection between unsteady vortex patterns (precessing vortex core (PVC) and helical instabilities) and the rate of fuel air mixing. The presence of unsteady helical vortex structures emanating from the swirler passage was shown to lead to "bursts" of increased fuel air mixing as the vortex structures propagated downstream. It is clearly of paramount importance that the presence of such features is considered during the fuel injector design stage in order to avoid the associated excitation of periodic frequencies in combusting flow, which could lead to increased noise levels and component fatigue.

Prediction of these phenomena requires time-resolved computational methods. Given current and near future computing power, direct numerical simulation (DNS) of practical engineering flows is still not realistic since the computational cost required to resolve all turbulent scales increases rapidly with Reynolds number Re (approximately as $Re^{9/4}$). The large eddy simulation (LES) computational fluid dynamics (CFD) methodology is well suited to the calculation of turbulent swirling flowfields as the stochastic nature of the flow is preserved and explicit computation of unsteady coherent structures is also clearly possible. The main drawback with LES is that very small time steps are required for solution stability and the computational costs are hence considerable. This is because the time scales associated with large-scale energy-containing flow features are many orders of magnitude larger than

Contributed by the International Gas Turbine Institute of ASME for publication in the JOURNAL OF ENGINEERING FOR GAS TURBINES AND POWER. Manuscript received April 11, 2008; final manuscript received April 11, 2008; published online November 20, 2008. Review conducted by Dilip R. Ballal. Paper presented at the ASME Turbo Expo 2008: Land, Sea and Air (GT2008), Berlin, Germany, June 9–13, 2008.

Copyright © 2009 by ASME

Downloaded 02 Jun 2010 to 171.66.16.109. Redistribution subject to ASME license or copyright; see http://www.asme.org/terms/Terms_Use.cfm

the typical time steps required for stability on numerical grids of sufficiently fine density to resolve the complex eddy structures adequately. The alternative unsteady Reynolds averaged Navier–Stokes (URANS) approach is much more computationally affordable, but questions still exist whether the statistical turbulence models used in URANS (mainly calibrated against 2D, steady, near equilibrium shear flows) are capable of adequate performance in fundamentally unsteady and 3D air swirl fuel injector flowfields (for discussion of the problems and potential of URANS methods, see Ref. [9]). The objective of the present work was, therefore, to compare the performance and cost implications of these two CFD methodologies, URANS and LES, for air swirl fuel injector flows.

Tang et al. [10] assessed the progress of applying LES techniques to high swirl confined flow under isothermal conditions; good agreement was found with experimental measurements for mean velocities, but no detailed examination of time-resolved features was undertaken. Garcia-Villalba et al. [11] investigated unconfined swirling jets under varying test conditions. Excellent agreement with experiment was obtained and large-scale coherent structures were predicted, as observed experimentally. Wegner et al. [12] used LES to investigate isothermal flow and mixing in the generic radial-fed swirler fuel injector studied experimentally by Midgley [6] and Janus et al. [13]. Good statistical agreement with experimental data was obtained and the presence of large-scale helical structures was identified via the λ_2-criterion proposed by Jeong and Hussain [14], emerging from within the swirler, although again no detailed comparison with experimental data on the spectral characteristics of these structures was carried out.

URANS methods are an attractive alternative to LES since the time-dependent features that have to be resolved are then restricted only to the coherent periodic motions and not the wide range of frequencies of broadband turbulence. Iaccarino et al. [15] showed good agreement between experiments URANS and LES for flow over a surface mounted cube. This flow is dominated by vortex shedding at frequencies unlikely to be strongly coupled to the turbulent energy-containing frequency range, so this success of URANS cannot necessarily be extrapolated to swirling flows and vortex breakdown. Wegner et al. [16], however, evaluated the performance of URANS against LES in predicting a PVC in an unconfined swirling flow. Overall, good agreement with experiment was achieved. Note that it was observed that use of the standard k-ε model did not lead to URANS, predicting a statistically stationary state containing a periodic PVC; initial appearance of precession was damped out with increased time. A Reynolds stress transport (RST) turbulence model was adopted, and this did result in successful URANS prediction of a PVC. However, the predicted levels of turbulence energy with URANS were far lower than measured, whereas LES was in good agreement with measured data for this statistic. This implies that the level of energy in the low frequency precession motion resolved by URANS was much too low. Given this observation, it is surprising that URANS then outperformed LES in predicting the dominant precession frequency; LES overpredicted this by some 20%, whereas the URANS error was only $\sim$2%. In free swirling flows, the PVC motion may again be dominant and there was no evidence in the cross-sectional velocity vector predictions shown in Ref. [15] of any multiple helical structures. Furthermore, it was noted in Ref. [15] that, for the free swirl flow conditions examined, the PVC precession period was five times greater than the integral time scale deduced from the LES data, which, like the vortex shedding example, would be beneficial to URANS accuracy. In the context of combustors, the effect of confinement may stabilize the flow and change the nature of the vortex breakdown, and it is therefore of interest to examine URANS performance as well for high swirl confined flows. This was done recently by Jochmann et al. [17], who, like in the study reported in Ref. [16], employed the k-ε turbulence model as well as a full second-order (RST) closure to perform URANS simulations of swirling flow. It is interesting to note that in Ref. [17], unlike for the free swirling flow results [16], both k-ε and RST models reproduced the spatial and temporal dynamics of the flow, despite the turbulence levels in the eddy viscosity model predictions being in some regions approximately five times higher than the RST results. The authors argued that one reason for similar results from two turbulence closures is that the PVC instability is an inviscid phenomenon, so that the details of the turbulence model may not matter. This conclusion may not extend beyond simulation of PVC breakdown to the more complex helical structure instability observed in the data of Midgley et al. [5–7] and in the data shown in Ref. [17]. The ability of URANS to predict the details of these structures was not explicitly discussed. The presence of both a PVC and rotating helical structures was evident in the power spectral density (PSD) plots in Ref. [17] deduced from Laser Doppler Anemometer measurements and URANS solutions. Three frequencies were identifiable as related to coherent motions at Strouhal numbers St $=0.15$, 0.51, and 0.66. These were interpreted in Ref. [17] as the lower St being due to an axial oscillation of the front stagnation point of the recirculation zone and the highest being the precession frequency. Based on arguments presented in Ref. [5] it is believed that it is more likely that St$=0.15$ is the PVC frequency and the two higher St are helical vortex frequencies associated with the particular details (dependent on the geometry and flow parameters) of the multiple vortex structures created in the swirling shear layer. Nevertheless, the results of Jochmann et al. [17] showed that URANS, with both turbulence closures, was able to identify the frequency of all three of these instabilities, although the relative amplitude between the 3St values was not in agreement with the measured data and, as observed also in Ref. [16], the associated energy in URANS predicted oscillations was much lower than that observed in the LDA data. No LES predictions of the same flowfield were provided in Ref. [17].

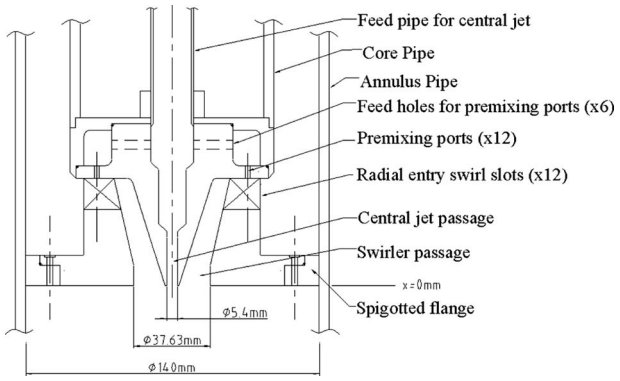


Fig. 1 Datum fuel injector geometry [6]

Based on the above discussion, the goal of the present work was to continue the work reported in Refs. [16,17] and contrast LES and URANS approaches for confined swirling flows as found in air swirl fuel injectors. The data of Midgley [6] were selected as validation data; these experiments have been analyzed in great detail [5,7] and contain (under different flow conditions) both a PVC and multiple helical vortex instabilities. Detailed spectral data are available, so an important focus of the work is to establish the accuracy with which URANS and LES can reproduce both PVC and multiple vortex flow structures.

2 Experimental Test Case

Midgley [6] employed laser sheet imaging (LSI) techniques to investigate a radially fed single swirl stream fuel injector based on an industrial gas turbine design (Fig. 1) under isothermal conditions. Previous tests with this type of fuel injector under combusting flow conditions have shown this particular design to be susceptible to undesirable combustor oscillations [18].

Downloaded 02 Jun 2010 to 171.66.16.109. Redistribution subject to ASME license or copyright; see http://www.asme.org/terms/Terms_Use.cfm

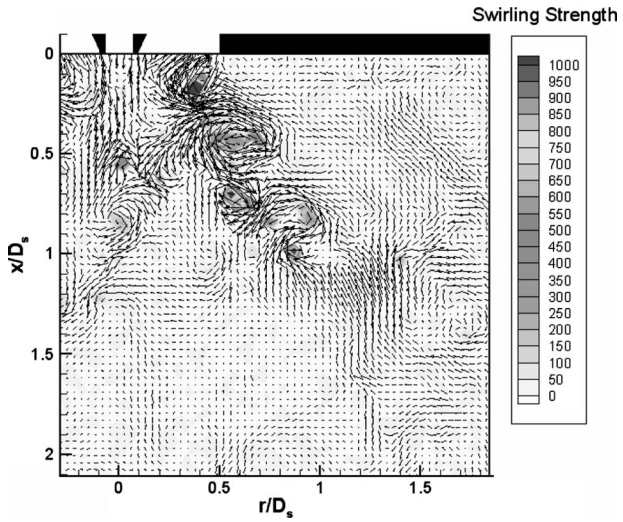


Fig. 2 *x-r* plane Reynolds-decomposed vectors and swirl strength contours [6]

Aerodynamic measurements both with and without the presence of the central jet [5] revealed high-energy-containing vortical structures embedded in the swirl stream shear layer, emerging from within the injector. These formed a quadruple vortex pattern that propagated down the main duct flow path. Instantaneous (Reynolds-decomposed) fluctuating velocity vectors in Fig. 2 clearly show the presence of these structures. Without the presence of the central jet a second unsteady event, namely, a precessing vortex core (PVC), defined as the rotation of the aerodynamic center about the geometric center, was also present. LES and URANS calculations of both jet and no-jet cases are presented below and compared with the PIV data gathered in [6]. Injector Swirl and Reynolds numbers of $S_N=0.77$ and $\mathrm{Re}=7.5\times10$ for the swirler passage and $S_N=0.0$ and $\mathrm{Re}=2.6\times10^4$ for the central jet passage (when flowing) define the flow conditions.

3 Numerical Techniques

For LES calculations an in-house code (LULES) developed at Loughborough University was used. For a detailed mathematical description of the code the reader is referred to Ref. [10] or Ref. [19]. URANS calculations were performed using FLUENT Version 6.2.16, adopting at this stage an eddy viscosity k-ε turbulence model. Spatial discretizations for LES and URANS predictions are both second order accurate, the former employing central differencing and the latter an upwind scheme. For LES, explicit Adams–Bashforth time-marching was used with a time step $\Delta t=1.0\times10^{-6}$ s to maintain solution stability. A second-order implicit temporal discretization was used for URANS calculations with a time step of $\Delta t=1.0\times10^{-3}$ s.

An identical computational domain was used (shown in the cross section in Fig. 3, the 3D solution domain was obtained by rotation through 360 deg) for both LES and URANS calculations and generated using ICEM CFD. To allow LES calculations to be carried out in parallel on four processors it has been divided into eight blocks.

Nodal distributions were based on a bi-geometric meshing scheme with a maximum stretch factor of 5% in any direction. As noted above, the domain was rotated about the centerline to create a polar type mesh with 80 nodes in the circumferential direction. In total the computational domain consists of ~900,000 cells. Inside the swirler 53 nodes were used in the longitudinal direction and 39 in the radial. This resolution is not sufficient to resolve the near-wall boundary layers where turbulent length scales are much smaller than the numerical grid; hence a wall function approach was used to calculate the instantaneous wall shear stress and a van

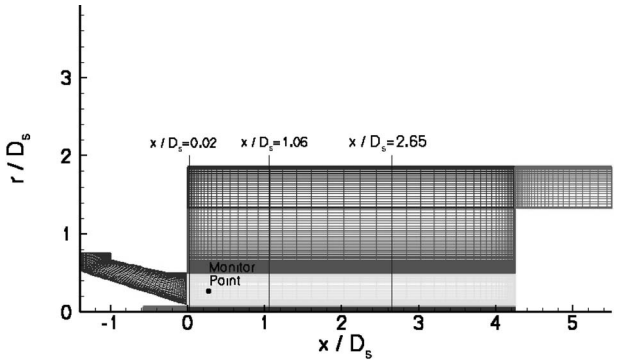


Fig. 3 Computational mesh

Driest-type damping function was implemented to reduce the eddy viscosity in near-wall regions. For further details, see Ref. [10].

Experimental data available in Ref. [6] have shown that the details of the individual swirler vane jet/wake structure disappear very quickly in the swirler passage downstream of the vane exit. Hence it was concluded that it was not necessary to resolve the flow through each individual vane (as done in Refs. [16,17], for example); this leads to unnecessary demands on computer memory and grid generation/multiblock structure complexities. From the experimental data of Midgley [6], swirler/central jet mass flow rates and swirler axial/tangential momentum flow rates, G_x and G_θ, were calculated via direct integration of measured fuel injector exit plane velocity profiles. These values were then used to specify axisymmetric radial and tangential velocity components at the radial swirler inlet to ensure that correct values for Reynolds and Swirl numbers were set in the calculations; this same practice was used for both URANS and LES solutions. For URANS calculations, values for k and ε were calculated based on an assumed turbulence intensity of 5% and a length scale set as the hydraulic diameter of the inlet duct.

4 Results and Discussion

Results presented in this section have been normalized using the swirler exit diameter, $D_s=37.63$ mm, and swirler exit bulk axial velocity, $V_{x,s}=1.99$ m/s, as reference length and velocity scales. Figures 4 and 5 show time-averaged streamlines, superimposed on time-averaged axial velocity contours for LES and URANS calculations. In order to obtain smooth statistics azimuthal averaging has also been applied to the LES data.

In both cases common qualitative features associated with strongly swirling confined flows, such as the formation of corner and central recirculation zones, are well represented. Separation of

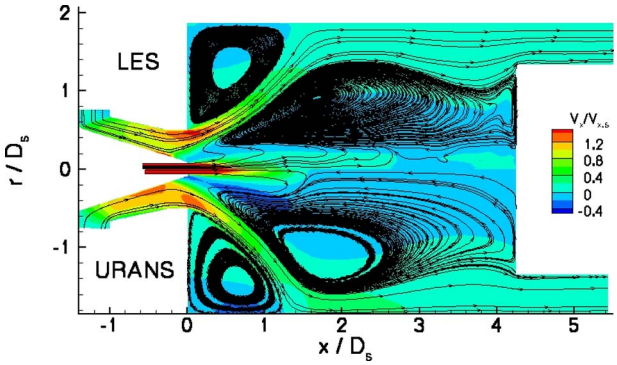


Fig. 4 Mean streamlines and mean axial velocity contours—with jet condition

Downloaded 02 Jun 2010 to 171.66.16.109. Redistribution subject to ASME license or copyright; see http://www.asme.org/terms/Terms_Use.cfm

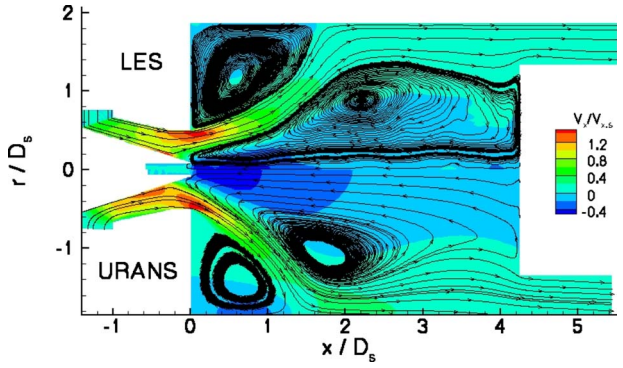


Fig. 5 Mean streamlines and mean axial velocity contours—no-jet condition

the mean flow is seen to occur upstream of the fuel injector exit plane inside of the annular swirl passage in both URANS and LES. Spencer et al. [5] determined this point as located between $x/D_s=-0.43$ and $x/D_s=-0.27$, which agrees reasonably well with LES and URANS, where $x/D_s\approx-0.15$.

In the with jet condition the swirl cone reattaches to the outer wall in the experiments [6] at $x/D_s=1.25$, while in the no-jet condition this location moved further downstream to a time-mean location of 1.75. The no-jet case also exhibited a greater degree of variation, $+0.85/-1.25D_s$ compared with $+/-0.5D_s$. It was suggested in Ref. [5] that the presence of a PVC in the no-jet case has a destabilizing influence and is responsible for the observed differences. The time-mean value of the swirl cone reattachment predicted is shown in Figs. 4 and 5 to be well captured by LES with mean locations of $x/D_s\approx1.3$ and $x/\approx D_s$ 1.6 for jet and no-jet conditions, respectively. URANS has not resolved these differences with a mean location of $x/D_s\approx1.3$ for both flow conditions. The reasons for this will be explored further below.

Radial profiles of time-averaged axial and tangential velocities for LES and URANS calculations, at the three axial locations indicated in Fig. 3, are compared with the experimental results in Figs. 6 and 7. Overall LES and URANS provide satisfactory representations of axial velocity at both flow conditions. For the first two profiles, axial velocity is predicted slightly better by LES: URANS discrepancies at these locations are attributed to variations in the reattachment of the swirl cone on the outer wall as discussed above. It is clear that while LES is able to capture the experimentally observed Rankine distribution of tangential velocity, URANS provides a particularly poor representation, quickly tending to a solid body rotation shape. This is due to the fact that any linear eddy viscosity model (such as the standard k-ε used here) has this well known tendency to develop solid body rotation profiles very quickly in swirling flows, see, for example, Ref. [20]; this could of course be remedied by moving to a RST model, as suggested by Wegner et al. [16].

In both with jet and no-jet configurations multiple vortical structures were observed in the measured data issuing from within the annular swirl passage. These formed a quadruple vortex pattern and propagated downstream with the bulk flow along helical paths. The clearest representation of these structures is obtained if r-θ plane measurements are examined via Reynolds decomposition (subtraction of the mean velocity field in the same r-θ plane from an instantaneous field), revealing only the fluctuating or unsteady flow structures. Streakline patterns may then be traced using the in-plane velocity components only to visualize the embedded structures. Figures 8 and 9 show such Reynolds decomposed streamlines for a randomly selected instantaneous measurement at the swirler exit for both test conditions.

For both flow conditions, LES and experiment are in close agreement, with four vortical structures clearly visible. In Refs. [5,6] the term "two-strong two-weak" was used to describe the observed vortex pattern in the with jet case. This refers to the fact that, as seen in the density of streaklines in the left-hand experimental picture in Fig. 8, two vortices, separated by π rad and rotating in the same direction as the bulk flow field, are of approximately equal and greater strength and exhibit greater coherence than the other two vortices. These are also separated by π rad but rotate in the opposite direction. In the no-jet flow condition, although four vortices are still observed, any coherence pattern is much weaker; each of the vortices displays its own individual streakline pattern (this change in coherence is better displayed in spatial correlation maps, see Fig. 12 below). The LES data for the no-jet case reflect this change very closely. As will be demonstrated below, it is the absence of a PVC in the with jet case

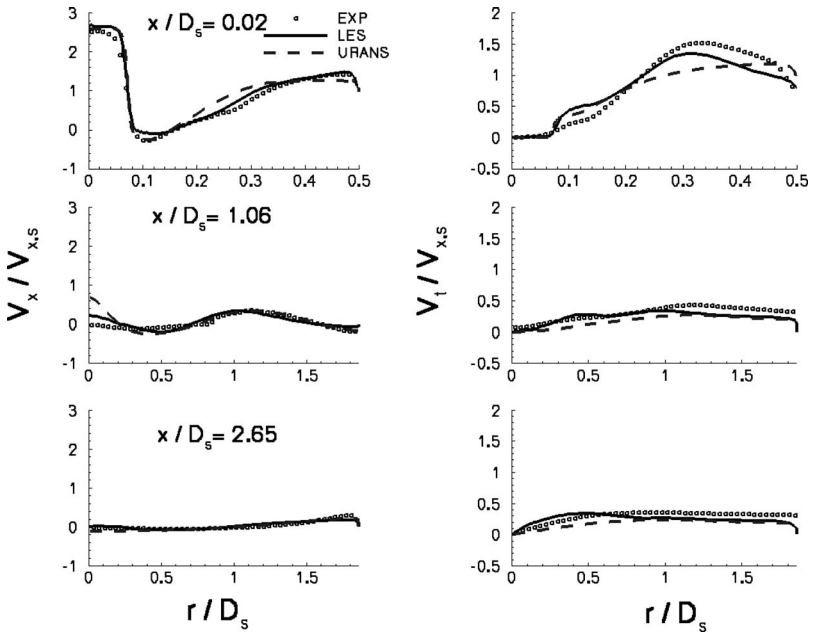


Fig. 6 Time-averaged axial (left) and tangential (right) velocity profiles for with jet condition: top $x/D_s=0.02$, middle $x/D_s=1.06$, and bottom $x/D_s=2.66$

Downloaded 02 Jun 2010 to 171.66.16.109. Redistribution subject to ASME license or copyright; see http://www.asme.org/terms/Terms_Use.cfm

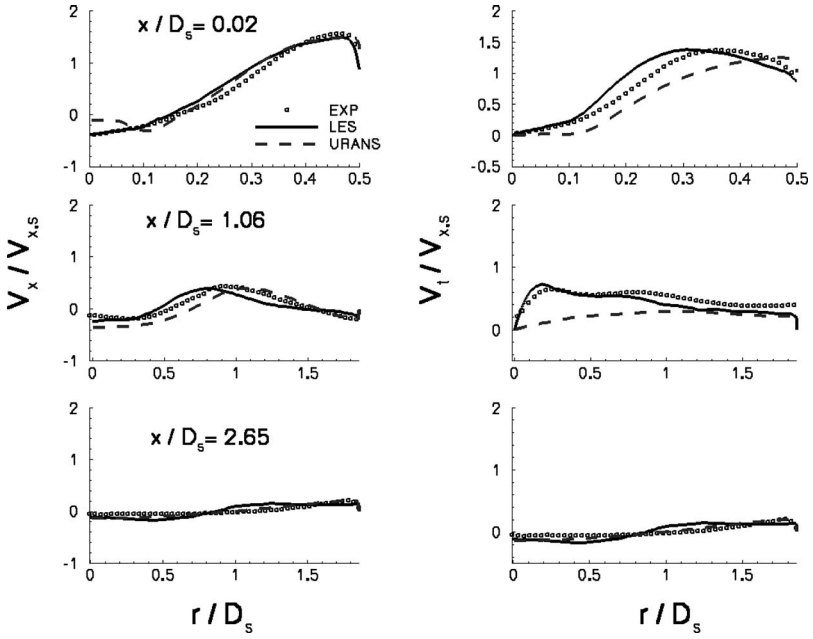


Fig. 7 Time-averaged axial (left) and tangential (right) velocity profiles for no-jet condition: top $x/D_s=0.02$, middle $x/D_s=1.06$, and bottom $x/D_s=2.66$

and its appearance in the no-jet case that is the reason for this change in coherence pattern. It should be borne in mind that it is this pattern and its change with flow condition that are responsible for fixing the absolute values of the periodic frequencies, which appear in the spectral data to be examined for the present experiment below and which has already been discussed above for the data of Jochmann et al. [17]. Although the URANS calculations in Fig. 8 show evidence of vortical structures emerging from within the swirler they are not in accordance with either experiment or LES. In the early stages of the URANS simulation four vortices were present but these became a two vortex pattern in the statistically stationary solution so that the URANS solution does not reflect the measured dynamics of the embedded helical vortices in the present experiment at all.

In order to make a quantitative assessment of the unsteady features observed in Fig. 8 a time trace of the instantaneous velocity components was recorded within the swirl stream at the monitor point indicated in Fig. 1 for both test conditions. A sample of the time trace obtained in the with jet condition is shown in Fig. 9.

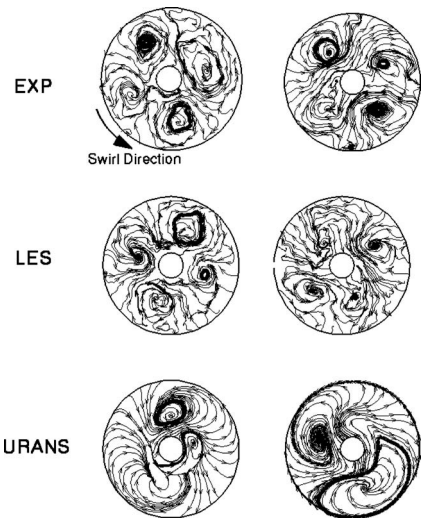


Fig. 8 Reynolds decomposed instantaneous streamlines at $x/D_s=0.02$ with jet (left) and no-jet (right) conditions

Figure 9 serves to provide a clear illustration of the inherent differences between LES and URANS predicted temporal dynamics. While LES simulates the broadband stochastic nature of the flow URANS is only able to resolve the ensemble or phase-averaged coherent unsteadiness. It is interesting to note that the magnitude of the velocity fluctuations is quite different, with the fluctuating amplitude much larger in the LES (although this contains both coherent and true turbulent energy contributions). The mean value, indicated by the horizontal line in each frame, is, however, almost identical.

In order to obtain spectral information (and allow the coherent part of the LES time-traces to be identified) the time histories of axial velocity were Fourier transformed directly via a standard fast Fourier transform (FFT) algorithm. Figures 10 and 11 show PSDs calculated from LES and URANS compared with the hot-wire data of Midgley [6] for with jet and no-jet conditions.

In the with jet condition the experimental spectrum (Fig. 10) exhibits distinct spikes, which correspond to various periodic unsteady events. Notice also that the periodic spikes are embedded well within the range of turbulent broadband frequencies. The interaction between coherent and stochastic processes seems fairly weak in the with jet case as the spikes are narrow; in contrast, stronger interaction (N.B. difficult for URANS to capture) is probable in the no-jet case as significant broadening in the vicinity of the periodic spikes is evident. For the with jet data, the primary spike at $St \approx 1.39$ corresponds to the vortices in the "two-strong" vortex pair (see Fig. 8) passing a fixed point, while the secondary spike, occurring at double the primary frequency, $St \approx 2.78$, corresponds to the two-strong two-weak pattern passing a fixed point. It can be seen that LES has been able to capture these frequencies with a remarkable degree of accuracy with Strouhal numbers of $St \approx 1.44$ and $St \approx 2.88$. Although the experimental spectrum for the no-jet condition, shown in Fig. 11, exhibits many similarities, there are clear differences. In contrast to the with jet condition the primary peak now occurs at $St \approx 0.69$. This of course corresponds to the strongest single vortex passing a fixed point (see Fig. 8), while the secondary spike occurring at double the primary St ≈ 1.39, corresponds to a vortex pair. Once again, frequencies predicted by the LES approach are in very close agreement with

Downloaded 02 Jun 2010 to 171.66.16.109. Redistribution subject to ASME license or copyright; see http://www.asme.org/terms/Terms_Use.cfm

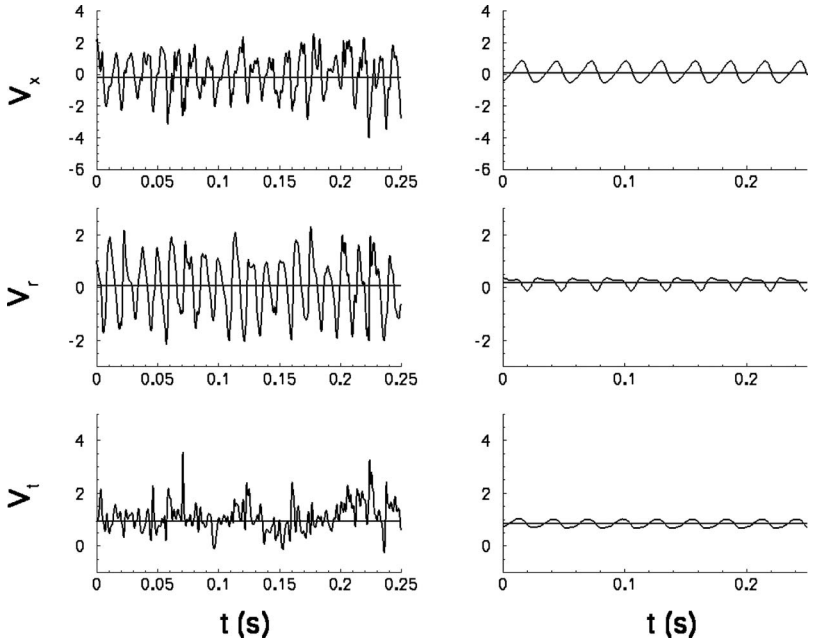


Fig. 9 Time history of instantaneous velocities at $x/D_s=0.27$ and $r/D_s=0.27$ for with jet condition LES (left) and URANS (right)

experiment, yielding St≈0.67 and St≈1.34. These spectral differences observed between with jet and no-jet conditions are now firmly attached to the details of the helical vortex structures shown in Fig. 8, and it is thus no surprise that, since LES has captured these structures accurately, the spectral peaks are simulated accurately. The change in the vortex pattern on removal of the central jet is due to the appearance in this case of a PVC. This additional unsteadiness has a relatively low characteristic frequency and is evident on examination and comparison of the lower end of the spectra (St<0.1) shown in Figs. 10 and 11. The increase in energy in the low St region in the no-jet case compared with the with jet case shows that the latter contains a PVC whereas the former does not (see Ref. [5] for more details. Note that this implies that there is no precession of the multiple vortex structures in either flow case; these are rotating rather than precessing about the geometric axis. The presence of a central jet has a stabilizing effect on the large recirculation region, "fixing" this on the geometric combustor axis. The absence of the central jet allows precession of the central recirculation zone, and this precession has a "blurring" effect on the vortical structures emanating from within the swirler, reducing their strength and coherence. Once again, LES has captured this switch between with jet and no-jet cases remarkably well and reflected the subtle spectral differences between with jet and no-jet conditions over the whole frequency range.

It is also very clear from Figs. 10 and 11 that the URANS predictions produce very poor spectral results and do not in any way represent either the particular frequencies associated with the shear layer vortex structures or is URANS sensitive to the difference between with jet and no-jet conditions, showing no evidence of a PVC in either case. This is unsurprising given that the coherent vortex structures captured by URANS are not in accordance with experimental observation. The absence of the PVC in the URANS results and its associated destabilizing influence helps to explain why the reattachment location of the swirl cone, shown in Figs. 4 and 5, is identical in the URANS with jet and no-jet conditions.

To gain further understanding of the size and interaction between the vortical structures emanating from within the swirler, spatial correlations of the radial velocity component at the swirler

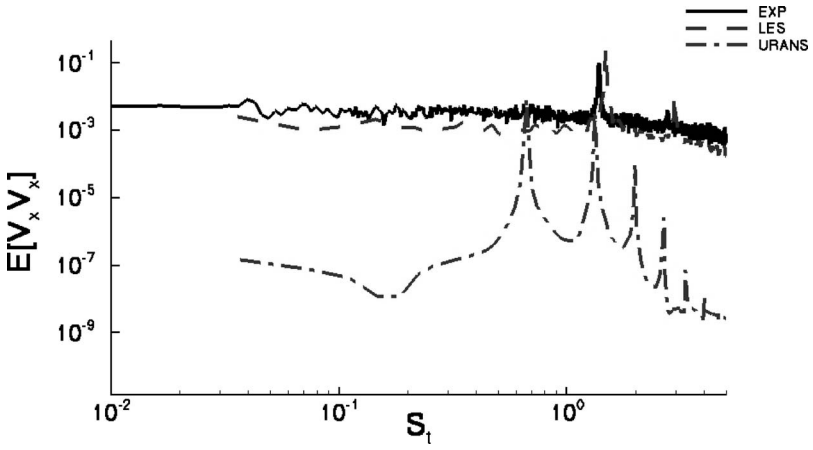


Fig. 10 PSD of axial velocity $x/D_s=0.27$ and $r/D_s=0.27$ with jet condition

Downloaded 02 Jun 2010 to 171.66.16.109. Redistribution subject to ASME license or copyright; see http://www.asme.org/terms/Terms_Use.cfm

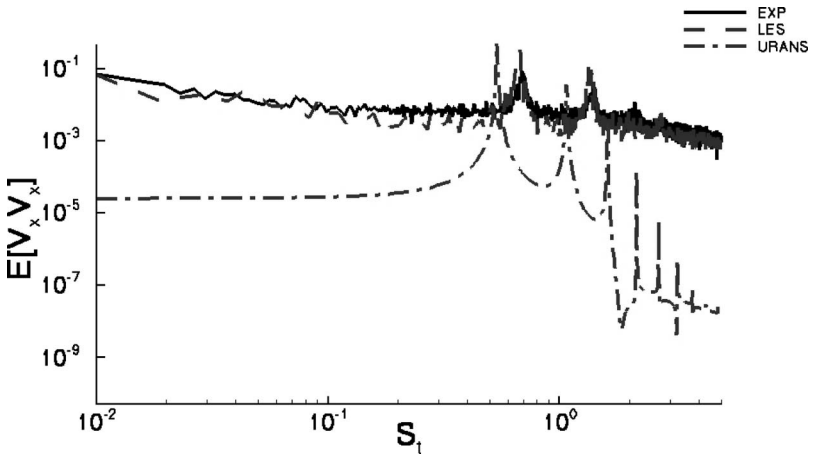


Fig. 11 PSD of axial velocity $x/D_s=0.27$ and $r/D_s=0.27$ no-jet condition

exit have been evaluated and are shown in Fig. 12 for with jet and no-jet conditions. The spatial correlation function, $R_{ij}(\mathbf{x},\Delta\mathbf{s})$, is defined as

$$\overline{R_{ij}(\mathbf{x},\Delta\mathbf{s})} = \frac{\overline{v_i(\mathbf{x},t)\cdot v_j(\mathbf{x}+\Delta\mathbf{s})}}{v_i'(\mathbf{x})v_j'(\mathbf{x})}$$

where $\Delta\mathbf{s}$ represents the separation vector between a reference point ($\mathbf{x}$) and any other point in the plane. The reference point is indicated by the black dot in Fig. 12 and is located at $x/D_s=0.02$, $r/D_s=0.175$, and $\theta=\pi$ rad.

In both flow conditions good agreement has been obtained between experiment and LES with the presence of four vortical structures clearly evident. For the with jet data, in the region located π rad from the reference point, high levels of positive correlation are observed, while in the regions located $\pi/2$ rad from the reference point, high levels of negative correlation are present. This is consistent with Fig. 8 and the interpretation given above, that two corotating strong vortices separated by π rad exist, separated by two weak vortices also separated by π rad but counter-rotating (i.e., negatively correlated). The experimental observations indicate that, although with jet and no-jet conditions exhibit very similar correlation patterns, the actual levels of correlation were notably lower in the latter case. This gives support to the argument that the presence of a PVC has a destabilizing effect on the helical vortices, reducing their strength and coherence in space and time. LES captures this subtle characteristic, accurately predicting reduced levels of correlation. Interestingly, despite the differences in the form of the coherent structures captured by URANS shown in Fig. 8, spatial correlations of radial velocity show some similarity with experiment in the with jet condition, although the correlation pattern is shifted to a smaller radius than that observed in the measured data. This, however, is not the case in the no-jet condition where URANS predicts a very different correlation pattern to the experiments, in stark contrast to LES.

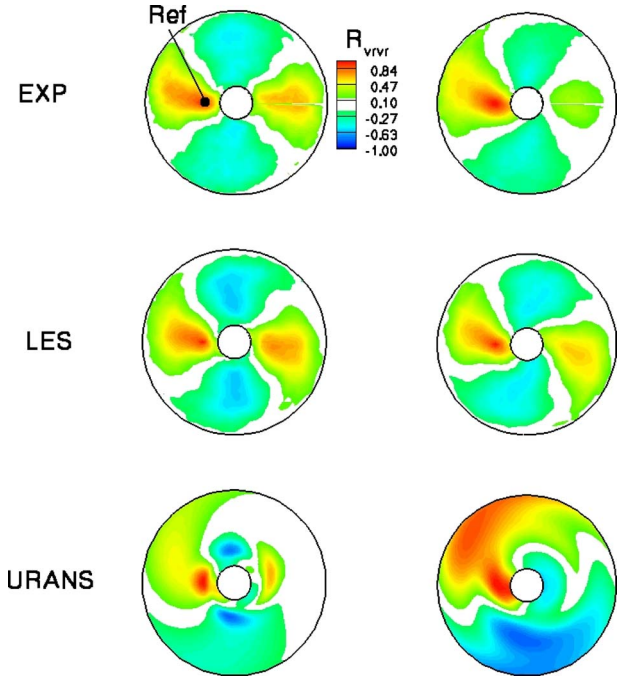


Fig. 12 Spatial correlations of the radial velocity swirler exit with jet (left) and no-jet (right) conditions.

As a final comment, a comparative estimate of computational cost between URANS and LES is provided. The characteristic convection time of the vortex pattern at the swirler exit, i.e., the time taken for one complete rotational period, is quantified via a reference time scale, T_s, defined as

$$T_s = \frac{\pi D_{s,\mathrm{mid}}}{V_{\theta,s}} \approx \frac{\pi D_{s,\mathrm{mid}} V_{x,s}\int_0^R r^2 dr}{G_\theta} = 0.02 \text{ s}$$

An average value of the swirler exit bulk tangential velocity, $V_{\theta,s}$, was calculated from the total tangential momentum flow rate, G_θ, evaluated by integration over the predicted profiles at the swirler exit. Assuming a mass flow based value for the average axial velocity allows a value for T_s to be estimated (20 ms). Using this characteristic time it is possible to make an assessment of the different computational requirements of LES and URANS by estimating the ratio of the number of CPU hours (using the computer resources and time steps adopted in the present study) required to resolve one rotational period of the vortex structures. Based on this LES requires approximately 40 times more computational resources (essentially due to the much smaller time step needed). This factor of ~40 is the main reason why URANS methods would certainly be preferred for design purposes, but then the fidelity of what can be obtained in this smaller CPU time has to be considered.

5 Conclusions

The results presented here have shown that both LES and URANS CFD approaches are able to capture many of the gross features of the time-averaged flow associated with strongly swirling confined flows very well. However, in the two test cases investigated (with jet and no-jet configurations) experimental data

Downloaded 02 Jun 2010 to 171.66.16.109. Redistribution subject to ASME license or copyright; see http://www.asme.org/terms/Terms_Use.cfm

revealed a degree of variation in some of these time-mean features, for example, swirl cone reattachment location, for which only LES returned the correct trend.

A quadruple vortex pattern emanating from within the swirler and observed experimentally has been successfully predicted by LES for both test cases. Spectral analysis found LES to be in excellent agreement with experiment, capturing all the subtle spectral differences between test cases over a broad frequency range. Although URANS calculations showed evidence of large-scale vortical structures at the swirler exit, they were not in accordance with experiment and, as a result, URANS was not able to produce the correct spectral characteristics. In the no-jet case an additional unsteady event, namely, a PVC, was present. Again, only LES was successful in reproducing this measured change between the two flow conditions. An analysis of the influence of the PVC on both the time-mean flowfield and the spectral characteristics was provided, with LES, via spectral and spatial correlation comparisons, producing excellent agreement with measured data.

As discussed in the Introduction, there are still questions regarding the applicability of URANS methods to the current class of the flow problem. Perhaps with use of a RST turbulence closure, the URANS performance presented here could have been improved, for example, in the capture of swirl; velocity profile shapes. However, it is not felt that this would have lead to correct reproduction of the multiple vortex pattern observed at both flow conditions, although clearly calculations with a RST model should be performed to confirm this, and this is currently underway. Equally, there are a few computational refinement tests (grid size, time step, and discretization errors) that may be influential and are ongoing, but it is not currently believed that these will change the results significantly. The most compelling argument for URANS is of course its relatively modest computational requirements—approximately one to two orders of magnitude less than that demanded by LES for the current flow. However, on the basis of the results presented here, unless URANS can demonstrate a much improved capture of the all-important frequency content of air swirl fuel injector flowfields, it cannot be recommended for use, and the increased cost of LES is believed to be an absolutely worthwhile expense because of the high fidelity of the predicted results in the important area of flow instabilities.

Acknowledgment

Funding to support this work was provided by UK EPSRC CASE Award No. 05000215. Thanks are also given to colleagues at Rolls-Royce and in the Loughborough University UTC (in particular, Mark Robinson) for many useful technical discussions.

Nomenclature

D_s = swirler exit diameter
$D_{s,\mathrm{mid}}$ = swirler exit midannulus diameter
G_θ, G_x = swirl and axial momentum flow rates
Re = Reynolds number (e.g., $\rho V_{x,s} D_s/\mu$)
R_{ij} = spatial correlation function
S_N = Swirl number
St = Strouhal number ($f D_s/V_{x,s}$)
T_s = swirler exit time scale
V_x, V_r, V_θ = time-mean velocities in the x, r, θ directions
$V_{x,s}, V_{\theta,s}$ = swirler exit bulk axial and swirl velocities
v_i, v_j = fluctuating velocity in the i,j direction
v_i', v_j' = rms turbulence intensity in the i,j direction
λ_2 = second invariant of the velocity gradient tensor
ρ = density
μ = viscosity

References

[1] Leibovich, S., 1978, "The Structure of Vortex Breakdown," Annu. Rev. Fluid Mech., **10**, pp. 221–246.
[2] Gupta, A. K., Lilley, D. G., and Syred, N., 1984, *Swirl Flows*, Abacus Press, UK.
[3] Lucca-Negro, O., and O'Doherty, T., 2001, "Vortex Breakdown: A Review," Prog. Energy Combust. Sci., **27**, pp. 431–481.
[4] Benjamin, T. B., 1962, "Theory of the Vortex Breakdown Phenomenon," J. Fluid Mech., **14**, pp. 593–629.
[5] Spencer, A., McGuirk, J. J., and Midgley, K., 2008, "Vortex Breakdown in Swirling Fuel Injector Flows," ASME J. Eng. Gas Turbines Power (to be published).
[6] Midgley, K., 2005, "An Isothermal Experimental Study of the Unsteady Fluid Mechanics of Gas Turbine Fuel Injector Flowfields," Ph.D. thesis, Loughborough University, UK.
[7] Midgley, K., Spencer, A., and McGuirk, J. J., 2005, "Unsteady Flow Structures in Radial Swirler Fed Fuel Injectors," ASME J. Eng. Gas Turbines Power, **127**, pp. 755–764.
[8] Midgley, K., Dianat, M., Spencer, A., Yang, Z., and McGuirk, J. J., 2007 "Scalar Measurements and Unsteady Simulations in High Swirl Confined Flows," *Proceedings of the International Gas Turbine Congress 2007*, Tokyo, Japan, Dec. 2–5.
[9] Hanjalic, K., 2005, "Will RANS Survive LES?" ASME J. Fluids Eng., **127**, pp. 831–839.
[10] Tang, G., Yang, Z., and McGuirk, J. J., 2002, "Large Eddy Simulation of Isothermal Confined Swirling Flow With Recirculation," *Engineering Turbulence Modelling and Experiments*, W. Rodi and N. Fueyo, eds., Elsevier, Oxford, UK, Vol. 5, pp. 885–894.
[11] Garcia-Villalba, M., Frölich, J., and Rodi, W., 2006, "Numerical Simulations of Isothermal Flow in a Swirl Burner," ASME Paper No. GT2006-90764.
[12] Wegner, B., Staufer, M., Sadiki, A., and Janicka, J., 2005, "Study of Flow and Mixing in a Generic GT Combustor Using LES," *Engineering Turbulence Modelling and Measurements*, Vol. 6, W. Rodi, ed., Elsevier, Oxford, pp. 845–854.
[13] Janus, B., Dreizler, A., and Janicka, J., 2005, "Experimental Study on Stabilisation of Lifted Swirl Flames in a Model GT Combustor," Flow, Turbul. Combust., **75**, pp. 293–315.
[14] Jeong, J., and Hussain, F., 1995, "On the Identification of a Vortex," J. Fluid Mech., **285**, pp. 69–94.
[15] Iaccarino, G., Obi, A., Durbin, P. A., and Behnia, M., 2003, "Reynolds Averaged Simulations of Unsteady Separated Flow," Int. J. Heat Fluid Flow, **24**, pp. 147–156.
[16] Wegner, B., Maltsev, A., Schneider, C., Sadiki, A., Dreizler, A., and Janicka, J., 2004, "Assessment of Unsteady URANS in Predicting Swirl Flow Instability Based on LES and Experiments," Int. J. Heat Fluid Flow, **25**, pp. 528–536.
[17] Jochmann, P., Sinigersky, A., Hehle, M., Schäfer, O., Koch, R., and Bauer, H. J., 2006, "Numerical Simulation of a Precessing Vortex Breakdown," Int. J. Heat Fluid Flow, **27**, pp. 192–203.
[18] Lartigue, G., Meier, U., and Bérat, C., 2004, "Experimental and Numerical Investigation of Self-Excited Combustion Oscillations in a Scaled Gas Turbine Combustor," Appl. Therm. Eng., **24**(11–12), pp. 1583–1592.
[19] Dianat, M., Yang, Z., Jiang, D., and McGuirk, J. J., 2006, "Large Eddy Simulation of Scalar Mixing in a Coaxial Confined Jet," Flow, Turbul. Combust., **77**, pp. 205–227.
[20] Hirai, S., Takagi, T., and Matsumoto, M., 1988, "Predictions of the Laminarisation Phenomena in an Axially Rotating Pipeflow," ASME J. Fluids Eng., **110**, pp. 424–430.

Downloaded 02 Jun 2010 to 171.66.16.109. Redistribution subject to ASME license or copyright; see http://www.asme.org/terms/Terms_Use.cfm

A Generalized Likelihood Ratio Test for Adaptive Gas Turbine Performance Monitoring

S. Borguet
e-mail: s.borguet@ulg.ac.be

O. Léonard
e-mail: o.leonard@ulg.ac.be

Turbomachinery Group,
University of Liège,
Chemin des Chevreuils,
1 4000 Liège, Belgium

Kalman filters are widely used in the turbine engine community for health monitoring purposes. This algorithm has proven its capability to track gradual deterioration with good accuracy. On the other hand, its response to rapid deterioration is a long delay in recognizing the fault and/or a spread of the estimated fault on several components. The main reason for this deficiency lies in the transition model of the parameters that is blended in the Kalman filter and assumes a smooth evolution of the engine condition. This contribution reports the development of an adaptive diagnosis tool that combines a Kalman filter and a secondary system that monitors the residuals. This auxiliary component implements a generalized likelihood ratio test in order to detect and estimate an abrupt fault. The enhancement in terms of accuracy and reactivity brought by this adaptive Kalman filter is highlighted for a variety of simulated fault cases that may be encountered on a commercial aircraft engine. [DOI: 10.1115/1.2967493]

Keywords: gas path analysis, adaptive estimation

1 Introduction

Predictive maintenance aims at scheduling the overhaul actions on the basis of the actual level of deterioration of the engine. The benefits are improved operability and safety as well as reduced life cycle costs. Generating reliable information about the health condition of the gas turbine is therefore a requisite and has been the subject of an intensive research in the community.

In this paper, *module performance analysis* is considered. Its purpose is to detect, isolate, and quantify the changes in engine module performance, described by so-called health parameters, on the basis of measurements collected along the gas path of the engine [1]. Typically, the health parameters are correcting factors on the efficiency and the flow capacity of the modules (fan, lpc, hpc, hpt, lpt, and nozzle), while the measurements are intercomponent temperatures, pressures, and shaft speeds.

Many techniques have been investigated to solve the diagnosis problem, ranging from optimal estimation to artificial intelligence as well as expert systems (see Ref. [2] for a detailed review). Among the various approaches, the popular Kalman filter [3] has received great attention from the researchers. This recursive, minimum-mean-squared-error algorithm has proven its capability to track engine wear with good accuracy. This *gradual deterioration* process (due to erosion, corrosion, or fouling, for instance) occurs during a normal operation of the engine and affects all major components at the same time. One reason for the ability of the Kalman filter to deal with that kind of degradation is that it assumes a "relatively" slow evolution of the health parameters to filter the measurement noise.

On the other hand, *rapid deterioration* may happen too. These faults, caused, for instance, by hot restarts or foreign/domestic object damage,[1] impact one (at most two) component(s) at a time. The time of occurrence of the event, as well as the impacted component and the magnitude of the fault, is typically unknown. The response of the Kalman filter to these short-time-scale variations in the engine condition is a long delay in recognizing the fault and/or a spread of the estimated fault over several components, which is termed "smearing" effect (see Ref. [4]).

To overcome these deficiencies, a strategy that combines a so-called single-fault isolator with a Kalman filter is proposed in Ref. [5]. The single-fault isolator consists of a bank of possible events that is examined whenever a residual is suspected to be representative of an abrupt fault. While very efficient, this solution implies the interaction between two different diagnosis tools. Moreover, the setup of the fault library requires significant knowledge and experience.

A broader way to tackle the problem at hand is to view it in the realm of *adaptive estimation* [6]. The basic idea consists in increasing the mobility of the health parameters momentarily in order to recognize a rapid degradation. Mathematically, it comes down to increasing the covariance of the health parameters on the basis of a statistical processing of the residuals. Several techniques have been explored in the literature, such as autocorrelation [7,8] and covariance matching [9]. In Ref. [10], the authors developed an adaptive Kalman filter for performance monitoring that integrates a covariance matching scheme.

Another attractive solution has been proposed in Ref. [11]. The transition model for the health parameters is modified so as to account for possible jumps in the parameters. This technique has been successfully applied in visual tracking [12] and is the backbone of the algorithm presented in this contribution. The newly developed diagnosis tool combines a Kalman filter, which relies on the assumption of a smooth variation of the health parameters, and a secondary system that monitors the residuals. This auxiliary component implements a *generalized likelihood ratio test* (GLRT) in order to detect and estimate a rapid fault. In that way, the performance of the Kalman filter is maintained under normal operation (long-time-scale deterioration), whereas the event detector acts as a fault compensator in the case of a sudden variation in the engine health. The enhancement in terms of accuracy and reactivity brought by this adaptive Kalman filter is illustrated for a variety of simulated fault cases that may be encountered on a commercial aircraft engine.

2 Description of the Method

The scope of this section is to provide the mathematical background of the adaptive algorithm. The generic diagnosis tool re-

[1] A domestic object damage is caused by an element of the engine (e.g., part of a blade) that breaks off and strikes a downstream flow path component.

Contributed by the International Gas Turbine Institute of ASME for publication in the JOURNAL OF ENGINEERING FOR GAS TURBINES AND POWER. Manuscript received April 1, 2008; final manuscript received April 2, 2008; published online October 13, 2008. Review conducted by Dilip R. Ballal. Paper presented at the ASME Turbo Expo 2008: Land, Sea and Air (GT2008), Berlin, Germany, June 9–13, 2008.

Copyright © 2009 by ASME

Downloaded 02 Jun 2010 to 171.66.16.109. Redistribution subject to ASME license or copyright; see http://www.asme.org/terms/Terms_Use.cfm

lying on a Kalman filter is briefly presented. Then, based on a model that can handle abrupt variations in the health parameters, the auxiliary component that performs the detection and estimation of the "jumps" is developed. Finally, the integration of this adaptive component with the Kalman filter is described.

2.1 The Engine Performance Simulation Tool. One of the master pieces of the gas path analysis approach is a simulation model of the engine. Considering a steady-state operation of the engine, these simulation tools are generally nonlinear aerothermodynamic models based on mass, energy, and momentum conservation laws applied to the engine flow path. Equation (1) represents such an engine model where $\mathbf{u}_k$ are the variables defining the operating point of the engine (e.g., fuel flow, altitude, and Mach number), $\mathbf{w}_k$ are the aforementioned health parameters, $\mathbf{y}_k$ are the gas path measurements, and k is the discrete time index.

$$\mathbf{y}_k = \mathcal{G}(\mathbf{u}_k, \mathbf{w}_k) \tag{1}$$

Within the frame of turbine engine diagnostics, the quantity of interest is the difference between the actual engine condition and a guessed one, $\hat{\mathbf{w}}_k^-$. Assuming a linear relationship between the measurements and the parameters as well as fixed operating conditions, the performance model (Eq. (1)) is reformulated according to Eq. (2).

$$\mathbf{y}_k = \mathbf{G}_k \mathbf{w}_k \tag{2}$$

where

$$\mathbf{G}_k = \frac{\partial}{\partial \mathbf{w}_k} \mathcal{G}(\mathbf{u}_k, \mathbf{w}_k)\Big|_{\mathbf{w}_k = \hat{\mathbf{w}}_k^-} \tag{3}$$

is the Jacobian matrix of the engine model around the health condition $\hat{\mathbf{w}}_k^-$. With some abuse of notation, $\mathbf{y}_k$ and $\mathbf{w}_k$ are now deviations of the measurements and the health parameters from their values at the linearization point.

2.2 An Improved Model for Adaptive Estimation. The core of the diagnosis tool is a Kalman filter that is to be made more responsive to abrupt degradation. The derivation of the Kalman filter (see, for instance, Ref. [13] in the particular scope of engine performance monitoring) implies that the system is formulated as a state-space model. Within the frame of adaptive estimation, it is proposed in Ref. [11] to express the state-space model under the following form:

$$\mathbf{w}_k = \mathbf{w}_{k-1} + \nu_k + \mathbf{\Delta}_\mathbf{w} \delta_{\tau,k} \tag{4}$$

$$\mathbf{y}_k = \mathbf{G}_k \mathbf{w}_k + \epsilon_k \tag{5}$$

Classical assumptions about the different variables of the model are the following:

- The health parameters $\mathbf{w}_k$ are considered as Gaussian random variables with initial condition $\mathbf{w}_0 \in \mathcal{N}(\hat{\mathbf{w}}_0, \mathbf{P}_{\mathbf{w},0})$.
- The random variable $\upsilon_k \in \mathcal{N}(0, \mathbf{Q}_k)$ is the so-called process noise that provides the required mobility to track gradual deterioration. It is assumed to be independent of $\mathbf{w}_k$.
- The random variable $\epsilon_k \in \mathcal{N}(0, \mathbf{R}_k)$ is the measurement noise that represents sensor inaccuracies. It is assumed to be uncorrelated with υ_k.

The last term in Eq. (4) accounts for a possible jump in the health parameters:

- $\mathbf{\Delta}_\mathbf{w}$ is a vector modeling the jump.
- τ is a positive integer that represents its time of occurrence.
- $\delta_{i,j}$ is the Kronecker delta operator.

Note that $\mathbf{\Delta}_\mathbf{w}$ and τ are regarded here as *unknown* parameters and not as random variables, which means that no prior distribution is attached to them.

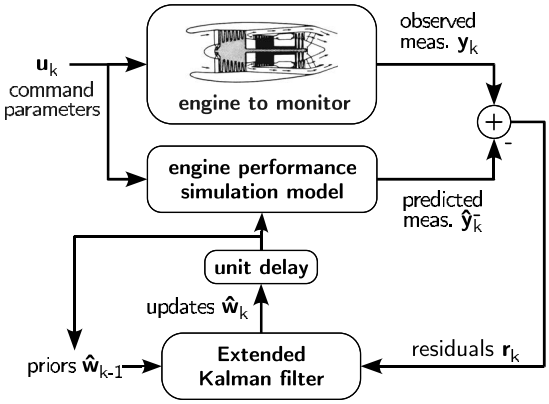


Fig. 1 Health parameter update mechanism using an extended Kalman filter

The strategy of adaptive estimation comes from viewing Eqs. (4) and (5) according to the following two different hypotheses:

- H_0: no jump up to now ($\tau > k$).
- H_1: a jump has occurred ($\tau \leq k$).

Under assumption H_0 (no jump), the Kalman filter provides an optimal estimation of the health parameters in the least-squares sense. Due to the mild nonlinearity of the system, the extended Kalman filter (EKF) is selected. The basic processing step of the EKF at time k is reported in algorithm 1 in a pseudocode style.

Line 1 is the prediction step: prior values of the health parameter distribution are generated by means of the transition model (Eq. (4)) under the no-jump assumption. Then, the data are acquired (line 2) and used in building the residuals $\mathbf{r}_k$, namely, the difference between the measurements and the model predictions (line 3). The Jacobian matrix is assessed on line 4 and subsequently used in the computation of the covariance matrix of the residuals $\mathbf{P}_{\mathbf{y},k}$ (line 5) and of the Kalman gain $\mathbf{K}_k$ (line 6). Loosely speaking, the gain weighs the uncertainty on the parameters versus the uncertainty on the measurements. Finally, the posterior distribution of the health parameters is generated at the correction step (line 7). To complete the description, Fig. 1 sketches the closed-loop structure of the generic diagnosis tool relying on the EKF. The engine performance model, actually embedded in the EKF, is represented outside of it in order to underline its importance in this *model-based* estimation process.

Algorithm 1 Basic step of the extended Kalman filter
1: $\hat{\mathbf{w}}_k^- = \hat{\mathbf{w}}_{k-1}$ and $\mathbf{P}_{\mathbf{w},k}^- = \mathbf{P}_{\mathbf{w},k-1} + \mathbf{Q}_k$
2: acquire $\mathbf{u}_k$ and $\mathbf{y}_k$
3: $\mathbf{r}_k = \mathbf{y}_k - \mathcal{G}(\mathbf{u}_k, \hat{\mathbf{w}}_k^-)$
4: compute Jacobian matrix as per Eq. (3)
5: $\mathbf{P}_{\mathbf{y},k} = \mathbf{G}_k \mathbf{P}_{\mathbf{w},k}^- \mathbf{G}_k^T + \mathbf{R}_k$
6: $\mathbf{K}_k = \mathbf{P}_{\mathbf{w},k}^- \mathbf{G}_k^T \mathbf{P}_{\mathbf{y},k}^{-1}$
7: $\hat{\mathbf{w}}_k = \hat{\mathbf{w}}_k^- + \mathbf{K}_k \mathbf{r}_k^-$ and $\mathbf{P}_{\mathbf{w},k} = (\mathbf{I} - \mathbf{K}_k \mathbf{G}_k) \mathbf{P}_{\mathbf{w},k}^-$

Under assumption H_1, the residuals $\mathbf{r}_k$ and the estimated parameters $\hat{\mathbf{w}}_k$ can be expressed as functions of the jump characteristics τ and $\mathbf{\Delta}_\mathbf{w}$. Given the first-order approximation on the measurement equation, the residuals $\mathbf{r}_k$ can be seen as the sum of two terms:

$$\mathbf{r}_k = \mathbf{r}_{k,H_0} + \mathbf{H}_{k,\tau} \mathbf{\Delta}_\mathbf{w} \tag{6}$$

where $\mathbf{r}_{k,H_0}$ are the residuals in the no-jump case, distributed as $\mathcal{N}(\mathbf{0}, \mathbf{P}_{\mathbf{y},k})$ and the second term represents the influence of a jump

Downloaded 02 Jun 2010 to 171.66.16.109. Redistribution subject to ASME license or copyright; see http://www.asme.org/terms/Terms_Use.cfm

$\mathbf{\Delta_w}$ that has occurred at time τ on the residuals at time k.

Similarly, we can split the estimated health parameters in a sum of two terms:

$$\hat{\mathbf{w}}_k = \hat{\mathbf{w}}_{k,H_0} + \mathbf{F}_{k,\tau}\mathbf{\Delta_w} \tag{7}$$

where $\hat{\mathbf{w}}_{k,H_0}$ are the estimated values in the no-jump case and the second term represents the influence of a jump $\mathbf{\Delta_w}$ that has occurred at time τ on the estimated values at time k.

As will be shown in the next section, the detection and estimation of the jump largely rely on the matrices $\mathbf{F}_{k,\tau}$ and $\mathbf{H}_{k,\tau}$. They can be computed from the system models (4) and (5) and the equations of the Kalman filter in Algorithm 1 (see the Appendix for a particular formulation implemented in this study or Ref. [11] for extensive details).

2.3 Event Detection by Means of the Generalized Likelihood Ratio Test. A common method to determine which hypothesis between H_0 and H_1 is true is to use the likelihood ratio test (LRT). In short, it is a statistical test in which a ratio is computed between the maximum probability of a result under two different hypotheses, so that a decision can be made between them based on the value of this ratio (see Ref. [14]). To apply the LRT, prior distributions for τ and $\mathbf{\Delta_w}$ have to be postulated. Moreover, the test does not directly yield estimates of those quantities. These two issues are clearly drawbacks in the present application. As a workaround, the GLRT, described in Ref. [14], is used. This procedure essentially consists in computing the maximum likelihood estimates $\hat{\tau}$ and $\hat{\mathbf{\Delta}}_{\mathbf{w},k}$, assuming that H_1 is true, and then in substituting these values into the usual LRT to decide whether a jump has happened.

Practically, the detection at time k of a hypothetic jump that occurred at time $\tau \leq k$ relies on the log-likelihood ratio

$$l_{k,\tau} = 2\log\frac{p(\mathbf{r}_1,\ldots,\mathbf{r}_k|H_1,\hat{\mathbf{\Delta}}_{\mathbf{w},k})}{p(\mathbf{r}_1,\ldots,\mathbf{r}_k|H_0)} \tag{8}$$

where

- $p(\mathbf{r}_1,\ldots,\mathbf{r}_k|H_1,\hat{\mathbf{\Delta}}_{\mathbf{w},k})$ is the conditional probability of observing the residual history if hypothesis H_1 is true,
- $p(\mathbf{r}_1,\ldots,\mathbf{r}_k|H_0)$ is the conditional probability of observing the residual history if hypothesis H_0 is true, and
- $\hat{\mathbf{\Delta}}_{\mathbf{w},k}$ is the maximum likelihood estimate of the jump,

$$\hat{\mathbf{\Delta}}_{\mathbf{w},k} = \arg\max_{\mathbf{\Delta_w}}\{p(\mathbf{r}_1,\ldots,\mathbf{r}_k|H_1,\mathbf{\Delta_w})\} \tag{9}$$

Since all conditional densities in Eq. (8) are Gaussian, the log-likelihood ratio writes down the following after some algebraic steps:

$$l_{k,\tau} = \mathbf{d}_{k,\tau}^T\mathbf{C}_{k,\tau}^{-1}\mathbf{d}_{k,\tau} \tag{10}$$

where matrix $\mathbf{C}_{k,\tau}$ is deterministic and vector $\mathbf{d}_{k,\tau}$ is a linear combination of the residuals,

$$\mathbf{C}_{k,\tau} = \sum_{j=\tau}^{k}\mathbf{H}_{j,\tau}^T\mathbf{P}_{\mathbf{y},j}^{-1}\mathbf{H}_{j,\tau} \tag{11}$$

$$\mathbf{d}_{k,\tau} = \sum_{j=\tau}^{k}\mathbf{H}_{j,\tau}^T\mathbf{P}_{\mathbf{y},j}^{-1}\mathbf{r}_j \tag{12}$$

Equations (11) and (12) show that the likelihood ratio (Eq. (10)) actually implements a matched filter, i.e., a correlation test between the variations in the residuals and the signature of a jump, represented by $\mathbf{H}_{k,\tau}$.

At each time step k, the likelihood ratio $l_{k,\tau}$ is computed for $\tau = 1,\ldots,k$ to perform the jump detection. Hence, the original implementation of the GLRT algorithm involves a growing bank of matched filters. To keep the problem tractable, the jump detection is restricted to a sliding data window of width M. If the window is sufficiently wide to ensure detection of all important faults, this approximation does not lead to serious difficulties.

So, for $k-M<\tau\leq k$, the likelihood ratio $l_{k,\tau}$ is computed. The value $\hat{\tau}$ that maximizes $l_{k,\tau}$ represents the most likely time at which a jump occurred during the last M time steps. The decision rule to choose between H_0 and H_1 is

$$l_{k,\hat{\tau}} \underset{H_0}{\overset{H_1}{\gtrless}} \eta \tag{13}$$

where η is a threshold value chosen to provide a reasonable tradeoff between false alarms and detection delay.

If hypothesis H_1 is verified at time step k, a jump has occurred at estimated time $\hat{\tau}$, and its maximum likelihood estimate is given by

$$\hat{\mathbf{\Delta}}_{\mathbf{w},k} = \mathbf{C}_{k,\hat{\tau}}^{-1}\mathbf{d}_{k,\hat{\tau}} \tag{14}$$

The latter relation provides a least-squares estimate of the jump $\mathbf{\Delta_w}$, assuming that τ is known and that no prior information is available about the value of the jump. In that case, $\mathbf{C}_{k,\hat{\tau}}^{-1}$ is the error covariance of the estimate $\hat{\mathbf{\Delta}}_{\mathbf{w}}$.

From a computational standpoint, it is interesting to note that recursive relations can be derived for the quantities involved in the GLRT when the detection scheme is limited to a buffer containing the latest M data points. These relations are provided in the Appendix.

2.4 Practical Implementation of the Adaptive Algorithm. Once a jump is detected by the GLRT algorithm, the maximum likelihood estimates $\hat{\tau}$ and $\hat{\mathbf{\Delta}}_{\mathbf{w},k}$ can be used directly to increment the parameters estimated by the Kalman filter,

$$\hat{\mathbf{w}}_k = \hat{\mathbf{w}}_{k,\mathrm{KF}} + \underbrace{(\mathbf{I}-\mathbf{F}_{k,\hat{\tau}})\hat{\mathbf{\Delta}}_{\mathbf{w},k}}_{\delta\hat{\mathbf{w}}_k} \tag{15}$$

where $\hat{\mathbf{w}}_{k,\mathrm{KF}}$ are the Kalman filter estimates, $\mathbf{I}\ \hat{\mathbf{\Delta}}_{\mathbf{w},k}$ is the contribution to the parameters of a jump that occurs at $\hat{\tau}$, and $\mathbf{F}_{k,\hat{\tau}}\hat{\mathbf{\Delta}}_{\mathbf{w},k}$ represents the response of the Kalman filter to the jump prior to its detection.

In some cases, the estimate of the jump may be quite inaccurate. To reflect this degradation in the quality of the estimate, caused by the jump, it is advised in Ref. [15] to increase the covariance matrix of the health parameters accordingly. This rise in parameter covariance results in an increased Kalman gain, i.e., an increased bandwidth. The filter can improve its response to the jump and hence compensate for inaccuracies in $\hat{\tau}$ and $\hat{\mathbf{\Delta}}_{\mathbf{w},k}$. The covariance modification is done through

$$\mathbf{P}_{\mathbf{w},k} = \mathbf{P}_{\mathbf{w},k,\mathrm{KF}} + \underbrace{(\mathbf{I}-\mathbf{F}_{k,\hat{\tau}})^T\mathbf{C}_{k,\hat{\tau}}^{-1}(\mathbf{I}-\mathbf{F}_{k,\hat{\tau}})}_{\delta\mathbf{P}_{\mathbf{w},k}} \tag{16}$$

Engine performance monitoring generally suffers from negative redundancy; it means that the number of health parameters, n, outweighs the number of measurements, m. As a consequence, the system is only partially observable and matrix $\mathbf{C}_{k,\tau}$ is singular. In that case, the pseudoinverse [16] usefully replaces the common inverse. The possible jump directions are then restricted to the observable subspace of the parameter space (see Ref. [17] for further details). Another possibility is to estimate the jump with a Bayesian approach. The introduction of prior knowledge about the jump focuses the search for a solution in a neighborhood of the a priori values. Note that this solution could also be used for fully observable systems in the case where some a priori information about the possible range of values for $\mathbf{\Delta_w}$ is available.

In the implemented GLRT system, the buffer of residuals $\mathbf{d}_{k,\tau}$ is reset immediately after each detection. This is done in order to

Downloaded 02 Jun 2010 to 171.66.16.109. Redistribution subject to ASME license or copyright; see http://www.asme.org/terms/Terms_Use.cfm

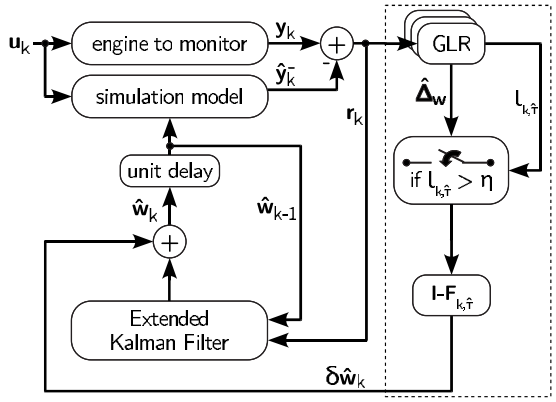


Fig. 2 Integration of the adaptive component with the Kalman filter

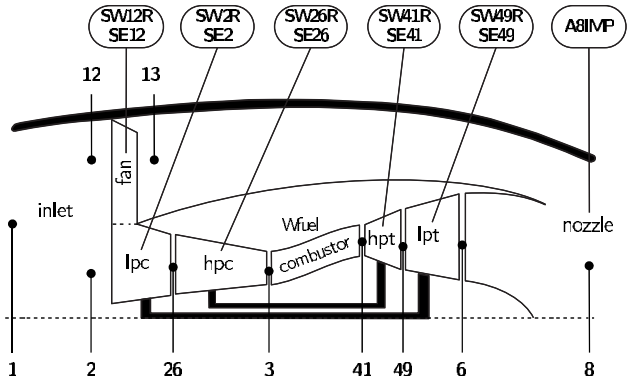


Fig. 3 Turbofan layout with station numbering and health parameter location

avoid possible instabilities due to multiple detections of the same jump, which would lead to "overcompensation." With this modification, the GLRT system can detect several successive jumps.

Two parameters are available to tune the GLRT system: the width M of the sliding window and the threshold η in the hypothesis testing (Eq. (13)). The selection of M is dictated by a trade-off between accurate jump estimation and minimum detection delay. The former suggests choosing M large enough to minimize the uncertainty $\mathbf{C}_{k,\hat{\tau}}^{-1}$ in the estimated jump, while the latter advocates a small-sized buffer. On the other hand, the threshold η is directly related to the probability of false alarms P_F in jump detection,

$$P_F = \int_{\eta}^{\infty} p(l = L|H_0)dL \tag{17}$$

where $p(l=L|H_0)$ is the probability density of $l_{k,\tau}$ conditioned on H_0, which is a chi-squared density with n degrees of freedom (see Ref. [14] for a proof). Specifying an allowable false alarm rate (small, but nonzero) gives the threshold value.

Figure 2 depicts the integration of the adaptive component, which comprises all the elements in the dashed box, with the Kalman filter. For the sake of clarity, only the most relevant data streams are sketched in the diagram. Briefly explained, the adaptive component works as follows:

- The GLR box performs the GLRT in three stages:

1. update of the quantities in the M-sized buffer according to the relations given in the Appendix
2. computation of the likelihood ratio by means of Eq. (10)
3. search for the maximum value of the likelihood ratio

The outputs of the GLR box are the estimated time of occurrence of the jump $\hat{\tau}$ (not represented), the estimated jump $\hat{\mathbf{\Delta}}_{\mathbf{w},k}$, and the maximum value of the likelihood ratio in the buffer $l_{k,\hat{\tau}}$.

- This value is compared with the threshold η in order to determine whether a jump has occurred.
- In case hypothesis H_1 is true, the increment in the parameters $\delta\hat{\mathbf{w}}_k$ due to the jump is computed and added to the Kalman filter estimate, as stated in Eq. (15). At the same time, the covariance matrix of the health parameters is also modified according to Eq. (16).

From a computational viewpoint, the aforementioned operations performed in the adaptive components are roughly equivalent to $M+1$ runs of a linear Kalman filter (i.e., no call to the nonlinear engine model) per time step. Yet, the most demanding part of the whole adaptive algorithm lies in the evaluation of the Jacobian matrix $\mathbf{G}_k$ and in the prediction of the measurements, which involves, in the case of centered differences, $2n+1$ calls to the nonlinear engine model. As a result, the overhead in CPU time needed by the adaptive algorithm is rather limited.

3 Application of the Method

3.1 Engine Layout. The application used as a test-case is a high bypass ratio, mixed-flow turbofan. The engine performance model has been developed within the frame of the OBIDICOTE[2] project and is detailed in Ref. [18]. A schematic of the engine is sketched in Fig. 3 where the location of the 11 health parameters and the station numbering are also indicated. One command variable, which is the fuel flow rate fed in the combustor, is considered here.

The sensor suite selected for diagnosing the engine condition is representative of the instrumentation available on-board contemporary turbofan engines and is detailed in Table 1 where the nominal accuracy of each sensor is also reported.

3.2 Definition of the Test-Cases. Simulated data have been generated to examine how the adaptive algorithm performs. Cruise conditions (Alt=10,668 m, Mach=0.8, and $\Delta T_{\mathrm{ISA}}=0$ K) are assumed. The flight sequence is 5000 s long, and the sampling rate is set to 2 Hz. Gaussian noise, whose magnitude is specified in Table 1, is added to the clean simulated measurements to make them representative of real data.

Engine wear due to normal operation is simulated by linearly drifting values of nearly all health parameters, starting from a healthy engine (all parameters at their nominal values) at $t=0$ s and with the following degradation at the end of the sequence ($t=5000$ s): −0.5% on SW12R, −0.5% on SE12, −0.4% on SW2R, −0.5% on SE2, −1.0% on SW26R, −0.7% on SE26, +0.4% on SW41R, −0.8% on SE41, and −0.5% on SE49. To demonstrate the improvements achieved with the adaptive estimation algorithm, a number of fault cases, summarized in Table 2, are superimposed one at a time to the global performance deterioration. While far from being exhaustive, these cases are representative of typical accidental component faults that can be expected on present turbofans and are added as a step change to engine wear at $t=2500$ s. This library of degradations (both distributed and localized) has been devised within the frame of the OBIDICOTE project too (see Ref. [19]) and has been used in a number of studies.

3.3 Definition of a Figure of Merit. The quality of the estimation performed by the generic diagnosis tool and the adaptive

[2]A Brite/Euram project for on-board identification, diagnosis, and control of turbofan engines.

Downloaded 02 Jun 2010 to 171.66.16.109. Redistribution subject to ASME license or copyright; see http://www.asme.org/terms/Terms_Use.cfm

Table 1 Selected sensor suite (uncertainty is three times the standard deviation)

Label	Uncertainty	Label	Uncertainty
p_{13}^0	±100 Pa	T_{13}^0	±2 K
p_3^0	±5000 Pa	T_3^0	±2 K
N_{lp}	±6 rpm	N_{hp}	±12 rpm
T_6^0	±2 K		

one is assessed in terms of the maximum root mean square error (RMSE) over the last 50 s of the sequence (i.e., over 100 samples),

$$\mathrm{RMSE} = \max\left(\sqrt{\frac{1}{100} \sum_{t=4950\ \mathrm{s}}^{5000\ \mathrm{s}} \left(\frac{\mathbf{w}_t - \hat{\mathbf{w}}_t}{\mathbf{w}^{\mathrm{hl}}} \right)^2} \right) \tag{18}$$

where $\mathbf{w}^{\mathrm{hl}}$ are the nominal values of the health parameters.

Given the stochastic character of the measurement noise, each test-case has been run 20 times. The RMSEs reported in Table 3 are the average values over the 20 runs in order to guarantee that they are statistically representative. A test-case characterized by an averaged maximum RMSE below 0.25% is declared successful, which is indicated by a check mark. This threshold corresponds to roughly three times the standard deviation of the identified health parameters (i.e., the square root of the diagonal terms of the covariance matrix $\mathbf{P}_{\mathbf{w},k}$).

Table 2 List of abrupt component faults

Label	Definition of the fault		Faulty component
a	−1% on SW12R	−0.5% on SE12	Fan
	−0.7% on SW2R	−0.4% on SE2	lpc
b	−1% on SE12		
c	−1% on SW26R	−0.7% on SE26	hpc
d	−1% on SE26		
e	−1% on SW26R		
f	+1% on SW41R		hpt
g	−1% on SW41R	−1% on SE41	
h	−1% on SE41		
i	−1% on SE49		lpt
j	−1% on SW49R	−0.4% on SE49	
k	−1% on SW49R		
l	+1% on SW49R	−0.6% on SE49	
m	+1% on A8IMP		Nozzle
n	−1% on A8IMP		

Table 3 Comparison of the figure of merit obtained with the generic EKF and with the adaptive algorithm (EKF+GLR)

Case	EKF		EKF+GLR	
Wear (**w**)	0.09%	✓	0.10%	✓
w+a	0.50%	-	0.12%	✓
w+b	0.27%	-	0.09%	✓
w+c	0.20%	✓	0.11%	✓
w+d	0.18%	✓	0.13%	✓
w+e	0.32%	-	0.12%	✓
w+f	0.21%	✓	0.09%	✓
w+g	0.43%	-	0.11%	✓
w+h	0.23%	✓	0.10%	✓
w+i	0.20%	✓	0.09%	✓
w+j	0.53%	-	0.57%	-
w+k	0.45%	-	0.09%	✓
w+l	0.40%	-	0.09%	✓
w+m	0.16%	✓	0.11%	✓
w+n	0.34%	-	0.15%	✓

4 Results

Both the generic and the adaptive diagnosis tools have been run on the previously described test-cases. The tuning parameters of the adaptive tool have been set to the following values: a sliding window of width $M=10$ time steps (i.e., 5 s) and a probability of false alarm $P_F=10^{-4}\%$. These settings were found satisfactory for the level of noise and the magnitude of the abrupt faults considered in the reported application.

Figure 4 depicts the tracking of engine wear with the extended Kalman filter. It can be seen that the identified values are in good agreement with the true ones, which is confirmed by a RMSE of 0.09%. This figure underlines the fact that the Kalman filter is able to filter the measurement noise and to give an accurate assessment of the level of deterioration of the gas turbine, provided that the evolution of the health parameters is "sufficiently" smooth.

The tracking of the engine condition with the EKF in the case where accidental fault **a** (fan+lpc) is superimposed to wear is sketched in Fig. 5. It can readily be seen that the Kalman filter is unable to follow the abrupt drift in the performance of the fan and the lpc. This fast variation is indeed not accounted for in the transition model of the health parameters that is blended in the Kalman filter. As a result, the fault is spread over multiple components such as the hpc (SW26R) and the lpt (SE49). Moreover, it can be noticed that several hundreds of seconds are required by the filter to (erroneously) recognize the abrupt fault.

When the adaptive algorithm is applied to the same fault case (wear+**a**), the identification of the health parameters is as shown in Fig. 6. The improvement with respect to the results discussed previously is obvious. First, the abrupt fault is localized on the fan and the lpc, and its magnitude is quite fairly assessed, the drop in SW2R being slightly overestimated. Second, the responsiveness for recognizing the fault has dramatically improved. The examination of Table 4 will show that the accidental event is detected and recognized a few seconds after it has happened. These two points greatly enhance the relevance of the results and provide a detailed insight on the temporal evolution of the engine condition.

Table 3 reports the figure of merit defined by Eq. (18) for the different fault-cases that have been considered in the present study. The first line is related to the case of engine wear (abbreviated **w** in the subsequent lines). For that case of long-time-scale deterioration, the performance of both diagnosis tools is essentially the same. Indeed, as long as the adaptive component does not issue any detection flag, the adaptive algorithm will be confounded with the generic one. This can be clearly seen from the schematic in Fig. 2.

Considering the cases involving the global drift in engine performance and one of the 14 component faults defined in Table 2, it can be seen that the EKF achieves a reasonable identification for a mere 6 cases out of 14. Furthermore, the figure of merit is a measure of the estimation accuracy at the end of the sequence but does not reflect the delay in fault recognition, which has been shown to be quite long from the analysis of Fig. 5.

On the other hand, the adaptive tool succeeds in solving all test-cases but case **w+j**. The figure of merit is roughly the same as for the case of pure engine wear (first line of the table), which hints at the capability of the adaptive component to estimate quite accurately the jump in engine health. The issue of timely recognition of the fault will be discussed in the next paragraph. The misdiagnosis of case **w+j** is due to a lack of observability of the health parameters of the turbines—more specifically the triplet SE41, SE49, and SW49R—with the sensor configuration used here. Figure 7 depicts the evolution of the health parameters of the hot section estimated with the adaptive algorithm. It can be noticed that the fault on SW49R is largely underestimated, while the efficiency drop (SE49) is simply not detected. On top of that, a false alarm on SE41 is issued, which leads to a wrong interpretation of the actual health condition of the engine.

To conclude the analysis of the result, it is worth taking a look

Downloaded 02 Jun 2010 to 171.66.16.109. Redistribution subject to ASME license or copyright; see http://www.asme.org/terms/Terms_Use.cfm

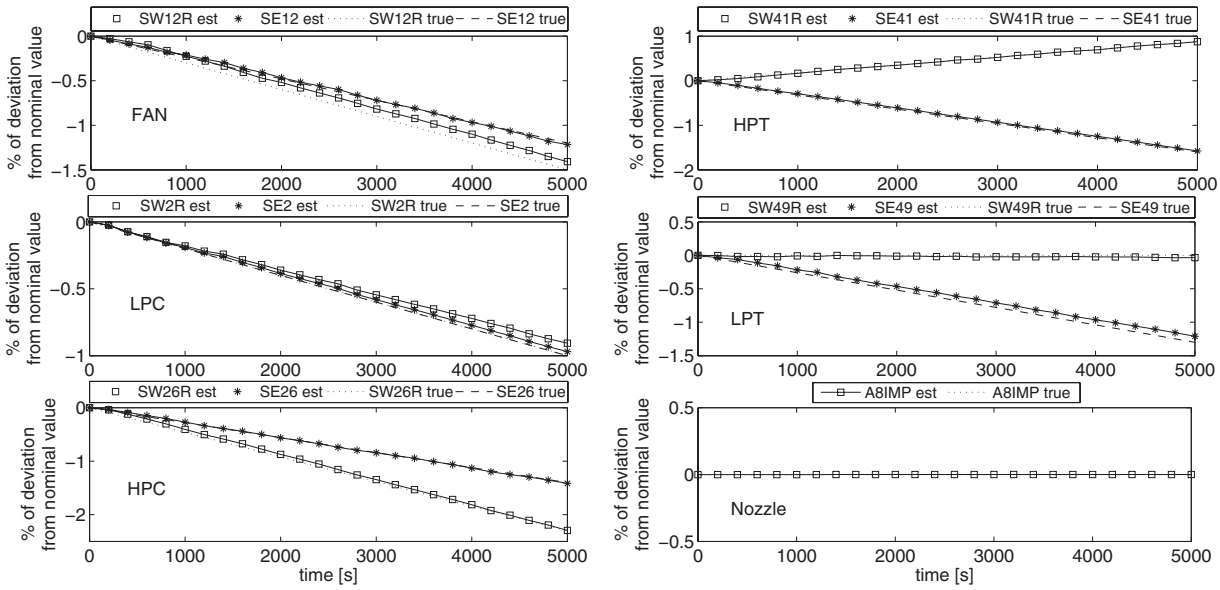


Fig. 4 Tracking of engine wear with the generic diagnosis tool. In the legends, "est" stands for estimated.

at the delay needed by the adaptive algorithm to recognize the fault. Recall that the adaptive component gives access to the time of detection of the jump, k_{det}, defined as the time at which the maximum likelihood ratio in the buffer exceeds the threshold, and to the estimated time of occurrence of the jump, $\hat{\tau}$, which is the time corresponding to the maximum value of the likelihood ratio in the buffer.

The middle column of Table 4 lists the delay between the occurrence of the fault τ_{true} and its detection k_{det} by the GLRT algorithm expressed in number of data samples, which is a more relevant quantity than the detection time itself. It can be noticed that the delay between the true time of occurrence of the fault (which is $\tau_{\text{true}}=2500.5$ s) and the time of detection amounts to a couple of samples. Most of the faults are detected four time steps after they appear. For fault cases $\mathbf{w}+\mathbf{b}$ and $\mathbf{w}+\mathbf{j}$, the delay is slightly longer. This is due to the fact that the signature of these faults on the measurements is somewhat weaker for the other cases. On the contrary, the delay for the hpt faults is a bit shorter since those faults cause a deeper variation in the measurements. As soon as the jump is detected, it is also estimated and subsequently added to the Kalman filter estimate in order to compensate for the rapid drift in the engine health. The estimation of the jump relies on a residual averaged over a few time steps, which provides some attenuation of the measurement noise. Looking at the right column of Table 4, one can notice that the time of occurrence of the jump is fairly well assessed. This probably constitutes a piece of information of secondary matter, but which might be helpful in some cases.

Given the fast detection of the jump, only a fraction of the buffer is actually used. One can thus think about shortening the width of the sliding window to spare memory space and computational time. Yet, the rapid detection of the jump is due to two causes. First, the abrupt fault has been introduced as a pure step (i.e., the full fault occurs in one time step); most rapid deterioration happen, however, over a few seconds or so rather than instantly. Second, we consider a static system so that a modification

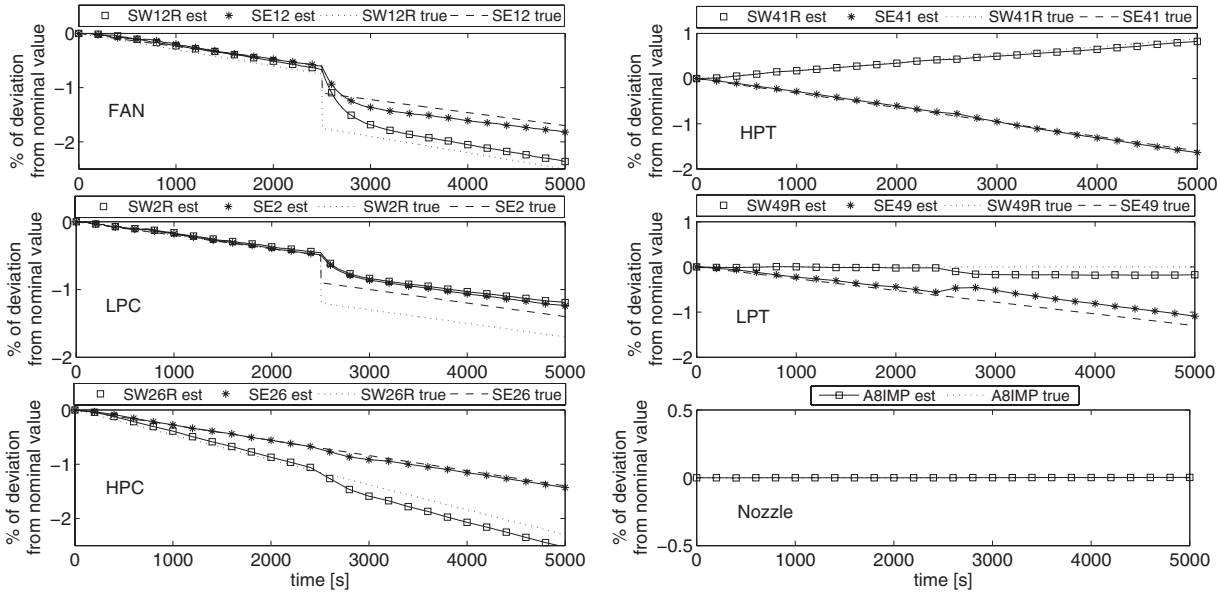


Fig. 5 Tracking of engine wear+fault a with the generic diagnosis tool. In the legends, "est" stands for estimated.

Downloaded 02 Jun 2010 to 171.66.16.109. Redistribution subject to ASME license or copyright; see http://www.asme.org/terms/Terms_Use.cfm

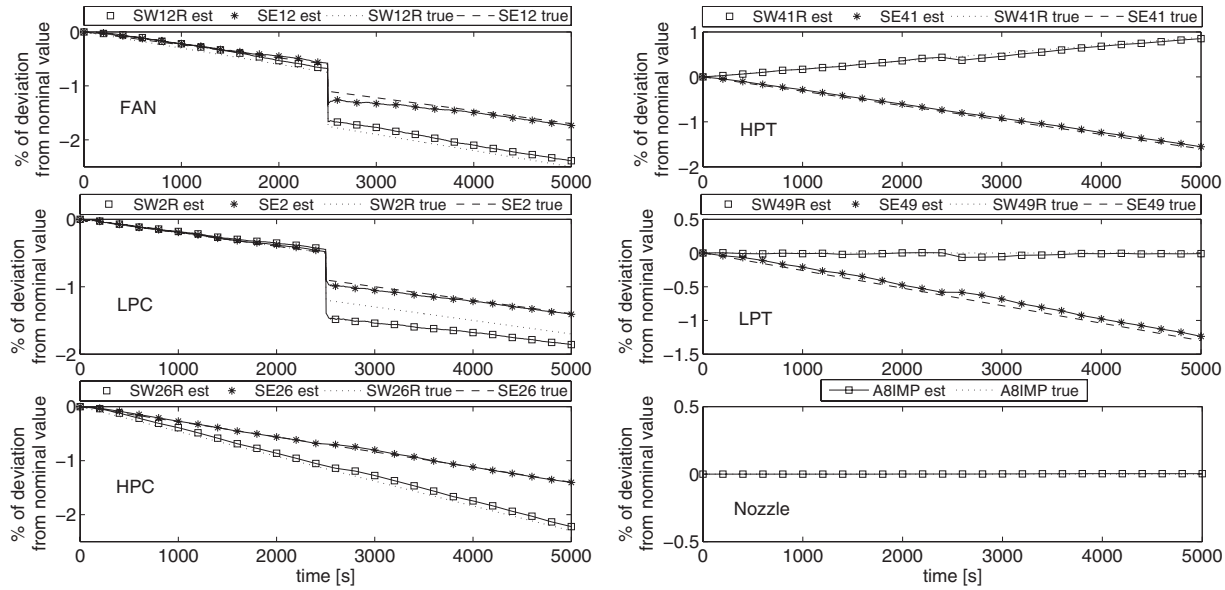


Fig. 6 Tracking of engine wear+fault a with the adaptive algorithm. In the legends, "est" stands for estimated.

in the state of the system instantaneously shows up in the measurements. The length of the buffer should be carefully selected with these two parameters in mind.

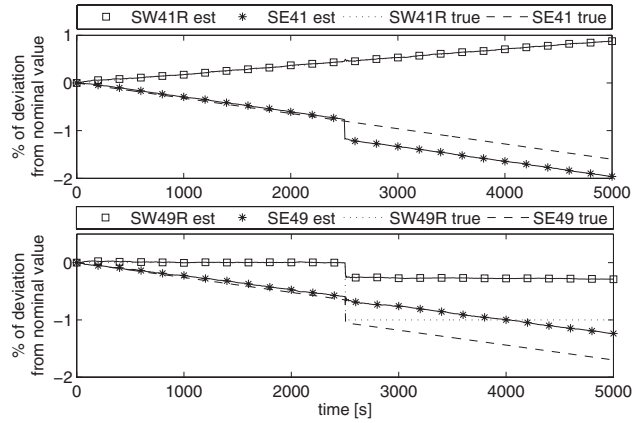


Fig. 7 Tracking of engine wear+fault j with the adaptive algorithm. In the legend, "est" stands for estimated.

Table 4 Detection delay $k_{\text{det}} - \tau_{\text{true}}$ and estimated time of jump $\hat{\tau}_{k_{\text{det}}}$. The true time of jump is $\tau_{\text{true}} = 2500.5$ s.

Case	$k_{\text{det}} - \tau_{\text{true}}$	$\hat{\tau}_{k_{\text{det}}}$
w+a	4	2500.5
w+b	9	2501.5
w+c	4	2500.5
w+d	4	2500.5
w+e	4	2500.5
w+f	2	2500.5
w+g	2	2500.5
w+h	2	2500.5
w+i	4	2500.5
w+j	6	2501
w+k	4	2500.5
w+l	4	2500.5
w+m	4	2500.5
w+n	4	2500.5

5 Discussion

The enhancements in fault recognition and estimation accuracy brought by the adaptive algorithm have been pointed out in the previous section. To complete the analysis of the results, additional issues that may lead to further developments of the proposed methodology are discussed in the following.

The first point concerns the estimation of the jump $\mathbf{\Delta_w}$ in the health parameters. In the present implementation of the adaptive component, $\mathbf{\Delta_w}$ is assumed to be totally free. It would be interesting to replace this unconstrained estimate with a selection of the most likely fault in a bank of predefined events, as in Ref. [5]. The modifications to the GLRT that need to be carried out in that case are described in Ref. [11]. However, this solution requires a great expertise for the definition of the fault library. In turn, it may be restricted to engine manufacturers. Moreover this implementation requires additional fault recognition logic for handling novel fault modes.

A second interesting development of the adaptive diagnosis tool consists in extending the fault coverage to system (and possibly sensor) malfunctions such as stuck bleed valves or mistuned variable stator vanes. These faults typically occur in an abrupt manner so that they could be kept constant in the Kalman filter (by assuming perfect knowledge about them, i.e., a tiny covariance) and be estimated only by the adaptive component in case a jump in the health condition is detected. Sensor biases could be dealt with in a similar fashion.

Information fusion comes to mind as a third axis for future research. Indeed, the adaptive component allows detection and estimation of a rapid deterioration. Once a jump is detected, another diagnosis tool could isolate the fault so that its result is fused with the fault estimated by the GLRT. Information fusion between model-based and data-driven diagnosis tools has already been investigated by the authors in previous publications [20,21] and has shown potential improvement in the assessment of the engine condition.

6 Conclusion

In this contribution, an adaptive algorithm for engine health monitoring has been developed. It combines a Kalman filter, which provides an accurate estimation of the health condition for long-time-scale deterioration (such as engine wear), and an adaptive component, which monitors the residuals and looks for abrupt

Downloaded 02 Jun 2010 to 171.66.16.109. Redistribution subject to ASME license or copyright; see http://www.asme.org/terms/Terms_Use.cfm

changes in the health condition. The adaptive component implements a generalized likelihood ratio test that detects and estimates rapid variations in the engine condition.

The advantages of the proposed approach have been pointed out. First, the performance of the Kalman filter is not degraded for slow evolutions of the engine condition. Second, the adaptive component acts as a fault compensator for the Kalman filter and can handle a variety of fault events. Third, the adaptive component is easily integrated with the generic diagnosis tool, while the increase in computational burden remains limited (about 15% in the present implementation). The improvement in estimation accuracy and fault recognition achieved by the adaptive diagnosis tool with respect to the generic one has been illustrated for a series of typical component fault cases that may occur on a turbofan engine.

Nomenclature

- $\hat{\cdot}$ = estimated value
- A8IMP = nozzle exit area (nominal value: 1.4147 m^2)
- hpc = high pressure compressor
- hpt = high pressure turbine
- k = discrete time index
- lpc = low pressure compressor
- lpt = low pressure turbine
- N = rotational speed
- p_i^0 = total pressure at station i
- SEi = efficiency factor of the component whose entry is located at section i (nominal value: 1.0)
- SWiR = flow capacity factor of the component whose entry is located at section i (nominal value: 1.0)
- T_i^0 = total temperature at station i
- $\mathbf{u}_k$ = actual command parameters
- $\mathbf{w}_k$ = actual but unknown health parameters
- $\mathbf{y}_k$ = observed measurements
- $\mathbf{\Delta_w}$ = unknown abrupt fault
- ϵ_k = measurement noise vector
- v_k = process noise vector
- τ = unknown time of occurrence of the abrupt fault
- $\mathcal{N}(\mathbf{m},\mathbf{R})$ = Gaussian probability density function with mean $\mathbf{m}$ and covariance matrix $\mathbf{R}$

Appendix: Recursive Relations for Computation of the GLRT

Jump detection by means of the GLRT requires that the likelihood ratio $l_{k,\tau}$ (Eq. (10)) be evaluated for all $k-M<\tau\leq k$. The necessary quantities for this calculation can be computed from the following equations:

$$\forall\, \tau \in k-M, k[$$

$$\mathbf{C}_{k,\tau} = \mathbf{C}_{k-1,\tau} + \mathbf{H}_{k,\tau}^T \mathbf{P}_{\mathbf{y},k}^{-1} \mathbf{H}_{k,\tau} \tag{A1}$$

$$\mathbf{d}_{k,\tau} = \mathbf{d}_{k-1,\tau} + \mathbf{H}_{k,\tau}^T \mathbf{P}_{\mathbf{y},k}^{-1} \mathbf{r}_k \tag{A2}$$

$$\mathbf{H}_{k,\tau} = \mathbf{G}_k(\mathbf{I} - \mathbf{F}_{k-1,\tau}) \tag{A3}$$

$$\mathbf{F}_{k,\tau} = \mathbf{F}_{k-1,\tau} + \mathbf{K}_k \mathbf{H}_{k,\tau} \tag{A4}$$

where $\mathbf{I}$ is the identity matrix but also the transition matrix of the health parameters in the application at hand.

For the most recent element in the buffer ($\tau=k$), the quantities are initialized according to

$$\mathbf{C}_{k,k} = \mathbf{G}_k^T \mathbf{P}_{\mathbf{y},k}^{-1} \mathbf{G}_k \tag{A5}$$

$$\mathbf{d}_{k,k} = \mathbf{G}_k^T \mathbf{P}_{\mathbf{y},k}^{-1} \mathbf{r}_k \tag{A6}$$

$$\mathbf{F}_{k,k} = \mathbf{K}_k \mathbf{G}_k \tag{A7}$$

References

[1] Volponi, A. J., 2003, "Foundation of Gas Path Analysis (Part I and II)," *Gas Turbine Condition Monitoring and Fault Diagnosis*, von Karman Institute Lecture Series No. 1, von Karman Institute, Rhode-Saint-Genèse, Belgium.

[2] Li, Y. G., 2002, "Performance-Analysis-Based Gas Turbine Diagnostics: A Review," Proc. Inst. Mech. Eng., Part A, **216**(5), pp. 363–377.

[3] Kalman, R. E., 1960, "A New Approach to Linear Filtering and Prediction Problems. ASME J. Basic Eng., **82**, pp. 35–44.

[4] Provost, M. J., 1994, "The Use of Optimal Estimation Techniques in the Analysis of Gas Turbines," Ph.D. thesis, Cranfield University.

[5] Volponi, A. J., 2003, "Extending Gas Path Analysis Coverage for Other Fault Conditions," *Gas Turbine Condition Monitoring and Fault Diagnosis*, von Karman Institute Lecture Series No. 1, von Karman Institute, Rhode-Saint-Genèse, Belgium.

[6] Mehra, R. K., 1972, "Approaches to Adaptive Filtering," IEEE Trans. Autom. Control, **17**(5), pp. 693–698.

[7] Mehra, R. K., 1970, "On the Identification of Variances and Adaptive Kalman Filtering," IEEE Trans. Autom. Control, **15**(2), pp. 175–184.

[8] Odelson, B., Rajamani, M., and Rawlings, J., 2006, "A New Autocovariance Least-Squares Method for Estimating Noise Covariances," Automatica, **42**, pp. 303–308.

[9] Jazwinski, A. H., 1969, "Adaptive Filtering," Automatica, **5**, pp. 475–485.

[10] Dewallef, P., Léonard, O., and Borguet, S., 2006, "An Adaptive Estimation Algorithm for Aircraft Engine Performance Monitoring," University of Liège, Technical Report No. 06-02.

[11] Willsky, A., and Jones, H., 1974, "A Generalized Likelihood Ratio Approach to State Estimation in Linear Systems Subject to Abrupt Changes," *Proceedings of the IEEE Conference on Decision and Control*, Phoenix, AZ, November, pp. 846–853.

[12] Bensalah, F., and Chaumette, F., 1994, "Real-Time Visual Tracking Using Abrupt Changes Detection," INRIA, Technical Report No. 2425.

[13] Dewallef, P., 2005, "Application of the Kalman Filter to Health Monitoring of Gas Turbine Engines: A Sequential Approach to Robust Diagnosis," Ph.D. thesis, University of Liège.

[14] van Trees, H. L., 1968, *Detection, Estimation and Modulation Theory*, Wiley, New York.

[15] Willsky, A., and Jones, H., 1976, "A Generalized Likelihood Ratio Approach to the Detection and Estimation of Jumps in Linear Systems," IEEE Trans. Autom. Control, **21**(1), pp. 108–112.

[16] Strang, G., 1988, *Linear Algebra and its Applications*, 3rd ed., Brooks-Cole, Pacific Grove, CA.

[17] Borguet, S., and Léonard, O., 2008, "A Study on Sensor Selection for Efficient Jet Engine Health Monitoring," *Proceedings of the 12th International Symposium on Transport Phenomena and Dynamics of Rotating Machinery*, Honolulu, HI, February, Paper No. ISROMAC-2008-20072.

[18] Stamatis, A., Mathioudakis, K., Ruiz, J., and Curnock, B., 2001, "Real-Time Engine Model Implementation for Adaptive Control and Performance Monitoring of Large Civil Turbofans," ASME Paper No. 2001-GT-0362.

[19] Curnock, B., 2000, "Obidicote Project—Work Package 4: Steady-State Test Cases," Rolls-Royce PLc, Technical Report No. DNS62433.

[20] Dewallef, P., Romessis, C., Léonard, O., and Mathioudakis, K., 2006, "Combining Classification Techniques With Kalman Filters for Aircraft Engine Diagnostics," ASME J. Eng. Gas Turbines Power, **128**(2), pp. 281–287.

[21] Borguet, S., and Léonard, O., 2007, "Coupling Principal Component Analysis and Kalman Filter Algorithms for On-Line Aircraft Engine Diagnostics," *Proceedings of the 18th International Symposium on Air Breathing Engines*, Beijing, China, Sept., Paper No. ISABE-2007-1275.

Downloaded 02 Jun 2010 to 171.66.16.109. Redistribution subject to ASME license or copyright; see http://www.asme.org/terms/Terms_Use.cfm

Cyclic Carbonation Calcination Studies of Limestone and Dolomite for CO_2 Separation From Combustion Flue Gases

Sivalingam Senthoorselvan[1]
e-mail: sivalingam@es.mw.tum.de

Stephan Gleis

Spliethoff Hartmut

Lehrstuhl Energiesysteme,
Technische Universität München (TUM),
Boltzsmannstrasse 15,
85748 Garching, Germany

Patrik Yrjas

Mikko Hupa

Combustion and Materials Chemistry,
Åbo Akademi Process Chemistry Centre,
Biskopsgatan 8,
FI-20500 Åbo, Finland

Naturally occurring limestone and dolomite samples, originating from different geographical locations, were tested as potential sorbents for carbonation/calcination based CO_2 capture from combustion flue gases. Samples have been studied in a thermogravimetric analyzer under simulated flue gas conditions at three calcination temperatures, viz., 750°C, 875°C, and 930°C for four carbonation calcination reaction (CCR) cycles. The dolomite sample exhibited the highest rate of carbonation than the tested limestones. At the third cycle, its CO_2 capture capacity per kilogram of the sample was nearly equal to that of Gotland, the highest reacting limestone tested. At the fourth cycle it surpassed Gotland, despite the fact that the $CaCO_3$ content of the Sibbo dolomite was only 2/3 of that of the Gotland. Decay coefficients were calculated by a curve fitting exercise and its value is lowest for the Sibbo dolomite. That means, most probably its capture capacity per kilogram of the sample would remain higher, well beyond the fourth cycle. There was a strong correlation between the calcination temperature, the specific surface area of the calcined samples, and the degree of carbonation. It was observed that the higher the calcination temperature, the lower the sorbent reactivity. The Brunauer–Emmett–Teller measurements and scanning electron microscope images provided quantitative and qualitative evidences to prove this. For a given limestone/dolomite sample, sorbent's CO_2 capture capacity depended on the number of CCR cycles and the calcination temperature. In a CCR loop, if the sorbent is utilized only for a certain small number of cycles (<20), the CO_2 capture capacity could be increased by lowering the calcination temperature. According to the equilibrium thermodynamics, the CO_2 partial pressure in the calciner should be lowered to lower the calcination temperature. This can be achieved by additional steam supply into the calciner. Steam could then be condensed in an external condenser to single out the CO_2 stream from the exit gas mixture of the calciner. A calciner design based on this concept is illustrated. [DOI: 10.1115/1.2969090]

Keywords: CO_2 separation, limestone and dolomite, carbonation, calcination

1 Introduction

Fossil fuels continue to dominate in the global energy mix despite its adverse effects on the environment and climate. This has caused the atmospheric concentration of CO_2, a major contributor to the green house effect, to increase from 280 ppm before the industrial revolution to ~365 ppm today. About one-third of all anthropogenic CO_2 emissions are from point sources, e.g., electric utility plants. Separation of CO_2 from the point sources and permanently storing it into suitable geological formations can be a major mitigation step for climate change [1] that would justify the continued utilization of fossil fuels for a foreseeable future power generation. On the other hand it is generally accepted that the cost associated with the separation of CO_2 from the flue gases introduces the largest economic penalty [2] to this mitigation option. For the existing combustion systems, the only proven commercially available technology to separate CO_2 is based on amine-based absorption system. However, this technology introduces severe efficiency penalties and added costs, which justify a range of emerging approaches. One of those approaches involves the separation of CO_2 at high temperatures (600–700°C) using carbonation reaction of CaO (Eq. (1)) [3]. The exothermic carbonation reaction is given in Eq. (1).

$$CaO(s) + CO_2(g) \rightarrow CaCO_3(s) \quad \Delta H = -178 \text{ kJ/mol} \qquad (1)$$

Once CaO has reached its ultimate conversion of $CaCO_3$, it can thermally be regenerated to CaO and CO_2 by heating $CaCO_3$ beyond the calcination temperature. The endothermic calcination reaction is given below:

$$CaCO_3(s) \rightarrow CaO(s) + CO_2(g) \quad \Delta H = +178 \text{ kJ/mol} \qquad (2)$$

The carbonation calcination reaction (CCR) scheme, based on reactions (1) and (2), alternates carbonations and calcinations over multiple cycles to capture CO_2 from flue gases. There are a number of advantages in this CCR based CO_2 capture with $CaCO_3$ as a sorbent material.

(a) Both carbonation and calcination reactions take place at high temperatures, essentially above 600°C, enabling the effective recovery of calcination energy in the carbonator. Nevertheless, at low temperature systems, the heat delivered to the sorbent regeneration cannot be recovered in a steam cycle.
(b) The CCR of the $CaO/CaCO_3$ system does not require pressurized conditions unlike the other sorption processes that need high pressures and/or low temperatures to en-

[1]Corresponding author.

Contributed by the International Gas Turbine Institute of ASME for publication in the JOURNAL OF ENGINEERING FOR GAS TURBINES AND POWER. Manuscript received April 9, 2008; final manuscript received April 15, 2008; published online October 14, 2008. Review conducted by Dilip R. Ballal. Paper presented at the ASME Turbo Expo 2008: Land, Sea and Air (GT2008), Berlin, Germany, June 9–13, 2008.

Copyright © 2009 by ASME

Downloaded 02 Jun 2010 to 171.66.16.109. Redistribution subject to ASME license or copyright; see http://www.asme.org/terms/Terms_Use.cfm

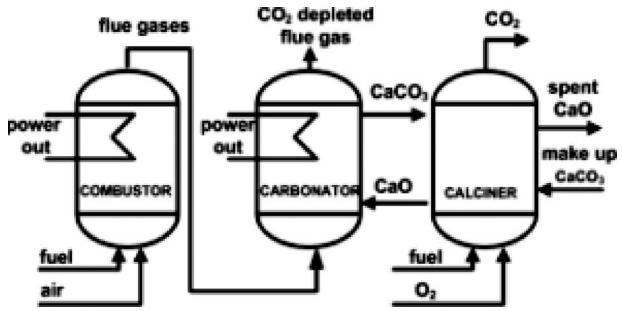


Fig. 1 CO_2 capture based on CCR integrated into a combustion process

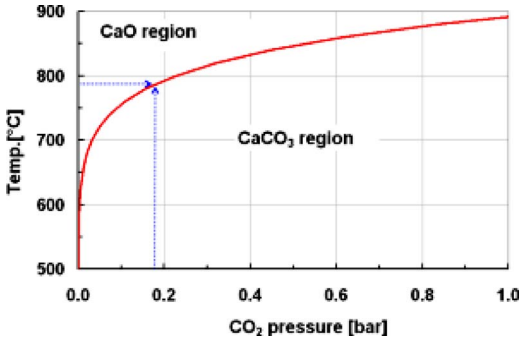


Fig. 2 Equilibrium partial pressure of CO_2 plotted against the temperature as obtained by thermodynamic calculations

hance the sorption efficiency [4]. Furthermore the carbonation temperature of CaO fits well in the domain of flue gas exit temperatures especially from that of the circulating fluidized bed (FB) based combustion systems. Moreover the fast reaction rate of CaO at temperatures above 600°C allows compact reactor designs [5].

(c) The sorption capacity of CaO is very high when compared with other processes. Under ideal conditions, the sorption capacities of monoethanolamine (MEA), silica gel, and activated carbon are 60 g, 13.2 g, and 88 g of CO_2/kg, respectively. In contrast, CaO-based process would capture 393 g of CO_2/kg, assuming a 50% conversion of CaO over repeated cycles [4].

(d) The high availability of $CaCO_3$ in nature as limestone and dolomite, its well geographical distribution on earth, and its low cost [6] allow this capture process to be implemented all over the world including fast developing countries such as China and India.

The CCR based sorption process, integrated with a combustion system, is illustrated in Fig. 1. Fuel and air mixture is combusted in the combustor, typically using a FB system. The flue gases from the combustor, at 650°C, pass through another FB called carbonator, where CO_2 reacts with CaO producing $CaCO_3$. Thus the CO_2 concentration in the flue gases is reduced to very low level. Equation (1) is an exothermic reaction, such that a substantial portion of the total power output is produced in this step besides that in the combustor. The carbonated sorbent ($CaCO_3$) then led to the third FB called calciner, where it is thermally regenerated to CaO and CO_2 at ~900°C. The required energy for the endothermic thermal regeneration process can either be supplied directly from the combustion of the same fuel in pure oxygen or by means of indirect heat transfer from the combustion chamber. The reason for using oxygen in the former case, instead of air, is to produce a pure CO_2 stream without air N_2 at the exit of the calciner. The sorbent is circulated between the carbonator and calciner while adding make up $CaCO_3$ to the calciner to replace spent CaO.

Spreadsheet calculations of mass and energy balance for the process in Fig. 1 showed that the fuel needed in the calciner is 1/3 of the fuel for the whole system. That means, oxygen requirement for this process is 1/3 of that of a stand alone oxyfuel process giving the same power output. Moreover, the capture cost with respect to the oxyfuel reference case is also reduced because of additional power extracted from the capture component itself (the carbonator) [7] in addition to reduced O_2 supply.

The CCR based sorption process can also be used in gasification of solids as a precombustion CO_2 capture technique. Lime enhanced gasification of solids (LEGSs) is a steam enhanced gasification process combined with CO_2 sorption. The LEGS process consists of a LEGS reactor and a regeneration unit. Hydrogen rich gas is generated in LEGS reactor from carbonaceous fuel. A simplified LEGS reaction equation neglecting other side reactions is as follows:

$$\text{fuel} + a\text{CaO} + b\text{H}_2\text{O} \rightarrow x\text{H}_2 + (a-z)\text{CaCO}_3 + y\text{C} + z\text{CaS} \quad (3)$$

In addition to the main reactions of steam reforming in Eq. (3), water gas shift reaction, CO_2 absorption, and capture of sulfur by CaO are also integrated. Exothermic CO_2 absorption, endothermic steam reforming, and slightly exothermic gasification reactions can be adjusted to minimize energy losses by a simple reactor design operated below 800°C. Apart from the production of hydrogen rich gas, a solid product consisting of $CaCO_3$, CaO, char, ash, and CaS is also produced during LEGS with coal. This solid product is separated from the gas and processed in a regenerator where CO_2 laden sorbent is regenerated and a high purity CO_2 stream is produced [8]. The generalized reaction equation is as follows:

$$(a-z)\text{CaCO}_3 + y\text{C} + z\text{CaS} + m\text{O}_2 \rightarrow (a-z)\text{CaO} + z\text{CaSO}_4 + (a-z+y)\text{CO}_2 \quad (4)$$

Figure 2 shows the thermodynamic relationship of the equilibrium partial pressure of CO_2, calculated by using HSC CHEMISTRY 5.0 software from Outokumpu Research Oy, Finland, as a function of the calcination temperature of the $CaO/CaCO_3$ system. The plot shows that, at a given temperature, a partial pressure of CO_2 (P_{CO2}) higher than equilibrium pressure (P_{eq}) favors carbonation and vice versa. For example, P_{eq} at 792°C is 0.2 bar (in Fig. 2 the point is indicated by arrows). Hence, at 792°C, calcination would be favored if the actual partial pressure of CO_2 were lower than 0.2 bar. On the other hand calcination at a P_{CO2} of 0.2 bar can be induced by increasing the temperature beyond 792°C.

However, there are a number of critical issues of the CCR based processes under investigation. Those are how fast and to what extent the desired carbonation and calcination reactions take place under process conditions and how these rate parameters vary in the subsequent cycles. Several studies on the reversibility of the carbonation/calcination reaction have shown that the recarbonation is far from reversible in practice [9]. Furthermore, the decay in maximum carbonation capacity with increasing number of cycles is a common feature, irrespective of limestone type and process conditions. The capture capacity decreases dramatically in the first 20 cycles and beyond that it tends to stabilize with a residual conversion of ~8 mol % for up to 500 cycles [10]. Another study explains the reasons for the sorbent deactivation as grain growth, limited diffusion of CO_2 through the $CaCO_3$ product layer, pore closure, and an overall shrinkage of the particle. All these factors play a role in limiting the maximum carbonation conversions [11].

It is evident that the reactivity of the naturally occurring carbonates decays drastically with increasing number of carbonation/calcination cycles. In a CCR loop, sorbent can either be utilized

Downloaded 02 Jun 2010 to 171.66.16.109. Redistribution subject to ASME license or copyright; see http://www.asme.org/terms/Terms_Use.cfm

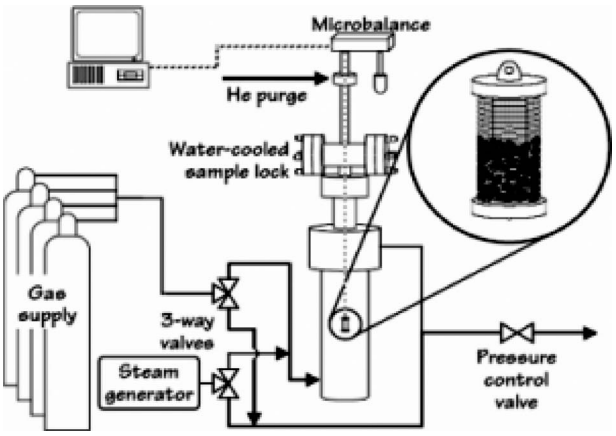


Fig. 3 TGA instrument used for the experiments with magnified sample holder

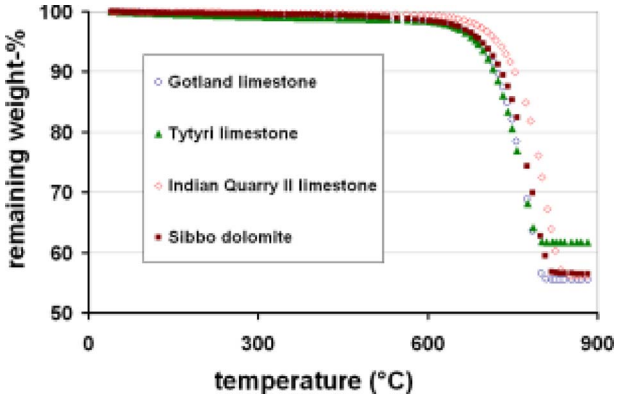


Fig. 4 Decomposition curves of the samples obtained by DTA coupled with TGA

for a maximum number of cycles (100 or more) or for a certain limited number of cycles (10–20). Sustaining the sorption capacity in the former case requires a huge reactor with decaying sorbents while the latter needs a relatively small reactor with large makeups. It is viable to deploy large makeup flows with naturally occurring $CaCO_3$ since it is cheap and abundant in nature.

In this work we have studied naturally occurring unique samples of limestone and dolomite from various geographical locations in a thermogravimetric analyzer (TGA). In a CCR based CO_2 capture scheme, we focused on the ways of sustaining the sorption capacity of sorbents by limiting the number of CCR cycles and varying calcination temperatures from 750°C to 930°C. Data gathered in this study could be useful in optimizing the operating conditions of this process, especially the calciner operating temperatures.

2 Experimental Methods

There were three limestone samples and a dolomite used for all the experiments. The Gotland limestone is from Sothern Sweden. The Tytyri limestone and Sibbo dolomite are from two different places in Finland and the particle sizes were between 120 μm and 180 μm. The third limestone named as Indian Quarry II originated from Ariyalur District, southern India, grounded, and sieved in the range 129–150 μm.

The carbonate contents of the samples were measured using differential thermal analyzer (DTA) model SDT Q600 Version 8.3, which is also coupled with thermogravimetric analyzer. The thermogravimetric measurements were the main interest in these tests. 10–20 mg of each sample, which had been grounded to a fine powder to avoid popping out of the sample holder during heat up, was transferred into a platinum holder. A heating rate of 20°C/min with a purge gas flow of 100 ml/min, 100% N_2 was set. The analyzer was run until the sample reached 1000°C.

The cyclic CCR studies were performed in a TGA, which is schematically illustrated in Fig. 3. The reactor is electrically heated with a heated section of 24.5 cm in height. It was constructed of Incoloy 800 and lined with quartz glass to minimize the risk of corrosion. The inner diameter of the quartz glass tube was 19 mm. The desired gas mixture of 2 l/min is supplied via mass flow controllers. This gas stream is preheated in the lower sections of the reactor chamber. A purge gas flow of (inert gas, usually helium) 0.4 l/min is supplied from the top of the reactor to protect the balance from corrosive gases.

The cylindrical sample holder was made with a fine mesh of Incoloy 800. The sample is placed in the shell between an inner core and the outer net, forming an ~1 mm sample layer. The outer diameter of the sample holder was 10 mm and the length was 20 mm. Once the desired conditions (temperature and gas composition) are established in the reactor, the sample holder is lowered into the reaction chamber. The weight of the sample and the temperature in the reaction chamber are recorded. The sample is weighed with an external balance before and after each run to verify the readings from TGA, which gives out a weight signal down to 10^{-5} g.

In all TGA runs, the carbonation conditions were kept unchanged at 650°C isothermal atmospheric gas flow of 20% CO_2 and 80% N_2 and carbonation time of 500 s. The temperature was chosen according to the $CaCO_3$ equilibrium data and from literature [10–12] as an optimum for the carbonation reaction. Flue gas CO_2 concentration would hardly ever be more than 20% for any type of fuel combusted in air. The calcination occurred in a 100% N_2 environment and the temperatures were changed to 930°C, 875°C, or 750°C. In addition to this Gotland was also calcined at 800°C. In each run, the CCR cycles were repeated for four times.

The $CaCO_3$ content (wt %) of samples can be calculated according to the stoichiometry of Eq. (2) and by knowing the initial and final weights (m_i and m_f) during the first calcination. In Eq. (5), m_s is the sample weight (m_s is equal to or greater than m_i depending on the moisture content of the respective sample).

$$\text{carbonate content} = \frac{(m_i - m_f)}{M_{CO_2}} \frac{M_{CaCO_3}}{m_s} \times 100 \tag{5}$$

The degree of CaO (mol %) into $CaCO_3$ conversion achieved (C_n) during a certain time interval between t_n and t_{n+1} can be calculated according to the stoichiometry of Eq. (1) and knowing weights of samples m_n and m_{n+1} at t_n and t_{n+1}, respectively. The amount of total conversion of CaO mol % to $CaCO_3$ during the carbonation cycle can also be calculated by integrating Eq. (6) for the whole carbonation period.

$$C_n = \frac{(m_{n+1} - m_n)}{(m_i - m_f)} \times 100 \tag{6}$$

Surface and internal textures of the raw calcined and carbonated samples were analyzed using scanning electron microscope (SEM). Two sets of samples were prepared for the SEM using epoxy resin and a carbon tape placed on an aluminum plate. The latter was used to see the internal structures by crushing the samples between two plates before placing on the carbon tape. The Brunauer–Emmett–Teller (BET) specific surface area analysis was also performed to measure the samples' specific surface areas. Carlo Erba Sorptomatic 1900 apparatus was used in calculating the surface areas of the samples before and after the calcination.

3 Results and Discussion

Figure 4 shows the decomposition curves of the samples obtained by thermogravimetric measurements in DTA cum TGA ana-

Downloaded 02 Jun 2010 to 171.66.16.109. Redistribution subject to ASME license or copyright; see http://www.asme.org/terms/Terms_Use.cfm

Table 1 Samples' particle size and its calculated carbonate content using data from DTA and TGA

Sample name	Particle size (μm)	Carbonate content
Gotland limestone	125–180	97.52
Tytyri limestone	125–180	84.25
Indian Quarry II	129–150	98.97
Sibbo dolomite	125–180	-

lyzer. The normalized weight percentages (the percentage of the measured weight to the initial weight of the sample) of the samples were plotted against the increasing temperature. The Tytyri limestone contained the lowest carbonate amount among them. Table 1 shows the calculated $CaCO_3$ contents. Gotland and Indian Quarry II have more than 95% of $CaCO_3$ while Tytyri contains just less than 85%.

It was not possible to do the same calculation for the Sibbo dolomite since it also contains $MgCO_3$. Though $MgCO_3$ decomposes at low temperatures, there was no clear distinction observed between $MgCO_3$ and $CaCO_3$ decomposition in Fig. 4. Dolomite $MgCO_3 \cdot CaCO_3$ breaks up to separate molecules ($MgCO_3$ and $CaCO_3$) at about 750°C. When breaking up, $MgCO_3$ calcines immediately. $CaCO_3$ also started to calcine at 750°C since there is no CO_2 in the system. Therefore the calcination data obtained in this case had no clue about the amount of $CaCO_3$ present in the sample.

The carbonate contents of the samples were also calculated using the TGA data for all runs and averaged values were compared with the values obtained from DTA, as tabulated in Table 2. Both values tallied very closely. DTA cum TGA values seemed higher than TGA, perhaps due to the higher calcination temperature of 1000°C used. The Sibbo dolomite contains 61.63 wt % of $CaCO_3$ as calculated by TGA data.

Figure 5 shows the conversion of CaO (mol %) to $CaCO_3$ of the Gotland sample for four consequent CCR cycles at which the samples were calcined at 930°C, 875°C, 800°C, and 750°C. The conversion of CaO mol % declined steadily with the number of cycles for all four calcination temperatures.

The higher the calcination temperatures, the lower the conversion. The conversion differences were less at low calcination temperatures of 750°C and 800°C along the number of cycles. However, the differences were significant between 800°C and 875°C except for the first cycle. The total conversions dramatically decayed with increasing number of cycles when the calcination temperature is 930°C. A similar trend was also observed with the rest of the samples.

The calcination rates were calculated for the Gotland during the first cycle at varying temperatures of 930°C, 875°C, 800°C, and 750°C and plotted in Fig. 6. It is clear that the higher the calcination temperature, the higher the calcination rate. The rate of calcination was almost the same at temperatures of 930°C and 875°C and the complete calcination was achieved within 200 s. Observed equal calcination rates may be due to the absence of CO_2 backpressure, which would be necessary to control the con-

Table 2 Comparison of calculated carbonate content by TGA experiments with that of the DTA and TGA

Sample name	Carbonate content calculated by TGA data	Calculated carbonate content by DTA cum TGA data
Gotland	94.64	97.52
Sibbo dolomite	61.63	-
IndianQuarry II	93.28	98.97
Tytyri	80.42	84.25

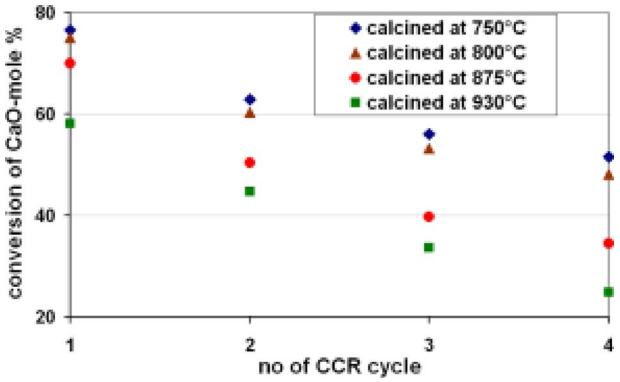


Fig. 5 Gotland limestone conversion of CaO (mol %) to $CaCO_3$ is plotted as a function of the number of cycles for a range of calcination temperatures from 750°C to 930°C

version rate of $CaCO_3$ into CaO beyond a certain temperature, e.g., 875°C. At 800°C, it took more than 400 s to fully decompose into CaO, which was double the time of that at 875°C. The calcination was very slow at 750°C and a complete conversion of $CaCO_3$ to CaO was reached at about 1400 s. At temperatures of 800°C and 750°C the calcination rates were slow, giving high total carbonation (CaO to $CaCO_3$) conversions. At 875°C and 930°C, the carbonation conversion was influenced by the temperature while the calcination rate was not.

The CaO to $CaCO_3$ conversions for all the samples calcined at 875°C are shown in Fig. 7. The Tytyri limestone exhibited the lowest conversion among other samples and along the number of cycles. Gotland and Indian Quarry II gave good conversions, more than 50 mol %, at first two cycles and then decayed faster to ~35 mol % at the fourth cycle. Contrary to all the limestones, the Sibbo dolomite reached the highest conversion of about 80 mol % at the first cycle and decayed relatively slowly by reaching 53 mol % during the fourth cycle. It should be noted that the $CaCO_3$ content of the Sibbo dolomite was 61 wt %, which was only 2/3 of that of the other limestones except for Tytyri.

Figure 8 shows the grams of CO_2 captured per kilogram of the parent sample along the number of CCR cycles. An interesting observation with the Sibbo dolomite was that at the second cycle it equalized to the Indian Quarry II's capture capacity and at the third cycle to that of the Gotland. It is clear at the fourth cycle that the Sibbo dolomite captured more CO_2 than Indian Quarry II and Gotland. It is likely that beyond the fourth cycle, Sibbo dolomite's capture capacity would remain higher than all tested limestones. It

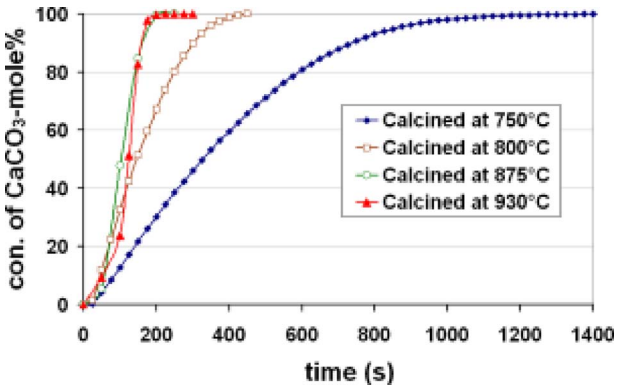


Fig. 6 Gotland limestone calcination ($CaCO_3$ to CaO conversion) rate during the first cycle for a range of calcination temperatures from 750°C to 930°C

Downloaded 02 Jun 2010 to 171.66.16.109. Redistribution subject to ASME license or copyright; see http://www.asme.org/terms/Terms_Use.cfm

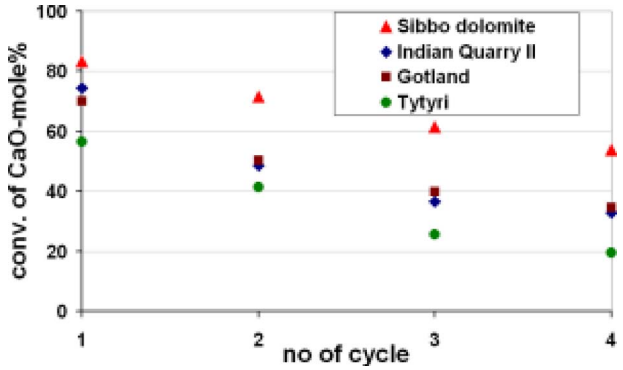


Fig. 7 Conversion of CaO (mol %) into $CaCO_3$ plotted as a function of the number of cycles for all four samples; the calcination temperature was 875°C

could be of great interest to know how many cycles this trend would prevail and to use such data to quantify the additional gains of using the Sibbo dolomite instead of the limestone in CCR loops.

The rate of carbonation is an important design parameter for the CCR based systems. Figure 9 shows the carbonation rate curves during the first cycle of all four samples tested. It can be observed that there is a fast reaction phase followed by a dramatic rate shift to a slow reaction phase. The fast reaction regime was completed within 100 s of carbonation and then it got shifted to a slow reaction phase said to be diffusion controlled. Sibbo dolomite's carbonation rate was the highest and the Tytyri was the lowest.

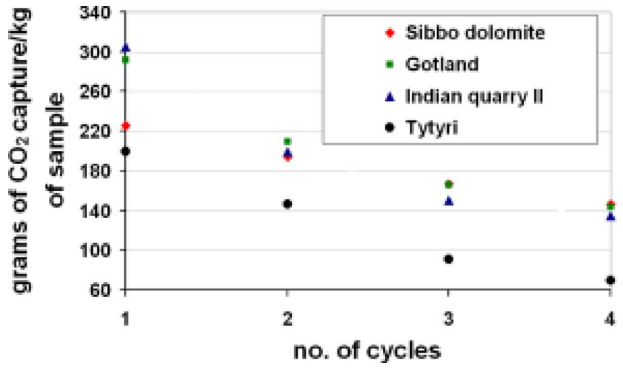


Fig. 8 CO_2 captured in grams per kilogram of parent samples plotted against the number of cycles; the calcination temperature was 875°C

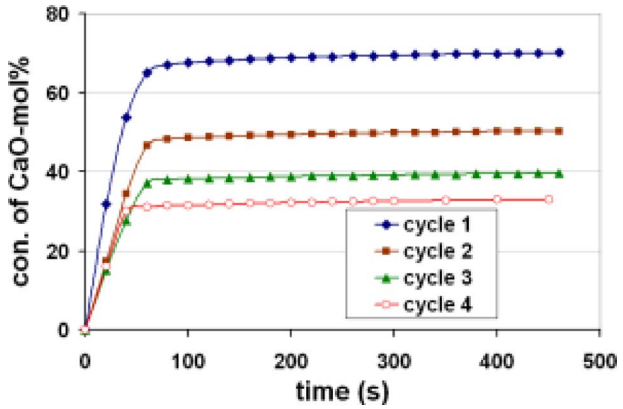


Fig. 9 Conversion of CaO (mol %) to $CaCO_3$ rates plotted during the first cycle for all four samples calcined at 875°C

Table 3 Decay coefficient *k* values calculated for Eq. (7)

k value	Gotland	Tytyri	Ind. Qua.	Sibbo
750°C calcination	0.22	0.24	0.24	0.1
930°C calcination	0.44	0.52	0.59	0.28

The other two limestones were also fairly highly reactive as dolomite. However, our interest is on the fast reaction regime occurs within 100 s, that determining the required volume of a carbonator.

Several semiempirical formulas were suggested in literature for the sorbent decay with increasing number of CCR cycles. Many of them are meant for a large number of cycles where the sorbent decayed to a residual conversion for, e.g., 8–10 CaO mol %. After that the conversion remained constant for as many as 500 cycles [10]. However, for a certain limited number of cycles, as in our case, it was proposed [12] that the decay of the sorbent activity was dependent on its conversion itself; i.e., the decay was slower at a lower conversion (CaO to $CaCO_3$) and vice versa. With the assumption that the rate of the decay is proportional to conversion, Eq. (7) was derived:

$$\alpha_N = \alpha_{N-1}(1 - k\alpha_{N-1}) \tag{7}$$

The k is the coefficient of decay and its values for the two different calcination temperatures of 750°C and 930°C were calculated by curve fitting exercise and were tabulated in Table 3. For the 750°C calcination, limestones' k values were smaller and almost the same, which means a slow and similar decaying rates at low temperature calcinations. In contrary, at a higher calcination temperature, the decaying rates were higher and different from each other. At 930°C calcination, the Indian Quarry II limestone decayed at the fastest rate despite its high initial conversion while the Tytyri showed a low rate regardless of its low initial conversion. The Sibbo dolomite had the lowest decaying rate in both temperatures and its decay rate at the highest calcination temperature was nearly the same as that of the limestones at low temperature (750°C).

The calculated conversions (CaO in mol % to $CaCO_3$) and the measured ones were plotted against each other in Fig. 10. The deviations seemed to confine within ±10%. Overall, the predictions were in good agreement with measured values while the best fits were observed at higher conversions, i.e., at low calcination temperatures, except the Tytyri at the first cycle. At 930°C calcinations, Sibbo dolomite conversions were overpredicted for the second and fourth cycles.

It is obvious that the low calcination temperature led to a high CaO to $CaCO_3$ conversion for all tested samples. It could be due to a slow release of CO_2 from $CaCO_3$, which left behind a CaO

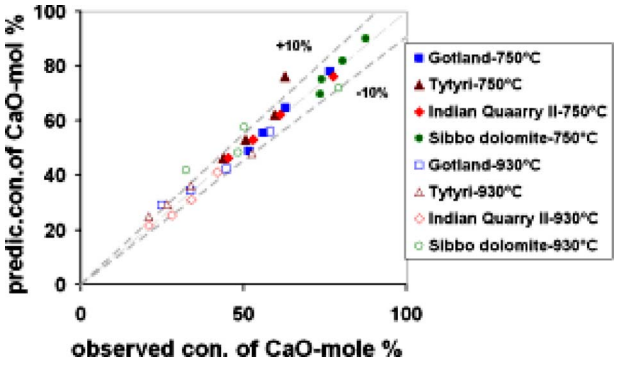


Fig. 10 Measured and predicted CaO (mol %) to $CaCO_3$ conversions by Eq. (7) for two different calcination temperatures of 750°C and 930°C; ±10% margins were marked

Downloaded 02 Jun 2010 to 171.66.16.109. Redistribution subject to ASME license or copyright; see http://www.asme.org/terms/Terms_Use.cfm

Table 4 BET surface areas of the selected samples

Sample name	Calcined at 750°C (m^2/g)	Calcined at 875°C (m^2/g)	Raw samp. (m^2/g)
Gotland	6.032	4.980	0.027
Sibbo dolom.	26.925	22.753	0.030

structure with a high surface area. The high surface area may be directly responsible for the enhanced reactivity. In order to prove this concept the samples from Gotland and Sibbo dolomites, fresh and once calcined at 750°C and 875°C, were sent for BET surface analysis. The results are in Table 4.

The BET surface areas of fresh and calcined samples of Gotland and Sibbo dolomites, along with the respective conversion (CaO in mol % to $CaCO_3$), are plotted in Fig. 11. The BET surface areas of the calcined samples were 200 times that of the fresh Gotland and more than 750 times that of the fresh Sibbo dolomite. Moreover, the higher the calcination temperatures, the lower the BET surface area. A slow release of CO_2 at low temperature produced a higher BET surface area. The calcined Sibbo dolomite showed nearly five times higher BET surface area than that of the Gotland for the same calcination conditions. Furthermore the calculated BET surface areas per mole CaO of the calcined samples at 875°C and 750°C of Sibbo were 3735 m^2/mol and 4420 m^2/mol CaO and that of the Gotland were 511 m^2/mol and 619 m^2/mol CaO, respectively. When compared with Gotland, CaO in the calcined Sibbo dolomite sample had a very high surface area, which was also shared by MgO. This may have been the reason behind the highest conversion (CaO in moles to $CaCO_3$) exhibited by the Sibbo dolomite in all the experiments. This BET measurement gave quantitative evidence for the highest reactivity of the Sibbo dolomite as well as the effect of the low calcination temperatures.

Similar studies had also been carried out with totally different samples, with varying process conditions, and with different aims in the number of listed references [10,13–15]. In Table 5 the measurement conditions of all these referred works are compared with

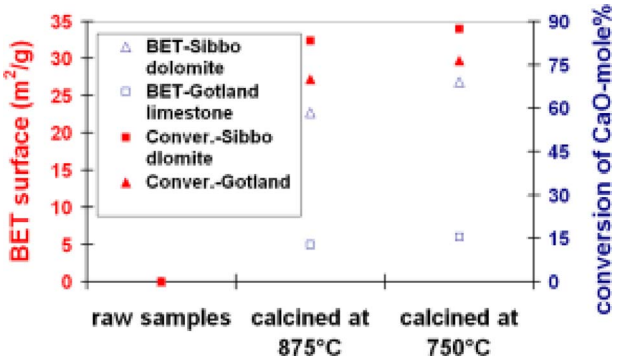


Fig. 11 Gotland and Sibbo dolomite—BET surface areas of CaO and respective CaO (mol %) conversion curves. The hollow signs belong to the secondary *Y*-axis.

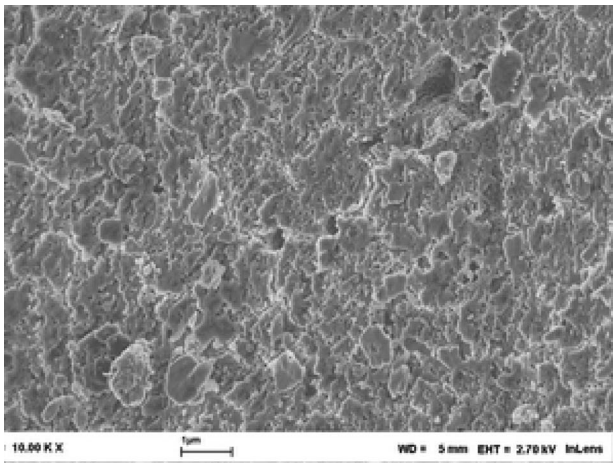


Fig. 12 SEM image of Gotland—calcined at 750°C and magnified to 10,000

our present work. Generally, it can be concluded from all these works that the decay in the maximum carbonation capacity along the CCR cycles was a common feature irrespective of limestone type and process conditions especially when comparing sorbent performance at a high number of cycles. However, for the limited number of cycles, the sorbent decay depends much on the calcination temperature rather than on the number of CCR cycles.

The SEM images of Gotland samples calcined at 750°C and 875°C with 100% N_2 are in Figs. 12 and 13. They had distinct differences over the surface textures between each other. The former consisted of plenty of sharp edges all over the surface, which, in fact, enhanced the specific surface area thus the reactivity. The latter had rather smooth edged surfaces, less surface area, and less reactivity. The same phenomenon was also evident in Figs. 14 and 15 where the Sibbo dolomite was calcined with the same conditions as the Gotland. These images provided qualitative evidence to the enhanced reactivity with low calcination temperatures.

It can be concluded that, for a given limestone/dolomite sample, the total CaO conversion is a function of the calcination temperature and the number of CCR cycles. In this study we focused on the certain number of cycles to sustain fairly high conversions, as explained in the Introduction. In this case, the challenge of achieving and retaining high reactivity along the CCR cycles depends on the calcination temperature. The lower the calcination temperature, the higher the conversion (CaO to $CaCO_3$) rates. It means that in a CCR loop, the calciner should be operated at a possible low temperature, which must also ensure achieving a reasonably high calcination rate.

According to the thermodynamic data (Fig. 2), the CO_2 partial pressure in the calciner determines the equilibrium temperature of the $CaCO_3$/CaO system and a slightly higher equilibrium temperature would favor the calcination reaction. In general, the calciners can be heated by either direct or indirect firing with oxygen and fuel, which would avoid the air nitrogen mixing with CO_2

Table 5 Comparison of reaction conditions of this work with previous works

Ref.	Calcination T (K)	Calcination P_{CO_2}	Carbonation T (K)	Carbonation P_{CO_2}	Particle sizes (μm)	Number CCR cycles (max)
This work	1023–1203	0.0	923	0.2	125–180	4
[10]	1123–1273	0.1	923	0.1	100–1000	500
[13]	1123–1223	0.0–1.0	923	0.1–1	100–800	40
[14]	1223	1	873	0.05	500	4
[15]	1023	0	1023	0.15	<10	5

Downloaded 02 Jun 2010 to 171.66.16.109. Redistribution subject to ASME license or copyright; see http://www.asme.org/terms/Terms_Use.cfm

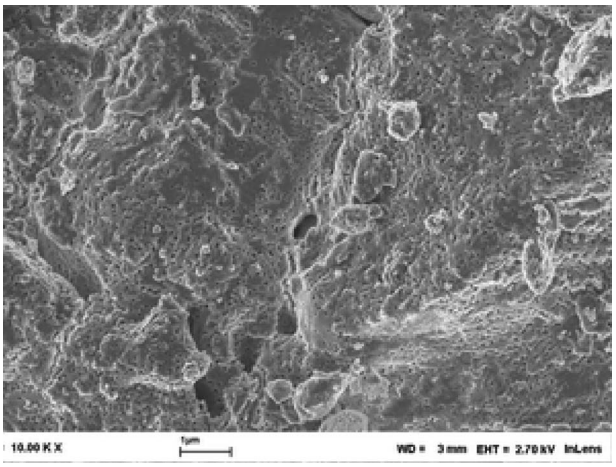


Fig. 13 SEM image of Gotland—calcined at 875°C and magnified to 10,000

stream. In both cases, the CO_2 partial pressure must be brought down to lower the calcination temperature (an atmospheric direct fired calciner would have a P_{CO2} of >0.9 bar). The steam could be the most suitable gas stream available in a power plant to be

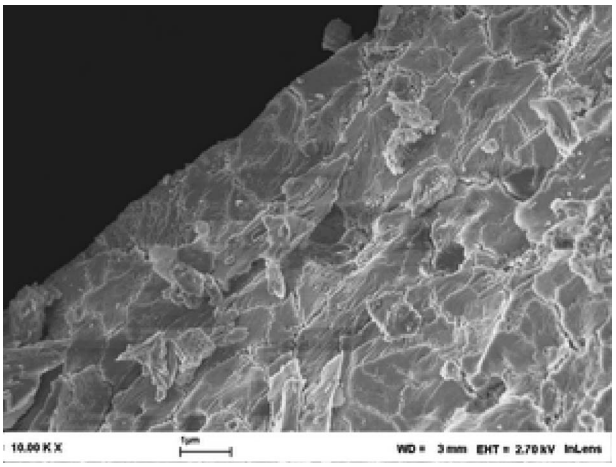


Fig. 14 SEM image of Sibbo dolomite—calcined at 750°C and magnified to 10,000

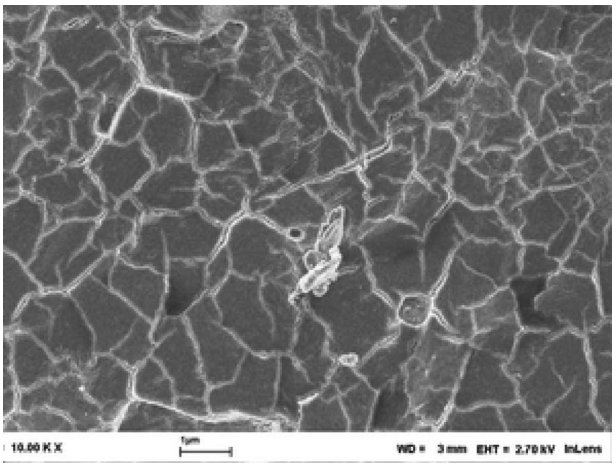


Fig. 15 SEM image of Sibbo dolomite—calcined at 875°C and magnified to 10,000

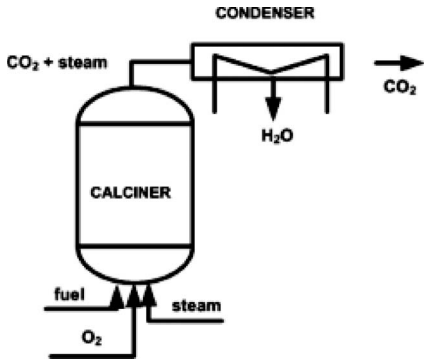


Fig. 16 Sketch of a calciner operated with steam supply

used in the calciner to bring down the CO_2 partial pressure. The supplied steam can then be separated from CO_2 using a condenser at the calciner exit. A calciner sketch with a steam supply is illustrated in Fig. 16.

4 Conclusions

CCR based CO_2 capture is an emerging technique that can be adapted into the existing and future power plants with reasonable investments and minimum energy penalties. Naturally occurring limestones or dolomite, cheap and abundant in nature, can be used as regenerative sorbents for this process. The fast decaying sorbent reactivity along the number of CCR cycles requires large reactor volumes and high recirculation rates within the loop to sustain the sorption capacity. The challenge here is to retain fairly high reactivity for a maximum number of cycles.

Three limestones and a dolomite sample from different geographical locations have been studied in a thermogravimetric analyzer under simulated flue gas conditions at three calcination temperatures of 750°C, 875°C, and 930°C for four CCR cycles. The reactivity and CO_2 capture capacity of the samples widely varied due to their origins and textures. The dolomite sample exhibited the highest rate of carbonation for all the test conditions. At 875°C calcination, the Sibbo dolomite's CO_2 capture capacity per kilogram of the sample reached the same as that of the Gotland—the highest reacting limestone tested during the third cycle. Beyond that the Sibbo dolomite's capture capacity per kilogram of the sample remained higher despite its low $CaCO_3$ content, amounting to 2/3 of that of the Gotland. The limestones' reactivities follow the following descending order: Gotland $>$ Indian Quarry II $>$ Tytyri.

The measured total carbonations of all the samples with the number of cycles were compared with those of the predicted values. The prediction was made based on the assumption that the decay rate, for a certain number of cycles (<20), was proportional to its own total carbonation conversion along the CCR cycles. The decay coefficient of the Sibbo dolomite was the lowest in all calcination temperatures and its value at the highest calcination temperature (930°C) was nearly the same as that of the tested limestones at the lowest calcination temperature (750°C). Since the Sibbo dolomite's decay coefficient is lower in all the limestones, its capture capacity per kilogram of the sample is likely to remain higher beyond the fourth cycle.

The higher the calcination temperature, the lower the sorbent reactivity. BET specific surface area measurements and SEM images provide quantitative and qualitative evidence for this observation. For a given limestone/dolomite sample, it can be stated that the sorbent reactivity is a function of the number of CCR cycles and the calcination temperature. In a CCR loop, if the sorbent is utilized for a certain number of cycles, the reactivity can only be increased by lowering the calcination temperature. According to the thermodynamic calculations, the CO_2 partial

Downloaded 02 Jun 2010 to 171.66.16.109. Redistribution subject to ASME license or copyright; see http://www.asme.org/terms/Terms_Use.cfm

pressure in the calciner has to be lowered to lower the calcination temperature. Lowering the CO_2 partial pressure in a calciner can be achieved by additional steam supply. The supplied steam would then be condensed in an external condenser to single out the CO_2 stream from the calciner exit gases.

Acknowledgment

S.S. would like to acknowledge the financial support from European Union via Marie Curie actions program under the INECSE project.

Peter Backman is highly acknowledged for performing and helping all the experiments. Dr. S. Murugesan is thanked for supplying Indian Quarry samples from southern India.

Nomenclature

k = proportionality coefficient or decay coefficient
m = mass (kg)
P = pressure (N m^{-2})
M = molecular weight (g/mol)
α = conversion of CaO (mol %)

Subscripts

eq = equilibrium
f = final
i = initial
s = sample

References

[1] Metz, B., Davidson, H., Loos, M., and Meyer, M., 2005, *Special Report on Carbon Dioxide Capture and Storage, Inter Governmental Panel on Climate Change*, Cambridge University Press, Cambridge.
[2] Herzog, H. J., 2001, "What Future for Carbon Capture and Sequestration?" Environ. Sci. Technol., **35**, pp. 148A–153A.
[3] Carlos Abanades, J., Edward Anthony, J., Dennis Lu, Y., Salvador, C., and Alvarez, D., 2004, "Capture of CO2 From Combustion Gases in a Fluidized Bed of CaO," AIChE J., **50**, pp. 1614–1622.
[4] Gupta, H., and Liang Fan, S., 2002, "Carbonation-Calcination Cycle Using High Reactivity Calcium Oxide for Carbon Dioxide Separation From Flue Ga," Ind. Eng. Chem. Res., **41**, pp. 4035–4042.
[5] Abanades, C. J., Edward Anthony, J., Wang, J., and Oakey, J., 2005, "Fluidized Bed Combustion Systems Integrating CO2 Capture With CaO," Environ. Sci. Technol., **39**, pp. 2861–2866.
[6] Abanades, J. C., Rbin Edwards, S., and Edward Anthony, J., 2004, "Sorbent Cost and Performance in CO2 Capture Systems," Ind. Eng. Chem. Res., **43**, pp. 3462–3466.
[7] Alvarez, D., and Abanades, C. J., 2005, "Determination of the Critical Product Layer Thickness in the Reaction of CaO With CO2," Ind. Eng. Chem. Res., **44**, pp. 5608–5615.
[8] Günter, S., Jörg, M., Roland, B. and Thorwarth, C., 2006, "An Overview on CO2 Capture Technologies and Current R&D Activities at IVD," presented at the Tenth International Conference on Boiler Technology, Szczyrk, Orle Gniazdo, Oct. 17–20.
[9] Abanades, C. J., and Alvarez, D., 2003, "Conversion Limits in the Reaction of CO2 With Lime," Energy Fuels, **17**, pp. 308–315.
[10] Grasa, G. S., and Abanades, J. C., 2006, "CO2 Capture Capacity of CaO in Long Series of Carbonation/Calcination Cycles," Ind. Eng. Chem. Res., **45**, pp. 8846–8851.
[11] Alvarez, D., and Carlos Abanades, J., 2005, "Pore-Size and Shape Effects on the Recarbonation Performance of Calcium Oxide Submitted to Repeated Calcination/Recarbonation Cycles," Energy Fuels, **19**, pp. 270–278.
[12] Wang, J., and Edward Anthony, J., 2005, "On the Decay Behavior of the CO2 Absorption Capacity of CaO-Based Sorbents," Ind. Eng. Chem. Res., **44**, pp. 627–629.
[13] Abanades, J. C., 2002, "The Maximum Capture Efficiency of CO2 Using a Carbonation/Calcination Cycle of CaO/CaCO3," Chem. Eng. J., **90**, pp. 303–306.
[14] Shimizu, T., Hirama, T., Hosoda, H., Kitano, K., Inagaki, M., and Tejima, K., 1999, "Twin Fluid-Bed Reactor for Removal of CO2 From Combustion Processes," Chem. Eng. Res. Des., **77**(1), pp. 62–68.
[15] Silaban, A., and Harrison, D. P., 1995, "High Temperature Capture of Carbon Dioxide: Characteristics of the Reversible Reaction Between CaO(s) and CO2(g)," Chem. Eng. Commun., **137**, pp. 177–190.

Downloaded 02 Jun 2010 to 171.66.16.109. Redistribution subject to ASME license or copyright; see http://www.asme.org/terms/Terms_Use.cfm

Wide Gap Braze Repair Using Vertically Laminated Repair Scheme

Doug Nagy

Xiao Huang[1]

Liburdi Turbine Services,
Dundas, ON, L9H 7K4, Canada

Repair of after-service gas turbine hot section superalloy components provides considerable saving in life-cycle cost of engines. Whereas a number of methods have been used in the past to repair these superalloy components, wide gap brazing technology has provided a practical alternative to repair difficult-to-weld alloys with substantial damages. In this paper, the historical development of wide gap repair technologies is reviewed first. Subsequently, the recent development in utilizing a vertically laminated structure to repair a large and deep gap (up to 16 mm) in one brazing cycle will be discussed. The microstructure resulted from this repair scheme will be evaluated and compared with conventional wide gap braze with slurry and that of the Liburdi powder metallurgy (LPM™) process. It is observed that in conventional wide gap brazing with premixed slurry, the presence of intermetallic compounds can be effectively reduced by reducing the ratio of braze alloy to gap filler, which, however, also contributes to the increased occurrence of macroscopic voids in the wide gap joint. The LPM™ method, on the other hand, can achieve a macroscopically void-free repair of gap (up to 6 mm) and minimize the formation of intermetallics. By using a vertically laminated repair scheme it is shown that the process is able to repair a deeper gap (up to 16 mm) with no macroscopic defects and reduced intermetallic compounds. [DOI: 10.1115/1.2967496]

1 Introduction

During gas turbine operations, hot section gas turbine components such as turbine blades and vanes are subjected to potential damages, including thermal fatigue cracks (vanes), creep (blades), surface degradation caused by oxidation, hot corrosion or erosion, and foreign object impact damage. These damages, if not repaired, will reduce engine operating efficiency and cause secondary damage to downstream components. Since many modern turbine components are costly to manufacture, effective repair and restoration, instead of replacement, can reduce the overall operating cost. High integrity repair joints are paramount to effective repair practice.

Current repair practices include fusion welding (tungsten inert gas (TIG), plasma transfer arc (PTA), and laser beam welding (LBW)), solid state diffusion, conventional brazing, and brazing derivatives. It has been well documented that fusion weld repair has limitation in repairing high strength precipitation hardened nickel-based superalloy, particularly ones with higher γ' formers (Al+Ti), since they are highly susceptible to hot cracking in weld metal and heat affected zone (HAZ), and strain-age cracking (post-weld heat treatment (PWHT)) in HAZ [1,2]. Furthermore, fusion welding can cause appreciable distortion when large damages are to be weld repaired.

An alternative joining technology to fusion welding is brazing. Braze repair is generally divided into two regimes: narrow gap (<250 μm) and wide gap (>250 μm) [3]. Traditional narrow gap brazing method employs a braze alloy with melting temperature above service temperature yet below the temperature that can cause metallurgical degradation to the component. Due to the addition of melting temperature depressant(s) in braze alloy, the ductility of the joint is inherently poor. An improvement to the brazing process is narrow gap diffusion brazing in which boron is used as a diffusible melting point depressant (MPD) [4,5]. A transient liquid-phase (TLP™) bonding process, developed at P&W (Pratt & Whitney, East Hartford, CT) [6,7] in 1970s, was the early form of diffusion brazing. At bonding temperature, the MPD within the interlayer diffuses into the base material. This resulted in a compositional change in the braze that raised the solidus of the interlayer and isothermal solidification in the bond region takes place. To achieve complete isothermal solidification and joint homogenization using the TLP™ process in narrow gap brazing, a long diffusion cycle is required. Therefore the TLP™ process is limited to a small gap or cracks [8].

When a wider joint needs to be filled entirely by a low melting braze alloy, the inclusion of an excessive MPD will result in the formation of brittle intermetallics such as borides and silicides. In addition to the brittle nature, the presence of these phases also reduces the remelting temperature of the joint and provides path for crack propagation [9], which reduces the resistance to fracture. The ductilities of the intermetallics are inversely ranked according to their hardness. The hardness of various phases commonly occurred in the Ni-based brazed joint is given in Table 1.

To overcome these limitations, wide gap brazing (WGB) was developed. In this case the braze alloy is blended with gap filler powder of similar composition to the base metal [11,12]. The braze alloy to gap filler ratio typically ranges from 1:2 to 1:4 [13]. The gap filler in WGB performs the following functions: (1) reduction of MPD in the joint, (2) bridge the faying surfaces, (3) act as a sink for MPD, (4) provide capillary pressure to draw molten braze alloy into cavity, and (5) present opportunities for further alloying in addition to gap filler metal [14]. In the development of WGB repair technology over the last 30 years, many companies have created their internal processes based primarily on different alloying compositions, filler alloy placements, and heat treatment cycles [15–28]. While most of these processes are proprietary in nature, Table 2 summarizes the reported features to each process [29].

The typical microstructure for a wide gap consists of an inhomogeneous microstructure of gap filler particles, surrounded by

[1]Also at Department of Mechanical and Aerospace Engineering, Carleton University, Ottawa, ON, K1S 5B6, Canada.

Contributed by the International Gas Turbine Institute of ASME for publication in the JOURNAL OF ENGINEERING FOR GAS TURBINES AND POWER. Manuscript received April 1, 2008; final manuscript received April 2, 2008; published online October 13, 2008. Review conducted by Dilip R. Ballal. Paper presented at the ASME Turbo Expo 2008: Land, Sea and Air (GT2008), Berlin, Germany, June 9–13, 2008.

Copyright © 2009 by ASME

Downloaded 02 Jun 2010 to 171.66.16.109. Redistribution subject to ASME license or copyright; see http://www.asme.org/terms/Terms_Use.cfm

Table 1 Microhardness of commonly occurred intermetallic phases in braze joint [3,10]

Phase	HV (0.05 g)
IN738	366–453
γ-Ni	321–378
Cr boride	1958–2210
Eutectic Ni silicide–Ni boride-γ-Ni	757–955
Eutectic Ni boride–Cr boride-γ-Ni	722–982
Centerline eutectic constituents Ni boride–Cr boride-γ-Ni	720 (25 g)

Table 3 Effect of the filler particle size on the WGB joint microstructure [30,33]. Substrate: Rene 95. Braze alloy: Ni-12W-10Cr-3.5Fe-3.5Si-2.5B and 50 μm powder size. Braze cycle: 1170°C/30 min.

Gap filler particle size (μm)	Microstructure characteristics
80–105	Large filler particles, large eutectic constituents
50–80	Larger amounts of discrete borides (40–50 μm)
40–50	Increased dispersion of discrete borides Increased occurrence of voids Increased surface area resulting in strong alloying reaction between the filler and the braze alloy and melting point increased rapidly and fluidity decreased leading to many small voids

the braze alloy with boride rich chains and clusters [30,31]. The addition of a gap filler had been reported to increase the ductility and fatigue crack resistance of the wide gap brazed prior to diffusion treatment [32]. However, the ductility of the WGB repaired region is generally limited to $<1-4\%$. Several critical parameters, namely, gap width, braze alloy to gap filler ratio, braze temperature and time, postbrazing heat treatment, and placement of gap filler and braze alloy, have been observed to affect the mechanical properties of the WGB joint. An improvement in mechanical properties has been observed to be associated with the reduction in size of the brittle intermetallic phases. For example, in one study of high temperature, tensile properties showed that the yielding strength and ductility fell by 10% when the gap width increased from 25 μm to 125 μm [10]. Conversely, increasing the brazing temperature from 1150°C to 1250°C reduces the amount of boride and increase the ductility and tensile strength of the wide gap joint [30]. One noticeable artifact of wide gap joining technique is the occurrence of voids when the braze ratio (braze alloy to filler alloy) decreases.

LPM process addresses the shortcomings by using a layered placement of gap filler and braze alloy. In this process, a solid state sintering of gap filler is used first to form a porous structure. Subsequently, infiltration of braze alloy into the porous gap filler by capillary action densifies the joint with minimum braze alloy, hence minimum melting point depressant. LPM process improves the mechanical properties of the joint due to the reduced intermetallics and voids [19–22]. In practice, this approach allows the

Table 2 Summary of wide gap repair processes

Trade name	Process	Reference
ADH (activated diffusion healing) (General Electric, Schenectady, NY)	Slurry of superalloy powder and lower-melting-point bonding alloy mixture	[15,16]
M-Fill™ (Avco Lycoming, Stratford, CT)	Ni plating of the faying surface Specially formulated filler alloy melts and bridge gap No capillary action employed	[17,18]
LPM™ (Liburdi Engineering, Dundas, ON, Canada)	Based on liquid-phase sintering principle Solid state sintering of a gap filler to form a porous structure Braze alloy containing MPD applied above the sintered region Infiltration of braze alloy into the gap filler by capillary action	[19–22]
Liquid phase diffusion sintering	Filler and gas filler mixture Melting of the filler metal above solidus Rearrangement of a gap filler by sliding and densification Melting of the gap filler Diffusion of MPD leads to isothermal solidification	[23]
Transient liquid-phase infiltration (TLI)	Skeleton formed by solid freeform fabrication (SFF) Infiltrant material with MPD such as Si, Cu, and C Liquid metal fills the skeleton void space and achieves isothermal solidification without significant dimensional change Controlled gating of the liquid and bulk compositions to prevent freeze-off of liquid and complete filling of powder-metal skeleton	[24,25]
Liquid phase diffusion bonding (LPDB or SermaFill) (Sermatch, Pottstown, PA)	Paste containing 80% of parent metal (IN 738)	[26]
Effective structural repair (ESR) (Howmet, Whitehall, MI)	Diffusion brazing Alloy blend of high melt and low melt powders NGB with thinner blend WGB with thicker blend	[27]
Supersolidus/transient liquid-phase sintering (LPS)	Powder mixture with 30–70% additive powder with MPD Freestanding sintering Sintering in the mushy zone	[28]

Downloaded 02 Jun 2010 to 171.66.16.109. Redistribution subject to ASME license or copyright; see http://www.asme.org/terms/Terms_Use.cfm

Table 4 Nominal compositions for substrate and gap filler (wt %)

Alloy	Al	C	Cr	Co	Fe	Mo	Nb	Ta	Ti	W	Zr	Ni
IN738	3.4	0.17	16	8.5	—	1.75	0.9	1.75	3.4	2.6	0.1	Bal.

Table 5 Composition and thermal properties of BNi-9

Product name	Composition	Solidus (°C)	Liquidus (°C)	Brazing temperature (°C)
BNi-9	Ni-15Cr-3.5B	1020	1050	1200

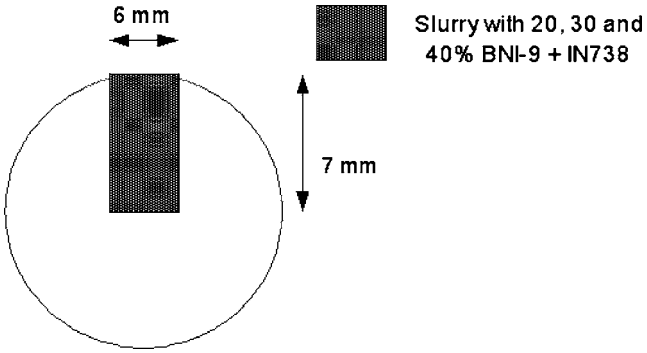


Fig. 1 Conventional wide gap brazing with slurry

repair joint to be as large as 6 mm. If a joint gap is greater than 6 mm, multiple steps are required. The size of eutectic constituents, discrete intermetallic compound, and voids were found to be sensitive to the gap filler particle size as summarized in Table 3 [30,33]. In light of the above review, the future wide gap development requires the following efforts: reduce the size and amount of intermetallic compounds in the joint, lower the diffusion heat treatment time required, and repair larger defects in a single step without significant porosity. In this study, the influence of braze alloy to gap filler ratio on the microstructure of the WGB joint, particularly boride and void formation, is first examined. Subsequently, a vertically laminated structure for large gaps (16 mm deep) is detailed and its microstructure is compared with that produced by WGB using premixed slurry and LPM™.

2 Materials and Experimental Procedure

The base alloy used in this study was cast IN738 bars fabricated by sophisticated alloys. Braze alloy BNi-9 and gap filler alloy IN738 were purchased from Praxair Surface Technologies, Inc. (Indianapolis, IN). The compositions of the materials are given in Tables 4 and 5. The substrate IN738 was machined to produce test specimens for wide gap brazing trials using cylindrically drilled cavity, as shown in Fig. 1. This geometry was used to study the effect of braze alloy (BNi-9) to gap filler (IN738) ratio on the microstructure of the joint.

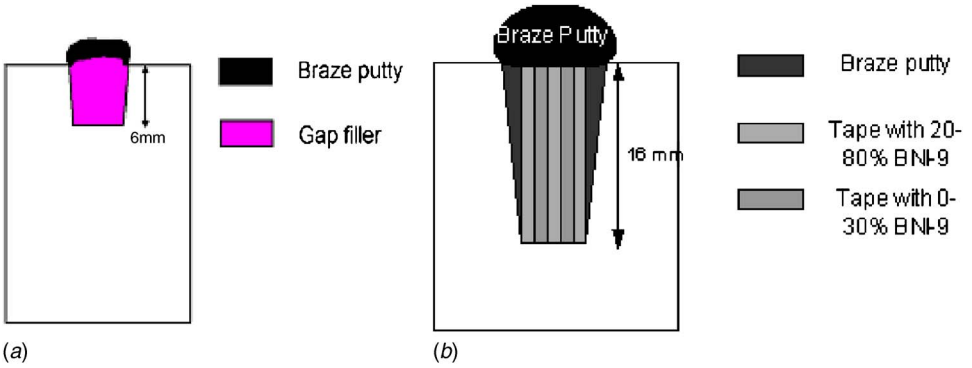


Fig. 2 LPM™ wide gap joint (*a*) and a vertically laminated structure (VLS) (*b*) (the width at the top of the cavity is about 1 mm in this configuration)

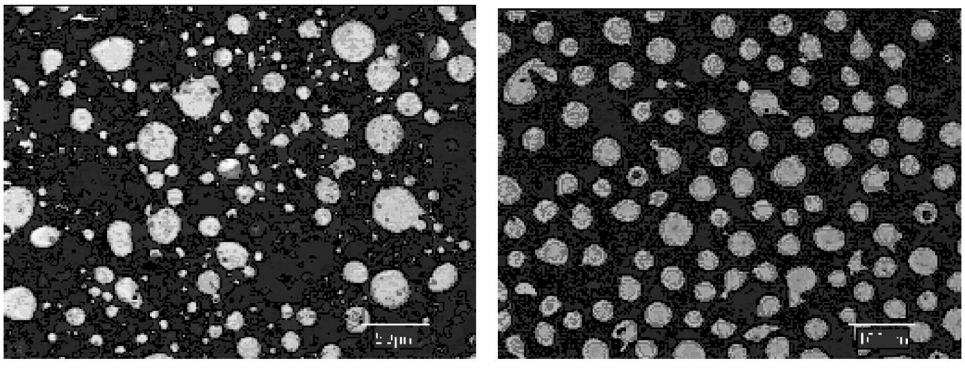


Fig. 3 IN738 (*a*) BNi-9 powder (*b*) in the as-received condition

Downloaded 02 Jun 2010 to 171.66.16.109. Redistribution subject to ASME license or copyright; see http://www.asme.org/terms/Terms_Use.cfm

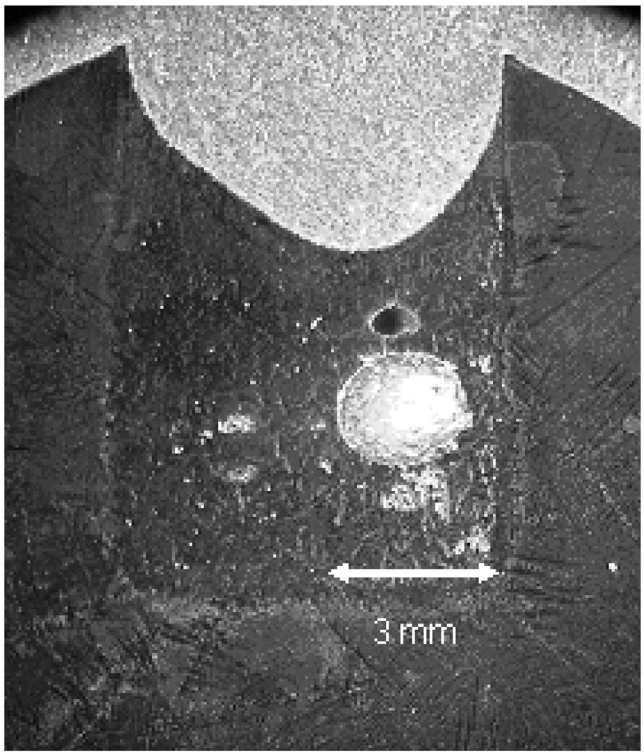


Fig. 4 40% BNi-9 WGB joint by slurring method showing a 2 mm interstitial void

For WGB repair with the LPM™ process, *U* grooves with 6 mm depth and 1 mm width were machined as shown in Fig. 1(*a*). It is believed that since the actual defects/cracks on turbine components will require substantial cleaning and grinding, the simulated *U* groove is representative of the repair process. Additionally, due to the use of braze putty, any irregularly shaped defects can be accommodated in this process.

For the vertically laminated structure, the samples were machined using a milling machine to generate *U* grooves as shown in Fig. 2(*b*). To better mimic the nature of a true repair, the walls were given a 10 deg slope. Also illustrated in the figures are the vertical placements of the braze alloy in the cavities. The number of braze layers is varied according to the width of the cavity with braze tape thickness ranging from 1 mm to 2 mm. The tapes were made of BNi-9 and IN738 with different mixing ratios. It is also to be noted that the sample or defect orientation did not play a role in this repair scheme. Furnace brazing was conducted in vacuum at 1200°C followed by furnace cooling. No postbrazing heat treatment was used for samples examined in this study.

3 Results

3.1 As-Received Powder Materials. The powder materials in the as-received condition were examined under an optical microscope to identity the shapes and powder size distributions. As shown in Fig. 3, the IN738 powder exhibits a wide range of size distribution with an average particle size of 10 μm, while BNi-9 powder assumes a uniform powder size distribution with majority of the particles in the 30–40 μm diameter range.

Three samples with different braze alloy to gap filler ratios (40%, 30%, and 20% braze alloys, respectively) were examined using optical microscopy and scanning electron microscopy (SEM). Examination under an optical microscope reveals large voids in all the joints. The sample with 40% BNi-9 contains large voids with their diameters up to 2 mm as shown in Fig. 4. With further reduction in braze alloy to gap filler ratio, the size and the number of voids increase. With the slurry method used in this study, it was not able to achieve defect-free joints for gaps of 7 mm or greater in one braze operation. As also reported in litera-

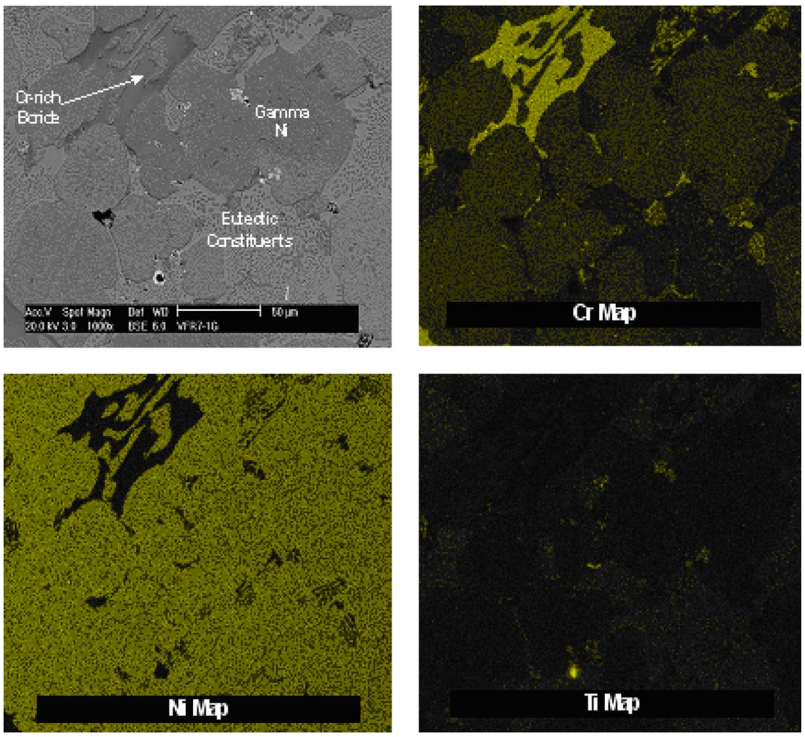


Fig. 5 Microstructure (BSE) and EDS maps of the WGB joint with 40% BNi-9; large Cr boride phases are observed to co-exist with a finer Ti boride phase [14]

Downloaded 02 Jun 2010 to 171.66.16.109. Redistribution subject to ASME license or copyright; see http://www.asme.org/terms/Terms_Use.cfm

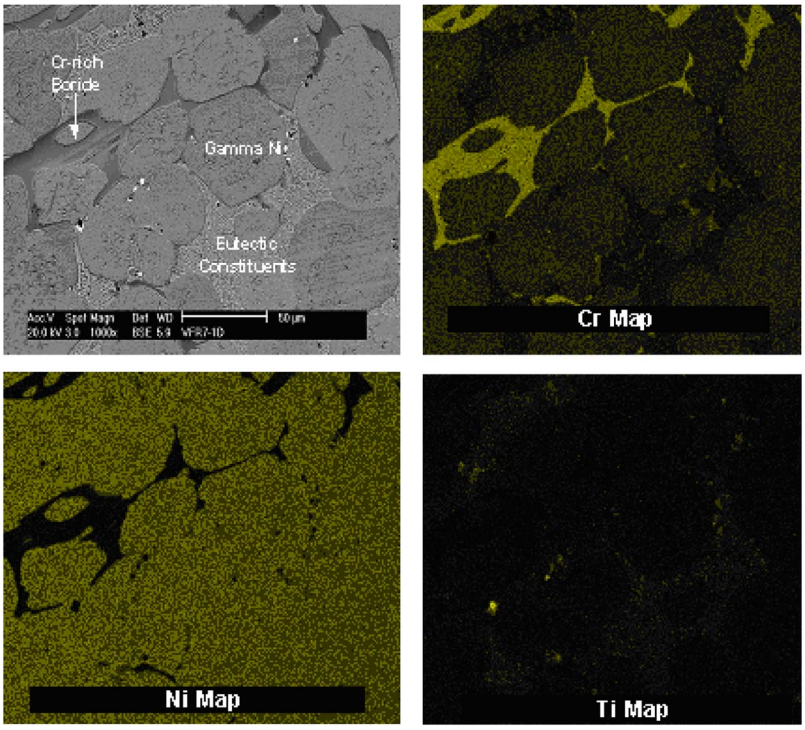


Fig. 6 WGB joint with 30% BNi-9 and 70% IN738 [14]

ture that when premixed slurry containing 30% braze alloy was used, the maximum depth of the gap was about 4 mm; beyond which large voids are very difficult to eliminate [34].

3.2 Effect of Braze Alloy to Gap Filler Ratio. SEM backscatter images and elemental maps for the WGB joints with 40%, 30%, and 20% BNi-9 are presented in Figs. 5–7, respectively. The microstructure of the joint with 40% BNi-9 is consisted of large primary γ-Ni particles, Cr-rich borides, and eutectic constituents. Small Cr-rich particles are also observed inside the γ-Ni particles.

Comparing the particle sizes of the large primary γ-Ni particles

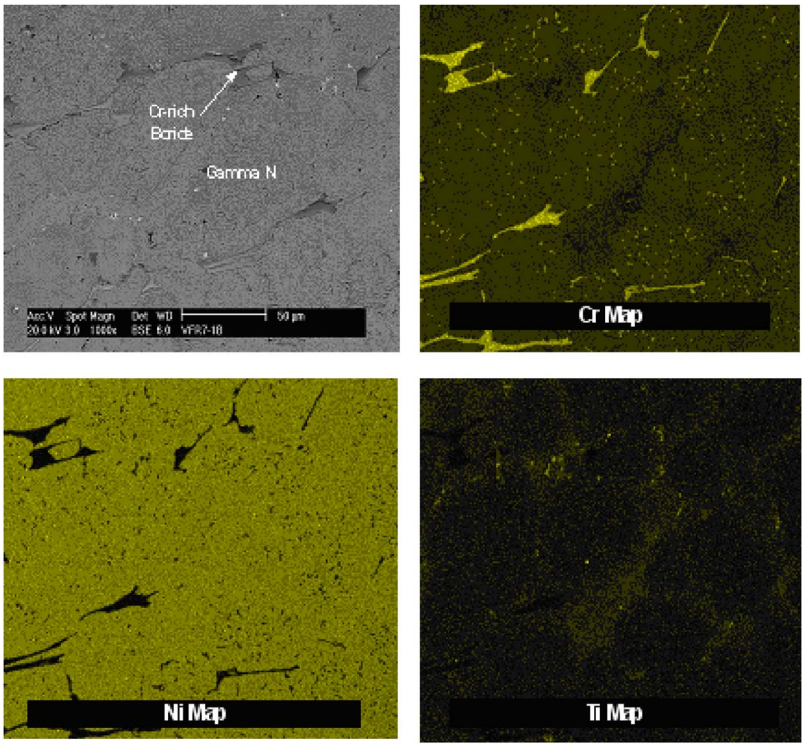


Fig. 7 WGB joint with 20% BNi-9; the size of Cr-rich boride has been reduced in comparison to Figs. 5 and 6 [14]

Downloaded 02 Jun 2010 to 171.66.16.109. Redistribution subject to ASME license or copyright; see http://www.asme.org/terms/Terms_Use.cfm

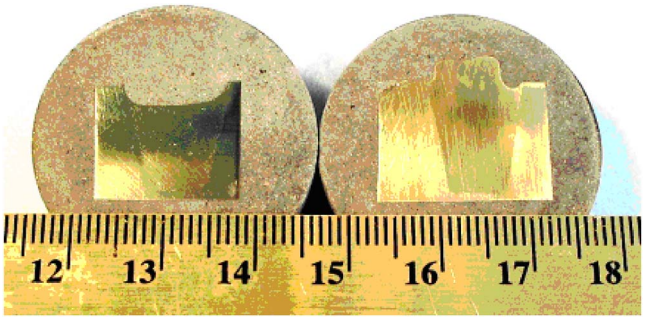
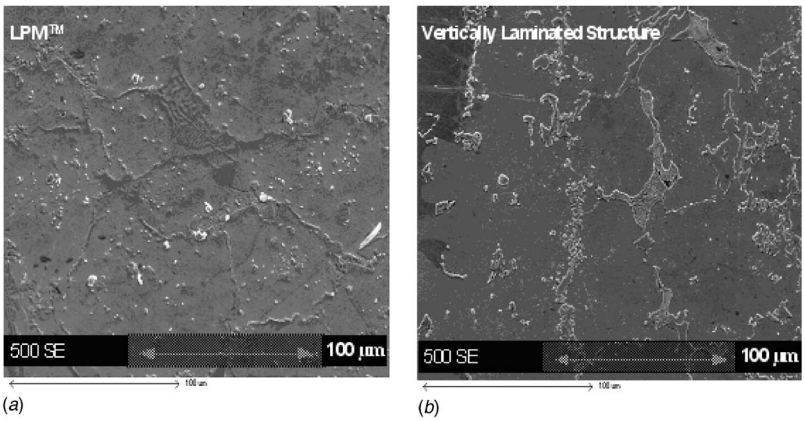


Fig. 8 WGB repaired joints using LPM™ (*a*) and vertically laminated configuration (*b*)

resemble that seen in the joint with 40% BNi-9. No obvious eutectic constituents are observed in Fig. 7 for the WGB joint with 20% BNi-9.

3.3 LPM™ and Vertically Laminated WGB Joints. In order to improve the joint integrity with reduced voids and borides, two different approaches, LPM™ and a vertically laminated structure, were used in this study to join the wide gaps. As illustrated in Fig. 2, the gap size used for the LPM™ repair process was similar in depth to that used for WGB with slurry. The repaired region, shown in Fig. 8(*a*), exhibits a dense structure with no macroscopic voids. The microstructure was further examined using SEM as shown in Fig. 9(*a*). Similar to the microstructure shown in Fig. 6 (30% BNi-9) three distinct regions are observed: primary γ-Ni, Cr-rich boride, and eutectic constituents. It should be noted that



(*a*) (*b*)

Fig. 9 Microstructure of WGB repaired joints using LPM (*a*) and a vertically laminated structure (*b*)

(Fig. 5) to that of IN738 powders shown in Fig. 3(*b*), it is believed that the original powder particles have been completely melted during the brazing cycle resulting in primary γ-Ni particles much larger than the original IN738 powder particles. Similar study suggested that the primary γ-Ni was formed directly from molten braze alloys [35]. The identification of the Cr-rich boride was based on our early study of B mapping using wavelength dispersive spectroscopy (WDS) [14].

It is also interesting to note that the eutectic constituents shown in Fig. 5 contained at least three components: γ-Ni, Ni-rich phase, and Cr-rich phase. In a Ni–Cr–B ternary filler [36], it has been predicted that a binary invariant eutectic reaction takes place at 1042°C as $L \rightarrow \gamma + Ni_3B$, while a ternary eutectic terminal reaction occurs at 997°C as $L \rightarrow$ fcc γ-Ni+Ni_3B+CrB. Further examining the eutectic constituents and Cr and Ni maps in Fig. 5, it is possible that both binary eutectic phases and ternary eutectic phases exist. It is also possible that some Ti boride formed during brazing as several Ti-rich particles are observed on the Ti-map (Fig. 5) and it may assume the form of TiB_2 since the free energy of formation for it was reported to be lower than that for CrB [37]. Further study with WDS is required to identify the nature of this phase since energy dispersive spectroscopy (EDS) is not capable of differentiating them.

With the reduction of BNi-9 from 40% to 30%, the microstructure of the WGB joint shown in Fig. 6 contains a reduced amount of Cr-rich borides and eutectic constituents. Other features are similar to the brazed joint with 40% BNi-9. Further reduction of BNi-9 to 20%, by contrast, resulted in significant changes to the microstructure. The shape of the primary γ-Ni seen in Fig. 5 has changed to a more irregular and the size of the Cr-rich boride is reduced, while the small Cr-rich particles inside the primary γ-Ni all the microstructures presented in this study are in the as-brazed condition with no diffusion or homogenization cycle incorporated.

The gap repaired with a vertically laminated structure was able to produce a defect-free joint for a depth of 16 mm, shown Fig. 8(*b*), in a single braze cycle at 1200°C. Further analysis with SEM showed a similar microstructure as LPM™ repaired joint but the Cr-rich borides and eutectic constituents are much smaller as illustrated in Fig. 9(*b*). It is also noticed that with the use of braze putty, the arrangement of braze tapes (braze alloy-rich or filler-rich) did not affect the microstructure of the braze joint.

4 Conclusion

It was observed in this study that the presence of intermetallic compounds can be effectively removed by reducing the ratio between braze alloy and gap filler. It, however, contributes to the increased occurrence of macroscopic voids in the 7 mm deep wide gap joint using slurry method. In contract, the LPM™ method can effectively repair a similar gap while at the same time eliminate macroscopic void and generate a microstructure similar to that of 30% BNi-9 in the slurry method. Furthermore, the repair scheme based on a vertically laminated structure was able to repair a 10 mm wide and 16 mm deep gap with no macroscopic defect and further reduction in the sizes of discrete Cr-rich boride and eutectic phases using a one-step braze process. Both high temperature tensile and fatigue properties for the gaps repaired using a vertically laminated structure are being tested and will be reported in our future communication. The effects of postbraze heating treatment on microstructure and mechanical properties are also being evaluated.

Downloaded 02 Jun 2010 to 171.66.16.109. Redistribution subject to ASME license or copyright; see http://www.asme.org/terms/Terms_Use.cfm

Acknowledgment

We like to thank our technicians, graduate and summer students, and our colleagues who have devoted their time and effort to prepare samples and conduct laboratory analyses, particularly Ms. K. Kott from Liburdi Engineering for preparing brazing procedures with a vertically laminated structure and SEM analysis. Special acknowledgment goes to Mr. M. Yao at Deloro Stellite for contributing experiment materials and Mr. H. Leon at Carleton University for conducting brazing trial using slurry mixture.

References

[1] Duval, D. S., and Owczarski, W. A., 1967, "Further Heat-Affected Zone Studies in Heat Resistant Nickel Alloys," Weld. Res. Suppl., Sept., pp. 423s–432s.
[2] Liburdi, J., and Lowden, P., 1985, "Repair Technologies for Gas Turbine Components," *AGARD Conference Proceedings on Advanced Joining of Aerospace Metallic Materials*, Sept., Vol. 398, pp. 22.1–22.12.
[3] Heikinheimo, L. S. K., Laukkanen, A., and Veivo, J., 2005, "Joint Characterization for Repair Brazing of Superalloys," Weld. World, **49**(5–6), pp. 5–12.
[4] Fritsche, B., and Satir-Kolorz, A., 2000, "Repair Brazing of Nickel-Based Turbine Blades," Weld. World, **44**(5), pp. 10–14.
[5] Gandy, D., Frederick, G., Stover, J., and Viswanathan, R., 2003, "Overview of Hot Section Component Repair Methods," www.my.epri.com.
[6] Duval, D. S., Owczarki, W. A., and Paulonic, D. F., 1974, "TLP Bonding—A New Method for Joining Heat Resistant Alloy," Weld. J. (Miami, FL, U.S.), **53**, pp. 203–214.
[7] Duval, D. S., 1970, U.S. Patent No. 3,530,568.
[8] Duvall, D. S., and Doyle, J. R., 1973, "Repair of Turbine Blades and Vanes," ASME Paper No. 73-GT-44.
[9] Fritsche, F., Satir-Kolorz, A., and Baumann, R., 2000, "Repair Brazing of Nickel-Based Turbine Blades," Weld. World, **44**(5), pp. 10–14.
[10] Ojo, O. A., Richards, N. L., and Chaturvedi, M. C., 2004, "Effect of Gap Size and Process Parameters on Diffusion Brazing of Inconel 738," Sci. Technol. Weld. Joining, **9**(3), pp. 209–220.
[11] McComas, C. C., and Stewart, D. C., 1987, "Repair of Surface Defects in Superalloy Articles," U.S. Patent No. 4,705,203.
[12] Ferrigno, S. J., Somerville, M., and Young, R., 1989, "Alloy Powder Mixture for Treating Alloys," U.S. Patent No. 4,830,934.
[13] Duval, D. S., Owczarski, W. A., Paulonic, D. F., and Schaefer, R. P., 1977, "Method for Repairing Surface Defects Using Metallic Filler Material," U.S. Patent No. 4,008,844.
[14] Huang, X., Yandt, S., Nagy, D., and Yao, M., 2007, "Effect of Ruthenium, Rhenium and Yttria Additions on the Microstructure of Wide Gap Brazing of IN738," ASME Paper No. GT2007-27129.
[15] Hopping, G. S., and Berry, T. F., 1970, "Activated Diffusion Bonding," Weld. Res. Suppl., Nov., pp. 505s–509s.
[16] Demo, W. D., and Ferrigno, S. J., 1992, "Brazing Method Helps Repair Aircraft Gas-Turbine Nozzles," Adv. Mater. Process., **141**(3), pp. 43–45.
[17] McMurray, J. H., and Miller, J. A., 1983, "Braze Filler Metal Composition and Process," U.S. Patent No. 4,394,347.
[18] Lee, J. W., McMurray, J. H., and Miller, J. A., 1985, "Development of a New Brazing Technique for Repair of Turbine Engine Components," Weld. J. (Miami, FL), **64**, pp. 18–21.
[19] Liburdi, J., and Ellision, K. A., 1993, "Novel Approach to the Repair of Vane Segment," International Gas Turbine and Aero Engine Congress, Cincinnati, OH, May 24–27, pp. 24–27.
[20] Ellison, K. A., Lowden, P., and Liburdi, J., 1994, "Powder Metallurgy Repair of Turbine Components," ASME J. Eng. Gas Turbines Power, **116**, pp. 237–242.
[21] Liburdi, J., Lowden, P., and Ellison, K., 1992, "Powder Metallurgy Repair Technique," U.S. Patent No. 5,156,321.
[22] Ellison, K. A., Lowden, P., and Liburdi, J., 1993, "Repair Joints in Nickel-Based Superalloys With Improved Hot Corrosion Resistance," ASME Paper No. 93-GT-247.
[23] Young, W. R., 1978, "Turbine Airfoil Repair," *Proceedings of the Conference on Materials Synergisms*, Kaimesha Lake, NY, Oct. 17–19, pp. 924–938.
[24] Lorenz, A., Sachs, E., Allen, S., Rafflenbeul, L., and Kernan, B., 2004, "Densification of a Powder-Metal Skeleton by Transient Liquid-Phase Infiltration," Metall. Mater. Trans. A, **35**(2), pp. 631–640.
[25] Lorenz, A., Sachs, E., and Allen, S., 2004, "Freeze-off Limits in Transient Liquid-Phase Infiltration," Metall. Mater. Trans. A, **35**(2), pp. 641–653.
[26] Miglietti, W., Kearney, J., and Pabon, L., 2001, "Liquid Phase Diffusion Bond Repair of Siemens V84.2, Row 2 Vanes and Alstom Tornado, Second Stage Stator Segments," ASME Paper No. 2001-GT-0510.
[27] Wustman, R. D., Hampson, L., Smith, J., and Suneson, M., 1996, "High Strength Diffusion Brazing Repairs for Gas Turbine Components," ASME Paper No. 96–GT-427.
[28] Bell, S., 1985, "Repair and Rejuvenation Procedures for Aero Gas-Turbine Hot Section Components," Mater. Sci. Technol., **1**, pp. 629–634.
[29] Tandon, R., and German, R. M., 1994, "Supersolidus-Transient Liquid Phase Sintering Using Superalloy Powders," Int. J. Powder Metall., **30**(4), pp. 435–443.
[30] Zhang, J., Zhang, Z., Sun, J., and Liu, X., 2000, "Effect of Gap Filler on Microstructure of Wide Gap Brazing Seam," Mineral. J., **41**(8), pp. 1073–1076.
[31] Juergon, W., and Malik, M. P., 1985, "Wide Gap Brazing in Maintenance of Turbine Guide Vanes," DVS-Ber., **98**, pp. 78–82.
[32] Yu, Y. H., and Lai, M. O., 1995, "Effect of Gap Filler and Brazing Temperature on Fracture and Fatigue of Wide Gap Brazed Joints," J. Mater. Sci., **30**, pp. 2101–2107.
[33] Li, X., Zhong, Q., and Cai, C., 2003, "Wide-Gap Brazing Between K403 and DZ4 Superalloys," J. Aeronaut. Mater., **23**(4), pp. 10–15.
[34] Lim, L. C., Lee, W. Y., and Lai, M. O., 1995, "Nickel Base Wide Gap Brazing With Preplacement Technique, Part I–Effect of Material and Process Parameters on Formation of Macrovoids," Mater. Sci. Technol., **11**, pp. 955–960.
[35] Tung, S. K., Lim, L. C., and Lai, M. O., 1995, "Microstructural Evolution and Control in BNi-4 Brazed Joints of Nickel 270," Scr. Mater., **33**(8), pp. 1253–1259.
[36] Ohsasa, K., Shinmura, T., and Narita, T., 1999, "Numerical Modeling of the Transient Liquid Phase Bonding Process of Ni Using Ni-B-Cr Ternary Filler Metal," J. Phase Equilib., **20**(3), pp. 199–206.
[37] Shrivastava, P. K., Tiwari, A. N., and Gopinathan, V., 1989, "Role of Boron in Fe- and Ni-Based Rapidly Solidified Microcrystalline Alloys," Key Eng. Mater., **38–39**, pp. 143–162.

Downloaded 02 Jun 2010 to 171.66.16.109. Redistribution subject to ASME license or copyright; see http://www.asme.org/terms/Terms_Use.cfm

The Performance Evaluation With Diffuser Geometry Variations of the Centrifugal Compressor in a Marine Engine (70 MW) Turbocharger

Hong-Won Kim
e-mail: khw007@hhi.co.kr

Jong-Il Park

Seung-Hyup Ryu

Seong-Wook Choi

Sang-Hak Ghal

Hyundai Industrial Research Institute,
Hyundai Heavy Industries Co., Ltd.,
1, Jeonha-Dong, Dong-Gu,
Ulsan 682-792, Korea

An examination of the condition of the flow leaving the impeller exit kinetic energy often accounts for 30–50% of the shaft work input to the compressor stage; for energy efficiency, it is important to recover as much of this as possible. This is the function of the diffuser, which follows the impeller. Effective pressure recovery downstream of an impeller is very important in order to realize a centrifugal compressor with a high efficiency and a high pressure ratio, and an appropriate selection of a diffuser for a specific impeller is a critical step in order to develop the compressor accordingly. The purpose of this study is to investigate the sensitivity of how compressor performances change as the vaned diffuser geometry is varied. Three kinds of vaned diffusers were studied and compared with its results. The first vaned diffuser type is based on a modified NACA airfoil, the second is a channel diffuser, and the third is a conformal transformation of NACA 65-(4A10)06 airfoil. A mean-line prediction method was applied to investigate the performance and stability for three kinds of diffusers. Computational fluid dynamic (CFD) analyses and a detailed interior flow pattern study have been done. In this study, the off-design behavior of three different types of diffusers, given by the mean-line prediction, was investigated using CFD results and the NACA 65 diffuser geometry, which satisfies a wider operating range and has a higher pressure recovery than the others, was selected. The numerical results were compared with experimental data for validation and showed good agreement. [DOI: 10.1115/1.2967733]

1 Introduction

The centrifugal compressor of a marine engine turbocharger is composed of an impeller, the first vaneless diffuser, a vaned diffuser, the second vaneless diffuser, and a volute casing. Usually, in the first vaneless diffuser, the front pinched vaneless diffuser is commonly employed to extend the operating range of an engine. The flow angle at the impeller exit is mostly a function of the density and the passage width. As the flow diffuses, the density increases and the flows turn toward the tangential direction. In practice, the frictional forces acting in the boundary layers also retard the flow close to the endwalls, and if the diffusion is allowed to proceed sufficiently, the radial motion in the endwall flow can cease altogether and the flow will move inwards toward the impeller, thereby setting up a recirculation in the diffuser. This limits the pressure rise obtainable and may ultimately result in a rotating stall or surge. Such instability can be controlled by limiting the passage width in a pinched vaneless diffuser.

The performance of the diffuser is measured by means of both the static pressure recovery coefficient

$$C_p = \frac{P_4 - P_2}{P_{02} - P_2} \tag{1}$$

and the total pressure loss coefficient

$$K = \frac{P_{02} - P_{04}}{P_{02} - P_2} \tag{2}$$

The design objective for a diffuser is to achieve the maximum static pressure recovery with the minimum total pressure loss, within other constraints of size and flow stability.

Exclusive of a vaneless diffuser, the vaned diffuser options that may be used are the channel (wedge) and airfoil (or cascade) diffusers shown in Fig. 1. The channel diffuser is normally a simple straight-sided passage formed by means of discrete wedge-shaped vanes. A distinct throat is formed at the inlet to the passage. Cascade diffuser vanes are usually based on a standard airfoil shape such as NACA 65 but can vary considerably in solidity (chord/pitch ratio). In low solidity diffusers the vane count is small and there is no overlap between adjacent vanes and therefore no throat, but even so, the performance of such diffusers is quite different from that of an equivalent vaneless diffuser.

Extensive sets of laboratory data are available for channel diffusers in the work of Japikse and Baines [1], for example. These give the static pressure recovery data as a function of the area ratio, diffuser length/width ratio, and many aerodynamic parameters, such as the Reynolds and Mach numbers and the inlet boundary layer blockage. It is generally evident from a performance map that the largest static pressure recovery occurs at a high length/width ratio, which implies a larger diffuser. Where the installation space for the turbocharger is limited, some compromise in the diffuser dimensions may be necessary. An attempt to increase the diffuser area ratio within the same overall size by increasing the divergence angle can be counterproductive after a certain point because the diffuser will stall, limiting the pressure rise that can be achieved.

Contributed by the International Gas Turbine Institute of ASME for publication in the JOURNAL OF ENGINEERING FOR GAS TURBINES AND POWER. Manuscript received April 3, 2008; final manuscript received April 7, 2008; published online October 14, 2008. Review conducted by Dilip R. Ballal. Paper presented at the ASME Turbo Expo 2008: Land, Sea and Air (GT2008), Berlin, Germany, June 9–13, 2008.

Copyright © 2009 by ASME

Downloaded 02 Jun 2010 to 171.66.16.109. Redistribution subject to ASME license or copyright; see http://www.asme.org/terms/Terms_Use.cfm

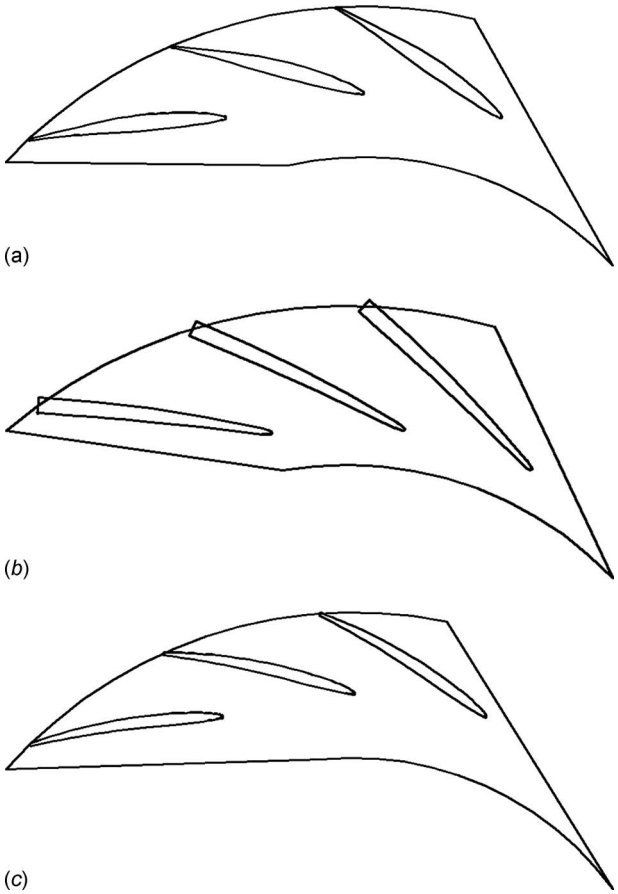


Fig. 1 Studied three different diffuser models: (*a*) airfoil diffuser (*A*-type), (*b*) channel diffuser (*B*-type), and (*c*) NACA 65-(4A10)06 (*C*-type)

For airfoil diffusers, the database is less extensive. For high solidity diffusers using a standard airfoil profile, cascade test data for that profile may be used effectively, but are less applicable to low solidity diffusers.

Laboratory data provide good guidance for the designer but cannot be relied on highly accurate estimates of the performance of compressor diffusers. The fundamental problem is that the flow leaving the impeller is highly distorted, unsteady, and turbulent, whereas almost all laboratory tests are made with a steady uniform inlet flow. Experience suggests that vaneless diffusers typically have static pressure recoveries in the range 0.45–0.6, airfoil diffusers in the range 0.55–0.70, and channel diffusers in the range 0.6–0.70.

In this study, three kinds of vaned diffusers were used. Figure 1(*a*) (*A*-type) is a design geometry based on the NACA airfoil. Figure 1(*b*) (*B*-type) is a channel diffuser. Figure 1(*c*) (*C*-type) is a diffuser designed by a conformal transformation of the NACA65-(4A10)06 airfoil. Dimensions of the applied vaned diffusers are shown in Table 1. The three different diffusers have a common impeller.

Table 1 List of studied diffusers

Type	Geometry	$R3/R2$	$R4/R2$	α_2(deg)	z	A_{th}	AR
A	Airfoil	1.2	1.46	17.8	18	0.95	1.21
B	Channel	1.2	1.55	16.8	19	0.95	1.28
C	NACA 65	1.2	1.45	18.5	18	1.00	1.21

The configuration of the vanes in the cascade diffuser comes from the conformal transformation of known airfoil sections from a rectilinear coordinate system to a curvilinear system. In the rectilinear system, the flow is uniform and parallel to the abscissa. In the curvilinear system, the flow is that of a spiral vortex emanating from a reference circle that connects the leading edges of the diffuser vanes. Figure 2 illustrates the flow field geometries and Fig. 3 shows the vane geometries.

The derivation of the transformation equations is as follows:

$$\theta = \frac{my + x}{m^2 + 1}, \quad r = r_3 \exp\left(\frac{mx - y}{m^2 + 1}\right), \quad m = \frac{C_{r3}}{C_{\theta 3}} \tag{3}$$

In this study, the off-design behavior of three different types of diffusers, given by the mean-line prediction, was investigated using CFD results and the best diffuser geometry, which satisfies a wider operating range and a higher pressure recovery than the others, was selected.

In the mean-line prediction method, the total pressure loss in vane rows is assumed to have three sources: skin friction, profile, and secondary flow losses. The loss calculations require quantities related to the lift, the loadings, and the equivalent diffusion ratio, wherein formulas come directly from treatments for two-dimensional cascades.

2 Mean-Line Prediction Method

The mean-line prediction method is very useful in estimating the performance and operating ranges for a compressor. It is an efficient method that saves time and cost. The current aerodynamic modeling generally draws on some well established techniques for analyzing conventional radial-flow diffuser geometries, and also on techniques for analyzing two-dimensional airfoil cascades of arbitrary solidity.

Here, the isentropic efficiency of the compressor impeller is defined as

$$\eta(\dot{m}, U)_{\text{impeller}} = \frac{\Delta h_{\text{ideal}}}{\Delta h_{\text{ideal}} + \Delta h_{\text{loss}}} - \Delta \eta_{\text{clearance}} \tag{4}$$

The Δh_{ideal} [2] is a function of slip factor and revolution and the loss Δh_{loss} [2] is equal to the sum of the incidence loss and friction loss.

To evaluate the performance of the vaneless diffuser, the equations of mass conservation, angular momentum, and radial equilibrium, as follows, are solved in this region. This set of equations was solved directly by the fourth order Runge–Kutta integration method. Also, this simple prediction is applied to both the interface for the impeller and the diffuser, as well as the interface for the diffuser and the volute.

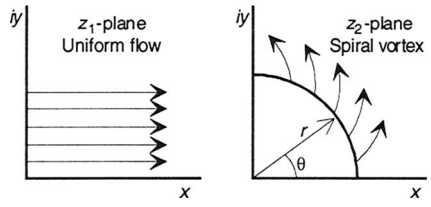


Fig. 2 Flow field geometries

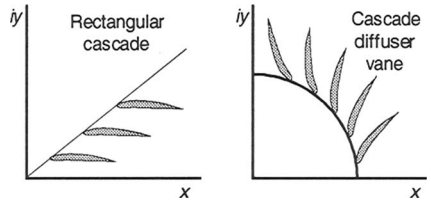


Fig. 3 Airfoil geometries

Downloaded 02 Jun 2010 to 171.66.16.109. Redistribution subject to ASME license or copyright; see http://www.asme.org/terms/Terms_Use.cfm

Meridional momentum equation

$$C_m \frac{dC_m}{dr} - \frac{C_\theta^2}{r} + C_f \frac{C_m \sqrt{C_\theta^2 + C_m^2}}{b \sin \phi} + \frac{1}{\rho} \frac{dp}{dr} = 0 \tag{5}$$

Tangential momentum equation

$$C_m \frac{dC_\theta}{dr} + \frac{C_m C_\theta}{r} + C_f \frac{C_\theta \sqrt{C_\theta^2 + C_m^2}}{b \sin \phi} = 0 \tag{6}$$

Continuity equation

$$\frac{1}{\rho} \frac{dp}{dr} + \frac{1}{C_m} \frac{dC_m}{dr} + \frac{1}{b} \frac{db}{dr} + \frac{1}{r} = 0 \tag{7}$$

Ideal gas state equation

$$p = \rho RT \tag{8}$$

Energy equation

$$T_0 = T + \frac{C^2}{2C_p} \tag{9}$$

Wall surface friction coefficient

$$c_f = 0.01 \times \left(\frac{1.8 \times 10^5}{\mathrm{Re}} \right)^{0.2} \tag{10}$$

where ϕ is the angle relative to the axis of rotation.

The flow angle at the vane exit is expressed as the sum of the vane exit angle and the two terms representing flow deviation are given by

$$\alpha_4 = \alpha_{4b} - \delta^* - \left(\frac{d\delta}{di} \right)_{\mathrm{ref}} (i - i_{\mathrm{ref}}) \tag{11}$$

$$\left(\frac{d\delta}{di} \right)_{\mathrm{ref}} = \exp\left[-\sigma_s \left\{ 3.3 - \left(\frac{3\left(\frac{\pi}{2} - \alpha_{3,\mathrm{ref}} \right)}{\pi} \right)^2 \right\} \right] \tag{12}$$

As mentioned, the nominal deviation, the deviation under the reference incidence operation, is formulated by Carter's rule [3], and the derivative of deviation with respect to incidence is calculated via a formula given by Aungier [4].

The reference incidence angle, one of the important quantities in calculating the diffuser performance, is recommended to use the modified formula originally based on the tangent difference rule by Dixon [5], as follows:

$$\tan \alpha_{3,\mathrm{ref}} - \tan \alpha_{4,\mathrm{ref}} = \frac{1.55}{1 + \frac{1.5}{\sigma_s}} f(\alpha_{4,\mathrm{ref}}) \tag{13}$$

An additional multiplying function, as a third order polynomial, is introduced to the tangent difference rule in order to extend the applicable range of the low-solidity vane exit angles.

With an empirical correlation, the equivalent diffusion ratio is expressed as the sum of two terms; the first term is derived from correlations of data for blades operating near conditions of minimum loss and the second term represents an additional contribution when the cascade is operated at an incidence different from the reference value. When it exceeds about 2.0, the cascade row is assumed to be stalled.

$$D_{\mathrm{eq}} = D_{\mathrm{eq1}} + D_{\mathrm{eq2}} \tag{14}$$

$$D_{\mathrm{eq1}} = \frac{\sin \alpha_4}{\sin \alpha_3} \left(1.12 + 0.61 \frac{\sin \alpha_3^2}{2 \sin \alpha_m} |C_L| \right) \tag{15}$$

$$D_{\mathrm{eq2}} = k \frac{\sin \alpha_4}{\sin \alpha_3} \left(\frac{180}{\pi} |i - i_{\mathrm{ref}}| \right)^{1.43} \tag{16}$$

$$p_{04} = p_{03} - \mathrm{LC}_{34} (p_{03} - p_3) \tag{17}$$

Table 2 Governing equations and boundary conditions

Governing equation		Mass conservation equation Momentum equation (x, y, z) Turbulent equation
Boundary condition	Operating fluid	Air
	Inlet pressure	101,325 (Pa, total pressure)
	Inlet temperature	25 (°C)
	Flow rates	40 m^3/s
	Interface	Mixing plane method
	Turbulent model	Standard k-ε equation Wall function y^+: 52 (average) at wall
	Wall	Adiabatic

$$\mathrm{LC}_{34} = \mathrm{LC}_{\mathrm{sf}} + \mathrm{LC}_{\mathrm{pr}} + \mathrm{LC}_{\mathrm{sec}} \tag{18}$$

Three sources of total pressure loss are accounted for in the analysis of the cascade diffuser; the skin friction loss coefficient, one of the three sources, is estimated using a formula analogous to that used for pipe flows, as follows:

$$\mathrm{LC}_{\mathrm{sf}} = c_f \frac{L_B}{d_H} \left(\frac{\bar{C}}{C_3} \right)^2 \tag{19}$$

For the blade profile loss, an empirical correlation by Lieblein [6] is utilized for the required drag characteristics of the vane row, which relates the blade wake momentum thickness to the ratio of maximum-to-exit velocity, i.e., the equivalent diffusion ratio. The profile loss coefficient is modeled as follows:

$$\mathrm{LC}_{\mathrm{pr}} = 2\sigma_s \frac{0.004}{1 - 1.17 \ln(D_{\mathrm{eq}})} \left(\frac{\sin \alpha_3}{\sin \alpha_m} \right)^2 \left(\frac{\sin \alpha_m}{\sin \alpha_4} \right)^3 \tag{20}$$

The secondary flow loss, a loss due to secondary flow, provides a way to represent lift dependent losses using the form by Howell [7], based on the experience with matching test data for specific axial-flow compressor geometry. The secondary flow loss coefficient is given, as follows, in which a value of 0.018 is only a tentative suggested value and caution is advised:

$$\mathrm{LC}_{\mathrm{sec}} = 0.018 C_L^2 \sigma_s \left(\frac{\sin \alpha_3}{\sin \alpha_m} \right)^2 \tag{21}$$

3 The Verification for the Numerical Analyses

For the verification of CFD analysis results, the compression ratio and the compressor exit total temperature and efficiency were compared with experimental data for the *C*-type diffuser. The number of grid cells was about 190,000 for the impeller and 50,000 for the diffuser. The analysis was done by a CFX, which is a commercial CFD program. Table 2 describes the governing equations and boundary conditions. The mixing plane method was adopted to the calculation of the interface between the impeller exit and the diffuser inlet. In order to accelerate the convergence of the CFD analysis, the mass flow condition of the design point at the compressor inlet was given. The volute of the compressor was not included in this analysis. Therefore, it is difficult to compare accurately the experimental operating point of the compressor in this analysis. However, taking into consideration the above assumptions, the deviations for efficiency and the compressor exit total temperature and pressure ratio (total to total) in Table 3 were satisfactory. The data are from Figs. 11–13. Figure 4 shows the configuration of the modeled compressor. The stable increases of static pressure at midspan for the impeller and the diffuser are shown in Fig. 5.

Experimental processes are as follows. First, starting air from a high air pressure vessel is supplied to the combustor chamber where air is ignited with LPG fuel. Burned gas flow to the turbine of the turbocharger and then the compressor is operated by a

Downloaded 02 Jun 2010 to 171.66.16.109. Redistribution subject to ASME license or copyright; see http://www.asme.org/terms/Terms_Use.cfm

Table 3 Comparison between analysis and experimental results

	Expt.	CFD
Pressure ratio (t-t)	3.71	3.75
Compressor exit total temperature (°C)	182	188
Efficiency (%)	86.1	83.8

common shaft of the turbine. Mass flow rate measurement is done at the flow nozzle and the surging and choking conditions are measured by the main pipe and the scavenging exhaust valve operation. Figure 6 illustrates the schematic view of the turbocharger test facilities.

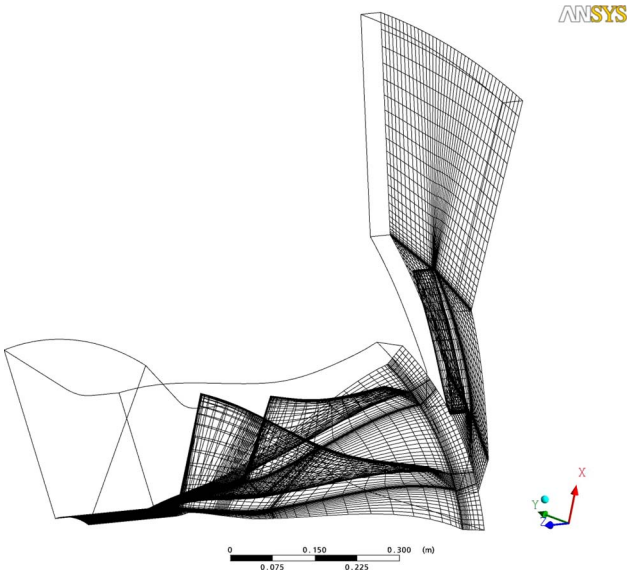


Fig. 4 Configuration for compressor modeling

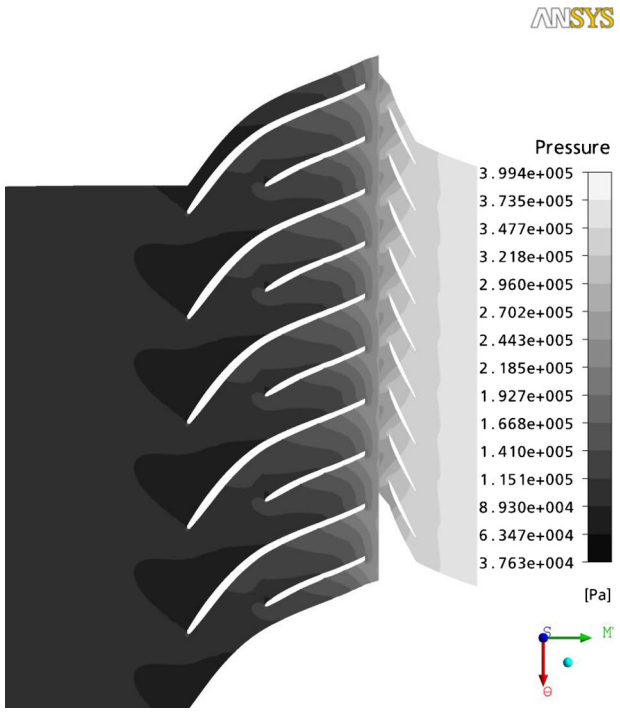


Fig. 5 Contours of the static pressure at midspan

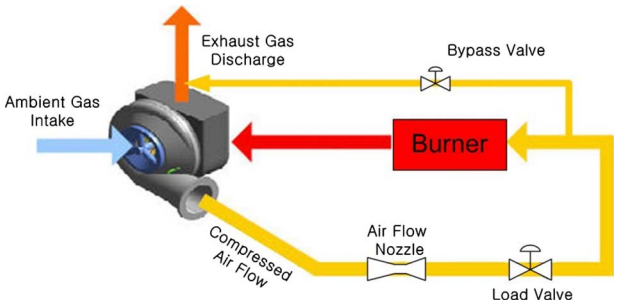


Fig. 6 Schematic view of the turbocharger test facilities

4 The Results and Discussion

Figure 7 shows the estimated operating range of the C-type diffuser with the mean-line prediction method. The maximum choke flow rate was determined when the Mach number at the inducer was 1.0. The throat blockage in the choke calculation was 0.015. The diffuser stall flow rate was determined when the equivalent diffusion ratio exceeds 2.0 or the Mach number is equal to unity due to reduced effective diffuser throat area.

Figure 8 shows the pressure recovery factor variation as the operating flow rate range is at a 100% revolution condition. The C-type diffuser has the highest pressure recovery factor (0.53) and has a wider operating range than the others.

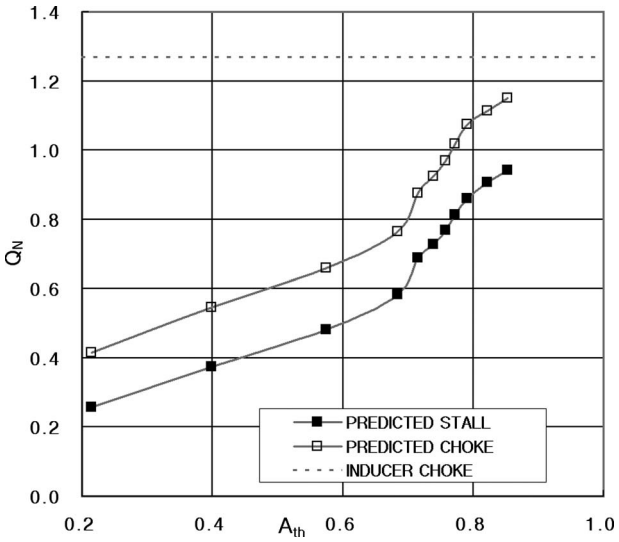


Fig. 7 Flow rates at the stall and choke conditions

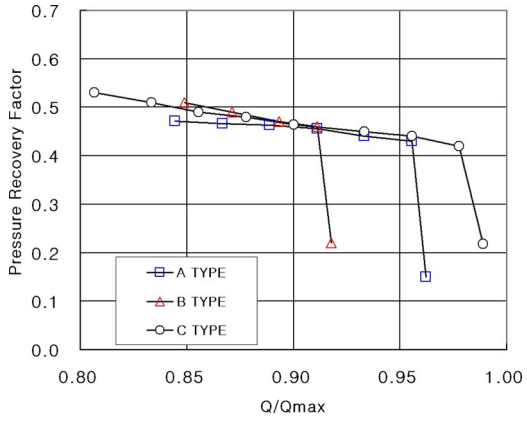


Fig. 8 Pressure recovery factor at different diffusers

Downloaded 02 Jun 2010 to 171.66.16.109. Redistribution subject to ASME license or copyright; see http://www.asme.org/terms/Terms_Use.cfm

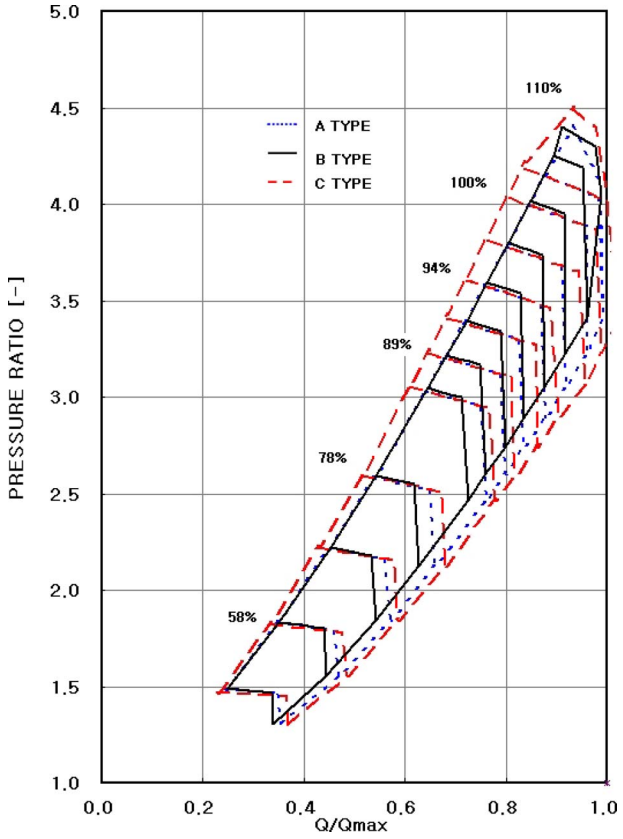


Fig. 9 Total pressure ratio versus flow rate (only predicted data)

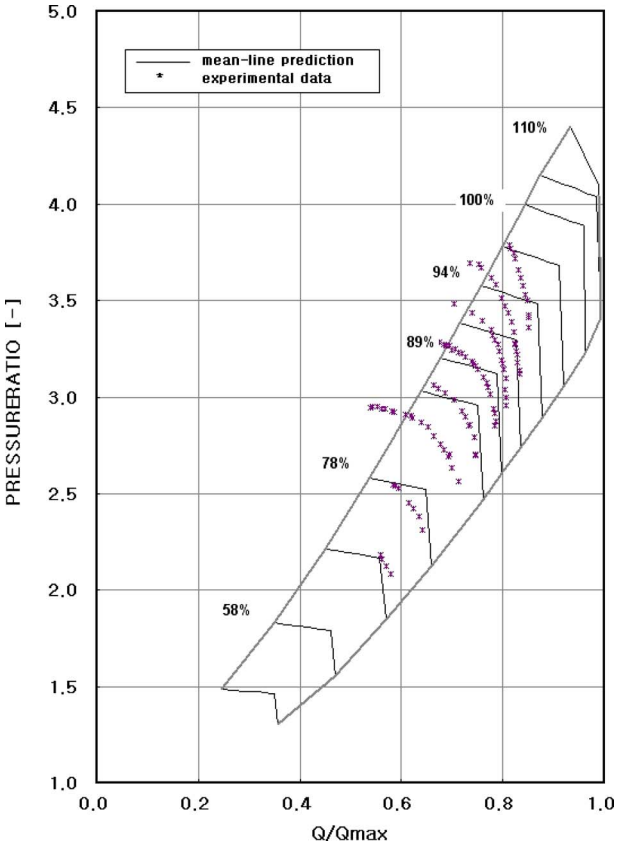


Fig. 10 *A*-type total pressure ratio versus flow rate (predicted and measured data)

Mean-line predictions for wide operating ranges were carried out on the three different diffusers, all with a common impeller.

Figure 9 shows a performance comparison of the *A*-, *B*-, and *C*-type diffusers. Although the *C*-type diffuser represents a slightly low compression ratio, the surging and choking margins are much larger than the two other diffusers. Its characteristics with experimental data are also depicted, as shown in Figs. 10–12. Point data were all measured.

From the measured data, the surge line of mean-line predictions was underestimated. Due to the possibility of system's danger, surge points were only measured for two or three operation conditions. In general, predicted data are considerably similar to measured data but compression slopes are different from measured data at high loads. The *B*-type diffuser has the lowest operating range among the diffusers. From the results in Table 4, the *C*-type diffuser is the best one with respect to the compression ratio, operating range, and size effect.

Although mean-line performance predictions were calculated for the three different diffuser models, three-dimensional viscous CFD analyses are necessary to confirm or to modify the diffuser loss models. Figures 13 and 14 show the static pressure and mach contours at midspan for the *C*-type diffuser. Figures 13 and 14 represent the flow acceleration and deceleration through the diffuser throat. The detailed CFD analysis results for the three diffusers are shown in Fig. 15. The *x*-axis represents the meridional length of the blade and the value of the *y*-axis represent the pressure value. From these results, it was found whether the diffuser shape design was reasonable or not. The important objective was to minimize the pressure difference between the pressure and the suction side. When the difference is bigger, pressure recovery and efficiency at the diffuser are smaller due to the secondary flow or separation. The minimum pressure difference and pressure recovery at the *C*-type diffuser was better than the *A* and *B*-type diffusers. The sudden pressure decrease and increase were shown at about the 10% position of the meridional distance; this position is the real diffuser throat.

Table 5 shows the comparison results between the mean-line prediction and the viscous CFD analysis at the design point for the *C*-type diffuser. The deviation is considerably smaller and the mean-line prediction is useful in evaluating the performance for a variety of diffusers [5–10].

5 Conclusions

In this study, the off-design behaviors of three different types of diffusers, given by mean-line prediction, were investigated, using CFD results and the best diffuser geometry, which satisfies wider operating range and a higher pressure recovery than the others, was selected. The numerical results were compared with the experimental data for validation. The comparison result shows good agreement with the experiment. The following conclusions are made based on this study.

(1) The mean-line prediction technique was efficiently verified by evaluating the performance and characteristics for the three different kinds of diffusers.
(2) The *C*-type diffuser (NACA 65-4A10) shows a much steeper surge line slope and a better surge operating margin

Downloaded 02 Jun 2010 to 171.66.16.109. Redistribution subject to ASME license or copyright; see http://www.asme.org/terms/Terms_Use.cfm

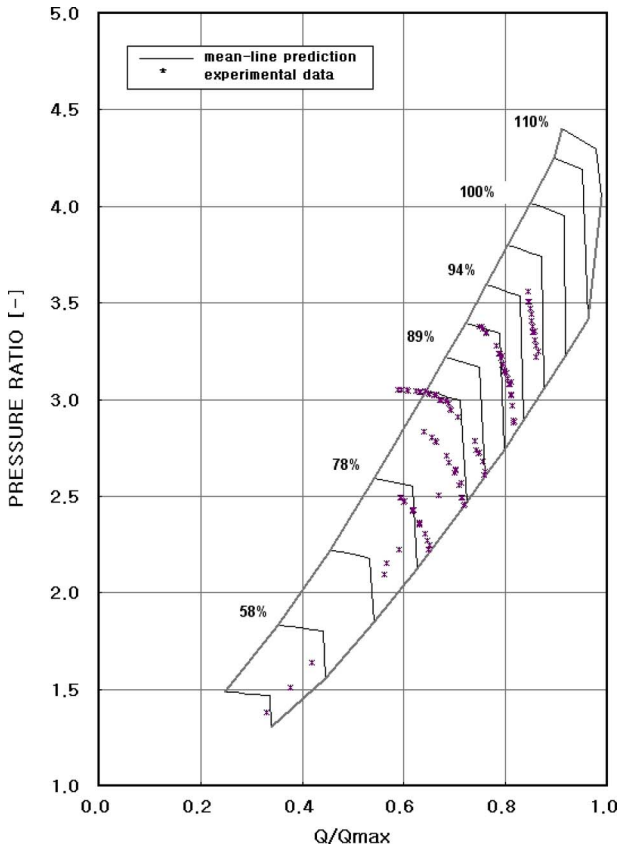


Fig. 11 *B*-type total pressure ratio versus flow rate (predicted and measured data)

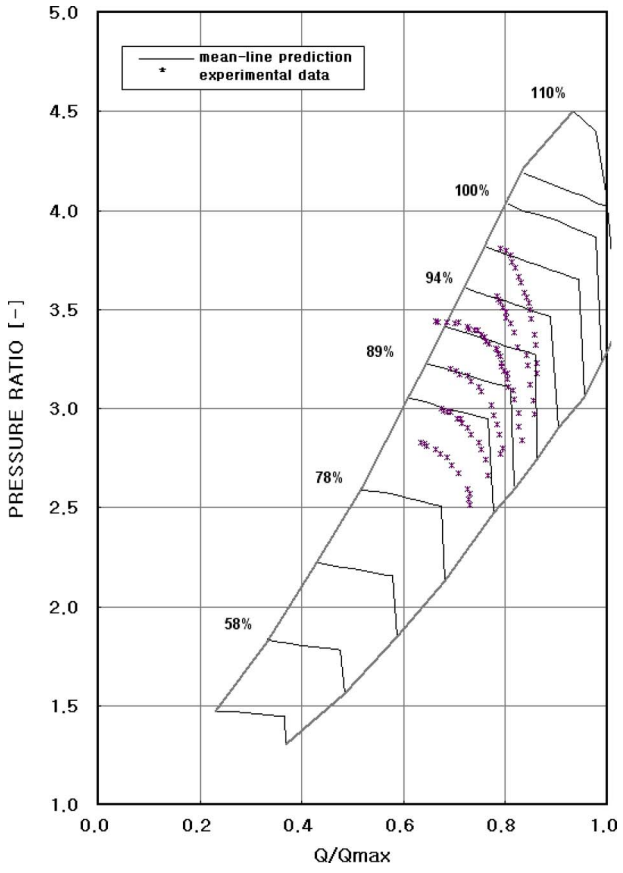


Fig. 12 *C*-type total pressure ratio versus flow rate (predicted and measured data)

Table 4 Performance comparison among the *A*, *B*, and *C* diffusers

	Compression ratio	Operating range	Size effect	Evaluation
A-type	Good	Bad	Good	2
B-type	Good	Bad	Bad	3
C-type	Good	Good	Good	1

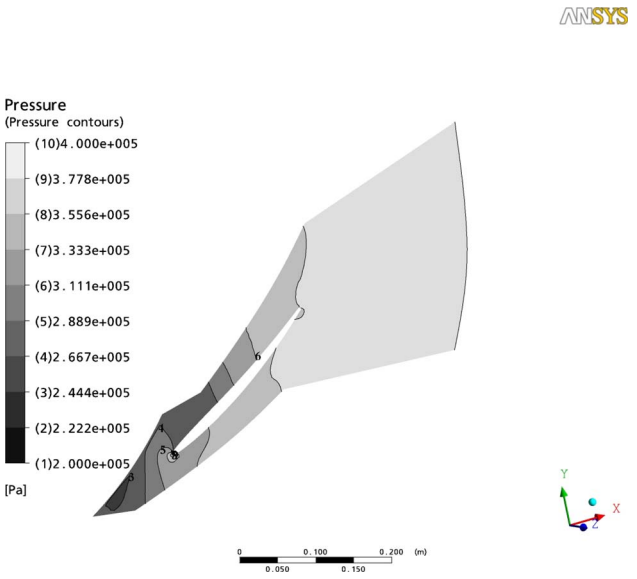


Fig. 13 Pressure contours at midspan

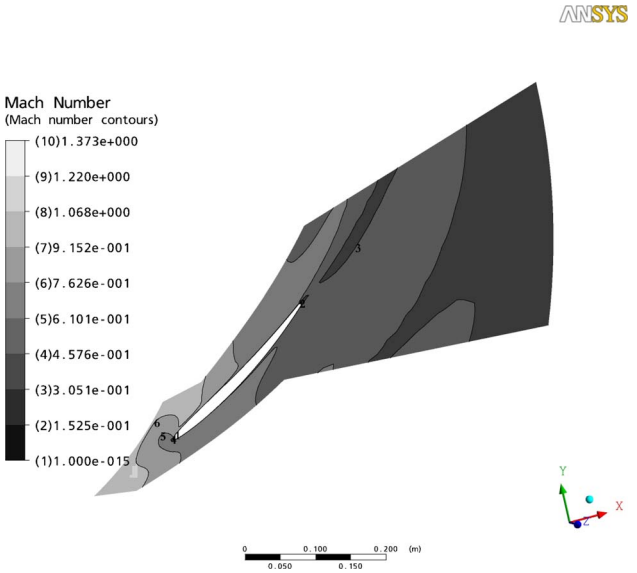


Fig. 14 Mach number contours at midspan

including compression ratio characteristics, than any other diffuser.

(3) From the measured data, the exact surging and choking lines were confirmed and its criteria were established. The surging flow rate was determined when the equivalent diffusion ratio exceeds 2.0 or when the Mach number is equal to unity due to the reduced effective diffuser throat area.

Downloaded 02 Jun 2010 to 171.66.16.109. Redistribution subject to ASME license or copyright; see http://www.asme.org/terms/Terms_Use.cfm

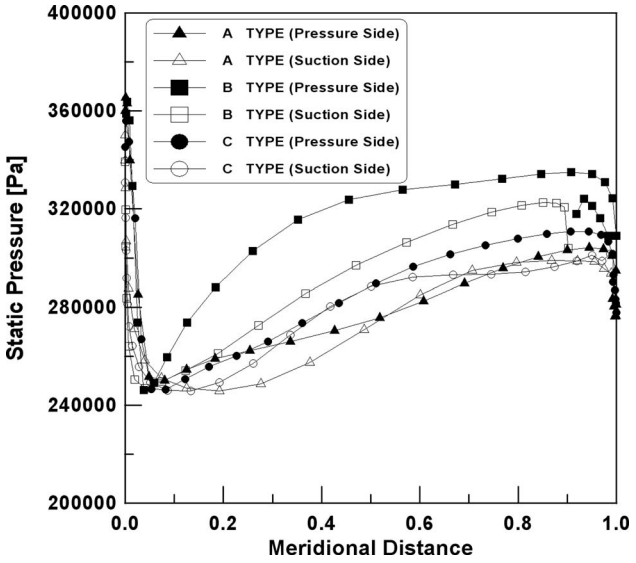


Fig. 15 Pressure distribution at midspan

Table 5 Comparison between the mean-line prediction and the CFD results

	Mean-line prediction	CFD
Pressure recovery factor	0.46	0.48
Pressure loss coefficient	0.21	0.27

Nomenclature

AR = diffuser area ratio (inlet versus outlet)
A_{th} = diffuser throat area divided by the NACA 65 throat area
K = pressure loss coefficient
C_p = pressure recovery factor; specific heat at constant pressure
Q = flow rate
Q_n = design point flow rate
C_L = lift coefficient
$\dot{m}$ = mass flow rates
δ^* = norminal deviation
σ_s = solidity
L_B = diffuser length
U = circumferential speed
Δh = enthalpy difference
d_H = diffuser width
LC = loss coefficient
P = pressure
R = gas constant
α = flow angle
Z = blade number
C = absolute velocity
ρ = density
b = diffuser width
T = temperature
i = incidence angle
C_f = friction coefficent
Re = Reynolds number
r = radius
η = efficiency

Subscripts

0 = stagnation
1 = impeller inlet
2 = impeller exit
3 = diffuser inlet
4 = diffuser exit
m = meridional direction
max = maximum
θ = tangential direction
r = radial direction
ref = reference
eq = equivalent
sf, pr = surface, profile
sec = secondary

References

[1] Japikse, D., and Baines, N. C., 1998, "Diffuser Design Technology," Concepts ETI, Inc.
[2] Jiang, W., Khan, J., and Dougal, R. A., 2005, "Dynamic Centrifugal Compressor Model for System Simulation," J. Power Sources, **158**, pp. 1333–1343.
[3] Carter, A. D. S., and Hughes, H. P., 1946, "A Theoretical Investigation Into the Effects of Profile Shape on the Performance of Aerofoils in Cascade," British ARC R&M 2384.
[4] Aungier, R. H., 1988, "A Systematic Procedure for the Aerodynamic Design of Vaned Diffusers," Flows in Non-Rotating Turbomachinery Components, ASME FED-Vol. 69, pp. 27–34.
[5] Dixon, S. L., 1978, *Fluid Mechanics, Thermodynamics of Turbomachinery*, Pergamon, Oxford.
[6] Lieblein, S., 1959, "Loss and Stall Analysis of Compressor Cascades," ASME J. Basic Eng., **81**, pp. 387–400.
[7] Howell, A. R., 1945, "Fluid Dynamics of Axial Compressor," Proc. Inst. Mech. Eng., **153**, p. 452.
[8] Kim, H.-W., Ryu, S.-H., Ghal, S.-H., Ha, J.-S., and Rhee, S.-K., 2005, "A Numerical Approach for the Design of the Compressor Impeller Exit Diameter Variations in a Marine Engine Turbocharger," ASME Paper No. GT-2005-68653.
[9] Japikse, D., 1996, "Centrifugal Compressor Design and Performance," Concepts ETI, Inc.
[10] Oh, J. S., 2002, "Investigation of Off-Design Performance of Vaned Diffusers in Centrifugal Compressors—Part II: A Low Solidity Cascade Diffuser," ASME Paper No. GT-2002-30388.

Downloaded 02 Jun 2010 to 171.66.16.109. Redistribution subject to ASME license or copyright; see http://www.asme.org/terms/Terms_Use.cfm

Design, Fabrication, and Performance of Foil Gas Thrust Bearings for Microturbomachinery Applications

Brian Dykas
US Army Research Laboratory,
21000 Brookpark Road,
Cleveland, OH 44135

Robert Bruckner

Christopher DellaCorte

Brian Edmonds

NASA Glenn Research Center
21000 Brookpark Road,
Cleveland, OH 44135

Joseph Prahl
Case Western Reserve University
10900 Euclid Avenue,
Cleveland, OH 44106

A methodology for the design and construction of simple foil thrust bearings intended for parametric performance testing and low marginal costs is presented. Features drawn from a review of the open literature are discussed as they relate to bearing performance. The design of fixtures and tooling required to fabricate foil thrust bearings is presented, using conventional machining processes where possible. A prototype bearing with dimensions drawn from literature is constructed, with all fabrication steps described. A load-deflection curve for the bearing is presented to illustrate structural stiffness characteristics. Start-stop cycles are performed on the bearing at a temperature of 425°C to demonstrate early-life wear patterns. A test of bearing load capacity demonstrates useful performance when compared with data obtained from the open literature.
[DOI: 10.1115/1.2966418]

1 Introduction

Foil gas bearings represent an enabling technology for advanced oil-free turbomachinery systems. Operating at high speeds and temperatures, these next-generation turbomachines will present tribological challenges that conventional oil-lubricated rolling element bearings may be unable to meet, including shaft speeds well above 3×10^6 DN (shaft diameter in millimeters multiplied by the shaft rotational speed in rev/min) and bearing temperatures in excess of 400°C [1]. Continued advancement of foil bearing technology will allow more widespread adoption of oil-free shaft supports in high speed rotating equipment.

As described by DellaCorte et al. [2], machine designers have been slow to adopt this technology into candidate systems due to the relatively small number of foil bearing manufacturers and a perception of risk. Beyond a specific expertise in the details of gas dynamic lubrication, the fabrication of foil bearings requires a technical knowledge of metallurgy, sheet metal forming, and tribology, dissuading many from attempting their manufacture and development. The information presented herein attempts to provide a basic methodology for the production of prototype thrust bearings for technology evaluation and research.

A further motive for describing the fabrication of foil thrust bearings is the relative dearth of information in the open literature regarding their design, construction, and performance, especially when compared with their journal bearing counterparts. The patent literature contains many references to design practices for the compliant structure supporting the top foil, but only a handful of authors have presented experimental evaluations of performance [3].

Those experimental evaluations are a necessary and critical part of the design effort. Valco and DellaCorte [4] recommended a four-step approach for transitioning foil bearing technology into specific turbomachines: (1) concept feasibility assessment, (2) bearing component development and testing, (3) simulated rotor system testing, and (4) turbomachinery system demonstration. This process provides a staged approach to bearing integration that mitigates technical risk with each step.

Performance guidelines have been established to predict journal bearing load capacity [1] and power loss performance [5] for the initial concept feasibility step. The open literature contains many examples of bearing component development and testing (see Ref. [2] for a brief discussion of journal bearing development history). Similar guidelines for foil thrust bearings have not yet been validated, however, and fewer details of thrust bearing development and testing are freely available. Simulated rotor testing can be performed with facilities such as described by Howard [6], but this type of testing focuses mostly on the radial (orbit) motion of the shaft, whereas thrust loading is more difficult to simulate. The net result is that foil thrust bearing tools have not experienced the same degree of development as those for journal bearings, increasing the technical risk in transitioning them to new turbomachines.

To ameliorate some of the challenges in thrust bearing development, DellaCorte et al. [7] suggested that oil-free turbomachine designs should attempt to minimize thrust loads to reduce load capacity requirements and improve design margin. They also suggested that with lower thrust loading, bearings can be sized smaller to reduce power loss and cooling requirements, driving overall system efficiency higher. Furthermore, lower thrust loads allow a reduction in rotating mass and inertia due to a smaller thrust runner, which can improve the rotordynamic characteristics of the shaft. While conventional rolling element bearing-supported machines are designed to always have a net positive thrust load to prevent skidding of the rolling elements, foil bearings do not require, nor do they benefit from this practice. Consequently, somewhat different design practices are required and employed in foil bearing-supported systems.

2 Background

Foil bearings are hydrodynamic bearings composed of compliant surfaces and generally employ a gaseous lubricant. In both geometries a rotating member drags the viscous process fluid into

Contributed by the International Gas Turbine Institute of ASME for publication in the JOURNAL OF ENGINEERING FOR GAS TURBINES AND POWER. Manuscript received March 28, 2008; final manuscript received April 8, 2008; published online October 1, 2008. Review conducted by Dilip R. Ballal. Paper presented at the ASME Turbo Expo 2008: Land, Sea and Air (GT2008), Berlin, Germany, June 9–13, 2008.

Copyright © 2009 by ASME

Downloaded 02 Jun 2010 to 171.66.16.109. Redistribution subject to ASME license or copyright; see http://www.asme.org/terms/Terms_Use.cfm

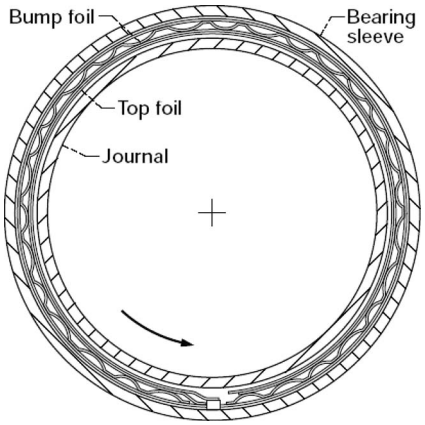


Fig. 1 Typical geometry of a modern foil journal bearing

a converging gap, raising the fluid pressure and providing a load carrying capacity. Figures 1 and 2 show the basic components of journal and thrust foil bearings.

Foil bearings were first reported in the open literature by Blok and Van Rossum [8]. These early tension-dominated oil-lubricated bearings were found to allow thicker fluid films than rigid geometry bearings under a given loading condition, and their compliance provides increased tolerance to misalignment, shock loading, rotor distortions due to centrifugal and thermal stresses, and other deviations from optimal geometry. This tolerance to component-level and system-level geometric distortions is particularly important when using a thin gas film as opposed to a relatively thick viscous oil film. Bending-dominated foil journal bearings followed, with a smooth sheet metal foil providing the bearing surface, and reinforced by a compliant foil support structure. Some of the earliest compliant thrust bearings were more of an outgrowth of predecessor step and tilting pad bearings than a revolution in design and function.

Common practice in modern foil bearings is to use corrugated "bump foils" to form the compliant structure, with many designs incorporating several layers of bump foils to tailor stiffness properties as a function of bearing loading [9]. The further use of "stiffener foils" between the top and bump foils is an established practice to allow optimization of the bearing deflection behavior. DellaCorte and Valco [1] provided a simple relationship to estimate journal bearing load capacity at various operating conditions, where it is found that the increased complexity of bearings with these features allows for several-fold improvements in bearing load capacity over the simplest designs.

The patent literature shows an abundance of alternative designs for foil journal bearings including multipad and overlapping "leaf" designs [10,11], with early foil thrust bearing designs employing similar configurations. However, the earliest foil thrust bearing patents incorporate more advanced design features than are seen in the first foil journal bearing patents. In the first appearance of a bump foil type thrust bearing in the patent literature [12], a bearing is described with multiple smooth foils tailored to provide speed- and load-dependent deflection behavior for increased load capacity.

This multistage deflection-dependent bearing stiffness is described as a key feature in modern high load capacity foil journal bearings, though more often achieved by multiple bump layers [9]. Furthermore, descriptions of variable stiffness in the radial [10] and azimuthal [13] directions of the pad appear in the early patents. A number of patents describe a stiffness distribution matching that of the pressure distribution as a technique to increase load capacity [14,15].

It is notable that in contrast to journal bearings, typical thrust bearing configurations result in large differences between runner surface velocities at the inner and outer diameters of the thrust pads. Bump foil structures must be designed to provide appropriate stiffness distributions to account for these gradients in runner surface velocity.

Another effect described in literature is crowning of the runner surface. Here, the heat input from viscous dissipation in the gas film leads to an axial temperature gradient in the thrust runner, resulting in a convex rotating surface. Early patents acknowledge the effectiveness of a compliant foundation in compensating for this phenomenon [10,14] and describe structural tailoring as a way to combat its deleterious effects [16]. Centrifugal stress distortions in the rotating runner can also be accommodated by a compliant bearing surface.

Tailoring of the bearing stiffness distribution to accommodate system-level effects, such as misalignment, also appears in the early literature. Gray and Heshmat [16] described a bearing whose outer sections are more compliant than inner sections, allowing increased deflection at the outermost radius of the bearing, preventing high speed rubbing contact.

Although a review of patent disclosures yields a wide array of techniques for increasing thrust bearing performance, only a few studies have been published providing experimentally measured

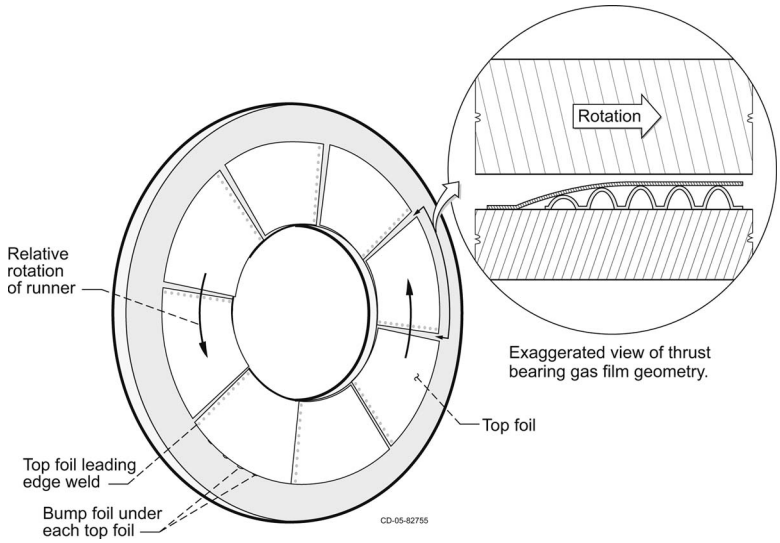


Fig. 2 Typical geometry of a modern foil thrust bearing

Downloaded 02 Jun 2010 to 171.66.16.109. Redistribution subject to ASME license or copyright; see http://www.asme.org/terms/Terms_Use.cfm

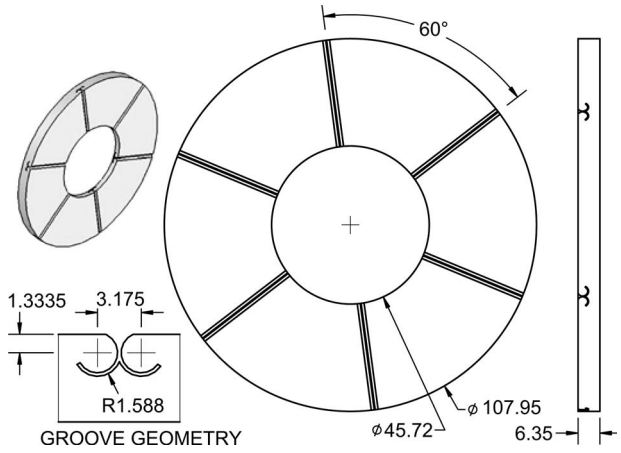


Fig. 3 Drawing of a bearing backing plate with foil-retaining slots (dimensions in millimeters)

bearing performance [17,18] with these focusing mainly on simpler bearing designs. Specific details of advanced bearing designs remain proprietary and protected under U.S. patent law, thereby restricting the availability of performance data for state-of-the-art bearings. Despite these restrictions, a number of advanced features are described in expired patents and are therefore freely available to would-be bearing designers. A modular foil thrust bearing architecture facilitates the parametric evaluation of the effectiveness of these features. In Secs. 3–6, a basic design is developed, fabricated, tested, and discussed. The primary purpose of this work, however, is to demonstrate the manufacturing process in order to stimulate more widespread adoption of the technology.

3 Design Features

The baseline test bearing is designed to have several discrete pads composed of three major components: a top foil to provide the stationary boundary for the hydrodynamic gas film, a bump foil structure to provide compliant support for the top foil, and the thrust bearing backing plate, as shown in Fig. 2. In more advanced bearings, multistage bump foils [9] and reinforcing stiffener foils [13] are generally incorporated into this basic design.

Many foil thrust bearing designs rely on the use of spot or tack welds to attach the foil members to the rigid backing plate. This attachment method can have adverse effects, as noted by Della-Corte et al. [2], particularly if the individual bearing components are heat treated prior to welding. Additionally, welding precludes the ability to remove and reinstall the foil components, which is conducive to rapid and inexpensive bearing design iterations as well as increased instrumentation access.

In an attempt to produce a versatile thrust bearing design that provides ample access for instrumentation, such as thermocouples and heat flux gauges affixed directly to the underside of the top foil, welding is not used. Instead, the backing plate is slotted to allow the top foils to be easily installed and removed, as shown in Fig. 3. For simplicity, a partial-arc circular slot is cut into the plate at the leading edge of each pad so that the top foil is restrained tangentially by a curled-over tab, as shown in Fig. 4. This attachment method is similar to a circular mounting slot proposed by Agrawal and Hockey [19]. An identical slot on the trailing edge allows the bump foil to be attached in the same manner. This provides higher stiffness at the trailing edge of the pad [20,21] to preserve the converging film under load. Alternate arrangements are also envisioned, including one or more bump foils attached at the leading edge of the pad or incorporating a stiffener foil attached at either the leading or trailing edge. As opposed to a configuration where many foil layers are fastened together in a stacked arrangement [21,22], this configuration requires a minimal amount of tooling and specialized forming equipment for subsequent iterations in design. The authors do not claim that this specific architecture will result in optimized performance, but it is conducive to relatively rapid and inexpensive technology evaluation, provided suitable test facilities are available.

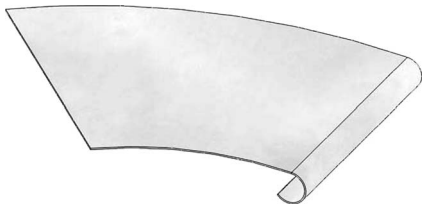


Fig. 4 Sketch of top foil with hinged leading edge

A further advantage of the curled-over leading edge of the top foil is that it provides a smooth transition region for the process fluid at the leading edge. Whereas welding the top foils to precision spacer blocks can, with care, provide better dimensional accuracy, the curled region provides increased tolerance to misalignment at the entrance region. It is also notable that this slot arrangement provides slight hinging motion to allow the top foil to seat on the bump foils more repeatably.

When the bearing is assembled, tack-welded shims are inserted into the curled slots at the inner and outer radii of the foil to prevent radial sliding of the foil components. The shims can be removed easily to allow mass-based measurements of top foil wear volume as well as attachment of fine gauge thermocouples, heat flux gauges, and other instrumentation. Although more elaborate methods can be used to constrain the top foil radial movement, such as set screws or other fasteners, the current method provides adequate performance, flexibility, and ease of manufacturing.

4 Tooling and Fabrication

Typically, foil thrust bearings consist of a discrete number of thrust pads, each having an arcuate shape where a top foil extends circumferentially with constant inner and outer diameters from the leading edge of the pad to the trailing edge. Since the top foil generally defines the boundaries of the gas film, the pad extent is taken in this configuration as the angular distance from leading to trailing edge of the top foil, independent of the details of the compliant understructure. Because this shape does not easily lend itself to common sheet metal forming equipment, the foil blanks used to construct the pads are cut around the perimeter using wire electrical discharge machining (EDM). Other methods commonly used as described in the open literature include stamping and chemical milling processes.

A bearing backing plate, as shown in Fig. 3, is first machined and surface ground to produce flat and parallel faces. The partial-arc slots needed to retain the foil components are then machined by wire EDM. Conveniently, slot thicknesses achievable by a single wire pass are appropriate to accommodate the practical range of foil thicknesses, leaving a small clearance in the hinge to permit motion. The backing plate is constructed from a nickel-based superalloy (Inconel 718) to allow heat treatment of the entire assembled bearing as well as to permit high temperature operation. However, other dimensionally stable materials, such as precipitation hardened stainless steel, can conceivably be used for this component as operational conditions dictate.

The top and bump foil blanks are cut from stacks of annealed Inconel X-750 foil by the same EDM process. Dimensions of the foil blanks are given in Figs. 5 and 6, where the bump foil has several azimuthal slits separating it into five individual bump strips, as described by Gray and Heshmat [16]. This configuration allows for variable bump spacing, which helps to accommodate

Downloaded 02 Jun 2010 to 171.66.16.109. Redistribution subject to ASME license or copyright; see http://www.asme.org/terms/Terms_Use.cfm

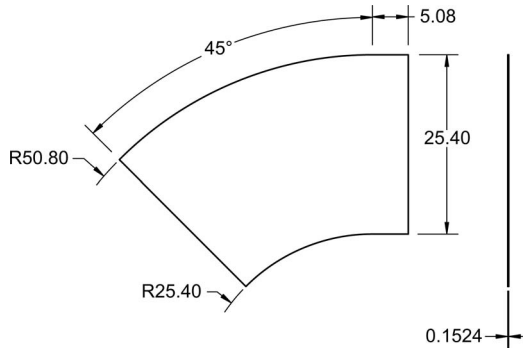


Fig. 5 Drawing of top foil blank (dimensions in millimeters)

the effects of varying surface velocity, thermal crowning, centrifugal dishing, and misalignment. The rectangular tabs are sized to fit into the backing plate slots.

There is a great deal of freedom in the design of the tooling required to form the bump foils. Although stamping or hydroforming methods may be appropriate for higher volume production designs, they are not as well suited to one-off prototype designs. For this application, a rather traditional set of conventionally machined dies is selected, and bump foil blanks are pressed into the dies for forming. This arrangement mimics the method reported by DellaCorte et al. [2], who described a set of bump foil dies for foil journal bearings that provide for relatively inexpensive fabrication of various bump configurations.

In practice, the same tooling intended to create bump foils for journal bearings can be adapted to press bump foils for thrust bearings. This tooling usually has parallel corrugations, and a thrust bearing bump foil blank can be pressed into that tooling in the same way as a journal bearing blank. This method is attractive in that it requires little additional equipment beyond what is required to fabricate journal bearings. However, to demonstrate an alternate configuration the authors have chosen an arrangement where all bumps are oriented radially.

The bump foil die begins as a circular disk constructed from a suitable steel, such as 15-5 PH [2], which has been ground flat and parallel. Channels are then machined into the disk, corresponding to the desired corrugated bump profiles. These channels have a profile achieved by milling 508 μm deep with a 3.175 mm ball end mill, which approximates the bump profiles, as described by Ruscitto et al. [23] and Heshmat et al. [24]. A number of different arrangements can be employed, including a conventional milling machine with the workpiece held on a rotary table or dividing head or with the piece held fixed in a computer numeric control (CNC) mill. This provides several options for a general machine shop to fabricate the tooling without specialized equipment.

Whereas the bump spacing in foil journal bearings is typically described by a linear bump pitch, the radially oriented bumps in this design are separated by prescribed angular separations. For

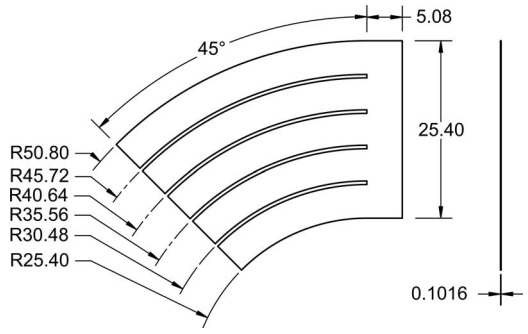


Fig. 6 Drawing of bump foil blank (dimensions in millimeters)

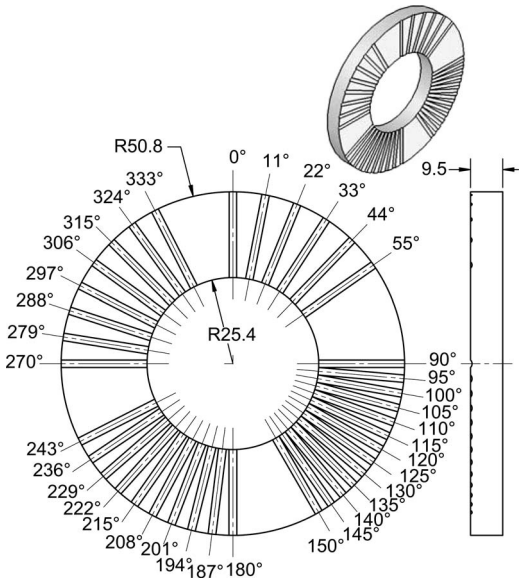


Fig. 7 Drawing of bump foil die with radial channels (dimensions in millimeters)

this work, the die disk has been divided into four sections where the radial channels are spaced by 5 deg, 7 deg, 9 deg, and 11 deg, respectively, as shown in Fig. 7. Each of these sections contains bump rows extending approximately 60 deg to allow construction of bearings with pad extents longer than the standard 45 deg shown here. To allow bump foils to be constructed with azimuthal strips of varying bump spacing, the plate is separated into five concentric rings using wire EDM. The rings can then be rotationally indexed to produce a wide array of different bump foil configurations, as shown in Fig. 8.

The bump foil blanks (Fig. 6) are arranged on the die to produce the desired bump layout and a 1.6 mm thick layer of polytetrafluoroethylene (PTFE) is placed over the foil, with a thick steel block resting on top (Fig. 9). This stack is then placed in a manual hydraulic press and approximately 20 MPa of pressure is applied to form the bump foils. Figure 10 shows the bump foil and PTFE after forming, where the cold flow behavior of the PTFE was found to produce better-formed bumps than the polyurethane and rubber sheets also tested. Because the bump foil is formed in a soft (annealed) state, the formed bump experiences very little spring-back when removed from the die, but this effect has not been quantitatively measured in the current work.

After formation of the top and bump foils, the hinged edges of the foils (Fig. 4) are curled in situ by bending them into the backing plate slots. A 3.2 mm diameter pin is used in conjunction with the backing plate to aid in the forming. Because this forming

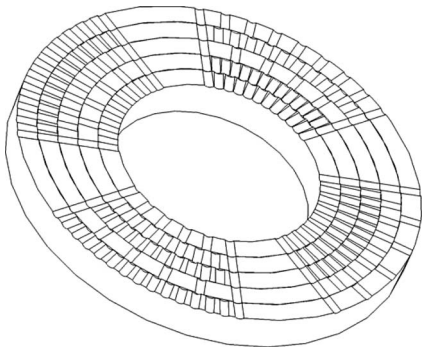


Fig. 8 Drawing of bump foil die with indexed concentric rings

Downloaded 02 Jun 2010 to 171.66.16.109. Redistribution subject to ASME license or copyright; see http://www.asme.org/terms/Terms_Use.cfm

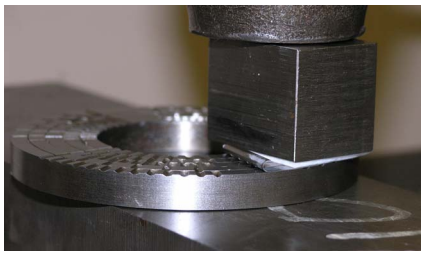


Fig. 9 Bump foil being formed in hydraulic press

operation is done by working the foil directly into the plate, no additional specialized fixtures and tools are required for this operation. Photographs of the prototype bearing during and after assembly are shown in Figs. 11 and 12.

Following the final forming steps of the foil members, metal straps are spot welded in the slots immediately adjacent to the inner and outer radii of the foils to prevent radial motion of the foils (shown in Fig. 12). Due to the arcuate nature of the pads, frictional torque exerts a radially inward force on the top foil when it is restrained on the leading edge, making the inner straps more critical to proper bearing operation. With the bearing fully assembled in this manner, there is a small amount of motion permitted in the hinge point of the top foil, though this is adjustable based on the thickness of the slot created by wire EDM. The bearing is then heat treated as an assembly.

To properly form the top foils during heat treatment, they are seated against the bump foils under a small compressive force of 2 kPa, based on the total top foil area. Circular plates appropriately massed for this purpose and compatible with the heat treatment temperatures have demonstrated acceptable performance in this study when rested on top of the bearing during the treatment. The Inconel X-750 alloy commonly used for bearing foils is generally supplied in the annealed or solution heat treated state, in



Fig. 10 Bump foil and PTFE after forming



Fig. 11 Prototype bearing with one top foil removed



Fig. 12 Photograph of assembled prototype bearing after heat treatment of foils

which it is formed into the appropriate bearing members. From these states, various heat treatments are possible to achieve desirable mechanical properties, some of which are described by DellaCorte et al. [2]. For information on the recommended heat treatments for Inconel X-750 as well as other nickel- and cobalt-based alloys, the reader is referred to AMS 2774A [25].

Prototype bearings are heat treated at 732°C for 16 h, followed by an air cool, per AMS 5698. Although this AMS specification is intended for cold drawn wire, it has been found to be appropriate for the thin foil employed in these bearings. This heat treatment is chosen because it provides acceptable elastic properties at elevated temperatures in excess of 540°C but does not require an inert gas or vacuum environment. In general practice, however, it may be desirable to conduct this heat treatment in a nonoxidizing atmosphere to better control the foil surface chemistry and prevent alloying constituents from being depleted due to surface oxidation.

5 Prototype Geometry

Based on the basic design principles outlined in Secs. 3 and 4 and dimensions available in the open literature, a prototype bearing geometry is selected, with relevant dimensions given in Table 1. These dimensions are chosen in most cases out of convenience and no attempt has been made to optimize performance by varying these parameters. For detailed analysis on foil thrust bearings as well as available geometry and performance data, the reader is referred to Refs. [3,17,18,20,26–30].

Foil thrust bearings typically contain four to eight pads with individual angular extents of approximately 45 deg and a ratio of outer radius to inner radius of about 2. Heshmat et al. [29] provided a detailed optimization study concerning these bearing parameters. The bearing described here contains six identical pads each with an angular extent of 45 deg and a radius ratio of exactly 2 to represent typical thrust bearing designs.

Table 1 Prototype bearing geometry

Inner diameter	5.08 cm
Outer diameter	10.16 cm
Pad angular extent	45 deg
Single pad area	7.6 cm^2
Number of pads	6
Total pad area	45.6 cm^2
Top foil coating	Bare Inconel X750
Top foil thickness	152 μm
Bump foil thickness	102 μm
Number of bump foil strips	5
Bump pitches (ID to OD)	5.36 mm, 5.19 mm, 4.65 mm, 3.77 mm, and 5.90 mm

Downloaded 02 Jun 2010 to 171.66.16.109. Redistribution subject to ASME license or copyright; see http://www.asme.org/terms/Terms_Use.cfm

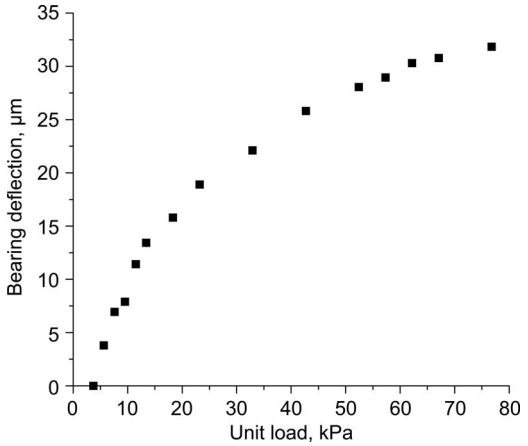


Fig. 13 Load-deflection curve for prototype bearing

Agrawal [22], who described a somewhat more complex foil thrust bearing than is undertaken in this study, noted that a bearing intended for a 50,000–100,000 rpm turbocompressor for an air cycle air conditioning system would typically have a 127–152 μm thick top foil and an overall diameter of 10.16 cm. Based on this guidance, the outer diameter of the prototype bearing is set at 10.16 cm, and the top foil thickness is chosen to be 152 μm.

While the individual bump geometry can vary widely, a bump depth of 500 μm is selected for the prototype bump foil die based on data taken from Refs. [3,13]. Although the referenced designs incorporate bumps that vary slightly in height along the extent of the pad, the bump heights in the prototype design are nominally equal, and the converging wedge geometry is developed from the hinged leading edge to the first bump. Iordanoff [17,18] provided comprehensive analysis of the gas film profile, which is a useful tool to improve on the bump geometry employed in this study. The radius of curvature for the bump is chosen to be 1.6 mm, as produced by a 3.2 mm diameter (1/8 in.) ball end mill. Bump foil thickness is chosen to be approximately 100 μm to mimic forming characteristics reported by DellaCorte et al. [2]. Each bump foil blank is divided into five bump strips of equal radial extent, ignoring the slit widths.

Heshmat [13] reported a radially varying compliance distribution that puts the stiffest bump strips at the radial center of the pad, a soft bump strip on the inner radius where unit loading is lightest and medium bump stiffness on the outer diameter where loads are moderate, but increased compliance is required to accommodate misalignment. This qualitative design is chosen for the prototype bearing bump foil in order to demonstrate the capabilities of the indexable tooling previously described. Starting from the innermost bump strip and progressing radially outward angular bump spacings of 11 deg, 9 deg, 7 deg, 5 deg, and 7 deg provide approximate midline bump pitches of 5.36 mm, 5.19 mm, 4.65 mm, 3.77 mm, and 5.90 mm, respectively.

6 Experimental Results

After assembly of a prototype bearing, several experimental tests are performed to verify proper bearing operation. A load-deflection test of the bearing is first performed to ensure that the chosen compliant structure provides aggregate stiffness characteristics within an appropriate range for a bearing of this size. Figure 13 shows the average deflection of the bearing for various applied loads, where the load is reported per unit pad area. This shows an incremental bearing stiffness per pad area in the range of 1–10 N/mm^3 for unit loadings of 7–70 kPa.

Following the load-deflection test, the bearing is subjected to elevated temperature (425°C) start-stop cycling against a PS304



Fig. 14 Wear pattern on top foil after start-stop cycling at high temperature

[31,32] solid lubricant-coated thrust runner to simulate the early surface-conditioning process that is expected to occur in a turbomachine application. During these cycles, a constant axial load of approximately 7 kPa is applied to the bearing as the runner is accelerated from rest to 20,000 rpm, held for a short time, and decelerated to a stop over a total-cycle period of about 15 s. This cycle profile exposes the bearing to dry sliding contact at low speeds as well as full-airborne operation at higher speeds, as would be experienced in practical applications. Figure 14 is a post-test photograph of a thrust bearing top foil, showing characteristic top foil wear after cycling at high temperature.

After this initial conditioning test of more than 1000 cycles, the bearing is run at a constant speed of 23,000 rpm while increasing axial load in increments of 4–10 N followed by several minutes of dwell time at each load. Load capacity is reached when a large increase in torque accompanies a very small increase in load. Figure 15 shows the load-torque curve at 23,000 rpm, where the load capacity is determined to be 125 N. This is a modest value of load capacity, but it demonstrates the viability of this bearing design for parametric studies.

To compare the load capacity performance of the prototype bearing to published data, it is important to take into account, at a minimum, the bearing geometry and operating speeds. DellaCorte and Valco [33] reported a simple rule-of-thumb model to aid in comparing the relative performance of various foil journal bearings, where the load capacity is estimated by a linear function of bearing surface velocity and bearing projected area, multiplied by a dimensional performance coefficient characteristic to the bearing design.

Their reported expression provides an estimate of bearing performance based on engineering first principles and corroborated by empirical data, and it is anticipated that a similar performance model can be developed for foil thrust bearings. The equivalent mathematical expression for thrust bearings, accounting for differences in geometry, is given as

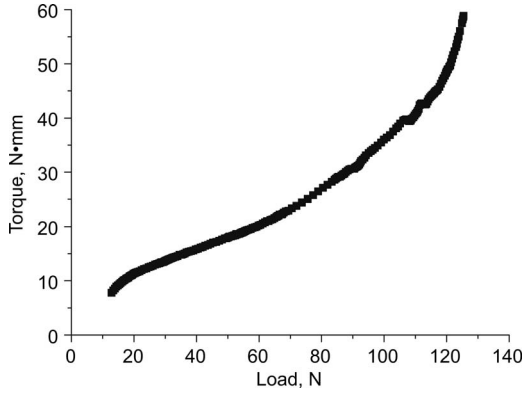


Fig. 15 Torque versus load at 23,000 rpm

Downloaded 02 Jun 2010 to 171.66.16.109. Redistribution subject to ASME license or copyright; see http://www.asme.org/terms/Terms_Use.cfm

$$W = D_t(\pi w D_m)(D_m N)$$

where W is the maximum steady-state load, $N(\mathrm{lb}_f)$; D_t is the load capacity coefficient, $(N/\mathrm{mm}^3\ \mathrm{krpm})$ $(\mathrm{lb}_f/\mathrm{in}^3\ \mathrm{krpm})$; w is the difference between the inner and outer top foil diameters or radial extent of the top foil, millimeters (inches); D_m is the average of the inner and outer top foil diameters, millimeters (inches); and N is the shaft speed in thousand rpm (krpm).

This expression estimates thrust bearing load capacity as proportional to the runner surface velocity at the radial center of the top foil and the total swept area of the bearing between the inner and outer radii of the foils. The bearing load capacity coefficient, when multiplied by these quantities, can provide a rough estimate of the maximum load the bearing can support, which is useful for feasibility and sizing studies.

Defined in this manner, the load capacity coefficient has units of force $\times$ time divided by length cubed or viscosity per length. Physically, this reflects the ratio of the gas viscosity to the minimum tolerable (characteristic) film thickness, which is related to bearing and runner geometry, surface roughness, and details specific to the bearing design. For advanced bearing designs that more efficiently shape the film thickness distribution, this characteristic minimum film thickness is lowered, and higher load capacity performance is achieved.

Many foil thrust bearings do not have top foils that fully populate the swept area between the inner and outer pad diameters. The above expression conspicuously omits a factor which accounts for the portion of bearing area populated with load carrying top foils; this a consequence of system-level considerations. As noted earlier, turbomachine design practices favor a thrust runner with a minimized outer diameter. As such, the design of foil thrust bearings should favor the smallest required outer diameter to support a given load with adequate margin and thus optimize the populated area to achieve that goal. If individual pads must have an angular separation to accommodate thermal management schemes or other design features, this expression for load capacity accounts for the associated spatial penalties and thus encourages the overall bearing design to be optimized.

It is notable that factors such as low-friction tribological coatings, effective thermal management, and highly smooth and flat surfaces have all been found to affect load capacity performance in foil thrust bearings [34], consistent with the physical interpretation of the load capacity coefficient as defined. As a result, a particular bearing design can exhibit a wide range of load capacity coefficients. However, this simple expression may be useful in comparing the relative performance of various bearings, holding other factors such as surface roughness and coatings constant.

The open literature contains few reports of experimentally measured foil thrust bearing load capacity. Furthermore, many of these load capacity data are reported without the combination of geometry and speed conditions necessary to calculate a load capacity coefficient according to the proposed expression. Nevertheless, a few data are available containing all the necessary information to estimate a load capacity coefficient.

While not the same structural configuration as the foil thrust bearings under study here, Licht [14] gave a load capacity equivalent to a D_t of 0.027 $\mathrm{lb}_f/\mathrm{in}.^3$ krpm for a type of compliant thrust bearing. Koepsel [27] reported achieving a steady load capacity corresponding to D_t of 0.091. Heshmat and Shapiro [3] discussed the development of two designs for foil thrust bearings, achieving load capacity coefficients of 0.034 and 0.048 at 80 krpm. It is notable that these two bearings were only about 50% and 67% populated with top foils, however. In a more recent study with a fully populated bearing running at speeds from 25 krpm to 40 krpm, Dykas [34] reported load capacities corresponding to a coefficient of 0.125 with a commercially available bearing. However, even these more recent data are obtained from a bearing design several years old; the authors are not aware of sufficient details on the load capacities of state-of-the-art foil thrust bearings in the open literature to report currently achievable coefficients. It is anticipated that these data will become more readily available in the near future. The single load capacity datum taken for the prototype bearing achieves an uncooled load capacity coefficient of 0.024 for a 75% populated bearing with bare Inconel X-750 foils and a runner surface roughness of $R_a = 0.36\ \mu\mathrm{m}$, demonstrating a useful load capacity for parametric study. Furthermore, a visual inspection of post-test bearing wear suggests poor pad-to-pad consistency, implying that better quality control may improve performance.

7 Concluding Remarks

Using design methodologies laid out by DellaCorte et al. [2], a basic foil thrust bearing design is outlined to demonstrate a modular bearing intended to provide rapid and low cost design iterations. The authors do not claim high load capacity or an optimized bearing, preferring instead to demonstrate the relative ease with which a simple foil thrust bearing can be constructed for experimental testing. With a modest investment in similar tooling, bearing backing plates, and foil material, marginal costs for subsequent bearing designs can be relatively low.

Initial performance data obtained from the test bearing described herein demonstrate a working prototype and thus verify the basic methods by which it has been constructed. Further refinements of these methods are easily achievable by foil bearing practitioners wishing to adopt a bearing architecture conducive to parametric testing and low cost.

Acknowledgment

The authors wish to acknowledge the support of the Fundamental Aeronautics Program Office, Subsonic Rotary Wing Project. Additionally, Charles Smalley, Jean Wells, and the students of the Pre-Apprentice Machining Program are acknowledged for their skill and effort in constructing much of the prototype tooling and hardware for this study.

References

[1] DellaCorte, C., and Pinkus, O., 2000, "Tribological Limitations in Gas Turbine Engines: A Workshop to Identify the Challenges and Set Future Directions," National Aeronautics and Space Administration, Report No. NASA TM 2000-210059.
[2] DellaCorte, C., Radil, K., Bruckner, R. J., and Howard, S. A., 2007, "Design, Fabrication and Performance of Open Source Generation I and II Compliant Hydrodynamic Gas Foil Bearings," National Aeronautics and Space Administration, Report No. NASA TM 2007-214691.
[3] Heshmat, H., and Shapiro, W., 1984, "Advanced Development of Air-Lubricated Foil Thrust Bearings," Lubr. Eng., **40**(1), pp. 21–26.
[4] Valco, M. J., and DellaCorte, C., 2002, "Emerging Oil-Free Turbomachinery Technology for Military Propulsion and Power Applications," *Proceedings of the 23rd U.S. Army Science Conference*, Dec. 2–5, Orlando, FL.
[5] DellaCorte, C., Radil, K., Bruckner, R. J., and Howard, S. A., 2007, "A Preliminary Foil Gas Bearing Performance Map," National Aeronautics and Space Administration, Report No. NASA TM 2007-214691.
[6] Howard, S. A., 2007, "A New High-Speed Oil-Free Turbine Engine Rotordynamic Simulator Test Rig," National Aeronautics and Space Administration, Report No. NASA TM 2007-214489.
[7] DellaCorte, C., Radil, K., Bruckner, R., Bauman, S., Puleo, B. S., and Howard, S. A., 2006, "Rotor Support Technology Developments for Long Life Closed Brayton Cycle Turbines," *Proceedings of the Space Technology and Applications International Forum—STAIF 2006*, Feb. 12–16, Albuquerque, NM, American Institute of Physics, New York.
[8] Blok, H., and van Rossum, J., 1953, "The Foil Bearing—A New Departure in Hydrodynamic Lubrication," Lubr. Eng., **9**(6), pp. 316–320.
[9] Heshmat, H., 1981, "Multi-Stage Support Elements for Compliant Hydrodynamic Bearings," U.S. Patent No. 4,300,806.
[10] Barnett, M., 1972, "Self-Pressurizing Bearings With Resilient Elements," U.S. Patent No. 3,635,534.
[11] Silver, A., 1979, "Foil Bearing Stiffener," U.S. Patent No. 4,153,315.
[12] Fortmann, W. E., 1978, "Dual Wedge Fluid Thrust Bearing Including Wave Spring," U.S. Patent No. 4,082,375.
[13] Heshmat, H., 1981, "Stepped, Split, Cantilevered Compliant Bearing Support," U.S. Patent No. 4,277,112.
[14] Licht, L., 1978, "Resilient Foil Thrust Bearings," U.S. Patent No. 4,116,503.
[15] Gu, A., and Nadjafi, R., 1993, "Foil Thrust Bearing With Varying Radial and Circumferential Stiffness," U.S. Patent No. 5,248,205.

Downloaded 02 Jun 2010 to 171.66.16.109. Redistribution subject to ASME license or copyright; see http://www.asme.org/terms/Terms_Use.cfm

[16] Gray, S., and Heshmat, H., 1981, "Support Element for Compliant Hydrodynamic Thrust Bearing," U.S. Patent No. 4,277,111.
[17] Iordanoff, I., 1998, "Maximum Load Capacity Profiles for Gas Thrust Bearings Working Under High Compressibility Number Conditions," ASME J. Tribol., **120**, pp. 571–576.
[18] Iordanoff, I., 1999, "Analysis of an Aerodynamic Compliant Foil Thrust Bearing: Method for a Rapid Design," ASME J. Tribol., **121**, pp. 816–822.
[19] Agrawal, G., and Hockey, E., 1982, "Foil Bearing Mounting," U.S. Patent No. 4,348,066.
[20] Ku, C. R., and Heshmat, H., 1992, "Compliant Foil Bearing Structural Stiffness Analysis: Part I—Theoretical Model Including Strip and Variable Bump Foil Geometry," ASME J. Tribol., **114**, pp. 394–400.
[21] Heshmat, H., 1999, "High Load Capacity Compliant Foil Hydrodynamic Thrust Bearing," U.S. Patent No. 5,961,217.
[22] Agrawal, G., 1984, "Hydrodynamic Fluid Film Thrust Bearing," U.S. Patent No. 4,462,700.
[23] Ruscitto, D., McCormick, J., and Gray, S., 1978, "Hydrodynamic Air Lubricated Compliant Surface Bearing for an Automobile Gas Turbine Engine I—Journal Bearing Performance," National Aeronautics and Space Administration, Report No. NASA CR 135368.
[24] Heshmat, H., Shapiro, W., and Gray, S., 1982, "Development of Foil Journal Bearings for High Load Capacity and High Speed Whirl Stability," ASME J. Lubr. Technol., **104**(2), pp. 149–156.
[25] Society of Automotive Engineers, 2005, *Heat Treatment Wrought Nickel Alloy and Cobalt Alloy Parts—Aerospace Material Specification AMS 2774A*, SAE, Warrendale, PA.
[26] Heshmat, H., 1991, "Analysis of Compliant Foil Bearings With Spatially Variable Stiffness," American Institute of Aeronautics and Astronautics, AIAA Paper No. AIAA-91-2102.
[27] Koepsel, W., 1977, "Gas Lubricated Foil Bearing Development for Advanced Turbomachines," Air Force Aero Propulsion Laboratory, Report No. AFAPL-TR-76-114.
[28] Heshmat, C. A., Xu, D. S., and Heshmat, H., 2000, "Analysis of Gas Lubricated Foil Thrust Bearings Using Coupled Finite Element and Finite Difference Methods," ASME J. Tribol., **122**, pp. 199–204.
[29] Heshmat, H., Walowit, J. A., and Pinkus, O., 1983, "Analysis of Gas Lubricated Compliant Thrust Bearings," ASME J. Lubr. Technol., **105**, pp. 638–646.
[30] Bruckner, R. J., 2004, "Simulation and Modeling of the Hydrodynamic, Thermal, and Structural Behavior of Foil Thrust Bearings," Ph.D. thesis, Case Western Reserve University, Cleveland, OH.
[31] DellaCorte, C., and Edmonds, B. J., 1999, "Self-Lubricating Composite Containing Chromium Oxide," U.S. Patent No. 5,866,518.
[32] DellaCorte, C., and Edmonds, B. J., 1995, "Preliminary Evaluation of PS300: A New Self-Lubricating High Temperature Composite Coating for Use to 800C," National Aeronautics and Space Administration, Report No. NASA-TM-107056.
[33] DellaCorte, C., and Valco, M. J., 2000, "Load Capacity Estimation of Foil Air Journal Bearings for Oil-Free Turbomachinery Applications," Tribol. Trans., **43**, pp. 795–801.
[34] Dykas, B. D., 2006, "Factors Influencing the Performance of Foil Gas Thrust Bearings for Oil-Free Turbomachinery Applications," Ph.D. thesis, Case Western Reserve University, Cleveland, OH.

Downloaded 02 Jun 2010 to 171.66.16.109. Redistribution subject to ASME license or copyright; see http://www.asme.org/terms/Terms_Use.cfm

Design and Performance Evaluation of a Trigeneration System Incorporating Hydraulic Storage and an Inverted Brayton Cycle

Matthew Blieske
e-mail: matthewblieske@mac.com

J. E. D. Gauthier
e-mail: donald_gauthier@carleton.ca

X. Huang
e-mail: xhuang@mae.carleton.ca

Carleton University Ottawa,
269 Chemin de la Colonie,
Val Des Monts, QC, J8N 4A4 Canada

To bring the economic benefit of trigeneration to small-scale users without incorporating expensive components, an inverted Brayton cycle (IBC) is employed, which makes use of the expander section already present in a microturbine. An air accumulator provides pressurized air, which is passed through the expander section of the same microturbine used to charge the accumulator. The air passing through the IBC is cooled due to expansion, simultaneously providing power and cooling the flow. As the microturbine is indirectly fired, the flow passing through the engine or IBC can be directly vented into the household—eliminating the need for additional heat exchangers. The size of the cycle studied is on the order of 10 kW(e), suitable for a domestic household; however, the system is easily scaled for larger commercial applications. The majority of the components in the system being studied are "off the shelf" products. A feasibility study was conducted to ensure that the proposed system is economically competitive with systems currently used, such as individual generation provided by an air conditioner (A/C), a high efficiency natural gas (NG) furnace, and grid power. Simulations were run for a full year based on the actual external temperature and the electrical and thermal loads for a single family detached dwelling located in Winnipeg, Canada. Performance data were generated using MATLAB™ while the economic performance was determined with time-based simulations conducted using SIMULINK™. The system is designed to allow energy islanding by providing for all household energy needs throughout the year; however, integration with a power grid is optional. It was found that the operating costs for the proposed trigeneration system in an energy islanding mode of operation were equivalent to or less than individual generation (A/C unit, NG furnace, and grid power) during heating modes of operation and were more expensive for cooling modes of operation. The yearly energy cost for the trigeneration system exceeded the individual generation costs by 30–40%; however, there remains much room for improvement to the trigeneration concept. All economic data were based on fair market energy prices as found in central Canada. [DOI: 10.1115/1.2966420]

1 Introduction

A key motivation behind developing the concept of trigeneration is to further improve distributed energy systems. Many studies and simulations have demonstrated lower specific capital costs for trigeneration systems over individual generation, in addition to a lower specific fuel consumption [1]. In applications where combined heating and power (CHP) does not make economic sense, the added value of an additional energy product may improve economical viability. By providing a cooling load, a trigeneration system enables a building or an industrial plant to produce all or a portion of the energy products consumed on site. In addition to reducing energy costs, trigeneration systems offer the option of total energy islanding—an option not possible with CHP.

The motivation behind this study is to design, model, and build a trigeneration system targeting the residential market,[1] which is capable of an energy islanding mode of operation. While residential cogeneration has been thoroughly explored [2,3], residential trigeneration has received much less attention. This may be due to the fact that with respect to small-scale applications, most methods of providing a cooling load investigated thus far require components with a very high capital cost, such as absorption chillers and boilers [4–7]. In addition to a high capital cost, many absorption chillers use toxic LiBr as the working fluid, which can pose a health risk should a leak occur. It is therefore highly desirable to design a system without harmful fluids or heavy metals. To accomplish this, an air accumulator employed as part of an inverted Brayton cycle (IBC) is used in lieu of lead acid batteries.

The objective of this study is to design and simulate a system that can provide complete residential trigeneration energy islanding at a low capital cost. The description and configuration of the system will be detailed first, followed by the results of the simulation with commentary.

2 System Configuration

The proposed system utilizes an indirectly fired gas turbine (IFGT) to keep combustion products separate from the working fluid passing through the microturbine. This allows the exhaust from the microturbine to be directly vented into the house for heating or cooling purposes. A network of heat exchangers was

[1]Patent pending.

Contributed by the International Gas Turbine Institute of ASME for publication in the JOURNAL OF ENGINEERING FOR GAS TURBINES AND POWER. Manuscript received March 28, 2008; final manuscript received April 3, 2008; published online October 1, 2008. Review conducted by Dilip R. Ballal. Paper presented at the ASME Turbo Expo 2008: Land, Sea and Air (GT2008), Berlin, Germany, June 9–13, 2008.

Copyright © 2009 by ASME

Downloaded 02 Jun 2010 to 171.66.16.109. Redistribution subject to ASME license or copyright; see http://www.asme.org/terms/Terms_Use.cfm

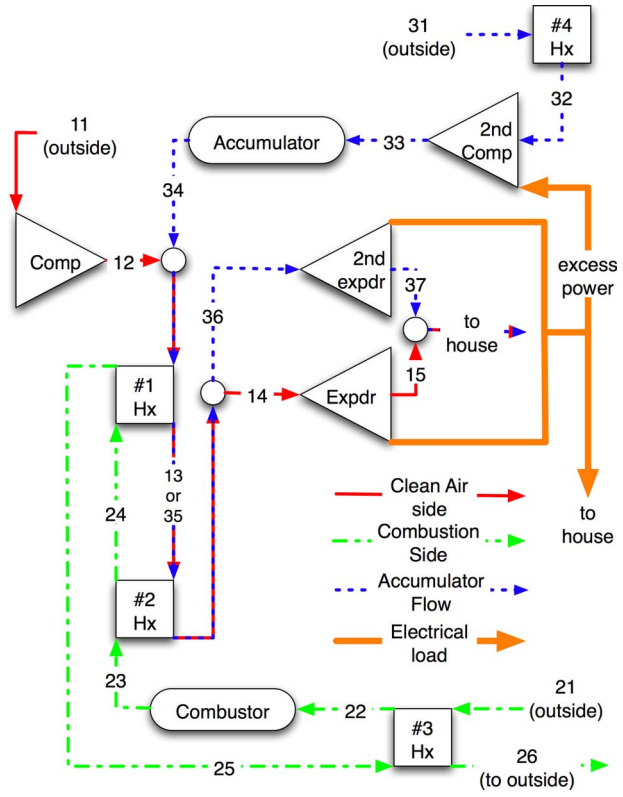


Fig. 1 System configuration for heating (ConFig. 1)

used to implement the IFGT concept in two configurations: one for producing the heating load and the other for producing the cooling load. These configurations can be seen in Figs. 1 and 2,

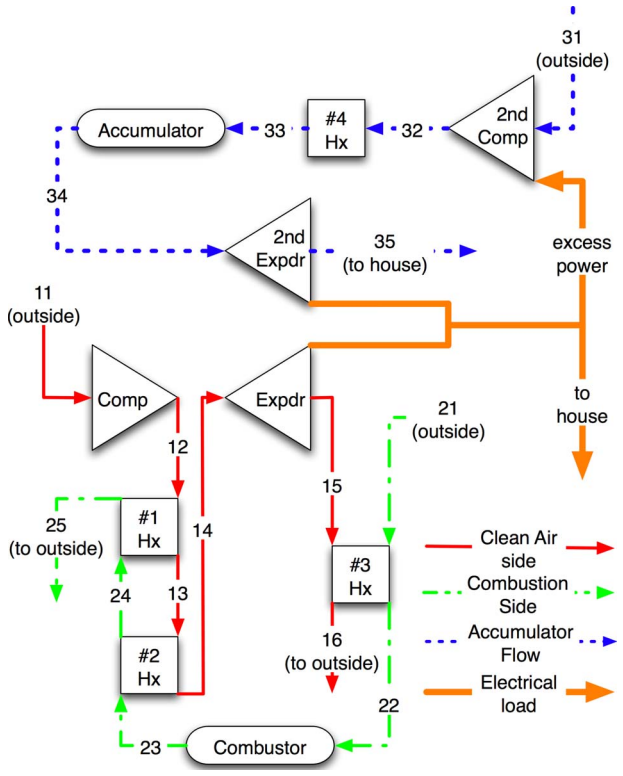


Fig. 2 System configuration for cooling (ConFig. 2)

respectively. Components such as duct fans and flow valves have been omitted for clarity. Note that the shaft connecting the compressor and expander of the microturbine has also been omitted. The station numbering convention used is as follows. The first number identifies the flow, 1 for microturbine flow, 2 for combustion flow, and 3 for accumulator flow. The second number denotes the station position in the flow, 1 for the inlet and so on.

Accumulator pressurization is accomplished using a compressor operating at $\Delta P = 4–6$ bars, labeled "2nd comp" in Figs. 1 and 2. As the microturbine produces electrical power in excess of the household demand (10 kW on design at $T_a = 288$ K), the difference is provided to the secondary compressor to charge the accumulator.

As shown in Figs. 1 and 2, the two configurations differ primarily in the heat exchanger flow configuration. ConFig. 1 does not cycle expander exhaust through the heat exchanger network (HEN), thereby providing a high temperature flow for household heating.

Conversely ConFig. 2 uses the expander exhaust to preheat the combustion air, as the high temperature expander exhaust is not required during the cooling load production. The #2 heat exchanger (#2 Hx) and the combustor are part of a natural gas atmospheric furnace similar to a conventional natural gas household furnace. The maximum cycle temperature (and by extension the thermal efficiency of the microturbine) is limited by the materials used to fabricate #2 Hx.

The other major difference between the two configurations is how the accumulator flow is used. When a heating load is desired, ConFig. 1 takes advantage of the elevated temperature at Station 32 provided by the secondary compressor. During discharge, the accumulator flow is directed through the HEN where the flow temperature is increased before discharge through the microturbine expander section. When a cooling load is required, the second compressor discharge flow (Station 32) is cooled using a heat exchanger (#4 Hx) buried inground before passing into the accumulator. This ensures that the air in the accumulator is at or below ambient, for use in the cooling load production. During discharge, the accumulator flow is vented directly into the expander section. Expansion through the expander produces electrical power and flow at a low temperature suitable for household cooling.

3 Load Profiles

To perform a detailed economic evaluation of the proposed system, a full year of operation is required for simulation. To accomplish this, high-resolution load data were obtained using an open source program called ESP-R [8]. This program is part of a project run by the Energy Systems Research Unit at the University of Strathclyde in the UK. After decades of development, contributions from Ph.D. theses, and several case studies, ESP-R has the ability to predict building thermal loads with a high degree of reliability. Factors such as solar gains, solar view factors, outside air infiltration, circulation, customizable duct/vent locations, lighting thermal gains, and occupant driven gains are incorporated into the model.

Included in ESP-R is a basic computer-aided design program that permits the user to build a simple geometry. This geometry is then used in modeling thermal loads. Figure 3 shows the geometry used in estimating the annual household thermal loads for the subject study. The parameters chosen in ESP-R were designed to reflect construction practices common to single family detached dwellings constructed in the 1950s to the 1980s:

- occupied by a four-person family
- no basement, two story, 1500 ft^2
- brick exterior walls with glass fiber insulation for a total relative strength index (RSI) value of 2.19
- ceiling of the secondary floor is insulated with an air gap for a total RSI value of 0.39
- solar view factors typical of a suburban environment

Downloaded 02 Jun 2010 to 171.66.16.109. Redistribution subject to ASME license or copyright; see http://www.asme.org/terms/Terms_Use.cfm

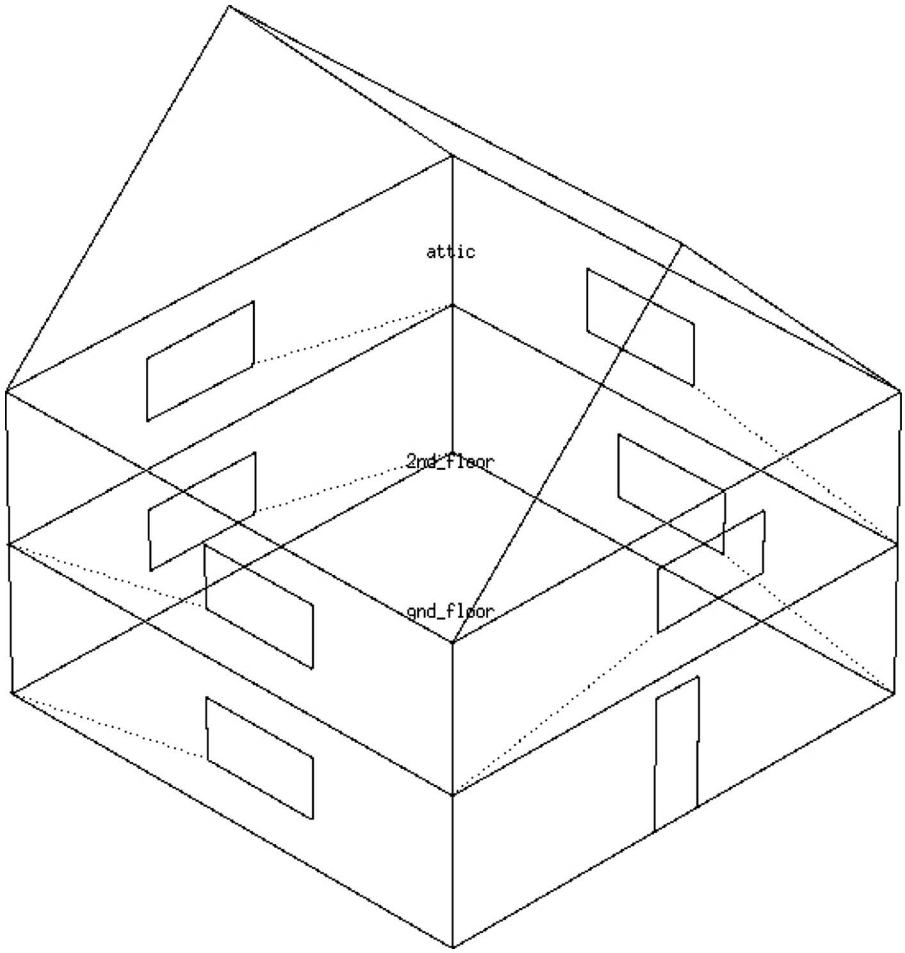


Fig. 3 Geometry used in ESP-R to model thermal loads

- double paned windows
- exterior surface of the ground floor subjected to an averaged ground temperature profile for Winnipeg, Canada [9]
- free air exchange between the first and second floors
- outside air infiltration set at 1 AC/h
- no internal walls
- volume of air on each floor and the attic varies in an isothermal manner
- ambient temperature, wind, sunshine, and precipitation data for Winnipeg, Canada in 2001 is used
- separate occupancy profiles are used for weekdays and weekends

In addition, an occupancy profile was specified that included latent and sensible gains from body heat, appliances, showers/baths, and lighting. Figure 4 is a sample of the output from the thermal simulation. While a full year was modeled in 5 min increments, only data for January and July are presented here.

The electrical profiles shown in Fig. 4 were taken from a project run by the International Energy Agency called Annex 42 [10]. This program is a partnership between several governmental organizations and universities around the world. The electrical profiles used for the simulation represent the consumption of an average detached single family Canadian household and is provided to Annex 42 by the Canadian Center for Housing Technology based in Ottawa, Canada. The electrical profile includes the consumption from air handling blowers used in the furnace and air conditioning systems.

Climatic data for Winnipeg, Canada were used for the load simulation as this region experiences extreme cold and very hot summers (−40–40°C). This climate requires significant heating and cooling loads, making it ideal for testing the performance of the trigeneration system under study.

In an effort to simplify the first iteration of the simulation, no hot water loads were used in the simulation. As hot water can be provided by the waste combustion exhaust, providing a hot water load will not incur any extra costs for the system under study. Providing hot water will increase costs for the independent generation system, making relative economic results from the simulation conservative.

4 Mathematical Model

As there are a number of components that require modeling, for ease of understanding, this section is broken into three subgroups: the HEN, turbomachinery, and IBC. Several assumptions impacting multiple subgroups are as follows:

- air was treated as a perfect gas and was assumed to be composed of 21% O_2 and 79% N_2
- no transient behavior was modeled
- $P_a = 101.325$ kPa
- no microturbine inlet pressure losses were assumed

4.1 Heat Exchanger Network. The following simplifications and assumptions were used in modeling the HEN performance:

- $\varepsilon = 0.9$ for all exchangers
- zero fouling was assumed
- $\Delta P_{hx} = 2\%$ (applied to each heat exchanger)
- $\eta_{comb} = 0.99$

Downloaded 02 Jun 2010 to 171.66.16.109. Redistribution subject to ASME license or copyright; see http://www.asme.org/terms/Terms_Use.cfm

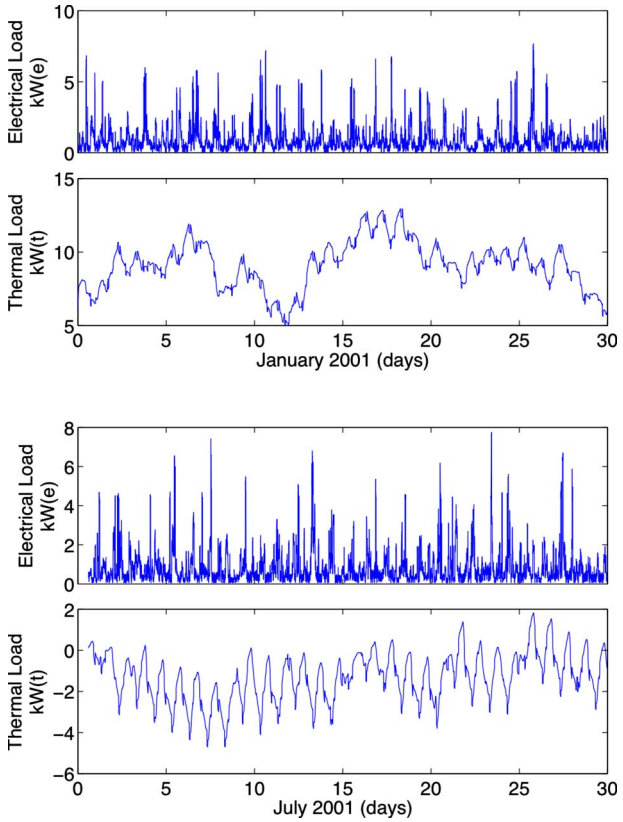


Fig. 4 Sample of load profiles estimated using ESP-R

- combustion side and air side mass flows are equal
- $T_{max}=1200$ K

Equations for heat exchanger (Eq. (1)) and the first law of thermodynamics (Eq. (2)) were applied to each exchanger in the network. With respect to Eqs. (1) and (2), the subscripts C and H stand for cold stream and hot stream, respectively.

$$\varepsilon = \frac{h_{C,\text{out}} - h_{C,\text{in}}}{h_{H,\text{in}} - h_{C,\text{in}}} \tag{1}$$

$$\dot{m}_C(h_{C,\text{out}} - h_{C,\text{in}}) = \dot{m}_H(h_{H,\text{in}} - h_{H,\text{out}}) \tag{2}$$

Using ConFig. 1 as an example, the following six equations result from the application of Eqs. (1) and (2) to the HEN:

$$\varepsilon = \frac{h_{13} - h_{12}}{h_{24} - h_{12}} \tag{3a}$$

$$\varepsilon = \frac{h_{14} - h_{13}}{h_{23} - h_{13}} \tag{3b}$$

$$\varepsilon = \frac{h_{22} - h_{21}}{h_{25} - h_{21}} \tag{3c}$$

$$h_{13} - h_{12} = h_{24} - h_{25} \tag{4a}$$

$$h_{14} - h_{13} = h_{23} - h_{24} \tag{4b}$$

$$h_{22} - h_{21} = h_{25} - h_{26} \tag{4c}$$

Equations (3*a*)–(3*c*) and (4*a*)–(4*c*) are then manipulated into the standard $Ax=b$ format by placing all unknown variables on the left hand side and all known variables on the right hand side of the equation as follows:

$$\begin{bmatrix} 0 & 0 & -1 & 0 & \varepsilon & 0 \\ -1 & 0 & 0 & \varepsilon & 0 & 0 \\ 1-\varepsilon & -1 & 0 & 0 & 0 & 0 \\ 0 & 0 & 1 & 0 & -1 & 1 \\ 1 & 0 & 0 & -1 & 1 & 0 \\ -1 & 1 & 0 & 1 & 0 & 0 \end{bmatrix} \times \begin{bmatrix} h_{13} \\ h_{14} \\ h_{22} \\ h_{24} \\ h_{25} \\ h_{26} \end{bmatrix} = \begin{bmatrix} (\varepsilon-1)h_{21} \\ (\varepsilon-1)h_{12} \\ -\varepsilon h_{23} \\ h_{21} \\ h_{12} \\ h_{23} \end{bmatrix} \tag{5}$$

After solving Eq. (5) for x, the specific fuel flow can be calculated using the following:

$$\ddot{m}_f = \frac{h_{23} - h_{22}}{\eta_{\text{comb}}} \tag{6}$$

A similar procedure as is outlined above was used for solving the HEN system of equations under ConFig. 2.

4.2 Turbomachinery. The following simplifications and assumptions were used in modeling turbomachinery components:

- $R=287$ J/kg K
- $\eta_c=0.75$ (at design and $T_a=288$ K)
- $\eta_t=0.84$ (at design and $T_a=288$ K)
- $\eta_m=0.96$
- CPR=4 (at design and $T_a=288$ K)
- microturbine expander discharges air at 2% above the P_a to account for the exhaust ducting losses
- no microturbine compressor overboard bleed or expander cooling flows

For the turbomachine compression and expansion processes, Eq. (7) was used to determine the isentropic discharge temperature. Note that the station numbers in Eqs. (7) and (8) are given for the compression across the microturbine compressor but are identical in form for the second compressor. While the expander uses the same form as Eq. (7), Eq. (9) is substituted in lieu of Eq. (8). Once an isentropic discharge temperature was determined, this was converted to an actual temperature using Eq. (8) and (9) through the use of an isentropic efficiency. A curve fit for $Cp(T)$ was taken from Ref. [11] for use in Eq. (7).

$$\int_{T_{11}}^{T_{12s}} \frac{Cp(T)}{T} dT - R \ln\left(\frac{P_{12}}{P_{11}}\right) = 0 \tag{7}$$

$$T_{12} = T_{11} + \frac{T_{11}}{\eta_c}\left(\frac{T_{12s}}{T_{11}} - 1\right) \tag{8}$$

$$T_{15} = T_{14} + T_{14}\eta_t\left(\frac{T_{15s}}{T_{14}} - 1\right) \tag{9}$$

For a required work output, the microturbine mass flow and the HEN fuel flow are calculated as follows:

$$\dot{m} = \frac{\dot{W}\eta_m}{(h_{14} - h_{15}) - (h_{12} - h_{11})} \tag{10}$$

$$\dot{m}_f = \ddot{m}_f \dot{m} \tag{11}$$

With the microturbine mass flow known, the heat load of the microturbine is calculated as follows:

$$\dot{Q} = \dot{m}(h_{15} - h_h) \tag{12}$$

To obtain a measure of confidence in design performance prediction, external validation was required. GASTURB™ 11 was used to confirm the results obtained using the above equations. GASTURB™ is a well established program that may be used to predict gas turbine performance. Although GASTURB™ does not provide a provision for modeling IFGT cycles, the HEN was treated as a "black box" in the GASTURB™ calculations by specifying a turbine (expander) inlet temperature (TIT) that matched what the HEN

Downloaded 02 Jun 2010 to 171.66.16.109. Redistribution subject to ASME license or copyright; see http://www.asme.org/terms/Terms_Use.cfm

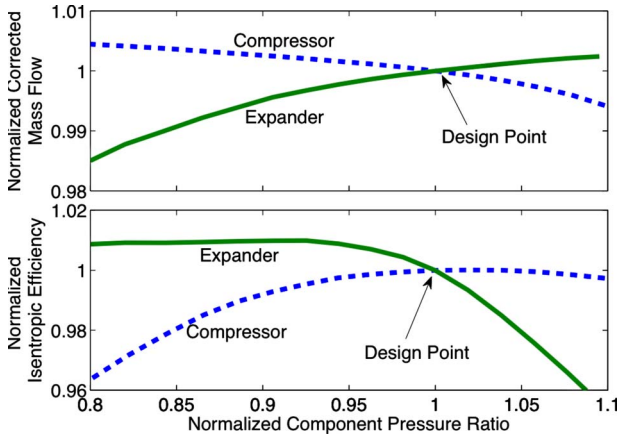


Fig. 5 Off-design performance of the microturbine compressor and expander normalized by design point values

provided. Key performance characteristics such as the mass flow, power output, and fuel consumption were predicted by GASTURB™ to be within 0.1% of what was predicted by the MATLAB™ model. Using this validation, off-design performance was predicted using a generic compressor and expander maps incorporated into GASTURB™. These maps represent an averaging of several actual turbomachinery maps to approximate conventionally designed compressors and expanders used in gas turbines. A constant speed operating line was modeled in GASTURB™ by varying the output power from the design to synchronous idle. Corrected compressor mass flow, compressor pressure ratio (CPR), expander pressure ratio (EPR), isentropic efficiencies, and corrected expander mass flow were then normalized by design point values to capture trends, as shown in Fig. 5. These normalized values were then multiplied by design point performance predictions from the MATLAB™ model to generate a constant speed off-design operating line.

The modeled system will run throughout the year; as a result, the ambient temperature will vary considerably. The corrected compressor mass flow (Eq. (13)) was used to evaluate the performance at temperatures other than the reference temperature of 15°C (288 K); P_{ref} and T_{ref} refer to standard ambient conditions of 101.325 kPa and 288 K, respectively. The variation of the maximum power with the ambient temperature was calculated by matching mass flows between the compressor and expander of the microturbine using the correlations in Fig. 5 and Eqs. (13) and (14). Off-design performance throughout the full ambient temperature range was calculated using the same methodology.

$$\dot{m}' = \frac{\dot{m}\dfrac{P_a}{P_{\text{ref}}}}{\sqrt{\dfrac{T_a}{T_{\text{ref}}}}} \tag{13}$$

$$\dot{m}_t' = \frac{\dot{m}_t\dfrac{P_{14}}{P_{\text{ref}}}}{\sqrt{\dfrac{T_{14}}{T_{\text{ref}}}}} \tag{14}$$

The second compressor was modeled using performance charts from a commercially available unit. Data for the compressor were digitized from which curve fits for the mass flow, power input, and isentropic efficiency were calculated without the need for Eq. (7); Eq. (8) was used to determine the discharge temperature. The second compressor operates at a constant pressure rise of 4 bars or 6 bars with an isentropic efficiency between 0.84 and 0.92 depending on the mass flow.

4.3 Inverse Brayton Cycle. The following simplifications and assumptions were used in modeling the IBC.

- Air in the accumulator is isothermal and isobaric.
- A polytropic exponent of $n=1.4$ (adiabatic) was assumed for compression during charging and for expansion during discharge.
- The accumulator was assumed to be a horizontal cylinder with spherical endcaps.
- A free convection boundary condition is applied to the outer surface.
- The accumulator internal surface temperature is equal to the bulk fluid temperature.
- The fluid in the accumulator is quiescent.
- The insulation thickness is $t=0.1$ m and the insulation thermal conductivity is $k_{\text{ins}}=0.038$ W/m K; the thermal resistance of the steel accumulator wall was treated as negligible.
- Radiation heat transfer from the exterior surface of the accumulator is negligible.

As the model was used in a time-based simulation, a set of equations had to be used that allowed variation in the inlet mass flow and the enthalpy while simultaneously calculating the accumulator temperature and pressure. The first law of thermodynamics was applied to a control volume enclosing the accumulator where e represents the specific energy of the system

$$\left(Q + W + \sum mh\right)_{\text{in}} - \left(Q + W + \sum mh\right)_{\text{out}} = m_2 e_2 - m_1 e_1 \tag{15}$$

The flow entering the accumulator is a moving fluid and does boundary work on the quiescent fluid in the accumulator. To account for this boundary work, the specific energy of the fluid in the accumulator is measured using internal energy while the specific energy of the incoming (or leaving) flow is measured using enthalpy. Heat addition or loss is present only in the form of heat transfer to ambient through the accumulator wall. Using these assumptions, a discrete form of Eq. (15) can be written as

$$\frac{\dot{m}_{\text{in}}h_{\text{in}} - \dot{m}_{\text{out}}h_{\text{out}} + m_1u_1 - \dot{Q}'_{\text{acc}}}{m_1 + \dot{m}_{\text{in}} - \dot{m}_{\text{out}}} - u_1 = u_2 - u_1 = \frac{du}{dt} \tag{16}$$

With respect to Eq. (16), subscripts 1 and 2 correspond to the accumulator state at the previous and current timesteps, respectively.

Pressure was modeled using the differential form of the perfect gas law

$$\frac{dP}{dt} = \frac{R}{V}(Tdm + mdT) \tag{17}$$

An explicit discrete differential form is required to implement Eq. (17) into a simulation marched in time given by

$$\frac{dP}{dt} = \frac{R}{V}[T_1(\dot{m}_{\text{in}} - \dot{m}_{\text{out}} - m_1) + m_1T_2] \tag{18}$$

Finally, $\dot{Q}'_{\text{acc}}$ must be estimated. Under a free convection assumption, the external convection coefficients must be estimated using empirical correlations. Equations (19) and (20) are averaged Nusselt number correlations for free convection around a horizontal cylinder [12] and a sphere [13], respectively,

$$\overline{\text{Nu}_D} = C\text{Ra}_D^n, \quad C = 1/8, \quad n = 1/3 \tag{19}$$

$$\overline{\text{Nu}_D} = 2 + \frac{0.589\text{Ra}_D{}^{1/4}}{(1 + [0.469/\text{Pr}]^{9/16})^{4/9}} \tag{20}$$

where the Rayleigh number is calculated as

Downloaded 02 Jun 2010 to 171.66.16.109. Redistribution subject to ASME license or copyright; see http://www.asme.org/terms/Terms_Use.cfm

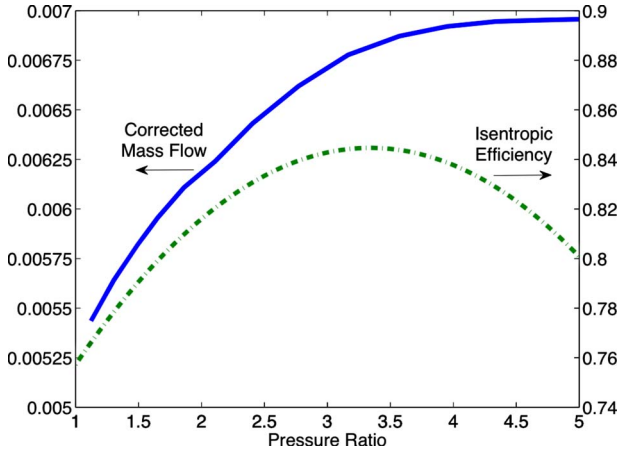


Fig. 6 Off-design performance of the second expander during the IBC operation

$$\mathrm{Ra}_D = \frac{g\beta(T_s - T_\infty)D^3}{\nu\alpha} \tag{21}$$

Equations (19)–(21) are then combined with Eq. (22) to produce an estimate for the average convective heat transfer coefficient, one for the cylindrical surface and one for the spherical endcaps

$$\bar{h} = \frac{\overline{\mathrm{Nu}_D}k}{D} \tag{22}$$

Using the assumption that the heat transferred through the insulation via conduction is equal to the heat dissipated through free convection, Eq. (23) is used to determine the external surface temperature of the accumulator where subscripts sp and cyl correspond to the spherical and cylindrical surfaces, respectively

$$\frac{k_{\mathrm{ins}}(T - T_s)(A_{\mathrm{sp}} + A_{\mathrm{cyl}})}{t} = [(\bar{h}A)_{\mathrm{sp}} + (\bar{h}A)_{\mathrm{cyl}}](T_s - T_\infty) \tag{23}$$

$\dot{Q}'_{\mathrm{acc}}$ is then determined by backsubstituting T_s into Eq. (23) and calculating the heat transfer through the accumulator wall or from the external surface of the accumulator via convection

$$\dot{Q}'_{\mathrm{acc}} = \frac{k_{\mathrm{ins}}(T - T_s)(A_{\mathrm{sp}} + A_{\mathrm{cyl}})}{t} = [(\bar{h}A)_{\mathrm{sp}} + (\bar{h}A)_{\mathrm{cyl}}](T_s - T_\infty) \tag{24}$$

The IBC has the potential to operate with pressure ratios of 1–7, depending on the load demand of the household. This range is significantly different from the pressure ratios of 3–3.76 experienced by the expander during microturbine operation. Hence a second expander with a design point tailored for typical mass flows and pressure ratios used in the IBC operation was used. Figure 6 gives the operating line used to model performance data for the second expander.

During cooling load production, the discharge flow from the second compressor is passed through a heat exchanger buried underground (Hx #4). The exchanger was assumed to be buried at a depth such that the heat capacity of the region surrounding the heat exchanger is infinite. An effectiveness of 0.95 was assumed for the exchanger. Under the infinite heat capacity assumption, the ground temperature adjacent to the exchanger was assumed to be constant at 8 °C (281 K) [9]. The cooled flow was then discharged to the accumulator.

It should be noted that the IBC expander load is controlled with the use of a virtual pressure regulator on the outlet of the accumulator. The effect of this regulator on the outlet flow from the accumulator has not been taken into account. Future iterations of the mathematical model will incorporate the effect of a pressure regulator.

During heating load production, the IBC flow is directed through the HEN to increase the flow temperature. Control over the maximum cycle temperature adds another degree of freedom, in addition to pressure regulation, with respect to controlling the work and heat output of the IBC.

5 Simulation Parameters

The mathematical model of the system described in Sec. 4 was incorporated into a SIMULINK™ simulation marched in time. This simulation provided control to the mathematical model to ensure that a comfortable temperature was maintained throughout the simulated dwelling while remaining within the operating envelopes of each system component, in addition to ensuring that the household electrical demand was met. The increase and decrease in the household temperature were calculated using a bulk heat capacity calculated using Eq. (25). The deviation of household temperature from the desired set point of 22 °C (295 K) is determined using Eq. (26)

$$C_h = \dot{m}_h C_{pa} \tag{25}$$

$$\Delta T_h = \int \frac{\dot{Q}_{\mathrm{load}} + \dot{Q} + \dot{Q}_{\mathrm{acc}} + \dot{Q}'_{\mathrm{acc}}}{C_h} \tag{26}$$

Simulation control allowed the household temperature to vary for no more than ±1.5 °C from the nominal set point.

Several discretization schemes provided with SIMULINK™ were experimented with to arrive at a solver-independent solution, with the goal of optimizing the solution accuracy and the CPU time. With the exception of the accumulator behavior, most trends in performance data were either linear or weakly quadratic in nature. As a result, higher order discretization schemes did not produce significantly different results from first order schemes such as the explicit Euler method. As the control system was based on switches that turned on or shut off components abruptly, the simulation solver had to be able to deal with a high occurrence of discontinuities. The first order Euler method using a fixed timestep was able to negotiate discontinuities without divergence.

It was desirable to choose as large a timestep as possible without significant penalty to the accuracy or without inducing solver instability. A timestep of 1 s was chosen, as larger timesteps resulted in solution instability. This instability threshold can be attributed to the high rate of change in accumulator pressure during discharge as the IBC pressure ratio approaches the atmospheric pressure. At a lower pressure ratio, less specific work is produced by the expander; hence a larger mass flow is required to satisfy a given electrical or thermal load. The accumulator pressure could drop below the atmospheric pressure between timesteps larger than 1 s, causing rapid solution divergence.

The economic performance of the proposed system was measured against the performance of a natural gas furnace, vapor compression air conditioner, and purchasing grid power as is common in many North American and European households. The thermal and electrical load profiles used in the model simulation were applied to the independent generation simulation as well. The following parameters were used in simulating individual generation.

- The natural gas furnace has a first law efficiency of 90%.
- The air conditioner operates with a constant coefficient of performance (COP) of 3.5 and provides 3 ton of cooling (10.55 kW).
- Electricity is purchased at 0.09 CAD/kW h.
- Natural gas is purchased at 0.40 CAD/m^3.

Energy prices used for simulating the independent generation were also used for simulating the trigeneration system. The air conditioner output load is assumed to remain constant irrespective of the outside air temperature. As the COP for air conditioners is

Downloaded 02 Jun 2010 to 171.66.16.109. Redistribution subject to ASME license or copyright; see http://www.asme.org/terms/Terms_Use.cfm

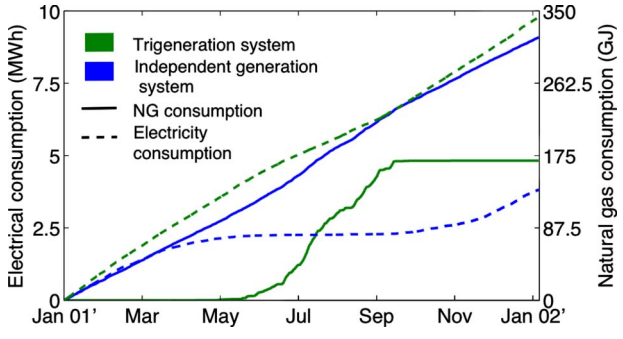


Fig. 7 Cumulative energy consumption of the individual generation and trigeneration systems

measured at an outside temperature of 27.8°C (82°F) as per Air-Conditioning and Refrigeration Institute (ARI) Standard 210-240-2006 [14], the cooling load will be underpredicted at temperatures below 27.8°C and overpredicted at temperatures above. As a rule of thumb, for each degree the condensing temperature is increased in a vapor compression cycle, the COP reduces by 2–4% [15]. To mitigate the error introduced with a constant COP assumption, future iterations of the independent generation simulation will not make this assumption.

6 Simulation Results

Using 5 min thermal and electrical load data, a full year was simulated in 1 s intervals; the yearly energy consumption is summarized in Fig. 7 for both systems. While overall operational costs are higher for the trigeneration system, it must be noted that costs are competitive during the heating mode, as shown in Fig. 8. Note that component performance parameters were intentionally selected to be extremely conservative. Hence the data presented in Figs. 7 and 8 represent a "worst case" scenario with much room for improvement.

The system had difficulty meeting cooling loads during peak summer conditions (sustained temperatures of more than 30°C) where the sustained cooling load exceeded 2 kW. To keep the household temperature within set point limits, the grid power was purchased and provided to the second compressor. This increased the mass flow into the accumulator during charging periods beyond what the microturbine alone could accomplish. Despite maintaining a comfortable household climate, Fig. 8 illustrates the negative impact that purchasing grid power had on economic performance. There is great potential for cooling cycle optimization as the second expander design point can be tailored as required. Unlike the microturbine expander, the second expander does not have to be matched to a compressor; therefore the design mass flow and pressure ratio can be used as variables in an optimization study.

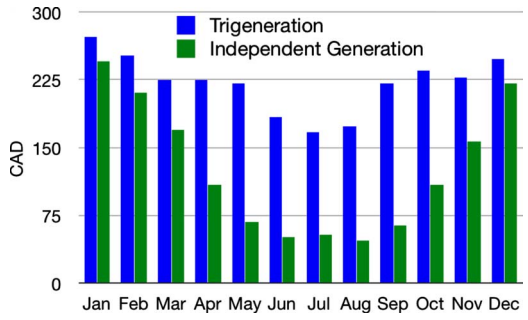


Fig. 8 Monthly noncumulative energy cost comparison for the trigeneration and independent generation systems

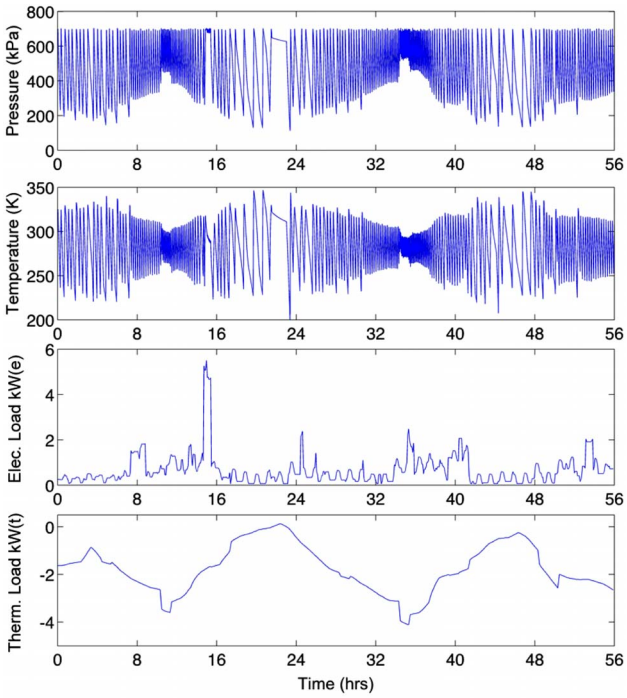


Fig. 9 Typical accumulator behavior in the cooling mode

It should be noted that conservative values for turbomachinery isentropic efficiencies were used to ensure that the results were not overoptimistic. Increasing the isentropic efficiency of the microturbine expander and/or compressor would allow more electrical energy to be fed to the second compressor during the cooling mode without increasing fuel consumption. This would reduce or eliminate the amount of supplementary grid power required to maintain a set point temperature during peak cooling load periods, thereby improving the economic performance during the cooling load production. An increase in the second expander efficiency would result in cooler exhaust temperatures, thereby increasing the cooling load capacity, again reducing or eliminating the quantity of grid power required during peak periods. An exciting conclusion one can draw from the results of the study at this point is that despite the poor economic performance of the system while in the cooling mode, there is significant room for improvement.

A conservative value for the maximum cycle temperature was selected (1200 K) to ensure a reasonable service life for Hx #2. The use of high temperature materials and special design would allow for maximum cycle temperature uprating. This in turn would increase the power input to the second compressor and a corresponding reduction in the supplementary grid power during cooling mode, without an increase in fuel consumption.

The accumulator behaved in a different manner depending on the system mode (heating or cooling). As seen in Fig. 9, periods of increased discharge/charging cycling correspond to periods of increased thermal load. Accumulator cycling was virtually invariant with respect to the electrical load, as the work output from the IBC expander almost always exceeded the demand given that the expander operates in a thermal load following manner the majority of the time.

Unlike the cooling mode, it was found that during the heat load production the accumulator behavior followed the electrical load rather than the thermal load, as shown in Fig. 10; periods of high electrical load correspond to periods of full accumulator blowdown.

The HEN does a good job of extracting heat from discharge flows in ConFig. 1, as the combustion flow is discharged at about 310 K. There is room for improvement for ConFig. 2, as the

Downloaded 02 Jun 2010 to 171.66.16.109. Redistribution subject to ASME license or copyright; see http://www.asme.org/terms/Terms_Use.cfm

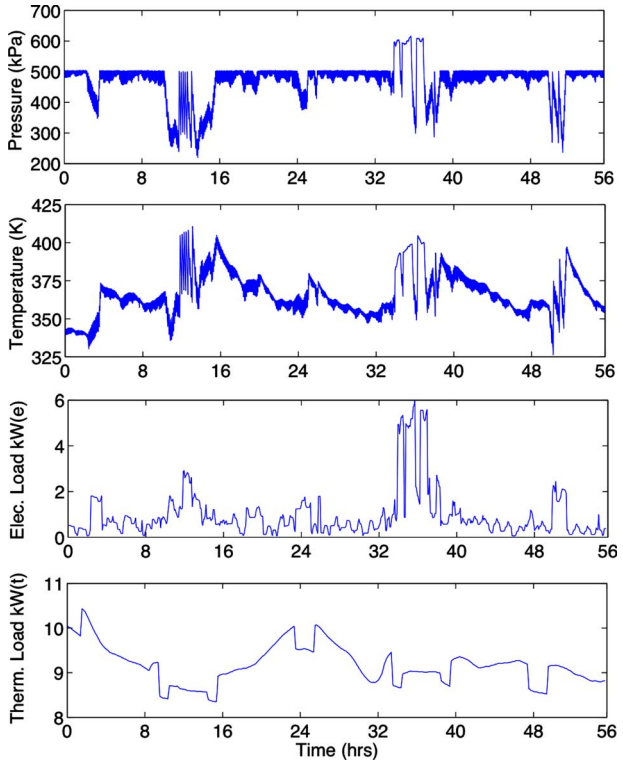


Fig. 10 Typical accumulator behavior in the heating mode

combustion flow is discharged at about 510 K, and the microturbine exhaust is discharged at about 350 K. Future iterations of the simulation will use these flows to provide a hot water load without an increase in fuel consumption. As the independent generation system would require additional fuel or electricity to satisfy a hot water load, the difference between the economic performance of the trigeneration and independent systems would decrease.

7 Conclusion

A full year high-resolution simulation of a trigeneration system incorporating the hydraulic storage and an inverse Brayton cycle with a microturbine was successfully conducted. Yearly operational costs for the system exceeded individual generation provided by the vapor compression air conditioner, natural gas furnace, and grid power by 30–40%; however, the trigeneration economic performance while producing a heat load was equal to or better than the individual system. As this economic evaluation represents a trigeneration system that has not been optimized, there is great potential for improvement via uprating and/or varying turbomachinery sizing.

Total energy islanding was achieved except during peak summer thermal loads. Supplementary grid power was required to maintain the household temperature when the cooling load exceeded about 2 kW. Improvements to the turbomachinery isentropic efficiency, increasing the household set point temperature during the peak cooling load, or uprating the maximum HEN temperature could reduce or eliminate the requirement for supplementary grid power and improve economic performance.

Many systems have been designed for the residential market that provide some measure of heating, cooling, or power; however, no other system discussed in open literature is capable of providing for all three energy products at a competitive capital cost for homeowners, making the system under study unique.

8 Future Work

Future iterations of the simulation will satisfy a hot water load. The accumulator pressure regulator will also be incorporated into the mathematical model. A sensitivity study should be conducted to determine which individual component variables have the greatest impact on economic performance. The results of such a study could be used in implementing a genetic algorithm based optimization of the trigeneration system. The economic performance of the system using different climatic data should be evaluated to determine which regions of the world are best suited for this technology.

Acknowledgment

Special thanks to Marianne Manning of the National Research Council's Canadian Centre for Housing Technology in Ottawa, Ontario for providing access to measured thermal and electrical load data. Gratitude is expressed toward Ian Beausoleil-Morrison, Associate Professor and Canada Research Chair at Carleton University for providing access to the ESP-R source code. Financial support is graciously provided by Dr. John Rogers of Innovative Materials Technology (IMT).

Nomenclature

C_{pa} = specific heat of air
$\bar{h}$ = accumulator free convective heat transfer coefficient
h_h = household ambient enthalpy
h_{in} = accumulator inlet enthalpy
h_{out} = accumulator outlet enthalpy
m_h = mass of air in the thermally controlled volume of dwelling
$\dot{m}$ = microturbine mass flow
$\dot{m}_{c2}$ = secondary compressor mass flow
$\dot{m}_{\text{in}}$ = accumulator inlet mass flow
$\dot{m}_{\text{out}}$ = accumulator outlet mass flow
$\dot{m}'$ = corrected microturbine compressor mass flow
$\dot{m}'_t$ = corrected expander mass flow
P_a = ambient pressure
$\dot{Q}$ = microturbine thermal output
$\dot{Q}_{\text{acc}}$ = accumulator thermal output
$\dot{Q}_h$ = household thermal load
$\dot{Q}'_{\text{acc}}$ = accumulator heat transfer load
R = universal gas constant
T_a = outside air temperature
$T_{\max}$ = maximum #2 Hx operating temperature
T_s = accumulator external surface temperature
T_∞ = household ambient temperature
$\dot{W}$ = microturbine electrical output
$\dot{W}_{c2}$ = secondary compressor electrical input
$\dot{W}_h$ = household electrical load
ΔP_{hx} = heat exchanger pressure loss
ε = heat exchanger effectiveness
η_c = compressor isentropic efficiency
η_{c2} = secondary compressor isentropic efficiency
η_{comb} = combustion efficiency
η_m = mechanical efficiency
η_t = expander isentropic efficiency

Acronyms

CAD = Canadian funds
Hx = heat exchanger
kW(e) = electrical output (kW)
kW(t) = thermal output (kW)
LHV = lower heating value
TELR = thermal to electrical load ratio

Downloaded 02 Jun 2010 to 171.66.16.109. Redistribution subject to ASME license or copyright; see http://www.asme.org/terms/Terms_Use.cfm

References

[1] Hernández-Santoyo, J., and Sánches-Cifuentes, A., 2003, "Trigeneration: An Alternative for Energy Savings," Appl. Energy, **76**, pp. 219–227.

[2] Stritih, U., and Butala, V., 2004, "Optimization of a Thermal Storage Unit Combined With a Biomass Boiler for Heating Buildings," Renewable Energy, **29**, pp. 2011–2022.

[3] Kaikko, J., Backman, J. L. H, Koskelainen, L., and Larjola, J., 2007, "Optimum Operation of Externally-Fired Microturbine in Combined Heat and Power Generation," ASME Paper No. GT2007–28264.

[4] Míguez, J. L., Murillo, S., Porteiro, J., and López, L. M., 2004, "Feasibility of a New Domestic CHP Trigeneration With Heat Pump: I. Design and Development," Appl. Therm. Eng., **24**, pp. 1409–1419.

[5] Kong, X. Q., Wang, R. Z., Wu, J. Y., Huang, X. H., Huangfu, D. W., Wu, D. W., and Xu, Y. X., 2005, "Experimental Investigation of a Micro-Combined Cooling, Heating and Power System Driven by a Gas Engine," Int. J. Refrig., **28**, pp. 977–987.

[6] Kong, X. Q., Wang, R. Z., and Huang, X. H., 2004, "Energy Efficiency and Economic Feasibility of CCHP Driven by Stirling Engine," Energy Convers. Manage., **45**, pp. 1433–1442.

[7] Godefroy, J., and Boukhanouf, S. R., 2007, "Design, Testing and Mathematical Modelling of a Small-Scale CHP and Cooling System (Small CHP-Ejector Trigeneration)," Appl. Therm. Eng., **27**, pp. 68–77.

[8] Energy Systems Research Unit, University of Strathclyde, 2007, www.esru.strath.ac.uk/programs/ESP-r.htm, accessed Sept.

[9] Williams, G. P., and Gold, L. W., 2007, "Ground Temperatures," National Research Council Digest, Report No. CBD-180.

[10] FC+Cogen-Sim, Annex 42, International Energy Association, 2007, http://cogen-sim.net, accessed Oct.

[11] Turns, S. R., 2000, *An Introduction to Combustion, Concepts and Applications*, 2nd ed., McGraw-Hill, Singapore.

[12] Morgan, V. T., 1974, "The Overall Convective Heat Transfer from Smooth Circular Cylinders," Adv. Heat Transfer, **11**, pp. 199–264.

[13] Churchill, S. W., 1983, "Free Convection Around Immersed Bodies," *Heat Exchange Design Handbook*, Hemisphere, New York.

[14] Air-Conditioning Refrigeration Institute, 2007, "Performance Rating of Unitary Air-Conditioning and Air-Source Heat Pump Equipment," ARI 210-240-2006, © 2006, www.ari.org, accessed Sept.

[15] Cengle, Y. A., and Boles, M. A., 2002, *Thermodynamics an Engineering Approach*, McGraw-Hill, New York, p. 568.

Downloaded 02 Jun 2010 to 171.66.16.109. Redistribution subject to ASME license or copyright; see http://www.asme.org/terms/Terms_Use.cfm

Ten Years of Experience With a Small Jet Engine as a Support for Education

O. Léonard
Professor
e-mail: o.leonard@ulg.ac.be

J. P. Thomas
FNRS Research Fellow
e-mail: jp.thomas@ulg.ac.be

S. Borguet
Research Engineer
e-mail: s.borguet@ulg.ac.be

Turbomachinery Group,
University of Liège,
Chemin des Chevreuils, 1
B-4000 Liège, Belgium

In 1997 the Turbomachinery Group of the University of Liège decided to acquire a small jet engine to illustrate the courses in propulsion and to provide the students with the opportunity to get some experience on data measurement, acquisition, and interpretation. Among others, the SR-30 engine from Turbine Technology Ltd. Chetek, WI was chosen. It consists of a single spool, single flow engine with a centrifugal compressor, a reversed combustion chamber, an axial turbine, and a fixed convergent nozzle. This engine was installed on a test bench allowing for manual control and providing fuel and oil to the engine. The original setup included measurements of intercomponent pressure and temperatures, exhaust gas temperature, and rotational speed. Since then both the engine and the test bench have been deeply modified. These modifications were led by a triple objective: the improvement and the enrichment of the measurement chain, the widening of the engine's operational domain, and, last but not the least, the wish to offer appealing hands-on projects to the students. All these modifications were performed at the University of Liège and were conducted by the students as part of their Master theses. Several performance models of the engine were developed to support data validation and engine condition diagnostic. This paper summarizes the developments conducted with and by the students, and presents the experience that was gained by using this engine as a support for education. [DOI: 10.1115/1.2967487]

Keywords: jet engine, test bench, hands-on projects, Master students

1 Introduction

The Department of Aerospace and Mechanical Engineering of the University of Liège, Belgium offers undergraduate and graduate programs leading to Bachelor, Master, and Ph.D. degrees in Aerospace, Mechanical, and Energetics Engineering. Air-breathing propulsion is one of the key issues of the Master in Aerospace engineering, whose objective is to train the students in advanced techniques of modeling, simulation, and measurements in the disciplines involved in aerospace: fluid mechanics, flight mechanics, solid mechanics, propulsion, and materials.

In 1997 the Turbomachinery Group of the University of Liège decided to acquire a small jet engine to illustrate the lessons in propulsion. The nature of the funding clearly oriented the project toward didactic activities more than research ones, although both are often coupled. The idea was to provide the students with the opportunity to get some experience on data measurement, acquisition, and interpretation.

The engine had to be not too big so that it can be operated in a university laboratory environment, without too drastic security measures, and not too small so that it offers enough didactic possibilities. Indeed there are quite a few jet engines for model aircrafts that are offered now at a reasonable price, but they are so small that it is unlikely that they can be equipped with a few sensors for intercomponent pressure and temperatures.

The SR-30 engine from Turbine Technology Ltd. was chosen among others. This was also the choice of other teams, such as Refs. [1–3]. The SR-30 is a single spool, single flow engine with a centrifugal compressor, a reversed combustion chamber, an axial turbine, and a fixed convergent nozzle (Fig. 1). This engine is installed on a test bench, which allows manual engine control and provides fuel, oil, and pressurized air for the starting procedure (Fig. 2).

Since 1997 both the engine and the test bench have been deeply modified. These modifications were led by a triple objective: the improvement and the enrichment of the measurement chain, the widening of the engine's operational domain, and, last but not the least, the wish to offer appealing hands-on projects to the students. The fittings and connections of the engine to the bench were completely changed and a load cell was added to measure the thrust. A variable area nozzle was mounted on the engine so as to modify the engine working line. Variable geometry inlet guide vanes were added ahead of the compressor wheel to modify the compressor characteristic. A servomotor was added to remotely operate the fuel valve and to control the engine using the acquisition system. Besides additional sensors were added such as a fuel flowmeter and an air flowmeter.

All these modifications were performed at the University of Liège and were conducted by the students as part of their Master theses. Several thermodynamical performance models of the engine were also developed to support data validation, new component design (inlet guide vane and nozzle), engine condition diagnostic, and engine control. This paper summarizes the developments conducted with and by the students, and presents the experience that was gained by using this engine as a support for education.

2 The Original Engine

The SR-30 engine from Turbine Technology Ltd. is 170 mm $\times$ 270 mm. It is a single spool, single flow engine with a centrifugal compressor, a reversed combustion chamber, an axial turbine, and a fixed convergent nozzle. This engine has the ability to run on different fuels, such as diesel, but using kerosene makes it easier to start. The design operating point is defined as

Contributed by the International Gas Turbine Institute of ASME for publication in the JOURNAL OF ENGINEERING FOR GAS TURBINES AND POWER. Manuscript received April 1, 2008; final manuscript received April 8, 2008; published online October 10, 2008. Review conducted by Dilip R. Ballal. Paper presented at the ASME Turbo Expo 2008: Land, Sea and Air (GT2008), Berlin, Germany, June 9–13, 2008.

Copyright © 2009 by ASME

Downloaded 02 Jun 2010 to 171.66.16.109. Redistribution subject to ASME license or copyright; see http://www.asme.org/terms/Terms_Use.cfm

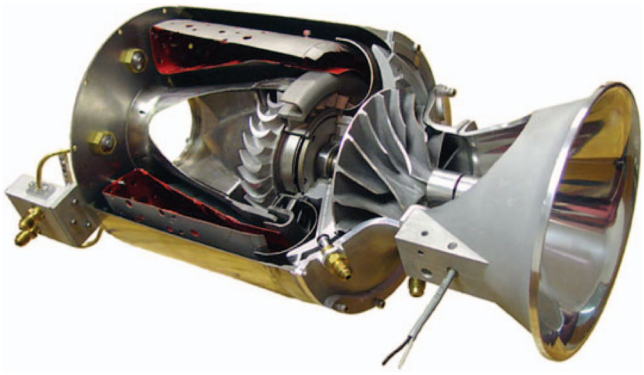


Fig. 1 Cutaway of the SR-30 engine

Thrust: 140 N	Fuel flow: 0.005 kg/s
EGT: 720°C	Airflow: 0.5 kg/s
Speed: 86,000 rpm	Compression ratio: 3.4

The engine is installed on a test bench, which allows manual engine control and provides fuel, oil, and pressurized air. In 1997 the original setup included measurements of some intercomponent pressure and temperatures, exhaust gas temperature (EGT), and rotational speed. The thrust was not directly measured but correlated with the pressure in the combustion chamber. Neither the airflow nor the fuel flow was available at that time. Since then significant modifications have been brought by the manufacturer [4]. The data acquisition is obtained with a National Instruments SCXI chassis and displayed with LABVIEW.

3 Hardware Modifications

During initial testing of the SR-30, it was found that some variables were mandatory in order to perform a complete energy balance on the jet engine: the thrust, the airflow, and the fuel flow. Also, it came out that it would be interesting to control the position of the engine equilibrium line. It was decided to build a variable area nozzle and to mount it downstream of the existing one, as a prolongation of the latter. Later it was also decided to build a variable geometry inlet guide vane to be mounted between the bell-mouth inlet and the compressor wheel, so as to be able to modify the compressor characteristic. Finally it was decided to explore the possibility of controlling the engine using the data acquisition system and a servomotor was added to remotely operate the fuel valve.

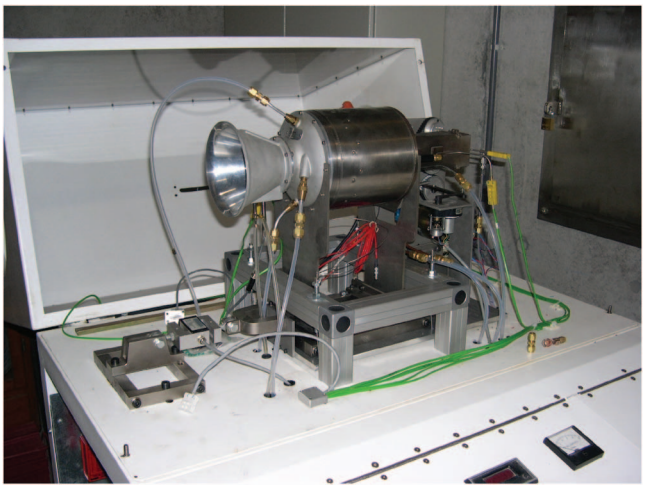


Fig. 2 SR-30 engine on its test bench

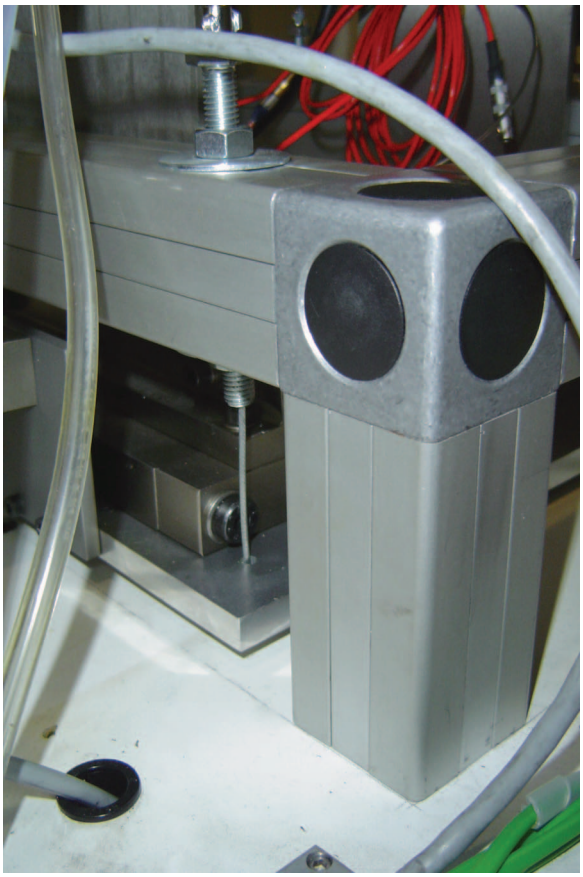


Fig. 3 Hanging plate supporting the engine and strapping system

These hardware modifications were all performed by students as part of their Master theses. They represent approximately 20 person-months of student work.

3.1 The Thrust Measurement. In its original configuration the jet engine was supported on two rigid "legs" and the thrust was actually a result of a correlation with the pressure in the combustion chamber.

To provide for free engine response to thrust, the support legs were removed and the engine was fixed on a rigid plate made of aluminum. This plate has also to support the (heavy) system used to actuate the variable area nozzle. The plate is free to react to the engine thrust as it hangs from the frame using four straps made from steel cables (Fig. 3). In order to improve the thrust response even further, all of the rigid tubing connections were replaced with flexible couplings (fuel and oil in and out, pressurized air in, and pressure and temperature measurements).

The load transducer is a commercially available standard load cell rated to 200 N (Sensy 2712). The sensitivity of this load cell is 1.85 mV/V. The load cell is mounted with two kneecaps to compensate for alignment errors. The jet engine is restrained axially by the load cell (Fig. 4). In order to calibrate the thrust measurement, a cable-pulley system was devised so that calibrated weights could be hung from the centerline of the jet engine. The system calibrated to a resolution of 0.2 N. The thrust measurement system also maintains zero and is repeatable.

3.2 The Airflow Measurement. The bell-mouth original nozzle (visible in Figs. 1 and 2) has been replaced with a calibrated nozzle (Fig. 5). The airflow is deduced from the difference between the ambient pressure and the static pressure measured by four holes at the throat of the flowmeter. The accuracy is 5 g/s.

Downloaded 02 Jun 2010 to 171.66.16.109. Redistribution subject to ASME license or copyright; see http://www.asme.org/terms/Terms_Use.cfm

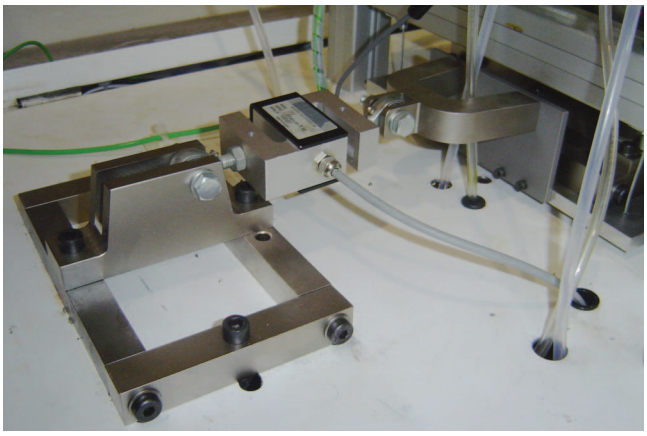


Fig. 4 Thrust measuring load cell

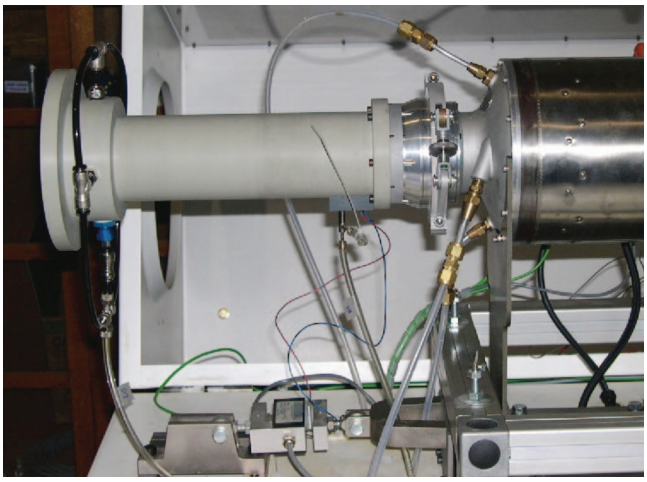


Fig. 5 Air flowmeter and variable geometry inlet guide vane

3.3 The Fuel Flow Measurement. The fuel flow is measured using a volumetric sensor similar to those used for diesel engines. The sensor consists of a cavity with a known reference volume that fills and empties according to the fuel flow sent to the injectors and to the fuel flow returning to the tank. A pulse is sent to an electronic device each time the cavity is filled up. The fuel flow is simply obtained by multiplying the frequency of this signal by the reference volume of the cavity. The accuracy is 0.5% of the full scale value.

3.4 The Variable Area Nozzle. The original engine is operated by controlling the fuel flow, which is injected into the combustion chamber. Varying the fuel flow allows traversing the equilibrium line of the engine from idle (around 40,000 rpm) to maximum speed (around 85,000 rpm). It was decided to add a second control parameter to the engine, in order to vary the position of the equilibrium line and to allow for the exploration of the compressor map. This has been done through the addition of a variable area convergent nozzle as a prolongation of the existing one. Figure 6 depicts a cut view of the SR-30 engine featured with the variable area nozzle.

The inlet section of the variable area nozzle is circular and fits the exit section of the original one. The outlet section is rectangular and has the same area as the inlet section (2462 mm^2). The transition from the circular inlet to the rectangular outlet is progressive and based on a combination of conical and plane surfaces. Two movable flaps allow decreasing the outlet section down to 20% of the initial area (which is far beyond the limits of the engine in terms of EGT). Of course as the outlet section area can only decrease compared with the original value the engine running line can only be shifted upward. However, a nozzle with a wider outlet section would have acted as divergent-convergent for most of the operating conditions, with the related pressure drop. This solution was not selected considering the relatively low total pressure (around 1.3 bars) at the turbine outlet section. It is recognized that this extra nozzle did not allow a sufficient exploration of the compressor characteristic since the operating points with the minimum loss could not be reached.

The variable area nozzle is 170 mm long and is made of Inconel 625 using an electro-erosion machine. It is mounted on the engine using the six original screws that are used to fix the rear plate to the original nozzle liner. The rotation of the two flaps is performed

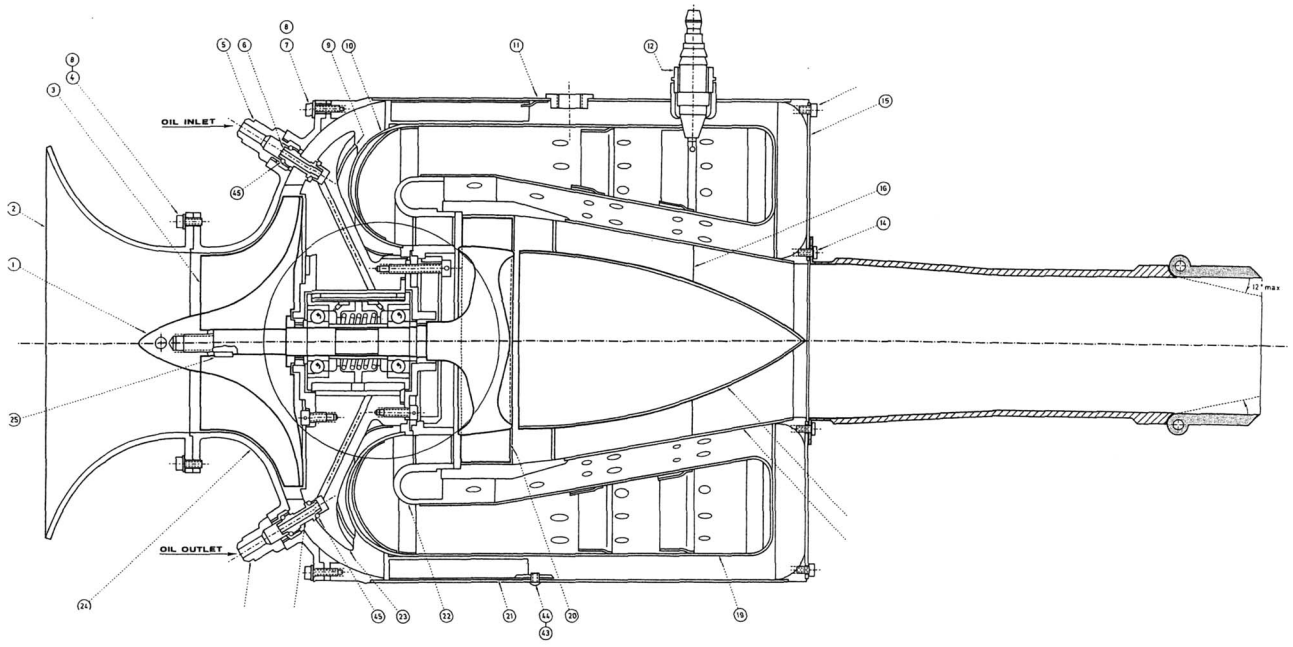


Fig. 6 The SR-30 and the variable area nozzle

Downloaded 02 Jun 2010 to 171.66.16.109. Redistribution subject to ASME license or copyright; see http://www.asme.org/terms/Terms_Use.cfm

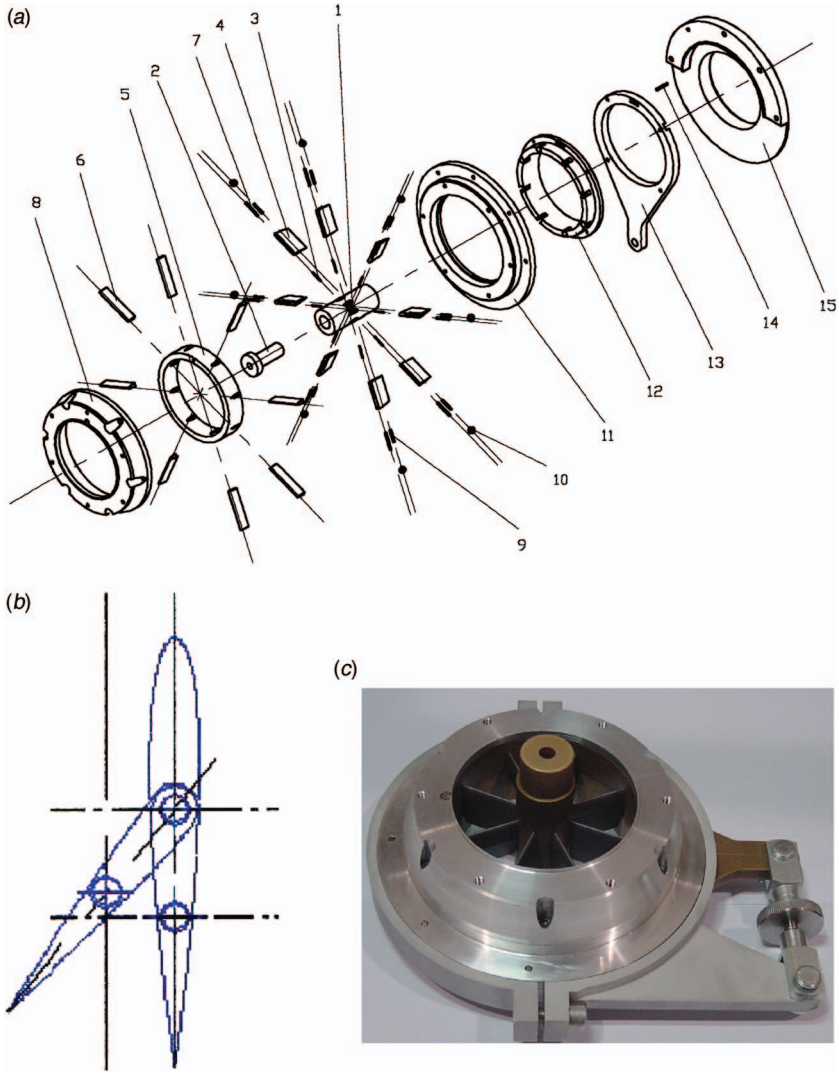


Fig. 7 Inlet guide vane

using a dc servomotor and a notched belt (visible in Fig. 8). It can be either operated manually or included in a control loop.

3.5 The Variable Geometry Inlet Guide Vane. With the same objective of controlling the operating point of the engine and widening its operational domain, it was decided to design and to build a variable geometry guide vane and to mount it between the original bell-mouth nozzle (or the flowmeter nozzle) and the inlet section of the compressor.

The inlet guide vane (IGV) system is made of eight blades that can be rotated by −40 deg to +40 deg around the radial direction. The flow entering the rotor is deflected either in the sense of rotation or in the opposite sense. According to the Euler equation, which relates the enthalpy rise to the angular momentum variation within the rotor, the characteristic map of the compressor is significantly modified by the rotation of the eight blades at the price of a (moderate) pressure drop. The rotation of the aft-part of the blades results from the circular movement of a ring operated by a radial arm (Fig. 7).

3.6 The Fuel Valve. The original engine was controlled purely manually, only by modifying the quantity of fuel injected into the combustion chamber. The fuel valve actually controls the quantity of fuel, which is allowed to return to the fuel tank. A fully open valve therefore corresponds to idle and a fully closed valve corresponds to maximum speed. The fuel flow ranges from 2 g/s to 5 g/s approximately.

The real-time acquisition system has a number of inputs but also two possible outputs that can pass 0/10 V signals. It was decided to take advantage of this feature to remotely operate the fuel valve, since it should open the way to a digital control of the engine via the acquisition system (described in Sec. 5).

To this end the mechanical control of the fuel valve (using a cable) was replaced with a dc servomotor controlled either by a PC or by an angular position sensor on the original throttle lever so that a manual control is still available. The dc motor is connected to the fuel valve via a reduction gear and a parallelogram mechanism (Fig. 8).

4 Modeling the SR-30 Engine

Turbine engines can be modeled at various levels of detail, ranging from simple algebraic relations to full 3D description of the gas path. Among this variety, aerothermodynamic models (also known as 0D models) are largely used throughout an engine program: for preliminary design and performance prediction, for the engine-airframe integration, as well as for the synthesis of the control laws, and for condition monitoring. As a direct application of the course of Propulsion Physics, a number of Master theses have been partly dedicated to the development of such a 0D

Downloaded 02 Jun 2010 to 171.66.16.109. Redistribution subject to ASME license or copyright; see http://www.asme.org/terms/Terms_Use.cfm



Fig. 8 Rear part of the engine and fuel valve operating system

model of the SR-30 turbojet, which has been subsequently used for control system design and performance diagnostics. Reported here is the setup of the latest model [5].

0D models allow the prediction of the overall performance of an engine such as net thrust and specific fuel consumption and the average thermodynamic state of the working fluid at intercomponent stations. As the name suggests, the resolution of such models lies at a component level. Modeling the engine cycle relies on the application of mass, momentum, and energy balances along the engine flow-path.

ECOSIMPRO [6] was selected as the platform for the development of the engine model. This general simulation tool is object-oriented and based on the concept of component to model a system. It allows focusing on the modeling task itself as it features a powerful equation solver as well as a graphical user interface (ECODIAGRAM) for building the model. Figure 9 depicts a schematic of the SR-30 model in ECODIAGRAM. The major components of the engine are the flowmeter (intake), the compressor, the burner, the turbine, and the convergent nozzle.

As a first step, a library of components is created in ECOSIMPRO. Each component can be seen as an operator whose purpose is to compute the thermodynamic state of the fluid (typically mass flow W, total temperature T^0, and pressure p^0) at the outlet of the module on the basis of the inlet conditions and some additional parameters. The modeling relies on the equations for mass, momentum, and energy balances and/or on empirical information derived from rig tests or computational fluid dynamics (CFD) calculations (e.g., compressor and turbine maps). A number of textbooks, see for instance Refs. [7,8], are dedicated to this task.

4.1 Thermodynamic Properties. The working fluids (air and combustion gases) are considered as semiperfect gases of variable specific heats. Accordingly, the constant-pressure specific heat C_p, the enthalpy h, and the entropy function Φ are defined as

$$C_p = C_p(T,\mathrm{FAR}) \tag{1}$$

$$h = h_{\mathrm{ref}} + \int_{T_{\mathrm{ref}}}^{T} C_p dT = h(T,\mathrm{FAR}) \tag{2}$$

$$\Phi = \Phi_{\mathrm{ref}} + \int_{T_{\mathrm{ref}}}^{T} \frac{C_p}{T} dT = \Phi(T,\mathrm{FAR}) \tag{3}$$

where FAR is the fuel-to-air ratio.

4.2 Atmospheric Conditions and Flowmeter. The engine is mounted on a test bench. In that configuration, ambient pressure and temperature are also the total conditions at the flowmeter inlet (Station 1). The effect of humidity is not taken into account in the present model.

$$p_1^0 = p_{\mathrm{amb}} \tag{4}$$

$$T_1^0 = T_{\mathrm{amb}} \tag{5}$$

The flowmeter is supposed adiabatic, but introduces a pressure drop measured by a total pressure recovery factor π_d. The thermodynamic state of the fluid at the flowmeter exit (Station 2) is

$$W_2 = W_1 \tag{6}$$

$$T_2^0 = T_1^0 \tag{7}$$

$$p_2^0 = \pi_d\, p_1^0 \tag{8}$$

where π_d is given by the ISA-1932 norm that was followed to build the flowmeter.

4.3 Compressor. This component actually stacks the inlet guide vane and the centrifugal stage. The governing equations for the compressor are the following:

$$W_3 = W_2 \tag{9}$$

$$p_3^0 = \pi_c\, p_2^0 \tag{10}$$

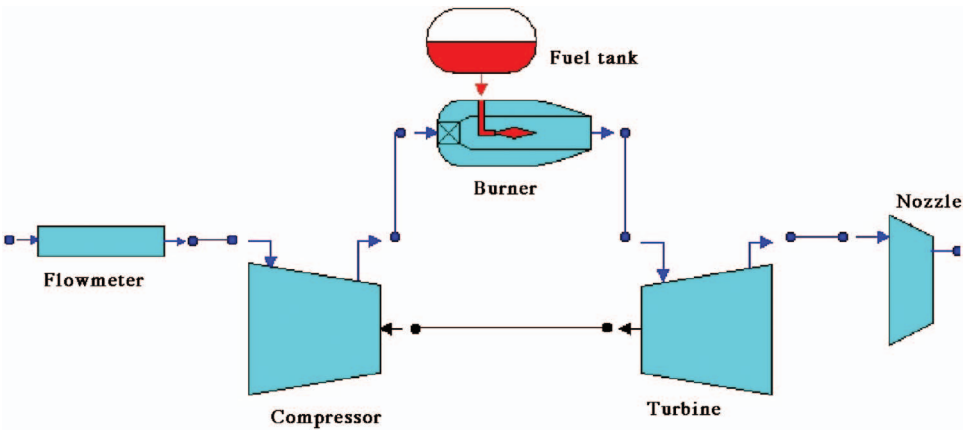


Fig. 9 Schematic of the ECOSIMPRO model

Downloaded 02 Jun 2010 to 171.66.16.109. Redistribution subject to ASME license or copyright; see http://www.asme.org/terms/Terms_Use.cfm

$$h_3^0 = h_2^0 + \frac{1}{\eta_c}(h_{3,\text{is}}^0 - h_2^0) \tag{11}$$

The isentropic outlet enthalpy $h_{3,\text{is}}^0$ is computed from the entropy function

$$\Phi_{3,\text{is}} = \Phi_2 + R\,\log(\pi_c) \tag{12}$$

The characteristic curves of the compressor have been worked out from a mean-line analysis [9] and are stored in the β-lines format to prevent numerical interpolation problems. Accounting for the effect of the inlet guide vane, the corrected inlet mass flow W_2^{std}, the pressure ratio π_c, and the isentropic efficiency η_c are functions of the corrected spool speed N_2^{std}, the β-coordinate, and the IGV stagger angle α_{IGV} as follows:

$$W_2^{\text{std}} = C_{W^{\text{std}}}\, f_{W^{\text{std}}}(N_2^{\text{std}}, \beta, \alpha_{\text{IGV}}) \tag{13}$$

$$\pi_c = C_\pi\, f_\pi(N_2^{\text{std}}, \beta, \alpha_{\text{IGV}}) \tag{14}$$

$$\eta_c = C_\eta\, f_\eta(N_2^{\text{std}}, \beta, \alpha_{\text{IGV}}) \tag{15}$$

where $C_{W^{\text{std}}}$, C_π, and C_η are so-called map scaling factors that are applied to the performances read in the map so that they match the actual compressor performances.

The power required to drive the compressor is given by

$$\text{PW}_c = W_3(h_3^0 - h_2^0) \tag{16}$$

4.4 Burner. The combustion chamber increases the enthalpy of the working fluid through the burning of fuel. The governing equations for this component are

$$W_4 = W_3 + W_F \tag{17}$$

$$p_4^0 = \pi_b\, p_3^0 \tag{18}$$

$$h_4^0 = \frac{\eta_b W_F \text{LHV} + W_3 h_3^0}{W_4} \tag{19}$$

where LHV stands for low heating value of the fuel.

The combustion efficiency η_b expresses the fact that the combustion process is incomplete. It is very well correlated with the air loading AL as follows:

$$\text{AL} = \frac{W_3}{\text{vol}(p_3^0)^{1.8} 10^{0.00145(T_3^0 - 400)}} \tag{20}$$

The pressure recovery factor π_b accounts for the friction losses and is evaluated according to

$$\pi_b = 1 - K_b\left(\frac{W_3\sqrt{T_3^0}}{p_3^0}\right)^2 \tag{21}$$

where K_b is a constant depending on the burner geometry and surface roughness.

4.5 Turbine. The constitutive equations for the turbine are quite similar to those of the compressor as follows:

$$W_5 = W_4 \tag{22}$$

$$p_5^0 = \pi_t\, p_4^0 \tag{23}$$

$$h_5^0 = h_4^0 + \eta_t(h_{5,\text{is}}^0 - h_4^0) \tag{24}$$

The isentropic outlet enthalpy $h_{5,\text{is}}^0$ is computed from the entropy function

$$\Phi_{5,\text{is}} = \Phi_4 + R\,\log(\pi_t) \tag{25}$$

Due to the moderate compressor pressure ratio, the turbine is unchoked for most of the operating regimes. Moreover, no map is available, be it from the manufacturer or from a mean-line analysis. As a workaround, Stodola's ellipsis is used for describing the pressure ratio π_t-corrected mass flow W_4^{std} relation

$$W_4^{\text{std}} = K_t\sqrt{1 - \pi_t^{n_t}} \tag{26}$$

where K_t and n_t are constant parameters that characterize the turbine stage. Stodola's model treats the turbine as a nozzle, as far as the $(W_4^{\text{std}}, \pi_t)$ curve is concerned, and therefore neglects the influence of the rotational speed on the stage characteristic.

Considering the isentropic efficiency η_t, a correlation with the inlet corrected mass flow is to be determined from the experimental measurements.

The available power generated by the turbine is given by

$$\text{PW}_t = \eta_m W_4(h_4^0 - h_5^0) \tag{27}$$

The mechanical efficiency η_m accounts for the loss generated in the bearings supporting the shaft.

4.6 Exhaust Nozzle. Assuming an adiabatic process, the constitutive equations write down

$$W_9 = W_5 \tag{28}$$

$$p_9^0 = \pi_n p_5^0 \tag{29}$$

$$T_9^0 = T_5^0 \tag{30}$$

where π_n represents the pressure loss across the nozzle and is modeled as the burner pressure loss (21).

The nozzle expansion ratio $\text{NER} = p_{\text{amb}}/p_9^0$ is subcritical for the whole operating range, which means that the static pressure in the exit plane p_9 is equal to the ambient pressure p_{amb} and the exhaust Mach number is subsonic. From the exit Mach number M_9 and total temperature T_9^0, the exhaust jet velocity V_9 can be computed with usual equations. A discharge coefficient C_D is introduced to account for the reduction of effective flow area due to the boundary layer. C_D is correlated with the NER as follows:

$$C_D = \frac{A_{9,\text{eff}}}{A_{9,\text{geom}}} = C_D(\text{NER}) \tag{31}$$

Finally, the thrust generated by the engine is assessed with a momentum balance between the engine inlet and outlet as follows:

$$FG = W_9 V_9 + A_{9,\text{eff}}(p_9 - p_{\text{amb}}) \tag{32}$$

The net thrust confounds with the gross thrust since the engine is not moving and the pressure term vanishes as the nozzle is unchoked.

4.7 Assembling the Components. To build the engine model, the basic modules presented in Secs. 4.1 through 4.6 are assembled following the general schematic of Fig. 9. Ensuring the conservation of mass, momentum, and energy throughout the engine generates constraints, which actually restrict the operating range of each component. The conservation principles translate into a set of nonlinear algebraic equations, also termed compatibility equations that are solved with ECOSIMPRO's built-in algorithms.

From an external point of view, the engine model can be seen as a vector-valued function

$$y = \mathcal{G}(u) \tag{33}$$

where u is the vector of command parameters that define the operating point of the engine (fuel flow, nozzle area, IGV angle, ambient temperature, and pressure) and y is the vector of measurements (total temperature and pressure at various stations, spool speed, and thrust).

4.8 Fitting the Engine Model to Test Data. Numerous parameters have appeared in the modeling of the components. Their values must be determined on the basis of experimental data collected on the engine so that the resulting model is representative of the actual engine behavior. This task is usually known as model

Downloaded 02 Jun 2010 to 171.66.16.109. Redistribution subject to ASME license or copyright; see http://www.asme.org/terms/Terms_Use.cfm

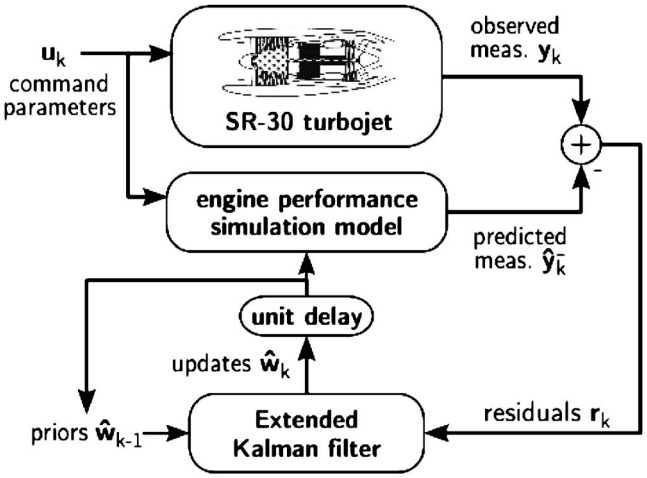


Fig. 10 Tuning procedure using an extended Kalman filter

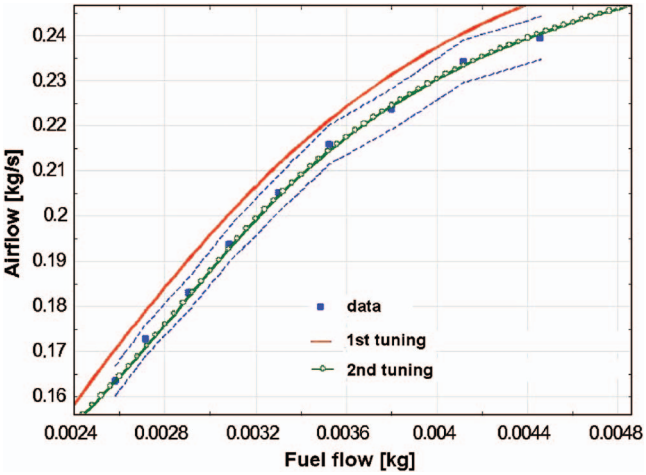


Fig. 12 Fuel flow—airflow curve

fitting/tuning. Data have been collected on the engine in the operating range 55,000–75,000 rpm per steps of 2500 rpm. The tests were conducted at a nominal IGV stagger and a fully opened nozzle.

Model fitting has been carried out in two stages. Raw estimations of the various parameters and correlations have been determined from a first tuning procedure applied to each component separately. As some important quantities are not available (e.g., turbine inlet total pressure p_4^0) or are at best rough indicators (e.g., turbine inlet total temperature T_4^0), the values of some parameters such as mechanical efficiency or burner pressure loss have been imposed to common values.

Second, a fine tuning of the model has been performed. The fitting parameters are now computed at a global level. To this end, they are considered as additional inputs w of the model:

$$y = \mathcal{G}(u,w) \tag{34}$$

The tuning task can be seen as the inverse problem of performance prediction. Knowing the command parameters u and the observed measurements y, the parameters w are modified so that the residuals between the experimental data and the model predictions are minimized in the least-squares sense. The minimization algorithm implements a Kalman filter (see Ref. [10] for details) developed in the Turbomachinery Group in the frame of research activities in health monitoring. Figure 10 sketches the general principle of the recursive tuning of model parameters.

Some results of the fitting procedure are sketched in Figs. 11 and 12. The blue dots are the experimental data, the dotted blue lines are the uncertainty bounds on the measurements, the red line is the model prediction after the first tuning step, and the green line is the model prediction after refining the parameter values with the Kalman filter.

Figure 11 depicts the evolution of the exhaust gas temperature T_9^0 with respect to the fuel flow. It can be seen that the model predictions are already within the uncertainty bounds for the higher operating regimes after the first tuning process. The second pass with the Kalman filter improves the results in the mid- and low-power regions.

Figure 12 represents the evolution of the airflow W_2 with respect to the fuel flow. For this particular quantity, the first tuning procedure is clearly unsuccessful as the prediction of airflow is outside the confidence limits for the whole operating line. The further fitting performed by the Kalman filter dramatically improves the quality of the mass flow prediction for the regimes considered. Conclusions similar to those drawn for Figs. 11 and 12 are valid for the other measurements.

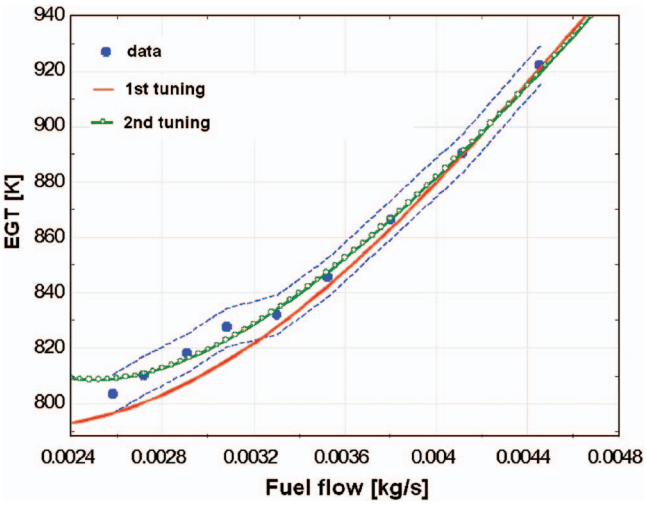


Fig. 11 Fuel flow—EGT curve

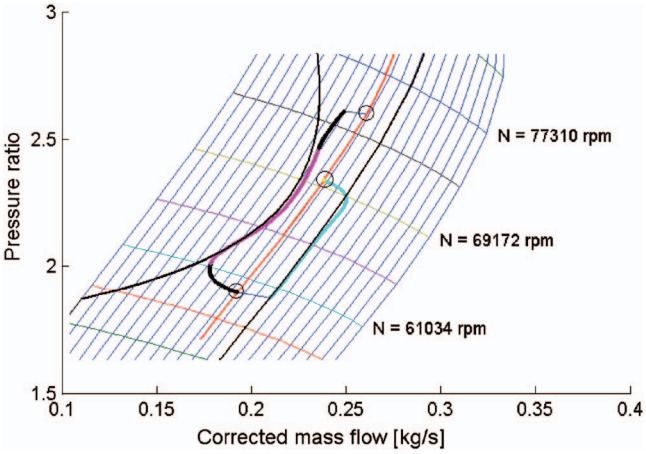


Fig. 13 Trajectory of the operating point for a deceleration followed by an acceleration in the compressor map: steady-line (red curve), limits on the mass flow (black curves), and steady operating points (black circles)

Downloaded 02 Jun 2010 to 171.66.16.109. Redistribution subject to ASME license or copyright; see http://www.asme.org/terms/Terms_Use.cfm

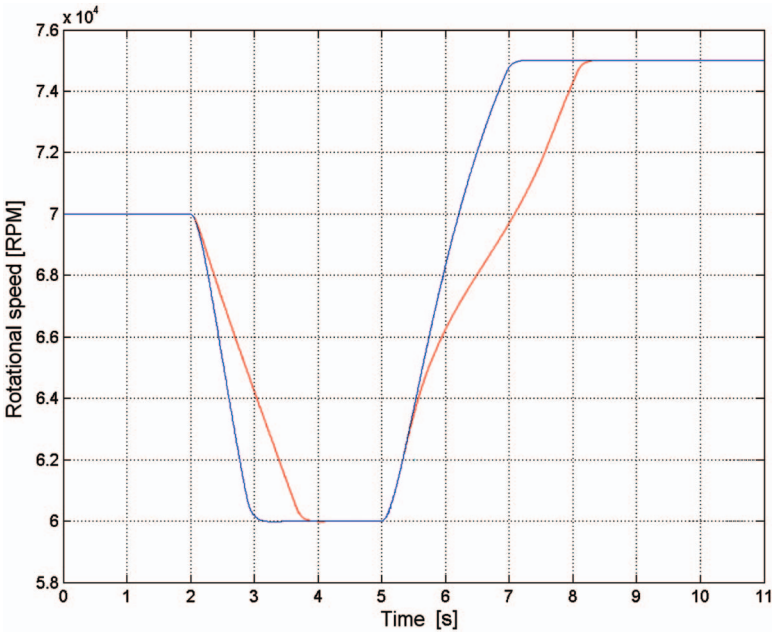


Fig. 14 Evolution of the rotational speed with (red line) and without (blue line) physical limits

5 Controlling the SR-30 Engine

A transient mathematical model of the engine can be made available by adding one equation to the steady-state model described above. This equation describes the evolution of the rotational speed with time by balancing the power developed by the turbine, the power required by the compressor, and the inertia of the rotating parts as follows:

$$J\left(\frac{2\pi}{60}\right)^2 N\frac{dN}{dt} = \mathrm{PW}_t - \mathrm{PW}_c \tag{35}$$

Whereas the dynamic behavior of the rotational speed is captured with some accuracy provided that the additional parameter J in Eq. (35) is correctly determined, the evolutions of the mass flow and the temperatures are more qualitatively captured. As the acquisition system is able to output signals and as the fuel valve is driven now by a dc motor, it was decided to explore the possibility of controlling the fuel flow injected into the engine corresponding to prescribed objectives.

The objectives are the minimization (at least the reduction) of the time required for transients, while avoiding the trespass of any physical limit of the engine. The rotational speed has been selected to play the role of the performance parameter from which a feedback action is determined, as it is the case on most of gas turbine engines. The physical limits are specified in terms of rotational speed (minimum and maximum levels), air and fuel flows (minimum and maximum values), and maximum EGT.

A controller has been devised for this virtual engine using MATLAB/SIMULINK. The control device includes the following elements: a feedforward action that generates a command, a feedback action that generates a correction of the feedforward in function of the error, one control action per physical limit, and an antiwindup device. The control strategy has to pursue the following objectives: reduction of the response time, zero static error, no violation of any of the physical limits, robustness against external perturbations, and sensor noise. A proportional-integral-derivative control law has been selected for the rotational speed (tuned with the performance index ITAE[1]), while a proportional-integral control law was selected for the air mass flow as well as for the EGT (for a very short response time).

An example of control sequence is depicted in Fig. 13. The engine decelerates from 70,000 rpm to 60,000 rpm, and stabilizes and accelerates up to 75,000 rpm. The operating point moves between the following physical limits: minimum fuel flow (yellow), maximum corrected mass flow (cyan), maximum fuel flow (black), minimum corrected mass flow (magenta), and maximum fuel flow again.

The corresponding evolution of the rotational speed is depicted in Fig. 14 (red curve). The latter is compared with the speed obtained in the absence of limits (blue curve). While the setting time is of the order of 10 s for the open-loop engine, it has been reduced to about 1 and 2 s for the unlimited maneuvers depicted here. Even in the case of limits, the closed-loop behavior remains very rapid. For several reasons these results obtained with the ECOSIMPRO transient mathematical model coupled to a MATLAB/SIMULINK controller could not be repeated on the test bench.

The dynamic behavior of the fuel valve actuation is characterized by a considerable inertia due to the parallelogram system (visible in Fig. 8). This means that if the dynamics of the closed loop is too rapid the inertia of the fuel valve is stronger than the damping, resulting in a violation of physical limits. This issue has shown to significantly limit the performance of the controller. The performance of the controller is even more limited by the acquisition frequency of 4 Hz and its associated time delay of 250 ms between the computation of the command signal and the moment at which the latter is applied.

For these reasons the control laws synthesized and tested with the mathematical model of the engine had to be significantly modified with a loss of performance. The bandwidth of the controller had to be drastically limited, i.e., the closed-loop behavior of the engine had to be smoothed to avoid instabilities.

Figure 15 illustrates the poor performance of the fuel controller facing an external perturbation introduced by a rapid opening of the variable area nozzle. The ejection velocity is reduced and so is the total pressure in the nozzle, inducing an acceleration of the engine spool. The rejection of this perturbation, while effective, is slow and oscillating.

The high frequency/small amplitude evolutions observed in Fig.

[1]Integral of time multiplied by absolute error: ITAE=$\int_0^T t|e(t)|dt$.

Downloaded 02 Jun 2010 to 171.66.16.109. Redistribution subject to ASME license or copyright; see http://www.asme.org/terms/Terms_Use.cfm

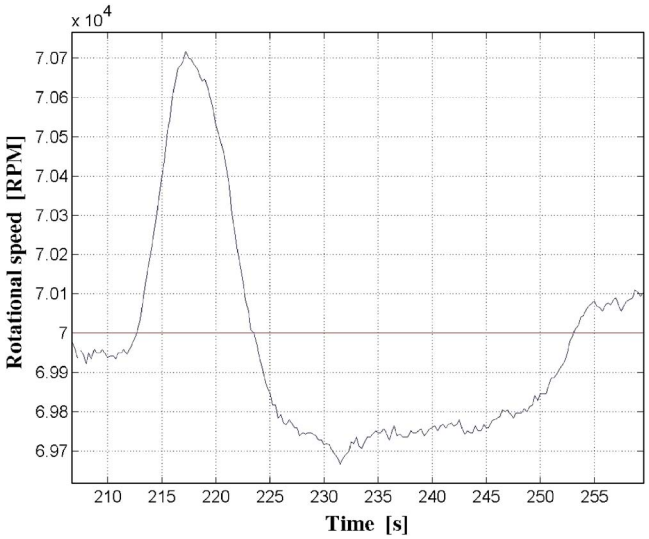


Fig. 15 Rejection of an external perturbation

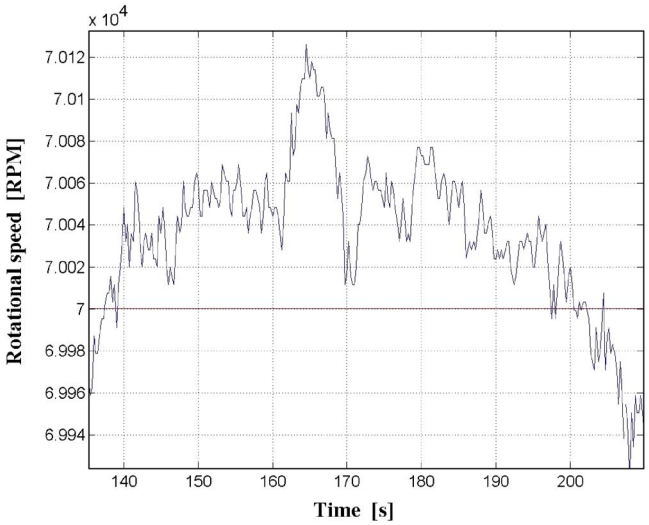


Fig. 16 Follow-up of a prescribed rotational speed

15 (and further in Fig. 16) are probably the consequence of additional poor features of the fuel valve actuator. The latter introduces strong nonlinearities due to internal friction forces, inducing parasitic movements of the fuel valve and degrading the transient performance of the whole system. The command noise characterizing the original fuel valve actuation is another issue. It is due to the necessary clearance in the kneecap mechanisms of the parallelogram system.

Figure 16 illustrates the result of the follow-up of an assigned value for the rotational speed equal to 70,000 rpm. The maximum error is about 100 rpm, but the mean error is below 50 rpm, which can be considered as rather successful considering the above mentioned shortcomings of the actuation system.

The replacement of the original fuel valve and its actuation system with a proportional electrical valve whose dynamics is fast enough seems to be the only way to overcome these problems. This solution has been implemented by Watanabe et al. [1] and has been undertaken this year in our group by a Master student.

6 Conclusions

The main characteristic of gas turbines, i.e., power density, is well illustrated by the SR-30 engine, which is a reliable and effective demonstrator of many aspects of gas turbine operation. As noted by other academic teams, the single-point one-dimensional instrumentation typical of this small scale engine makes it somewhat difficult to obtain accurate results. However, the SR-30 is an excellent opportunity for the students to learn about the limitations of simplifying assumptions and about the difficulty associated with data acquisition, treatment, and interpretation.

The development of a computer model of the engine has shown that, by coupling principles of thermodynamics and mechanics to measured data and to a smart parameter identification procedure, it is possible to obtain meaningful results, despite the lack of information about component performance (no compressor nor turbine maps are available). These results would not have been obtained without the additional instrumentation, i.e., airflow, fuel flow, or thrust measuring devices.

The modifications of the test bench to implement these additional sensors, the design, the development, and the implementation of additional components for the engine itself, such as an inlet guide vane or a variable area nozzle, as well as the tentative to control the engine via the acquisition system, represented very appealing projects for the students. These projects were also quite successful in terms of educational objectives because they implied a deep understanding of the physics of many phenomena.

Acknowledgment

This work has been performed by the following Master students: Pierre-Yves Hanquet (thrust measurement), Anthony Mignon (variable area nozzle), Pierre Seronveaux (actuation via dc motors), Benoît Vertessen (design of the inlet guide vane), Claude Mockels (integration of the inlet guide vane), Jean-Philippe Thomas (new thrust measurement frame and control of the engine), Khanh Mai Quoc (identification of the engine model), and François Denis (proportional electrical fuel valve). The success of the SR-30 in our laboratory is also due to the strong support of its manufacturer, despite the distance.

Nomenclature

A = area
FG = thrust
h, h^0 = enthalpy, total enthalpy
J = spool inertia
N = spool speed
p, p^0 = pressure, total pressure
PW = power
R = gas constant
T, T^0 = temperature, total temperature
W, W_F = air mass flow, fuel mass flow
η = isentropic efficiency
Φ = entropy function
π = pressure ratio

Subscripts and Superscripts

1 = intake inlet
2,3 = compressor inlet, compressor outlet
4,5 = turbine inlet, turbine outlet
9 = exhaust
b = burner
c = compressor
t = turbine
amb = ambient
is = isentropic
std = corrected for standard conditions

References

[1] Watanabe, A., lmen, S. M., Leland, R., Whitaker, K. W., and Trevino, L. C., 2004, "Soft Computing Applications on SR-30 Turbojet Engine," AIAA Paper No. 2004–6444.
[2] Perez-Blanco, H., 2003, "Activities Around the SR-30 Minilab at PSU," *Proceedings of the 2003 American Society for Engineering Education Annual*

Downloaded 02 Jun 2010 to 171.66.16.109. Redistribution subject to ASME license or copyright; see http://www.asme.org/terms/Terms_Use.cfm

Conference and Exposition, The American Society for Engineering Education, Nashville, TN.
[3] Witkowski, T., White, S., Ortiz Dueas, C., Strykowski, P., and Simon, T., 2003, "Characterizing the Performance of the SR-30 Turbojet Engine," *Proceedings of the 2003 American Society for Engineering Education Annual Conference and Exposition*, The American Society for Engineering Education, Nashville, TN.
[4] Turbine Technologies Ltd, http://www.turbinetechnologies.com
[5] Mai, Q.-K., 2006, "Simulation of the Performance of the SR-30 Turbojet (in French)," M.S. thesis, University of Liège, Liège, Belgium.
[6] EcosimPro by EA Internacional, http://www.ecosimpro.com
[7] Mattingly, J. D., 1996, *Elements of Gas Turbine Propulsion*, McGraw-Hill, Singapore.
[8] Walsh, P. P., and Fletcher, P., 1998, *Gas Turbine Performance*, Blackwell Science, Oxford.
[9] Vertessen, B., 2001, "Design of a Variable Guide Vane for the SR-30 Turbojet (in French)," M.S. thesis, University of Liège, Liège, Belgium.
[10] Dewallef, P., 2005, "Application of the Kalman Filter to Health Monitoring of Gas Turbine Engines: A Sequential Approach to Robust Diagnosis," Ph.D. thesis, University of Liège, Liège, Belgium.

Downloaded 02 Jun 2010 to 171.66.16.109. Redistribution subject to ASME license or copyright; see http://www.asme.org/terms/Terms_Use.cfm

Effect of Side Feed Pressurization on the Dynamic Performance of Gas Foil Bearings: A Model Anchored to Test Data

Tae Ho Kim
Postdoctoral Research Associate
e-mail: taeho21c@tamu.edu

Luis San Andrés
Mast-Childs Professor
Fellow ASME
e-mail: lsanandres@mengr.tamu.edu

Texas A&M University Turbomachinery Laboratory,
Texas A&M University,
College Station, TX 77843-3123

Comprehensive modeling of gas foil bearings (GFBs) anchored to reliable test data will enable the widespread usage of these bearings into novel high speed turbomachinery applications. GFBs often need a forced cooling gas flow, axially fed through one end of the bearing, for adequate thermal management. This paper presents rotordynamic response measurements on a rigid rotor supported on GFBs during rotor speed run-up and coastdown tests with the GFBs supplied with increasing feed gas pressures to 2.8 bars. Rotor speed run-up tests to 35 krpm show that the bearing end side feed gas pressurization delays the onset speed of rotor subsynchronous whirl motions. The test data validate closely the predictions of the threshold speed of instability and the whirl frequency ratio derived from a GFB model that implements the axial evolution of gas circumferential flow velocity as a function of the imposed side feed pressure. Rotor speed coastdown tests from 25 krpm with a low feed pressure of 0.35 bar evidence a nearly linear synchronous rotor response for small and moderately large imbalance mass distributions. A structural finite element rotordynamics model integrates linearized synchronous speed GFB force coefficients and predicts synchronous responses, amplitude, and phase angles, agreeing with the test data. The analysis and measurements demonstrate the profound effect of the end side feed gas pressurization on the rotordynamic performance of GFBs.
[DOI: 10.1115/1.2966421]

Keywords: gas foil bearing, external pressurization, rotordynamic stability, imbalance response

Introduction

Gas foil bearings (GFBs) using engineered solid lubricants (coatings) have demonstrated an ultimate specific load of 680 kPa (100 psi) and high temperature operation to 650°C [1,2]. Figure 1 depicts the configuration of a "second generation" type [1] GFB consisting of a single arcuate top foil and five corrugated bump strip layers. The leading edge of the top foil is free, while its trailing edge is spot welded to the bearing housing. Beneath the top foil, the five bump strip layers, each with five bumps, are split into five axial segments. One end of the bump strip layers is spot welded to the bearing housing while the other end is free, thus providing an engineered structural stiffness varying around the bearing circumference. Dry-friction between the bumps and the top foil and the bumps and the bearing inner surface provides energy dissipation (damping) well in excess of that obtained in simpler gas bearing configurations [3,4].

In operation, GFBs develop a hydrodynamic film pressure that separates the rotating shaft and the top foil. As rotor speed and load increase, the minute gas film becomes stiffer than the underlying elastic support structure; and hence, the bearing force performance depends greatly on the material properties and geometrical configuration of the top foil and the bump strip layers. Chen et al. [5] and DellaCorte et al. [6] fully described the materials and manufacturing processes to construct first and second generation type GFBs. These relevant publications, also offering some limited experimental validations, enable the widespread knowledge of a, until recently, protected technology. To date, however, GFB design is still largely empirical, each bearing being a custom piece of hardware, with resulting variability even in identical units, and limited scalability.

Thermal management is an issue of importance for the reliable performance of GFBs in high temperature environments. The engineered coatings applied to the top foil and the rotor surface ensure low-friction operation and little wear, and reduce the likelihood of thermal seizure and bearing failure. Often, a cooling gas flow is forced through the foil bearing underlying structure to carry away heat generated by a hot component, for example. This highly effective cooling method [7] controls the thermal growth of components and changes in material properties, reduces thermal gradients, and prevents hot spots in the bearings; hence extending their life [8]. With an adequate supply of cooling flow into a GFB supporting the hot end of a microgas turbine, Ref. [9] describes the successful endurance tests conducted to 120 krpm at an operating temperature of 800°C.

Since 2003, the authors have conducted a comprehensive research program to develop experimentally validated computational models predicting the static and dynamic forced responses of GFBs, to identify the structural characteristics of second generation foil bearings, and to measure the rotordynamic performance of a rigid rotor supported on the test GFBs. The research products to date include the following:

(a) An extensive test database for nonlinear foil bearing structural deflections versus static and dynamic applied forces, along with the identification of bearing structural stiffness and energy dissipation loss factor as a function of load amplitude, excitation frequency, and shaft temperature [10–13].

Contributed by the International Gas Turbine Institute of ASME for publication in the JOURNAL OF ENGINEERING FOR GAS TURBINES AND POWER. Manuscript received March 28, 2008; final manuscript received March 29, 2008; published online October 2, 2008. Review conducted by Dilip R. Ballal. Paper presented at the ASME Turbo Expo 2008: Land, Sea and Air (GT2006), Berlin, Germany, June 9–13, 2008.

Copyright © 2009 by ASME

Downloaded 02 Jun 2010 to 171.66.16.109. Redistribution subject to ASME license or copyright; see http://www.asme.org/terms/Terms_Use.cfm

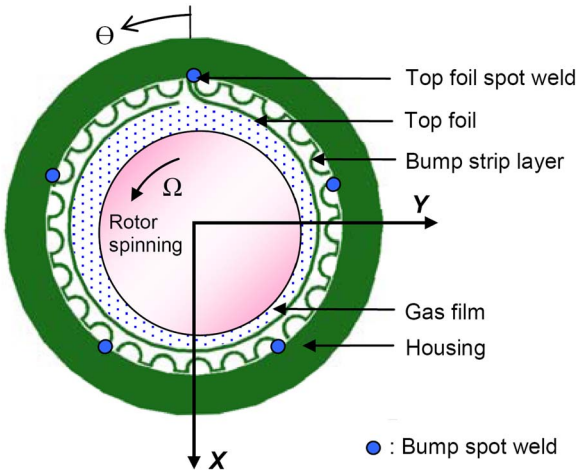


Fig. 1 Schematic of "second generation" bump type foil bearing

(b) An independent experimental database for rotordynamic measurements acquired in a test rigid rotor supported on GFBs for shaft speeds to 50 krpm, various mass imbalance distributions, and increasing levels of gas pressurization forced through one side end of the test bearings [14,15]. The measurements revealed the effect of side pressurization, customarily used for cooling, on ameliorating amplitudes of rotor synchronous response and even eliminating subsynchronous motions.

(c) Accurate computational predictive models, evolving from a simple tool [16] to a more elaborate one [17] that presently integrates the gas film to a shell finite element model of the top foil and the underlying bump strip layers structure. Predictions for GFB load capacity and minimum film thickness in the noted references agree within 15% with the relevant test data of Ruscitto et al. [18], while predictions of rotor dynamic response using linearized bearing force coefficients reproduce closely the measured amplitude of synchronous response and the onset of subsynchronous whirl motions for the test rotor-GFB system, as reported in Ref. [14].

References [16,17,19] provide comprehensive reviews of prior art in the analysis of GFBs and note the near absence of model predictions compared against reliable (noncommercial) test data. In particular, Ref. [19] includes further comparisons of GFB load and torque to test the data collected by Kim et al. [20]. San Andrés and Kim [19] also advanced a simple nonlinear structural model for GFB forced performance that, in conjunction with a rotordynamics transient response model, predicts with exactness the amplitude and rich frequency content of measured rotor responses. For rotor speed operation above a system natural frequency, the typical hardening nonlinearity in the foil bearing structure induces rotor motions with multifrequencies, super- and subsynchronous.

There is no GFB predictive model that accounts for the effect of side flow pressurization on modifying the bearing forced response and making it less prone to induce subsynchronous whirl motions and/or rotordynamic instability. Presently, this paper presents additional rotor response measurements with GFBs supplied with increasing levels of side pressurization and compares the test data to predictions from an enhanced computational model that incorporates the axial evolution of gas film circumferential flow velocity due to an imposed feed pressure, axially supplied through a bearing end. The correlation between predicted and measured onset speeds of instability and whirl subsynchronous frequency is very good. The experimentally benchmarked code presently aids industry to advance further GFB technology.

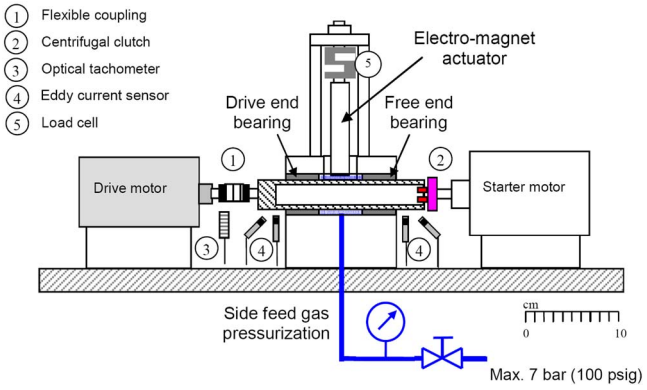


Fig. 2 Layout of rotor-GFBs test rig and instrumentation

Rotordynamic Measurement of Shaft Motions in Test Rotor-GFB System

Figure 2 depicts a simple layout of the test rig and instrumentation. References [14,15] detail the geometry and materials of the test rotor and second generation GFBs procured from a commercial vendor and are shown schematically in Fig. 1. In brief, the hollow rotor weighs 1 kg, and the GFB length L and diameter $2R_J$ are 38.1 mm. The measured sway radial clearance c is 40 μm and 70 μm for the drive and free end GFBs, respectively. A 0.75 kW ac motor with maximum speed of 50 krpm drives the test rotor through a flexible coupling. In addition, a 1.49 kW router ac motor and a centrifugal clutch aid in the startup of the test rotor. The clutch is typically disengaged once the rotor lifts off from its bearings (~8 krpm). Pressurized air, 7 bar (100 psi gauge) maximum, flows through the midsection of the rig housing and enters a test bearing at one of its axial ends; the other end being exposed to ambient pressure P_a.

Rotordynamic response measurements are conducted for various sets of imbalance distributions and feed pressures P_s. Two pairs of orthogonally positioned eddy current sensors located at both rotor ends record the lateral rotor motions along the horizontal and vertical planes. The eddy current sensors have a 2 mm linear range and sensitivity of 7.87 mV/μm $\pm$ 5%

Figure 3 shows a schematic of a GFB and a journal rotating with angular speed Ω. An imposed pressure differential $P_s - P_a$ forces a cooling flow through the foil bearing. The graph depicts the evolution of gas velocities, circumferential and axial, through inner and outer flow regions. The inner flow, between the rotating

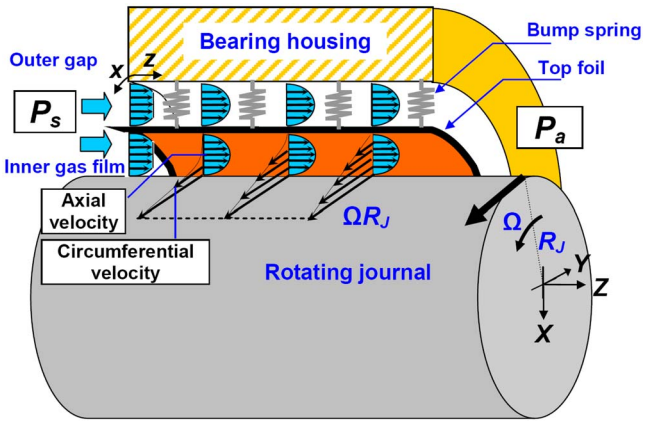


Fig. 3 Flow induced by side pressure in a foil bearing: schematic of the evolution of gas velocities within the inner and outer flow regions, i.e., between the journal and the top foil underneath top foil and bearing housing, respectively

Downloaded 02 Jun 2010 to 171.66.16.109. Redistribution subject to ASME license or copyright; see http://www.asme.org/terms/Terms_Use.cfm

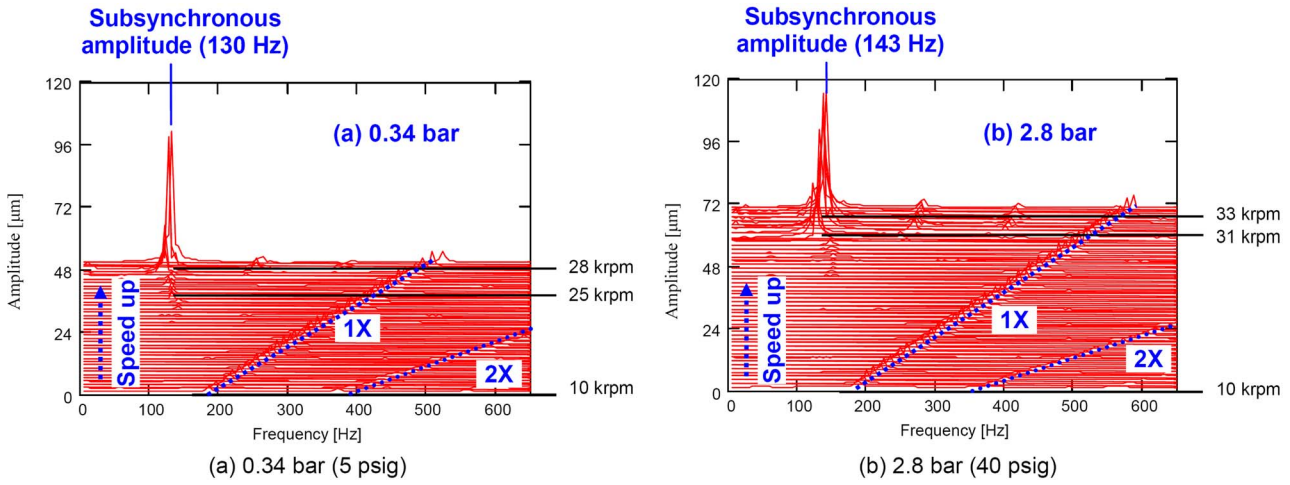


Fig. 4 Waterfalls of rotor free end vertical displacements measured during speed run-up from 10 krpm. Base line imbalance condition and air feed gauge pressures (*a*) 0.34 bar (5 psi gauge) and (*b*) 2.8 bars (40 psi gauge).

journal and the top foil, is characterized by a minute film thickness h. The outer flow forced through the back side of the top foil has a much larger characteristic length, typically a bump height h_b.

Onset Speed of Subsynchronous Motions. The rotor speed run-up (acceleration) tests from 10 krpm (minimum motor control speed) reveal the onset speed N_{os} of subsynchronous rotor motions for operation with increasing side feed pressures. Figures 4(*a*) and 4(*b*) display waterfall plots of vertical motions recorded at the rotor free end for side feed gauge pressures of 0.35 bar (5 psi gauge) and 2.8 bars (40 psi gauge), respectively. The lines labeled 1× and 2× denote synchronous and twice synchronous rotor motions. Subsynchronous motions with large amplitudes are evident as the rotor speed increases above a certain threshold value.

Figure 5 depicts the amplitudes of rotor synchronous and subsynchronous motions recorded at the rotor free end for feed pressures of 0.35 bar (5 psi gauge), 1.4 bars (20 psi gauge), and 2.8 bars (40 psi gauge). With a low feed pressure of 0.35 bar, the onset speed of subsynchronous motion is just 25 krpm. Note the severity of the subsynchronous rotor motions at the highest speed (~33 krpm). On the other hand, the rotor onset speed N_{os} delays to 30.5 krpm as the side feed pressure increases to 2.8 bars.

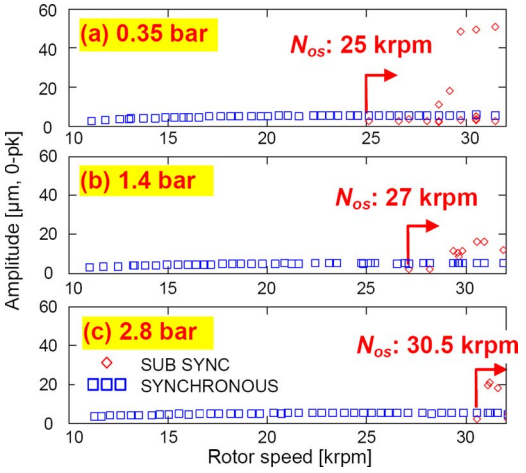


Fig. 5 Measured amplitudes of synchronous and subsynchronous rotor motions versus shaft speed for increasing air feed gauge pressure. Vertical displacements (*X*-direction) at rotor free end. N_{os}: onset speed of subsynchronous motion.

At a shaft speed of 30 krpm (500 Hz), the fast Fourier transform (FFT) of rotor motions shown in Fig. 6 reveal the severity of subsynchronous amplitudes and its relation to the level of bearing side pressurization. The frequency of subsynchronous whirl corresponds with a rigid body natural frequency of the rotor-GFB system. This natural frequency changes little with increases in the feed pressure. Figure 7 shows the dramatic effect of the bearing end side pressurization on reducing the total amplitude of rotor motion while rotating at 30 krpm. Recall that, for a low level of external pressurization, rotor motions are mainly composed of large whirl amplitudes at the system natural frequency. For $P_s \geq 2.8$ bars, rotor subsynchronous whirl motions disappear, i.e., the test system is rotordynamically stable at 30 krpm.[1]

Synchronous Response Amplitude and Phase Angle (Rotor Coastdown Tests). With a feed (gauge) pressure of 0.35 bar (5 psi gauge), imbalance response measurements are conducted during rotor speed coastdown tests from 25 krpm. Imbalance masses are added into the rotor end planes at a radius r_e of 15.11 mm, and producing in-phase and out-of-phase distributions. The assumption of linearity for the rotor-GFB system response is to be verified using increasing masses m_e of 55 mg, 110 mg, 165 mg, and 330 mg, i.e., one, two, three, and six times the smallest mass. For the 55 mg mass, the imbalance distance $u_e = (m_e\, r_e/M)_{\mathrm{DE,FE}}$ equals 1.3 μm and 2.3 μm at the rotor drive end and free end, respectively.

The recorded rotor synchronous responses are subtracted using a base line response (amplitude and phase) and normalized by multiplying the ratio of the smallest imbalance mass to the actual used [19]. Figure 8 presents the normalized rotor amplitudes and phase angles of the measured rotor synchronous response for the applied sets of small to large imbalance masses. The figure displays the vertical motions at the rotor drive end for an out-of-phase imbalance distribution.

For the smallest to moderately large imbalance masses (55–165 mg), the test data evidence nearly identical normalized amplitudes and phase angles, i.e., characteristic of a linear system. On the other hand, with a large imbalance mass of 330 mg, the

[1]The importance of the feed pressure effect on foil bearing stability was unknown prior to testing. Hence, a gas flow meter was not readily available at the time of the measurements. This omission will be corrected in future experimentation.

Downloaded 02 Jun 2010 to 171.66.16.109. Redistribution subject to ASME license or copyright; see http://www.asme.org/terms/Terms_Use.cfm

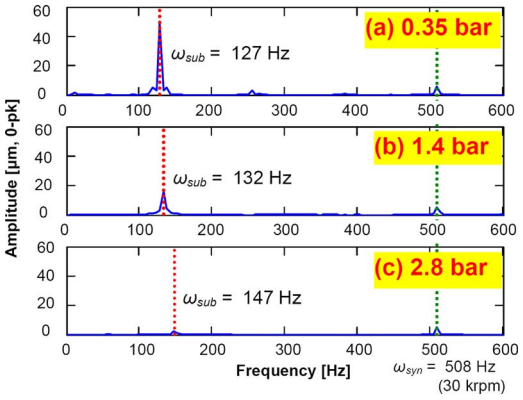


Fig. 6 Spectra of measured rotor free end vertical motions for increasing feed (gauge) side pressures and operation at 30 krpm (500 Hz)

peak amplitude around the critical speed ω_{cr} increases significantly. At this imbalance condition, the rotor-GFB system shows an apparent nonlinear behavior, demonstrating a response similar to that obtained from a system with a "hardening stiffness." The critical speed of the rotor-bearing system decreases by ~3 krpm when compared to those speeds estimated from the responses obtained with the smallest to moderate imbalance masses. A phase angle of ~90 deg determines a similar system natural frequency for all imbalance conditions. With the large imbalance mass, the phase angle increases more rapidly around the natural frequency, thus denoting a marked reduction in effective bearing damping. Kim [15] presented more imbalance response measurements obtained for increasing side pressures to 3 bars. These results are not shown for brevity.

Analysis of Gas Foil Bearing Forced Performance

As a conclusion of their GFB experimental work, San Andrés et al. [14] noted that the axial flow rate induced by side pressurization retards the development of the mean circumferential flow velocity u_c, as is commonly asserted in annular pressure seals [21,22]. For a centered journal operation, the gas mean flow circumferential velocity u_c varies along the axial coordinate z as [21]

$$u_c = \frac{\Omega R_J}{2}(1 - e^{-\delta z}) + \alpha \Omega R_J e^{-\delta z} \tag{1}$$

where

$$\delta = 12\mu/(\dot{m}_z c^2), \quad \dot{m}_z = \frac{c^2}{24\mu\Re T}\frac{(P_s^2 - P_a^2)}{L} \tag{2}$$

$\Re = 287$ J/kg K, and $\mu = 1.87 \times 10^{-5}$ Pa s is the air viscosity at room temperature. $\dot{m}_z$ is the axial flow rate through the film, and α is an inlet flow preswirl factor, hereby taken as null since in the tests the pressurized airflow impinged directly into one end of the bearing. Note that as $z \to \infty$, $u_c \to 0.5\Omega R_J$, i.e., 50% of rotor surface speed.

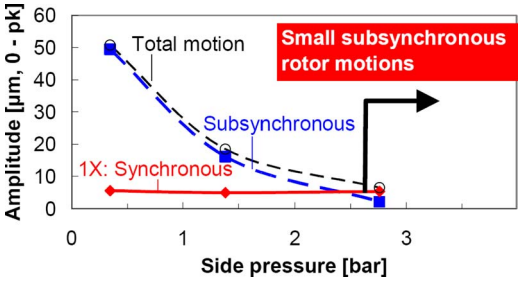


Fig. 7 Measured amplitudes of total shaft motion, and synchronous and subsynchronous components versus magnitude of bearing side (gauge) gas pressure at 30 krpm (500 Hz)

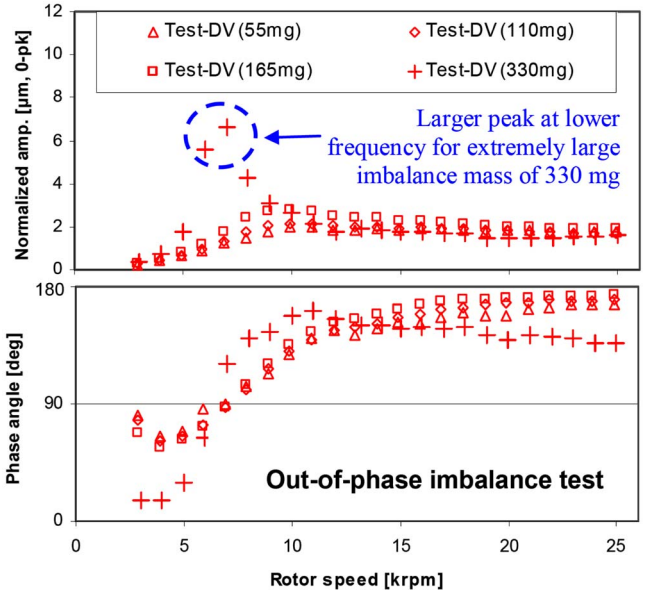


Fig. 8 Measured normalized amplitude and phase of synchronous rotor response for out-of-phase imbalance masses of 55 mg, 110 mg, 165 mg, and 330 mg. Measurements at drive end bearing, vertical plane (DV) with base line subtraction. Bearing end feed pressure at 0.34 bar (5 psi gauge) gauge.

Considering an isothermal,[2] isoviscous, and ideal gas ($\rho = P/\Re T$), a modified Reynolds equation incorporating the evolution of circumferential flow velocity for determination of the hydrodynamic film pressure P is

$$\frac{\partial}{\partial x}\left(\frac{Ph^3}{12\mu}\frac{\partial P}{\partial x}\right) + \frac{\partial}{\partial z}\left(\frac{Ph^3}{12\mu}\frac{\partial P}{\partial z}\right) = u_c\frac{\partial (Ph)}{\partial x} + \frac{\partial (Ph)}{\partial t} \tag{3}$$

in the film region $(0 < x = \Theta R_J < 2\pi R_J,\ 0 < z < L)$.

The boundary conditions for the gas film pressure are $P(\Theta, 0) = P_s$ and $P(\Theta, L) = P_a$ at the bearing inlet and discharge axial planes, respectively; and, at the leading and trailing edges (Θ_l, Θ_t) of a top foil $P(\Theta_\eta, z)_{\eta = l,t} = P_{\text{sub}}(z)$. The axial distribution of the gas pressure P_{sub} in the outer flow region (underneath the top foil) is approximately[3]

$$P_{\text{sub}}(z) = \left[P_s^2\left(1 - \frac{z}{L}\right) + P_a^2\left(\frac{z}{L}\right)\right]^{0.5} \tag{4}$$

The film thickness h for an aligned journal is $h = c + e_X \cos(\Theta) + e_Y \sin(\Theta) + w_d$, where (e_X, e_Y) are journal center displacements and w_d is the elastic deflection field of the underlying support structure. w_d is due to the pressure difference $\{P - P_{\text{sub}}\}$ and a function of the material, thickness, and geometry of the top foil, and elastic support structure. See Ref. [17] for details on the shell FE model of the top foil and integration with the bump layer stiffness distribution.

As in Refs. [16,17], small amplitude journal motions about an equilibrium position render partial differential equations (PDEs) for the zeroth- and first-order pressure fields; and from which, prediction of the GFB reaction forces and frequency dependent

[2]The effect of temperature on the operation of the test GFBs was minimal, i.e., no significant changes in measured bearing and shaft temperatures were recorded during the experiments.

[3]The flow of gas through the outer region underneath the top foil is only axial, not greatly restricted by the bump strip layers.

Downloaded 02 Jun 2010 to 171.66.16.109. Redistribution subject to ASME license or copyright; see http://www.asme.org/terms/Terms_Use.cfm

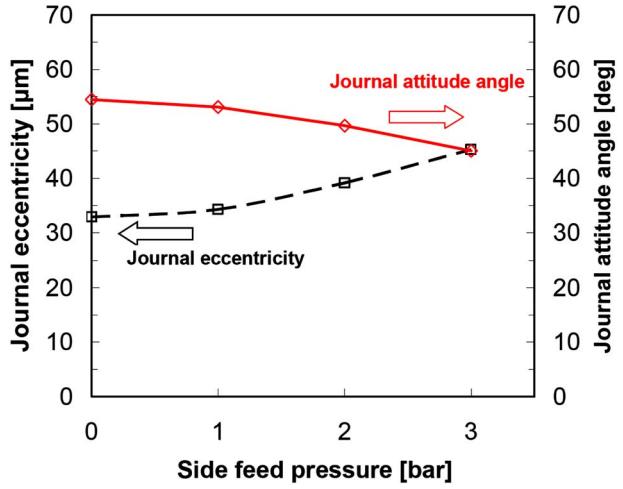


Fig. 9 Predicted GFB journal eccentricity and attitude angle versus side feed (gauge) pressure. Static load 4.9 N. Rotor speed: 30 krpm (500 Hz).

force coefficients, stiffness, and damping $(K_{\alpha\beta}, C_{\alpha\beta})$ $\alpha\beta = X, Y$ follow. The predictive model includes the effect of an empirically derived structural loss factor $\gamma = 0.2$ [19] that represents mechanical energy dissipation from dry-friction in the test foil bearing structure. The current model does not include thermal energy transport considerations since these were unimportant for the laboratory test conditions. During the rotordynamic tests, insignificant changes ($<5\,^{\circ}$C) in the temperature of the test GFBs were recorded.

Model predictions follow for the free end test GFB operating with a static load of 4.9 N (*X*-direction). For rotor operation at 30 krpm (500 Hz), Fig. 9 shows that as the bearing end feed pressure increases, the predicted journal eccentricity increases and the journal attitude angle decreases. Note that the test measurements with side feed pressurization show small static rotor motions along the horizontal direction as the rotor speed increases, thus implying a reduction in cross-coupled effects, see Ref. [15]. As the bearing side feed pressure increases, the minimum film thickness ranges from 35 μm to 25 μm and the drag torque decreases from 1.6 N μm to 1.3 N μm. The axially fed gas flow forced by side pressurization retards the evolution of the gas film velocity in the circumferential direction, thus decreasing the bearing drag torque and minimum film thickness, as depicted in Fig. 10.

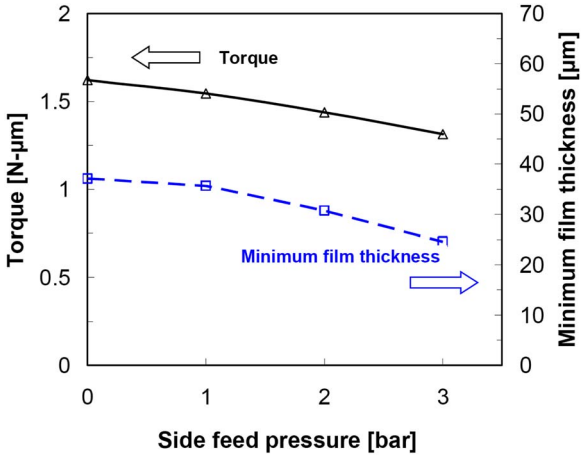


Fig. 10 Predicted GFB drag torque and minimum film thickness versus side feed (gauge) pressure. Static load 4.9 N. Rotor speed: 30 krpm (500 Hz).

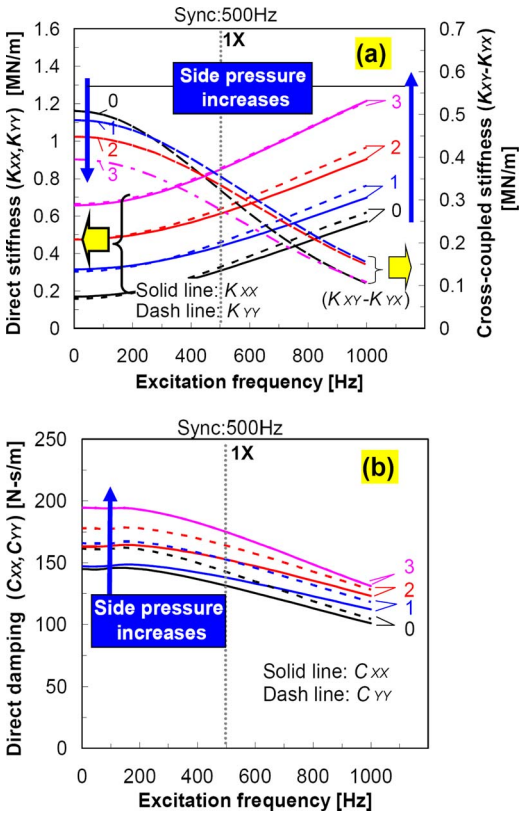


Fig. 11 Effect of bearing side pressurization on predicted GFB force coefficients; (*a*) direct and cross-coupled stiffnesses and (*b*) direct damping coefficients. The numbers denote magnitude of side feed pressure, P_s [bar (gauge)]. Static load 4.9 N ($\frac{1}{2}$ rotor weight), rotor speed: 30 krpm (500 Hz). Bearing structural loss factor $\gamma = 0.20$.

Figure 11 shows predicted (a) direct (K_{XX}, K_{YY}) and cross-coupled $(K_{XY} - K_{YX})$ stiffnesses and (b) direct (C_{XX}, C_{YY}) damping coefficients versus excitation frequency at a shaft speed of 30 krpm (500 Hz). Direct stiffnesses and damping coefficients grow as the bearing side pressure increases. Most importantly, the difference $(K_{XY} - K_{YX})$ decreases at low frequencies denoting a net gain in bearing stability. Note also that all bearing force coefficients depend strongly on the excitation frequency.

A simple eigenvalue analysis of the test rotor-GFBs follows Lund's approach [23] to determine stability parameters; namely, system critical mass and whirl frequency ratio (WFR). The WFR equals the ratio of whirl frequency at the onset of subsynchronous motions to the threshold shaft speed N_{os}. For a shaft speed of 30 krpm and $\frac{1}{2}$ rotor mass of 0.5 kg, Fig. 12 reveals a magnitude of bearing side feed pressure $\geqslant 2.9$ bars to ensure stable rotor

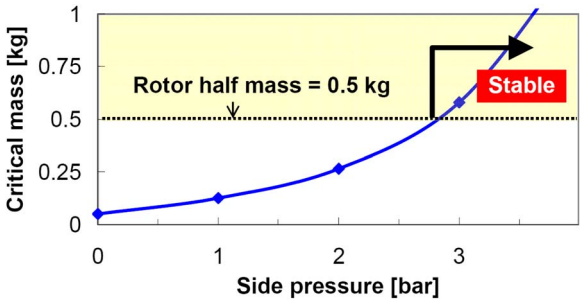


Fig. 12 Predicted critical mass versus side feed pressure for operation of GFB. Static load 4.9 N. Speed: 30 krpm (500 Hz).

Downloaded 02 Jun 2010 to 171.66.16.109. Redistribution subject to ASME license or copyright; see http://www.asme.org/terms/Terms_Use.cfm

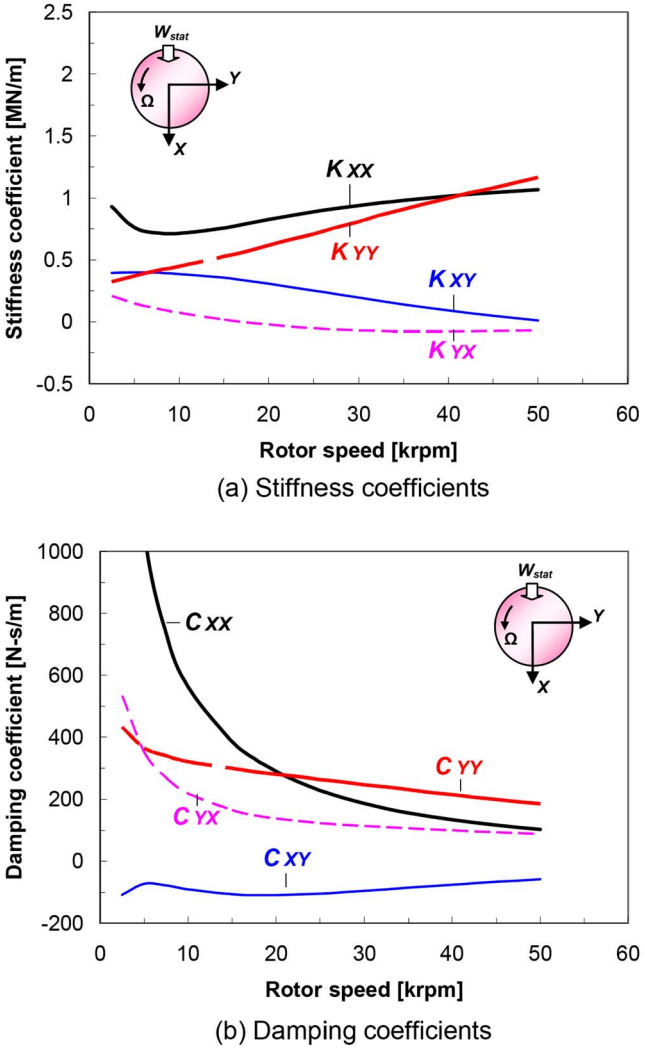


Fig. 13 Predicted synchronous stiffness and damping coefficients versus rotor speed for drive end GFB supporting static load of 6.6 N (*X*-direction). Structural loss factor γ=0.2. Bearing side feed pressure at 0.34 bar (5 psi gauge) gauge.

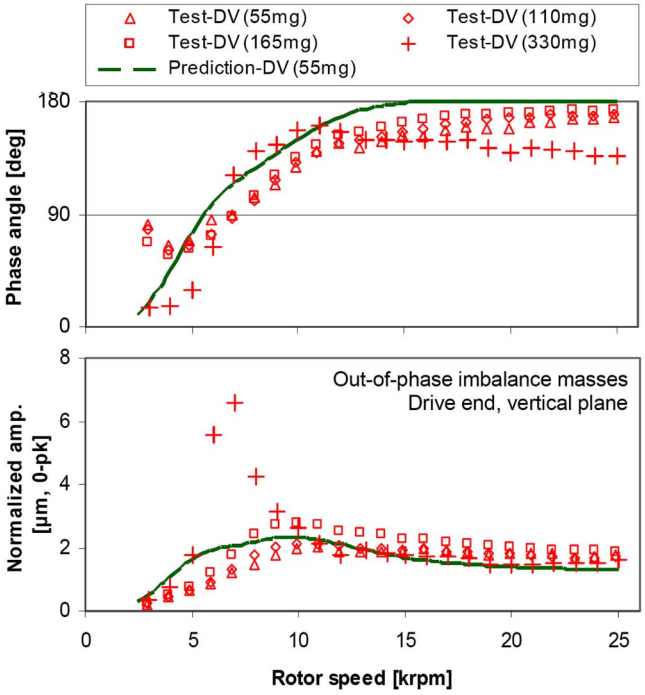


Fig. 14 Predicted and measured phase angles and normalized rotor amplitude of synchronous response for increasing out-of-phase imbalance mass distributions (drive end bearing, vertical plane). Bearing side feed pressure at 0.34 bar (5 psi gauge) gauge.

operation, i.e., free of subsynchronous whirl. Note that in Fig. 7, the measured rotor subsynchronous whirl motions disappear for side feed pressures $\geq$2.8 bars, i.e., the test system becomes rotordynamically stable. At P_s=3 bars, the predicted whirl frequency is 165 Hz, i.e., WFR=0.33=165 Hz/500 Hz; while that determined from the measurements is 147 Hz, i.e., WFR=0.29=147 Hz/508 Hz. The predicted threshold rotor speed of instability agrees well with the measured magnitude.

Predicted Rotor Synchronous Responses and Comparisons to Test Data

A FE rotordynamics model integrates the linearized GFB force coefficients to predict the synchronous response of the test rotor. Note that test measurements of rotor synchronous response verify the linearity of the test rotor-GFB system for small to moderately large imbalance masses (see Fig. 8). Figure 13 presents the predicted synchronous speed force coefficients (stiffness and damping) versus the rotor speed for the drive end GFB. The magnitudes of direct stiffness (K_{XX},K_{YY}) are larger than those of cross-coupled stiffness (K_{XY},K_{YX}), in particular, at high rotor speeds, thus favoring stable rotor performance. The direct damping coefficients (C_{XX},C_{YY}) drop rapidly as the rotor speed increases. At rotor speeds lower than 20 krpm, C_{XX} is larger than C_{YY}. However, C_{YY} becomes larger than C_{XX} at higher rotor speeds.

Figure 14 shows a comparison of predicted rotor synchronous responses (phase angle and normalized amplitude) to the test results acquired during rotor speed coastdown tests (see also Fig. 8). The predicted response based on linearized bearing force coefficients shows (obviously) a unique normalized amplitude and phase angle. In general, the predictions are in good agreement with the test data (phase angle and amplitude) for small to moderately large imbalance masses, i.e., 55–165 mg, i.e., those test conditions that reveal the characteristic response of a linear system. The rotor critical speed ω_{cr}, i.e., speed at which the rotor amplitude is the largest, occurs at a rotor speed larger than the system natural frequency ω_n depending on the system damping ratio ξ, i.e., $\omega_{cr}=\omega_n/\sqrt{1-2\xi^2}$ [24].

On the other hand, for the largest imbalance mass of 330 mg, the comparison evidences a large discrepancy, in particular, for rotor amplitudes around the system critical speed and phase angle above that speed. The increase in test normalized rotor amplitude and different trends in phase angle from those obtained for small to moderate imbalances are attributed to a system nonlinearity introduced by the foil bearings' strong (hardening) stiffness characteristics [10,19]. As the rotor speed increases well above the critical speed, all predicted and measured synchronous rotor amplitudes approach the imbalance displacements u of 1.3 μm and 2.3 μm at the drive and free end bearing locations, respectively.

A simple one degree of freedom system model is implemented to identify the mechanical parameters representing each bearing. The method uses the measured rotor synchronous responses for small to moderately large imbalance masses and with a side feed gauge pressure of 0.34 bar (5 psi gauge). From the tests, a phase angle equal to 90 deg determines the location of the undamped natural frequency ω_n. The effective stiffness coefficient (K_{eff}) follows from $K_{\text{eff}}=\omega_n^2 M$, where M is the known fraction of rotor

Downloaded 02 Jun 2010 to 171.66.16.109. Redistribution subject to ASME license or copyright; see http://www.asme.org/terms/Terms_Use.cfm

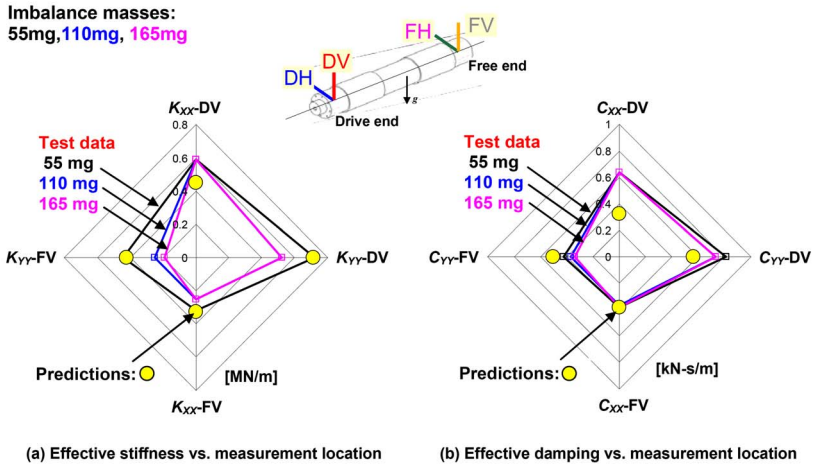


Fig. 15 Effective GFB stiffness and damping coefficients estimated from rotor response measurements for small and moderately large imbalance masses. Predictions obtained at a rotor speed of 10 krpm.

mass that each bearing supports. The effective damping coefficient C_{eff} is estimated from [24]

$$C_{\text{eff}} = 2\xi\sqrt{K_{\text{eff}}M}, \quad \xi = \sqrt{\frac{1}{2}\left\{1 - \left(\frac{\omega_n}{\omega_{\text{cr}}}\right)^2\right\}} \tag{5}$$

Note that the damping ratio ξ approaches zero as the critical speed ω_{cr} moves toward the natural frequency ω_n.

Figure 15 shows the representation of the mechanical parameters of the rotor-GFB system identified while crossing the system critical speed (~10 krpm). The symbols DV and FH denote measurements at the rotor drive end-vertical plane and at the rotor free end-horizontal plane, respectively. The drive end bearing with a smaller nominal radial clearance (40 μm) shows larger stiffness and damping coefficients than those for the free end bearing, which has a larger nominal radial clearance (70 μm). From Eq. (5), the estimated damping ratios ξ are ~0.5 around the natural frequency for small to moderate in-phase imbalance distributions, thus showing a well-damped system.

The test data compared to predictions of direct stiffness and damping coefficients at the system critical speed (10 krpm) show good agreement, thus validating the rotordynamic model of rotor-GFB system for small to moderately large imbalance masses. Reference [15] reports further test data (rotor synchronous responses and identified bearing mechanical parameters) and predictions for increasing in-phase and out-of-phase rotor imbalance masses.

Conclusions

A successful implementation of GFBs into high temperature applications requires adequate thermal management procedures. Often, pressurized air is forced through a GFB to carry away heat conducted from a hot component, for example. In recent experimental work, bearing side pressurization also reveals a profound impact on the rotordynamic response and the stability of a test rotor-GFB system.

Dynamic response measurements are conducted on a rigid rotor supported on GFBs during rotor speed run-up and coastdown tests with the GFBs supplied with increasing feed pressures to 2.8 bars (40 psi gauge). Rotor speed run-up tests further demonstrate the beneficial effect of the bearing end side pressurization on delaying the onset speed of rotor subsynchronous motions. FFTs at 30 krpm show that the total amplitude of motion, mainly composed of whirl motions at the natural frequency, reduce dramatically with increasing side feed pressures. For $P_s \geq 2.8$ bars, the rotor subsynchronous whirl motions disappear, i.e., the test system becomes rotordynamically stable. Rotor speed coastdown tests from 25 krpm with a low side pressure of 0.35 bar evidence nearly linear synchronous rotor responses for small to moderately large imbalance mass distributions. Alas, for the largest imbalance condition, the rotor response demonstrates a nonlinear characteristic akin to that of a hardening stiffness system.

Analysis also advances a model of GFB with side pressurization. A FE model of the top foil is coupled to the gas film model modified by the evolution of gas flow circumferential velocity, a function of the imposed side feed pressure. Predicted direct stiffnesses and damping coefficients increase as the magnitude of feed pressure rises, while the difference in cross-coupled stiffnesses, directly related to rotor-bearing system stability, decreases. A simple eigenvalue analysis of the test rotor-GFBs predicts that side feed pressurization delays the threshold speed of instability. The predictions are in close agreement with the test results of threshold rotor speed of instability and whirl frequency ratio, thus validating the model of GFBs with side feed pressurization. A rotordynamics model integrating the linearized GFB force coefficients predicts the synchronous response of the test rotor operating with small and moderately large imbalance masses. The model predictions of rotor synchronous response (amplitude and phase angle) agree very well with the test results recorded for small to moderately large imbalance masses. The agreement between the identified mechanical parameters of the test GFBs, while crossing the system critical speed, and the predicted direct stiffness and damping coefficients is also very good.

As a final observation, although external pressurization aids to improve GFB rotordynamic performance, a too large supplied cooling gas flow may penalize sensibly the efficiency and the performance of the turbomachinery.

Acknowledgment

This material is based on the work supported by the National Science Foundation under Grant No. 0322925. The support of the Turbomachinery Research Consortium is gratefully acknowledged. Thanks to Foster-Miller Technologies for providing the test foil bearings.

Nomenclature

$C_{\alpha\beta}$ = damping coefficients (N s/m), $\alpha, \beta = X, Y$
C_{eff} = effective damping coefficient (N s/m)
c = nominal radial clearance of GFBs (m)
DV, DH = drive end bearing, vertical and horizontal planes

Downloaded 02 Jun 2010 to 171.66.16.109. Redistribution subject to ASME license or copyright; see http://www.asme.org/terms/Terms_Use.cfm

e_X, e_Y = journal eccentricity component (m), $e=\sqrt{e_X^2+e_Y^2}$
FV, FH = free end bearing, vertical and horizontal planes
h = gas film thickness (m)
h_b = bump height (m)
K_{eff} = effective stiffness coefficient (N/m)
$K_{\alpha\beta}$ = stiffness coefficients (N/m), $\alpha,\beta=X,Y$
L = bearing axial width (m)
M_{DE}, M_{FE} = fraction of rotor mass at drive and free end bearings (kg), 0.66 kg and 0.36 kg
m_e = mass imbalance (mg), $m_e \ll M$
$\dot{m}_z$ = axial mass flow rate per unit circumferential length and film thickness ($\text{kg}/(\text{m}^2)$)
N_{os} = onset speed of subsynchronous rotor motions (rpm), $\Omega\ (30/\pi)$
P = hydrodynamic pressure in gas film (Pa)
P_a = ambient pressure (Pa)
P_s = side feed gas pressure (N/m^2)
P_{sub} = gas pressure in outer flow region (behind or back of top foil) (N/m^2)
R_J = shaft radius (m)
r_e = radius for location of imbalance masses (m), r_e = 15.11 mm
T = temperature (K)
t = time (s)
u_c = mean circumferential flow velocity (m/s)
u_e = $m_e r_e/M$, imbalance displacement (μm)
w_d = top foil transverse deflection (m)
X,Y,Z = coordinate system for the inertial axes (m)
$x(=R_J\Theta),z$ = coordinate system on plane of bearing (m)
α = inlet gas flow preswirl factor
ρ = gas density (kg/m^3)
γ = structural damping loss factor (−)
μ = gas viscosity (Pa s)
$\Re$ = ideal gas constant (J/kg K)
Θ = top foil angular coordinate (rad)
Ω = rotor angular velocity (rad)
$\Omega_{\text{threshold}}$ = threshold speed of instability (Hz)
W_{stat} = static load (N)
ω = whirl frequency (rad)
ω_{cr} = critical speed (rad/s)
$\omega_{\text{threshold}}$ = whirl frequency of unstable motions (Hz)
ω_n = natural frequency of system (Hz)
ξ = damping ratio (−)
WFR = whirl frequency ratio (−), $\omega_{\text{threshold}}/\Omega_{\text{threshold}}$

Subscripts

$\alpha,\beta=X,Y$ = directions of perturbation for first-order pressure fields
l,t = top foil leading and trailing edges
Syn, Sub = components of synchronous and subsynchronous vibrations

References

[1] DellaCorte, C., and Valco, M. J., 2000, "Load Capacity Estimation of Foil Air Journal Bearings for Oil-Free Turbomachinery Applications," STLE Tribol. Trans., **43**(4), pp. 795–801.
[2] Heshmat, H., 1994, "Advancements in the Performance of Aerodynamic Foil Journal Bearings: High Speed and Load Capacity," ASME J. Tribol., **116**, pp 287–295.
[3] Peng, J.-P., and Carpino, M., 1994, "Coulomb Friction Damping Effects in Elastically Supported Gas Foil Bearings," STLE Tribol. Trans., **37**(1), pp. 91–98.
[4] Howard, S., DellaCorte, C., Valco, M.-J., Prahl, J.-M., and Heshmat, H., 2001, "Dynamic Stiffness and Damping Characteristics of a High-Temperature Air Foil Journal Bearing," STLE Tribol. Trans., **44**(4), pp. 657–663.
[5] Chen, H. M., Howarth, R., Geren, B., Theilacker, J. C., and Soyars, W. M., 2000, "Application of Foil Bearings to Helium Turbocompressor," *Proceedings of the 30th Turbomachinery Symposium*, Houston, TX, Sep. 17–20, pp. 103–113.
[6] DellaCorte, C., Radil, K., Bruckner, R., and Howard, S., 2007, "Design, Fabrication and Performance of Open Source Generation I and II Compliant Hydrodynamic Gas Foil Bearings," NASA/TM-2007-214691.
[7] Radil, K., DellaCorte, C., Bruckner, R., and Zessoteck, M., 2007, "Thermal Management Techniques for Oil-Free Turbomachinery Systems," STLE Tribol. Trans., **50**, pp. 319–327.
[8] Bauman, S., 2005, "An Oil-Free Thrust Foil Bearing Facility Design Calibration, and Operation," NASA/TM-2005-213568.
[9] Heshmat, H., Tomaszewski, M. J., and Walton, J. F., 2006, "Small Gas Turbine Engine Operating With High-Temperature Foil Bearings," ASME Paper No. GT2006-90791.
[10] Rubio, D., and San Andrés, L., 2006, "Bump-Type Foil Bearing Structural Stiffness: Experiments and Predictions," ASME J. Eng. Gas Turbines Power, **128**, pp. 653–660.
[11] Rubio, D., and San Andrés, L., 2007, "Structural Stiffness, Dry Friction Coefficient, and Equivalent Viscous Damping in a Bump-Type Foil Gas Bearing," ASME J. Eng. Gas Turbines Power, **129**, pp. 494–502.
[12] Kim, T. H., Breedlove, A. W., and San Andrés, L., 2008, "Characterization of Foil Bearing Structure for Increasing Shaft Temperatures: Part I—Static Load Performance," ASME Paper No. GT2008-50567.
[13] Kim, T. H., Breedlove, A. W., and San Andrés, L., 2008, "Characterization of Foil Bearing Structure for Increasing Shaft Temperatures: Part II—Dynamic Force Performance," ASME Paper No. GT2008-50570.
[14] San Andrés, L., Rubio, D., and Kim, T. H., 2007, "Rotordynamic Performance of a Rotor Supported on Bump Type Foil Gas Bearings: Experiments and Predictions," ASME J. Eng. Gas Turbines Power, **129**(3), pp. 850–857.
[15] Kim, T. H., 2007, "Analysis of Side End Pressurized Bump Type Gas Foil Bearings: A Model Anchored to Test Data," Ph.D. thesis, Texas A&M University, College Station.
[16] Kim, T. H., and San Andrés, L., 2005, "Heavily Loaded Gas Foil Bearings: A Model Anchored to Test Data," ASME J. Eng. Gas Turbines Power, **130**, p. 0125041.
[17] San Andrés, L., and Kim, T. H., 2007, "Improvements to the Analysis of Gas Foil Bearings: Integration of Top Foil 1D and 2D Structural Models," ASME Paper No. GT2007-27249.
[18] Ruscitto, D., McCormick, J., and Gray, S., 1978, "Hydrodynamic Air Lubricated Compliant Surface Bearing for an Automotive Gas Turbine Engine I-Journal Bearing Performance," NASA CR-135368.
[19] San Andrés, L., and Kim, T. H., 2008, "Forced Nonlinear Response of Gas Foil Bearing Supported Rotors," Tribol. Int., **41**(8), pp. 704–715.
[20] Kim, T.-H., Lee, Y.-B., Kim, C.-H., and Lee, N.-S., 2003, "A Study on the Reliability of an Air Foil Journal Bearing for High Speed Turbomachinery," J. Fluid Machinery (Korean Fluid Machinery Association), **6**(2), pp. 7–14.
[21] Black, H. F., Allaire, P. E., and Barrett, L. E., 1981, "Inlet Flow Swirl in Short Turbulent Annular Seal Dynamics," *Proceedings of the Ninth International Conference in Fluid Sealing*, BHRA Fluid Engineering, Leeuwenborst, The Netherlands, Apr. 1–3, pp. 141–152.
[22] Childs, D., 1993, *Turbomachinery Rotordynamics*, Wiley, New York, Chap. 5.
[23] Lund, J. W., 1968, "Calculation of Stiffness and Damping Properties of Gas Bearings," ASME J. Lubr. Technol., **90**, pp. 793–803.
[24] Ginsberg, J. H., 2001, *Mechanical and Structural Vibration—Theory and Application*, Wiley, New York, pp. 135–139.

Downloaded 02 Jun 2010 to 171.66.16.109. Redistribution subject to ASME license or copyright; see http://www.asme.org/terms/Terms_Use.cfm

Arnaud Sternchüss[1]
e-mail: arnaud.sternchuss@ecp.fr

Etienne Balmès

Laboratoire MSSMAT,
École Centrale Paris,
Grande Voie des Vignes,
92295 Châtenay-Malabry Cedex, France

Pierrick Jean

Jean-Pierre Lombard

Snecma (Safran Group),
Site de Villaroche,
Rond-point René Ravaud,
77550 Moissy-Cramayel Cedex, France

Reduction of Multistage Disk Models: Application to an Industrial Rotor

The present study deals with the reduction of models of multistage bladed disk assemblies. The proposed method relies on the substructuring of the rotor into sectors. The bladed disks are coupled by intermediate rings, which remove the problem of incompatible meshes. The sectors are represented by superelements whose kinematic subspaces are spanned by a set of cyclic modeshapes and a set of normal modes when their left and right interfaces are fixed. The first step is to compute the cyclic modeshapes that are defined on the full rotor by enforcing the uncoupling of the spatial Fourier harmonics. This leads to a family of subproblems parametrized by the harmonic coefficient, similar to the classical approach used to deal with tuned bladed disks. The subsequent reduction process leads to compact reduced models whose accuracy has been extensively tested on simple but realistic academic models. The proposed methodology was then applied to an industrial rotor to conduct an analysis at a wider scale. This case was also the occasion to point out the fact that the assembly of individual disk models into a rotor model is really straightforward and provides an efficient tool to observe and predict coupled phenomena. [DOI: 10.1115/1.2967478]

1 Introduction

This study presents an industrial application of the authors' reduction technique to determine the modal characteristics of assemblies of bladed disks.

The current industrial practice is to model separately each bladed disk of the rotor. When such disks are cyclically symmetric, their dynamics are fully determined from that of a small portion, typically a bladed sector. This configuration no longer holds in real rotors due to mistuning, which significantly alters this behavior since it can strongly localize the strain energy [1]. Therefore, full-scale analyses require huge models, all the more since many nearly identical computations are needed to cover the entire space of parameters (mistuning coefficients, rotation speed, and temperature). To address this issue, many reduction techniques have been developed such as those of Lim et al. [2], Feiner and Griffin [3,4], and Sternchüss et al. [5], among others, that rely on synthesis techniques using either component or system modes.

Such reduced representations would be a good starting point for dealing with multistage rotors. However, as underlined by Bladh et al. [6], the critical point is the choice of the boundary conditions that would properly represent interstage coupling, which is the main cause of discrepancies between single stage and multistage dynamics, since this coupling ratio controls the spread of the strain energy over many disks. Song et al. [7], Laxalde et al. [8], and Sternchüss and Balmès [9] proposed recently efficient computer mode synthesis (CMS) techniques that include such coupling directly into the formulation of the reduced problem.

The first part of this paper updates the methodology developed in Ref. [9]. This method consists in a decomposition of the disks into sector superelements connected with each other through intersector elements and interdisk ring elements. The updates mostly concern the formulation of the problems that lead to the cyclic modeshapes as defined by Laxalde et al. [8] and the process used to generate the subspaces in which the kinematics of the sector superelements are sought. The assembly of the problem remains really straightforward, leading to a very compact model whose accuracy is driven by the choice of the reduction bases. The main results obtained for a simple academic model that evaluates the accuracy of the proposed technique are described throughout this section.

The second part of this paper then presents the application of the methodology to a subset of a realistic industrial rotor provided by Snecma. From these results, the concluding section provides some guidelines for the practical use of such a reduction method in a global design process.

2 Multistage Reduction at Fixed Speed

The considered structure is presented in Fig. 1. It is composed of two bladed disks nominally tuned $\mathcal{D}^1$ and $\mathcal{D}^2$ with 12 and 15 blades, respectively, connected with a volumic interface $\mathcal{R}$. The disks are meshed with brick elements and the ring is meshed with tetrahedrons obtained by a Delaunay tessellation (MATLAB function delaunay3) between the nodes of the aft rim of disk $\mathcal{D}^1$, denoted $\mathcal{I}_a^1$, and the front rim of disk $\mathcal{D}^2$, denoted $\mathcal{I}_f^2$. The material is titanium whose properties are $E=120$ GPa, $\nu=0.33$, and $\rho=4700$ kg m^{-3}. The radii at the roots of the blades are 200 mm and 205 mm, respectively, and the radii at their tips are 280 mm and 285 mm, respectively. Their thickness varies from 6 mm at the root to 2 mm at the top. Their widths are 43 mm and 46 mm at the top. The frequency bandwidth of interest for this study is [0,14], if all frequencies are normalized with respect to the lower flexible natural frequency of the rotor.

2.1 Coupled Mechanical Problem. The meshes of the aft rim $\mathcal{I}_a^1$ of $\mathcal{D}^1$ and the front rim $\mathcal{I}_f^{\mathcal{R}}$ of $\mathcal{R}$ are identical to avoid problems of incompatibility. For the same reasons, the meshes of the aft rim $\mathcal{I}_a^{\mathcal{R}}$ of $\mathcal{R}$ and the front rim $\mathcal{I}_f^2$ of $\mathcal{D}^2$ are identical. Due to the way it is meshed, the interdisk ring $\mathcal{R}$ has a single element along the z direction, thus it has no interior degree of freedom (DOF) when it is made of first order elements. $\mathcal{D}^1$ and $\mathcal{D}^2$ have N^1 and N^2 DOFs, respectively. These two DOF sets are *disjoint*. The total number of DOF is $N=N^1+N^2$. The discrete displacement $\{q\}$ is continuous at the interface between two adjacent substructures:

[1]Corresponding author.

Contributed by the International Gas Turbine Institute of ASME for publication in the JOURNAL OF ENGINEERING FOR GAS TURBINES AND POWER. Manuscript received March 31, 2008; final manuscript received April 11, 2008; published online October 9, 2008. Review conducted by Dilip R. Ballal. Paper presented at the ASME Turbo Expo 2008: Land, Sea and Air (GT2008), Berlin, Germany, June 9–13, 2008.

Copyright © 2009 by ASME

Downloaded 02 Jun 2010 to 171.66.16.109. Redistribution subject to ASME license or copyright; see http://www.asme.org/terms/Terms_Use.cfm

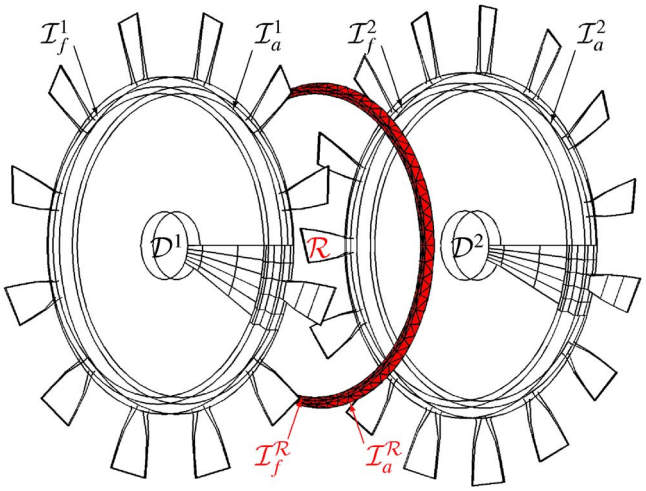


Fig. 1 Sample assembly

$$\{q_a^1\} = \{q_f^{\mathcal{R}}\} \quad \text{and} \quad \{q_f^2\} = \{q_a^{\mathcal{R}}\} \tag{1}$$

The particular geometry of $\mathcal{R}$ implies that its DOF is fully determined by $\{q^{\mathcal{R}}\} = \{q_f^{\mathcal{R}} \;\; q_a^{\mathcal{R}}\}^\top$.

In the frequency domain, if an external load $\{f_e(\omega)\}$ is given, the discrete displacement $\{q(\omega)\}$ satisfies

$$[Z(\omega)]_{N\times N}\{q(\omega)\}_{N\times 1} = \{f_e(\omega)\}_{N\times 1} \tag{2}$$

The dynamic stiffness matrix $[Z]$ of the rotor is

$$[Z(\omega)] = \begin{bmatrix} Z^1(\omega) & 0 \\ 0 & Z^2(\omega) \end{bmatrix} + [Z^{\mathcal{R}}(\omega)] \tag{3}$$

where $[Z^1]$, $[Z^{\mathcal{R}}]$, and $[Z^2]$ stand for the dynamic stiffness matrices of $\mathcal{D}^1$, $\mathcal{R}$, and $\mathcal{D}^2$, respectively.

2.2 Spatial Harmonic Content. Let us consider a single disk $\mathcal{D}^d$ in its nominal configuration. Under the assumption of cyclic symmetry, it is made of N_s^d identical angular sectors, numbered from 0 to $N_s^d - 1$, generated by successive rotations of a reference sector. Let θ^d be the rotation of angle $\alpha^d = 2\pi/N_s^d$ around the z axis. Since the discrete geometry is invariant whatever the rotation $(\theta^d)^s$, the discrete displacement $\{q^{d,s}\}$ is paired with its Fourier harmonic coefficients $\{\hat{q}_\delta^d\}$ such that, in the local basis of sector $\mathcal{S}^{d,s}$, it is written [5,10] as

$$\forall s \in \mathbb{N}_{N_s^d - 1}, \quad \{q^{d,s}\} = \Re\left(\sum_{\delta=0}^{N_s^d/2} \{\hat{q}_\delta^d\} e^{\mathbf{i}s\delta\alpha^d} \right) \tag{4}$$

The spatial harmonic DOF vectors $\{\hat{q}_\delta^d\}$ are defined on the reference sector $\mathcal{S}^{d,0}$ and are *complex quantities*, except for $\delta = 0$ and $\delta = N_s^d/2$, if N_s^d is even, multiplied by a dephasing factor that depends on the harmonic coefficient δ and the sector number s. Throughout the rest of the paper, the terms associated with harmonic coefficient $N_s^d/2$ are systematically kept, even if N_s^d is odd, in order to avoid dealing with different cases.

As stated by Eq. (4), there exists a duality between the physical DOF vector $\{q^d\}$ and the harmonic DOF vector $\{\hat{q}^d\}$:

$$\begin{aligned} \{q^d\} &= \{q^{d,0} \quad q^{d,1} \quad q^{d,2} \quad \cdots \quad q^{d,N_s-1}\}^\top \\ \{\hat{q}^d\} &= \{\hat{q}_0^d \;\; \Re(\hat{q}_1^d) \;\; \Im(\hat{q}_1^d) \;\; \Re(\hat{q}_{N_s^d/2-1}^d) \;\; \cdots \;\; \Im(\hat{q}_{N_s^d/2-1}^d) \;\; \hat{q}_{N_s^d/2}^d\}^\top \end{aligned} \tag{5}$$

where $\Re$ and $\Im$ stand for the real and imaginary parts of a complex quantity. The relation between these DOF vectors is

$$\{q^d\} = [E^d \otimes I_{N^{d,0}}]\{\hat{q}^d\} \tag{6}$$

where $[I_{N^{d,0}}]$ is the identity matrix whose size is the number of physical DOF of sector $\mathcal{S}^{d,0}$ and $\otimes$ is the Kronecker product. The block-column $[E_\delta^d]$ that corresponds to coefficient δ is

$$\begin{aligned} [E_0^d] &= [1 \quad \cdots \quad 1 \quad \cdots \quad 1]^\top \\ [E_\delta^d] &= \begin{bmatrix} 2 & 2\cos(\delta\alpha^d) & \cdots & 2\cos(s\delta\alpha^d) & \cdots & 2\cos((N_s^d-1)\delta\alpha^d) \\ 0 & -2\sin(\delta\alpha^d) & \cdots & -2\sin(s\delta\alpha^d) & \cdots & -2\sin((N_s^d-1)\delta\alpha^d) \end{bmatrix}^\top \\ [E_{N_s^d/2}^d] &= [1 \quad \cdots \quad (-1)^s \quad \cdots \quad (-1)^{N_s^d-1}]^\top \end{aligned} \tag{7}$$

When dealing with an assembly of two disks, the assumption about the ring states that any physical DOF belongs either to disk $\mathcal{D}^1$ or to disk $\mathcal{D}^2$. Therefore, the global DOF vector $\{q\}$ is

$$\{q\} = \begin{bmatrix} E^1 \otimes I_{N^{1,0}} & 0 \\ 0 & E^2 \otimes I_{N^{2,0}} \end{bmatrix} \{\hat{q}\} \tag{8}$$

where $\{q\} = \{q^1 \;\; q^2\}^\top$ and $\{\hat{q}\} = \{\hat{q}^1 \;\; \hat{q}^2\}^\top$.

Thanks to this, the spectral content of the modes of the whole rotor can be determined *relatively to each disk*. Figure 2 displays the result for the 74 first flexible modes of the sample rotor. For a given mode and a given disk $\mathcal{D}^d$, the amplitudes of the harmonic DOF vectors are normalized such that

$$\max_{\delta \in \{0, N_s^d/2\}} \|\hat{q}_\delta^d\|_1 = 1 \tag{9}$$

which allows to isolate the dominating harmonic. This figure also clearly shows, on the one hand, that the modes come in families and suggests, on the other hand, that they come in pairs. A closer look at the frequencies associated with these near-pairs of modes indicates that they are very close but different. Moreover, this figure confirms the fact that some modes are multiharmonic.

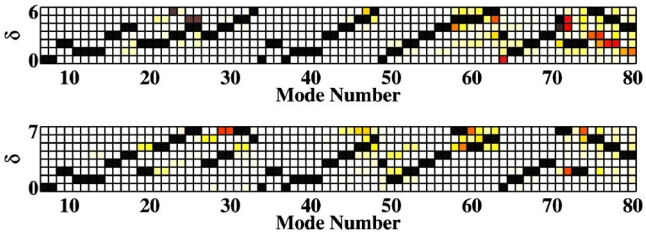


Fig. 2 Spatial spectrum of the 74 first flexible modes of the sample rotor

Downloaded 02 Jun 2010 to 171.66.16.109. Redistribution subject to ASME license or copyright; see http://www.asme.org/terms/Terms_Use.cfm

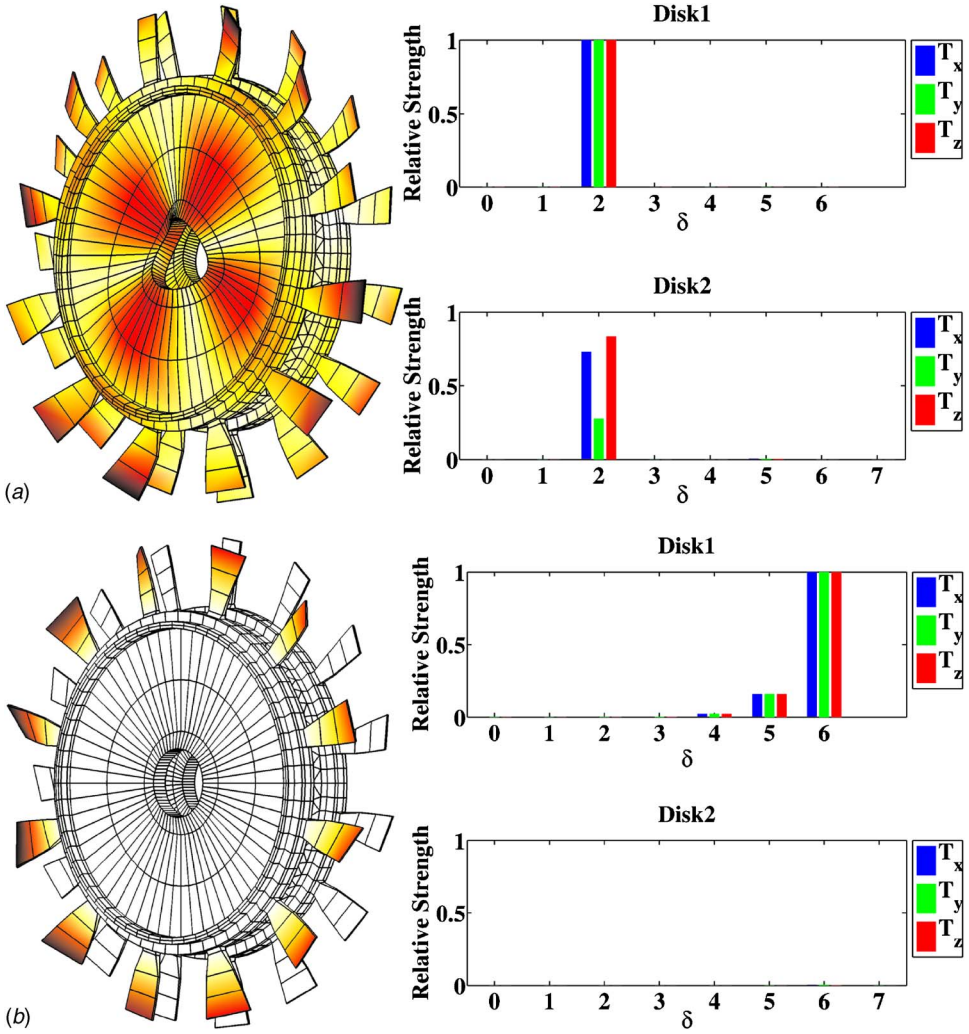


Fig. 3 (*a*) Monoharmonic coupled mode at $f=4.25$ and (*b*) multiharmonic localized mode at $f=2.99$ and their harmonic content

With the previous diagram, some particular modes can be identified, as described in Fig. 3. The harmonic DOF vectors are here normalized such that

$$\max_{d\in\{1,2\}}\left(\max_{\delta\in\{0,N_s^d/2\}}\|\hat{q}_\delta^d\|_1\right)=1 \tag{10}$$

One then finds monoharmonic coupled modes, such as the near-pair of modes at $f=4.25$ and $f=4.26$ that seems to correspond to $\delta=2$. Thus, the ring participates in theses modes, but its lack of symmetry does not affect the motion very much. On the contrary, the mode at $f=2.99$, which is localized to disk $\mathcal{D}^1$ is multiharmonic and the perturbation lies in the asymmetry of the ring, even though its participation is small.

2.3 Monoharmonic Eigensolutions. From the previous study of the complete rotor, the main conclusion to be drawn is that modes are not always monoharmonic. According to this, monoharmonic solutions such as defined by Laxalde et al. [8,11] are not necessarily modes of the full rotor. In the following section, the theory associated with monoharmonic solutions is recalled and the error between them and the eigenmodes is qualified.

Let us consider the two disks $\mathcal{D}^1$ and $\mathcal{D}^2$ connected with a volumic interface $\mathcal{R}$ without interior DOF, as presented in Fig. 1. The physical displacement is substituted by its Fourier decomposition (Eq. (8)) in the coupled problem in Eq. (2). If one considers that any disk $\mathcal{D}^d$, $d\in\{1,2\}$, is tuned, its dynamic stiffness $[Z^d]$ is obtained from that of its reference sector $[Z^{d,0}]$ through $[Z^d]=[I_{N_s^d}\otimes Z^{d,0}]$. The projection of the latter matrix onto the subspace generated by the Fourier matrix $[E^{d^\top}\otimes I_{N^{d,0}}]$ is

$$[\hat{Z}^d]=[E^{d^\top}\otimes I_{N^{d,0}}][I_{N_s^d}\otimes Z^{d,0}][E^d\otimes I_{N^{d,0}}]=[E^{d^\top}E^d]\otimes[Z^{d,0}]$$
$$=\begin{bmatrix} N_s^dZ^{d,0} & 0 & \cdots & 0 & 0\\ 0 & 2N_s^dZ^{d,0} & \cdots & 0 & 0\\ \vdots & \vdots & \ddots & \vdots & \vdots\\ 0 & 0 & \cdots & 2N_s^dZ^{d,0} & 0\\ 0 & 0 & \cdots & 0 & N_s^dZ^{d,0}\end{bmatrix} \tag{11}$$

Thanks to Eq. (11), the projection of the block-diagonal matrix containing the dynamic stiffnesses of both disks in Eq. (3) is really straightforward:

$$\begin{bmatrix} E^1\otimes I_{N^{1,0}} & 0\\ 0 & E^2\otimes I_{N^{2,0}}\end{bmatrix}^\top\begin{bmatrix} Z^1 & 0\\ 0 & Z^2\end{bmatrix}\begin{bmatrix} E^1\otimes I_{N^{1,0}} & 0\\ 0 & E^2\otimes I_{N^{2,0}}\end{bmatrix}$$
$$=\begin{bmatrix}\hat{Z}^1 & 0\\ 0 & \hat{Z}^2\end{bmatrix} \tag{12}$$

$[\hat{Z}^{\mathcal{R}}]$ is defined such that

Downloaded 02 Jun 2010 to 171.66.16.109. Redistribution subject to ASME license or copyright; see http://www.asme.org/terms/Terms_Use.cfm

$$[\hat{Z}^{\mathcal{R}}] = \begin{bmatrix} E^1 \otimes I_{N^{1,0}} & 0 \\ 0 & E^2 \otimes I_{N^{2,0}} \end{bmatrix}^{\top} [Z^{\mathcal{R}}] \begin{bmatrix} E^1 \otimes I_{N^{1,0}} & 0 \\ 0 & E^2 \otimes I_{N^{2,0}} \end{bmatrix} \tag{13}$$

If $[Z^{\mathcal{R}}]$ is decomposed into blocks indexed by dd' that couple disks $\mathcal{D}^d$ and $\mathcal{D}^{d'}$, the blocks indexed by dd' in $[\hat{Z}^{\mathcal{R}}]$ are then

$$[\hat{Z}^{\mathcal{R}}_{dd'}] = [E^d \otimes I_{N^{d,0}}]^{\top} [Z^{\mathcal{R}}_{dd'}] [E^{d'} \otimes I_{N^{d',0}}] \tag{14}$$

The different blocks indexed by dd' can themselves be decomposed into blocks indexed by $\delta\delta'$ that couple a shape of harmonic δ on disk $\mathcal{D}^d$ to a shape of harmonic δ' on $\mathcal{D}^{d'}$:

$$[\hat{Z}^{\mathcal{R}}_{dd',\delta\delta'}] = [E^d_{\delta} \otimes I_{N^{d,0}}]^{\top} [Z^{\mathcal{R}}_{dd'}] [E^{d'}_{\delta'} \otimes I_{N^{d',0}}] \tag{15}$$

This interharmonic coupling prevents the mechanical problem from being decomposed into individual subproblems for every harmonic coefficient as it could be done in the monodisk analysis. This also implies that the free vibration modes of the rotor can only be monoharmonic if the interharmonic coupling coefficients in Eq. (15) have a negligible influence. In the present formulation, the submatrices indexed by $\delta\delta'$, $\delta \neq \delta'$, in the blocks $[\hat{Z}^{\mathcal{R}}_{dd'}]$ are neglected, so that harmonics are decoupled.

$$[\hat{Z}^{\mathcal{R}}_{dd'}] = [\hat{Z}^{\mathcal{R}}_{dd',\delta\delta}] + \cancel{[\hat{Z}^{\mathcal{R}}_{dd',\delta\neq\delta'}]} \tag{16}$$

With this approximation, $[\hat{Z}^{\mathcal{R}}_{\delta}]$ is defined retroactively such that

$$[\hat{Z}^{\mathcal{R}}_{\delta}] = \begin{bmatrix} E^1_{\delta} \otimes I_{N^{1,0}} & 0 \\ 0 & E^2_{\delta} \otimes I_{N^{2,0}} \end{bmatrix}^{\top} [Z^{\mathcal{R}}] \begin{bmatrix} E^1_{\delta} \otimes I_{N^{1,0}} & 0 \\ 0 & E^2_{\delta} \otimes I_{N^{2,0}} \end{bmatrix} \tag{17}$$

The approximation error can be quantified from $[\hat{Z}^{\mathcal{R}}_{dd',\delta\neq\delta'}]$. In future work, this error estimation will be integrated into a residual iteration technique in order to enrich the subspaces of approximation in the subsequent reduction process.

From the structures of the harmonic matrices in Eqs. (12) and (17), one obtains a class of parametrized problems with respect to δ.

If $\delta=0$,

$$\left(\begin{bmatrix} N^1_s Z^{1,0} & 0 \\ 0 & N^2_s Z^{2,0} \end{bmatrix} + [\hat{Z}^{\mathcal{R}}_0] \right) \begin{Bmatrix} \hat{q}^1_0 \\ \hat{q}^2_0 \end{Bmatrix} = \{0\}$$

$$\begin{bmatrix} c^1_l - c^1_r & 0 \\ 0 & c^2_l - c^2_r \end{bmatrix} \begin{Bmatrix} \hat{q}^1_0 \\ \hat{q}^2_0 \end{Bmatrix} = \{0\} \tag{18}$$

Else,

$$\left(2 \begin{bmatrix} N^1_s Z^{1,0} & 0 & 0 & 0 \\ 0 & N^1_s Z^{1,0} & 0 & 0 \\ 0 & 0 & N^2_s Z^{2,0} & 0 \\ 0 & 0 & 0 & N^2_s Z^{2,0} \end{bmatrix} + [\hat{Z}^{\mathcal{R}}_{\delta}] \right) \begin{Bmatrix} \Re(\hat{q}^1_{\delta}) \\ \Im(\hat{q}^1_{\delta}) \\ \Re(\hat{q}^2_{\delta}) \\ \Im(\hat{q}^2_{\delta}) \end{Bmatrix} = \{0\}$$

$$\begin{bmatrix} c^1_l - c^1_r e^{2\mathbf{i}\pi\delta\alpha^1} & 0 \\ 0 & c^2_l - c^2_r e^{2\mathbf{i}\pi\delta\alpha^2} \end{bmatrix} \begin{Bmatrix} \hat{q}^1_{\delta} \\ \hat{q}^2_{\delta} \end{Bmatrix} = \{0\} \tag{19}$$

The equations that come first in the problems above are not sufficient to define a cyclic modeshape. An observation equation that states how the shapes are dephased between two adjacent sectors is added to each problem. The observation matrices $[c^d_r]$ and $[c^d_l]$ are used to isolate the right and left interface DOFs.

In the second problem, the projection of the dynamic stiffness matrix of any of the disks is equivalent to duplicate this matrix. This is not the case for the ring, which leads to near-pair eigensolutions. For thinner meshes of the ring, the near-pair solutions would converge to exact pairs. Throughout the rest of this paper, only the solutions without aliasing are considered:

$$\delta \leq \min_d \left(\frac{N^d_s}{2} \right)$$

This is referred to as "one to one nodal diameters" by Laxalde et al. [8,11].

As an illustration, the near-pair of eigensolutions at $f=4.25$ with $\delta=2$ is presented in Fig. 4. The chosen representation focuses on the solution that is really computed for a sector of the rotor and then restored to the whole structure.

It seems that they share some common properties as displayed in Figs. 3(*a*) and 4. The modal assurance criterion (MAC) is 0.989 for both modes and their frequency relative errors are 0.031 and 0.033, respectively. This excellent correlation states that this near-pair of monoharmonic solutions is locally (in terms of frequency) a near-pair of modes.

Finally, a classical frequency versus nodal diameter diagram is displayed in Fig. 5 either for the eigensolutions of the rotor or the modes of the individual disks when considered free-free. This graph shows significant discrepancies, which can be explained by the fact that the interstage interfaces are not exactly fixed when the disks are assembled together, but they are not free either. Ac-

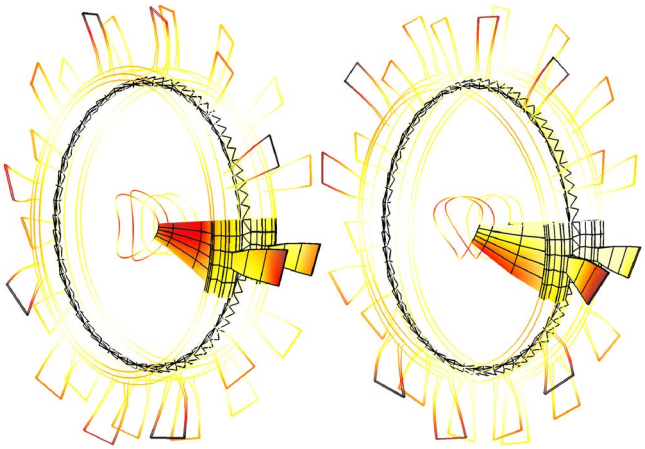


Fig. 4 Near-pair of monoharmonic solutions with $\delta=2$ at $f=4.25$

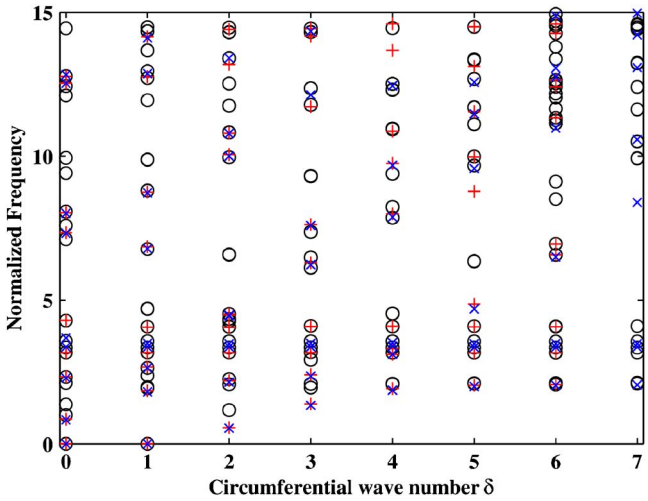


Fig. 5 Normalized frequency versus nodal diameter diagram for the monoharmonic eigensolutions of the rotor (○) and for the eigenmodes of disks $\mathcal{D}^1$ (+) and $\mathcal{D}^2$ (×) in free-free condition

Downloaded 02 Jun 2010 to 171.66.16.109. Redistribution subject to ASME license or copyright; see http://www.asme.org/terms/Terms_Use.cfm

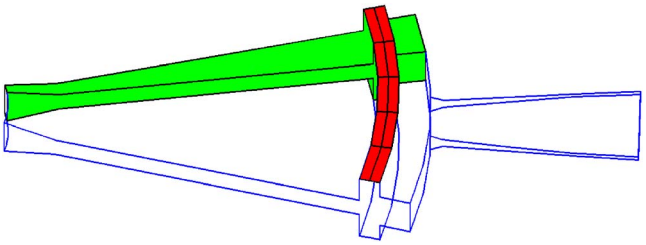


Fig. 6 Sector model: sector superelement with an intersector slice and the trace of the mesh of the ring

curate boundary conditions to apply to individual disks would be somewhere between free and fixed, depending on the modeshape.

2.4 Model Reduction. According to Sec. 2.3, monoharmonic solutions are not modes, but they will be used to approximate the kinematics of the bladed sectors, in order to build a reduced model of the rotor. To do so, each bladed sector is represented as a superelement that allows the following.

1. To target a set of eigenmodes from a set of monoharmonic solutions. Since it is assumed that each eigenmode is the linear combination of monoharmonic solutions whose frequencies lie in the vicinity of the corresponding natural frequency, the targeting of an eigenmode is, in fact, the targeting of the narrow frequency range where its harmonic components are found. It is also possible to select a subset of the harmonics a modeshape is made of. In practice, only the monoharmonic solutions with low δ are selected, since only these modeshapes account for disk-dominated motion at low frequencies [1].
2. To include blade-dominated motion into the reduced model by adding a set of modes of the individual sectors with their left and right interfaces clamped. Such modeshapes are used since fewer of them are required to account for blade-dominated motion than cyclic modeshapes with high δ at low frequencies.

2.5 Degrees of Freedom of the Superelements. Three types of generalized DOF are assigned to each sector superelement, they are defined in correspondence to a subset of physical DOF:

1. DOF that belong to the intersector elements (green area in Fig. 6)
2. DOF that belong to the interdisk ring (red area in Fig. 6)
3. purely interior DOF (the other DOF)

Generalized DOF Sets (i) and (ii) can be joint. In the previous approach [9], since the generalized DOF are paired with physical DOF, the compatibility between the two clockwisely consecutive sectors was ensured by keeping the physical finite elements with at least one node that belongs to the left interface. In the present updated technique, each slice of intersector elements is also condensed into a superelement whose generalized DOF are those of its two neighboring sector superelements, as illustrated in Figs. 6 and 7. The reduced rotor model keeps only the interdisk ring unchanged.

2.6 Subspaces of Motion. Let us consider a sector $\mathcal{S}^{d,s}$ with the following.

1. A set of eigenmodes $[\Phi_{\text{fix}}^{d,s}]$ of this sector with its left and right interfaces both clamped. These modes can differ from a sector to another.
2. A set of monoharmonic solutions $[\Re([\Phi_{\text{rcyc}}^{d,s}])\ \Im([\Phi_{\text{rcyc}}^{d,s}])]$ whose harmonics δ are selected for a particular reason (design). These modeshapes are identical for all the sectors of a given disk.

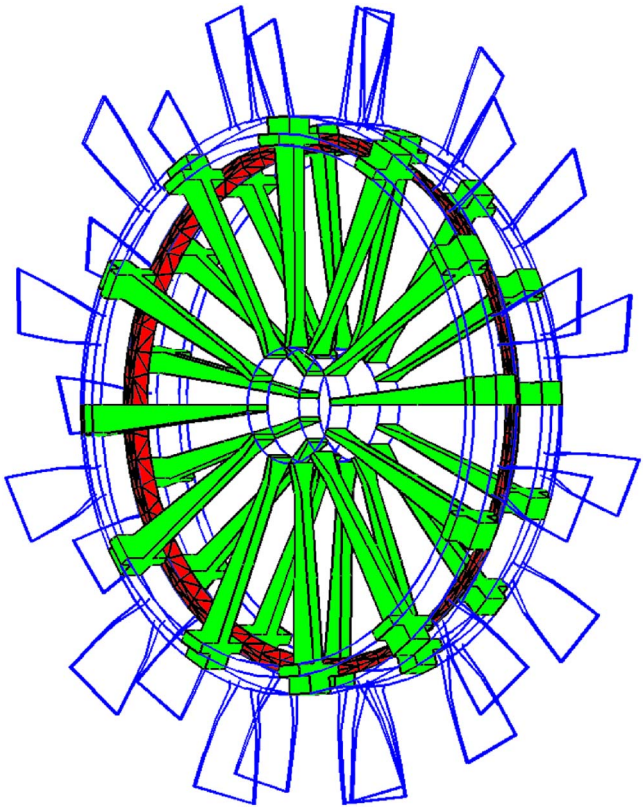


Fig. 7 Reduced rotor model: sector superelements connected with intersector slices and the ring

The initial set of vectors is

$$[T_{\text{init}}^{d,s}] = [[\Phi_{\text{fix}}^{d,s}]\ \Re([\Phi_{\text{rcyc}}^{d,s}])\ \Im([\Phi_{\text{rcyc}}^{d,s}])] \tag{20}$$

The sorting order of these vectors is critical to ensure a good condition number of the resulting matrices, since iterative procedures of orthonormalization are used to turn the initial set of vectors into the bases of the kinematic subspaces. In the present reduction process, an "orthogonal maximum sequence" [12] is used to orthogonalize the vectors. The main advantage of the orthogonal maximum sequence (OMS) is that it is faster than the standard or modified Gramm–Schmidt procedure. At step n of this algorithm, a sensor is placed at the physical DOF where vector n has its maximum and the latter physical DOF is defined as the generalized DOF associated with vector n. The remaining vectors are processed so that their observability is zero with respect to the current sensor. This process is repeated until all sensors are placed. It leads to a basis $[T_M^{d,s}]$ that relates the generalized DOF $\{q_M^{d,s}\}$ to the physical DOF of sector $\mathcal{S}^{d,s}$ thanks to

$$\{q^{d,s}\} = [T_M^{d,s}]\{q_M^{d,s}\} \tag{21}$$

Even though it is never explicitly built, the subspace in which the approximate solutions are sought is given by

$$[T_M] = \begin{bmatrix} T_M^{1,0} & \cdots & 0 & 0 & \cdots & 0 \\ \vdots & \ddots & \vdots & \vdots & & \vdots \\ 0 & \cdots & T_M^{1,N_s^1-1} & 0 & \cdots & 0 \\ 0 & \cdots & 0 & T_M^{2,0} & \cdots & 0 \\ \vdots & & \vdots & \vdots & \ddots & \vdots \\ 0 & \cdots & 0 & 0 & \cdots & T_M^{2,N_s^1-1} \end{bmatrix} \tag{22}$$

and the generalized DOF vector $\{q_M\}$ is related to the physical DOF vector $\{q\}$ thanks to

Downloaded 02 Jun 2010 to 171.66.16.109. Redistribution subject to ASME license or copyright; see http://www.asme.org/terms/Terms_Use.cfm

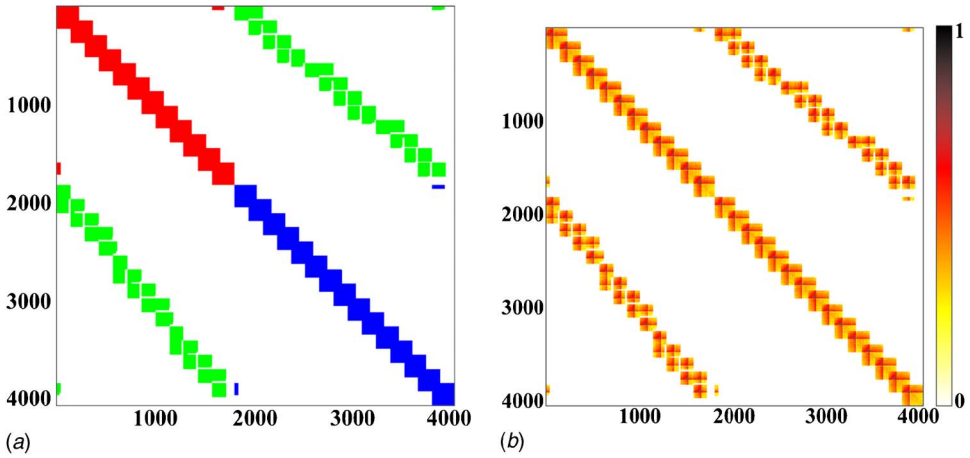


Fig. 8 Reduced stiffness matrix $[K_M]$ (*a*) global shape: upper left blocks belong to disk $\mathcal{D}^1$, lower right blocks belong to disk $\mathcal{D}^2$, off-diagonal blocks belong to ring $\mathcal{R}$, and (*b*) actual matrix

$$\{q\} = [T_M]\{q_M\} \tag{23}$$

2.7 Assembly of the Superelementary Matrices. Instead of computing the reduced matrices by the direct projection

$$[Z_M] = [T_M]^\top [Z][T_M]$$

where $[Z]$ is defined in Eq. (3), a two-step procedure is followed.

• Step 1. The physical finite element matrices of the sectors are projected onto their own kinematic subspace:

$$[Z_M^{d,s}] = [T_M^{d,s}]^\top [Z^{d,s}][T_M^{d,s}] \tag{24}$$

where $[Z^{d,s}]$ is the dynamic stiffness of sector $\mathcal{S}^{d,s}$. These reduced matrices are then assembled with respect to the generalized DOF associated with the superelements. This operation leads to the reduced matrices of both sector and intersector superelements.

• Step 2. The matrices of the ring are projected onto the kinematic subspaces of the neighboring disks with respect to the interdisk generalized DOF.

$$[Z_M^{\mathcal{R}}] = [T_M]^\top [Z^{\mathcal{R}}][T_M] \tag{25}$$

In order to avoid using the full matrix of modeshapes $[T_M]$, $[Z_M^{\mathcal{R}}]$ is built iteratively sector by sector. The reduced dynamic stiffness $[Z_M]$ is finally assembled with respect to the full set of generalized DOF.

All the reduced matrices are relatively sparse. Besides, they have the remarkable form displayed in Fig. 8 for the assembly of two tuned disks with 12 and 15 blades. The diagonal blocks and four off-diagonal blocks derive from the projection of the sector matrices. The latter blocks can be divided into two groups, the first with 12 blocks and the second with 15 blocks. The interdisk coupling is contained both in the diagonal blocks that are derived from the matrices of the intersector joints and in the off-diagonal blocks that are derived from the matrices of the ring. Apart from these remarks, the reduced matrices have no other properties, which could impact their eigenvalues or eigenvectors.

Note that the generalized load can be obtained from the physical load with the same procedures.

2.8 Numerical Results. Once the reduced matrices and load vectors have been assembled, it is possible to compute the free or forced response of the rotor.

The generalized eigenmodes are solutions of the homogeneous problem, as follows:

$$[Z_M(\omega)]\{q_M(\omega)\} = \{0\} \tag{26}$$

The physical modeshapes are then restored to the full structure thanks to Eq. (23). These modeshapes can be compared with those computed with the full model.

In the case of the sample rotor with 12 and 15 blades, different sets of monoharmonic solutions with $\delta \in \{0,5\}$ were computed for various targeted frequency ranges and were used to reduce the rotor problem, as displayed in Fig. 9(*a*). 250 generalized modes, comprised between $f=0$ and $f=15$, were compared with the assumed corresponding modes of the rotor in the same frequency range, referred to as reference modes. The resulting relative error in frequency is plotted in Fig. 9(*b*). A modeshape correlation index, based on a MAC)is reported in Fig. 9(*c*). As can been seen in these figures, the maximum of the relative error in frequency is

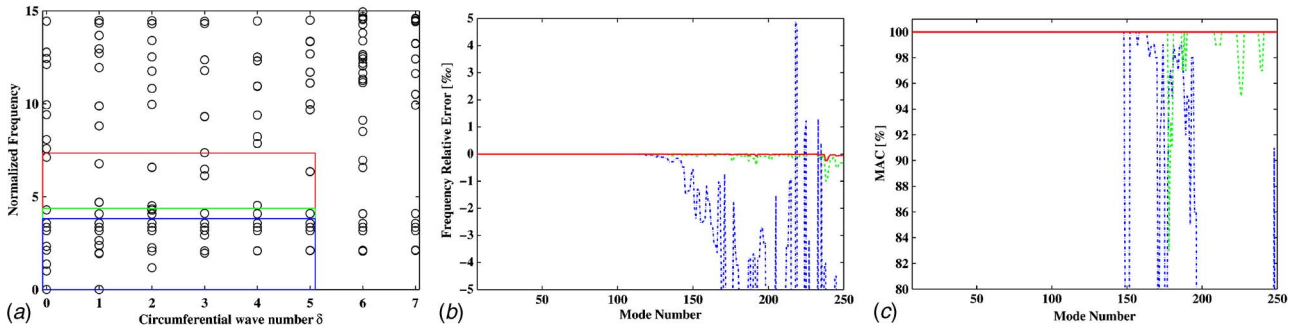


Fig. 9 (*a*) Targeted frequency ranges, (*b*) frequency relative error, and (*c*) modeshape correlation between reference and generalized modes

Downloaded 02 Jun 2010 to 171.66.16.109. Redistribution subject to ASME license or copyright; see http://www.asme.org/terms/Terms_Use.cfm

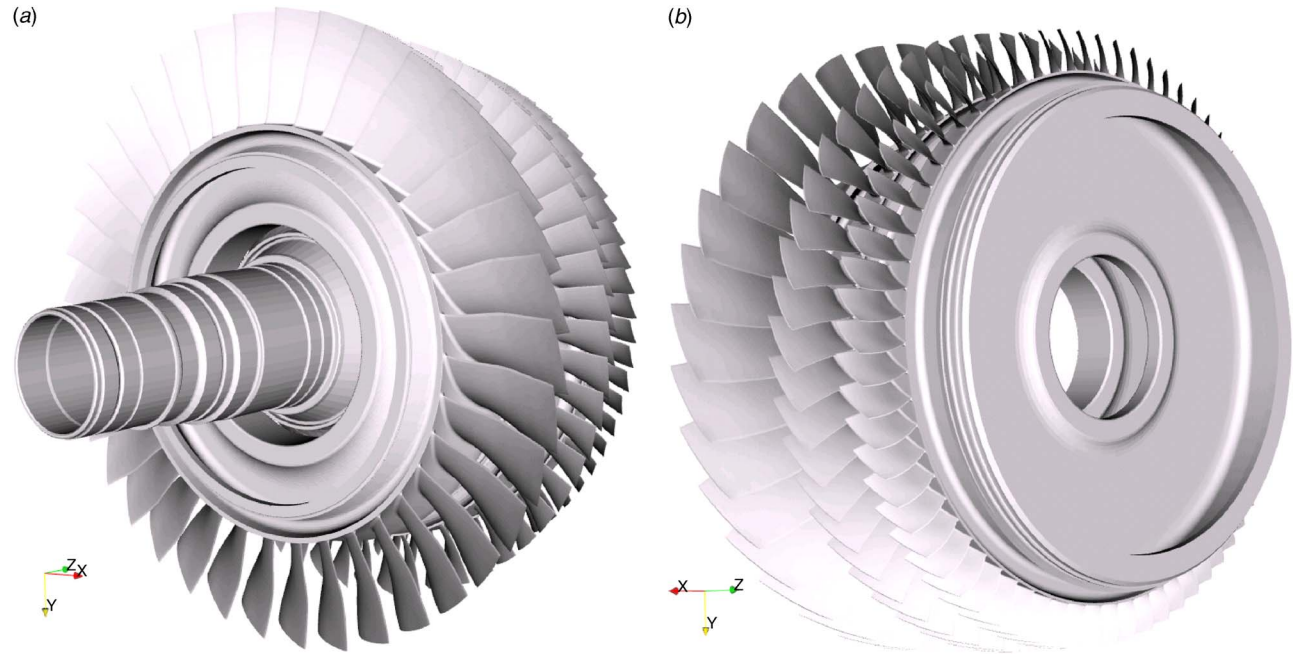


Fig. 10 Industrial three stage high pressure (HP) compressor: (*a*) front and (*b*) rear

below 0.1% and the modeshape correlation is excellent as soon as subspace $[T_M]$ includes enough vectors. A future development of this work is to define a priori error estimators, probably based on the identified source of error underlined in the monoharmonic computation section.

3 Application to an Industrial Model

The industrial model to which the methodology described in Sec. 2 is applied is a part of the numerical model of a compressor in development: it is depicted in Fig. 10. It is composed of three integrally bladed disks (blisks), whose characteristics are reported in Table 1. The full finite element model of the assembly is made of 11,289,230 tetrahedrons connecting 2,629,002 nodes, which leads to 7,887,006 DOFs. The materials of the stages are special alloys of titanium. Since the finite element model is quite huge as is, only the linear elements were considered at the time of the present study, but computations with quadratic elements are planned.

As described in the beginning of this paper, one uses interdisk rings built from a Delaunay tessellation between the nodes of the regarding rims of two adjacent disks. Since the nominal geometries of the sectors of two connected stages are such that they are bonded together, a preprocessing of the geometries is required to slightly translate the nodes of the flanges of disks $\mathcal{D}^1$ and $\mathcal{D}^3$ so that the interdisk rings can fill the empty spaces created between the flange of disk $\mathcal{D}^1$ (respectively, disk $\mathcal{D}^3$) and the rim of disk $\mathcal{D}^2$, such as depicted in Fig. 11. Two sets of nodes have to be moved for each flange.

- The first set is translated longitudinally.
- The second set is translated radially.

Table 1 Description of the finite element model

Stage	No. of sectors	No. of nodes/s	No. of elements/s	No. of DOF/s	Type of elements
1	36	16,343	65,170	49,029	Tetra4
2	56	9,566	36,815	28,698	Tetra4
3	70	23,104	97,860	69,312	Tetra4

This operation does not affect the integrity of the finite element mesh of such parts. Note that the bolting system is not included in the model.

The minimal set of elements to describe the geometry of the full assembly is presented in Fig. 12, since the bladed disks can be generated by circular repetitions of their initial sector. This allows huge memory savings because only this minimal geometry is stored.

3.1 Monoharmonic Shapes. The latter minimal geometry is perfectly suited for the computation of the cyclic modeshapes. A classical graph of normalized frequencies versus nodal diameter is plotted in Fig. 13. It compares the cyclic solutions of the assembly to the modes of the individual disks in free-fix ($\mathcal{D}^1$), fix-fix ($\mathcal{D}^2$), and fix-free ($\mathcal{D}^3$) conditions. Frequencies are normalized with respect to the frequency of the first flexible 0 diameter solution of the rotor.

From Fig. 13, it is noted that coupled solutions are found inside a triangle that has $\delta=0$, $f=0$ as a summit, and $\delta=0$ and $f=\delta$ as edges (when f is normalized, as stated before). In this region of high to moderate disk coupling as δ increases, there are noticeable differences between the frequencies of the rotor solutions and the disk natural frequencies. This comes from the fact that a fix condition at interstage interfaces is too stiff and disk modes that are similar to solutions of the rotor are higher in frequency. On the contrary, modes of the disks with free rims would be below rotor solutions since a free condition at the interstage interfaces is far too soft. Ideal boundary conditions to apply to a monodisk analysis so that multistage effects are properly described would be between free and fix conditions, and they would vary according to the considered diameter solution.

Everywhere else, it can be seen that many monoharmonic solutions are close to modes of the individual disks, merely due to the following.

1. A small disk-blade coupling, which tends to confine the strain energy on the blades [1]. In this case, the global motion is very similar to that of the individual disks whatever their boundary conditions are, since the latter do not affect the blade-dominated motion due to the low coupling ratio between the disk and the blades.

Downloaded 02 Jun 2010 to 171.66.16.109. Redistribution subject to ASME license or copyright; see http://www.asme.org/terms/Terms_Use.cfm

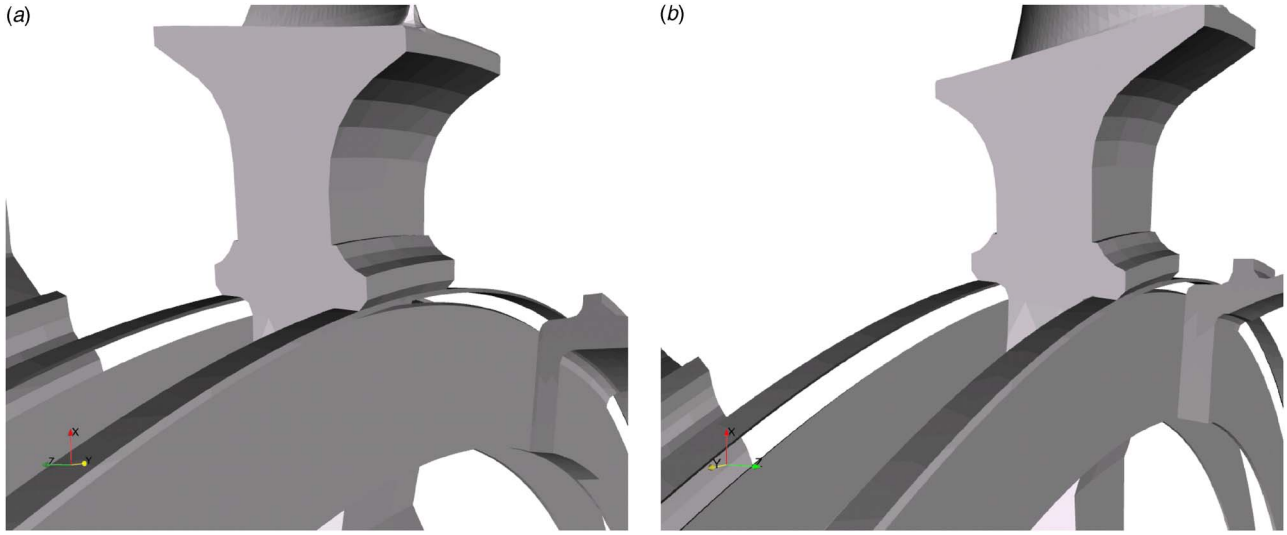


Fig. 11 Details of the rings (*a*) between $\mathcal{D}^1$ and $\mathcal{D}^2$ and (*b*) between $\mathcal{D}^2$ and $\mathcal{D}^3$

2. A small disk-disk coupling, which tends to confine the strain energy on a single disk.

Besides, a phenomenon of aliasing occurs for monoharmonic solutions that have a strong participation of disk $\mathcal{D}^1$ (respectively, $\mathcal{D}^2$). Typical modeshapes are plotted in Figs. 14–17. Notice that the computation of the strain energy in Fig. 14(*b*) provides useful information since the maximum of strain energy is located at the rim between disks $\mathcal{D}^1$ and $\mathcal{D}^2$ and not at the tip of the blades as expected because of the 2S1 shape.

3.2 Model Reduction and Results. A reduced model of this assembly was built from a set of cyclic solutions with $\delta \in \{0,2\}$ and $f \in [0,16.13]$. This reduced model has 44,342 generalized DOFs. To capture all the modes in the normalized frequency range [0,19.5], 900 modes were computed. Before restoring the modeshapes to the whole structure or a subset of physical DOF, a convenient way to describe the generalized modes is to perform a Fourier spatial analysis of the reduced modeshapes. Working with the reduced modeshapes instead of the full modeshapes is possible because without mistuning all the superelements of a given disk share the same kinematic subspace. Figures 18–20 in which the color varies from white (harmonic relative amplitude equals 0) to black (harmonic relative amplitude equals 1) then show that, as expected, modes come first by near-pairs and second by families.

The participation factor on each disk, in the sense of Eq. (27), is plotted in parallel to these spectra.

$$\forall d \in \{1,2,3\}, \quad R^d = \frac{\{q_M^d\}^\top [K_M^d] \{q_M^d\}}{\{q_M\}^\top [K_M] \{q_M\}} \tag{27}$$

It is mandatory to examine both graphs together to avoid hasty conclusions in terms of multiharmonicity of modes. Indeed, a mode that looks multiharmonic on a given disk can be so if its participation relative to that disk is very small: The analysis of an almost zero signal leads to a spectrum that shows multiple harmonics, but it does not indicate that the generalized displacement is almost zero on this disk. Special attention must be paid to the fact that a physical indicator, such as the kinetic energy, should be used to avoid normalization problems between the kinematic subspaces defined on each disk. For instance, Modes 118–180 are clearly localized to disk $\mathcal{D}^3$ according to Fig. 18 but seem to be multiharmonic on disks $\mathcal{D}^1$ and $\mathcal{D}^2$. The only multiharmonic modes of the reduced model are observed on disk $\mathcal{D}^3$ for $\delta > 22$ (if δ is considered as the dominating harmonic in these particular cases), as described in Fig. 21 where the shape of Mode 428 at $f = 10.23$ is restored to the whole assembly, and its weighted spectrum in the sense of Eq. (10) is plotted. From the latter figures, it

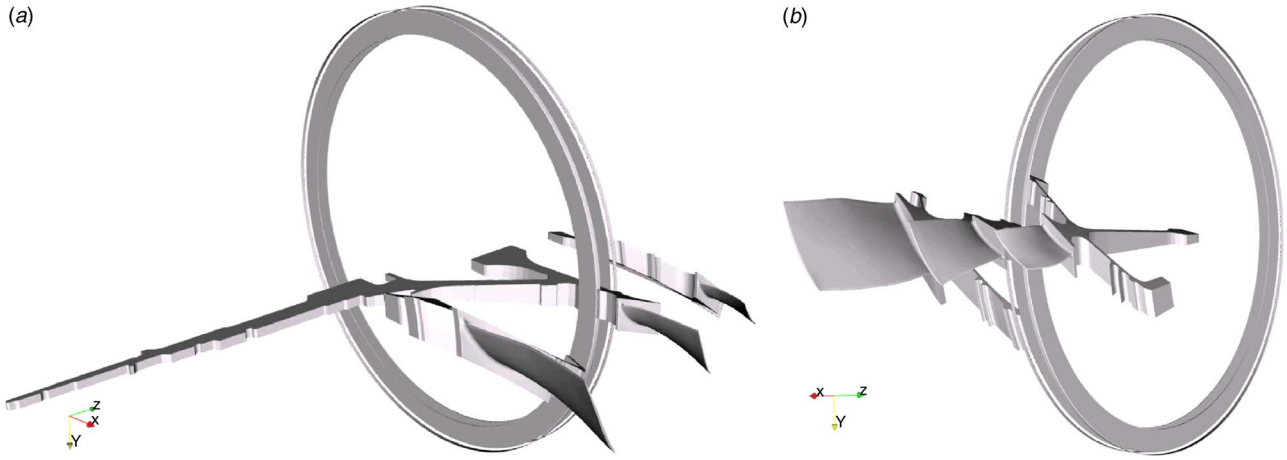


Fig. 12 Sector models and rings used in the computation of cyclic modeshapes: (*a*) front and (*b*) rear

Downloaded 02 Jun 2010 to 171.66.16.109. Redistribution subject to ASME license or copyright; see http://www.asme.org/terms/Terms_Use.cfm

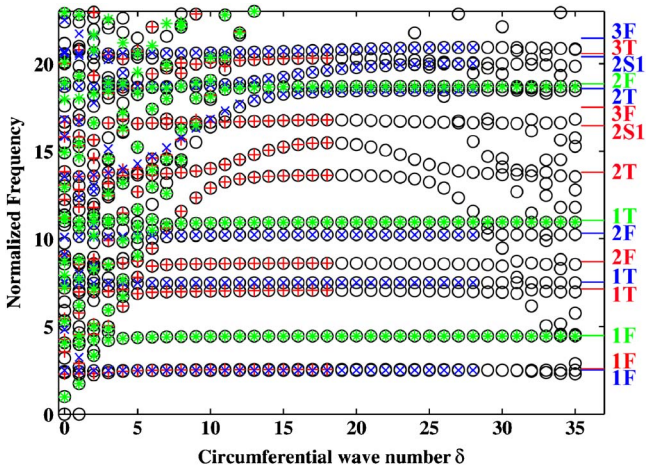


Fig. 13 Normalized frequencies of the cyclic solutions for the rotor (○) and the modes of disk $\mathcal{D}^1$ (+), disk $\mathcal{D}^2$ (×), and disk $\mathcal{D}^3$ (∗) in free-fix, fix-fix, and fix-free condition. Horizontal lines refer to blade frequencies of each stage.

can be concluded that almost all modes are monoharmonic, like that of Fig. 22.

3.3 Recovery of Modeshapes and Postprocessing. Postprocessing the restored modeshapes on the full rotor would be a very expensive numerical effort, since storing the 900 generalized modes represents about 305 Mbytes, whereas storing the 900 modes once restored represents 53 Gbytes. A procedure of partial recovery of the modeshapes has been developed. Given a selection of elements where the quantities of interest (energies and stresses) are assumed to be located, the generalized response is restored to the physical DOFs of these elements only. These locations can be given as follows.

- Either by a spatial Fourier analysis of the generalized displacement or the strain energy associated with each superelement, which leads to recoveries to full sector models.
- If the generalized displacement appears to be monoharmonic, a procedure of pairing between monoharmonic solutions and generalized modes (not described here) returns useful information where to look for stresses or energies.

As an illustration, the generalized mode at $f=15.89$ can be manually paired with the monoharmonic solution with $\delta=1$ at $f=15.53$ depicted in Fig. 14. Figure 23 displays the strain energy and the Von Mises stress distributions on a subset of physical finite elements that belong to disk $\mathcal{D}^1$. This figure shows that, for this generalized mode and this disk, the Von Mises stress is maximum on the disk and, as expected, has a high value in the middle of the blade tip due to the 2S1 shape. Nevertheless, the monoharmonic solution has a strong participation of disk $\mathcal{D}^2$ and a recovery extended to that disk should be computed.

4 Conclusion

In the present paper, the authors updated and then applied the reduction technique they developed to deal with multistage assem-

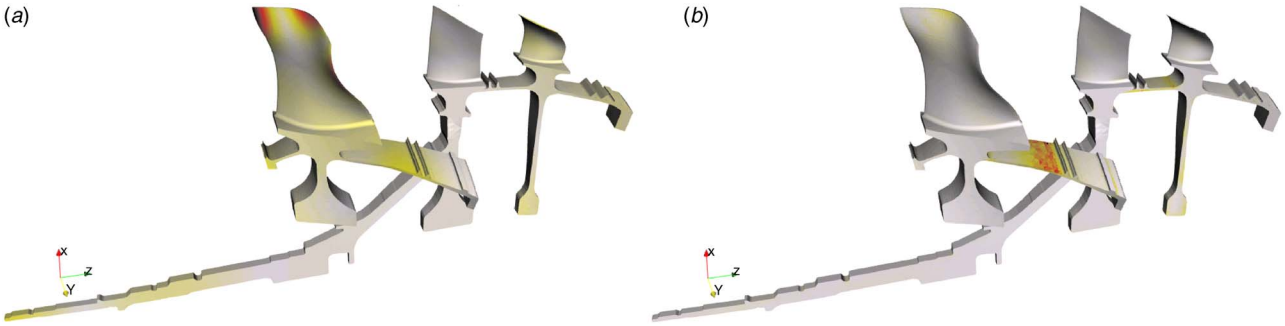


Fig. 14 Coupled cyclic solution with $\delta=1$ at $f=15.53$: (*a*) modeshape and (*b*) density of strain energy. Blade shapes are 2S1, 2F, and 1T.

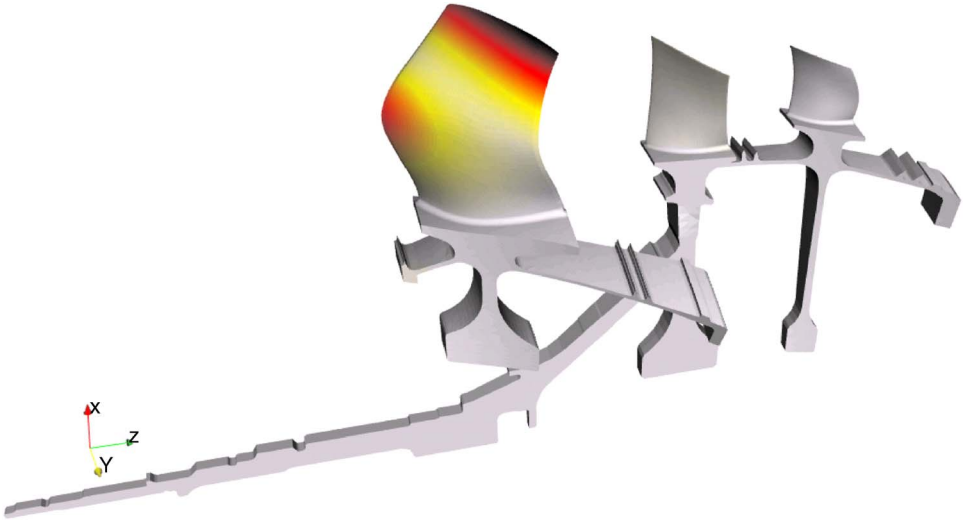


Fig. 15 Cyclic solution localized to disk $\mathcal{D}^1$ with $\delta=4$ at $f=8.63$. Blade shape is 2F.

Downloaded 02 Jun 2010 to 171.66.16.109. Redistribution subject to ASME license or copyright; see http://www.asme.org/terms/Terms_Use.cfm

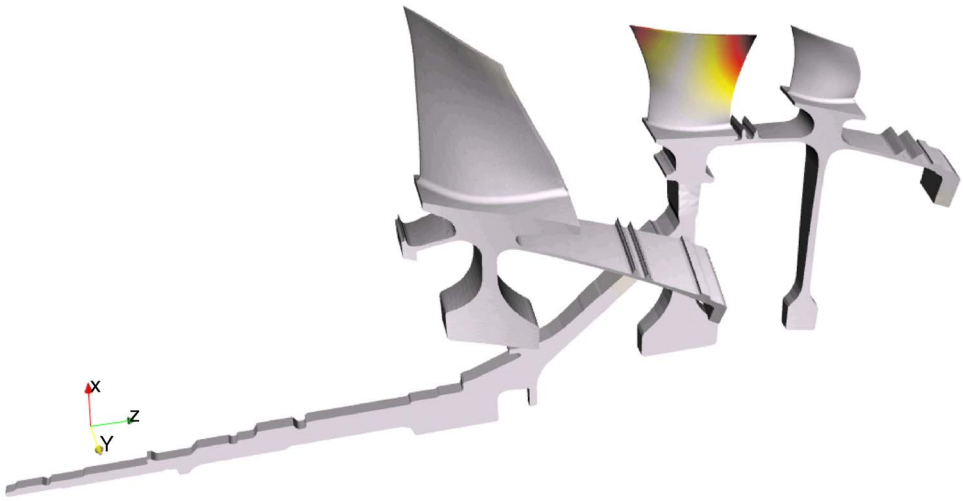


Fig. 16 Cyclic solution localized to disk $\mathcal{D}^2$ with $\delta=2$ at $f=7.47$. Blade shape is 1T.



Fig. 17 Cyclic solution localized to disk $\mathcal{D}^3$ with $\delta=0$ at $f=5.35$. Blade shape is 1F.

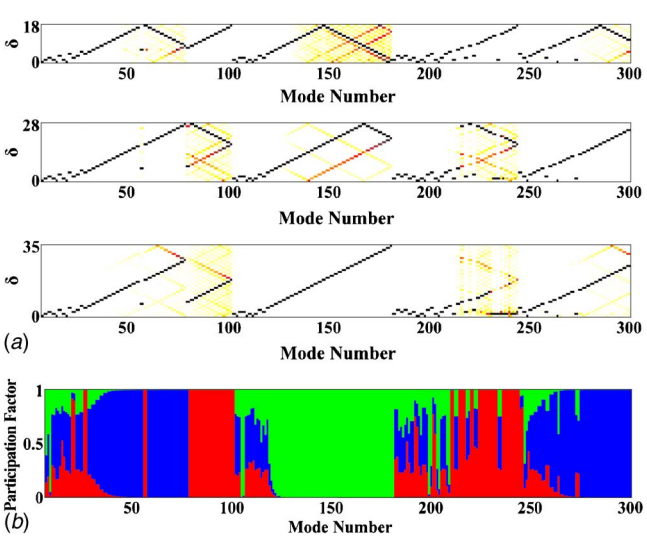


Fig. 18 Generalized modes 7 to 300 ($f\in[1,7.52]$): (*a*) Spatial harmonic content; (*b*) participation factor in strain energy for disks $\mathcal{D}^1$ (down), $\mathcal{D}^2$ (middle), and $\mathcal{D}^3$ (up)

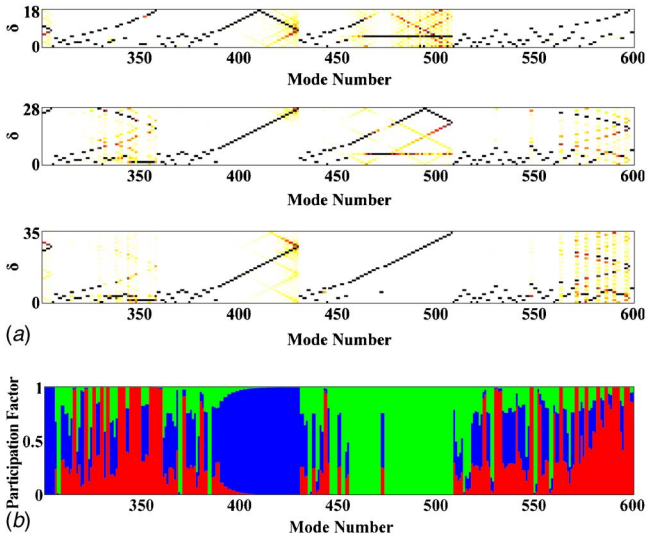


Fig. 19 Generalized odes 301–600 ($f\in[7.52,13.74]$): (*a*) Spatial harmonic content; (*b*) participation factor in strain energy for disks $\mathcal{D}^1$ (down), $\mathcal{D}^2$ (middle), and $\mathcal{D}^3$ (up)

Downloaded 02 Jun 2010 to 171.66.16.109. Redistribution subject to ASME license or copyright; see http://www.asme.org/terms/Terms_Use.cfm

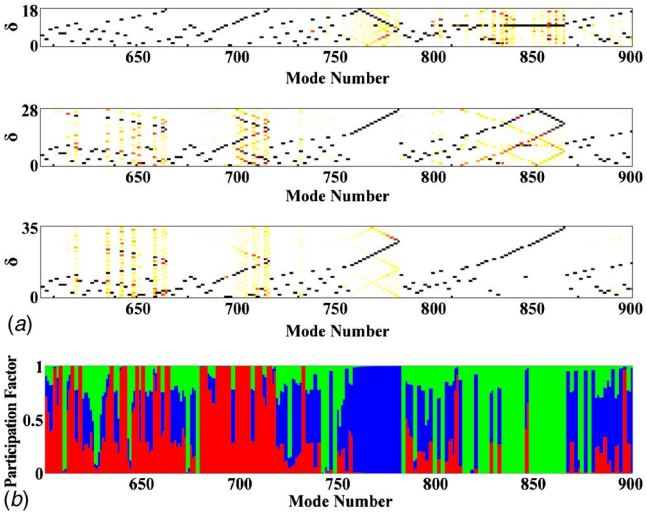


Fig. 20 Generalized modes 601–900 ($f \in [13.76, 19.57]$): (*a*) Spatial harmonic content; (*b*) participation factor in strain energy for disks $\mathcal{D}^1$ (down), $\mathcal{D}^2$ (middle), and $\mathcal{D}^3$ (up)

blies of bladed disks [9] to a realistic rotor model. The results obtained for this industrial rotor allow to give some guidelines to use efficiently the previous method in a real industrial environment.

1. In the proposed methodology, a set of monoharmonic solutions is computed. Such solutions already contain much valuable information in terms of coupling or regions of high density of strain energy or high stress levels.
2. These solutions are used to build a compact reduced model that represents the multistage model with a controlled accuracy. In future work, the error estimator derived from the monoharmonic computations will be integrated into an iterative procedure of enrichment of the subspaces built to approximate the kinematics of the sectors.
3. On the one hand, if a spectral analysis shows that the generalized modes of interest are spatially monoharmonic, it means that they potentially correspond to monoharmonic solutions, given by a manual or automatic pairing process. This property will be exploited in future work, especially in forced response computations.
4. On the other hand, if some of the modes of interest are multiharmonic, the response is computed with the reduced model.
5. In every case, the response can be restored to a subset of elements chosen either from an a priori analysis of the

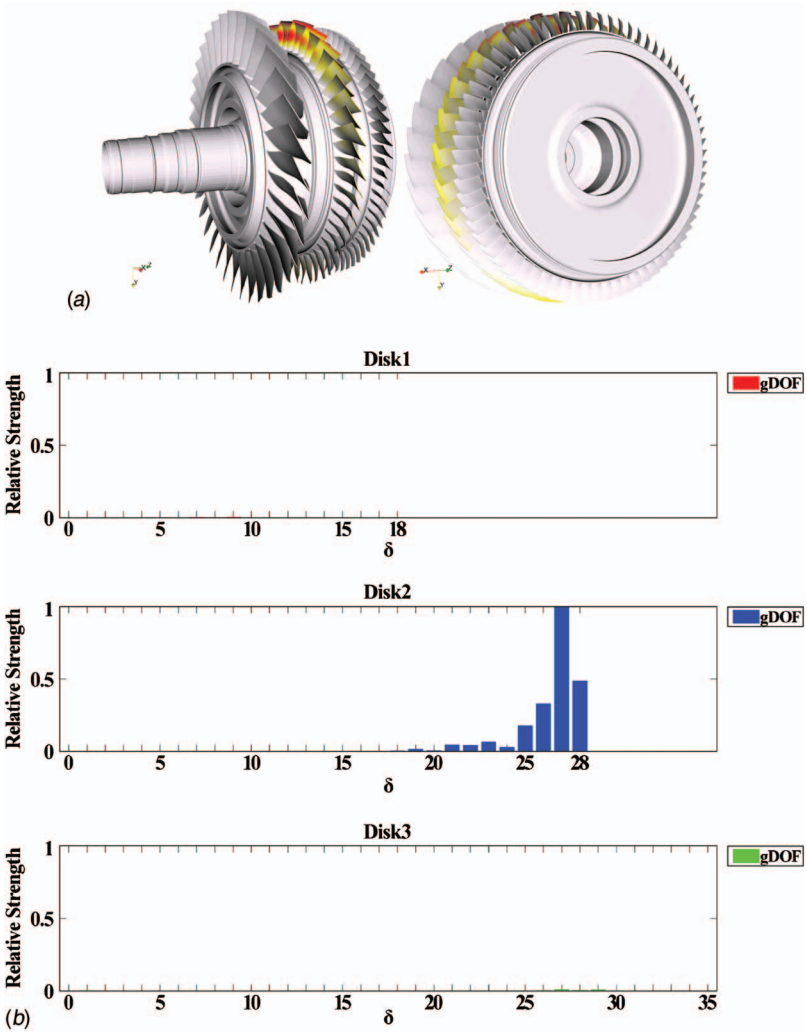


Fig. 21 Restored mode at $f=10.23$ localized to disk $\mathcal{D}^2$: (*a*) modeshape and (*b*) spatial harmonic content for disks $\mathcal{D}^1$ (up), $\mathcal{D}^2$ (middle), and $\mathcal{D}^3$ (down)

Downloaded 02 Jun 2010 to 171.66.16.109. Redistribution subject to ASME license or copyright; see http://www.asme.org/terms/Terms_Use.cfm

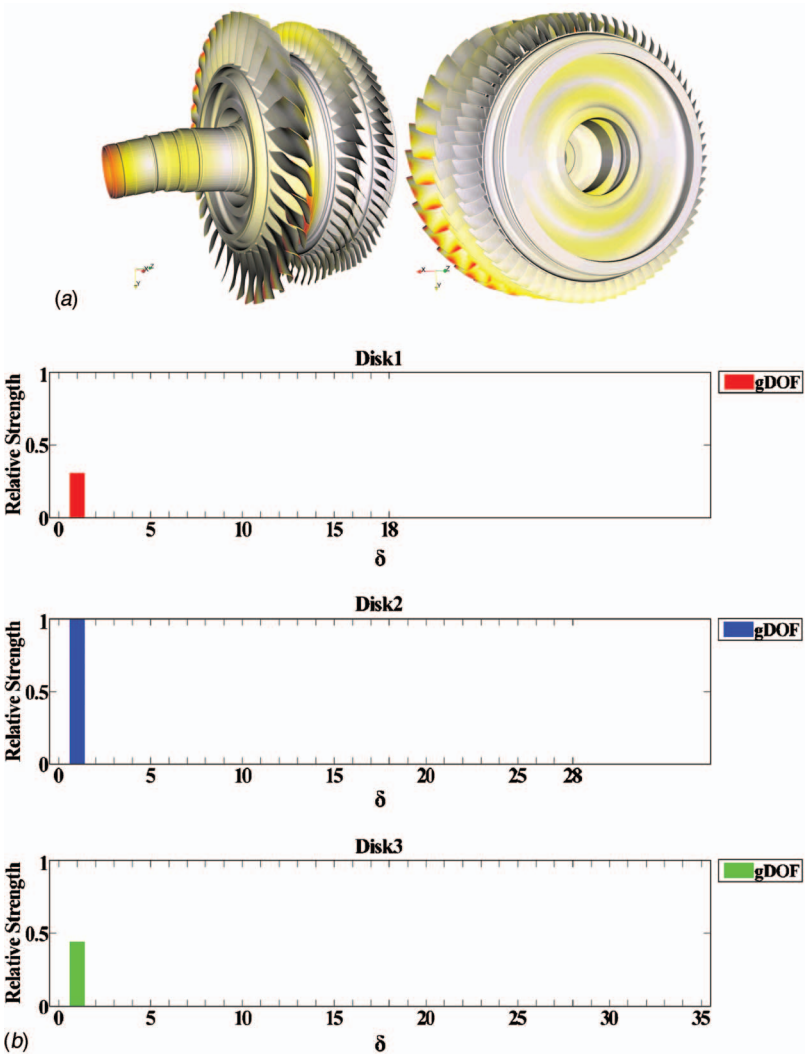


Fig. 22 Restored mode at f=15.89 with strong coupling: (*a*) modeshape and (*b*) spatial harmonic content for disks $\mathcal{D}^1$ (up), $\mathcal{D}^2$ (middle), and $\mathcal{D}^3$ (down)

monoharmonic solutions or from an a posteriori analysis of the spatial spectrum of the generalized modes.

The proposed methodology is already implemented within the Structural Dynamics Toolbox [13] with critical use of the superelement capabilities of this library. Internal element formulations are used although imports from SAMCEF and NASTRAN have also been done for verification. The structural dynamics toolbox (SDT) (for use in MATLAB®)switch to use NASTRAN as the eigenvalue solver for SDT based models was sometimes used for very large models. The SDT/OPENFEM export to VTK format was used to generate some of the figures included in this paper with ParaView. Developments specific to this study, grouped as the embryo of SDT/ROTOR package, are as follows:

1. preprocessing tools to assemble sector models and mesh rings using an automated volume mesher
2. monoharmonic rotor computations
3. sector superelement building from a set of monoharmonic multistage solutions and fixed sector modes
4. postprocessing tools for harmonic and generalized coordinate viewing

Acknowledgment

Thanks go to Snecma for its technical and financial support. This work takes place in the framework of the MAIA Mechanical Research and Technology Program sponsored by CNRS, ONERA, and SAFRAN Group.

Nomenclature

$\mathcal{I}$ = interface
$\mathcal{D}$ = disk
$\mathcal{R}$ = interdisk ring
$\mathcal{S}$ = sector
$[c]$ = observation matrix
$[E]$ = harmonic recovery matrix
$[I]$ = identity matrix
$[K]$ = stiffness matrix
$[M]$ = mass matrix
$[Z]$ = dynamic stiffness matrix
$[\Phi]$ = matrix of eigenvectors
$[T]$ = basis of a subspace
$\{f_e\}$ = external load vector

Downloaded 02 Jun 2010 to 171.66.16.109. Redistribution subject to ASME license or copyright; see http://www.asme.org/terms/Terms_Use.cfm

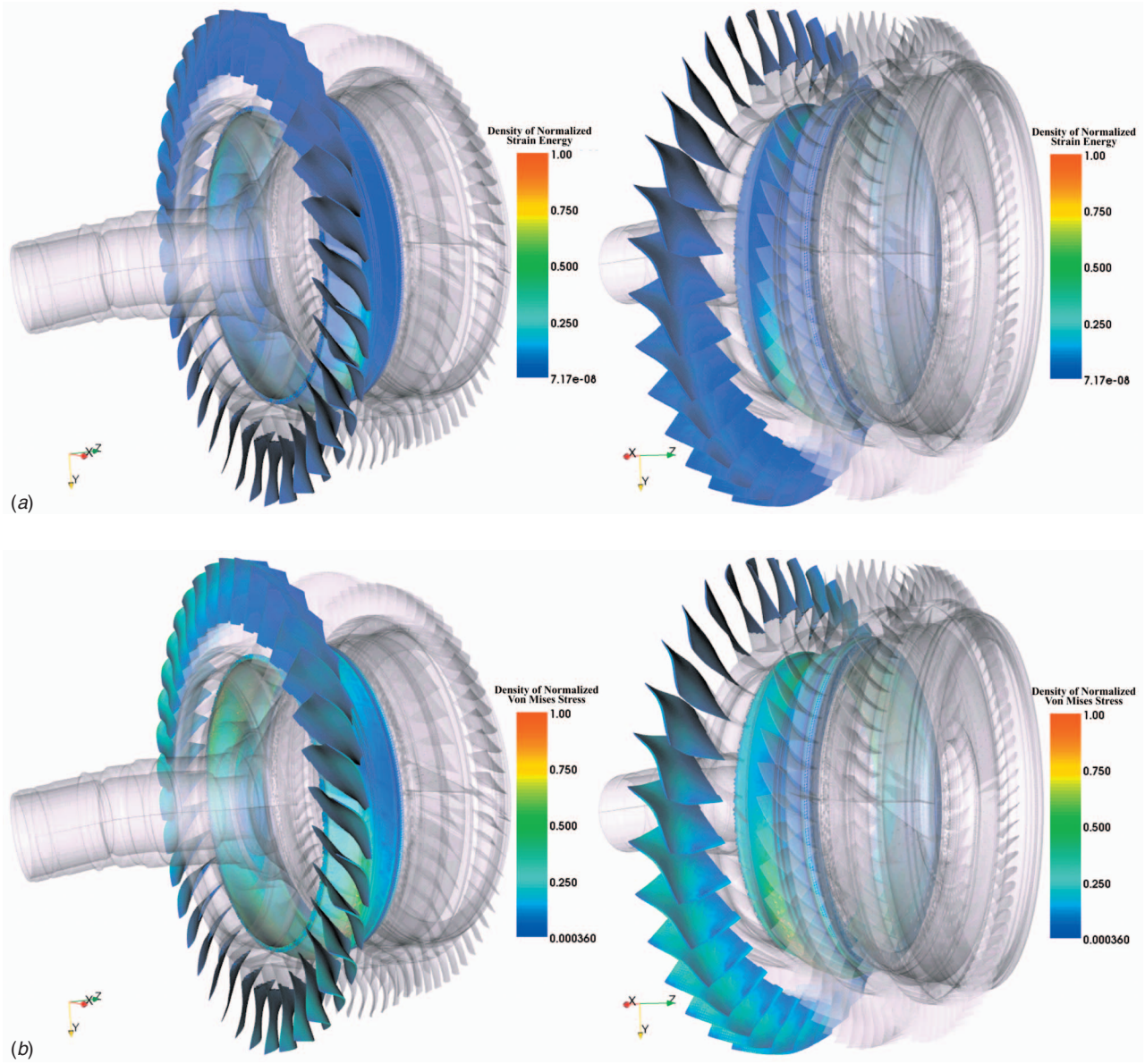


Fig. 23 Partial postprocessing of the generalized mode at f=15.89 on disk $\mathcal{D}^1$: (*a*) normalized density of strain energy and (*b*) normalized distribution of Von Mises stress

$\{q\}$ = DOF vector
$\{\hat{q}\}$ = harmonic DOF vector
α = sector angle
δ = Fourier harmonic
$\mathbf{i}$ = $\sqrt{-1}$
ω = natural frequency
f = normalized frequency
N = number of degrees of freedom
N_s = number of sectors
R = participation factor in strain energy
$\bar{*}$ = complex conjugate
$*_a$ = quantity relative to aft interface
$*_f$ = quantity relative to front interface
$*_c$ = quantity relative to complementary domain
$*_l$ = quantity relative to left interface
$*_r$ = quantity relative to right interface
$*_M$ = quantity relative to multistage reduction
$*_\delta$ = quantity relative to harmonic δ
$*^d$ = quantity relative to disk d
$*^{d,s}$ = quantity relative to sector s of disk d
$*^{\mathcal{R}}$ = quantity relative to interdisk ring $\mathcal{R}$

References

[1] Castanier, M. P., and Pierre, C., 2006, "Modeling and Analysis of Mistuned Bladed Disk Vibration: Status and Emerging Directions," J. Propul. Power, **22**(2), pp. 384–396.
[2] Lim, S. H., Castanier, M. P., and Pierre, C., 2004, "Vibration Modeling of Bladed Disks Subject to Geometric Mistuning and Design Changes," *Proceedings of the 45th AIAA/ASME/ASCE/AHS/ASC Structures, Structural Dynamics and Materials Conference*, Palm Springs, CA.
[3] Feiner, D. M., and Griffin, J. H., 2004, "Mistuning Identification of Bladed Disks Using a Fundamental Mistuning Model–Part I: Theory," ASME J. Turbomach., **126**, pp. 150–158.
[4] Feiner, D. M., and Griffin, J. H., 2004, "Mistuning Identification of Bladed Disks Using a Fundamental Mistuning Model–Part II: Application," ASME J. Turbomach., **126**, pp. 159–165.
[5] Sternchüss, A., and Balmès, E., 2006, "On the Reduction of Quasi-Cyclic Disks With Variable Rotation Speeds," *Proceedings of the International Conference on Advanced Acoustics and Vibration Engineering (ISMA)*, Leuven, Belgium, pp. 3925–3939.
[6] Bladh, R., Castanier, M. P., and Pierre, C., 2003, "Effects of Multistage Coupling and Disk Flexibility on Mistuned Bladed Disk Dynamics," ASME J.

Downloaded 02 Jun 2010 to 171.66.16.109. Redistribution subject to ASME license or copyright; see http://www.asme.org/terms/Terms_Use.cfm

Eng. Gas Turbines Power, **125**, pp. 121–130.
[7] Song, S. H., Castanier, M. P., and Pierre, C., 2007, "System Identification of Multistage Turbine Engine Rotors," ASME Paper No. GT2007-28307.
[8] Laxalde, D., Lombard, J.-P., and Thouverez, F., 2007, "Dynamics of Multi-Stage Bladed Disk Systems," ASME Paper No. GT2007-27083.
[9] Sternchüss, A., and Balmès, E., 2007, "Reduction of Multistage Rotor Models Through Cyclic Modeshapes," ASME Paper No. GT2007-27974.
[10] Ewins, D. J., 1973, "Vibration Characteristics of Bladed Disk Assemblies," J. Mech. Eng. Sci., **15**(3), pp. 165–186.
[11] Laxalde, D., Dupeux, J., and Lombard, J.-P., 2006, "Analyse Dynamique des Structures Cycliques Multi-Étages," *Actes du XVè Colloque Vibrations, Chocs et Bruit*, Lyon, France.
[12] Balmès, E., 2005, "Orthogonal Maximum Sequence Sensor Placements Algorithms for Modal Tests, Expansion and Visibility," *Proceedings of the International Modal Analysis Conference*, Orlando, FL.
[13] Balmès, E., Bianchi, J.-P., and Leclère, J.-M., 2007, Structural Dynamics TOOLBOX 6.0 (for use with MATLAB), SDTools, Paris, France.

Downloaded 02 Jun 2010 to 171.66.16.109. Redistribution subject to ASME license or copyright; see http://www.asme.org/terms/Terms_Use.cfm

Nonlinear Numerical Prediction of Gas Foil Bearing Stability and Unbalanced Response

Sébastien Le Lez

Mihaï Arghir

Jean Frêne

Laboratoire de Mécanique des Solides,
Université de Poitiers,
Téléport 2-SP2MI,
Boulevard Marie et Pierre Curie,
BP 30179,
86962 Futuroscope Chasseneuil Cedex, France

One of the main interests of gas foil bearings lies in their superior rotordynamic characteristics compared with conventional bearings. A numerical investigation on the stability limit and on the unbalanced response of foil bearings is presented in this paper. The main difficulty in modeling the dynamic behavior of such bearings comes from the dry friction that occurs within the foil structure. Indeed, dry friction is highly nonlinear and is strongly influenced by the dynamic amplitude of the pressure field. To deal with these nonlinearities, a structural dynamic model has been developed in a previous work. This model considers the entire corrugated foil and the interactions between the bumps by describing the foil bearing structure as a multiple degrees of freedom system. It allows the determination of the dynamic friction forces at the top and at the bottom of the bumps by simple integration of ordinary differential equations. The dynamic displacements of the entire corrugated sheet are then easily obtained at each time step. The coupling between this structural model and a gas bearing prediction code is presented in this paper and allows performing full nonlinear analyses of a complete foil bearing. The bearing stability is the first investigated problem. The results show that the structural deflection enhances the stability of compliant surface bearings compared with rigid ones. Moreover, when friction is introduced, a new level of stability is reached, revealing the importance of this dissipation mechanism. The second investigated problem is the unbalanced response of foil bearings. The shaft trajectories depict a nonlinear jump in the response of both rigid and foil bearings when the value of the unbalance increases. Again, it is evidenced that the foil bearing can support higher mass unbalance before this undesirable step occurs. [DOI: 10.1115/1.2967481]

1 Introduction

A spectacular mass reduction in a rotating machine can be achieved by increasing the rotational speed, which allows reducing the diameters while increasing the efficiency. Due to the low viscosity of their lubricant, gas bearings are good candidates for such high speed turbomachines. However, this low viscosity leads to two main disadvantages lying in low load capacities and limited damping levels. To overcome these limitations, the concept of gas foil bearing appeared in the mid-1960s. For such bearings, an elastic and dissipative structure is added between the housing and the rotating shaft. For the past decades, several types of foil bearings (tape type, leaf type, bump type, etc.) have been designed. Among all these designs, the bump-type foil bearing is now considered to be the most efficient [1,2].

This type of bearing is made of one or several corrugated sheets covered by a smooth top foil (Fig. 1). The corrugated and flat top sheets are welded at one end and free at the other end. Due to rotor speed, the gas pressure is applied on the top foil, which pushes radially the corrugated foil. As this foil is welded at a single extremity, the bumps slide along the circumferential direction and dry friction occurs with both the housing and the top foil. When the bearing is submitted to vibrations (unbalance mass, shocks, self-excited vibrations, etc.), the relative displacements within the foil structure contribute to the energy dissipation and to the overall stability of the system.

In 1983, Heshmat et al. were the first to study theoretically the behavior of a foil journal and thrust bearing [3,4]. The foil structure was considered to be a simple elastic foundation and a formula from Ref. [5] was adapted to compute the stiffness of the individual bumps. This allowed the easy calculation of the dynamic stiffness of the bearing. Due to its simplicity, this model is still attractive and has been used recently by Peng and Khonsari [6,7].

In 1996, Iordanoff proposed a similar formula for the static stiffness of a single bump, which included the friction between the corrugated foil and the housing [8]. This approach had the advantage of considering different formulas for the case of the bump with a fixed end and the bump with both ends free. Following an idea from 1995 [9], San Andres and Kim added a structural damping factor to this formula as an input parameter and computed the dynamic coefficients of a complete foil bearing [10]. They showed that the structural energy dissipation leads to higher damping coefficients. A similar study was also performed for a bearing with double strip layers [11].

However, due to the asymmetry of the foil bearing (the foils have a welded edge and a free edge), more realistic models of the structure have been looked for. In 1992, Ku and Heshmat introduced a model that took into account the elastic deformation of the bumps, the friction between the corrugated foil, the top foil, and the housing, as well as the interactions between the bumps [12]. Carpino and Talmage presented in 2003 a fully coupled finite element model of a foil bearing [13]. The finite element structural model described the behavior of the top foil supported by an elastic foundation, and a viscous dissipation of the subfoil was added in 2006 [14]. The relative displacements between the housing, the corrugated sheet, and the top foil are perturbed as function of the shaft displacements and the Coulomb friction is modeled as an equivalent viscous friction. This allows determining the dynamic coefficients of the foil bearing, and the results showed that high values of the friction coefficient can lead to low energy dissipation

Contributed by the International Gas Turbine Institute of ASME for publication in the JOURNAL OF ENGINEERING FOR GAS TURBINES AND POWER. Manuscript received March 31, 2008; final manuscript received April 2, 2008; published online October 9, 2008. Review conducted by Dilip R. Ballal. Paper presented at the ASME Turbo Expo 2008: Land, Sea and Air (GT2008), Berlin, Germany, June 9–13, 2008.

Copyright © 2009 by ASME

Downloaded 02 Jun 2010 to 171.66.16.109. Redistribution subject to ASME license or copyright; see http://www.asme.org/terms/Terms_Use.cfm

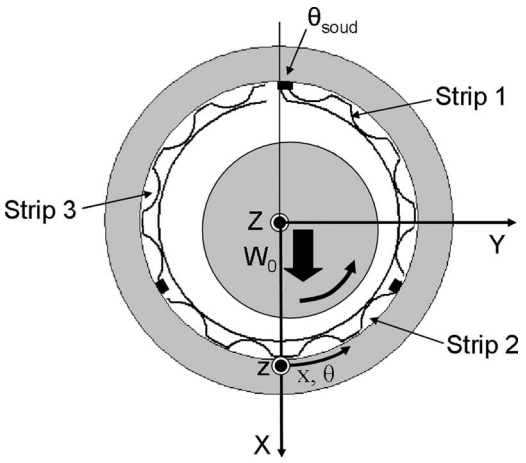


Fig. 1 Coordinate system of the foil bearing

levels. The influence of the stiffness along the axial direction was also studied, concluding that a structural model should consider the bearing in its totality [15].

The main idea of the model used in the present paper is to consider that the bump interactions must be taken into account to correctly describe the structural behavior, which was evidenced by previous finite element simulations [16]. The general formulation of the structural model is briefly explained [17] as well as its extension to a dynamic and dissipative model [18]. The model does not make any simplifying energetic considerations to replace the nonlinear Coulomb damping as an equivalent linear one and is therefore well suited to perform nonlinear dynamic analyses. The orbit method is thus used in the present work to determine the stability limit and the unbalance response of foil bearings.

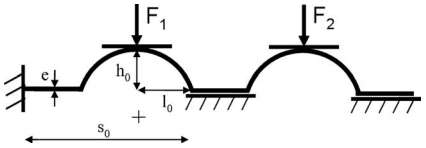


Fig. 2 Two bump strip

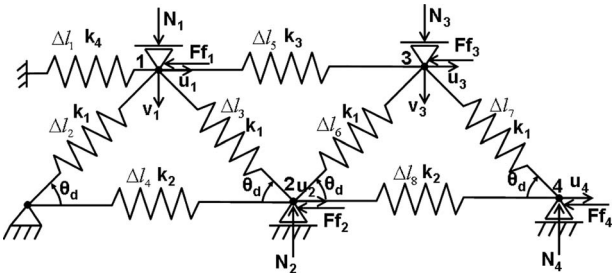


Fig. 3 The 6 DOF model

2 Theoretical Analysis

2.1 The Foil Bearing Structural Model. The mathematical model of the elastic structure is first presented for a strip made of two bumps (Fig. 2) and then it is extended to an arbitrary number of bumps. The model considers the continuous foil structure as an equivalent discrete one with a restricted number of nodes linked by linear springs. For instance, the model depicted in Fig. 3 has 6 degrees of freedom, namely, two vertical displacements, v_1 and v_3, and four horizontal displacements $u_1, \ldots, u_4$; this is the minimum required for describing the coupling between two successive bumps. The elementary characteristics of the bump strip model are the stiffnesses k_i and the transmission force angle θ_d that can be analytically expressed for each type of bump.

The elementary stiffnesses and transmission force angles are determined by using energetic methods for two kinds of boundary conditions (Fig. 4): no rotation and free rotation. This distinction is necessary in order to correctly take into account the last bump of the strip located at the free end.

The analytic calculations use the classical linear elasticity approach. First the bending moments and normal loads are calculated in all regions of the elementary structures. Then the elastic deformation energy is estimated and Castigliano's theorem is used to express the elementary spring stiffness or the transmission force angles. The complete mathematical development and the resulting relations for k_i and θ_d are given in Ref. [17]. The global stiffness matrix of the whole structure is derived from the expression of the potential energy. To determine this potential energy, the elongation of the elementary springs needs to be expressed. For more clarity these elongations will be first expressed for the strip constituted of two bumps having the same elementary characteristics k_i and θ_d shown in Fig. 3. Then the results will be extended to the general case of n bumps with the last bump having different elementary characteristics k_{ibis} and θ_{dbis}. The elongations of the eight springs are depicted in Fig. 3. The model is considered to be linear, i.e., the final configuration is close from the initial configuration. Hence the eight elongations are as follows:

$$\Delta l_1 = u_1, \quad \Delta l_5 = u_3 - u_1$$

$$\Delta l_2 = u_1 c - v_1 s, \quad \Delta l_6 = u_3 c - v_3 s - u_2 c$$
$$\Delta l_3 = u_2 c - u_1 c - v_1 s, \quad \Delta l_7 = u_4 c - u_3 c - v_3 s \tag{1}$$

$$\Delta l_4 = u_2, \quad \Delta l_8 = u_4 - u_2$$

where $c = \cos\theta_d$ and $s = \sin\theta_d$. The potential energy is as follows:

$$E_{\text{pot}} = \tfrac{1}{2}\{k_1(\Delta l_2^2 + \Delta l_3^2 + \Delta l_6^2 + \Delta l_7^2) + k_2(\Delta l_4^2 + \Delta l_8^2) + k_3 \Delta l_5^2 + k_4 \Delta l_1^2\} \tag{2}$$

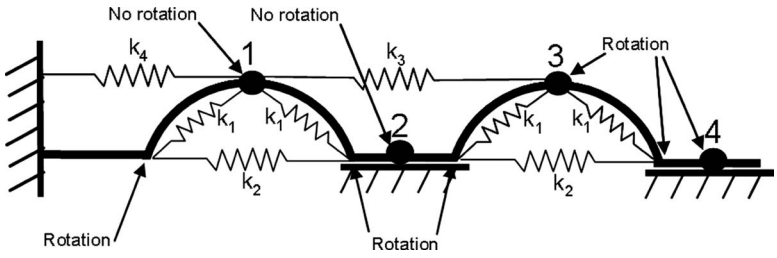


Fig. 4 Boundary conditions for calculating the elementary stiffnesses

Downloaded 02 Jun 2010 to 171.66.16.109. Redistribution subject to ASME license or copyright; see http://www.asme.org/terms/Terms_Use.cfm

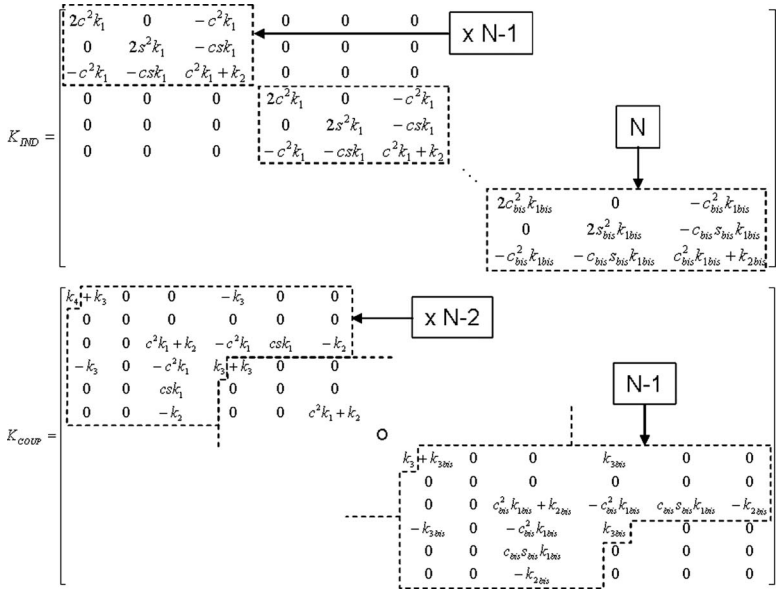


Fig. 5 Stiffness matrices

This leads to the following:

$$E_{\text{pot}} = \tfrac{1}{2}\{k_1(2u_1^2c^2 + 2v_1^2s^2 + 2u_2^2c^2 + 2u_3^2c^2 + 2v_3^2s^2 + u_4^2c^2 - 2u_1u_2c^2 - 2v_1u_2cs - 2u_2u_3c^2 + 2u_2v_3cs - 2u_3u_4c^2 - 2v_3u_4cs) + k_2(2u_2^2 + u_4^2 - 2u_2u_4) + k_3(u_1^2 - 2u_1u_3 + u_3^2) + k_4u_1^2\} \quad (3)$$

The foil is represented by a linear elastic system.

$$[K]\{U\} = \{F\} \quad (4)$$

Therefore, the stiffness matrix can be easily calculated because the potential energy is a quadratic form of the stiffness matrix.

$$\begin{bmatrix} 2c^2k_1 + k_3 + k_4 & 0 & -c^2k_1 & -k_3 & 0 & 0 \\ 0 & 2s^2k_1 & -csk_1 & 0 & 0 & 0 \\ -c^2k_1 & -csk_1 & 2c^2k_1 + 2k_2 & -c^2k_1 & csk_1 & -k_2 \\ -k_3 & 0 & -c^2k_1 & 2c^2k_1 + k_3 & 0 & -c^2k_1 \\ 0 & 0 & csk_1 & 0 & 2s^2k_1 & -csk_1 \\ 0 & 0 & -k_2 & -c^2k_1 & -csk_1 & c^2k_1 + k_2 \end{bmatrix} \begin{Bmatrix} u_1 \\ v_1 \\ u_2 \\ u_3 \\ v_3 \\ u_4 \end{Bmatrix} = \{F\} \quad (5)$$

For the general case of n bumps, the vector of generalized coordinates is defined as

$$U = [u_1 \quad v_1 \quad u_2 \quad \cdots \quad u_{2n-1} \quad v_{2n-1} \quad u_{2n}]^T \quad (6)$$

The global stiffness matrix can be seen as the sum of two matrices. The first one represents the stiffness of the bumps taken individually and the second one represents the coupling between the bumps. These matrices are given in Fig. 5 for the general case of n bumps. The last blocs of the matrices are different from the others due to the different transmission force angle θ_{dbis} and stiffnesses $k_{1\text{bis}}$, $k_{3\text{bis}}$ of the last bump.

2.2 The Dynamic Structural Model. The dynamic model of the structure is developed by supposing that, due to the small mass of steel foils, the foil bearing structure can be considered as a lightweight advanced friction damper. For such dampers, it is generally assumed that the inertia forces may be neglected compared with the friction and elastic forces; the damper element is thus considered of negligible mass. This assumption has also been verified by previous finite element simulations revealing that the kinetic energy of the structure could be neglected [16]. It is further supposed that the damping effects of the foil bearing structure arise only from Coulomb friction forces and the material damping is negligibly small. The dynamic characteristics of the foil structure can then be described by the time derivative of Eq. (4).

$$[K]\{\dot{U}\} = \{\dot{F}\} \quad (7)$$

$$\{\dot{U}\} = \{\dot{u}_1 \quad \dot{v}_1 \quad \dot{u}_2 \quad \cdots \quad \dot{u}_{2n-1} \quad \dot{v}_{2n-1} \quad \dot{u}_{2n}\}^T \quad (8)$$

$$\{\dot{F}\} = \{-\dot{F}_{f1} \quad \dot{N}_1 - \dot{F}_{f2} \quad \cdots \quad -\dot{F}_{f2n-1} \quad \dot{N}_{2n-1} - \dot{F}_{f2n}\}^T \quad (9)$$

These unsteady friction forces render the system of first order differential equations highly nonlinear because friction leads to stick-slip transitions at bump contacts.

The crucial point of the dynamic model is then the appropriate formulation of the unsteady Coulomb friction forces. The traditional model of a friction element in series with a spring is a good candidate but the resulting mathematical model is very stiff. In order to enable an efficient numerical integration, Petrov and Ewins introduced a regularization of the dynamic friction force that is used in the present dynamic model [19].

Downloaded 02 Jun 2010 to 171.66.16.109. Redistribution subject to ASME license or copyright; see http://www.asme.org/terms/Terms_Use.cfm

$$\dot{F}_{fi} = k_t(\dot{u}_i - 1/c_t \tan(\pi F_{fi}/2\mu_f N_i)) \tag{10}$$

This model is based on an approximation of the *sign* function intended to smooth out discontinuities. It allows the formulation of differential equations by describing the friction forces in a continuous way over the whole process of motion for all possible states of the friction contact, i.e., stick, slip, and stick-slip transitions, with no explicit determination of stick-slip transitions. This model is introduced in Eq. (7) and yields the node velocities:

$$\{\dot{U}\} = ([K] + [A])^{-1}\{D\} \tag{11}$$

$$[A] = \begin{bmatrix} k_t & 0 & 0 & & & & \\ 0 & 0 & 0 & & & & \\ 0 & 0 & k_t & & & & \\ & & & \ddots & & & \\ & & & & k_t & 0 & 0 \\ & & & & 0 & 0 & 0 \\ & & & & 0 & 0 & k_t \end{bmatrix}, \quad \{D\} = \begin{Bmatrix} g_1 \\ \dot{N}_1 \\ g_2 \\ \vdots \\ g_{2n-1} \\ \dot{N}_{2n-1} \\ g_{2n} \end{Bmatrix} \tag{12}$$

where the unsteady friction force given by Eq. (10) was expressed as

$$\dot{F}_{fi} = k_t \dot{u}_i - g_i \tag{13}$$

$$g_i = g(F_{fi}, N_i) = k_t \tan(\pi F_{fi}/2\mu_f N_i)/c_t \tag{14}$$

The tangential velocities $\dot{u}_i$ that appear in the definition of the friction forces can be extracted from $\{\dot{U}\}$:

$$\overbrace{\begin{Bmatrix} \dot{u}_1 \\ \dot{u}_2 \\ \vdots \\ \dot{u}_{2n-1} \\ \dot{u}_{2n} \end{Bmatrix}}^{\{\dot{X}\}} = \overbrace{\begin{bmatrix} 1 & 0 & 0 & & & & \\ 0 & 0 & 1 & & & & \\ & & & \ddots & & & \\ & & & & 1 & 0 & 0 \\ & & & & 0 & 0 & 1 \end{bmatrix}}^{[C]} \cdot \begin{Bmatrix} \dot{u}_1 \\ \dot{v}_1 \\ \dot{u}_2 \\ \vdots \\ \dot{u}_{2n-1} \\ \dot{v}_{2n-1} \\ \dot{u}_{2n} \end{Bmatrix} \tag{15}$$

$$\{\dot{X}\} = [C]\{\dot{U}\} = [C]([K] + [A])^{-1}\{D\} \tag{16}$$

The time derivative friction forces vector $\{\dot{F}_f\}$ is expressed by casting Eq. (13) in matrix form:

$$\begin{Bmatrix} \dot{F}_{f1} \\ \dot{F}_{f2} \\ \vdots \\ \dot{F}_{f2n-1} \\ \dot{F}_{f2n} \end{Bmatrix} = \overbrace{\begin{bmatrix} k_t & 0 & & & \\ 0 & k_t & & & \\ & & \ddots & & \\ & & & k_t & 0 \\ & & & 0 & k_t \end{bmatrix}}^{[B]} \cdot \begin{Bmatrix} \dot{u}_1 \\ \dot{u}_2 \\ \vdots \\ \dot{u}_{2n-1} \\ \dot{u}_{2n} \end{Bmatrix} - \begin{Bmatrix} g_1 \\ g_2 \\ \vdots \\ g_{2n-1} \\ g_{2n} \end{Bmatrix} \tag{17}$$

$$\{\dot{F}_f\} = [B]\{\dot{X}\} - [C]\{D\} \tag{18}$$

With these notations the friction forces can then be expressed by using Eq. (16):

$$\{\dot{F}_f\} = ([B][C]([K] + [A])^{-1} - [C])\{D\} = [G]\{D\} \tag{19}$$

In the system of $2n$ differential equations (19), $[G]$ is a full scalar matrix and $\{D\}$ contains the normal loads. The g part of the friction forces renders the system of first order differential equations highly nonlinear. The numerical integration is then performed by using Gear's stiff method. The method can be made very efficient by providing an analytically calculated Jacobian matrix [18].

2.3 Integration of the Model in a Foil Bearing Prediction Code. An existing gas bearing prediction code has been adapted to include the structural deformation of foil air bearings. This code allows the numerical solution of the compressible Reynolds equation in the frame of the finite volume method of discretization. An original aspect of the numerical solution is an upwind procedure borrowed from aerodynamics [20].

For the foil bearing prediction code, it is assumed that the top foil and the corrugated sheet remain in contact. The boundary conditions for the fluid film pressure are as follows:

$$P\left(z = -\frac{L}{2}, \theta\right) = P\left(z = \frac{L}{2}, \theta\right) = P(z, \theta = \theta_{\text{soud}}) = P_{\text{ref}} \tag{20}$$

The coupling between the fluid film and the deformable structure takes place in the expression of the film thickness. Most of the results present in literature use a bump static stiffness K_S to calculate this film thickness:

$$h_i = C_0 - C_0\varepsilon \cos(\theta_i - \varphi) + \frac{P_i - P_{\text{ref}}}{K_S} \tag{21}$$

Frequently this static stiffness is determined for a single bump without taking into account the interactions between the bumps [3,8].

Since the model developed in this paper gives directly the displacements of the top of the bumps, its integration in the foil bearing code is relatively simple. The average pressure on a bump is calculated for each iteration step in the resolution of the Reynolds equation. These loads are then applied to the structural model, which gives in return the vertical (or radial) displacements of the top of the bumps (v_i). The deflections of the structure δ_i can then be expressed in the center of the mesh cells by linear interpolation.

$$h_i = C_0 - C_0\varepsilon \cos(\theta_i - \varphi) + \delta_i \tag{22}$$

The clearance C_0 is a not well defined parameter for foil bearings. For instance, if there is interference between the shaft and the top foil (preload), the clearance does not exist in the usual sense. In the present paper it is assumed that the foil bearing has no preload and an initial clearance C_0=31.8 μm.

3 Results

3.1 Stationary Analysis. There are very few published experimental data allowing the validation of foil bearing prediction codes. In 1978, Ruscitto et al. presented the experimental minimum film thickness of a first generation foil bearing as function of the applied static load [21]. The dimensions, the geometry, and the working conditions of the foil bearing are given in Table 1.

The results obtained with the n degrees of freedom (NDOF) model are compared in Figs. 6 and 7 to the experimental data from Ref. [21] as well as with the theoretical results from Ref. [10] obtained by using Iordanoff's formula. The coordinate system of the bearing and the angular location of the top foil's spot weld are shown in Fig. 1. The welding is thus located at 180 deg (upward), i.e., at the opposite of the static load, which is oriented downward. Two rotating speeds of the shaft are considered: 30,000 rpm (Fig. 6) and 45,000 rpm (Fig. 7).

Figures 6 and 7 depict the minimum film thickness versus the load. The correlation is satisfactory for moderate to heavy loads, but discrepancies are obtained for light loads where the structure plays a less significant role. Although the structural models are totally different, few differences on the minimal film thickness appear between the theoretical results from Ref. [10] and those obtained with the NDOF model. This should not be interpreted as if the structural models have no influence on the calculated bear-

Downloaded 02 Jun 2010 to 171.66.16.109. Redistribution subject to ASME license or copyright; see http://www.asme.org/terms/Terms_Use.cfm

Table 1 Dimensions and working conditions of the foil bearing

Bearing length (mm)	38.1
Bearing diameter (mm)	38.1
Clearance (μm)	31.8
Geometry of the bumps	
Number of strips	1 or 5
Numbers of bumps per strip	26 or 5
Top foil welding angle (Fig. 1)	180 deg
Foil thickness (μm)	102
Pitch (mm)	4.572
Bump half length (mm)	1.778
Initial bump height (mm)	0.508
Bump foil Young's modulus (GPa)	214
Bump foil Poisson's ratio	0.29
Friction coefficient (if not indicated)	0.1
Working conditions	
Rotation speed (if not indicated) (rpm)	30 000
Dynamic viscosity of the air (Pa s)	1.82×10^{-5}
External pressure (Pa)	10^5

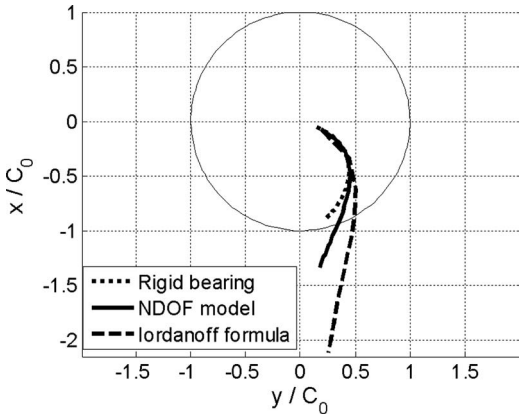


Fig. 8 Static equilibrium locus curve—influence of the structural model

ing characteristics. Figure 8 represents the static equilibrium locus curve of the foil bearing and of a rigid bearing having the same initial clearance. The foil bearing structure is modeled either by using Iordanoff's formula (no bump interactions) or by using the NDOF model (taking into account the interactions between the bumps). The static load varies from 10 N to 260 N and the initial clearance, which constitutes an impassable limit for the rigid bearing, is represented by the thin line.

The two prediction methods give different results. A soft structure, as the one obtained by neglecting the bump interactions, allows reaching eccentricity ratios much larger than unity. The stiffer is the structure, the smaller is the maximal eccentricity before contact.

3.2 Nonlinear Stability Analysis. To perform a nonlinear transient analysis of the bearing, the unsteady pressure field and the dynamic displacements of the structure have to be calculated at each time step. Pressures are obtained from the numerical solution of the transient and compressible Reynolds equation:

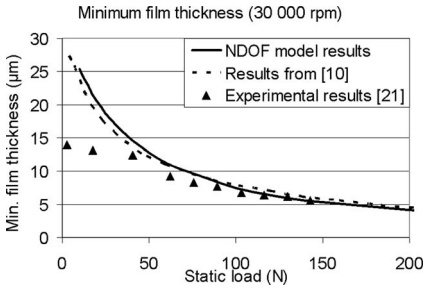


Fig. 6 Minimum film thickness at 30,000 rpm

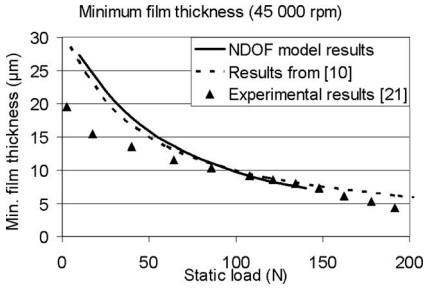


Fig. 7 Minimum film thickness at 45,000 rpm

$$\frac{\partial}{\partial x}\left(\frac{ph^3}{12\mu}\frac{\partial p}{\partial x}\right)+\frac{\partial}{\partial z}\left(\frac{ph^3}{12\mu}\frac{\partial p}{\partial z}\right)=\frac{\partial}{\partial x}\left(\frac{pVh}{2}\right)+\frac{\partial}{\partial t}(ph) \quad (23)$$

The film thickness, as well as its changing rate, is given by

$$h^{it}=C_0-x^{it}\cos(\theta)-y^{it}\sin(\theta)+\delta^{it} \quad (24)$$

$$\frac{\partial h}{\partial t}=-\dot{x}^{it}\cos(\theta)-\dot{y}^{it}\sin(\theta)+\frac{\delta^{it}-\delta^{it-1}}{\Delta t} \quad (25)$$

The dynamic deflections of the structure δ and the pressure must be determined simultaneously. To do so, the dynamic NDOF model is solved between the initial time t^{it-1} and the final time t^{it} for each iteration on the Reynolds equation. The initial conditions at t^{it-1} are the friction forces obtained at the previous time step. To solve the differential system of equations, the loading forces acting on the bumps must be accessible for every $t\in[t^{it-1},t^{it}]$. Therefore, it is supposed that the pressure variation between t^{it-1} and t^{it} is linear:

$$N(t)=N^{it-1}+\frac{N^{it}-N^{it-1}}{\Delta t}(t-t^{it-1}) \quad (26)$$

$$\dot{N}(t)=\frac{N^{it}-N^{it-1}}{\Delta t} \quad (27)$$

where the normal loads N^{it} are updated at each iteration of the Reynolds equation.

The stability analysis is performed by using the orbit method. The shaft is supported by two identical foil bearings (given in Table 1) and is supposed to be rigid, symmetric, perfectly aligned, and to have a total mass $2M$. Its initial location is far from the equilibrium position. After some rotating periods, the journal will either reach its static equilibrium position, or describe some limit cycles, or have some oscillatory motions increasing until the contact with the top foil occurs. The trajectories of the journal center are calculated from the equations of motion:

$$M\begin{Bmatrix}\ddot{x}\\ \ddot{y}\end{Bmatrix}+\begin{Bmatrix}F_x\\ F_y\end{Bmatrix}=\begin{Bmatrix}W_0\\ 0\end{Bmatrix} \quad (28)$$

3.2.1 Fixed Equilibrium Position. The static equilibrium position is first imposed by a fixed static load (W_0=50 N) at a constant rotation speed (30,000 rpm), and different rotor masses are considered. For instance, this case may be encountered for a vertical machine tool where the static load comes from the machining resistant force. With a fixed static load, the loaded bearing is stable even if the rotor mass is very low. When the rotor mass exceeds a certain value (critical mass), the bearing then becomes

Downloaded 02 Jun 2010 to 171.66.16.109. Redistribution subject to ASME license or copyright; see http://www.asme.org/terms/Terms_Use.cfm

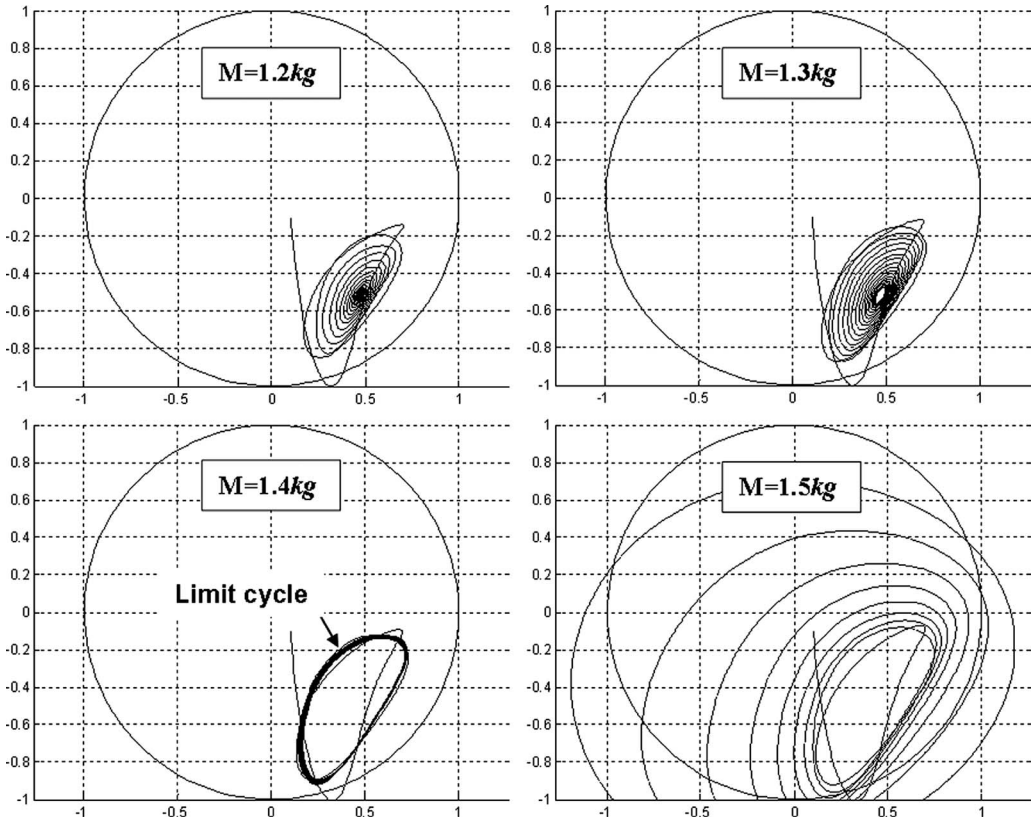


Fig. 9 Foil bearing stability, single strip without friction, μ_f=0

unstable.

The first stability analysis is performed for a single strip constituted of 26 bumps with no friction (μ_f=0) and the results are depicted in Fig. 9. The first observation is that the structural deformation, without energy dissipation, strongly enhances the bearing stability. Indeed the critical mass is around 1.4 kg (limit cycle) whereas the critical mass of a rigid bearing with the same initial clearance is 1.1 kg, which represents a gain of 22%.

The influence of the dry friction on the foil bearing stability is shown in Fig. 10. Logically, the dry friction within the structure contributes to the foil bearing stability by dissipating some energy out of the system. The critical mass is now around 1.8 kg, which represents another gain of 22%.

The same analysis was repeated for different friction coefficients values, up to μ_f=0.5. An increase in the value of the friction coefficient from 0.1 to 0.2 leads to a larger critical mass of 1.9 kg. However, the results are almost identical for μ_f=0.2 and μ_f=0.3. For larger values of the friction coefficient, the critical mass slightly decreases, which leads to the existence of an optimal friction coefficient for the bearing stability.

A similar behavior was obtained for a foil bearing constituted of five strips along the circumference, containing five bumps each (Table 1). The results for both foil bearings are summarized in Fig. 11. In this example, few differences are observed between the single strip case and the multiple strip case. Both bearings exhibit an optimal friction coefficient around 0.2–0.3.

The influence of the top foil's spot weld location has also been addressed. The coordinate system used to define this location is depicted in Fig. 1. Four spot weld locations have been tested (0 deg, 90 deg, 180 deg, and 270 deg) for both bearings (respectively, with one and five strips). The friction coefficient is fixed at μ_f=0.1 and the mass of the shaft at M=1.8 kg. The results for the bearing constituted of a single strip are represented in Fig. 12.

It clearly appears that the spot weld location plays an important role for the bearing stability. The bearing is at the stability limit when the spot weld is located at 180 deg (upward). A welding point located at 90 deg (on the right hand side) renders the bearing stable whereas a welding point located at 270 deg (on the left hand side) renders the bearing unstable. When the spot weld is located at 0 deg (downward), the bearing cannot support the 50 N static load because of the imposed pressure boundary condition at the weld point. The same influence of the spot weld location has also been observed for the bearing constituted of five strips. The only configuration that allows both bearings to be close from the stability limit is the upward position (180 deg) of the top foil welding point.

Therefore, in the case of a single top foil, it should be preferable to put the welding in the diverging zone, i.e., between 90 deg and 180 deg. Some extended simulations also showed that these spot weld locations allow reaching the maximum load capacity for a given minimum film thickness.

3.2.2 Variable Equilibrium Position. In this subsection, the static load imposed to the bearing comes only from the shaft weight $W_0=Mg$, and the stability analysis is performed by varying M or Ω. The first investigation for the single strip bearing was to find the critical mass of the rotor at a given constant rotation speed (30,000 rpm). The process remains identical and the results are presented in Fig. 13.

The critical mass represents the minimum mass of the rotor, which leads to a stable behavior of the bearing. The presence of dry friction allows a gain of 19% by reducing the critical mass to M=5.65 kg for μ_f=0.15 instead of M=6.95 kg for μ_f=0. The existence of an optimal friction coefficient also appears in this figure. Under the same conditions, the calculated critical mass of a rigid bearing with the same initial clearance is 9.05 kg.

The second investigation was to find the threshold speed of instability of the single and multiple strip bearings for a given shaft mass of M=5 kg. The results are depicted in Fig. 14 as function of the friction coefficient.

Downloaded 02 Jun 2010 to 171.66.16.109. Redistribution subject to ASME license or copyright; see http://www.asme.org/terms/Terms_Use.cfm

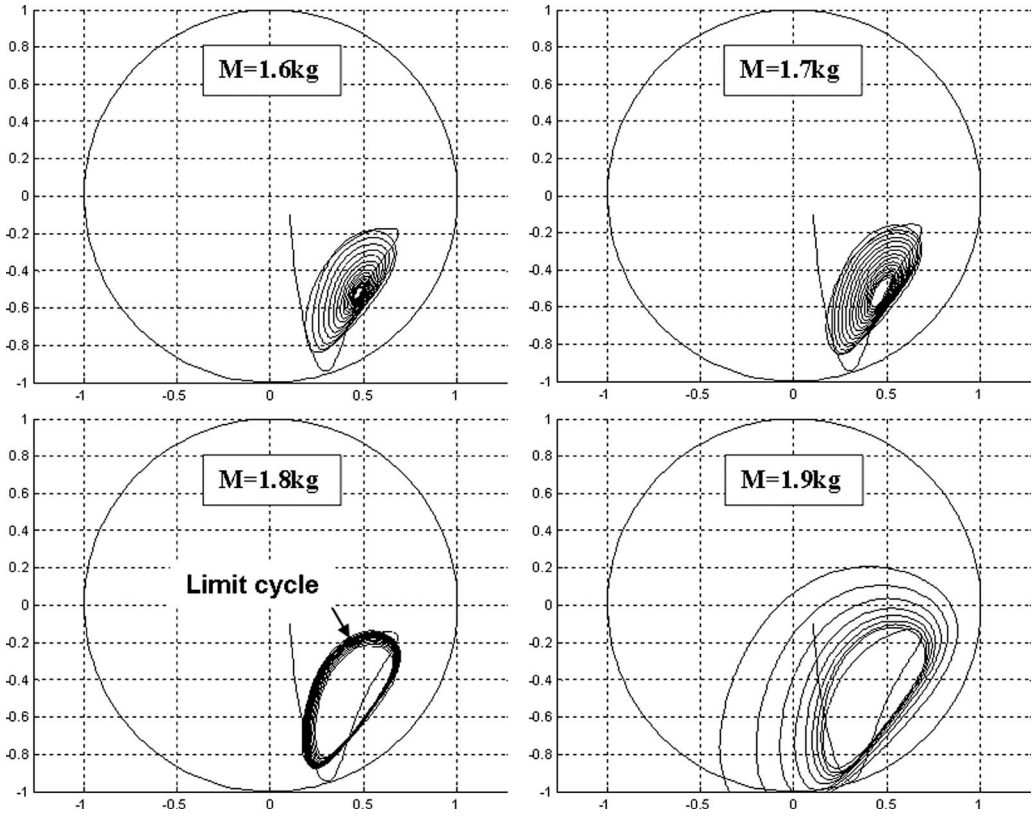


Fig. 10 Foil bearing stability, single strip with friction, μ_f=0.1

Although the global shape of the two curves is the same, some differences appear according to the type of structure (number of corrugated strips) studied. In this sample case, the optimal friction coefficient seems so be around μ_f=0.25 for the single strip bearing and around μ_f=0.35 for the five strip bearing.

3.3 Nonlinear Unbalanced Response. The unbalanced responses of the two foil bearings are calculated by solving the following equations of motion:

$$M\begin{Bmatrix}\ddot{x}\\ \ddot{y}\end{Bmatrix}+\begin{Bmatrix}F_x\\ F_y\end{Bmatrix}=\begin{Bmatrix}W_0\\ 0\end{Bmatrix}+Me_b\Omega^2\begin{Bmatrix}\cos(\Omega t)\\ \sin(\Omega t)\end{Bmatrix} \quad (29)$$

3.3.1 Arbitrary Static Load. The equilibrium position is first considered to be defined by W_0=50 N at 30,000 rpm and the rotor mass is fixed at M=0.5 kg, which ensures a stable operation. The relative eccentricity e_b/C_0 of the mass unbalance varies from 0.01 to 0.5. These unbalance values are used to investigate the foil bearing behavior from low unbalance conditions, corresponding to a well balanced rotor, to ultimate unbalance conditions, leading to the contact and probably to the destruction of the bearing. The results will then allow a comparison between the foil bearing and the rigid bearing dynamic load capacities.

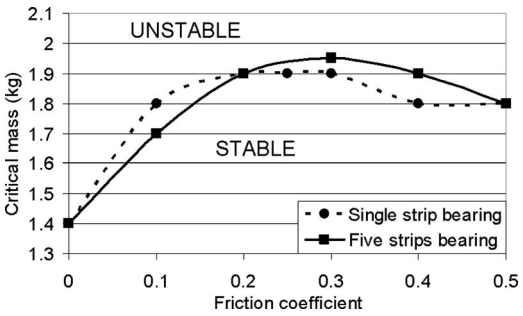


Fig. 11 Influence of the friction coefficient on the foil bearing stability

Simulations are performed from the equilibrium position for 20 shaft revolutions with 512 time steps per period. The trajectories of the shaft center for the last three revolutions are plotted in order to visually check that the limit cycle is obtained. For a foil bearing, the journal center can exceed the initial clearance circle because of the structural deflection. The results obtained for the single strip bearing are shown in Fig. 15.

An important gap exists between the response obtained for e_b =0.4C_0 and the one obtained for e_b=0.45C_0. This jump is evidenced in Fig. 16 where the relative vibration amplitudes (along the vertical axis $|X|/C_0$ and along the horizontal axis $|Y|/C_0$) are plotted as function of the mass unbalance.

The same study was performed for the five strip bearing, and the resulting trajectories are plotted in Fig. 17. For the eccentricity values of e_b=0.45C_0 and e_b=0.5C_0, a contact between the shaft and the top foil occurs rapidly (the calculated minimal film thickness is below an arbitrary value of 1 μm). However the fact that, at a given time step, the minimum film thickness is slightly smaller for the five strip bearing does not allow to conclude that its dynamic load capacity is smaller than the one of the single strip bearing.

This bearing analysis shows a special feature because the shaft motion is asynchronous for unbalances e_b=0.3C_0 and e_b =0.35C_0, needing two revolutions to describe its limit cycle. In Fig. 17, the unbalanced response for e_b=0.3C_0 is marked with the black dots, the unbalanced response for e_b=0.35C_0 is marked with the white dots, and the circle corresponding to the initial clearance is plotted with the thick line.

The calculated trajectories for e_b=0.3C_0 and e_b=0.35C_0 remain asynchronous, whatever the number of simulated revolutions (up to 120). Their Poincaré maps are given in Fig. 18, showing a

Downloaded 02 Jun 2010 to 171.66.16.109. Redistribution subject to ASME license or copyright; see http://www.asme.org/terms/Terms_Use.cfm

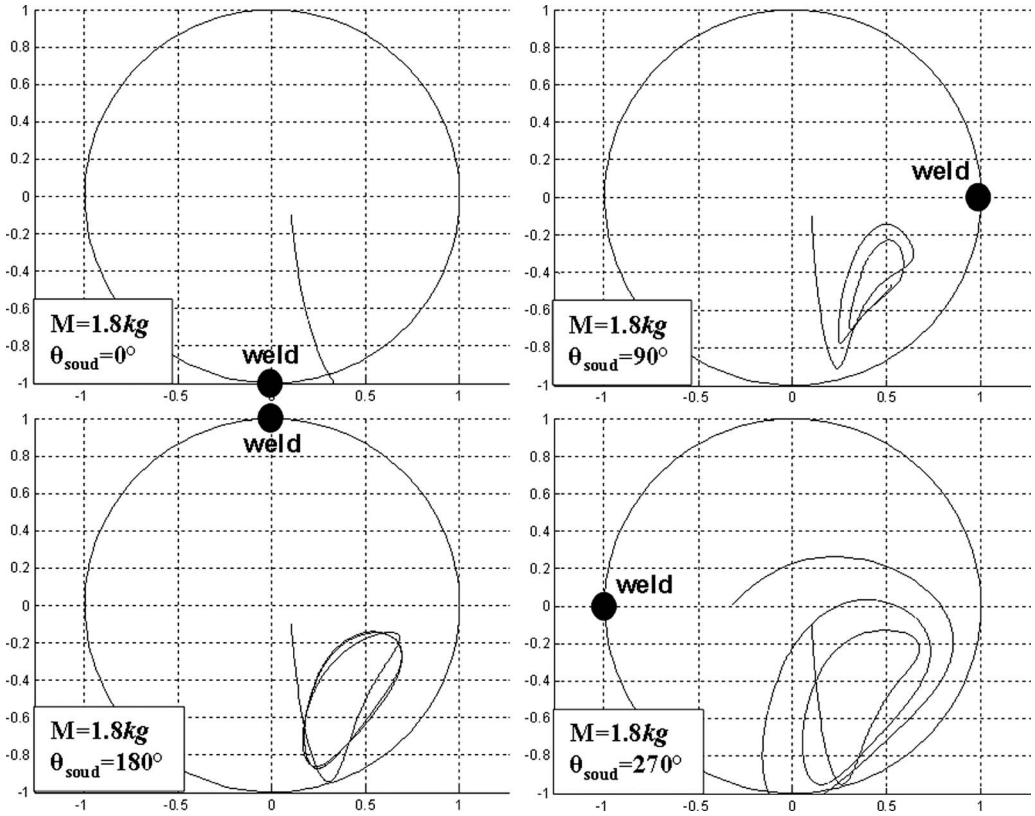


Fig. 12 Influence of the spot weld location on the foil bearing stability, single strip

typical two-frequency signature.

A fast Fourier transform (FFT) analysis of the motions along $\vec{X}$ and $\vec{Y}$ shows that other frequencies exist in addition to the synchronous one (500 Hz) and vary with the mass unbalance values. These additional frequencies are mainly $\Omega/2=250$ Hz and $2\Omega=1000$ Hz. Other subsynchronous frequencies also exist but remain small for all mass unbalance values.

The amplitudes of these three main frequencies are detailed in Fig. 19 as function of the mass unbalance. For more readability, the values of the 500 Hz component are given on the right vertical axis and those of the 250 Hz and 1000 Hz are given on the left vertical axis (different orders of magnitude).

An important increase in the $\Omega/2=250$ Hz component is observed just before the nonlinear response jump. This increase is responsible for the asynchronous trajectories obtained for $e_b=0.3C_0$ and $e_b=0.35C_0$. The FFT analysis also describes an increase in the component $2\Omega=1000$ Hz with the unbalanced load. Once the response jump has occurred, the motion of the shaft becomes synchronous again. To sum up, Fig. 20 depicts the maximum amplitude of motion, defined by $(\sqrt{|X|^2+|Y|^2})/C_0$, as function of the unbalance load for both foil bearings and for a rigid bearing with an identical initial clearance.

The response jump of both foil bearings occurs for more important unbalance levels (>50%) than the response jump of the rigid bearing. This jump, which was also described in Ref. [22], seems to be a general characteristic of circular bearings. It can lead to a contact between the journal and the bearing, resulting in the destruction of the system. From this point of view, both foil bearings exhibit a better dynamic behavior than the rigid bearing. As for the stability analysis, few differences are observed between the single strip and the five strip foil bearings (the inclination angles of the elliptical trajectories are, however, not the same). It

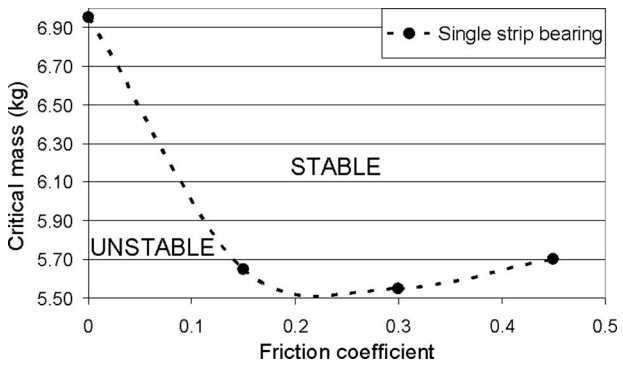


Fig. 13 Influence of the friction coefficient on the critical mass, 30,000 rpm, static load $W_0=Mg$

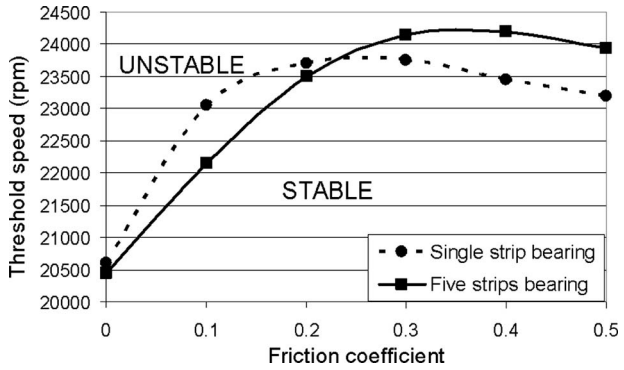


Fig. 14 Influence of the friction coefficient on the threshold speed of instability, $M=5$ kg, $W_0=Mg$

Downloaded 02 Jun 2010 to 171.66.16.109. Redistribution subject to ASME license or copyright; see http://www.asme.org/terms/Terms_Use.cfm

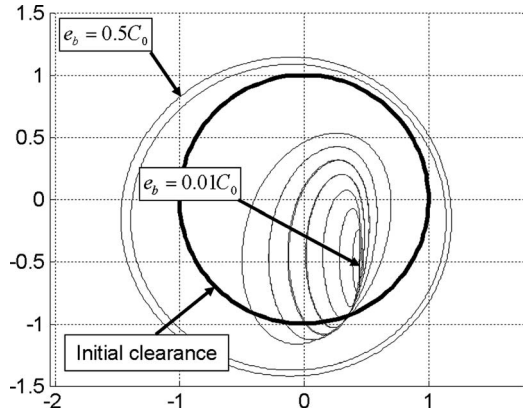


Fig. 15 Foil bearing nonlinear unbalanced response (single strip)

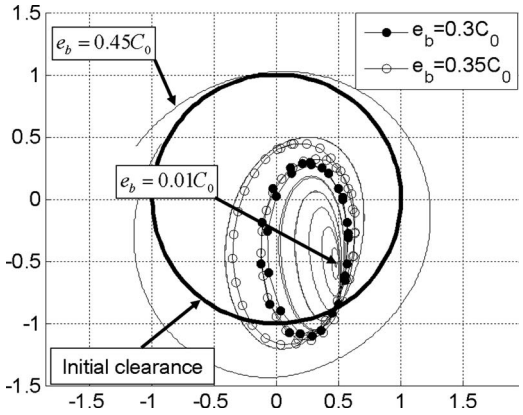


Fig. 17 Foil bearing nonlinear unbalanced response (five strips)

was shown in a previous paper that the dynamic behavior under uniform pressure distribution of two five-bump strips is better than the dynamic behavior of a single ten-bump strip [8]. This result suggests that, depending on the studied case, several strips will lead at least to the same dynamic behavior and maybe to an improved one.

3.3.2 Static Load Due to the Rotor Weight. In this last subsection, the static load is considered to be generated only by the rotor mass ($M=5$ kg). A stable case for the foil bearing and for the rigid bearing corresponds to $\Omega=18{,}000$ tr min^{-1}. The unbalanced eccentricity values used for the five strip bearing lie between $e_b/C_0=0.01$ and $e_b/C_0=0.125$. The journal trajectories are depicted in Figs. 21 and 22.

For the last unbalanced value $e_b/C_0=0.125$, the shaft has a complex motion and finally touches the structure after several revolutions (Fig. 22). The FFT analysis of the journal motions along $\vec{X}$ and $\vec{Y}$ is represented in Fig. 23. The synchronous component (300 Hz) clearly appears on these Fourier decompositions. Nevertheless, a subsynchronous component (100 Hz), less than $\Omega/2$, exists and has a greater magnitude value than the synchronous one (in the former example, Fig. 19, the subsynchronous frequency amplitudes remained always an order of magnitude less than the synchronous frequency amplitude). In this case, the mass unbalance may have activated the hydrodynamic instability of the bearing whereas the static equilibrium position was theoretically stable. However, other dynamic effects could be responsible for this subsynchronous frequency, and some deeper investigations have to be performed with some more elaborate nonlinear analysis tools.

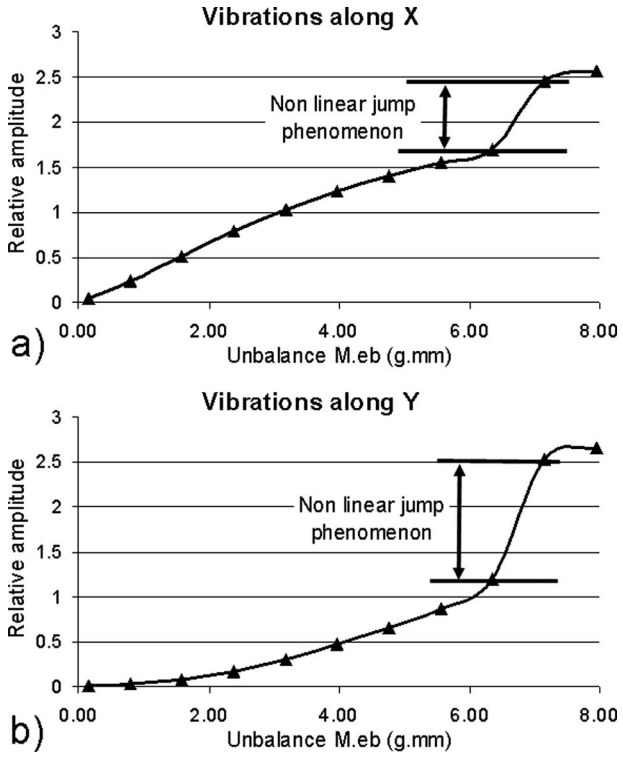


Fig. 16 Foil bearing nonlinear unbalanced response (single strip), nonlinear jump phenomenon

Figure 24 depicts the maximum amplitude of motion, still defined by $(\sqrt{|X|^2+|Y|^2})/C_0$, as function of the unbalanced load either for the five strip foil bearing or for the rigid bearing. For these working conditions, the foil bearing can once again support 50% higher unbalance levels than the rigid bearing. According to the ISO 1940/1 (which is more permissive than the API 617), a balance quality grade G2.5 leads to a permissible residual unbalance of 13.26 g mm. This value is located at the beginning of the rigid bearing jump, thus indicating that, for this given dynamic load, it should be safer to use a foil bearing.

4 Summary and Conclusions

An analytical model of the structure, fully developed and validated in former papers, has been implemented in a foil bearing prediction code. This model offers two main advantages that consist in taking into account the entire corrugated foil behavior and in considering the nonlinear behavior of dry friction.

The results concerning the foil bearing stationary behavior were compared with those obtained by considering the bumps as independent springs. The minimum film thickness predicted by both models agrees reasonably with experimental data taken from literature. On the other hand, important differences appear between the two models, notably on the predicted maximal eccentricity that can be reached before contact.

An important aspect of the NDOF model is that it allows performing dynamic simulations without the need to introduce other parameters than the value of the friction coefficient. Depending on the studied case, the simulations then take a few minutes to 1 h on a standard personal computer (PC).

The stability analysis has first evidenced that the structural deflection itself renders the bearing much more stable than a rigid bearing of same initial clearance. The introduction of dry friction then allows doubling this stability gain. Two kinds of bearings have been studied (single strip and five strips along the circumference), and they both show the existence of an optimal friction coefficient that maximizes the bearing stability.

Downloaded 02 Jun 2010 to 171.66.16.109. Redistribution subject to ASME license or copyright; see http://www.asme.org/terms/Terms_Use.cfm

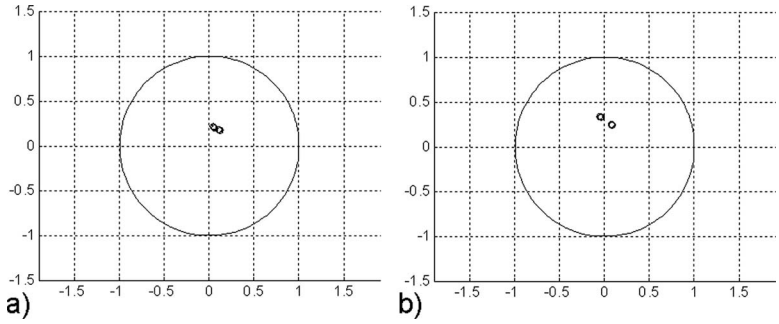


Fig. 18 Poincaré maps obtained for unbalanced values of (*a*) $e_b=0.3C_0$ and (*b*) $e_b=0.35C_0$

The unbalanced responses show a nonlinear step when the unbalanced load exceeds a certain limit. This jump can lead to the contact between the shaft and the top foil and hence can lead to the destruction of the system. The physical origins of this nonlinear jump phenomenon are still not well established and some extended investigations, using more elaborate analysis tools, could lead to some interesting information. Generally, the journal trajectories remain synchronous once this jump has occurred. However, for the five strip bearing, a 1/3 subsynchronous frequency appeared for high unbalanced load. Finally, all numerical cases demonstrated that the foil bearings can accept much larger unbalances than the rigid one.

The almost linear evolution of the maximum amplitudes with small unbalance values inevitably leads to the question of the use of linear dynamic coefficients to compute the foil bearing response. The authors have shown in previous papers that the dynamic characteristics of the compressible film and of the foil bearing structure, taken separately, were greatly affected by the excitation amplitude and were therefore nonlinear [18,20]. For the cases studied in this paper, the nonlinearities arising from both the

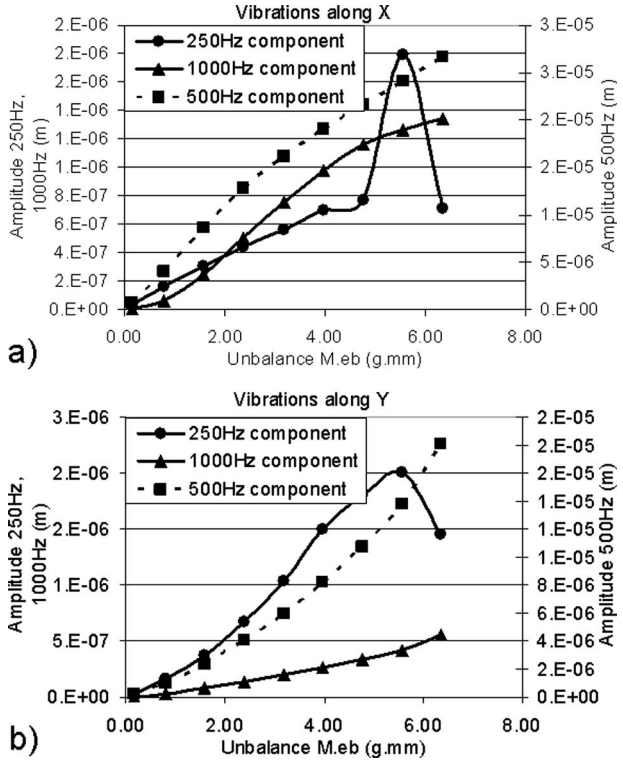


Fig. 19 Foil bearing nonlinear unbalanced response (five strips), FFT analysis

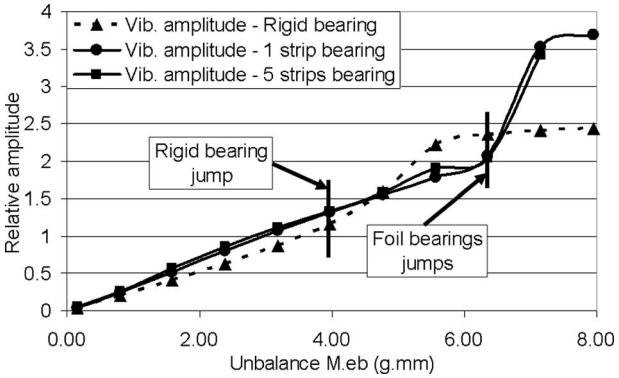


Fig. 20 Unbalanced response for both foil bearings and for the rigid bearing

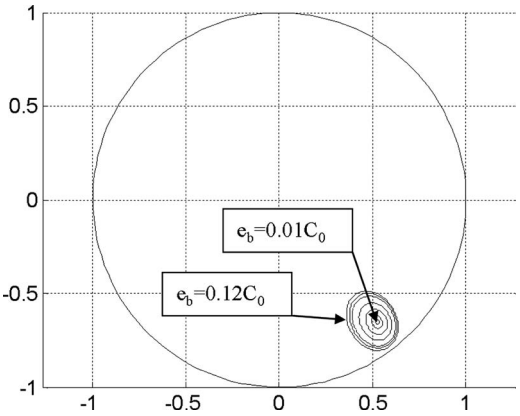


Fig. 21 Foil bearing nonlinear unbalanced response (five strips, $\Omega=18{,}000$ rpm)

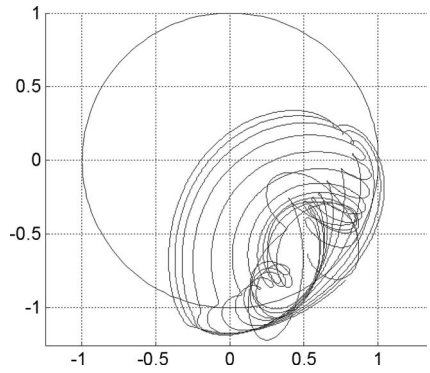


Fig. 22 Shaft trajectory for an unbalanced eccentricity $e_b=0.125C_0$

Downloaded 02 Jun 2010 to 171.66.16.109. Redistribution subject to ASME license or copyright; see http://www.asme.org/terms/Terms_Use.cfm

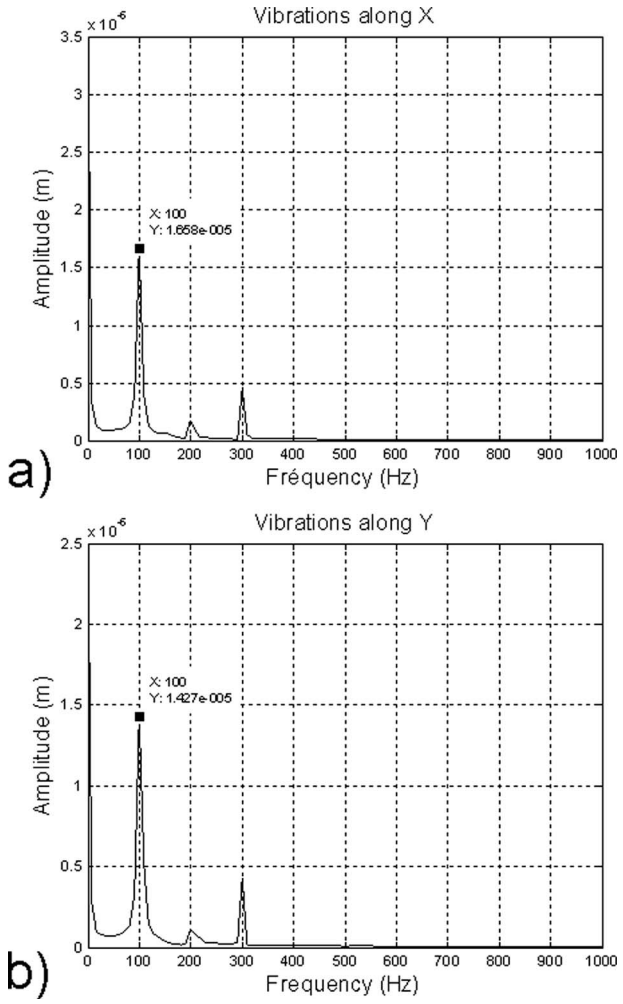


Fig. 23 FFT analysis of the shaft motion, $e_b=0.125C_0$

structure and the fluid film seem to have compensated each other for small unbalance values. Nevertheless it would be hazardous to conclude that these nonlinearities always compensate each other for all the possible designs and operating conditions.

Dynamic coefficients are usually calculated with the small perturbation assumption that considers infinitesimal displacements of the shaft around the static equilibrium position. If nonlinear damping (dry friction) is considered, as in the NDOF model, the dynamic perturbation compared with the static pressure is too low to initiate sliding between the foils. Hence the calculated dynamic coefficients cannot render the dissipative effect of the structure. Alternative methods can be used to compute "dynamic coefficients" as function of the amplitude excitation [23,24]. However, these methods require the orbit size knowledge, which can be exactly determined only by performing nonlinear dynamic analysis. Therefore, the authors would still recommend performing nonlinear dynamic analyses of rotor bearing systems, at least to check the results obtained with the classical rotordynamic force coefficient approach.

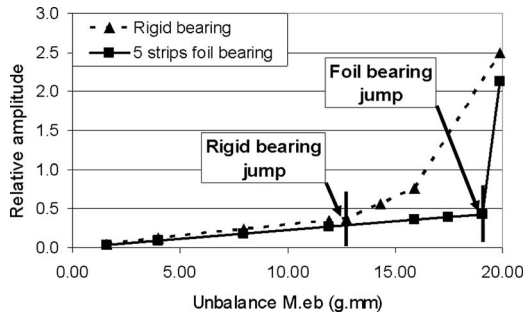


Fig. 24 Unbalanced response for the five strip foil bearing and for the rigid bearing ($\Omega=18{,}000$ rpm)

Acknowledgment

The authors wish to thank Turbomeca and Microturbo as well as MAIA work group for supporting this activity.

Nomenclature

- $A\ 3n\times3n$ = matrix defined by Eq. (12) (N m^{-1})
- $B\ 2n\times2n$ = matrix defined by Eq. (17) (N m^{-1})
- c = cosine of the transmission force angle (=cos(θ_d))
- c_{bis} = cosine of the last bump transmission force angle
- c_t = control parameter for the sign function approximation (s m^{-1})
- $C\ 2n\times3n$ = matrix defined by Eq. (15)
- C_0 = initial bearing clearance (m)
- $D\ 3n$ = vector defined by Eq. (12) (N s^{-1})
- e = foil thickness (m)
- e_b = unbalanced eccentricity (m)
- E_{pot} = potential energy (N m)
- F = external load vector (N)
- F_b = load applied on the bump b (N)
- F_{fi} = friction force at node i (N)
- $F_{x,y}$ = fluid film reaction force in direction $\vec{X},\vec{Y}$ (N)
- g = gravitational acceleration (m s^{-2})
- g_i = functions defined by Eq. (14) (N s^{-1})
- $G\ 2n\times3n$ = matrix defined by Eq. (19)
- h = film thickness (m)
- h_0 = bump height (m)
- k_i = elementary spring stiffness (N m^{-1})
- k_{ibis} = last bump elementary spring stiffness (N m^{-1})
- k_t = asperity stiffness at the contact interface (N m^{-1})
- K = global stiffness matrix (N m^{-1})
- K_{COUP} = coupling stiffness matrix (N m^{-1})
- K_{IND} = individual bump stiffness matrix (N m^{-1})
- K_S = static structural stiffness (N m^{-3})
- l_0 = bump half length (m)
- M = half mass of the rotor (kg)
- n = number of bumps
- N_i = normal load at node i (N)
- P = pressure (Pa)
- P_{ref} = reference pressure (Pa)
- s = sine of the transmission force angle (=sin(θ_d))
- s_{bis} = sine of the last bump transmission force angle
- s_0 = bump pitch (m)
- t = time (s)
- u_i = horizontal displacements of the structure nodes (m)
- U = general coordinate vector (m)
- v_i = vertical displacements of the structure nodes (m)
- V = linear shaft speed (m s^{-1})
- W_0 = static load of the bearing (N)
- x,y = shaft location in the Cartesian coordinate system (m)
- $\dot{X}$ = vector of the node horizontal velocities (m s^{-1})
- Δl_i = elementary spring elongation (m)

Downloaded 02 Jun 2010 to 171.66.16.109. Redistribution subject to ASME license or copyright; see http://www.asme.org/terms/Terms_Use.cfm

Δt = time increment (s)
δ = foil deflection (m)
ε = relative eccentricity
φ = attitude angle (rad)
μ = dynamic viscosity (Pa s)
μ_f = friction coefficient
θ_d = transmission force angle (rad)
θ_{dbis} = last bump transmission force angle (rad)
θ_{soud} = angular position of the top foil spot weld (rad)
θ = angular position (rad)
Ω = rotating speed (rad s^{-1})

Superscript

$\cdot$ = derivative with respect to time

Coordinate Systems

$(\vec{x},\vec{y},\vec{z})$ = cylindrical coordinate system
$(\vec{X},\vec{Y},\vec{Z})$ = Cartesian coordinate system

References

[1] Chen, M. H., Howarth, R., Geren, B., Theylacker, J. C., and Soyars, W. M., 2001, "Application of Foil Bearings to Helium Turbocompressor," *Proceedings of the 30th Turbomachinery Symposium*, Texas A&M University, Houston, TX, September 17–20.

[2] Braun, M. J., Choy, F. K., Dzodzo, M., and Hsu, J., 1996, "Steady-State and Transient Dynamic Simulation of a Continuous Foil Bearing," STLE Tribol. Trans., **39**(2), pp. 322–329.

[3] Heshmat, H., Walowit, J. A., and Pinkus, O., 1983, "Analysis of Gas-Lubricated Foil Journal Bearings," ASME J. Lubr. Technol., **105**, pp. 647–655.

[4] Heshmat, H., Walowit, J. A., and Pinkus, O., 1983, "Analysis of Gas-Lubricated Compliant Thrust Bearings," ASME J. Lubr. Technol., **105**, pp. 638–646.

[5] Walowit, J. A., and Anno, J. N., 1975, *Modern Developments in Lubrication Mechanics*, Applied Science, London, UK, Chap. 7.

[6] Peng, Z. C., and Khonsari, M. M., 2004, "Hydrodynamic Analysis of Compliant Foil Air Bearings With Compressible Air Flow," ASME J. Tribol., **126**, pp. 542–546.

[7] Peng, Z. C., and Khonsari, M. M., 2004, "On the Limiting Load-Carrying Capacity of Foil Bearings," ASME J. Tribol., **126**, pp. 817–818.

[8] Iordanoff, I., 1999, "Analysis of an Aerodynamic Compliant Foil Thrust Bearing: Method for a Rapid Design," ASME J. Tribol., **121**, pp. 816–822.

[9] San Andres, L., 1995, "Turbulent Flow Foil Bearings for Cryogenic Applications," ASME J. Tribol., **117**, pp. 185–195.

[10] Kim, T. H., and San Andres, L., 2005, "Heavily Loaded Gas Foil Bearings: A Model Anchored to Test Data," ASME Paper No. GT 2005-68486.

[11] Kim, T. H., and San Andres, L., 2005, "Analysis of Gas Foil Bearings With Piecewise Linear Elastic Supports," ASME Paper No. WTC 2005-63397.

[12] Ku, C. P., and Heshmat, H., 1992, "Compliant Foil Bearing Structural Stiffness Analysis—Part I: Theoretical Model Including Strip and Variable Bump Foil Geometry," ASME J. Tribol., **114**, pp. 394–400.

[13] Carpino, M., and Talmage, G., 2003, "A Fully Coupled Finite Element Formulation for Elastically Supported Foil Journal Bearings," STLE Tribol. Trans., **46**(4), pp. 560–565.

[14] Carpino, M., and Talmage, G., 2006, "Prediction of Rotor Dynamic Coefficients in Gas Lubricated Foil Journal Bearings With Corrugated Sub-Foils," STLE Tribol. Trans., **49**, pp. 400–409.

[15] Carpino, M., and Talmage, G., 2007, "Sub-Foil Stiffness Effects in Gas Lubricated Foil Journal Bearings," *Proceedings of the STLE Conference*, Philadelphia, May 6–10.

[16] Le Lez, S., Arghir, M., and Frene, J., 2007, "Static and Dynamic Characterization of a Bump-Type Foil Bearing Structure," ASME J. Tribol., **129**, pp. 75–83.

[17] Le Lez, S., Arghir, M., and Frene, J., 2007, "A New Bump-Type Foil Bearing Structure Analytical Model," ASME J. Eng. Gas Turbines Power, **129**(4), pp. 1047–1057.

[18] Le Lez, S., Arghir, M., and Frene, J., 2007, "A New Foil Bearing Dynamic Structural Model," *Proceedings of the STLE/ASME International Joint Tribology Conference*, ASME Paper No. IJTC2007-44110.

[19] Petrov, E. P., and Ewins, D. J., 2004, "Generic Friction Models for Time-Domain Vibration Analysis of Bladed Disks," ASME J. Turbomach., **126**, pp. 184–192.

[20] Arghir, M., Le Lez, S., and Frene, J., 2006, "The Finite Volume Solution of the Compressible Reynolds Equation—Linear and Non Linear Analysis of Gas Bearings," Proc. Inst. Mech. Eng., Part J: J. Eng. Tribol., **220**, pp. 617–627.

[21] Ruscitto, D., Mc Cormick, J., and Gray, S., 1978, "Hydrodynamic Air Lubricated Compliant Surface Bearing for an Automotive Gas Turbine Engine I-Journal Bearing Performance," NASA, Technical Report No. CR-135368.

[22] Adams, M. L., 2001, *Rotating Machinery Vibration*, Dekker, New York.

[23] Carpino, M., and Talmage, G., 2006, "Prediction of Rotor Dynamic Coefficients in Gas Lubricated Foil Journal Bearings With Corrugated Sub-Foils," STLE Tribol. Trans., **49**, pp. 400–409.

[24] Le Lez, S., Arghir, M., and Frêne, J., 2008, "Non Linear Dynamic Analysis of Foil Bearings," *Proceedings of the ISROMAC Conference*, Honolulu, HI, February 17–22, Paper No. ISROMAC12-2008-20082.

Downloaded 02 Jun 2010 to 171.66.16.109. Redistribution subject to ASME license or copyright; see http://www.asme.org/terms/Terms_Use.cfm

C. Hunter Cloud
e-mail: chcloud@BRGmachinery.com
BRG Machinery Consulting,
703 Highland Avenue,
Charlottesville, VA 22903

Eric H. Maslen
e-mail: ehm7s@virginia.edu

Lloyd E. Barrett
e-mail: leb@virginia.edu

University of Virginia,
Charlottesville, VA 22904

Damping Ratio Estimation Techniques for Rotordynamic Stability Measurements

Rotor stability is most commonly estimated using methods derived from a simple single degree of freedom system. When the modes of more complex systems, such as rotors, are closely spaced, we demonstrate that such methods can yield very poor estimates of the modal stability (damping ratio). Multiple output backward autoregression (MOBAR) is proposed as an alternative approach and is demonstrated to yield reasonably accurate estimates of modal damping even when modes are closely spaced. The performance of the MOBAR approach is then examined on an experimental rotor in tilt-pad bearings, demonstrating good performance in a realistic measurement setting.
[DOI: 10.1115/1.2967484]

1 Introduction

Rotordynamic instability is a persistent concern for turbomachinery manufacturers and end-users. Often requiring time-intensive design solutions, self-excited instabilities can affect users in a variety of ways, from costly failures to schedule delays to production losses. Shop testing has long served to help identify rotordynamic problems before reaching the field. While such testing can help verify unbalance response performance and predictions, even full-speed, full-load, pressure testing (ASME PTC 10 Type 1 test) does not provide a clear measurement of a machine's stability level or margin.

To measure stability level, an external excitation must be applied during operation and the response measured. Proven excitation devices, sensors, and data acquisition hardware for conducting the necessary stability tests are all available technologies. Using these measurements, the problem becomes one of how to estimate the damping ratio of the primary mode of interest, typically a rotor's first forward whirling mode. Currently, there is no clear consensus for which stability measurement techniques should be used for rotor systems. No systematic analytical or experimental studies have been performed to quantitatively assess the validity of common test and estimation techniques for stability evaluation. With only a few exceptions, most of the published damping ratio measurements have used single degree of freedom (SDOF) estimation techniques. The limitations of using such SDOF estimators for stability measurements have not been widely discussed in the literature. These gaps must be resolved especially since stability measurements during shop or field testing will certainly grow in practice due to the new stability targets now in place [1].

One objective of this paper is to provide the rotordynamicist with a clear understanding of the limitations of SDOF damping estimation techniques for rotor stability measurements. As an alternative, an existing general-purpose time domain estimation technique—backward autoregression—is introduced. Simulations and application on an experimental rotor system indicate that this technique is an excellent candidate for accurately measuring rotor stability.

Contributed by the International Gas Turbine Institute of ASME for publication in the JOURNAL OF ENGINEERING FOR GAS TURBINES AND POWER. Manuscript received March 31, 2008; final manuscript received April 13, 2008; published online October 10, 2008. Review conducted by Dilip R. Ballal. Paper presented at the ASME Turbo Expo 2008: Land, Sea and Air (GT2008), Berlin, Germany, June 9–13, 2008.

2 Challenges

Our overall objective is to measure or estimate the damped eigenvalues from measurements of an operating rotor system. This objective places our effort in the field of experimental modal analysis or, more generally, system identification. Success in any system identification effort means that proper consideration is given to the testing and analytical needs that a particular structure imposes. From the modal testing perspective, data should be acquired using methods of excitation and response measurement, which minimize alteration of the structure's dynamics [2] and, maximize the signal-to-noise ratio (SNR) of the modes of interest. Modal SNR denotes a mode's response relative to other contributing signals such as noise, other modes, and response due to the ambient excitations. Excitation should be high to maximize modal SNR but low enough to avoid responses so large that nonlinearities become significant.

Rotor systems present several practical modal testing challenges because the rotor must be spinning during the measurement. First, rotation implies significant but unmeasurable internal excitations (unbalance, misalignment, and aerodynamic), which produce additional response in the measurements [3,4]. Second, rotation complicates application of external forcing to the spinning rotor in order to adequately excite the modes of interest [3].

Once the necessary data are acquired, the next step in the system identification process is the modal parameter estimation effort. The selection of the modal parameter estimation technique is considered the most important yet most difficult task of the entire system identification process [5]. Its selection must consider the specific parameters needed for the identification, the type, the availability, and the quality of test data, as well as the system's underlying dynamic behavior and its influence on the parameters.

From the rotor stability perspective, the parameters needed for identification are those that characterize the damped eigenvalue of the mode of interest, typically the rotor's first forward whirling mode. This mode and the other underdamped modes of the system possess a pair of complex conjugate eigenvalues or poles of the form

$$\lambda_i = -\zeta_i\omega_i \pm j\omega_{d_i} = -\zeta_i\omega_i \pm j\omega_i\sqrt{1-\zeta_i^2} \tag{1}$$

in which the real part of the eigenvalue is the product of each i^{th} mode's damping ratio ζ_i and its undamped natural frequency ω_i. The mode's damped natural frequency ω_{d_i} is the frequency at which the mode will freely oscillate.

Consideration of a system's dynamic behavior and its influence on the parameters needed for identification is another key element in the estimation technique selection process. The dynamics gov-

Copyright © 2009 by ASME

Downloaded 02 Jun 2010 to 171.66.16.109. Redistribution subject to ASME license or copyright; see http://www.asme.org/terms/Terms_Use.cfm

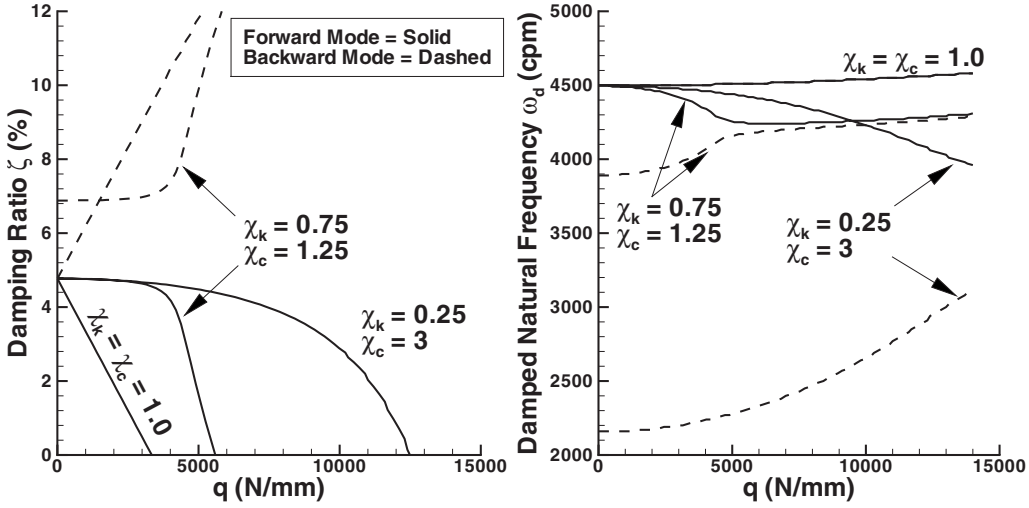


Fig. 1 Rigid rotor stability sensitivity for selected conditions

erning rotor systems require a unique modal analysis treatment due to their asymmetric or non-self-adjoint nature [6]. An even stronger challenge is presented by repeated or close modes, as is a characteristic of rotor systems where sister mode pairs (one forward and one backward) exist.

To examine the effect of closely spaced sister modes' interaction, consider a simple point mass or rigid rotor mounted within a fluid film bearing: a classic rotor system example. With two degrees of freedom, this rotor system exhibits planar whirling motions and is governed by only two modes of vibration. The linearized equations of motion for this system are given by

$$\begin{bmatrix} m_s & 0 \\ 0 & m_s \end{bmatrix} \begin{Bmatrix} \ddot{x} \\ \ddot{y} \end{Bmatrix} + \begin{bmatrix} \chi_c C_{yy} & 0 \\ 0 & C_{yy} \end{bmatrix} \begin{Bmatrix} \dot{x} \\ \dot{y} \end{Bmatrix} + \begin{bmatrix} \chi_k K_{yy} & q \\ -q & K_{yy} \end{bmatrix} \begin{Bmatrix} x \\ y \end{Bmatrix} = \begin{Bmatrix} f_x \\ f_y \end{Bmatrix} \tag{2}$$

in which m_s is the mass of the rotor. Forces acting on the rotor mass may be either independent of rotor motion (f_x and f_y) or motion dependent. Motion dependent or feedback forces are produced by the stiffness and damping characteristics of the bearing. The parameters χ_c and χ_k adjust the level of horizontal to vertical anisotropy by scaling the vertical principle damping C_{yy} and the principle stiffness K_{yy}. For an isotropic system, $\chi_k = \chi_c = 1$.

Motions in the two directions are coupled by the cross-coupled stiffness q. The skew-symmetric character of fluid components is represented by reversing the sign of q in the vertical equation of motion. Positive q in Eq. (2) produces feedback forces, which tend to destabilize the forward whirling mode.

For simplicity and practical purposes, gyroscopics are not considered in this system. Gyroscopic effects tend to be relatively weak for the machines of primary interest here, multistage between-bearing designs. These machines' level of support anisotropy typically dictates the closeness of lower sister modes.

To explore the influence of anisotropy and cross-coupling on system stability, we pursue an example single mass rotor with rotor mass (m_s=0.9 kg), vertical stiffness (K_{yy}=35,024 N/mm (200×10^3 lbf/in.)), and vertical damping (C_{yy}=7 N s/mm (40.5 lbf s/in.)). For simplicity, it is assumed that the bearing's stiffness and damping properties are constant with both rotor speed and motion frequency.

Two combinations of stiffness and damping anisotropy were selected along with the isotropic condition. Figure 1 presents the variation in stability as cross-coupled stiffness is varied. The forward mode's stability variation under these three conditions is typical of industrial rotor systems. The isotropic condition's linear stability variation is typically predicted for a rotor mounted on tilting pad journal bearings with between-pad loading with minimum clearance and maximum preload. With a modest amount of anisotropy in stiffness and damping (χ_k=0.75 and χ_c=1.25), the stability sensitivity curve of the forward mode is similar to a rotor with load-between-pad bearings at maximum clearance and minimum preload. The highly anisotropic condition is typical of a very heavy rotor supported by load-on-pad bearings.

For the case of isotropic stiffness and damping ($\chi_k = \chi_c = 1$), the forward and backward mode damping levels clearly diverge as q is applied. As Wohlrab [7] observed, anisotropy tends to increase stability robustness against cross-coupled stiffness. The isotropic system has a linear stability sensitivity curve with a forward mode stability threshold (ζ=0) near q=3300 N/mm. For the system with moderate anisotropy, the two modes' damping ratios are fairly insensitive to cross-coupling until q=4000 N/mm, where the forward mode's stability begins to quickly decline to its stability threshold of 5600 N/mm.

The two modes' base (q=0) damped natural frequencies are no longer equal in the anisotropic case. However, as cross-coupling is increased, their frequencies converge. At the q level where their damping ratios become very sensitive to q, their natural frequencies are once again nearly equal and remain so.

Frequency response functions (FRFs) were calculated for the three different bearing conditions at the three levels of cross-coupled stiffness. Different types of external forcing were applied to generate the FRFs: directional forcing in the x and y directions and circular forcing in the direction of rotation. The FRFs were calculated relative to the simulated x_p and y_p probes located, respectively, at 45 deg and 135 deg from the horizontal.

Figure 2 presents the isotropic condition's directional FRFs with several levels of cross-coupled stiffness. For brevity, only the FRFs measured by probe x_p due to horizontal forcing are shown. Since this system is isotropic, the other FRFs are identical. Three curves are displayed in each FRF, the forward and backward modes' responses and the total response. The total response is the sum of the forward and backward modes' contributions and represents what would be measured during a test. Modal contributions were calculated by decoupling the equations of motion with the system's left and right eigenvectors [6].

Examining Fig. 2, both modes actually contribute to the response even though only a single peak is present in the measured FRFs. The forward mode's contribution becomes increasingly dominant as the stability threshold is approached. This can be attributed to the cross-coupling's disparate effect on the two modes' ζ levels observed in Fig. 1.

Downloaded 02 Jun 2010 to 171.66.16.109. Redistribution subject to ASME license or copyright; see http://www.asme.org/terms/Terms_Use.cfm

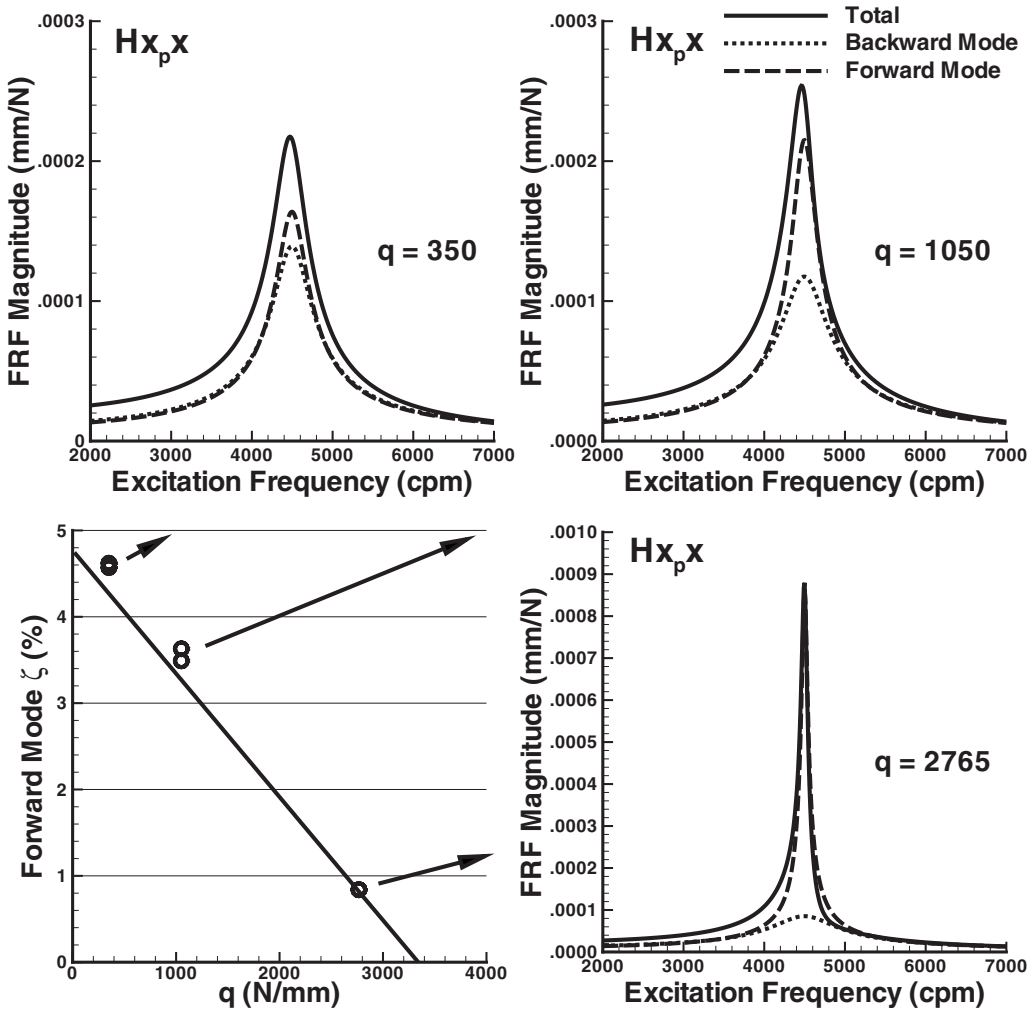


Fig. 2 FRFs for rigid rotor with isotropic bearing and directional excitation

However, many rotor systems are not isotropic. The challenges for a moderately anisotropic system become apparent when observing the FRFs in Fig. 3. Once again, for brevity purposes, only the $H_{x_p x}$ frequency response functions are displayed for each level of cross-coupling q. Even though anisotropy has separated the modes' natural frequencies, only one peak is observed in the measured FRFs. The interaction between the two modes' contributions is heavily dependent on the excitation and response direction. For this system, shaking vertically maximizes the forward mode's response while horizontal perturbation promotes the backward mode.

A popular stability measurement technique is to apply a forward whirling circular excitation to the rotor in an effort to excite the forward mode [8]. However, the circular FRFs in Fig. 4 contradict the commonly held perception that forward circular excitation results in only forward mode response. Unlike the isotropic situation, forcing an anisotropic system in this manner generates response from both modes. Only near the stability threshold does the circular excitation effectively isolate the forward mode contribution.

3 SDOF Damping Estimators

The primary attraction of SDOF estimation techniques is their simplicity. The simplest ones, logarithmic decrement, amplification factor, and phase slope, require little computational effort. Other more elaborate SDOF methods, which involve data curve fitting aspects, are still being developed [9]. Regardless of their complexity, all of them share the fundamental SDOF assumption that the variation in response around a resonance is dominated by one mode of vibration. The contribution of other modes' contribution is assumed to be essentially constant around the resonance [10].

The two most popular SDOF damping estimation techniques are the amplification factor and the logarithmic decrement. The amplification factor uses frequency response measurements. It is defined from the half-power point bandwidth $\Delta\omega_{\mathrm{HP}}$ and the peak resonant frequency ω_r by

$$Q \equiv \frac{\omega_r}{\Delta\omega_{\mathrm{HP}}} \tag{3}$$

It is then easily established that, for a SDOF system, the damping ratio may be computed from Q by

$$\zeta \approx \frac{1}{2Q} \quad \text{for } Q \gg 1 \tag{4}$$

The logarithmic decrement, or log decrement, is based in the time domain. Using a mode's free decay or ring-down response about an equilibrium condition, the log decrement is defined by

$$\delta \equiv \frac{1}{n_{\mathrm{cycle}}} \ln\left[\frac{y(t_0)}{y(t_0 + n_{\mathrm{cycle}} T_d)}\right] \tag{5}$$

where the response amplitude at some time $y(t_0)$ is divided by its corresponding amplitude after undergoing n_{cycle} cycles of vibra-

Downloaded 02 Jun 2010 to 171.66.16.109. Redistribution subject to ASME license or copyright; see http://www.asme.org/terms/Terms_Use.cfm

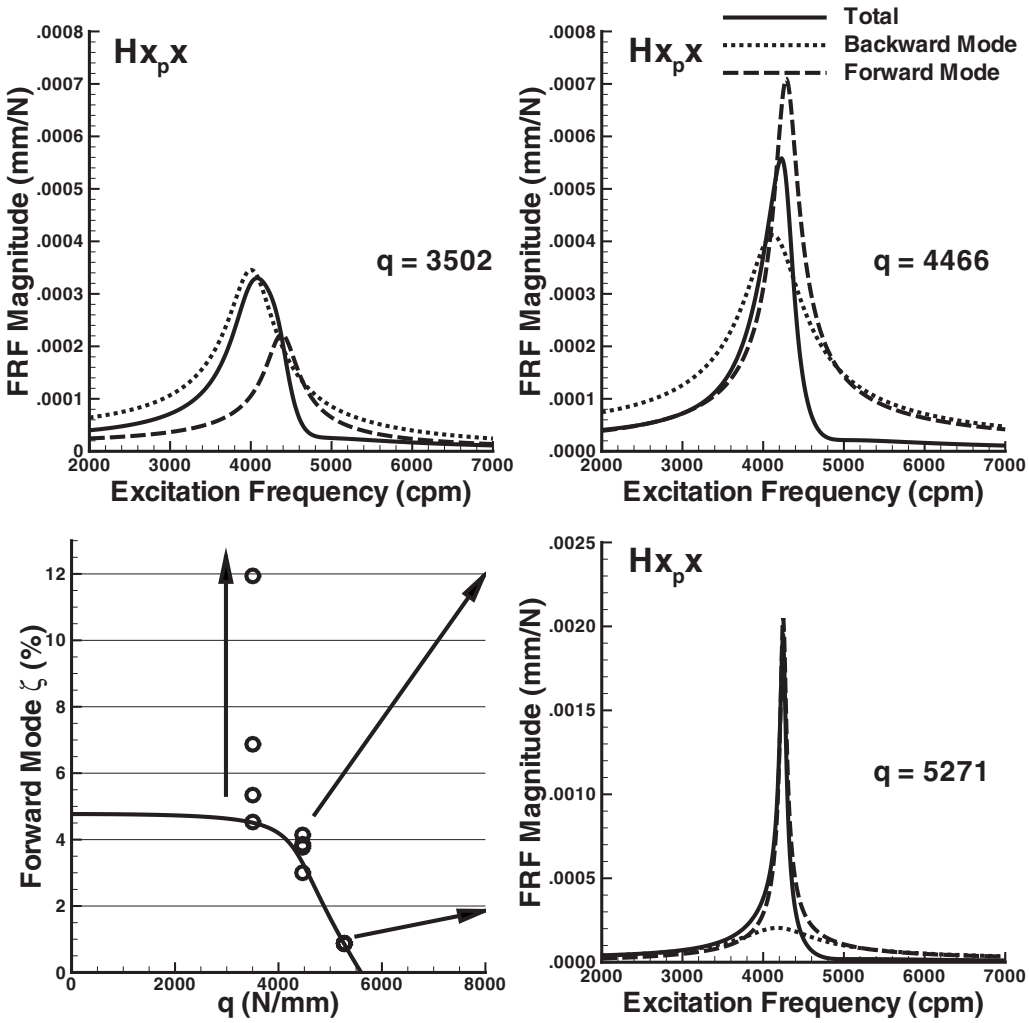


Fig. 3 FRFs for rigid rotor with χ_k=0.75, χ_c=1.25 and directional excitation

tion with period T_d. The damping ratio of the excited mode can be estimated from the log decrement measurement by

$$\zeta = \frac{\delta}{\sqrt{\delta^2 + 4\pi^2}} \tag{6}$$

For light damping, this relationship simplifies to

$$\zeta \approx \frac{\delta}{2\pi} \quad \text{for} \quad \zeta \ll 1 \tag{7}$$

The American Petroleum Institute (API) has chosen log decrement as the stability indicator instead of damping ratio. However, this study will use damping ratio as the *stability level indicator* to avoid confusion with log decrement as a *stability measurement technique*. For reference, API's stability specification requires that a turbomachine must exhibit a predicted log decrement of 0.1 or greater [1]. Using Eq. (6), a log decrement of 0.1 equates to a damping ratio of 0.0159.

To investigate the reliability of these two popular SDOF damping estimators, the simulated rigid rotor system with known eigenvalues will be examined. Although gyroscopic effects are not considered in either system, bearing stiffness and damping anisotropy along with destabilizing cross-coupled stiffness will be varied to examine the SDOF estimates' ability to resolve different stability levels and modal proximity.

Shaking the rigid rotor in both the horizontal and vertical directions produces four FRFs, two for each measurement probe. Therefore, four Q estimates are produced for each level of cross-coupling. Figures 2 and 3 present the resulting amplification factor estimates on the stability sensitivity curves.

For the isotropic bearing condition (χ_k=χ_c=1) with horizontal and vertical excitations, the amplification factor estimates achieve good agreement with the actual stability levels. This is especially true near the stability threshold where the forward mode dominates and the SDOF assumption is valid.

Such consistently accurate estimation is not achieved for the moderately anisotropic condition (χ_k=0.75 and χ_c=1.25) in Fig. 3. Near the stability threshold, the amplification factor estimates are unbiased because the forward mode dominates the response. However, the stability measurements can be very inaccurate at higher stability margins. Such inaccuracy can be attributed to the interaction between the forward and backward sister modes. Figure 4 shows some improvement using forward circular excitation but significant errors in the estimates remain.

Impulses were applied to the rigid rotor system for damping estimation using log decrement. Rotating at 10,000 rpm with a steady-state vibration amplitude of 25.4 μm (1.0 mil) p-p, the rotor was subjected to an impulse large enough to generate a peak transient amplitude of four times the synchronous response.

Figure 5 displays the transient response for the isotropic system where a horizontal impulse generated prominent decaying oscillations. Choosing which successive peaks should be used for the log decrement calculation is not a clear choice. The damping esti-

Downloaded 02 Jun 2010 to 171.66.16.109. Redistribution subject to ASME license or copyright; see http://www.asme.org/terms/Terms_Use.cfm

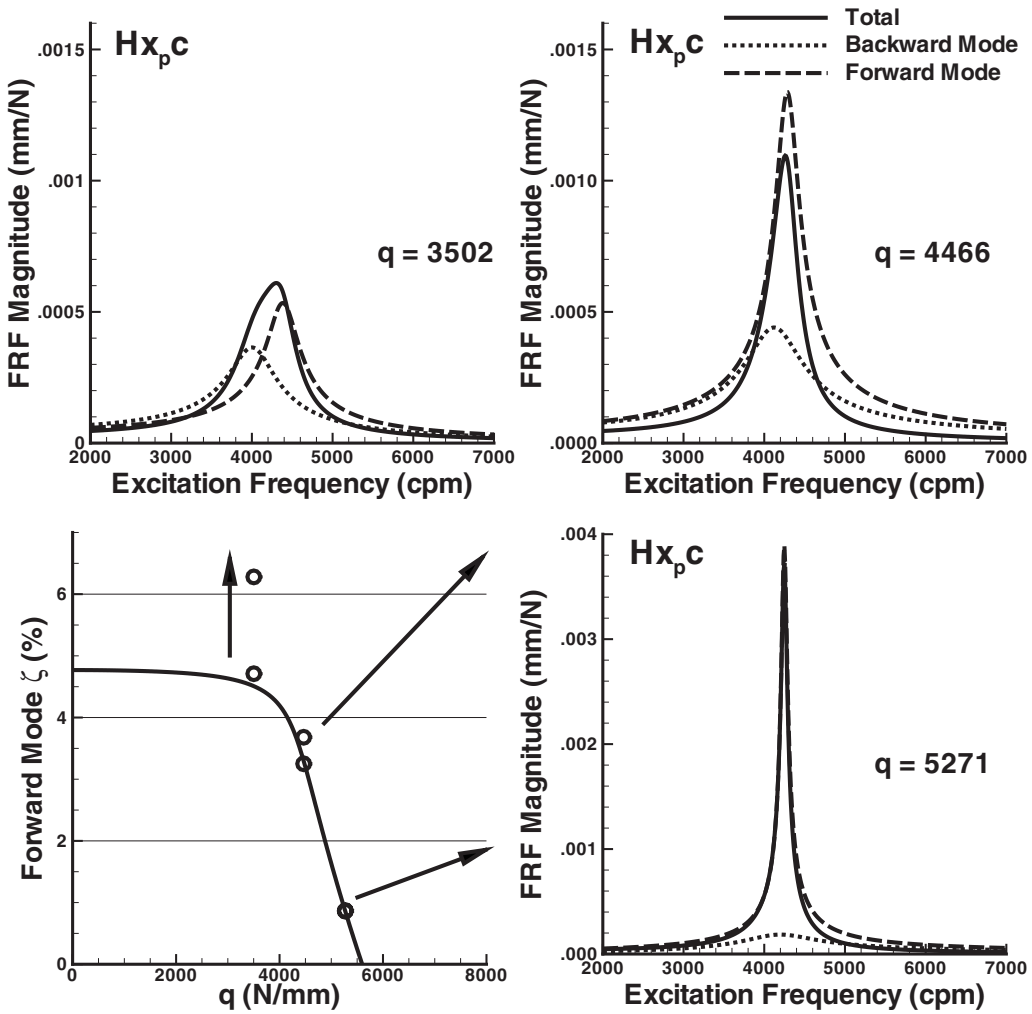


Fig. 4 FRFs for rigid rotor with χ_k=0.75, χ_c=1.25 and forward circular excitation

mates shown are based on the two successive peaks, which occur in the first 25 ms. Relative to the forward mode's actual damping level of 4.27%, the damping ratio estimates using the log decrement in Fig. 5 are poor.

Eliminating the synchronous vibration significantly improves the accuracy of the log decrement estimates: ζ=4.75% for the $x-$ probe and 4.72% for the $y-$ probe. However, even in this idealized analysis where the synchronous response can be exactly removed, some estimation error remains (both measurements should yield ζ=4.27%). This relatively small error is of concern because of the idealistic nature of the simulated test, a test on a system with only two modes, without noise, and with sufficient impulse strength to excite the forward mode. Furthermore, this ideal system lacks other excitations outside the synchronous range. If the steady-state excitation were near in frequency to the modes of interest, it could not be easily filtered. Therefore, any damping estimation error experienced in this ideal situation will likely be amplified when testing a more complex real machine. The same can be said of the amplification factor estimation errors shown earlier.

Overall, this evaluation of Q and δ highlights their difficulties in estimating the stability of even the simplest rotor systems. The amplification factor performs reasonably well for the two extremes of modal proximity, the isotropic and highly anisotropic condition. With appropriate excitation, such performance is expected for the highly anisotropic condition since the modes' frequencies are well separated and there is a little interaction between the forward and backward sister modes.

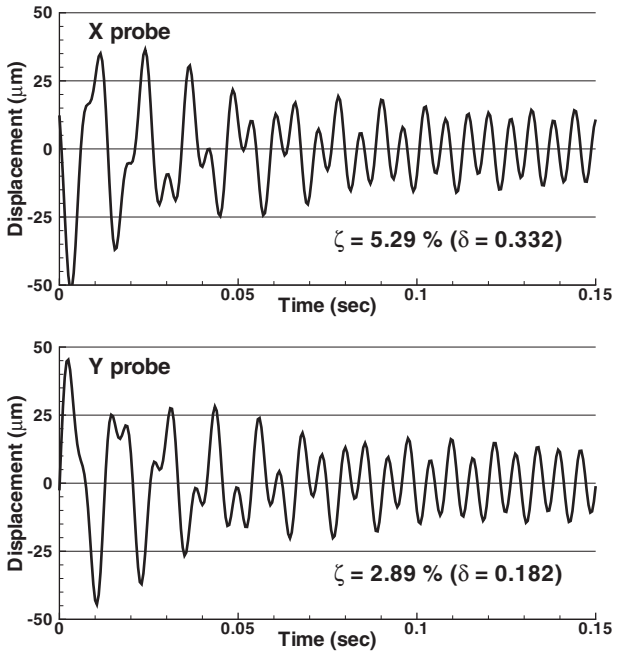


Fig. 5 Rigid rotor probe waveforms due to horizontal impulse (χ_k=χ_c=1, q=350 N/mm)

Downloaded 02 Jun 2010 to 171.66.16.109. Redistribution subject to ASME license or copyright; see http://www.asme.org/terms/Terms_Use.cfm

The amplification factor also achieves good accuracy at the other extreme where the sister modes' frequencies are identical. However, real rotor systems seldom exhibit repeated modes either because the level of q is inadequate or because of gyroscopic effects. Furthermore, Q's accurate damping estimates for the isotropic system are largely due to the fact that the mode of interest here, the first forward mode, is the least damped.

Close modal proximity, as seen in the moderately anisotropic system examined, has long been recognized as the downfall of SDOF techniques, regardless of their complexity [9]. The ever-present potential for close proximity and interaction between rotor's forward and backward sister modes suggests that a multiple degree of freedom (MDOF) parameter estimation technique is needed for reliable rotor stability assessment.

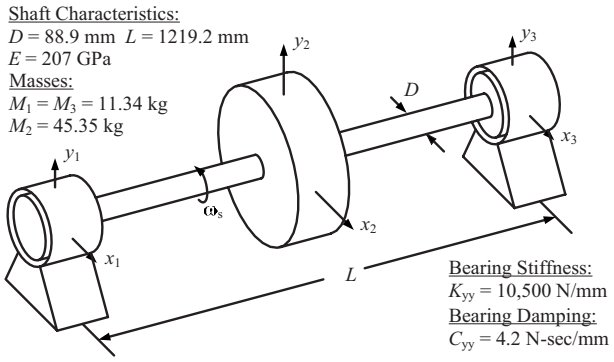


Fig. 6 Three mass rotor system

4 MDOF Time Domain Parameter Estimation

MDOF techniques apply curve fitting processes to the data allowing simultaneous identification of multiple modes. These fitting techniques eliminate the SDOF methods' assumption that the data are dominated by a single mode. With a large number of MDOF techniques available and continually emerging, it is impossible to evaluate all of them. Furthermore, there is no single technique that performs well for all situations [10]. Given these factors, this investigation focused on trying to identify a technique that (1) accommodates rotor systems' non-self-adjoint dynamic structure, (2) can estimate damping ratio accurately for close modes with relatively light damping levels ($\zeta < 10\%$), (3) requires relatively few response output locations, (4) handles noise and internal excitations, and (5) does not require measurement of the test excitation.

MDOF techniques are generally classified as either time domain or frequency domain techniques. In the structural dynamics community, frequency domain techniques are used with wide success. Unfortunately, frequency domain techniques require FRFs where the input excitations are measured. They also suffer from spectral resolution limitations and leakage effects created by the Fourier transform. Spectral resolution is the ability to distinguish the responses of two close signals, clearly an issue for a rotor's potentially close sister modes. In damping estimation, leakage tends to cause overestimation [2].

This investigation was led toward time domain methods by the helicopter community. Helicopter rotor stability measurements pose challenges very similar to those of turbomachinery rotors: Their response contains rotational speed harmonics and the contributions of very close lightly damped modes that are sometimes difficult to excite [11]. Likewise, stability testing time is a critical factor and can be extremely costly. Practical test conditions preclude measurement or precise knowledge of the test excitation. Although measuring test excitation has not been a major concern for turbomachinery stability testing to date (especially with the recent popularity of magnetic actuators), eliminating the need to do so is certainly attractive, especially for field testing.

Autoregression, moving average (MA), and autoregressive moving average (ARMA) are the three fundamental time series analyses applicable to a wide variety of systems and processes. A simple AR model of a noisy discrete sampled output process takes the form

$$y[n] = -a_1 y[n-1] - a_2 y[n-2] - \cdots - a_p y[n-p] + w[n] = -\sum_{i=1}^{p} a_i y[n-i] + w[n] \quad (8)$$

in which $w[n]$ is assumed to be a zero mean white Gaussian noise sequence and p is the order of the model's linear regressors, a_i. The term "autoregression" implies that $y[n]$ is predicted using its own previous values [5]. Using subsequent values instead of prior values (Eq. (8)), a backward AR model takes the form

$$y[n] = -b_1 y[n+1] - b_2 y[n+2] - \cdots - b_p y[n+p] + w[n] = -\sum_{i=1}^{p} b_i y[n+i] + w[n] \quad (9)$$

where b_i are the backward regression parameters. Using N samples, a system of linear equations can be solved to determine these regression parameters, which form the characteristic polynomial equation of the AR model. Solving for this polynomial's roots, one can obtain the estimated poles or eigenvalues that are participating in the response. The modal damping estimates are calculated using the real and imaginary parts of each pole.

Using a backward AR technique developed by Kumaresan and Tufts [12], Tasker and Chopra [11] performed extensive evaluations of simulated helicopter rotor systems with close modes at various damping levels in the presence of noise and rotational speed harmonics. They found that the backward AR technique could very accurately identify the damping of close modes.

Based on Tasker and Chopra's experience, backward AR was selected as a candidate MDOF technique for our damping estimation purposes. Significant accuracy improvements to this method may be realized by simultaneously including the measurements from multiple outputs in the identification technique [13]. In particular, Hung et al. [14] have extended the backward AR technique to address an output vector of arbitrary dimension. This extended method—multiple output backward autoregression—is referred to as MOBAR.

When multiple response signals are available, the MOBAR technique achieves better accuracy, with less bias and deviation due to noise, for damping estimation than using only a single output [11,13,14]. Such performance has been attributed to richer modal information in the data set, which also reduces the necessary time block needed for analysis. MOBAR also provides the flexibility of using different types of response signals (acceleration, velocity, and displacement) simultaneously in the same data matrices [14]. Given these demonstrated abilities, MOBAR appears particularly well suited to rotor stability measurement.

4.1 Three Mass Rotor Example. With six modes contributing to the response, the isotropic three mass rotor supported in fluid film bearings is a simple, but more realistic, model for representing the dynamics of a complex turbomachine. Figure 6 shows this system where the massless shaft is supported by two identical journal bearings at Masses 1 and 3. While not shown, the response is measured using simulated probes at each bearing, which are oriented 45 deg from the horizontal x axis. The level of bearing stiffness and damping anisotropy is controlled, as in the rigid rotor system, using the χ_k and χ_c factors. The same bearing conditions will be analyzed for the three mass rotor. However, cross-coupling q is now only applied at the midspan, Mass 2.

Steady-state synchronous vibration of approximately 25.4 μm (1.0 mil) p-p at the bearing probes was generated using equal

Downloaded 02 Jun 2010 to 171.66.16.109. Redistribution subject to ASME license or copyright; see http://www.asme.org/terms/Terms_Use.cfm

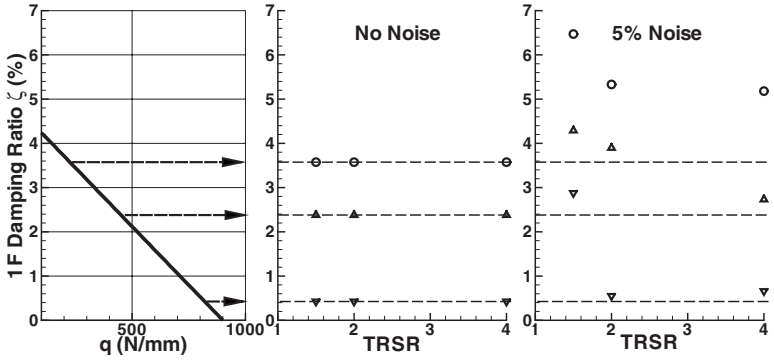


Fig. 7 MOBAR damping estimates for three mass rotor ($\chi_k=\chi_c=1$, horizontal impulse)

unbalances at 0 deg, 90 deg, and 180 deg placed at the three masses, respectively. Rotating at 10,000 rpm, impulse excitation was applied to Mass 1. This nonideal location mimics the external excitation restrictions on an actual machine [8,15]. The magnitude of the impulse was varied to investigate how the level of excitation influences the estimates. The transient response strength ratio (TRSR) compares the maximum transient response amplitude to the steady-state amplitude (25 μm *p-p*). A ratio of 4 indicates that the impulse caused the response (at any of the bearing probes) to be four times the steady-state vibration amplitude due to unbalance. To examine the MOBAR's performance under noisy conditions, white noise was added to the four simulated bearing probe responses. The noise level was set at a percentage of the steady-state rms vibration amplitude.

For two of the bearing design cases, Figs. 7 and 8 present the actual stability characteristics and the MOBAR damping estimates from the simulated impulse testing at three stability levels. The noise and low response strength ratio degrades the accuracy of the estimates. Overall, however, the estimates are very accurate, particularly at high TRSR. One clear exception is the isotropic bearing condition with $q=225$ N/mm and 5% noise. Shortly, it will be examined how this estimate can be improved through choice of excitation.

For the anisotropic bearing design at high noise levels, the MOBAR technique was unable to identify the first forward mode using a horizontal impulse. However, changing the impulse direction to vertical produced very accurate results because the forward mode is more vertically oriented.

Figure 9 presents the actual and identified poles for one of the moderately anisotropic system's q levels ($q=661$ N/mm). As expected, the vertical impulse excites not only the first forward mode but also the second (945 rad/s) and third (1346 rad/s) vertically oriented modes. Fairly accurate estimates for these higher modes are obtained. The backward mode is also identified because its orientation, with this level of q, is more easily excited by vertical excitation. The synchronous vibration component at 10,000 cycles/min (1047.2 rad/s) is identified as simply an undamped pole near the Im(λ) axis.

Given an impulse's directional nature and its ability to excite many modes, the question remains whether or not these estimates could be improved with a different type of excitation, one that improves the first forward mode's SNR. The blocking type test [15] is aimed at providing this capability. A type of tuned-sinusoidal method [2], blocking testing effectively tries to isolate a mode by exciting at its natural frequency in its predominant direction. Such testing is extremely suitable where magnetic actuators are available. Tasker and Chopra used this excitation technique for helicopter blades simulations as part of their evaluation of the backward AR technique [11].

To perform a blocking test of a rotor system, the following procedure is suggested.

1. *Perform sine sweep tests.* Given that a shaker device is available for blocking excitation, several sine sweeps should be performed through the expected frequency range. Although input measurement is not important during these sweeps, input direction should be varied to identify any modal directionality.
2. *Select blocking direction and frequency for the mode of interest.*
3. *Select blocking input amplitude.* While exciting the rotor in the selected fashion, amplitude selection is done by varying the excitation level until the desired response amplitude is achieved. As discussed before, this selection becomes a bal-

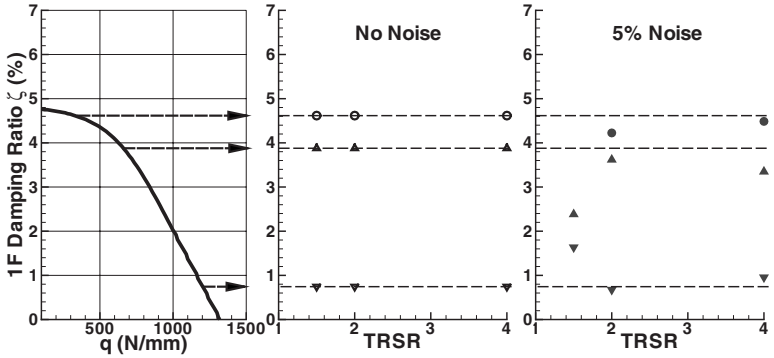


Fig. 8 MOBAR damping estimates for three mass rotor ($\chi_k=0.75$, $\chi_c=1.25$, open symbols=horizontal impulse, solid symbols=vertical impulse)

Downloaded 02 Jun 2010 to 171.66.16.109. Redistribution subject to ASME license or copyright; see http://www.asme.org/terms/Terms_Use.cfm

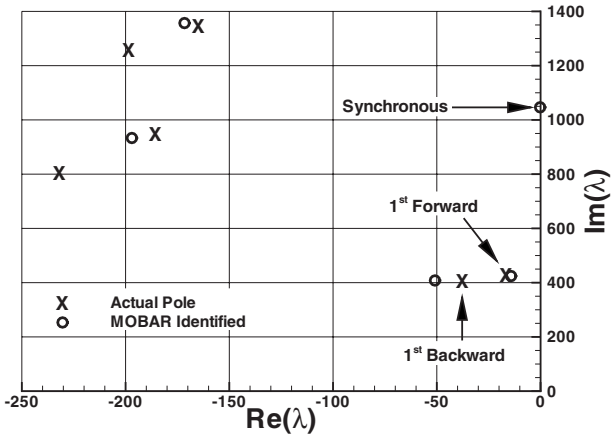


Fig. 9 Actual versus MOBAR estimated poles (χ_k=0.75, χ_c =1.25, q=661 N/mm, 5% noise, vertical impulse)

ance of maximizing SNR while avoiding large nonlinear effects.

4. *Apply blocking excitation and record free decay.* For estimation purposes, it is important to know when blocking excitation is eliminated within the recorded transient response. This point establishes the start of the free decay portion needed for analysis.

Such a procedure was performed for the simulated three mass rotor system on isotropic and moderately anisotropic bearings. Blocking excitation levels were varied to achieve the same three TRSR levels studied for the impulse-type of excitation. For the isotropic situation, forward circular blocking was used and the resulting blocking test free decay is shown in Fig. 10. This figure also presents the resulting MOBAR damping estimates. Excellent accuracy was obtained signifying the improved SNR of the first forward mode relative to that obtained by impulse excitation (Fig. 7).

The MOBAR technique, in combination with blocking testing, will serve as the stability measurement tool for the experimental portion of this study. Their application on an actual rotor system will help demonstrate their potential for stability measurement of industrial machines.

5 Experiments

The experimental rig consisted of a 1.55 m (61 in.) long rotor supported by two tilting pad journal bearings and incorporates three magnetic actuators. Figure 11 displays the overall rig layout. Two of the magnetic actuators, designated Actuators 1 and 2, were located between the journal bearings for application of cross-coupling stiffness. These locations correspond to those of various destabilizing components, such as oil and labyrinth seals, found in industrial between-bearing machines. The third actuator or shaker was located at the outboard end, where previous industrial stability measurement investigations [8,16] applied external excitation. Five planes of vibration were monitored using eddy current proximity probes. With a midspan diameter of 90 mm (3.5 in.) and a bearing span of 1.22 m (48 in.), the shaft was made of AISI 4340 steel.

Each 70 mm (2.75 in.) diameter tilting pad bearing consisted of five, 52.3 mm (2.06 in.) long steel pads, oriented in the load-between-pad configuration. Two sets of bearings were tested, one set with 0.3 preload pads (m_p=0.3) and the other with 0.1 preload pads. With their assembled clearance maintained at approximately 173 μm (6.8 mils) diametral, the two sets' preloads were varied through pad machined clearance differences. Both designs shared common bearing housings and ball pivots. Thus, preload was changed by installing new pads with a different pad machined bore. Complete details of the rig are given in Ref. [17].

5.1 Base Stability Testing. Base stability testing was conducted to examine the stability performance as a function of speed with no actuator cross-coupled stiffness. To maximize modal SNR, blocking tests were conducted for these stability measurements.

Using the actuator control system's sinusoid generator, the shaker actuator was used to excite the rotor at the desired blocking frequency and direction. The amplitude of the shaker blocking

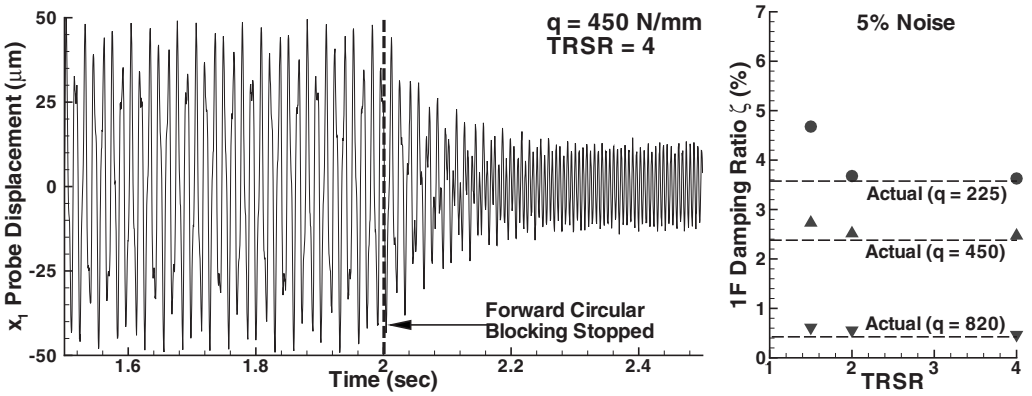


Fig. 10 Isotropic rotor with forward circular blocking and the resulting MOBAR estimates

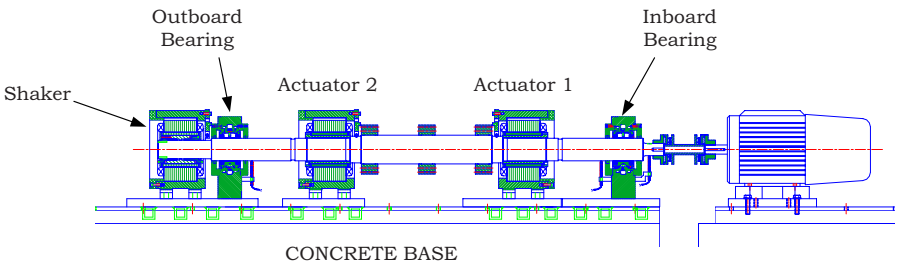


Fig. 11 Rig layout

Downloaded 02 Jun 2010 to 171.66.16.109. Redistribution subject to ASME license or copyright; see http://www.asme.org/terms/Terms_Use.cfm

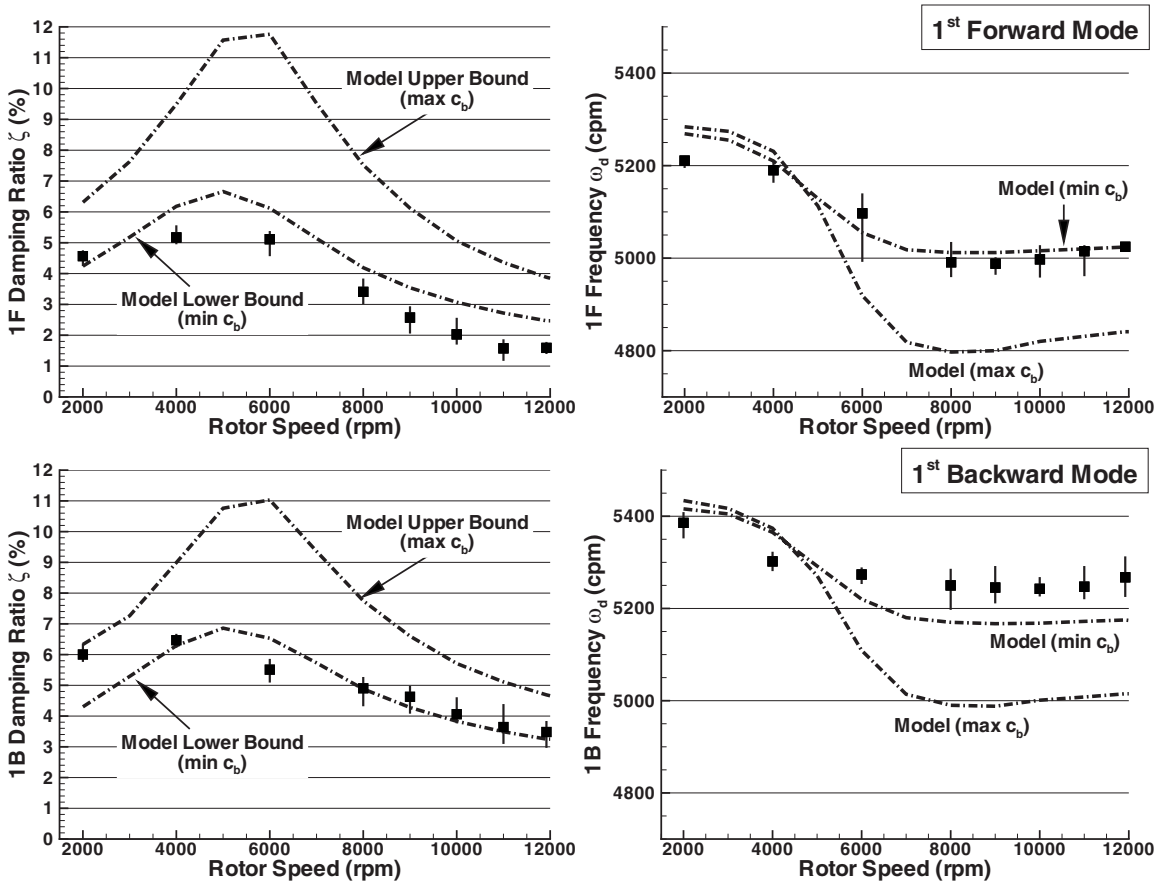


Fig. 12 First forward and backward mode base stability measurements versus predictions (m_p=0.3)

excitation was limited to keep unfiltered vibration at the journal bearings less than 38 μm (1.5 mils) *p-p* for linearity concerns. Upon turning off the shaker's nonsynchronous blocking excitation, the transient decay was recorded for use with the MOBAR technique. Five blocking tests were recorded for each direction of excitation. All ten radial probe channels were used in the estimation process.

Base stability measurements using this blocking test procedure were conducted at eight different speeds from 2000 rpm to maximum speed. For the 0.3 preload bearing design, Fig. 12 presents the results of these measurements for the first forward and backward modes. The left two plots give the measured damping ratios, and the right two plots show the modes' damped natural frequency characteristics. Stability measurements based on horizontal blocking are presented with the forward mode characteristics, whereas the backward mode characteristics are associated with vertical blocking measurements.

For each measurement shown in Fig. 12, the ζ and ω_d estimates are averages of estimates obtained from the five blocking tests. The vertical bars on each measurement indicate the range of estimates obtained, serving as an indicator of the estimate's uncertainty. Typical uncertainties were $\pm 0.2\%$ for damping ratios and ± 20 cycles/min (± 0.3 Hz) for damped natural frequencies.

The backward mode consistently has larger damping and a higher damped natural frequency than its sister forward mode. The lone exception occurs at 6000 rpm where both modes possess similar damping levels. Above 8000 rpm, the two modes' modal parameter deviations remain fairly constant with an approximately two percentage point difference in damping and an approximately 200 cycles/min (3.3 Hz) frequency separation. Because gyroscopic effects are not significant, the backward mode is the higher frequency sister mode due to the anisotropic support effects.

Approximate bounds for model predictions are also shown in Fig. 12. These are based on a system model including the shaft, bearings, and flexible support pedestals. The rotor and pedestal models were reconciled using modal testing to improve accuracy. The tilting pad bearing dynamics were calculated using the algorithm developed by He [18]. Stability predictions were determined using the bearings' full coefficients, which result in frequency dependent reduced coefficients [19]. Without component test data to correlate and reconcile their dynamics, the bearings represent the greatest uncertainty in the overall system model. Therefore, predictions were based on the two extreme combinations of the bearings' assembled clearance (c_b), preload, and inlet oil temperatures.

Throughout the speed range, both modes' damping and frequency measurements correlate the closest with the model's bound that is based on the bearings' minimum assembled clearance. For the first forward mode, the model typically overpredicts damping by approximately one percentage point but achieves excellent accuracy with respect to frequency. The opposite is true for the backward mode's predictions, which correlate better with the damping measurements than their frequency.

5.2 Stability Sensitivity Testing. To examine the effect of cross-coupled stiffness on machine stability, cross-coupling was induced through the appropriate feedback relationship between Actuator 2 and its adjacent sensor. The first forward and backward modes' stability sensitivities were measured for cross-coupling ranging from the base condition up to the onset of instability. Damped eigenvalues of the two modes were measured through blocking with the shaker.

For the 0.1 preload bearing design, Figs. 13 and 14 present the ζ and ω_d estimates obtained from blocking tests aimed at identi-

Downloaded 02 Jun 2010 to 171.66.16.109. Redistribution subject to ASME license or copyright; see http://www.asme.org/terms/Terms_Use.cfm

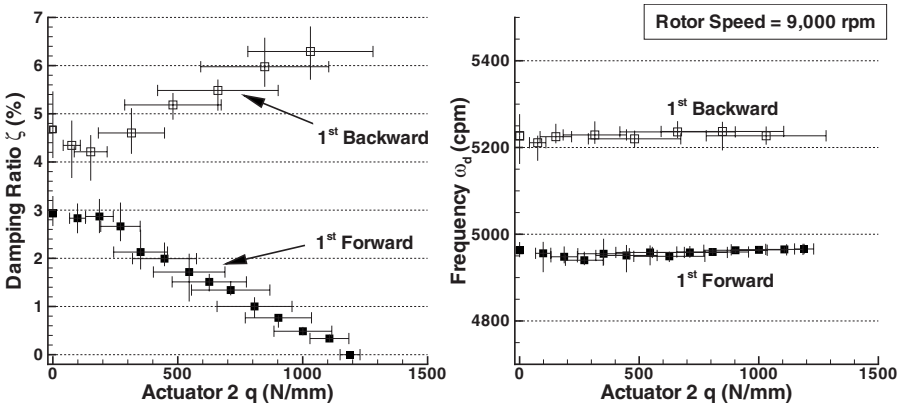


Fig. 13 First forward and backward mode stability sensitivity curve measurements at 9000 rpm (m_p=0.1)

fying the first forward and first backward modes as cross-coupling was varied at Actuator 2. The stability threshold points are where ζ equals 0. These thresholds were determined by increasing the actuator cross-coupled stiffness until the rotor exhibited unstable vibrations (increasing with time).

Examining the measurements in Figs. 13 and 14, the forward mode's damping declines almost linearly with increasing cross-coupling. The backward mode's damping linearly increases at nearly the same rate. Both modes' frequencies remain almost constant up to the stability threshold. Going from 9000 rpm to maximum speed decreases both modes' damping levels and the first mode's stability threshold.

The first forward mode's stability sensitivity curve measurements and predictions are given in Fig. 15. While overpredicting the damping, the model's lower bound provides the most accurate prediction. However, while the measurements show an almost linear decline of the mode's stability, the model's lower bound forecasts a region where the mode's damping is insensitive to additional cross-coupling. This indicates that the model is overpredicting the degree of anisotropy in the bearing system.

The stability sensitivity curve measurements and predictions for first backward mode are also given in Fig. 15. The backward

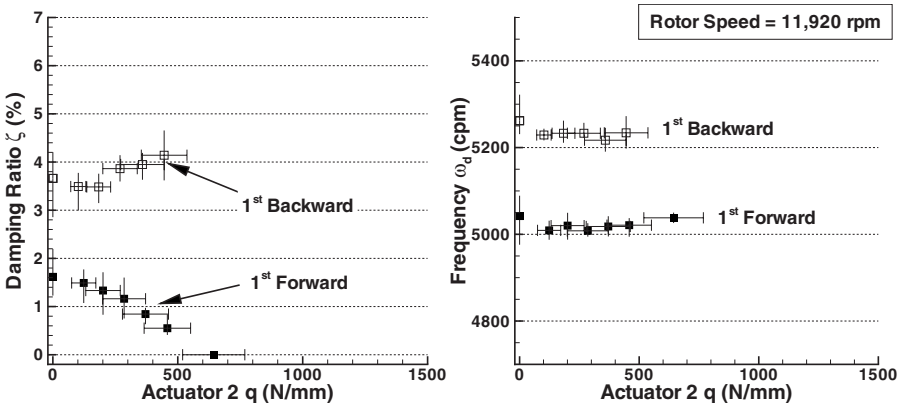


Fig. 14 First forward and backward mode stability sensitivity curve measurements at maximum speed (m_p=0.1)

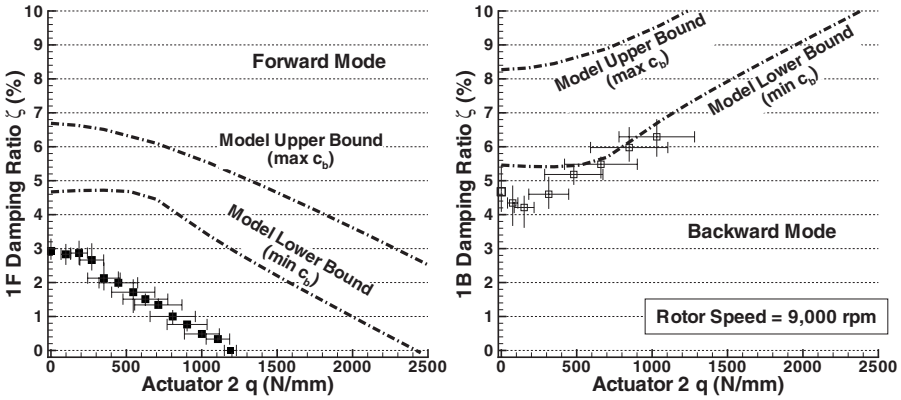


Fig. 15 First forward and backward mode stability sensitivity curve measurements versus predictions at 9000 rpm (m_p=0.1)

Downloaded 02 Jun 2010 to 171.66.16.109. Redistribution subject to ASME license or copyright; see http://www.asme.org/terms/Terms_Use.cfm

mode's damping measurements are slightly overpredicted by the model's lower bound, particularly for q levels less than 500 N/mm. However, good correlation is achieved at higher cross-coupling levels.

6 Conclusions

Widely used SDOF techniques for estimating modal damping from experimental measurements are not adequate for application to rotordynamic identification where closely spaced modes render the underlying assumptions invalid. A powerful alternative is offered by the MOBAR technique, which has been demonstrated both by simulation and by experiment to yield good estimates of both modal frequency and modal damping using only the time series response of a transient (impact) experiment. When more sophisticated experiments are possible—blocking excitation—then MOBAR does an excellent job of rejecting measurement noise and synchronous response while discriminating closely spaced modes. Comparison of measured modal frequencies and damping ratios to those predicted by a well established tilt-pad bearing model shows modest agreement in trend but suggests that the bearing model tends to overpredict relative machine stability.

Acknowledgment

The authors are grateful to ExxonMobil Research and Engineering for funding the majority of this work. Sincere thanks also go to Rotating Machinery Technology, Dresser-Rand, Petrobras, A-C Compressor, National Instruments, and Cooper Cameron for their generous contributions.

References

[1] API, 2002, *Axial and Centrifugal Compressors and Turboexpanders for Petroleum, Chemical and Gas Industry Services*, 7th ed., American Petroleum Institute, Washington, DC, Paper No. STD 617.

[2] Maia, N., and Silva, J., eds., 1997, *Theoretical and Experimental Modal Analysis*, Research Studies, Baldock, England.

[3] Bucher, I., Ewins, D. J., and Robb, D. A., 1996, "Modal Testing of Rotating Structures: Difficulties, Assumptions, and Practical Approach," *Proceedings of the Sixth International Conference on Vibrations in Rotating Machinery, IMechE*, Oxford, England, pp. 539–562.

[4] Nordmann, R., 1984, "Identification of Modal Parameters of an Elastic Rotor With Oil Film Bearings," ASME J. Vib., Acoust., Stress, Reliab. Des., **106**, pp. 107–112.

[5] Ljung, L., 1999, *System Identification: Theory for the User*, 2nd ed., Prentice-Hall, Englewood Cliffs, NJ.

[6] Nordmann, R., 1982, "Modal Parameter Identification and Sensitivity Analysis in Rotating Machinery," *Proceedings of the Conference on Rotordynamic Problems in Power Plants, IFToMM*, Rome, Italy, pp. 95–102.

[7] Wohlrab, R., 1976, "Einfluß der Lagerung auf die Laufstabilität Einfacher Rotoren mit Spalterregung," Konstruktion, **28**, pp. 473–478.

[8] Moore, J. J., Walker, S. T., and Kuzdzal, M. J., 2002, "Rotordynamic Stability Measurement During Full-Load Full-Pressure Testing of a 6000 psi Re-Injection Centrifugal Compressor," *Proceedings of the 31st Turbomachinery Symposium*, Texas A&M University, pp. 29–38.

[9] Phillips, A. W., and Allemang, R. J., 1996, "Single Degree-of-Freedom Modal Parameter Estimation Methods," *Proceedings of the 14th International Modal Analysis Conference*, Honolulu, HI, pp. 253–260.

[10] Ewins, D. J., 2000, *Modal Testing: Theory, Practice and Application*, 2nd ed., Research Studies, Baldock, England.

[11] Tasker, F., and Chopra, I., 1990, "Assessment of Transient Analysis Techniques for Rotor Stability Testing," J. Am. Helicopter Soc., **35**(1), pp. 39–50.

[12] Kumaresan, R., and Tufts, D. W., 1982, "Estimating the Parameters of Exponentially Damped Sinusoids and Pole-Zero Modeling in Noise," IEEE Trans. Acoust., Speech, Signal Process., **ASSP-30**(6), pp. 833–840.

[13] Tasker, F., and Chopra, I., 1990, "Multi-Output Implementation of a Modified Sparse Time Domain Technique for Rotor Stability Testing," *Proceedings of the Structures, Structural Dynamics and Materials Conference*, pp. 1871–1884, Paper No. AIAA-90-0946-CP, AIAA/ASME/ASCE/AHS.

[14] Hung, C. F., and Ko, W. J., 2002, "Identification of Modal Parameters From Measured Output Data Using Vector Backward Autoregressive Model," J. Sound Vib., **256**(2), pp. 249–270.

[15] Kanki, H., Fujii, H., Hizume, A., Ichimura, T., and Yamamoto, T., 1986. "Solving Nonsynchronous Vibration Problems of Large Rotating Machineries by Exciting Test in Actual Operating Condition," *Proceedings of the International Conference on Rotordynamics IFToMM*, Tokyo, Japan, pp. 221–225.

[16] Baumann, U., 1999, "Rotordynamic Stability Tests on High-Pressure Radial Compressors," *Proceedings of the 28th Turbomachinery Symposium*, Texas A&M University, pp. 115–122.

[17] Cloud, C. H., 2007, "Stability of Rotors Supported by Tilting pad Journal Bearings," Ph.D. thesis, University of Virginia, Charlottesville.

[18] He, M., 2003, "Thermoelastohydrodynamic Analysis of Fluid Film Journal Bearings," Ph.D. thesis, University of Virginia, Charlottesville.

[19] Brockett, T. S., and Barrett, L. E., 1993, "Exact Dynamic Reduction of Tilting-Pad Bearing Models for Stability Analyses," STLE Tribol. Trans., **36**(4), pp. 581–588.

Downloaded 02 Jun 2010 to 171.66.16.109. Redistribution subject to ASME license or copyright; see http://www.asme.org/terms/Terms_Use.cfm

Measurements of Leakage and Power Loss in a Hybrid Brush Seal

Luis San Andrés
Mast-Childs Professor
Fellow ASME
e-mail: lsanandres@mengr.tamu.edu

José Baker
Graduate Research Assistant
e-mail: jbakerv@tamu.edu

Adolfo Delgado
Graduate Research Assistant
e-mail: adelgam@tamu.edu

Mechanical Engineering Department,
Texas A&M University,
College Station, TX 77843

Simplicity, low cost, and easy replacement make labyrinth seals the primary seal type in gas turbines. However, excessive leakage and potential for rotordynamic instability are well known issues. Brush seals effectively control leakage in air breathing engines, albeit only applied for relatively low pressure differentials. Hybrid brush seals (HBSs) are an alternative to resolve poor reliability resulting from bristle tip wear while also allowing for reverse rotation operation. The novel configuration incorporates pads contacting the shaft, which under rotor spinning lifts off due to the generation of a hydrodynamic pressure. The ensuing gas film prevents intermittent contact, thus lowering the operating temperature and thermal distortions and even eliminating bristle wear. The hybrid brush seal improves sealing, is more durable and reliable than conventional brush seals, and allows reverse shaft rotation without seal damage. This paper presents measurements of power loss and leakage in a HBS for increasing pressure differentials over a range of rotor speeds. The test HBS, Haynes-25 bristle pack (~850 bristles/cm) and 45 deg lay angle, is 166.4 mm in diameter and integrates 20-arcuate pads connected with thin electrical-discharge machined webs (EDM-webs) to the seal casing. The webs are designed with low radial stiffness to allow for rotor excursions and high axial stiffness to avoid pad pitching motions resulting from high pressure differentials across the seal. Measured drag power at low rotor speeds (<11 m/s at 1300 rpm) decreases as the pressure differential across the seal increases. At a fixed rotor speed, a significant drop in drag torque (and drag power) ensues as the supply pressure increases, thus demonstrating that a gas film separates the rotor from the seal pads. Additionally, the operating temperature measured at the rotor/seal interface remains approximately constant (~24 °C) during tests with shaft rotation (power loss and drag torque measurements) under pressurized conditions, indicating that the rotor and seal pads are not in contact. Flow rate measurements at room temperature (25 °C) show an improved sealing ability with a leakage reduction of about 36% when compared with a first generation shoed-brush seal. The HBS calculated effective clearance (~50 μm) is approximately 70% smaller than the radial clearance (~180 μm) of an ideal noncontacting seal with similar rotor diameter. Improved brush seal technology will increase the efficiency of gas turbines while also aiding to improve the engine stability and to reduce vibrations.
[DOI: 10.1115/1.2967497]

1 Introduction

Current and future operational conditions in turbomachinery, i.e., increasing pressure differentials, operating temperatures, and rotational speeds, demand effective interface clearance control to reduce leakage and consequently to improve power delivery. Incorporating state-of-the-art sealing components in turbomachinery reduces leakage and power losses with savings in fuel consumption and operation and maintenance costs and increases engine reliability.

Chupp et al. [1] presented a comprehensive review of seals in steam and gas turbines, discussed the different sealing environments in turbomachinery, and highlighted the benefits resulting from proper clearance control. In a high pressure turbine, a 0.0254 mm (0.001 in.) blade tip clearance change gives up to a 0.1% decrease in specific fuel consumption and a 1°C drop in exhaust gas temperature. Turbomachinery designers must consider operational conditions (i.e., pressure differentials, temperatures, and rotor speeds) and material characteristics (thermal and structural behaviors) for a specific application. A minimal change in any of these factors does affect overall engine efficiency and dynamic behavior. The reference provides, for static, dynamic, and advanced design seals, the seal materials and manufacturing processes. Seal geometries, typical applications and locations within a turbomachine, and seal life are thoroughly described.

The review in Ref. [1] details well known advantages and disadvantages of labyrinth seals and brush seals commonly used in dynamic sealing applications. Labyrinth seals are comprised of circumferential knife-edge teeth to make a tortuous axial path that restricts gas flow from a high pressure region into a low pressure region. Labyrinth seals provide satisfactory sealing at a low manufacturing cost, albeit their leakage control effectiveness is highly dependent on maintaining, at all times, a tight radial clearance between the seal and the rotor. Transient large amplitude rotor excursions and partial rubbing of the rotor against the labyrinth teeth lead to an increase in leakage and a reduction in engine efficiency. Importantly enough, labyrinth seals are also prone to develop cross-coupled (follower) forces with the potential of inducing rotordynamic instability [2,3].

Brush seals improve power and efficiency in turbomachinery by overcoming the limitations associated with labyrinth seals. Initially implemented in aerospace applications, brush seals are presently an essential component in rotating machinery for power gen-

Contributed by the International Gas Turbine Institute of ASME for publication in the JOURNAL OF ENGINEERING FOR GAS TURBINES AND POWER. Manuscript received April 1, 2008; final manuscript received April 2, 2008; published online October 10, 2008. Review conducted by Dilip R. Ballal. Paper presented at the ASME Turbo Expo 2008: Land, Sea and Air (GT2008), Berlin, Germany, June 9–13, 2008.

Copyright © 2009 by ASME

Downloaded 02 Jun 2010 to 171.66.16.109. Redistribution subject to ASME license or copyright; see http://www.asme.org/terms/Terms_Use.cfm

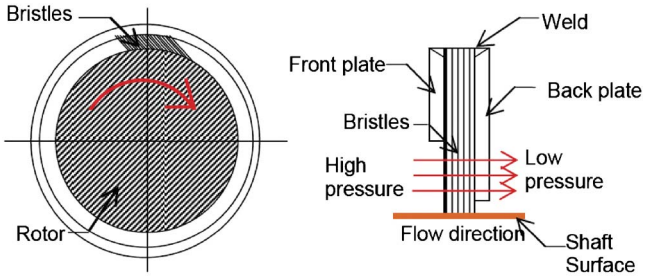


Fig. 1 Axial and cross-sectional views of conventional brush seal

eration. Commercially available brush seals, as depicted in Fig. 1, consist of packed metallic bristles of fine diameter clamped between a front plate on the upstream (high pressure region) and a backing plate on the downstream (low pressure region). Bristles are slanted at an angle (i.e., lay angle) in the direction of rotor spinning. The bristles bend rather than buckle during transient radial excursions of the rotor.

Ferguson [4] praised the brush seal as the first simple and functional sealing alternative to labyrinth seals in gas turbines. Leakage measurements in a single stage brush seal show a 90% reduction compared with leakage recorded in a five-teeth labyrinth seal with a 0.75 mm radial clearance. Chupp and Dowler [5] presented experimental results revealing that multiple brush seals installed in series withstand higher pressure drops and reduce secondary leakage in a shorter axial span than with a labyrinth seal. Incidentally, Conner and Childs [6] measured rotordynamic coefficients for a four-stage brush seal operating at increasing pressure ratios, shaft speed, fluid prerotation, and seal spacing. Identified cross-coupled stiffnesses are quite low and generally negative, thus having a stabilizing effect opposite to that in labyrinth seals.

Currently, the primary limitations of conventional brush seals include excessive bristle wear as identified by Proctor and Delgado [7], localized heat generation during shaft rotation (thermo-mechanical distortion) as observed by Dogu and Aksit [8], and an inherent inability to withstand high pressure differentials. Operation under these unfavorable conditions can permanently damage a brush seal and increase its leakage. In addition, conventional brush seals cannot accommodate shaft rotation in both directions, an issue of importance in some aircraft gas turbines.

Justak [9] introduced the first generation shoed-brush seal (SBS), see Fig. 2. This improved brush seal design accommodates shaft rotation in both directions at the same time it eliminates bristle tip wear, pad/rotor contact, and thermal distortions by means of a hydrodynamic gas film lifting the pads as the rotor spins. Delgado and San Andrés [10] presented a sound identification method to extract structural stiffness and damping characteristics from a 153 mm diameter shoed-brush seal by using single frequency shaker loads on a controlled motion test rig and without shaft rotation. A structural loss factor and a dry friction coefficient

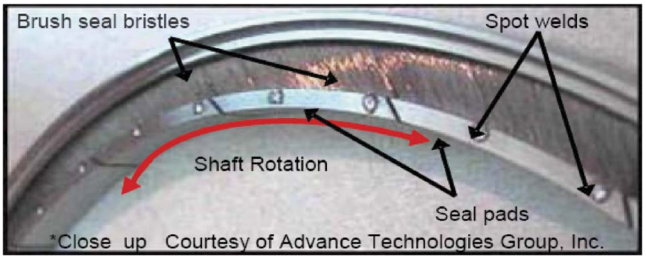


Fig. 2 Close-up view of first generation SBS



Fig. 3 Close-up view of HBS

represent the energy dissipated by the bristles and the dry friction interaction of the brush seal bristles rubbing against each other, respectively.

Delgado et al. [11] presented a comprehensive analysis for predicting the rotordynamic force coefficients in a SBS. The physical model couples the gas film hydrodynamic forces generated in the thin gap between the rotor and a shoe and the structural characteristics (stiffness and damping) from the bristle pack underneath. Predictions show that the operating gas film clearance and pressure differential do not significantly affect the shoed-brush seal force coefficients. The analysis does not account for the variation of the frictional forces acting within the bristle pack due to increasing pressure differentials.

Justak [12] introduced the hybrid brush seal (HBS), a second generation shoed-brush seal, shown in Fig. 3. In a HBS, the arcuate pads connect to the seal casing through electrical-discharge machined webs (EDM-webs). The novel construction eliminates reliability issues associated with the spot-welded connections originally used. More importantly, the thin beam connections (webs) provide a high axial stiffness while maintaining a low radial stiffness, thus reducing pad and rotor wear and secondary flow (leakage) by eliminating pad pitching motions caused by the large pressure differential imposed across the seal.

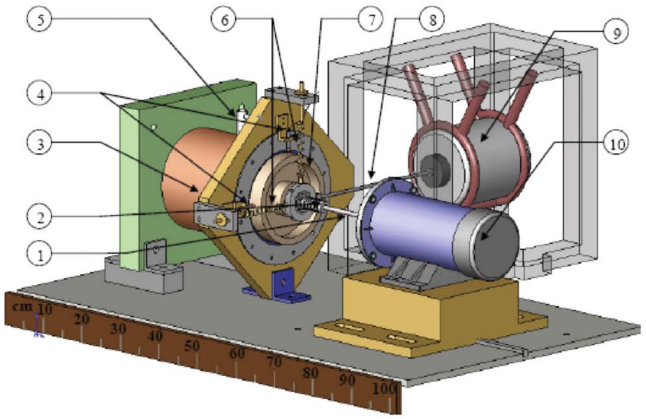
Justak and Crudgington [13] evaluated the performance and design of a HBS under static (no rotation) and with shaft rotation conditions (maximum operating speed of 15,000 rpm). The seal was tested in both ambient temperature and high temperature test rigs at pressure differentials ranging from 0 kPa to 300 kPa to simulate engine conditions. Performance of the test seal is characterized in terms of a semi-empirical effective clearance parameter (C_E) derived from the measured flow rate (leakage) across the seal, inlet pressure, and temperature. As the pressure differential across the HBS increases (i.e., 103–207 kPa) the effective clearance increases a little over 20%, representing a minimal increase in leakage across the seal. Additionally, a gradual temperature decrease at the rotor/seal interface and a constant power input during tests with shaft rotation and increasing pressure differential provide evidence for a gas film separating the seal pads from the rotor surface.

Chupp et al. [1] reviewed the SBS and its successor, the HBS, noting their state-of-the-art development. The present paper shows measurements of HBS leakage, power loss, and drag torque obtained at low rotor speeds (<1300 rpm) for increasing pressure differentials and at room temperature. The tests aim to characterize the performance of the test seal. In terms of the leakage measurements, the HBS shows a superior leakage performance over the first generation SBS, with a nearly 36% leakage reduction over the test pressure range.

2 Test Rig and Hybrid Brush Seal

Figure 4 depicts the rotordynamic test rig and instrumentation for hybrid brush seal evaluation. A slender steel shaft is affixed to the base of a cylindrical steel vessel via two tapered roller bearings, and the free end of the shaft holds a steel disk. A dc motor (746 W) drives the overhanging disk/shaft assembly at the shaft free end through a flexible coupling. The test brush seal (166.4

Downloaded 02 Jun 2010 to 171.66.16.109. Redistribution subject to ASME license or copyright; see http://www.asme.org/terms/Terms_Use.cfm



1	Quill shaft	6	Soft centering springs
2	Flexible coupling	7	Rotor
3	Pressurization vessel	8	Stinger
4	Eddy current sensors	9	Electromagnetic shaker
5	Supply pressure inlet	10	DC motor

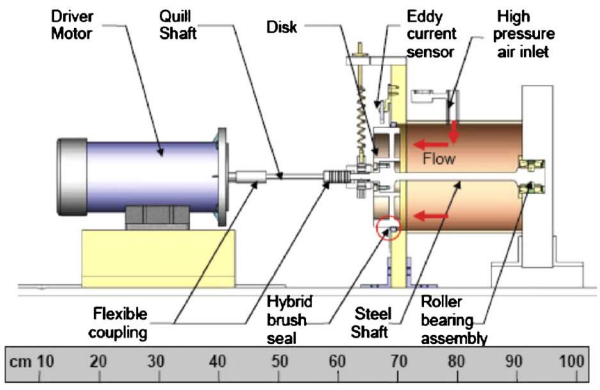


Fig. 4 Rotordynamic test rig for a HBS: (top) isometric view and (bottom) cross-sectional view

mm in diameter at the pad circumference) is secured atop of the vessel with a retainer ring. The seal assembly is a 0.381 mm (0.015 in.) nominal radial interference fit with the disk. Two eddy current sensors, 90 deg apart, are secured on the front plate of the cylindrical vessel and face the outer diameter of the steel disk. The sensors record the disk displacements along two orthogonal directions in the vertical plane.

A slender rod (stinger) connects an electromagnetic shaker to the free end of the shaft. The magnitude of the periodic load is controlled with a piezoelectric load cell fastened at one end of the stinger. Two soft springs located at the drive end of the shaft, in the vertical and horizontal directions, allow centering the rotor free end with respect to the test seal. The springs connect to the shaft through a ball bearing enclosed within an aluminum housing. A pressurized air line, feeding into the cylindrical housing, is instrumented with multiple pressure taps, a turbine flow meter, a static pressure transducer, and thermocouples.

Figure 5 shows a detailed cutaway view of the steel vessel and rotor/shaft assembly. The figure details the location of the HBS, the bearing assembly, one of the coil springs, and the eddy current sensor in the vertical direction.

In contrast to conventional brush seals, a HBS can accommodate shaft rotation in both directions, and it also eliminates bristle tip wear, pad/rotor contact and thermal distortions. Figure 6 shows a schematic profile view of the HBS. Once the HBS is pressurized, the pad design allows for a hydrostatic lift-off effect prior to shaft rotation. This effect is further enhanced by the hydrodynamic action generated by the rotation of the shaft.

Table 1 details the dimensions and material properties for the

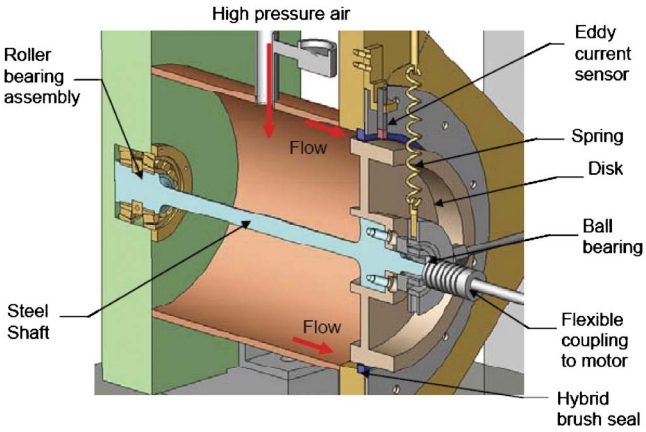


Fig. 5 Detailed view of disk/shaft assembly

test hybrid brush seal and Table 2 gives the air flow conditions for the leakage measurements obtained at ambient temperature, T_u. A turbine flow meter (± 0.2 SCFM) and a strain gauge pressure sensor (± 0.3 kPa) measure flow rate across the seal and upstream (supply) pressure P_s, respectively. The discharge pressure P_d is ambient (101 kPa).

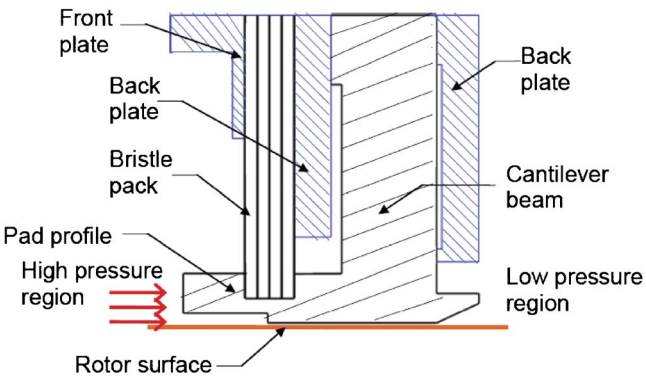


Fig. 6 Schematic profile view of the HBS (not to scale)

Table 1 Dimensions and material properties of test HBS

Physical properties	Magnitude
Rotor diameter, D_j	167.1 mm
Brush seal (pads) inner diameter, Ds_i	166.4 mm
Brush seal (retainer) outer diameter, D_o	183.1 mm
Brush seal width, B_w	8.53 mm
Radial interference between rotor and seal, R_i	0.381 mm
No. of pads	20
Width of pads	7.23 mm
Bristle lay angle, α	45 deg
Bristle modulus of elasticity, E	22.48×10^4 MPa
Bristle density (circumference)	850 bristle/cm

Table 2 Flow conditions for leakage measurements in a HBS

Fluid:Air	Magnitude
Absolute supply pressure (upstream), P_s	101–307 kPa
Absolute discharge pressure (downstream), P_d	101 kPa
Temperature upstream, T_u	22–25.5 °C
Specific gas constant, R	0.287 kJ/kg K

Downloaded 02 Jun 2010 to 171.66.16.109. Redistribution subject to ASME license or copyright; see http://www.asme.org/terms/Terms_Use.cfm

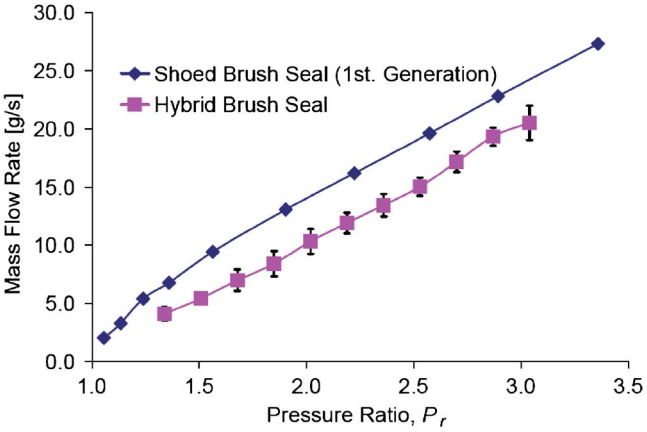


Fig. 7 Test flow rates for first generation SBS and HBS versus supply to discharge pressure ratio under static conditions (no shaft rotation)

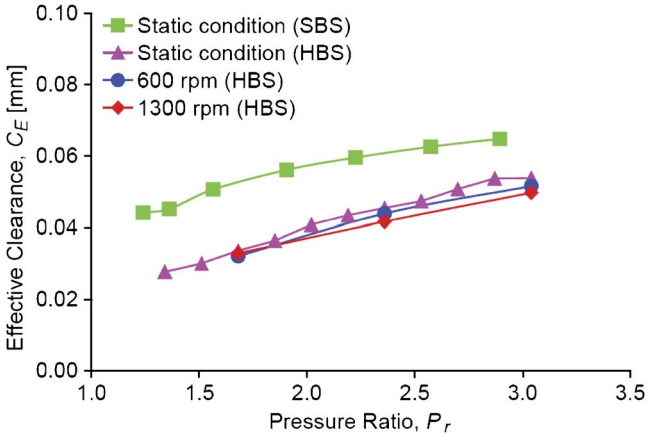


Fig. 9 Calculated effective clearance for SBS and HBS versus supply pressure to discharge pressure ratio at static condition (no rotation) and selected shaft speeds (600 rpm and 1300 rpm)

3 Experimental Results

Leakage (flow rate) in the hybrid brush seal is measured for increasing supply pressures (P_s up to 307 kPa) at ambient temperature (~25°C), under static (no shaft rotation) conditions and at low rotor speeds (<1300 rpm).

Leakage characteristics. Figure 7 depicts the measured mass flow rate versus pressure ratio ($P_r=P_s/P_d$) under static conditions (i.e., without shaft rotation) for the HBS and a first generation SBS tested at identical feed pressure conditions by Delgado and San Andrés [10]. Note that both test seals have an interference fit to the rotor. The HBS shows a better sealing performance over its predecessor, reducing overall leakage by about 36% over the test pressure range. This sealing improvement is due to the larger axial stiffness of the pads, which improves the pads' (shoes) ability to resist axial and twisting motions induced by the pressure differential. Eight independent trials were conducted to confirm the repeatability of the measurements for each pressure condition. In Fig. 7, error bars denote a rather low uncertainty, less than 5.0% of the leakage measurement.

In terms of HBS leakage versus rotational speed, test results in Fig. 8 indicate that the flow rate for each supply pressure (P_s) remains nearly constant, i.e., independent of rotor speed. The test results indicate that HBS leakage depends mainly on the pressure differential across the seal. Most leakage air flows through the minute air gap formed between the seal pads and rotor. This hydrostatic lift-off is induced primarily by the increasing pressure differential across the seal rather than shaft rotation.

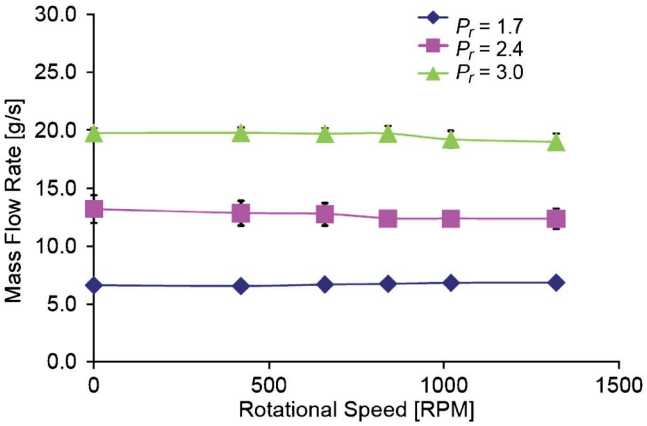


Fig. 8 Test flow rate for HBS versus rotor speed for increasing supply to discharge pressure ratios

Labyrinth seals remain as the standard seal element for rotating machinery that requires restricting gas flow from high to low pressure regions. Due to this circumstance, a brush seal manufacturer, Justak [9], compares leakage performance of brush seals to that of a noncontacting annular seal in terms of an effective clearance, C_E, defined as

$$c_E = \dot{m}\frac{\sqrt{T_u + 273.15}}{P_s \pi D_j \varphi} \tag{1}$$

where

$$\varphi = \begin{cases} \sqrt{\dfrac{2}{\gamma-1}\left(\dfrac{\gamma}{R}\right)P_r^{-(\gamma+1)/\gamma}\left(P_r^{(\gamma-1)/\gamma}\right)-1}, & P_r \le 1/p_{\text{choke}} \\ \sqrt{\dfrac{\gamma}{R}\left(\dfrac{2}{\gamma+1}\right)^{(\gamma+1)/(\gamma-1)}}, & P_r > 1/p_{\text{choke}} \end{cases} \tag{2}$$

where $P_r=(P_s/P_d)$ is a supply to discharge pressure ratio, $\gamma=1.4$ is the gas specific heat ratio, and $p_{\text{choke}}=(2/(\gamma+1))^{\gamma/(\gamma-1)}=0.53$ is the gas choke pressure ratio. The *effective* clearance, thought to represent that of an ideal "one-sharp tooth" labyrinth seal [9], does not account for a discharge or loss coefficient, typically <1. Thus, the actual clearance of the noncontacting seal may be larger than that hereby reported as effective.

Figure 9 depicts the calculated effective clearance (C_E) from the leakage data recorded for the SBS and HBS at static conditions (i.e., no shaft rotation). Additionally, the HBS effective clearance is shown for two rotor speeds, 600 rpm and 1300 rpm. The derived effective clearances for the SBS and HBS are a fraction of a typical labyrinth seal clearance. For nonrotating conditions, the HBS shows a lower effective clearance, ~30% in average, than that of the SBS over the test pressure range. The HBS effective clearances at 600 rpm and 1300 rpm are similar to the effective clearance calculated for no shaft rotation condition. The largest effective clearance is just over 0.050 mm at the highest test pressure ratio, $P_r=3.0$.

Power loss measurements. Rotating tests to characterize the hybrid brush seal performance in terms of drag power and torque are conducted for rotor speeds (ω_s) ranging from 400 rpm to 1300 rpm (a surface speed of ~11 m/s) and increasing supply pressure (P_s) to discharge pressure (P_d) ratios, $P_r=P_s/P_d$. In the case of no external pressurization, i.e., $P_r=1.0$, no air flows across the seal as the rotor spins.

Downloaded 02 Jun 2010 to 171.66.16.109. Redistribution subject to ASME license or copyright; see http://www.asme.org/terms/Terms_Use.cfm

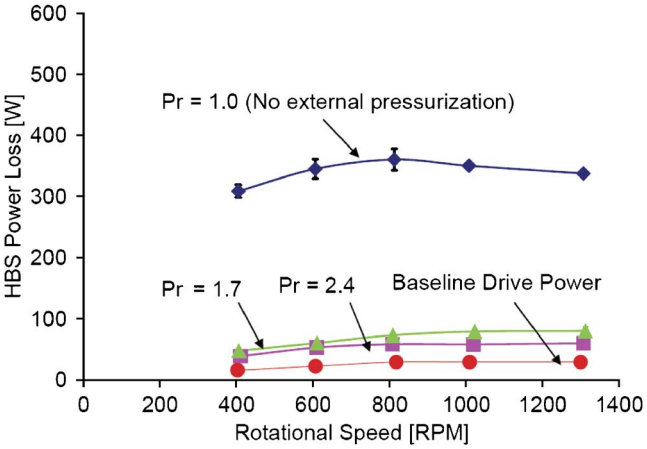


Fig. 10 Test power loss for HBS versus rotational speed for increasing supply to discharge pressure ratios

Power losses are derived from the drive motor electric power, i.e., voltage ***x*** current, at each test rotor speed. Prior to installing the HBS, a baseline drive power is recorded to account for the frictional drag arising from the roller bearings located at the base of the cylindrical vessel and the windage drag on the large steel disk. Subsequently, the power loss due to the HBS is determined by recording the motor drive power and subtracting the baseline power for identical operating conditions, pressure, and rotational speed. The drag torque is estimated by dividing the HBS power by the rotational speed (ω_s). The baseline power related to motor drag and disk windage is quite small (~25 W maximum), see Fig. 10. Note that the baseline power is not affected by increasing the supply pressure since without the HBS in place the area through which the air flows is rather large.

Figure 10 shows the HBS power loss versus rotational speed for increasing supply to discharge pressure ratios, $P_r = P_s / P_d$. Maximum power loss (~350 W) occurs at $P_r = 1.0$ due to the high contact forces at the rotor/seal interface and remains approximately constant over the test speed range. Power losses for a HBS decrease by about 90% from $P_r = 1.0$ to 1.7 over the test speed range.

Figure 11 shows the resultant drag torque versus rotational speed for increasing supply to discharge pressure ratios, $P_r = P_s / P_d$. Static breakaway torque measured at 0 rpm, i.e., torque required to initiate shaft rotation, drops significantly from $P_r = 1.0$ to 1.7 evidencing hydrostatic lift-off that causes the seal pads

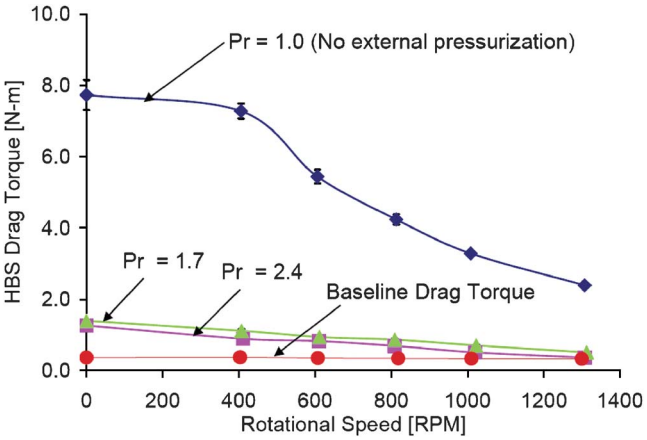


Fig. 11 Drag torque for HBS versus rotational speed for increasing supply to discharge pressure ratios

to separate from the rotor surface prior to actual shaft rotation. Drag torque decreases by about 50% from $P_r = 1.0$ to 1.7 over the test speed range. The hydrostatic lift-off effect is further enhanced by the hydrodynamic film action created once the rotor spins. The results denote a significant reduction in the *contact* forces between seal pads and rotor surface that should be apparent during rotor startup and actual steady operation. Hence, rotor and seal pads' wear are virtually eliminated. For reference, the Appendix presents measurements to assess the wear condition of the seal pads and rotor after testing with shaft rotation and under both pressurized and nonpressurized conditions. It is thought that the hydrodynamic lift-off effect will become more noticeable at higher rotational speeds. Additionally, a low constant operating temperature (~24°C) at the rotor/seal interface during the rotating tests with external pressurization evidences the absence of intermittent contact between the seal pads and rotor. Recall that power loss and drag torque estimations depicted in Figs. 10 and 11, respectively, correspond to a HBS with a radial interference of 0.381 mm (0.015 in.) with the rotor prior to external pressurization.

4 Conclusions

Gas turbines typically use labyrinth seals to restrict leakage between stages. Labyrinth seals inevitably wear, thus increasing their leakage and at times inducing harmful rotordynamic instability. Brush seals also effectively restrict secondary flows, but since the seal bristles are in contact with the rotor, they also wear and can induce severe shaft thermal bow. HBSs resolve poor reliability resulting from bristle tip wear while also allowing for reverse shaft rotation operation. A hybrid brush seal incorporates pads that are designed to contact the shaft. Under rotor spinning, hydrodynamic gas film pressure generates a force that lifts the pads off the rotor journal. The gas film prevents intermittent contact, which lowers the shaft operating temperature, reduces thermal distortions, and even eliminates bristles' wear. This paper presents results from laboratory experiments that quantify the leakage and power loss performance of a hybrid brush seal. Measurements show the advantages of a hybrid brush seal over a first generation SBS. Hybrid brush seals overcome the main deficiencies associated with the rotor and seal wear and low pressure differential capability of conventional brush seals.

Flow rate (leakage) measurements demonstrate a better sealing performance of the HBS with respect to a first generation SBS. This sealing improvement is due to the increase in axial stiffness provided by the EDM-webs connecting the shoes to the seal casing. The pitching motions of the pads caused by the pressure differentials across the seal are effectively prevented by the better support. Furthermore, the bristle bed in the HBS is now a secondary seal to the gas film riding pad element. In addition, the empirically derived effective clearances for the SBS and HBS are a fraction of an ideal noncontacting seal, with the HBS effective clearance being lower (~30% in average) than that of the SBS effective clearance.

Power loss and drag torque measurements performed on a HBS at low rotor speeds (i.e., a maximum surface speed of 11 m/s at 1300 rpm) reveal a surprising relation with respect to the increasing pressure differentials imposed on the seal. Maximum power losses (~350 W) occur without external air pressurization. Power losses decrease by approximately 90% over the test speed range of 400–1300 rpm as the seal is pressurized, which provides evidence for the generation of a hydrodynamic gas film separating the seal pads from the rotor surface. Most importantly, the breakaway torque drops by more than 50% as the HBS is pressurized, thus indicating that the seal pads lift off hydrostatically prior to actual shaft rotation. The hydrostatic lift-off effect is further enhanced by the hydrodynamic action caused by rotor spin. Thus, when pressurized, the HBS drag torque is lowest at rotor startup and steady operating conditions, a finding in direct opposition to that of typical brush seals. Power loss and drag torque measured under ex-

Downloaded 02 Jun 2010 to 171.66.16.109. Redistribution subject to ASME license or copyright; see http://www.asme.org/terms/Terms_Use.cfm

ternal pressurization, i.e., P_r=1.7 and 2.4, show no significant variation with increasing rotor speeds. Additionally, a low constant temperature (~24°C) at the rotor/seal interface also indicates the absence of intermittent contact between the rotor and hybrid brush seal pads.

Currently, tests and modeling to identify hybrid brush seal rotordynamic force coefficients are being conducted for increasing rotor speeds and excitation frequency. A high temperature experimental facility under construction will characterize HBS performance at higher shaft speeds and feed pressures, thus simulating actual engine conditions. Additional testing will further establish the reliable performance of the hybrid brush seal and will provide predictive tools facilitating the design, application, and improvement of this promising sealing technology.

Acknowledgment

Thanks to Siemens Power Generation Inc. for supporting the work and to Mr. John Justak, Advanced Technology Group, for providing the test seal (www.advancedtg.com).

Nomenclature

B_w = brush seal width (mm)
C_E = effective clearance of the ideal noncontacting seal (mm)
D_j = rotor diameter (mm)
Ds_i = brush seal inner diameter (mm)
D_o = brush seal outer diameter (mm)
E = bristle modulus of elasticity (Pa)
g = gravitational acceleration (9.81 m/s^2)
L = shaft length (0.284 m)
$\dot{m}$ = mass flow rate (g/s)
p_{choke} = static pressure/stagnation pressure at Mach 1
P_d = absolute discharge pressure (Pa)
P_r = pressure ratio (P_s/P_d)
P_s = absolute supply pressure (Pa)
R = specific gas constant (J/kg K)
R_i = radial interference between rotor and seal (mm)
T_u = upstream (supply) temperature (°C)
α = bristle lay angle (deg)
γ = gas specific heat ratio
φ = gas flow function, Eq. (2)
ω_s = rotor speed (rad/s)

Appendix: Evaluation of Disk and Seal Wear

The rotor and seal were disassembled to inspect their surfaces after ten combined hours of rotation at pressurized (~8 h) and nonpressurized conditions (~2 h). Figure 12 shows the surface profile of the disk along its axial span. Note that the scale for the ordinate (i.e., surface profile) is in micrometers and the abscissa (i.e., axial length) is in millimeters. Measurements show disk wear of nearly 60 μm at the seal location. The significant surface wear

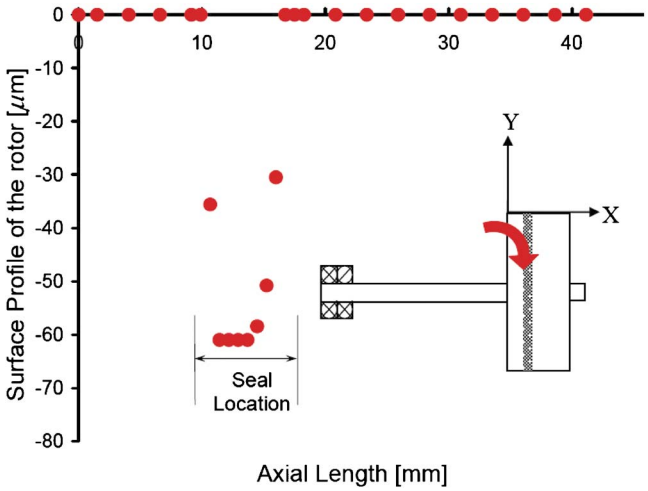


Fig. 12 Surface profile of the disk along its axial span; estimation of wear after 10 h of operation (tests with shaft rotation)

of the disk occurred during tests performed with shaft rotation and without pressure differential across the HBS (P_r=1.0). The HBS pads show no measurable wear after the 10 h of rotational tests.

References

[1] Chupp, R. E., Hendricks, R. C., Lattime, S. B., and Steinetz, B. M., 2006, "Sealing in Turbomachinery," J. Propul. Power, **22**(2), pp. 313–349.
[2] Benkert, H., and Wachter, J., 1980, "Flow Induced Spring Coefficients of Labyrinth Seals for Applications in Turbomachinery," NASA, Report No. CP2133.
[3] Childs, D., and Vance, J. M., 1997, "Annular Gas Seals and Rotordynamics of Compressors and Turbines," *Proceedings of the 26th Turbomachinery Symposium*, Houston, TX, Sept. 16–18, pp. 201–220.
[4] Ferguson, J. G., 1988, "Brushes as High Performance Gas Turbine Seals," ASME Paper No. 88-GT-182.
[5] Chupp, R. E., and Dowler, C. A., 1993, "Performance Characteristics of Brush Seals for Limited Life Engines," ASME J. Eng. Gas Turbines Power, **115**, pp. 390–396.
[6] Conner, J. K., and Childs, D., 1993, "Rotordynamic Coefficient Test Results for a Four-Stage Brush Seal," J. Propul. Power, **9**(3), pp. 462–465.
[7] Proctor, M. E., and Delgado, I. R., 2004, "Leakage and Power Loss Tests Results for Competing Turbine Engine Seals," NASA, Report No. TM-2004-213049.
[8] Dogu, Y., and Aksit, M. F., 2005, "Brush Seal Temperature Distribution Analysis," ASME Paper No. GT2005-69120.
[9] Justak, J. F., 2002, "Robust Hydrodynamic Brush Seal," U.S. Patent No. 6,428,009.
[10] Delgado, A., and San Andrés, L., 2005, "Measurements of Leakage, Structural Stiffness and Energy Dissipation Parameters in a Shoed Brush Seal," Sea Technol., **2005**(12), pp. 7–10.
[11] Delgado, A., San Andrés, L., and Justak, J. F., 2004, "Analysis of Performance and Rotordynamic Force Coefficients of Brush Seals With Reverse Rotation Ability," ASME Paper No. GT2004-53614.
[12] Justak, J. F., 2007, "Hydrodynamic Brush Seal," U.S. Patent No. 7,182,345.
[13] Justak, J. F., and Crudgington, P. F., 2006, "Evaluation of a Film Riding Hybrid Seal," AIAA Paper No. 2006-4932.

Downloaded 02 Jun 2010 to 171.66.16.109. Redistribution subject to ASME license or copyright; see http://www.asme.org/terms/Terms_Use.cfm

Nonlinear Stochastic Dynamics, Chaos, and Reliability Analysis for a Single Degree of Freedom Model of a Rotor Blade

Pankaj Kumar
Gas Turbine Design Department,
Bharat Heavy Electricals Limited,
Hyderabad-502032, India

S. Narayanan
Department of Mechanical Engineering,
Indian Institute of Technology Madras,
Chennai-600036, India

In turbomachinery, the analysis of systems subjected to stochastic or periodic excitation becomes highly complex in the presence of nonlinearities. Nonlinear rotor systems exhibit a variety of dynamic behaviors that include periodic, quasiperiodic, chaotic motion, limit cycle, jump phenomena, etc. The transitional probability density function (PDF) for the random response of nonlinear systems under white or colored noise excitation (delta-correlated) is governed by both the forward Fokker–Planck (FP) and backward Kolmogorov equations. This paper presents efficient numerical solution of the stationary and transient form of the forward FP equation corresponding to two state nonlinear systems by standard sequential finite element (FE) method using C^0 shape functions and Crank–Nicholson time integration scheme. For computing the reliability of system, the transient FP equation is solved on the safe domain defined by D barriers using the FE method. A new approach for numerical implementation of path integral (PI) method based on non-Gaussian transition PDF and Gauss–Legendre scheme is developed. In this study, PI solution procedure is employed to solve the FP equation numerically to examine some features of chaotic and stochastic responses of nonlinear rotor systems.
[DOI: 10.1115/1.2967720]

Keywords: Fokker–Planck equation, path integral, finite element method, chaos, reliability, nonlinear stochastic dynamics, blade vibration

1 Introduction

The forced vibration analysis of bladed disk assemblies subjected to unsteady aerodynamics forces is an important part of the design of a gas turbine engine [1]. Exciting forces in many situations in gas turbine blade vibration problems, such as due to an uneven pressure distribution and turbulence of the fluid in the flow path, are stochastic [2,3]. Nonlinearities may also arise from the dry friction damper, solid-fluid interaction forces, etc. [4]. When nonlinear systems are subjected to wide band, parametric and combined white noise, and harmonic excitation, complex dynamic phenomena, such as jump, bifurcations, dynamic instabilities, and chaotic motion are observed, which may severely restrict the operational range of the rotor [5]. Thus, the determination of nonlinear system responses to random excitation is of importance in order to understand their dynamics, as well as the design in the context of gas turbine bladed engine vibration problems [6]. However, nonlinear analysis of rotating machines poses difficulties in obtaining the analytical nonlinear model of the rotor from complicated aerodynamics and also from the lack of techniques to further analyze that model.

The transitional PDF for the random response of nonlinear systems under white noise excitation is governed by the FP equation. The closed-form solution of the FP equation is available only for a few low dimensional nonlinear systems. The limitations and difficulty of solving the FP equation have given rise to a number of approximate analytical approaches [7–9]. The approximate method to solve the FP equation [10] is based on the implicit or explicit assumption that the stationary probability densities of the states of the nonlinear oscillator can be approximated as jointly Gaussian. This assumption implies that the excitation and/or the nonlinearity are weak. Direct Monte Carlo simulation (MCS), while often regarded as less elegant than other methods, can be used to solve problems of significantly higher complexity. Its accuracy is, in principle, independent of the type of nonlinearity and dimensionality of the system. However, the method requires large computational resources.

In recent years, a number of numerical methods for the solution of the FP equation have been developed, and also for stochastic, chaotic, and reliability analyses. Numerical methods based on the Markov vector assumptions have been proposed for the solution of the FP equation, such as the PI method by Wehner and Wolfer [11], Naess and Moe [12], Yu et al. [13], and Lin and Yim [14] and the FE method by Langley [15], Spencer and Bergman [16], Pankaj and Narayanan [17], Wojtkiewicz et al. [18], and Kunert [19]. All of the numerical solution techniques developed for the FP equation up to now are confined to a phase space vector dimension of order <4. The numerical methods also suffer from difficulties of treating higher dimensional problems, requirement of large computer memory, and loss of accuracy of the PDF in the tail regions. It is a challenge to solve the FP equation for higher dimensional problems using the numerical technique.

This paper presents modified numerical methods to solve the FP equation for obtaining the stochastic response and transient statistics and for the reliability analyses of a number of single degree of freedom (SDOF) nonlinear systems representative of a rotor blade excited by wide band random excitation. The chaotic response of the nonlinear systems subjected to harmonic excitation combined with noise is also investigated. The numerical solution of the stationary as well as transient system is obtained by standard sequential FE method using the C^0 shape function and the Crank–Nicholson time integration scheme. The transient solution has importance especially in estimating the first passage probability. A boundary value problem is formulated for the first passage probability, the probability of the response exceeding a

Manuscript received April 3, 2008; final manuscript received April 4, 2008; published online October 13, 2008. Review conducted by Dilip R. Ballal.

Copyright © 2009 by ASME

Downloaded 02 Jun 2010 to 171.66.16.109. Redistribution subject to ASME license or copyright; see http://www.asme.org/terms/Terms_Use.cfm

threshold level for the first time, in terms of the FP equation. The FE method is applied to the Van der Pol oscillator, which provides good agreement with exact results.

A new PI method based on the non-Gaussian transition PDF and the Gauss–Legendre integration scheme is employed to the solution of the FP equation and to obtain the response of the SDOF system excited by white noise. This method is useful in reducing the computational cost and time. The PI solution procedure is also employed to solve the FP equation numerically to examine some features of the chaotic and extreme behaviors of a stochastic nonlinear system. It is observed that the presence of external noise has a significant effect on the transition between different response states and between co-existing attractors and the probability of a large excursion is increased as the noise intensity increases.

2 Fokker–Planck Equation

Nonlinear dynamical systems subjected to white noise excitation may be modeled with an n-dimensional vector Itô stochastic differential equations (SDEs) of the form

$$\frac{d\mathbf{X}}{dt} = \mathbf{m}(\mathbf{X}) + \mathbf{G}(\mathbf{X})\mathbf{W}(t) \tag{1}$$

where $\mathbf{X}$ is an R^n valued stochastic process representing the response of the system. $\mathbf{m}(\mathbf{X})$ and $\mathbf{G}(\mathbf{X})$ are the drift vector and the diffusion matrix, respectively, which depend on the response and system parameters. $\mathbf{W}(t)$ is an m-dimensional uncorrelated vector of white noise with $E[\mathbf{W}_i(t)]=E[\mathbf{W}_j(t)]=0$ and $E[\mathbf{W}_i(t_1)\mathbf{W}_i(t_2)] = 2\mathbf{D}_i\delta(\tau)$, where $\tau=t_2-t_1$, $\mathbf{D}_i$ is the spectral density of the ith excitation, and $\delta(\tau)$ is the Dirac delta function. The aforementioned system forms a Markov vector process in R^n, the behavior of which is completely determined by the transition PDF $p(\mathbf{X},\mathbf{t}|\mathbf{X}_0)$. The FP equation associated with Eq. (1) can be derived from the Itô form [20]

$$d\mathbf{X}(\mathbf{t}) = \mathbf{m}(\mathbf{X})d\mathbf{t} + \mathbf{G}(\mathbf{X})d\mathbf{B}(\mathbf{t}) \tag{2}$$

where $\mathbf{B}(t)$ is a vector Wiener process and $\mathbf{m}(\mathbf{X})$ is the Wong and Zakai corrected drift vector [21]. The corresponding FP equation for the system is given by [22]

$$\frac{\partial p}{\partial t} = -\sum_{i=1}^{n}\frac{\partial[m_i(\mathbf{X})p]}{\partial x_i} + \sum_{i=1}^{n}\sum_{j=1}^{n}\frac{\partial^2[h_{ij}(\mathbf{X})p]}{\partial x_i \partial x_j} \tag{3}$$

where h_{ij} is the ijth element of the matrix $\mathbf{H}(\mathbf{X})=\mathbf{G}(\mathbf{X})\mathbf{D}\mathbf{G}^{\mathrm{T}}(\mathbf{X})$ and $p=p(\mathbf{X},\mathbf{t}|\mathbf{X}_0)$ is the transition PDF of $\mathbf{X}(t)$ with the normalization condition

$$\int_{R^n} p(\mathbf{X},\mathbf{t}|\mathbf{X}_0)d\mathbf{X} = 1 \tag{4}$$

and subjected to the initial condition centered at $\mathbf{X}_0$ in the phase space

$$\lim_{t\to 0} p(\mathbf{X},\mathbf{t}|\mathbf{X}_0) = \delta(\mathbf{X}-\mathbf{X}_0) \tag{5}$$

Additionally a zero flux condition will be imposed at infinity given by

$$p(\mathbf{X}_i,\mathbf{t}) \to 0 \quad \text{as } \{\mathbf{X}_i\} \to \pm\infty, \quad i=1,2,\ldots,n \tag{6}$$

3 Finite Element Approach

The first step in the numerical solution of an initial and boundary value problem is the spatial discretization by which the transformation of a system of partial differential equations to a system of ordinary differential equations is achieved. The weighted residual statement for the problem given by Eq. (3) is integrated by parts to produce the weak form of the equations and the shape functions are chosen, which are defined for a finite region of the domain only. In this way, a set of linear equations is constructed in which the unknowns are the values of the joint PDF at a number of nodes in the domain. These equations are then solved by standard matrix methods.

The relevant portion Ω of the phase space is divided into M elements with m nodes and spanning the domain Ω_e. The PDF within the eth element is interpolated according to the following scheme

$$\hat{p}(\mathbf{X},\boldsymbol{t}|\mathbf{X}_0) = \sum_{s=1}^{m} N_s(\mathbf{X})p_s^e(\mathbf{X},\boldsymbol{t}|\mathbf{X}_0), \quad X\in\Omega \tag{7}$$

where $N_s(\mathbf{X})$, $s=1,2\ldots,m$ are the element shape functions, m is the number of nodes in a single element, and the p_s^e are the values of the PDF at the nodes. Converting Eq. (3) into the weak form and choosing the shape functions such that the residuals are orthogonal to the shape functions we get

$$\sum_{e=1}^{M}\int_{\Omega e}\left[\frac{\partial\hat{p}}{\partial t}N_r(\mathbf{X})d\mathbf{X} + \sum_{i=1}^{n} m_i(\mathbf{X})\hat{p}(\mathbf{X})\frac{\partial}{\partial x_i}[N_r(\mathbf{X})]d\mathbf{X} - \sum_{i=1}^{n}\sum_{j=1}^{n}\frac{\partial}{\partial x_i}\left[N_r(\mathbf{X})\frac{\partial}{\partial x_j}[h_{ij}(\mathbf{X})\hat{p}(\mathbf{X})]d\mathbf{X}\right] = 0 \tag{8}$$

Substituting Eq. (7) into Eq. (8) and expanding give

$$\sum_{e=1}^{M}\sum_{s=1}^{m}[\dot{p}_s^e(\mathbf{X},\boldsymbol{t}|\mathbf{X}_0)C_{rs}^e + p_s^e(\mathbf{X},\boldsymbol{t}|\mathbf{X}_0)\mathbf{K}_{rs}^e] = 0 \tag{9}$$

where

$$C_{rs}^e = \int_{\Omega e} N_r(\mathbf{X})N_s(\mathbf{X})d\mathbf{X} \tag{10}$$

and

$$K_{rs}^e = \int_{\Omega e}\left[\sum_{i=1}^{n} m_i(\mathbf{X})\mathbf{N}_s\frac{\partial}{\partial x_i}[N_r]d\mathbf{X} - \sum_{i=1}^{n}\sum_{j=1}^{n}\frac{\partial}{\partial x_i}[N_r]\frac{\partial}{\partial x_j}[h_{ij}N_s]d\mathbf{X}\right] \tag{11}$$

Globally assembling all elements, a set of n equations can be constructed, which in matrix form is given by

$$\boldsymbol{C}\dot{\boldsymbol{p}} + \boldsymbol{K}\boldsymbol{p} = 0 \tag{12}$$

with initial condition $\boldsymbol{p}(0)=\boldsymbol{p}$ where $\boldsymbol{p}$ is a vector containing the values of the joint PDF at the nodal points. Having addressed the issue of spatial discretization, the next step is temporal discretization, which converts the system of first order ordinary differential equations (ODEs) to a set of linear algebraic equations. So, this equation is further discretized in time using the θ method giving the recurrence relation

$$[\boldsymbol{C}-\Delta t(1-\theta)\boldsymbol{K}]\boldsymbol{p}(t+\Delta t) = [\boldsymbol{C}+\Delta t\theta\boldsymbol{K}]\boldsymbol{p}(t) \tag{13}$$

where $0\leqslant\theta\leqslant 1$ and Δt is time step. The Crank–Nicholson scheme is applied with $\theta=0.5$.

For the stationary solution of the FP equation, the matrix equation (12) becomes a system of n homogeneous linear equations

$$\boldsymbol{K}\boldsymbol{p} = 0 \tag{14}$$

where n is the number of nodal points in the computational mesh, $\boldsymbol{K}\in R^n\times R^n$, and $\boldsymbol{p}\in R^n$. This system admits both a trivial solution $\boldsymbol{p}=0$ and a nontrivial solution through the enforcement of the normalization condition.

The nontrivial solution is obtained by first fixing the PDF $\boldsymbol{p}^C$ at the node corresponding to the origin as unity [15]. This degree of freedom becomes constrained and is treated as an additional

Downloaded 02 Jun 2010 to 171.66.16.109. Redistribution subject to ASME license or copyright; see http://www.asme.org/terms/Terms_Use.cfm

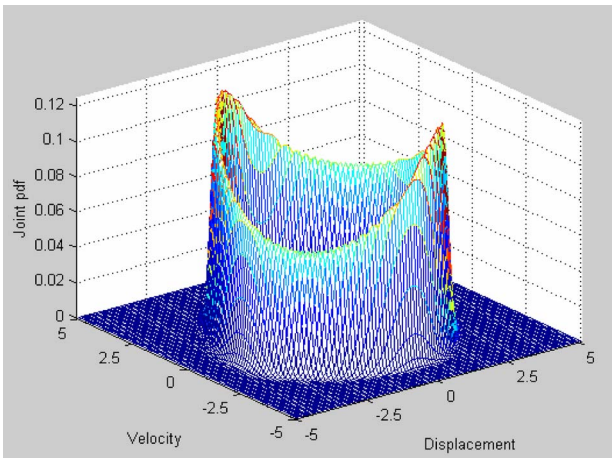


Fig. 1 Joint PDF for the Van der Pol oscillator with ξ=0.1 and D=0.1

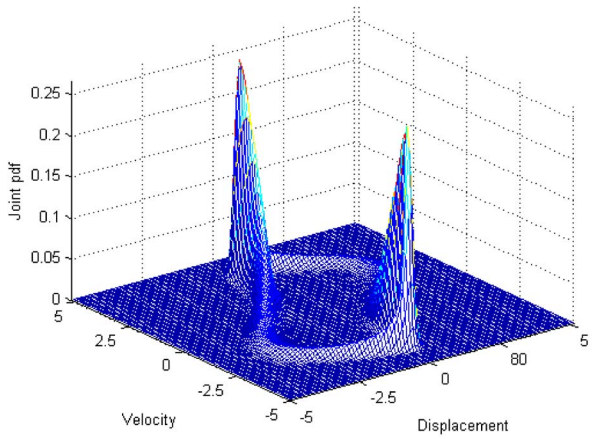


Fig. 2 Joint PDF for the Van der Pol oscillator with ξ=1.0 and D=0.1

boundary condition. The solution of Eq. (14) is reduced to the solution of a system of $(n-1)$ nonhomogeneous equations given by

$$\boldsymbol{K}^r\boldsymbol{p}^r = -\boldsymbol{f}^r \tag{15}$$

where $\boldsymbol{K}^r \in R^{n-1} \times R^{n-1}$, $\boldsymbol{p}^r \in R^{n-1}$, and $\boldsymbol{f}^r \in R^{n-1}$. The reduced matrix $\boldsymbol{K}^r$ is obtained by removing the cth row and column from the original matrix $\boldsymbol{K}$ and the reduced nodal density vector $\boldsymbol{p}^r$ is obtained from the original nodal density vector $\boldsymbol{p}$ by removing the cth component. The vector $\boldsymbol{f}^r$ is the cth column of $\boldsymbol{K}$ after removing the cth component. The solution of the stationary FP equation is obtained by enforcing the normalization condition given in Eq. (4).

The accuracy of the FE method based on numerical procedure as described above will be illustrated by application to two specific cases of the Van der Pol oscillator driven by stationary Gaussian white noise.

$$\ddot{X} + 2\xi[X(t)^2 - 1]\dot{X}(t) + X(t) = W(t) \tag{16}$$

Case 1. The values of ξ and D are taken as 0.1 and 0.1, respectively, in this case, which represents an intermediate case between linear and distinctly nonlinear behaviors. The grid domain is taken as $[-5,5]\times[-5,5]$, which is divided into 100 elements per dimension, each having 2^n nodes, where n is the dimensionality. The stationary joint PDF distribution obtained by this method is presented in Fig. 1. The figure clearly displays the limit cycle behavior of the oscillator.

Case 2. For the second case, ξ=1.0 and D=0.1, in which the case nonlinear behavior is strongly dominant. The time step used was Δt=0.005 s. The joint PDF obtained by the FE method for this case is shown in Fig. 2. The limit cycle behavior of the oscillator is even more pronounced in the present case.

The comparison of Figs. 1 and 2 shows that with the increase in the intensity of nonlinearity, the joint PDF becomes increasingly singular in the region of maximum excursion, reflecting the approach toward a "square wave" response.

3.1 Two-Dimensional Transient Solution. The transient behavior is of importance to many systems, especially relating to the first passage problem where failure can occur long before stationarity is reached. The hardening Duffing oscillator subjected to white noise excitation in the following form

$$\ddot{X} + 2\xi\dot{X} - X + \gamma X^3 = W(t) \tag{17}$$

is considered, to illustrate the efficacy of the FE based numerical procedure in solving for the transient PDF. Here ξ and γ are constants and $W(t)$ is an independent zero mean Gaussian white noise processes with

$$E[W(t)W(t+\tau)] = 2D\delta(\tau) \tag{18}$$

The corresponding FP equation is given by

$$\frac{\partial p}{\partial t} = \frac{\partial[(2\xi X_2 - X_1 + \gamma X_1^3)p]}{\partial X_2} - X_2\frac{\partial p}{\partial X_1} + (DX_1^2)\frac{\partial^2 p}{\partial X_2^2} \tag{19}$$

where $X_1 = X$ and $X_2 = \dot{X}$. The values of the parameters chosen are ξ=0.2, γ=0.1, and D=0.4 with a bivariate Gaussian initial distribution with zero mean and a variance of 0.5 in both dimensions. This system is particularly interesting since it has a bimodal stationary density function for small multiplicative excitation and is thus non-Gaussian. The grid size is chosen as $[-10,10]\times[-10,10]$, which is divided into 100 elements per direction. The time step Δt of $\pi/1000$ proved sufficient for good accuracy and a final time 10π was observed long enough for convergence to stationary conditions. The joint PDF of this system is given in Fig. 3 at two instants of time.

4 Reliability

The preceding works are concerned with the analysis of the response, namely, computing the joint PDF of the state vector. Such a characterization of the structural response provides useful insight into the manner in which structural uncertainties propagate, but it does not provide adequate information for reliability analyses. In recent years, a number of probability based codes have been formulated as a basis for safety analysis and design providing a consistent framework for the systematic assessment of the reliability of a structure.

Failure criteria in mechanics are normally defined in terms of load effects, such as stresses and deformations. Let $\mathbf{S}$ denote a vector of such effects and $g(\mathbf{s})=0$ denote the limit-state surface in the outcome space of $\mathbf{S}$. Without loss of generality, the function $g(\cdot)$ is formulated such that $g(\mathbf{s})>0$ defines the safe state and $g(\mathbf{s})\leqslant 0$ defines the failure state. The probability of failure of the structure, then, is

$$P_f = \int_{g(\mathbf{s})\leqslant 0} f_{\mathbf{s}}(\mathbf{s})\mathrm{d}\mathbf{s} \tag{20}$$

where $f_{\mathbf{s}}(\mathbf{s})$ $\mathrm{d}\mathbf{s}$ denotes the joint PDF of $\mathbf{S}$. The first excursion failure is an important failure criterion and a number of results have been published [16,23] on the solution of the backward Kolmogorov equation by the FE method for the system of two and three dimensions, leading to the definition of first passage of the

Downloaded 02 Jun 2010 to 171.66.16.109. Redistribution subject to ASME license or copyright; see http://www.asme.org/terms/Terms_Use.cfm

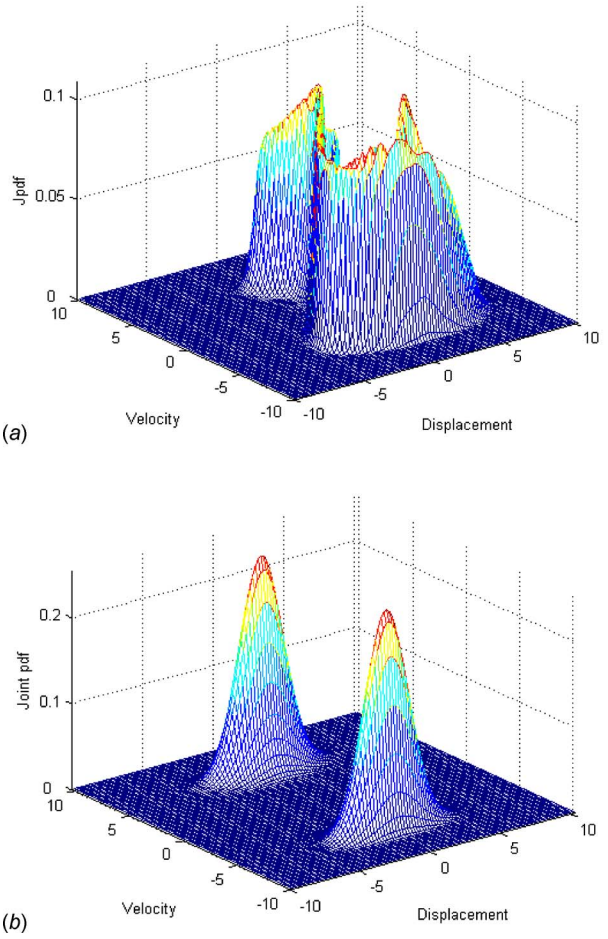


Fig. 3 Joint PDF for the hardening Duffing oscillator: (*a*) t =2.827 s and (*b*) t=31.419 s

dynamical system over the entire phase of initial conditions. While the backward equation would seem to be a more natural approach to the solution of the first passage problem, the forward or FE equation can also be utilized to solve for the first passage problem. Consider the partially open domain Ω shown in Fig. 4, where the transition PDF is defined to be zero in the second and fourth quadrants at a distance B from the x_2 axis. These boundaries, which prevent the clockwise trajectory from re-entering the safe region once outside, were proposed by Crandall [23].

An initial boundary value problem for the transition probability density of the oscillator is given by

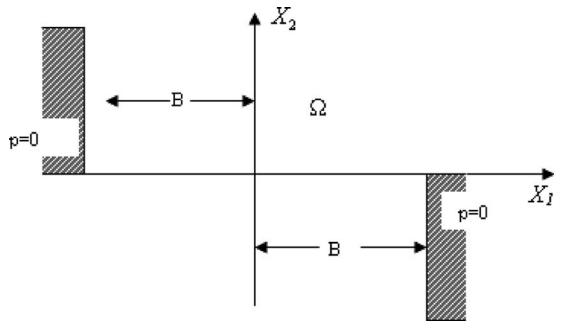


Fig. 4 Phase space safe domain for *D*-barriers for the first passage problem

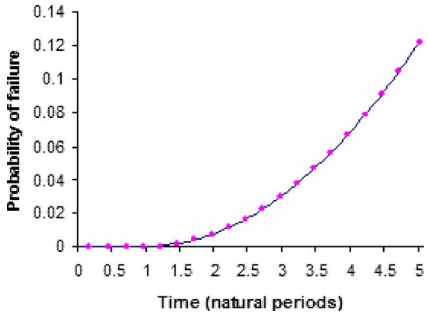


Fig. 5 Probability of failure versus time in natural periods for the Van der Pol system: B=3, ξ=0.5, and D=1; (—) forward solution and (●) backward solution

$$\frac{\partial p}{\partial t} = D\frac{\partial^2 p}{\partial X_2^2} - \frac{\partial}{\partial X_1}[m_1(X_1,X_2)p] - \frac{\partial}{\partial X_2}[m_2(X_1,X_2)p] \quad (21)$$

where $p=p(X_1,X_2,t|X_{01},X_{02};\Omega)dX_1dX_2$ is the probability of being between X_1 and X_1+dX_1 and X_2 and X_2+dX_2 at time t having started at X_{01},X_{02}, and not having previously left and re-entered Ω. The initial condition is given by

$$p(X_1,X_2,t|X_{01},X_{02};\Omega) = \delta(X_1 - X_{01})\delta(X_2 - X) \quad (22)$$

and the boundary conditions, depicted in Fig. 4, by

$$p(B,X_2,t;\Omega) = 0, \quad X_2 < 0 \quad (23)$$

$$p(-B,X_2,t;\Omega) = 0, \quad X_2 > 0 \quad (24)$$

$$p(X_1,X_2,t;\Omega) \to 0, \quad |X_2| \to \infty \quad (25)$$

The discretization process and equation for the numerical solution of the above equations by the FE method are very similar to that of solving Eqs. (7)–(13). The probability of failure of the oscillator can then be expressed in terms of the conditional transition PDF as follows

$$P_f(t) = 1 - \iint_{\Omega} p(\mathbf{X},t;\Omega)d\mathbf{X} \quad (26)$$

The accuracy of the FE method based numerical procedure as described above will be illustrated by application on the Van der Pol oscillator (Eq. (16)). The drift vector coefficients are given by

$$\mathbf{m}(\mathbf{X}) = \begin{bmatrix} X_2 \\ -2X_2\xi(X_1^2 - 1) - X_1 \end{bmatrix} \quad (27)$$

The oscillator parameters are given by ξ=0.5, excitation parameter D=1, and initial conditions are given by [0,0] and σ^2=1/9. The barriers are placed at B=3. While no exact solution exists in literature for the first excursion failure probability, the verification of the procedure is accomplished by comparing results through numerical solutions of the backward equation, which have been compared with the MCS, as reported in Ref. [16]. Comparisons of the results from the forward and backward equations are given in Fig. 5, showing good agreement.

5 Path Integration Method

The PI method denotes a general procedure for the solution of the FP equation following the evolution in time of the conditional PDF of the Markov vector process from a specified set of initial conditions. The method exploits the almost Gaussian nature of the Markov vector locally, making it possible to express the transition PDF of the Markov process in closed form for a very short time step. The Markov character can then be invoked to build a global (in time) solution from local (in time) transition PDFs. However, the response of nonlinear systems to Gaussian excitation is non-Gaussian. Thus for the Gaussian response assumption to work,

Downloaded 02 Jun 2010 to 171.66.16.109. Redistribution subject to ASME license or copyright; see http://www.asme.org/terms/Terms_Use.cfm

one has to take extremely small time steps and space intervals in the PI procedure for improving the accuracy of the PDF. To overcome this difficulty, a new non-Gaussian transition PDF based on the Gauss–Legendre integration scheme [13], by which the non-Gaussian PDF can be expressed as a series of normal distributions [24], is proposed in this paper, which allows for a coarse space grid size and time steps, thereby reducing the computational effort. The evaluation of the PDF $p(\mathbf{X},t)$ is obtained from

$$p(\mathbf{X},t) = \int_R p(\mathbf{X},t|\mathbf{X}^0,t_0)p(\mathbf{X}^0,t_0)d\mathbf{X}^0 \tag{28}$$

where R is the range of the n-dimensional state space for $\mathbf{X}$ and $p(\mathbf{X}^0,t_0)$ is the initial probability density of $\mathbf{X}$ (t) at $t=t_0$. By dividing the time interval (t,t_0) into N small time intervals of length $\Delta t=(t-t_0)/N$, $p(\mathbf{X},t|\mathbf{X}^0,t_0)$ can be expressed as

$$p(\mathbf{X},t|\mathbf{X}^0,t_0) = \int_{R^{2(N-1)}} \cdots \int \prod_{i=1}^{N} p(\mathbf{X}^i,t_i|\mathbf{X}^{i-1},t_{i-1})d\mathbf{X}^1 \cdots d\mathbf{X}^{N-1} \tag{29}$$

which when substituted into Eq. (28) gives

$$\begin{aligned} p(\mathbf{X},t) = & \int_R p(\mathbf{X},t|\mathbf{X}^{N-1},t_{N-1})d\mathbf{X}^{N-1} \int_R \\ & \times p(\mathbf{X}^{N-1},t_{N-1}|\mathbf{X}^{N-2},t_{N-2}) \\ & \times d\mathbf{X}^{N-2} \cdots \cdots \int_R p(\mathbf{X}^2,t_2|\mathbf{X}^1,t_1) \\ & \times d\mathbf{X}^1 \int_R p(\mathbf{X}^1,t_1|\mathbf{X}^0,t_0)p(\mathbf{X}^0,t_0)d\mathbf{X}^0 \end{aligned} \tag{30}$$

where $t_0<t_1<t_2<\ldots t_N<t$. This expression shows that a long-term evolution of the PDF can be expressed in a series of short-term evolutions.

5.1 Numerical Implementation. In general, the PI is carried out over a reduced range of the state space, provided that the probability of evolution outside this range is negligible, in which case a typical step of probability evolution from t_{i-1} to t_i can be expressed as

$$p(\mathbf{X}^i,t_i) = \int_{R_S} p(\mathbf{X}^i,t_i|\mathbf{X}^{i-1},t_{i-1})p(\mathbf{X}^{i-1},t_{i-1})d\mathbf{X}^{i-1} \tag{31}$$

where R_s represents the reduced state range, within an n-dimensional rectangle. PI procedures employ an interpolation scheme to express the PDFs on the continuous domain in terms of their values at discrete grid points. PI based on the Gauss–Legendre integration scheme is equivalent to replacing implicitly the function to be integrated directly with an interpolation polynomial of a certain order, avoiding additional computation required by most explicit interpolation procedures, such as the cubic B-spline interpolation. The values of the PDFs can be obtained at the Gauss-quadrature points in subintervals without explicit interpolation and the desired accuracy can be achieved with enough Gaussian points.

The integral of Eq. (31) can be discretized into the following composite Gauss–Legendre quadrature form [13]

$$p(\mathbf{X}^i,t_i) = \sum_{k=1}^{K} \frac{z_k}{2} \sum_{l=1}^{L_k} q_{kl}p(x_{kl}^{i-1},t_{i-1})p(x^i,t_i|x_{kl}^{i-1},t_{i-1}) \tag{32}$$

where K is the number of subintervals, L_k is the number of quadrature points in the subinterval K, z_k is the length of the subinterval K, each x_{kl} is the position of a Gauss-quadrature point, and q_{kl} is its corresponding weight. Equation (32) can be used to calculate the PDF at any point x^i at step i, provided that the PDF values are known at step $i-1$. To proceed to step $i+1$, however, only the following PDFs at the Gauss points are required:

$$p(x_{mn}^i,t_i) = \sum_{k=1}^{K} \frac{z_k}{2} \sum_{l=1}^{L_K} q_{kl}p(x_{kl}^{i-1},t_{i-1})p(x_{mn}^i,t_i|x_{kl}^{i-1},t_{i-1})$$

$$m=1,\ 2,\ \ldots,K \text{ and } n=1,2,\ \ldots,L_m \tag{33}$$

Equation (33) provides a scheme to calculate the evolution of the PDF step by step, starting from a given initial PDF. With the adoption of the Gauss–Legendre quadrature rule, the evolution of a continuous PDF is approximated by stepwise evolutions at discrete Gauss points. This procedure is an enhanced random walk model where the probability transits among the grid points and each transition is multiplied by a predetermined weight.

An adjustable non-Gaussian transition PDF can be expressed as a product of a Gaussian PDF and a polynomial function, which is a truncated version of an infinite expansion. Thus the transition PDF from x_{kl} at t_{i-1} to x_{mn} at t_i is assumed in non-Gaussian form as

$$\begin{aligned} p(x_{mn}^i,t_i|x_{kl}^{i-1},t_{i-1}) = & \frac{1}{\sqrt{2\pi}\sigma(t_i)} \exp\left\{-\frac{[x_{mn}^i-m_1(t_i)]^2}{2\sigma^2(t_i)}\right\} \\ & \times \left[\sum_{n=0}^{\infty} a_n \mathrm{He}_n\left\{\frac{[x_{mn}-m_1(t_i)]}{\sigma(t_i)}\right\}\right] \end{aligned} \tag{34}$$

where $\mathrm{He}_n[\cdot]$ is the nth Hermite polynomial and $\sigma^2(t_i)=E[x^2]-[E(x)]^2=m_2(t_i)-[m_1(t_i)]^2$. The polynomial is written as a sum of the Hermite polynomials because their orthogonality with respect to the normalized Gaussian PDF makes it relatively easy to obtain the expression for the coefficients a_n. In particular, multiplying both sides of Eq. (34) by the k_{th} Hermite polynomial and integrating give

$$E\left[\mathrm{He}_k\left\{\frac{[x_{mn}-m_1(t_i)]}{\sigma(t_i)}\right\}\right] = a_k M_{kk} = a_k k! \tag{35}$$

where M_{jk} is an operator, such that $M_{jk}=0$ for $j\neq k$ and for $j=k$ gives $M_{kk}=k!$. Substituting each of the first three Hermite polynomials into this expression gives $a_0=1$ and $a_1=a_2=0$. Equation (34) can be written in terms of the Gram–Charlier series of Type A[3] as follows:

$$\begin{aligned} p(x_{mn}^i,t_i|x_{kl}^{i-1},t_{i-1}) = & \frac{1}{\sqrt{2\pi}\sigma(t_i)} \exp\left\{-\frac{[x_{mn}^i-m_1(t_i)]^2}{2\sigma^2(t_i)}\right\} \\ & \times \left[1+\sum_{n=3}^{N} a_n \mathrm{He}_n\left\{\frac{[x_{mn}-m_1(t_i)]}{\sigma(t_i)}\right\}\right] \end{aligned} \tag{36}$$

where $\mathrm{He}_n(\theta)$ stands for Hermite polynomial of order n given by

$$\mathrm{He}_n(\theta) = (-1)^n \exp\left\{\frac{\theta^2}{2}\right\} \frac{\partial^n}{\partial\theta^n} \exp\left\{-\frac{\theta^2}{2}\right\} \tag{37}$$

The next three coefficents in the series are simply related to the cumulants of $\mathbf{X}$ as $a_n=\kappa_n(X)/(n!\sigma_X^n)$ for $n=3$, 4, and 5. For $n\geq 6$, the relationships are more complicated. In practice, though, one may not wish to consider terms with $n\geq 5$ anyway, because of computational complexities associated with the higher order polynomials around the tails of the probability densities. In fact, attention is commonly limited to $n=3$ and $n=4$, which provide one antisymmetric and one symmetric correction to the Gaussian PDF.

Each transition PDF $p(x_{mn}^i,t_i|x_{kl}^{i-1},t_{i-1})$ in Eq. (33) is now assumed to be non-Gaussian, which depends only on the conditional mean, variance, and few higher moments of X_{mn} (t_i). If this conditional mean, variance, and required higher order moments are determined, then the transition PDF can be constructed in the non-Gaussian form given in Eq. (36) and then the calculation

Downloaded 02 Jun 2010 to 171.66.16.109. Redistribution subject to ASME license or copyright; see http://www.asme.org/terms/Terms_Use.cfm

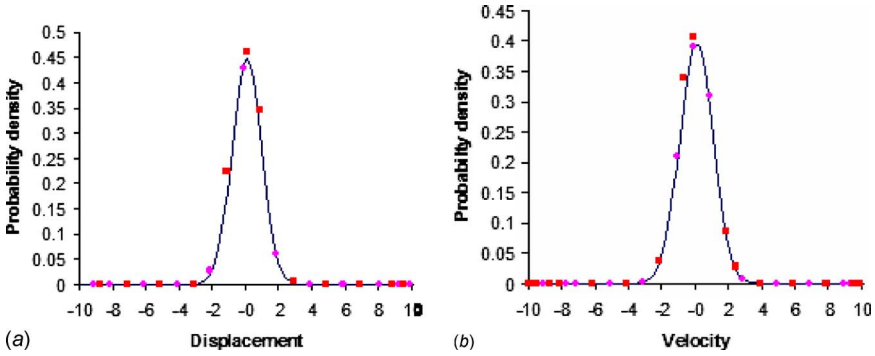


Fig. 6 Marginal PDF of (*a*) displacement and (*b*) velocity for the white noise excited Duffing oscillator; (—) exact results, (●), FEM, (■) PI method

described in Eq. (33) is straightforward.

Equation (36) can be interpreted as an expansion of a non-Gaussian PDF as a series of normal distributions. This density is of unit area, mean m_i, and variance σ^2 independent of the choice of the parameter a_n as a result of orthogonality relations between the Hermite polynomial and the standard normal distribution. However, these truncated series approximations may lead to a negative PDF in certain regions, which cannot be completely eliminated. The negative values of the transition PDF arising in a few situations are of a very low order $(10^{-5}-10^{-6})$ and are assumed to be zero.

For time-invariant systems, it is convenient to divide the time range into N equal steps $\Delta t=(t-t_0)/N$; thus $p(x^i_{mn},t_i|x^{i-1}_{kl},t_{i-1})$ remains unchanged for every time step. It needs to be calculated only once and stored for repeated use in all subsequent steps. If the system is not time-invariant, then the transition PDF $p(x^i_{mn},t_i|x^{i-1}_{kl},t_{i-1})$ must be computed for each time step.

To illustrate the performance and capability of the PI based numerical procedure for solving the FP equation, the following examples are presented together with the results.

The hardening Duffing oscillator subjected to white noise is considered as the first example.

$$\ddot{X}+2\beta\dot{X}+X+\lambda X^3=\sigma W(t) \tag{38}$$

where $W(t)$ is a unit Gaussian white noise. For $\sigma=\sqrt{4\beta}$, the system has an exact solution [12] given by

$$p_s(X_1,X_2)=C\exp\left\{-\frac{1}{2}\left(X_1^2+\frac{\lambda}{2}X_1^4+X_2^2\right)\right\} \tag{39}$$

where C is the normalization constant. The parameter β does not appear in the expression for p_s due to the specific choice of σ. For path integration, the parameters chosen are $\beta=0.25$ and $\lambda=0.2$. The initial distribution was assumed to be Gaussian with the probability density

$$p(X^{(0)},\dot{X}^{(0)})=\frac{1}{2\pi\theta_1\theta_2}\exp\left\{-\left(\frac{(X^\circ-\mu_1)^2}{2\theta_1}-\frac{(\dot{X}^\circ-\mu_2)^2}{2\theta_2}\right)\right\} \tag{40}$$

where $\mu_1=-2.0$, $\mu_2=-1.8$, $\theta_1=0.1$, and $\theta_2=0.1$. The evolution of the probability density is computed with a time step of $\Delta t=0.25$ and within a reduced state space $[-10,10]\times[-10,10]$, which is divided into 60 uniform subintervals in each direction with two quadrature points in each subinterval. For the graphical presentation, only the marginal stationary probability densities of X and $\dot{X}$ are shown in Figs. 6(*a*) and 6(*b*), respectively. It is seen that the agreement is very good, except for a slight overshoot in the central part of the marginal PDF. The stability of the numerical scheme depends on the intensity of white noise as well as on the degree of nonlinearity.

Next, the softening Duffing oscillator with external excitation is considered.

$$\ddot{X}+2\beta\dot{X}-X+\lambda X^3=\sigma W(t) \tag{41}$$

where $W(t)$ is a unit Gaussian white noise. The system has an exact solution for the case $\sigma=\sqrt{4\beta}$ given as [12]

$$p_s(X_1,X_2)=C\exp\left[\frac{X_1^2}{2}-\frac{X_2^2}{2}-\frac{\lambda X_1^4}{2}\right] \tag{42}$$

where C is the normalization constant. The parameters chosen are $\beta=0.2$, $\lambda=0.1$, and $\sigma^2=0.8$. The reduced rectangular state domain $[-10,10]\times[-10,10]$ is divided into 50 uniform subintervals in each direction with two quadrature points in each subinterval. The evolution of the probability density is computed with a time step $\Delta t=0.50$ s. Reducing the time step further did not change the computed PDF significantly. The initial distribution is the same as that of the previous example. The marginal PDF of the displacement and velocity obtained by the PI method compared very well with the analytical results, as well as with the FE solution, as shown in Figs. 7(*a*) and 7(*b*), but the accuracy in the tail region is not as good as required for reliability analysis.

6 Chaotic Dynamics

The effects of noise on the nonlinear dynamical system exhibiting chaotic behavior have been of interest in recent years [14,19]. Very few studies of the chaotic behavior in rotor dynamics have been performed. Sunderrajan and Noah [5], in their study of nonlinear dynamics of rotor systems, have shown complex behavior like chaos and have traced the routes of chaos through an arc continuation method. The phenomenon of rubs in turbomachinery is highly nonlinear and may lead to chaos. In addition to the harmonic or periodic excitation in rotor systems, if noise is also present due to rubs, the analysis of such systems and the analysis of the evolution of the probability density of the response become complex. However, the evolution of the probability density of the response of nonlinear systems driven by a combination of deterministic periodic excitation and white noise excitation can be described by a corresponding FP equation.

If the nonlinear system exhibits chaotic behavior due to the deterministic excitation and, if in addition, a stochastic excitation is also present, the response of the nonlinear system to the combination of the deterministic and random excitations may consist of coexisting chaotic and stochastic parts and it becomes difficult to distinguish between the two behaviors. A number of works have been reported in literature considering this problem [14]. In this paper, the effect of noise on chaotic nonlinear systems is considered. The two well Duffing system consisting of negative linear stiffness and positive cubic nonlinearity is considered. This

Downloaded 02 Jun 2010 to 171.66.16.109. Redistribution subject to ASME license or copyright; see http://www.asme.org/terms/Terms_Use.cfm

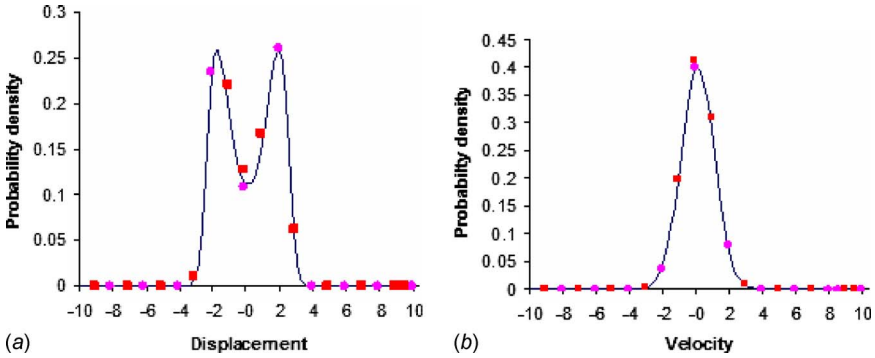


Fig. 7 Marginal PDF of the (*a*) displacement and (*b*) velocity. Key as in Fig. 6.

system may be used to model the forced vibration of a buckled rotor blade. The response of this system is given by

$$\ddot{X} + 2\beta\dot{X} - X + X^3 = f_0 \cos \omega t \tag{43}$$

which is chaotic for the values of the parameters $\beta=0.075$, $\omega=1.0$, and $f_0=0.3$[25]. The Poincaré section, which is a stroboscopic projection of the phase points corresponding to a sampling period $2\pi/\omega$, is shown in Fig. 8, which has the familiar strange attractor and fractal appearance typical of the chaotic attractor.

Assume that the above Duffing oscillator is subjected to additional Gaussian white noise excitation given by

$$\ddot{X} + 2\beta\dot{X} - X + X^3 = f_0 \cos \omega t + W(t) \tag{44}$$

Expressing Eq. (44) in state space form we get

$$\begin{pmatrix} \dot{X}_1 \\ \dot{X}_2 \end{pmatrix} = \begin{pmatrix} X_1 \\ X_2 - X_2^3 \end{pmatrix} + \begin{pmatrix} 0 \\ -2\beta X_1 + f_0 \cos \omega t + W(t) \end{pmatrix} \tag{45}$$

The corresponding FP equation is given by

$$\frac{\partial p}{\partial t} = -\frac{\partial (X_1 p)}{\partial X_2} - \frac{\partial(-2\beta X_1 + X_2 - X_2^3 + f_0 \cos \omega t)p}{\partial X_1} + \frac{D}{2}\frac{\partial^2 p}{\partial X_1^2} \tag{46}$$

6.1 Numerical Procedure. The numerical approach of obtaining the joint PDF by the PI method is based on a discrete lattice representation. By discretizing the probability domain at the ends of the segment (i.e., pre- and poststate), the short time PDF is converted to the transition tensor and the PDF at the poststate is obtained by accumulating all contributions from the prestate. The desired PDF can be obtained by the above procedure.

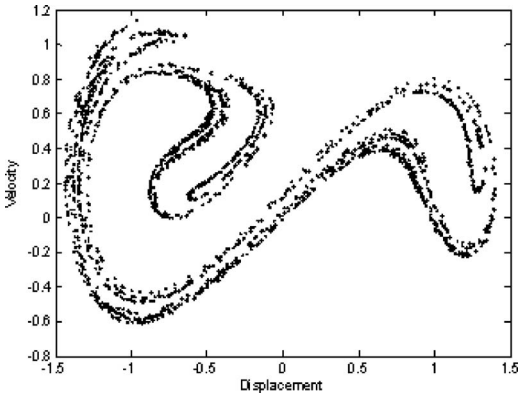


Fig. 8 A strange attractor for the Duffing oscillator given by Eq. (43) with $\beta=0.075$, $\omega=1.0$, and $f_0=0.3$

Using a multidimensional histogram representation for the probability density, the path sum can be implemented numerically. For convenience, just consider a one-dimensional system. The probability domain at time t is discretized into a finite number of elements represented by the function π as follows

$$p(x,t) = \sum_{i=1}^{N} \pi(x - x^i) p_i(t) \tag{47}$$

where

$$\pi(x - x^i) = \begin{cases} 1, & \left(x^i - \dfrac{\Delta x^{i-1}}{2}\right) \leqslant x \leqslant \left(x^i + \dfrac{\Delta x^i}{2}\right) \\ 0 & \text{otherwise} \end{cases} \tag{48}$$

The PDF at time $t+\Delta t$ can be obtained by summing up all the probability mass propagated from time t and normalizing afterward

$$p_i(t + \Delta t) = T_{ij}(\Delta t) p_j(t) \tag{49}$$

where the transition tensor T_{ij} is a banded matrix representing the Gaussian nature of the short time probability centered about the time dependent drift. Here, this histogram procedure is used in two dimensions [14]. For numerical calculation the initial conditions are assumed deterministic. They are represented by a product of two Dirac delta functions given by

$$p(x,t_0) = \delta(x_1 - x_{10})\delta(x_2 - x_{20}) \tag{50}$$

which resembles a dot with virtually zero area in phase space.

A time averaged density can serve as an invariant measure for both deterministic and noisy chaos [26] as follows

$$p_{\text{av}}(x_1,x_2) = \frac{1}{t_n}\int_0^{t_n} p(x_1,x_2,t)dt \tag{51}$$

where $t_n \gg 0$. The invariant measure on x_1 can be defined as

$$p_{\text{av}}(x_1) = \int_{-\infty}^{\infty} p_{\text{av}}(x_1,x_2)dx_2 \tag{52}$$

Figure 9 shows the time averaged probability density for the noisy chaotic attractors with the noise intensity at 0.02 (dashed line) and 0.07 (solid line). The invariant measure indicates that the probability of a large excursion is increased as the noise intensity increases. With this measure, the design incorporating extreme excursion induced failure in a noisy chaotic system may be derived.

7 Conclusion

In this paper, the FP equation is solved by the modified FE and the PI method to predict the stochastic and chaotic response, tran-

Downloaded 02 Jun 2010 to 171.66.16.109. Redistribution subject to ASME license or copyright; see http://www.asme.org/terms/Terms_Use.cfm

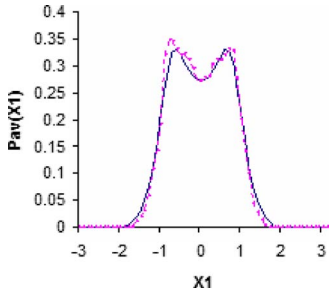


Fig. 9 Invariant measure on X_1: (●) noise intensity at 0.02 and (—) noise intensity at 0.07

sient statistics and reliability analysis of a number of SDOF nonlinear systems representative of a rotor blade subjected to random excitation. A non-Gaussian transition probability density approximation scheme in conjunction with the PI method is proposed for the solution of the FP equation associated with some nonlinear dynamical systems. The examples considered show the efficacy of the proposed method. The method is useful in reducing the computational time and cost due to a reduced number of time steps on the coarse grid. However, problems of accuracy and negative probability densities in certain regions have been observed. The transient FP equation is solved for the safe domain using the FE method. Using the time averaged probability density as an invariant measure, the probability of a large excursion is estimated. Numerical results show that the presence of external noise has a significant effect on the transition between different response states and between co-existing attractors, and the probability of a large excursion is increased as the noise intensity increases.

References

[1] Srinivasan, A. V., 1997, "Flutter and Resonant Vibration Characteristics of Engine Blade," ASME J. Eng. Gas Turbines Power, **119**(4), pp. 742–775.

[2] Griffin, J. H., and Hoosac, T. M., 1984, "Model Development and Statistical Investigation of Turbine Blade Mistuning," ASME J. Vib., Acoust., Stress, Reliab. Des., **106**, pp. 204–210.

[3] Cha, D. and Sinha, A., 1999, "Statistics of Response of a Mistuned Baded Disk Assembly Subjected to White Noise and Narrow Band Excitation," ASME J. Eng. Gas Turbines Power, **119**, pp. 710–717.

[4] Bread, C., Green, J. S., Vahdati, M., and Imregun, M., 2001, "A Non-Linear Integrated Aeroelasticity Method for the Prediction of Turbine Forced Response With Friction Damper," Int. J. Mech. Sci., **43**, pp. 2715–2736.

[5] Sunderrajan, P., and Noah, S. T., 1997, "Dynamics of Forced Nonlinear Systems Using Shooting/Arc-Length Continuation Method-Application to Rotor Systems," ASME J. Vibr. Acoust., **119**, pp. 9–20.

[6] Sogliero, G., and Srinivasan, A. V., 1980, "Fatigue Life Estimates of Mistuned Blades Via a Stochastic Approach," AIAA J., **18**(83), pp. 318–323.

[7] Roberts, J. B., and Spanos, P. D., 1990, *Random Vibration and Statistical Linearization*, Wiley, New York.

[8] Crandall, S. H., 1963, "Perturbation Techniques for Random Vibration of Nonlinear Systems," J. Acoust. Soc. Am., **35**(11), pp. 1700–1705.

[9] Wojtkiewicz, S. F., and Spencer, B. F., Jr., and Bergman, L. A., 1996, "On the Cumulant-Neglect Closure Method in Stochastic Dynamics," Int. J. Non-Linear Mech., **31**(3), pp. 657–684.

[10] Nigam, N. C., 1983, *Introduction for Random Vibration*, MIT, Cambridge, MA.

[11] Wehner, M. F., and Wolfer, W. G., 1983, "Numerical Evaluation of Path-Integral Solutions to Fokker–Planck Equation," Phys. Rev. A, **27**(5), pp. 2663–2670.

[12] Naess, A., and Moe, V., 2000, "Efficient Path Integration Method for Nonlinear Dynamics System," Probab. Eng. Mech., **15**, pp. 221–231.

[13] Yu, J. S., Cai, G. Q., and Lin, Y. K., 1997, "A New Path Integration Procedure Based on Gauss–Legendre Scheme," Int. J. Non-Linear Mech., **32**, pp. 759–768.

[14] Lin, H. and Yim, S. C. S., 1994, "A Path Integral Procedure for the Analysis of a Noisy Nonlinear System," *Proceedings of the Second International Conference on Computational Stochastic Mechanics*, Spanos, Athens, June 12–15, pp. 371–377.

[15] Langley, R. S., 1985, "A Finite Element Method for the Statistics of Non-Linear Random Vibration," J. Sound Vib., **101**(1), pp. 41–54.

[16] Spencer, B. F., and Bergman, L. A., 1991, "Numerical Solution of the Fokker–Planck Equation for First Passage Probability," *Computational Stochastic Mechanics*, P. D. Spanos and C. A. Brebbia, eds., Elsevier, Southampton, pp. 359–370.

[17] Kumar, P., and Narayanan, S., 2006, "Solution of Fokker–Planck Equation by Finite Element and Finite Difference Methods for Nonlinear System," Sadhana: Proc., Indian Acad. Sci., **31**(4), pp. 455–473.

[18] Wojtkiewicz, S. F., Bergman, L. A., and Spencer, B. F., Jr., 1994, "Robust Numerical Solution of the Fokker–Planck–Kolmogorov Equation for Two Dimensional Stochastic Dynamical Systems," Department of Aeronautical and Astronautical Engineering, University of Illinois at Urbana-Champaign, Technical Report No. AAE 94-08.

[19] Kunert, A., 1991, "Efficient Numerical Solution of Multidimensional Fokker–Planck Equations With Chaotic and Nonlinear Random Vibration," *Vibration Analysis: Analytical and Computational*, T. C. Huang, eds., Vol. DE-37, pp. 57–60.

[20] Soong, T., and Grigoriu, M., 1993, *Random Vibration of Mechanical and Structural Systems*, Prentice-Hall, Englewood Cliffs, NJ.

[21] Wong, E., and Zakai, M., 1965, "On the Relation Between Ordinary and Stochastic Differential Equation," Int. J. Eng. Sci., **3**, pp. 213–229.

[22] Risken, H., 1989, *The Fokker–Planck Equation: Methods of Solution and Applications*, Springer-Verlag, New York.

[23] Crandall, S. H., 1970, "First Crossing Probabilities of the Linear Oscillator," J. Sound Vib., **12**(3), pp. 285–299.

[24] Zhang, D. S., Wei, G. W., Kouri, D. J., and Hoffman, D. K., 1997, "Numerical Method for the Nonlinear Fokker–Planck Equation," Phys. Rev. E, **56**(1), pp. 1197–1206.

[25] Naess, A., 2000, "Chaos and Nonlinear Stochastic Dynamics," Probab. Eng. Mech., **15**, pp. 37–47.

[26] Jung, P., and Hänggi, P., 1990, "Invariant Measure of a Driven Nonlinear Oscillator With External Noise," Phys. Rev. Lett., **65**, pp. 3365–3368.

Downloaded 02 Jun 2010 to 171.66.16.109. Redistribution subject to ASME license or copyright; see http://www.asme.org/terms/Terms_Use.cfm

Measurements Versus Predictions for the Rotordynamic Characteristics of a Five-Pad Rocker-Pivot Tilting-Pad Bearing in Load-Between-Pad Configuration

Clint R Carter
Graduate Research Assistant
e-mail: crcarter@dow.com

Dara W. Childs
The Leland T. Jordan Professor of Mechanical Engineering
e-mail: dchilds@tamu.edu

Turbomachinery Laboratory,
Texas A&M University,
College Station, TX 77843-3123

Rotordynamic data are presented for a rocker-pivot tilting-pad bearing in the load-between-pad configuration for unit loads over the range 345–3101 kPa and speeds over the range 4000–13,000 rpm. The bearing was directly lubricated through a leading-edge groove with the following specifications: Five pads, 0.282 preload, 60% offset, 57.87 deg pad arc angle, 101.587 mm (3.9995 in.) rotor diameter, 0.1575 mm (0.0062 in.) diametral clearance, and 60.325 mm (2.375 in.) pad length. Dynamic tests were performed over a range of frequencies to investigate frequency effects on the dynamic stiffness coefficients. Under most test conditions, the direct real parts of the dynamic stiffnesses could be approximated as quadratic functions of the excitation frequency and accounted for with the addition of an added-mass matrix to the conventional [K][C] matrix model to produce a frequency-independent [K][C][M] model. Measured added-mass terms in the loaded direction approached 60 kg. At low speeds, "hardening" direct dynamic stiffness coefficients that increased with increasing frequency were obtained, which produced negative added-mass terms. No frequency dependency was obtained for the direct damping coefficients. The dynamic experimental results were compared to predictions from a bulk-flow computational fluid dynamics analysis. The static load direction in the tests was y. The direct stiffness coefficients K_{xx} and K_{yy} were slightly overpredicted. Measured direct damping coefficients C_{xx} and C_{yy} were insensitive to changes in either the load or speed in contrast to predictions of marked C_{yy} sensitivity for changes in the load. Only at the highest test speed of 13,000 rpm were the direct damping coefficients adequately predicted. Measurable cross-coupled stiffness coefficients were obtained for the bearings with K_{xy} and K_{yx} being approximately equal in magnitude but opposite in sign—clearly destabilizing. However, the whirl frequency ratio was found to be zero at all test conditions indicating infinite stability for the bearing. [DOI: 10.1115/1.2967728]

Introduction

Tilting-pad (TP) journal bearings have long been the bearing of choice for high-speed turbomachines. The inherent stability of the bearing gives it substantial advantages over fixed-arc journal bearings. Figure 1 illustrates the "rocker-pivot" pad TP bearing used in this study. The rocker pivot allows pad rotation about the contact axis of the pad and the bearing shell (parallel to the rotor axis). For load-on-pad (LOP) and load-between-pad (LBP) conditions, this bearing is expected to produce negligible destabilizing forces

In 1964, Lund [3] calculated the stiffness and damping coefficients for a single fixed nonrotational pad and then summed the contributions from each pad to find the combined effect of the pad assembly. This procedure is "Lund's pad assembly method." Lund's design curves do not account for frequency dependency, and for many years the common assumption was that the coefficients should be calculated at the synchronous frequency. Several authors have produced calculated results for tilting-pad bearings showing a significant frequency dependency for the coefficients in a $[K][C]$ model; Warner and Soler [4] raised the issue in 1975.

One of the first experimental investigations of the phenomenon was conducted by Ha and Yang [5]. They performed experiments on a five-pad TP bearing with a 300 mm journal in the LOP configuration. The bearing had zero preload and the pivot position was centered. The bearing was excited at frequencies that varied from 0.6 to 0.9 times the running speed. They found a slight decrease in the stiffness coefficients as well as a slight increase in the damping coefficients with increasing frequency. The results were limited by low speeds, loads, and amplitudes of excitation but were significant because they gave the first measured indication of frequency dependency.

Wygant [6] tested a five-pad rocker-pivot TP bearing with an L/D ratio of 0.75, journal diameter of 70 mm, a bearing clearance of 81.3 μm, a pad clearance of 91.4 μm, and a 50% offset in both LOP and LBP configurations. All tests were run at 900 rpm and the unit loads ranged from 0.133 kN to 0.534 kN. He excited the bearing using a single frequency excitation Ω with two linearly independent orbits, producing frequency-dependent $[K(\Omega)]$ and $[C(\Omega)]$ matrices. Wygant examined the effect of variable frequency excitation on the stiffness and damping coefficients by exciting the bearing at 0.5, 1, and 2 times the running speed. For

Contributed by the International Gas Turbine Institute of ASME for publication in the JOURNAL OF ENGINEERING FOR GAS TURBINES AND POWER. Manuscript received April 3, 2008; final manuscript received April 10, 2008; published online October 13, 2008. Review conducted by Dilip R. Ballal. Paper presented at the ASME Turbo Expo 2008; Land, Sea and Air (GT2008), Berlin, Germany, June 9–13, 2008.

Copyright © 2009 by ASME

Downloaded 02 Jun 2010 to 171.66.16.109. Redistribution subject to ASME license or copyright; see http://www.asme.org/terms/Terms_Use.cfm

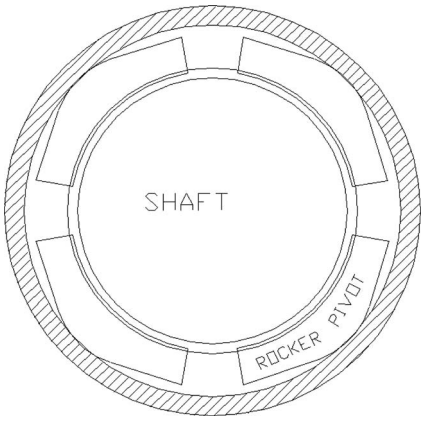


Fig. 1 Rocker-pivot tilting-pad bearing [1,2]

synchronous excitation, the following rms relevant uncertainties are cited: C_{xx} (15.5%) and C_{yy} (14.66%). Significantly better uncertainties were obtained at the $0.5X$ and $2X$ excitation frequencies. He found the direct stiffness coefficients to decrease with increasing frequency (consistent with Refs. [4,5]) and the direct damping coefficients to increase slightly (consistent with Ref. [5]).

Dmochowski [7] tested a 99 mm diameter ($L/D=0.4$) five-pad rocker-pivot TP bearing in a LBP configuration. The bearing was run at 8990 rpm (150 Hz) with an applied load of 4.0 kN. He also tested a 100 mm diameter ($L/D=1$) five-pad rocker-pivot-pad TP bearing in the LOP configuration. The preload for the bearings was 0.3; the offset was not specified. He used a multifrequency excitation approach with a frequency range up to 300 Hz with an increment of 10 Hz. The test results show a fair amount of scatter; however, the direct real dynamic-stiffness coefficients were reasonably fitted with a quadratic curve (netting a frequency-independent stiffness and mass model), and the direct imaginary dynamic-stiffness coefficients were reasonably fitted with a linear curve (netting a frequency-independent damping model). His model included the influence of pad contact flexibility and did a generally good job of predicting the measured results.

Ikeda et al. [8] performed tests for a large 580 mm (20.8 in.) diameter four-pad TP bearing in the LBP configuration. Aside from its larger size, their bearing is the same as the one tested in this paper. It was made by the same manufacturer and has the same wedge-shaped leading-edge groove (LEG) to facilitate direct lubrication. Synchronous excitation testing was done to obtain the stiffness and damping coefficients. They found that the direct stiffness coefficients increased linearly with the Sommerfeld number but that the stiffness coefficients were overpredicted by their Reynolds-equation code. The direct damping coefficients remained almost constant regardless of the loading or speed condition, in contrast with predictions of a linear increase with an increasing Sommerfeld number.

Recent investigations into the frequency dependency of TP bearing rotordynamic coefficients have been undertaken by Rodriguez and Childs [9] and Al-Ghasem and Childs [10]. Rodriguez and Childs tested a 116.8 mm (4.6 in) diameter flexure-pivot-pad bearing in a LOP configuration to obtain rotordynamic coefficients and to observe frequency effects. A 50% offset was provided. The bearing was tested for a range of speeds from 4000 rpm to 12,000 rpm with multifrequency excitation over the range of 20–300 Hz in 20 Hz increments. Frequency-dependent real dynamic-stiffness coefficients were found and accounted for with frequency-independent mass terms that approached 40 kg. The imaginary direct dynamic-stiffness coefficients were linear functions of excitation frequency; hence, a constant (frequency independent) direct damping coefficient accurately modeled the measured result. Al-Ghasem and Childs [10] tested the same bearing in a LBP load condition, obtaining basically the same results. Predictions from the bulk-flow and Reynolds-equation models were compared to measurements. For excitation frequencies at or below the running speed, predictions from the two models were very close. For higher frequencies, the bulk-flow model did a modestly better job, producing a slightly larger added-mass coefficient.

Test Rig Description

The testing apparatus shown in Fig. 2 was designed by Kaul [11] and implemented by Culotta [12]. Originally designed to test oil seals, this test rig has been adapted to test pressure-dam, TP, and flexure-pivot-pad bearings. The test bearing is placed at the center of the rotor, which is supported on both ends by hybrid ceramic ball bearings that are lubricated with a mist lube system. The bearing is supported in a housing that is attached to the support bearing pedestals via "pitch stabilizers." The pitch stabilizers consist of two pairs of three opposed turnbuckles that are spaced at 120 deg arcs around the housing. They allow the bearing housing to move freely in the radial direction yet prevent pitch and yaw rotations and axial movement. Power is delivered to the rotor via a 65 kW (90 hp) air turbine and flexible coupling. Speed can be varied from 0 rpm to 16,000 rpm. ISO VG32 oil is supplied to the test bearing housing via a gear pump in varying quantities up to 90 l/min.

Static and Dynamic Loading. A range of static external loads is applied from a pneumatic loader to the test bearing for speeds ranging from 4000 rpm to 13,000 rpm. The static loader can apply a steady load up to 22 kN in the y direction. The hydraulic shakers shown in Fig. 3 provide dynamic loads that are parallel and perpendicular to the static load.

A pseudo-random waveform that includes all frequencies from 20 Hz to 320 Hz in 20 Hz intervals is the input signal to the hydraulic shakers. The amplitude and phase of the waveform components are determined to minimize the peak force required from the shaker while providing adequate response amplitudes within the bearing. The shakers apply forces to the bearing housing via stingers. A stinger is rigidly attached to the bearing housing at one end and attached to the shaker via a load cell that is used to record the loads imposed by the shaker.

Instrumentation. As shown in Fig. 3, two piezoelectric accelerometers are attached to the bearing housing to record its acceleration components. Eddy-current proximity probes are placed in the x and y axes of the bearing housing to measure the displacement of the bearing relative to the rotor. Two probes are placed in a plane at the drive end, and two more are placed in a parallel plane at the nondrive end. Because measurements are taken in two parallel planes, both the pitch and yaw of the stator housing can be measured prior to testing and then eliminated.

Pad temperatures are monitored via embedded thermocouples that are installed just below the Babbitt surface of the pad. Thermocouples are also installed in the bearing housing to monitor the oil inlet and exit temperatures. Fluid pressure probes measure the oil inlet and exit pressures. A turbine flow meter is used to measure the bearing flow rate.

Test Bearing. A five-pad rocker-pivot TP bearing with a 60% pivot offset was tested. Lubrication is applied directly to a pad via the LEG, as shown in Fig. 4. The wedge shape of the leading edge is called a "flow director." It wipes and redirects hot carryover oil away from the cool oil that is being injected into the leading-edge recess. This design was pioneered by Ball and Byrne [13]. Table 1 provides details of the bearing geometry.

Predictions

As applied to bearings the lubrication theory has traditionally been based on the Reynolds equation obtained from the Navier–

Downloaded 02 Jun 2010 to 171.66.16.109. Redistribution subject to ASME license or copyright; see http://www.asme.org/terms/Terms_Use.cfm

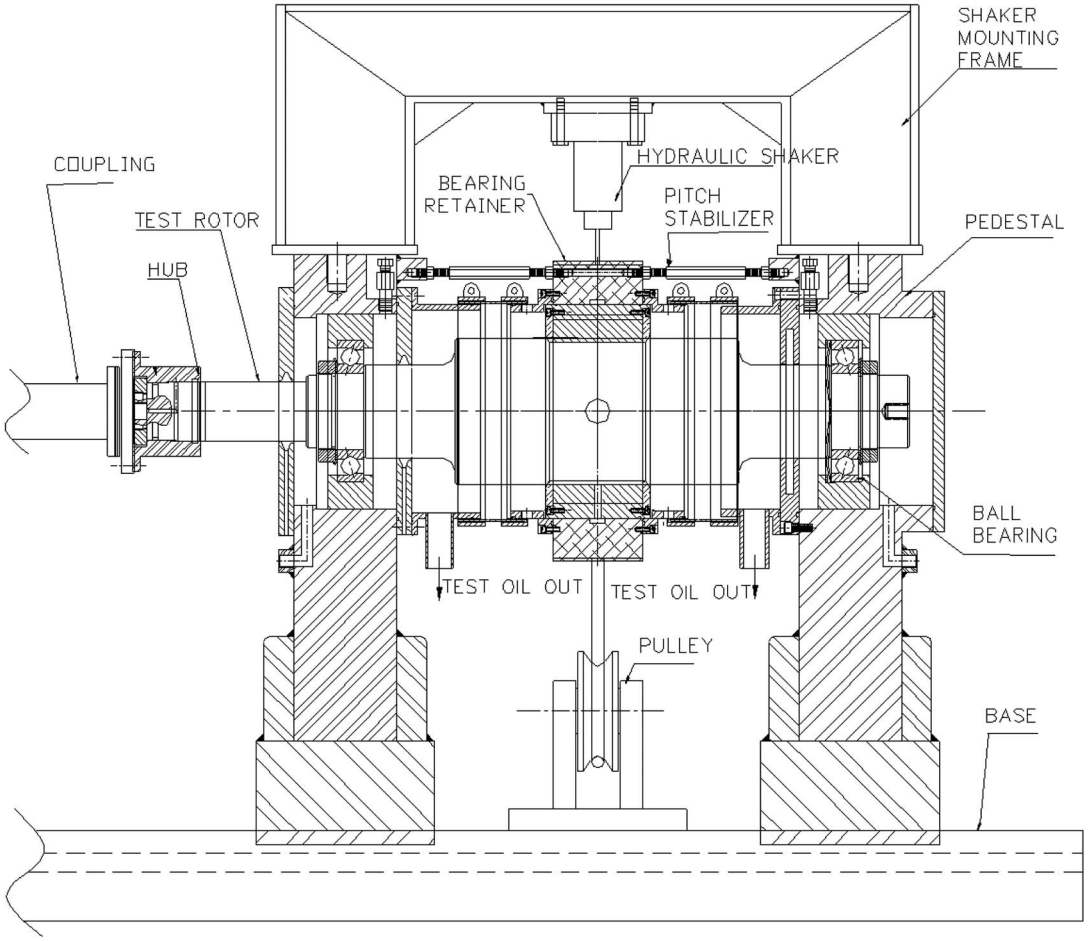


Fig. 2 Cross-sectional view of the test stand [2]

Stokes equations once the temporal and convective acceleration terms are dropped. However, Reinhardt and Lund [14] reported that purely laminar flows can lead to inertial effects stating that Reynolds numbers as small as 100 could produce substantial inertial effects that will not be predicted by the Reynolds equation. Incorporating their findings into a linearized bearing model requires the mass matrix of Eq. (1). The bearing reaction forces are modeled with stiffness $[K]$, damping $[C]$, and added-mass matrices $[M]$. Each coefficient in the matrices is designated by the subscripts (xx, yy) or (xy, yx); the former represent direct, and the latter represent cross-coupled coefficients.

$$-\begin{bmatrix} f_{bx} \\ f_{by} \end{bmatrix} = \begin{bmatrix} K_{xx} & K_{xy} \\ K_{yx} & K_{yy} \end{bmatrix} \begin{bmatrix} \Delta x \\ \Delta y \end{bmatrix} + \begin{bmatrix} C_{xx} & C_{xy} \\ C_{yx} & C_{yy} \end{bmatrix} \begin{bmatrix} \Delta \dot{x} \\ \Delta \dot{y} \end{bmatrix} + \begin{bmatrix} M_{xx} & M_{xy} \\ M_{yx} & M_{yy} \end{bmatrix} \begin{bmatrix} \Delta \ddot{x} \\ \Delta \ddot{y} \end{bmatrix} \tag{1}$$

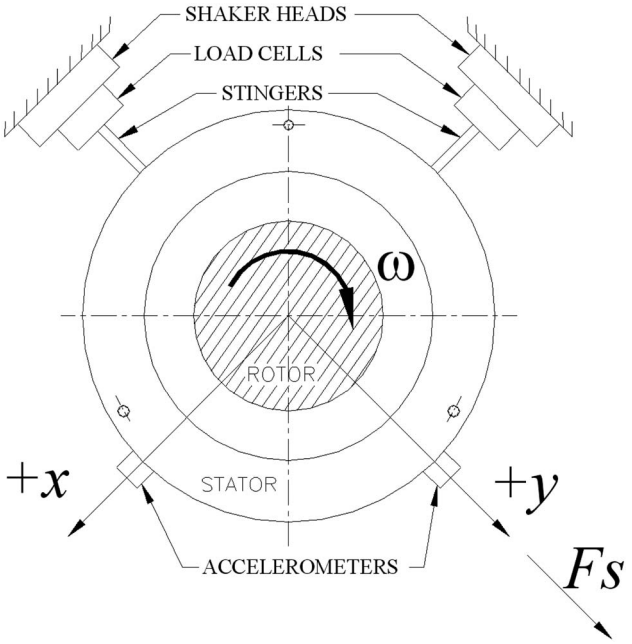


Fig. 3 Exciter head shown attached to the stator via stingers and load [2]

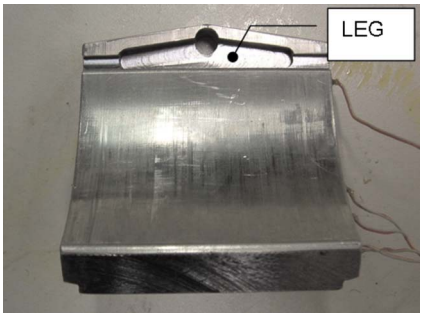


Fig. 4 Photo of the leading edge groove

Downloaded 02 Jun 2010 to 171.66.16.109. Redistribution subject to ASME license or copyright; see http://www.asme.org/terms/Terms_Use.cfm

Table 1 Bearing design specifications

No. of pads	5
Configuration	LBP
Pad arc angle	57.87 deg
Pivot offset	60%
Rotor diameter	101.587 mm (3.9995 in.)
Pad axial length	60.325 mm (2.375 in.)
Diametrical pad clearance	0.221 mm (0.0087 in.)
Diametrical bearing clearance	0.1575 mm (0.0062 in.)
Preload	0.282
Radial pad clearance (C_p)	0.1105 mm (0.00435 in.)
Radial bearing clearance (C_b)	0.0792 mm (0.00312 in.)
Pad polar inertia	0.000249 kg m^2
Pad mass	0.44 kg (0.96 lb m)
Lubricant type	ISO VG32

A bulk-flow model developed by San Andrés [15] was used for this study. The code has an option for a Reynolds-equation analysis. For a fixed-geometry bearing, a Reynolds-equation model can only produce the stiffness and damping matrices of a conventional $[K][C]$ model and not the added-mass matrix. Rodriguez and Childs [9] and Al-Ghosem and Childs [10] state that the Reynolds-equation model predicted their measured added-mass terms adequately due to the reduction in the degrees of freedom from the initial 12 degrees (four pads times three degrees of freedom) to the two rotor degrees of freedom. The bulk-flow analysis gave comparable results to the Reynolds model out to running speed, but gave modestly better agreement with experimental results at higher excitation frequencies. Based on those results, the bulk-flow model was used in this study.

Experimental Procedure

Table 2 below lists the various conditions for which the bearing was tested. These conditions vary from 4000 rpm to 13,000 rpm and from 345 kPa to 3101 kPa. Each test condition in Table 2 included a static and a dynamic test. After reaching a steady-state operating condition, a pseudo-random waveform input signal was sent sequentially to the x and then the y hydraulic shakers. Each *test* consisted of one *shake* in the x direction followed by another shake in the y direction. Each shake contains a waveform that is repeated 32 times with the data being averaged in the frequency domain. Ten tests are performed on the bearing for each test condition to perform a statistical repeatability analysis. Hence, for each condition there are $32 \times 10 = 320$ waveforms applied to the bearing in both the x direction and perpendicular y direction.

Dynamic-Stiffness Coefficients. The dynamic data sets are used to determine the rotordynamic stiffness, damping, and added-mass coefficients using a process described by Childs and Hale [16] and Rouvas and Childs [17]. After applying Newton's second law to the stator in both the x and y directions the equation of motion is

$$M_s \begin{bmatrix} \ddot{x}_s \\ \ddot{y}_s \end{bmatrix} = \begin{bmatrix} f_x \\ f_y \end{bmatrix} - \begin{bmatrix} f_{bx} \\ f_{by} \end{bmatrix} \tag{2}$$

In this equation, M_s is the mass of the stator, $\ddot{x}_s$ and $\ddot{y}_s$ are the stator acceleration components, f_x and f_y are the force components induced by the hydraulic shakers, and f_{bx} and f_{by} are the bearing reaction force components. Substituting Eq. (1) into Eq. (2) and applying a fast Fourier transform (FFT) produces

$$\begin{bmatrix} \boldsymbol{F}_x - M_s \boldsymbol{A}_x \\ \boldsymbol{F}_y - M_s \boldsymbol{A}_y \end{bmatrix} = - \begin{bmatrix} \boldsymbol{H}_{xx} & \boldsymbol{H}_{xy} \\ \boldsymbol{H}_{yx} & \boldsymbol{H}_{yy} \end{bmatrix} \begin{bmatrix} \boldsymbol{D}_x \\ \boldsymbol{D}_y \end{bmatrix} \tag{3}$$

Equation (3) contains $\boldsymbol{H}_{ij}$ dynamic stiffness functions that are related to the rotordynamic coefficients through

$$\boldsymbol{H}_{ij} = K_{ij} - \Omega^2 M_{ij} + j(\Omega C_{ij}) \tag{4}$$

Equation (4) shows the predicted $\boldsymbol{H}_{ij}$ term to be composed of the following real and an imaginary components

$$\mathrm{Re}(\boldsymbol{H}_{ij}) = K_{ij} - \Omega^2 M_{ij} \tag{5}$$

$$\mathrm{Im}(\boldsymbol{H}_{ij}) = \Omega C_{ij} \tag{6}$$

Equation (5) shows that estimates of the stiffness and added-mass coefficients can be obtained by curve-fitting $\mathrm{Re}(\boldsymbol{H}_{ij})$ with a quadratic function of Ω, and Eq. (6) states that estimates of the damping coefficients are found as the slope of $\mathrm{Im}(\boldsymbol{H}_{ij})$. The coefficients are referred to as "estimates" because they are not directly measured. Instead they are derived from a limited set of dynamic stiffness data, which can introduce sampling error. This error makes it necessary to introduce uncertainty terms, which can indicate the accuracy of the estimate. The uncertainty is found by using a 95% confidence interval that measures the error bound for the estimate of the slope or intercept.

Equation (3) contains two equations for the four unknown $\boldsymbol{H}_{ij}$ dynamic-stiffness functions. Four independent equations are found by shaking the stator separately in the x and y directions, netting

$$\begin{bmatrix} \boldsymbol{F}_{xx} - M_s \boldsymbol{A}_{xx} & \boldsymbol{F}_{xy} - M_s \boldsymbol{A}_{xy} \\ \boldsymbol{F}_{yx} - M_s \boldsymbol{A}_{yx} & \boldsymbol{F}_{yy} - M_s \boldsymbol{A}_{yy} \end{bmatrix} = - \begin{bmatrix} \boldsymbol{H}_{xx} & \boldsymbol{H}_{xy} \\ \boldsymbol{H}_{yx} & \boldsymbol{H}_{yx} \end{bmatrix} \begin{bmatrix} \boldsymbol{D}_{xx} & \boldsymbol{D}_{xy} \\ \boldsymbol{D}_{yx} & \boldsymbol{D}_{yy} \end{bmatrix} \tag{7}$$

Recall that each test condition involves 32 separate excitations with averaging in the frequency domain to produce each dynamic-stiffness function $\boldsymbol{H}_{ij}$.

Results and Predictions

A baseline test is performed to find the dynamic coefficients of the test-rig structure alone. The bearing housing is connected to the test rig through the pitch stabilizers as well as numerous hoses. The pitch stabilizers add a small amount of stiffness. The hoses connected to the bearing housing will also add some damping. When a dynamic test is performed, each of these components may contribute to the final rotordynamic coefficients. Because we are interested only in the bearing coefficients, all of the test-structure contributions must be subtracted from the final results. To get the

Table 2 Test matrix

	Oil flow (l/min)	Unit load				
		345 (50)	1034 (150)	1723 (250)	2412 (350)	3101 (450)
4,000 rpm	12.5	×	×	×	×	NA
7,000 rpm	20.8	×	×	×	×	×
10,000 rpm	20.8	×	×	×	×	×
13,000 rpm	30.3	×	×	×	×	×

Downloaded 02 Jun 2010 to 171.66.16.109. Redistribution subject to ASME license or copyright; see http://www.asme.org/terms/Terms_Use.cfm

baseline contribution, a "dry-shake" test is performed at zero speed with no lubricant. The $\boldsymbol{H}_{ij}$ dry-shake test results are subtracted from the actual bearing test results.

Dynamic-Stiffness Coefficients. Measured dynamic-stiffness coefficients were obtained for the test conditions in Table 2. The $\boldsymbol{H}_{ij}$ coefficients associated with the highest-speed/lowest-load condition (13,000 rpm, 345 kPa) are shown in Figs. 5(*a*)–5(*c*). The "bars" in the data reflect the repeatability uncertainties from 32 repeated tests at the same operating condition. Figure 5(*a*) shows fairly good agreement between the measured and predicted $\mathrm{Re}(\boldsymbol{H}_{xx})$ and $\mathrm{Re}(\boldsymbol{H}_{yy})$ coefficients. The model predicts $\mathrm{Re}(\boldsymbol{H}_{xx}) = \mathrm{Re}(\boldsymbol{H}_{yy})$; however, the measurements generally show $\mathrm{Re}(\boldsymbol{H}_{yy}) > \mathrm{Re}(\boldsymbol{H}_{xx})$. At low frequencies, these results will produce $K_{yy}K_{xx}$ and (unpredicted) stiffness orthotropy. Measured differences in bearing clearances in two orthogonal directions showed very small differences, so the observed orthotropy was not caused by bearing crush. The predicted curvature agrees well for $\mathrm{Re}(\boldsymbol{H}_{xx})$; however, the observed curvature for $\mathrm{Re}(\boldsymbol{H}_{yy})$ is greater than predicted. These results indicate that M_{xx} will be well predicted, but M_{yy} underpredicted.

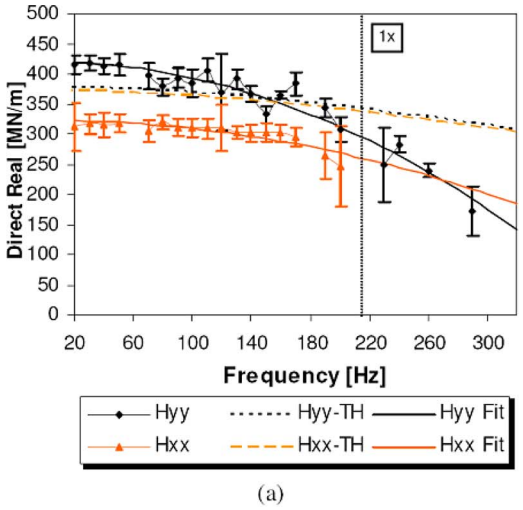
Figure 5(*b*) illustrates $\mathrm{Re}(\boldsymbol{H}_{yx})$ and $\mathrm{Re}(\boldsymbol{H}_{xy})$. The model predicts near zero values for these functions. At low excitation frequencies, the measured $\mathrm{Re}(\boldsymbol{H}_{xy})$ is approximately equal to $-\mathrm{Re}(\boldsymbol{H}_{yx})$, predicting destabilizing cross-coupled stiffness coefficients. Both functions have the same positive curvature, predicting negative and approximately equal m_{xy} and m_{yx} coefficients.

As shown in Fig. 5(*c*), the model predicts $\mathrm{Im}(\boldsymbol{H}_{xx}) = \mathrm{Im}(\boldsymbol{H}_{yy})$ versus measurements that show $\mathrm{Im}(\boldsymbol{H}_{yy}) > \mathrm{Im}(\boldsymbol{H}_{xx})$ implying $C_{yy} > C_{xx}$. The predictions and measurements predict a near zero intercept for both functions at zero frequency. Shown in Table 3 are the rotordynamic coefficients for both the measured and predicted bulk-flow results at 13,000 rpm and 345 kPa. The uncertainties associated with the measured coefficients are also shown. Measured results for $\mathrm{Im}(\boldsymbol{H}_{xy})$ and $\mathrm{Im}(\boldsymbol{H}_{yx})$ were consistently erratic functions of the excitation frequency and are not illustrated.

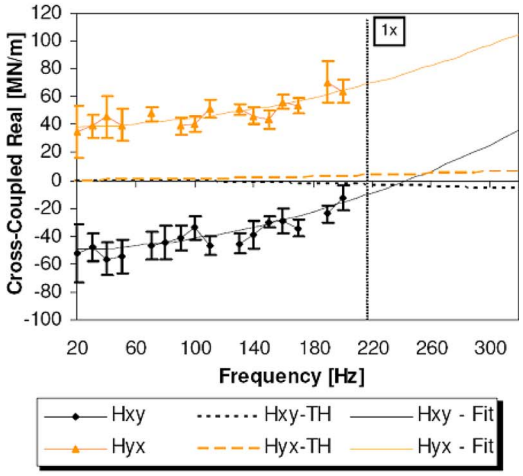
Stiffness Coefficients. Figure 6 show the effect of increasing unit load on the stiffness coefficients. The plots show that the stiffness is a generally linear function of load, shifting to a parabolic function at higher unit loads. K_{yy} is well modeled at the lower loads; however, as the load increases the code tends to overpredict. By contrast, the unloaded-stiffness coefficient K_{xx} is well modeled at all loads for the 4000 rpm and 7000 rpm cases and slightly overpredicted at the higher speeds. Stiffness orthotropy is minimal at the lower unit loadings but increases rapidly with increasing load. Measured orthotropy is modestly but consistently higher than predicted.

The cross-coupled coefficients are relatively small compared to the direct coefficients for all conditions. However, at the higher speeds they are generally equal in magnitude and opposite in sign. Hence, they could cause the bearing to destabilize, and their impact on stability will be addressed via the whirl frequency ratio (WFR).

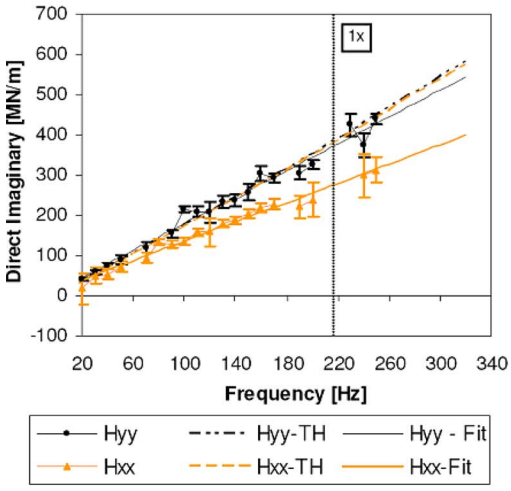
Damping Coefficients. Figure 7 shows the damping-coefficients' variation due to changes in the unit load at various speeds. The measured damping coefficients are almost completely insensitive to changes in the load. The direct damping is modeled adequately at low loads; however, it is greatly overpredicted with increasing load, especially in the loaded direction. As the speed increases, the predictions became more reliable; however, the damping is always overpredicted. The cross-coupled damping coefficients were found to be small relative to the direct coefficients and have a minimal impact on rotordynamics. At many test conditions, their small size made measurement difficult, leading to small absolute magnitudes but large relative uncertainties of the same order of magnitude as the coefficients themselves. For this reason the cross-oupled damping coefficients could not generally be estimated reliably and are not published here.



(a)



(b)



(c)

Fig. 5 LBP dynamic-stiffness coefficients at 13,000 rpm and 345 kPa for (*a*) direct real, (*b*) cross-coupled real, and (*c*) direct imaginary

Downloaded 02 Jun 2010 to 171.66.16.109. Redistribution subject to ASME license or copyright; see http://www.asme.org/terms/Terms_Use.cfm

Table 3 Rotordynamic coefficients at 13,000 pm and 345 kPa

	Units	Measured	Bulk flow	Uncertainty
K_{yy}	MN/m	420.11	375.84	11.18
K_{xx}	MN/m	322.66	370.44	7.45
C_{yy}	kN s/m	263.96	288.62	19.09
C_{xx}	kN s/m	191.13	285.39	12.65
M_{yy}	kg	68.87	17.86	8.39
M_{xx}	kg	34.42	17.62	9.90
K_{yx}	MN/m	38.20	0.07	4.24
K_{xy}	MN/m	−49.97	−0.19	8.44
M_{yx}	kg	−16.53	−1.66	5.41
M_{xy}	kg	−21.22	1.65	11.23

Added-Mass Coefficients. Direct and cross-coupled added-mass coefficients are shown in Fig. 8 versus unit loading. At 4000 rpm, M_{xx} and M_{yy} became more negative as the load increased. The negative values are consistent with our earlier observation that Re($\boldsymbol{H}_{xx}$) and Re($\boldsymbol{H}_{yy}$) increase with increasing excitation frequency. At the other speeds, there is no consistent change in M_{xx} and M_{yy} due to a change in unit loading. M_{xy} and M_{yx} are also shown versus the unit load. They both have negative signs, implying that they have no direct impact on the bearing's stability characteristic. The agreement between measurements and the prediction for the mass coefficients is only fair.

Whirl Frequency Ratio. The whirl frequency ratio characterizes the stability characteristics of a bearing. A plain journal bearing will have a WFR of about 0.5, and a TP bearing is normally assumed to have zero whirl frequency ratio. The WFR was calculated using San Andrés' [15] result that includes the fluid inertia terms. Despite the presence of destabilizing cross-coupled stiffness coefficients, zero WFR values were calculated for all conditions.

Static Data. The locus plot in Fig. 9(*a*) shows both the experimental and predicted changes in position of the bearing due to the increasing static load applied in the *y* direction by the pneumatic loader (vertically downward in Fig. 9(*a*)). Some measured cross coupling effects are present at all load conditions as shown by the deviation from the *y* axis in the loci plots. This is confirmed by the existence of small cross-coupled stiffness terms obtained by the dynamic test in Fig. 6.

The predictions in Fig. 9(*a*) for each condition show almost no cross coupling effects as are expected for a tilt pad bearing. Hence, the cross coupling seen in the experimental results mentioned above was not predicted by the code.

The plots in Fig. 9(*b*) show the relationship between the dynamic and static stiffnesses. The dynamic stiffness was obtained during the dynamic test and is simply the stiffness coefficient obtained at the zero frequency *y* intercept. The static stiffness was obtained by plotting the static load versus the bearing displacement and recording the slope of this curve at the various conditions. This slope is the static stiffness. The plot displays a good correlation between the two stiffness values except at the lowest load condition.

Summary, Discussion, and Conclusion

Measured rotordynamic-coefficient results are presented for a five-pad rocker-pivot TP bearing in the LBP configuration over a

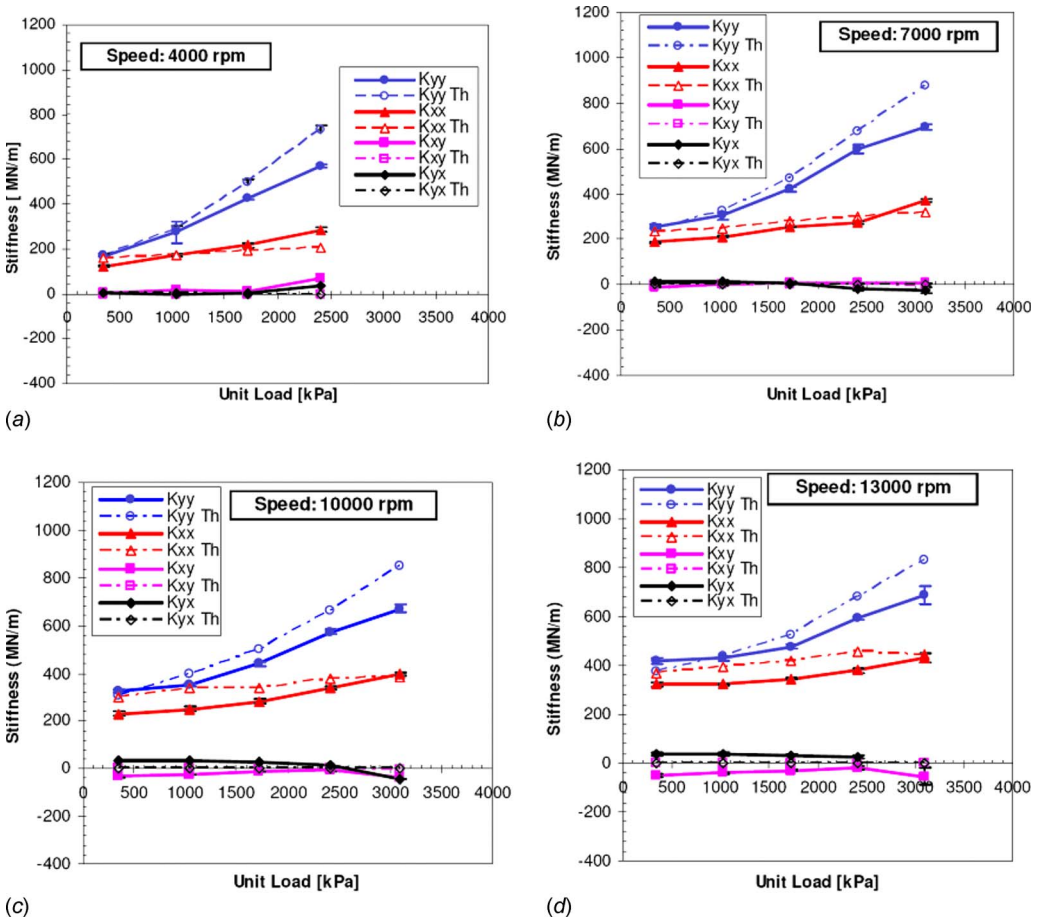


Fig. 6 LBP direct and cross-coupled stiffness coefficients versus the load for varying speeds: (*a*) 4000 rpm, (*b*) 7000 rpm, (*c*) 10,000 rpm, and (*d*) 13,000 rpm

Downloaded 02 Jun 2010 to 171.66.16.109. Redistribution subject to ASME license or copyright; see http://www.asme.org/terms/Terms_Use.cfm

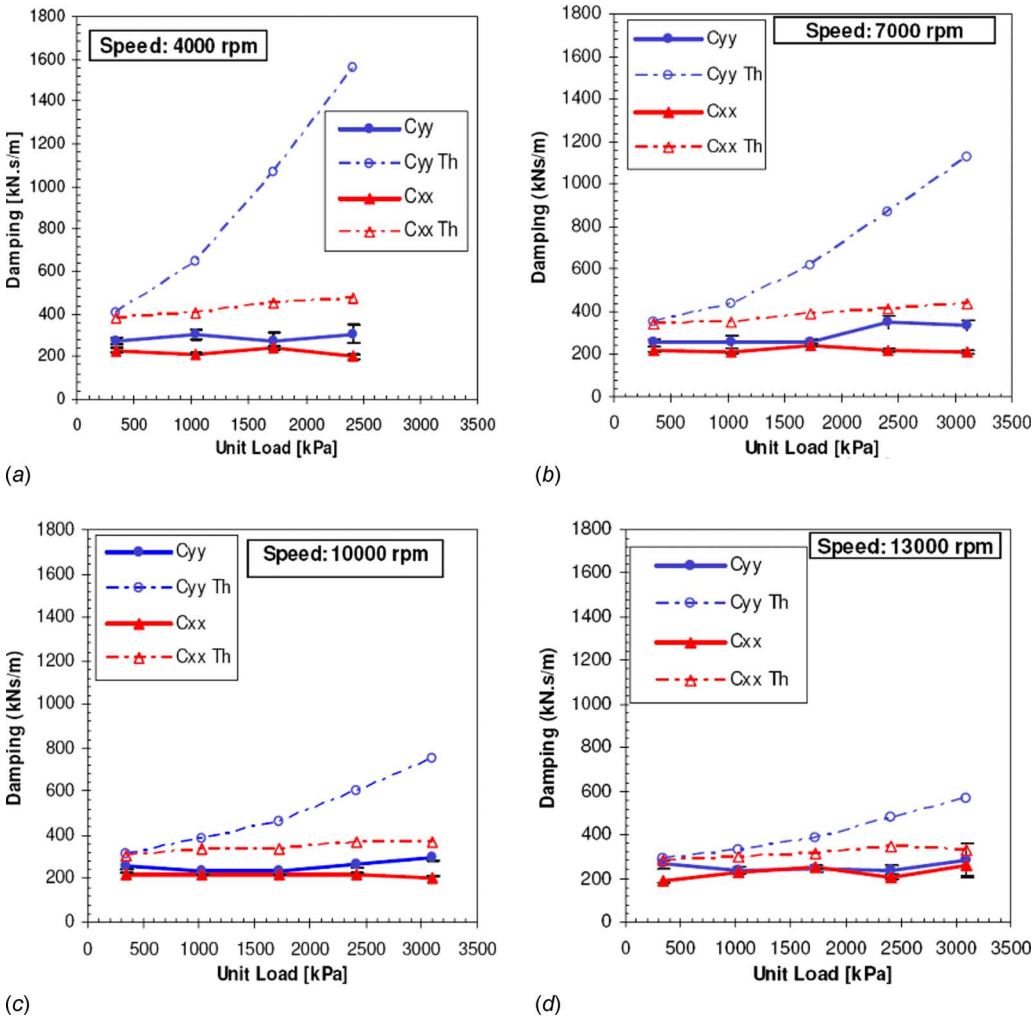


Fig. 7 LBP direct damping coefficients versus the load for varying speeds: (*a*) 4000 rpm, (*b*) 7000 rpm, (*c*) 10,000 rpm, and (*d*) 13,000 rpm

range of speeds and unit loads. The bearing was excited with a pseudo-random wave excitation from 20 to 320 Hz. Two different models can be used to define the bearing's rotordynamic coefficients. If a conventional $[K][C]$ model is chosen, the $[K]$ coefficients will be strongly frequency dependent because the real portions of the measured dynamic-stiffness coefficients vary with the excitation frequency. For the bearing tested here, a $[K][C][M]$ model works well and eliminates the frequency dependency. Both direct and cross-coupled added mass terms were measured; however, M_{xy} and M_{yx} were both negative and approximately equal. Hence, their contribution to the $[M]$ matrix will not directly impact the rotor stability. The added-mass terms tend to be small compared to the rotor's mass that they will be supporting and might cause a slight reduction in the natural frequency and critical speeds. They can be readily absorbed by finite element method-based rotordynamics codes.

The question of frequency dependency in rotordynamic coefficients largely centers on the direct-damping coefficients. $K_{xx}(\Omega)$ or $K_{yy}(\Omega)$ dependency seems to be reasonably predicted by the Reynolds-equation or bulk-flow models and can be readily accounted for by added-mass coefficients that remove the dependency. $C_{yy}(\Omega)$ and $C_{xx}(\Omega)$ dependency requires an iterative solution for the stability analysis with $\Omega=\omega_{n1}$, where ω_{n1} is the rotor's first natural frequency. Possible frequency dependency of the damping coefficients at precession frequencies that are higher than the running speed is irrelevant to the stability issue.

The present test results showed no frequency dependency in the direct damping coefficients. This outcome is consistent with Dmochowski's measurements. Comparisons to Wygnant's LBP measured results are complicated by his large uncertainties at a synchronous frequency that admit to various possible lines connecting his three frequency data points. However, from the $0.5X$ to $1X$ frequency range, Wygnant has data at Sommerfeld numbers of 0.0738, 0.222, and 0.738 but only show an increase in the $C_{yy}(\Omega)$ coefficient for a Sommerfeld number of 0.222. For the remaining two load conditions, Wygnant shows no frequency variation. For $C_{xx}(\Omega)$, a small increase (on the same order as the uncertainty) is observed from the $0.5X$ to $1X$ excitation frequency ratio. Marked differences between the present study and Wygnant's in test procedures, load and speed ranges, and bearing dimensions may account for differing outcomes and conclusions.

The identification and test procedure methods used here were used previously to measure dynamic-stiffness coefficients for hole-pattern-stator annular gas seals that have strong frequency-dependent characteristics. The measured dynamic coefficient results for these seals could not be modeled with a $[K][C][M]$ model. This method does not restrict the present measured outcomes to the quadratic functions used to identify added-mass and stiffness coefficients from measured $\mathrm{Re}(\boldsymbol{H}_{ij})$ functions. The data simply produce these outcomes. Similarly, the measured linear

Downloaded 02 Jun 2010 to 171.66.16.109. Redistribution subject to ASME license or copyright; see http://www.asme.org/terms/Terms_Use.cfm

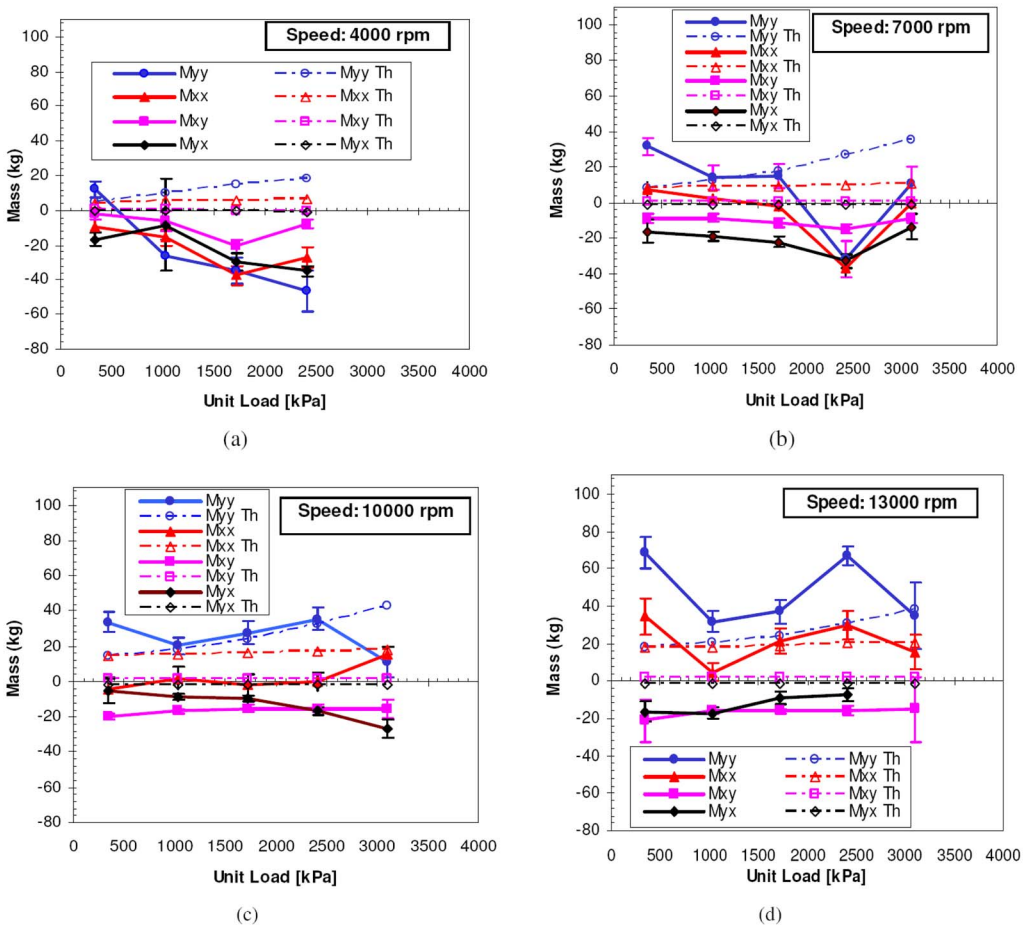


Fig. 8 LBP direct mass coefficients versus the load for varying speeds: (*a*) 4000 rpm, (*b*) 7000 rpm, (*c*) 10,000 rpm, and (*d*) 13,000 rpm

dependence of $\mathrm{Im}(\boldsymbol{H}_{ij})$ on Ω produces constant frequency-independent damping coefficients. It is not an a priori requirement of the procedure.

A summary of all measured rotordynamic-coefficient results is provided below.

Stiffness. The direct stiffness coefficients depended strongly on the applied unit load, much more so than the speed. They generally increased linearly with load, shifting to a quadratic dependence at higher unit loads. Stiffness orthotropy was apparent in test results, significantly more than predicted, and it became more pronounced at the heavier unit loads. The theory generally provided good agreement with measurements, only slightly overpredicting the stiffness coefficients.

Damping. The imaginary component of the direct dynamic-stiffness coefficient increased linearly with the excitation frequency. Consequently, the direct damping coefficients could be

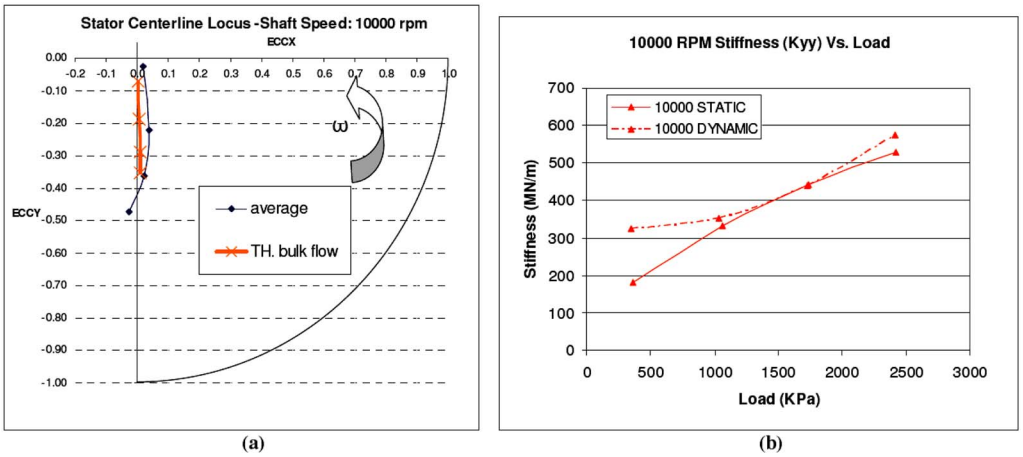


Fig. 9 (*a*) Measured and predicted loci plots at 10,000 rpm from 345 kPa to 2412 kPa and (*b*) comparison of dynamic-stiffness coefficients to the static stiffness at 10,000 rpm

Downloaded 02 Jun 2010 to 171.66.16.109. Redistribution subject to ASME license or copyright; see http://www.asme.org/terms/Terms_Use.cfm

closely modeled with constant (frequency-independent) coefficients. These coefficients generally remain constant regardless of the speed. Their observed insensitivity to changes in the unit loads is in direct conflict with predictions. At stated earlier, other researchers [7] noted similar behavior with this type of bearing. The model used here significantly overpredicted the direct damping coefficients. However, this model does not account for the contact flexibility between the pad and the bearing housing. Properly accounting for this flexibility might well produce better predictions [7].

Added mass. Large direct added-mass coefficients were found, which approached 60 kg. Direct coefficients in the loaded direction were significantly higher than in the unloaded direction. They depended significantly more on the running speed than the unit loading, rising steadily with the increasing speed. The coefficients were generally overpredicted at lower speeds and underpredicted at higher speeds. The 4000 rpm test conditions produced negative direct added-mass terms reflecting direct dynamic-stiffness coefficients that increased with the excitation frequency. This outcome was not predicted by the model, which predicted a small but positive added mass. Tests produced negative cross-coupled mass terms that were roughly equal. They would be expected to have no impact on stability.

A stability analysis of the bearing was undertaken based on the calculation of the whirl frequency ratio from measured rotordynamic coefficients. The whirl frequency ratio was zero for all conditions, predicting infinite stability.

Nomenclature

A_{ij} = Fourier transforms for the measured stator acceleration (e.g., A_{ij} is the acceleration in the j direction, due to an excitation force in the i direction), (L/t^2)

C_{ij} = direct and cross-coupled damping coefficients (Ft/L)

C_b = radial bearing clearance (L)

D = bearing diameter (L)

$\boldsymbol{D}_{ij}$ = Fourier transforms for the measured stator relative motion (L)

$\boldsymbol{F}_{ij}$ = Fourier transforms for the measured stator force (F)

F_s = static force applied by the pneumatic loader (F)

$f_{bx}\, f_{by}$ = bearing reaction force component in the x and y directions, respectively (F)

$f_x\, f_y$ = measured excitation force component in the x and y directions (F)

$\boldsymbol{H}_{ij}$ = direct and cross-coupled dynamic stiffnesses (F/L)

j = $\sqrt{-1}$

K_{ij} = direct and cross-coupled stiffness coefficients (F/L)

L = pad length (L)

M_s = mass of the stator (M)

M_{ij} = direct and cross-coupled added-mass coefficients (M)

P = bearing unit load (Fs/LD) (F/L^2)

R = bearing radius (L)

$\ddot{x}_s\ \ddot{y}_s$ = absolute acceleration of the stator in the x and y directions (L/t^2)

$\Delta x\ \Delta y$ = relative motion between the rotor and the stator in the x and y directions (L)

Ω = excitation frequency of the stator $(1/t)$

FFT = fast Fourier transform

LBP = load-between-pad

rms = root mean square

TP = tilting-pad bearing

WFR = whirl frequency ratio

Subscripts

x, y = x (unloaded) and y (loaded) directions

i, j = x, y

References

[1] Al-Ghasem, A., 2004, "Measurement of Rotordynamic Coefficients for a High Speed Flexure-Pivot Tilting-Pad Bearing (Load Between Pad) Configuration," MS thesis, Texas A&M University, College Station, TX.

[2] Rodriguez, L., 2004, "Experimental Frequency-Dependent Rotordynamic Coefficients for a Load-on-Pad, High Speed, Flexible-Pivot Tilting-Pad Bearing," MS thesis, Texas A&M University, College Station, TX.

[3] Lund, J. W., 1964, "Spring and Damping Coefficients for the Tilting-Pad Journal Bearing," ASLE Trans., **7**, pp. 342–352.

[4] Warner, R. E., and Soler, A. I., 1975, "Stability of Rotor-Bearing Systems With Generalized Support Flexibility and Damping and Aerodynamic Cross-Coupling," ASME J. Lubr. Technol., **97**, pp. 461–471.

[5] Ha, H. C., and Yang, S. H., 1999, "Excitation Frequency Effects on the Stiffness and Damping Coefficients of a Five-Pad Tilting Pad Journal Bearing," ASME J. Tribol., **121**, pp. 517–522.

[6] Wygant, K., 2001, "The Influence of Negative Preload and Non-Synchronous Excitations on the Performance of Tilting Pad Journal Bearings," Ph.D. thesis, University of Virginia, Charlottesville, VA.

[7] Dmochowski, W., 2006, "Dynamic Properties of Tilting-Pad Journal Bearings: Experimental and Theoretical Investigation of Frequency Effects Due to Pivot Flexibility," *Proceedings of ASME Turbo Expo 2006: Power for Land, Sea and Air*, Barcelona, Spain, May 8–11.

[8] Ikeda, K., Hirano, T., Yamashita, T., Mikami, M., and Sakakida, H., 2004, "An Experimental Study of Static and Dynamic Characteristics of a 580 mm (22.8 in) Diameter Direct Lubrication Tilting Pad Journal Bearing," *ASME/STLE International Joint Tribology Conference*, Long Beach, CA, Oct. 24–27.

[9] Rodriguez, L., and Childs, D., 2004, "Experimental Rotordynamic Coefficient Results for a Load-on-Pad Flexible-Pivot Tilting-Pad Bearing With Comparison to Predictions From Bulk-Flow and Reynolds Equation Models," ASME J. Tribol., **128**, pp. 378–387.

[10] Al-Ghasem, A., and Childs, D., 2006, "Rotordynamic Coefficients: Measurements Versus Predictions for a High Speed Flexure-Pivot Tilting-Pad Bearing (Load-Between-Pad Configuration)," ASME J. Eng. Gas Turbines Power, **128**(4), pp. 896–906.

[11] Kaul, A., 1999, "Design and Development of a Test Setup for the Experimental Determination of the Rotordynamic and Leakage Characteristics of Annular Bushing Oil Seals," Texas A&M University, M.S. Report.

[12] Culotta, V., 2004, "Theory Versus Experiment of the Rotordynamic and Leakage Characteristics of Smooth Annular Bushing Breakdown Oil-Seals," MS thesis, Texas A&M University, College Station, TX.

[13] Ball, J. H., and Byrne, T. R., 1998, "Tilting Pad Hydrodynamic Bearing for Rotating Machinery," Patent No. 5,795,076.

[14] Reinhardt, E., and Lund, J., 1975, "The influence of Fluid Inertia on the Dynamic Properties of Journal Bearings," ASME J. Lubr. Technol., **97**, pp. 159–167.

[15] San Andrés, L. A., 1991, "Effect of Eccentricity on the Force Response of a Hybrid Bearing," STLE Tribol. Trans., **34**, pp. 537–544.

[16] Childs, D., and Hale, K., 1994, "A Test Apparatus and Facility to Identify the Rotordynamic Coefficients of High-Speed Hydrostatic Bearings," ASME J. Tribol., **116**, pp. 337–344.

[17] Rouvas, C., and Childs, D., 1993, "A Parameter Identification Method for the Rotordynamic Coefficients of a High Reynolds Number Hydrostatic Bearing," ASME J. Vibr. Acoust., **115**, pp. 264–270.

Downloaded 02 Jun 2010 to 171.66.16.109. Redistribution subject to ASME license or copyright; see http://www.asme.org/terms/Terms_Use.cfm

Relationship of Influence Coefficients Between Static-Couple and Multiplane Methods on Two-Plane Balancing

John J. Yu
GE Energy,
1631 Bently Parkway South,
Minden, NV 89423
e-mail: john.yu@ge.com

This paper demonstrates analytical relationship of influence coefficients between static-couple and multiplane methods on two-plane balancing as well as its application. For the static-couple approach, cross-effects are defined between static weights and couple response as well as between couple weights and static response, thus making it possible to offset both static and couple vibration vectors effectively with appropriate combination of static and couple weights. Relationship of influence coefficients between static/couple and individual probe due to static/couple weights is also given. Static, couple, or individual probe influence coefficients due to static or couple weights can be obtained directly without having to place static or couple trial weights if influence coefficients used in the multiplane approach are known. From static and couple influence data as well as cross-effects, influence data for the multiplane approach can be obtained directly as well without having to place any trial weights at either plane. The above findings and conversion equations are obtained analytically and verified by experimental results. Conversion of influence coefficients from multiplane to static-couple format can determine whether static or couple weights are more effective as well as running vibration modes, while conversion from static-couple to multiplane format can determine which balance plane is more effective. [DOI: 10.1115/1.2968866]

1 Introduction

Unbalance accounts for majority of high vibration problems in rotating machines. High synchronous forces and vibration amplitudes due to mass unbalance produce excessive stresses on the rotor and also affect bearings and casing, thus reducing the life span of the machine. The source of unbalance may be imperfect manufacturing process including assembly variation and material nonhomogeneity. Though rotors are typically balanced by manufacturers before they are installed for service, unbalance may still occur afterward due to various reasons. These include deposits or erosion on and shifting of rotating parts as well as thermal effects. Therefore, in many cases, field balance is required to reduce synchronous vibration level. Topics on balancing have been of great interest to rotor dynamic researchers and engineers [1,2].

Typically a turbine, compressor, or generator section is supported by two bearings. This often requires two-plane balancing for most cases where cross-effects among different sections through couplings are trivial. There are a few papers discussing two-plane balancing with amplitude [3] or phase [4] only. These approaches would often require more runs in the field and may increase both the time and the cost for users of rotating machinery. The influence coefficient method is typically used for field trim balancing. There are basically two approaches to apply this method. The first one is to treat it as a multiplane balance problem involving a 2×2 matrix of complex influence coefficients, as Thearle [5] first presented in 1934. In this approach, two direct influence coefficients along with two cross-effect influence coefficients are generated so that correction weights at two balance planes can be determined. The second one is to treat it as two single-plane balance problems using static and couple components, respectively. The latter approach has been used extensively in the field [6,7].

Having valid influence coefficient data makes balance much easier. Influence coefficient data can be employed to save trial runs for many machines of the same design or for future balance on the same machine. For two-plane balancing with influence coefficients, either static-couple or multiplane approach can be used. However, no relationship of influence coefficients was given between these two approaches. It was also sometimes believed that static-couple balance could not reduce both static and couple vibration vectors successfully because static (couple) weights affect couple (static) response.

In this paper, the multiplane approach with 2×2 influence coefficient matrix is first presented followed by the static-couple approach. In the latter approach, cross-effects between the static (couple) weights and the couple (static) component are introduced. Then analytical relationship of influence coefficients between these two approaches is derived on two-plane balancing. Real examples are given to verify the developed analytical conversion formulas as well as to show their application.

2 Multiplane Method

As shown in Fig. 1, synchronous 1X vibration vectors are expressed as $\vec{A}_1$ and $\vec{A}_2$ measured by probes 1 and 2, respectively. Their orientations α_1 and α_2 are defined by phase lagging relative to their probe orientation (Fig. 1 shows the instant when Keyphasor® pulse occurs). Balance weights at weight planes 1 and 2 are expressed as $\vec{W}_1$ and $\vec{W}_2$ with their orientations β_1 and β_2 referenced to the probe orientation, respectively. Assuming that the system is linear, changes in 1X vibration vectors due to weight placement can be given by

Contributed by the International Gas Turbine Institute of ASME for publication in the JOURNAL OF ENGINEERING FOR GAS TURBINES AND POWER. Manuscript received March 28, 2008; final manuscript received April 16, 2008; published online October 14, 2008. Review conducted by Dilip R. Ballal. Paper presented at the ASME Turbo Expo 2008: Land, Sea and Air (GT2008), Berlin, Germany, June 9–13, 2008.

Copyright © 2009 by ASME

Downloaded 02 Jun 2010 to 171.66.16.109. Redistribution subject to ASME license or copyright; see http://www.asme.org/terms/Terms_Use.cfm

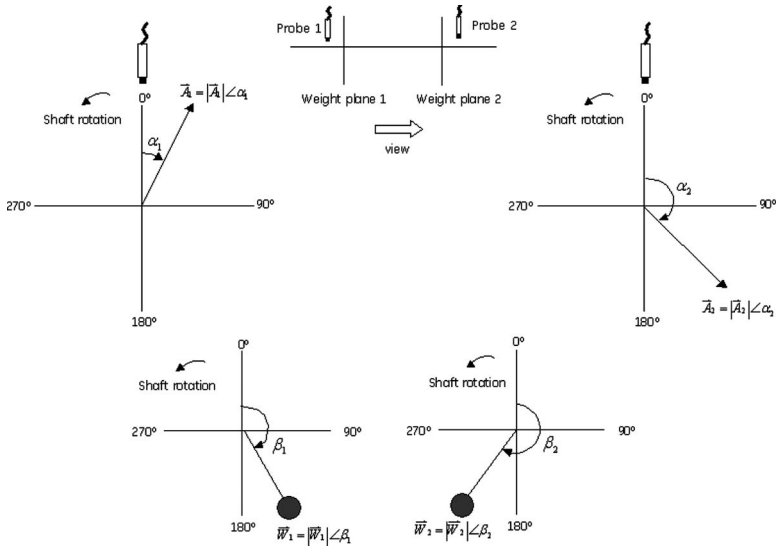


Fig. 1 Diagram of vibration and weight vectors when the Keyphasor pulse occurs

$$\begin{bmatrix} \vec{h}_{11} & \vec{h}_{12} \\ \vec{h}_{21} & \vec{h}_{22} \end{bmatrix} \begin{Bmatrix} \vec{W}_1 \\ \vec{W}_2 \end{Bmatrix} + \begin{Bmatrix} \vec{A}_1^{(0)} \\ \vec{A}_2^{(0)} \end{Bmatrix} = \begin{Bmatrix} \vec{A}_1^{(1)} \\ \vec{A}_2^{(1)} \end{Bmatrix} \tag{1}$$

where $\vec{h}_{11}$, $\vec{h}_{12}$, $\vec{h}_{21}$, and $\vec{h}_{22}$ form the 2×2 influence coefficient matrix. Superscripts "(0)" and "(1)" represent status without and with weights $\vec{W}_1$ and $\vec{W}_2$, respectively. Typically the four influence coefficients, through two trial runs, can be computed as follows:

$$\begin{bmatrix} \vec{h}_{11} & \vec{h}_{12} \\ \vec{h}_{21} & \vec{h}_{22} \end{bmatrix} = \begin{bmatrix} \vec{A}_1^{(1)} - \vec{A}_1^{(0)} & \vec{A}_1^{(2)} - \vec{A}_1^{(0)} \\ \vec{A}_2^{(1)} - \vec{A}_2^{(0)} & \vec{A}_2^{(2)} - \vec{A}_2^{(0)} \end{bmatrix} \begin{bmatrix} \vec{W}_1^{(1)} & \vec{W}_1^{(2)} \\ \vec{W}_2^{(1)} & \vec{W}_2^{(2)} \end{bmatrix}^{-1} \tag{2}$$

where superscript (0) represents status without weights and superscripts (1) and "(2)" denote status with the first and second sets of weights. Note that the two sets of weights must be chosen in a way that the weight matrix is not singular.

3 Static-Couple Method

In the static-couple approach, as shown in Fig. 2, vibration vectors at both ends of the shaft are expressed as combination of static and couple components as follows:

$$\vec{S} = \frac{\vec{A}_1 + \vec{A}_2}{2}, \quad \vec{C} = \frac{\vec{A}_1 - \vec{A}_2}{2} \tag{3}$$

where $\vec{S}$ and $\vec{C}$ are defined as static and couple components, respectively.

The static influence coefficient is computed based on vectorial changes in $\vec{S}$ due to the static weights $\vec{W}_S$ (which can be sometimes placed as one weight in the middle balance plane), as shown in Fig. 2. The couple influence coefficient is calculated based on vectorial changes in $\vec{C}$ due to the couple weights $\vec{W}_C$ (180 deg apart at two ends). When the static (couple) component is dominant, the static (couple) weight approach alone may be adopted. In the case that both components are high, up to four runs are often used to balance both static and couple components. However, cross-effects of static weights to the couple component or couple weights to the static component have often been neglected when

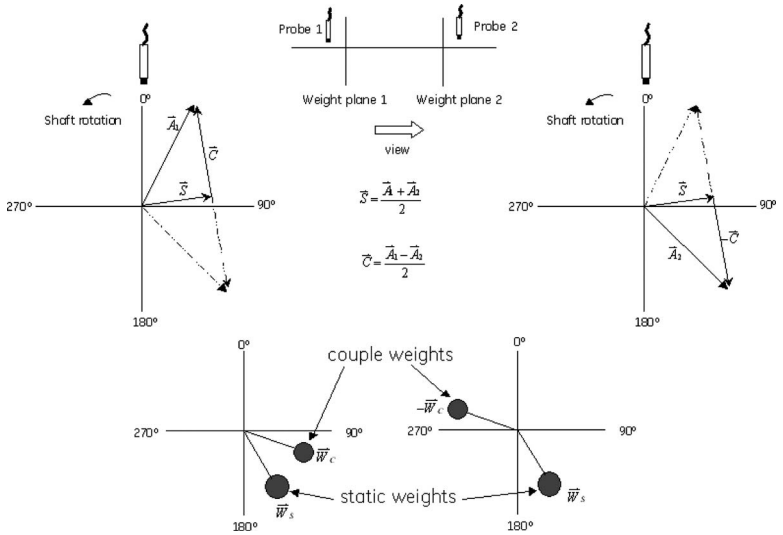


Fig. 2 Diagram of static/couple vibration and weight vectors when the Keyphasor pulse occurs

Downloaded 02 Jun 2010 to 171.66.16.109. Redistribution subject to ASME license or copyright; see http://www.asme.org/terms/Terms_Use.cfm

performing balance. A nonsymmetric rotor with respect to its two ends or strongly influenced by its adjacent section via coupling might have significant cross-effects.

This paper introduces the following static-couple balance model to include these cross-effects:

$$\begin{bmatrix} \vec{H}_{SS} & \vec{H}_{SC} \\ \vec{H}_{CS} & \vec{H}_{CC} \end{bmatrix} \begin{Bmatrix} \vec{W}_S \\ \vec{W}_C \end{Bmatrix} + \begin{Bmatrix} \vec{S}^{(0)} \\ \vec{C}^{(0)} \end{Bmatrix} = \begin{Bmatrix} \vec{S}^{(1)} \\ \vec{C}^{(1)} \end{Bmatrix} \tag{4}$$

where superscripts (0) and (1) represent status without and with static weight(s) $\vec{W}_S$ and/or couple weights $\vec{W}_C$. Equation (4) also applies to the case where the static weight $\vec{W}_S$ is placed in the middle plane instead of two end planes. The above four influence coefficients can be computed by placing static/couple weights. Having vibration data before and after static weight(s) placement $\vec{W}_S$ (without couple weights) yields

$$\vec{H}_{SS} = \frac{\Delta \vec{S}_S}{\vec{W}_S} \tag{5}$$

and

$$\vec{H}_{CS} = \frac{\Delta \vec{C}_S}{\vec{W}_S} \tag{6}$$

where $\Delta \vec{S}_S$ is the static vibration component with static weight(s) −static vibration component without static weight(s) and $\Delta \vec{C}_S$ is the couple vibration component with static weight(s)−couple vibration component without static weight(s).

Similarly, having vibration data before and after couple weight placement $\vec{W}_C$ (without static weights) yields

$$\vec{H}_{CC} = \frac{\Delta \vec{C}_C}{\vec{W}_C} \tag{7}$$

and

$$\vec{H}_{SC} = \frac{\Delta \vec{S}_C}{\vec{W}_C} \tag{8}$$

where $\Delta \vec{C}_C$ is the couple vibration component with couple weight(s)−couple vibration component without couple weights and $\Delta \vec{S}_C$ is the static vibration component with weight(s)−static vibration component without couple weights.

Equations (5) and (7) have been widely used to compute the effect of static weight(s) to the static component and the effect of couple weights to the couple component, respectively. However, the cross-effect of static weight(s) to the couple component or couple weights to the static component has not been introduced so far and has often been assumed to be zero. In a real rotor where asymmetry exists due to rotor structure or coupling effects, the cross-effect could be significant. Equations (6) and (8) include these cross-effects. After both static and couple balancing without considering the cross-effects, residual unbalance response could still be high. However, if these four influence coefficients are obtained, both the static and couple vibration components can be effectively reduced by applying appropriate static and couple weights. Thus synchronous vibration levels at plane 1 ($\vec{A}_1 = \vec{S} + \vec{C}$) and plane 2 ($\vec{A}_2 = \vec{S} - \vec{C}$) will be reduced accordingly.

Equation (4) shows that vibration can be effectively reduced using the static-couple approach by including cross-effects. There appears no need to reduce the static (or the couple) component perfectly with the static (or the couple) weights before making a trial run with the couple (or the static) weights, if both the static and couple weights are going to be tried. After trial runs with static and couple weights, respectively, all direct and cross-effects can be obtained, as shown in Eq. (4).

When the static or the couple component appears to be larger, only static weight(s) or couple weights are sometimes used. An optimized static or couple weight solution can be obtained to include the cross-effect.

Sometimes one needs to know individual probe influence due to static or couple weights. The static weight influence to probes near planes 1 and 2 can be given by

$$\vec{h}_{1,S} = \frac{\Delta \vec{A}_{1,S}}{\vec{W}_S} \tag{9}$$

and

$$\vec{h}_{2,S} = \frac{\Delta \vec{A}_{2,S}}{\vec{W}_S} \tag{10}$$

where

$\Delta \vec{A}_{1,S} = \vec{A}_1$ with static weight(s) $- \vec{A}_1$ without static weight(s)

$\Delta \vec{A}_{2,S} = \vec{A}_2$ with static weight(s) $- \vec{A}_2$ without static weight(s)

Similarly, the couple weight influence to probes near planes 1 and 2 can be given by

$$\vec{h}_{1,C} = \frac{\Delta \vec{A}_{1,C}}{\vec{W}_C} \tag{11}$$

and

$$\vec{h}_{2,C} = \frac{\Delta \vec{A}_{2,C}}{\vec{W}_C} \tag{12}$$

where

$\Delta \vec{A}_{1,C} = \vec{A}_1$ with couple weights $- \vec{A}_1$ without couple weights

$\Delta \vec{A}_{2,C} = \vec{A}_2$ with couple weights $- \vec{A}_2$ without couple weights

Combining Eqs. (5), (9), and (10) yields (note that $\Delta \vec{S}_S = (\Delta \vec{A}_{1,S} + \Delta \vec{A}_{2,S})/2$)

$$\vec{H}_{SS} = \tfrac{1}{2}(\vec{h}_{1,S} + \vec{h}_{2,S}) \tag{13}$$

Combining Eqs. (6), (9), and (10) yields (note that $\Delta \vec{C}_S = (\Delta \vec{A}_{1,S} - \Delta \vec{A}_{2,S})/2$)

$$\vec{H}_{CS} = \tfrac{1}{2}(\vec{h}_{1,S} - \vec{h}_{2,S}) \tag{14}$$

Combining Eqs. (7), (11), and (12) yields (note that $\Delta \vec{C}_C = (\Delta \vec{A}_{1,C} - \Delta \vec{A}_{2,C})/2$)

$$\vec{H}_{CC} = \tfrac{1}{2}(\vec{h}_{1,C} - \vec{h}_{2,C}) \tag{15}$$

Combining Eqs. (8), (11), and (12) yields (note that $\Delta \vec{S}_C = (\Delta \vec{A}_{1,C} + \Delta \vec{A}_{2,C})/2$)

$$\vec{H}_{SC} = \tfrac{1}{2}(\vec{h}_{1,C} + \vec{h}_{2,C}) \tag{16}$$

Using Eqs. (13)–(16), individual probe influence vectors near plane 1 or 2 due to static or couple weights can also be expressed in terms of static or couple influence vectors as follows:

$$\vec{h}_{1,S} = \vec{H}_{SS} + \vec{H}_{CS} \tag{17}$$

$$\vec{h}_{2,S} = \vec{H}_{SS} - \vec{H}_{CS} \tag{18}$$

$$\vec{h}_{1,C} = \vec{H}_{SC} + \vec{H}_{CC} \tag{19}$$

$$\vec{h}_{2,C} = \vec{H}_{SC} - \vec{H}_{CC} \tag{20}$$

Downloaded 02 Jun 2010 to 171.66.16.109. Redistribution subject to ASME license or copyright; see http://www.asme.org/terms/Terms_Use.cfm

Note that all the above equations apply to cases where static weights are placed either at the middle balance weight plane only or at two end balance weight planes with the same amount of weights in the same orientation. Couple weights are always defined throughout the paper as placement at two end balance planes with the same amount of weights in the opposite orientation (180 deg apart).

4 Relationship of Influence Coefficients Between the Two Methods

When performing balance in the field, sometimes the number of weights or the amount of weights (heavy metal weights may not be allowed due to high temperature on some rotors such as high pressure (HP) section) is limited at balance planes. In this case, even if a 2×2 influence coefficient matrix is available that may lead to placement of a large amount of weights at two end planes, one would prefer to use less amount of static or couple weights only to reduce vibration to acceptable levels. Using either static or couple weights would depend on which component is dominant and which weight placement is more efficient (having sensitivity of static and couple influence vectors would help to determine). Having influence vectors for static and couple weights with the same phase lag reference for weights and vibration vectors (suggested to use for balancing, preferably aligned to the probe orientation), one would be able to see how the rotor is running before, after, or close to the translational, pivotal, or other bending modes based on phase lag angle of static and couple influence vectors. The above-mentioned questions can be answered by conversion of influence vectors from the multiplane method to the static-couple method.

On the other hand, one would also need to know influence vectors expressed in terms of multiplane method from known static and couple influence vectors in some cases. Sometimes only one end balance plane can be used due to unavailable empty holes or slot section for weights or difficult access on the other end plane. In thermal bow/rub situations, calculating additional unbalance (caused by thermal bow) using vibration excursion vectors compensated by the normal running condition vectors based on the multiplane influence model would help to determine the thermal bow/rub location (close to balance plane 1 or 2). Using the 2×2 multiplane method would also directly lead to weight placement at planes 1 and 2. Those would require conversion of influence vectors from the static-couple method to the multiplane method.

Applying arbitrary static weights $\vec{W}_S$ only at planes 1 and 2, Eq. (1) after replacing $\vec{W}_1$ and $\vec{W}_2$ each with $\vec{W}_S$ can be reformulated to

$$\tfrac{1}{2}(\vec{h}_{11}+\vec{h}_{12})\vec{W}_S=\tfrac{1}{2}(\vec{A}_1^{(1)}-\vec{A}_1^{(0)}) \tag{21a}$$

$$\tfrac{1}{2}(\vec{h}_{21}+\vec{h}_{22})\vec{W}_S=\tfrac{1}{2}(\vec{A}_2^{(1)}-\vec{A}_2^{(0)}) \tag{21b}$$

Applying the same static weights $\vec{W}_S$ only at planes 1 and 2, Eq. (4) after setting $\vec{W}_C=0$ can be reformulated to

$$\vec{H}_{SS}\vec{W}_S=\vec{S}^{(1)}-\vec{S}^{(0)} \tag{22a}$$

$$\vec{H}_{CS}\vec{W}_S=\vec{C}^{(1)}-\vec{C}^{(0)} \tag{22b}$$

Addition of Eqs. (21*a*) and (21*b*) followed by subtraction of Eq. (22) with application of Eq. (3) yields

$$\vec{H}_{SS}=\tfrac{1}{2}(\vec{h}_{11}+\vec{h}_{22}+\vec{h}_{12}+\vec{h}_{21}) \tag{23}$$

Subtraction of Eq. (21) from Eq. (21) followed by subtraction of Eq. (22) with application of Eq. (3) yields

$$\vec{H}_{CS}=\tfrac{1}{2}(\vec{h}_{11}-\vec{h}_{22}+\vec{h}_{12}-\vec{h}_{21}) \tag{24}$$

Similarly, applying arbitrary couple weights $\vec{W}_C$ only at planes 1 and 2, Eq. (1) after replacing $\vec{W}_1$ with $\vec{W}_C$ and $\vec{W}_2$ with $-\vec{W}_C$ can be reformulated to

$$\tfrac{1}{2}(\vec{h}_{11}-\vec{h}_{12})\vec{W}_C=\tfrac{1}{2}(\vec{A}_1^{(1)}-\vec{A}_1^{(0)}) \tag{25a}$$

$$\tfrac{1}{2}(\vec{h}_{21}-\vec{h}_{22})\vec{W}_C=\tfrac{1}{2}(\vec{A}_2^{(1)}-\vec{A}_2^{(0)}) \tag{25b}$$

Applying the same static weights $\vec{W}_C$ at planes 1 and 2, Eq. (4) after setting $\vec{W}_S=0$ can be reformulated to

$$\vec{H}_{SC}\vec{W}_C=\vec{S}^{(1)}-\vec{S}^{(0)} \tag{26a}$$

$$\vec{H}_{CC}\vec{W}_C=\vec{C}^{(1)}-\vec{C}^{(0)} \tag{26b}$$

Addition of Eqs. (25*a*) and (25*b*) followed by subtraction of Eq. (26*a*) with application of Eq. (3) yields

$$\vec{H}_{SC}=\tfrac{1}{2}(\vec{h}_{11}-\vec{h}_{22}-\vec{h}_{12}+\vec{h}_{21}) \tag{27}$$

Subtraction of Eq. (25*b*) from Eq. (25*a*) followed by subtraction of Eq. (26*b*) with application of Eq. (3) yields

$$\vec{H}_{CC}=\tfrac{1}{2}(\vec{h}_{11}+\vec{h}_{22}-\vec{h}_{12}-\vec{h}_{21}) \tag{28}$$

Thus, conversion equations of influence vectors from the multiplane method to the static-couple method are given by Eq. (23) (direct static influence vector), Eq. (24) (cross-effect of the couple component due to static weights), Eq. (27) (cross-effect of the static component due to couple weights), and Eq. (28) (direct couple influence vector). Combining Eqs. (23), (24), (27), and (28), conversion of influence vectors from the static-couple method to the multiplane method can also be given by

$$\vec{h}_{11}=\tfrac{1}{2}(\vec{H}_{SS}+\vec{H}_{CC}+\vec{H}_{SC}+\vec{H}_{CS}) \tag{29}$$

$$\vec{h}_{12}=\tfrac{1}{2}(\vec{H}_{SS}-\vec{H}_{CC}-\vec{H}_{SC}+\vec{H}_{CS}) \tag{30}$$

$$\vec{h}_{21}=\tfrac{1}{2}(\vec{H}_{SS}-\vec{H}_{CC}+\vec{H}_{SC}-\vec{H}_{CS}) \tag{31}$$

$$\vec{h}_{22}=\tfrac{1}{2}(\vec{H}_{SS}+\vec{H}_{CC}-\vec{H}_{SC}-\vec{H}_{CS}) \tag{32}$$

Combining Eqs. (13)–(16) and (29)–(32) yields influence vectors with the multiplane method expressed by individual probe influence vectors due to static and couple weights as follows:

$$\vec{h}_{11}=\tfrac{1}{2}(\vec{h}_{1,S}+\vec{h}_{1,C}) \tag{33}$$

$$\vec{h}_{12}=\tfrac{1}{2}(\vec{h}_{1,S}-\vec{h}_{1,C}) \tag{34}$$

$$\vec{h}_{21}=\tfrac{1}{2}(\vec{h}_{2,S}+\vec{h}_{2,C}) \tag{35}$$

$$\vec{h}_{22}=\tfrac{1}{2}(\vec{h}_{2,S}-\vec{h}_{2,C}) \tag{36}$$

Combining Eqs. (33)–(36), individual probe influence vectors due to static or couple weights can also be expressed in terms of influence vectors with the multiplane method as follows:

$$\vec{h}_{1,S}=\vec{h}_{11}+\vec{h}_{12} \tag{37}$$

$$\vec{h}_{2,S}=\vec{h}_{21}+\vec{h}_{22} \tag{38}$$

$$\vec{h}_{1,C}=\vec{h}_{11}-\vec{h}_{12} \tag{39}$$

$$\vec{h}_{2,C}=\vec{h}_{21}-\vec{h}_{22} \tag{40}$$

Note that all the above equations in this section apply to cases where static weights are placed at two end balance weight planes. In case the static weight is defined as placement at the middle balance plane, Eqs. (27), (28), (39), and (40) are still valid.

Downloaded 02 Jun 2010 to 171.66.16.109. Redistribution subject to ASME license or copyright; see http://www.asme.org/terms/Terms_Use.cfm

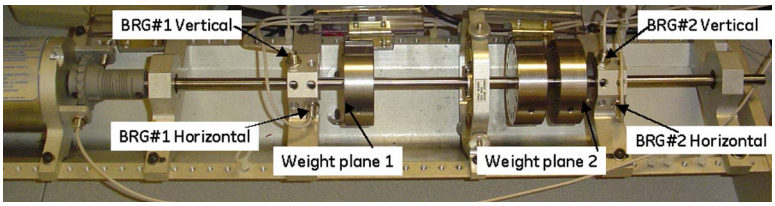


Fig. 3 Rotor kit for balance calculations

5 Real Example One (Verification)

The first real example presented here is mainly to verify the above-developed equations of influence coefficient conversion between multiplane and static-couple methods. In this example, a Bently Nevada™ RK-4 rotor kit was used, as shown in Fig. 3. A shaft with the diameter and length of 0.01 m and 0.56 m, respectively, was supported by two brass bushing bearings and driven by a 75 W motor. Three 0.8 kg disks were attached to the shaft with one close to bearing No. 1 and two close to bearing No. 2, thus having asymmetry mass distribution with respect to the two bearings. The rotor was also supported by a midspan spring to prevent excessive bow in the middle of the shaft. The data acquisition and processing system consisted of two pairs of *X-Y* displacement proximity probes, one speed probe and one Keyphasor probe for speed and phase measurement. Two balance weight planes 1 and 2 are located adjacent to bearing Nos. 1 and 2 as well as their corresponding proximity probes. The shaft was rotated in the counterclockwise direction when viewed from the motor to the rotor kit.

In this example, the running speed for balance was set at 4800 rpm for demonstration. Since higher amplitudes occurred in the horizontal direction at the running speed, influence coefficient calculations were carried out in terms of vibration readings measured by the two horizontal probes located 90 deg right to the top, as shown in Fig. 3. From an initial run without any balance weight placement, synchronous vibration vectors at bearing Nos. 1 and 2 in the horizontal direction were as follows:

$$\vec{A}_1^{(0)} = 5.962 \text{ mils pp} \angle 88 \text{ deg}$$

$$\vec{A}_2^{(0)} = 3.742 \text{ mils pp} \angle 260 \text{ deg}$$

With the following two 0.4 g weights placed at planes 1 and 2 (see Fig. 4):

$$\vec{W}_1^{(1)} = 0.4 \text{ g} \angle 225 \text{ deg}, \quad \vec{W}_2^{(1)} = 0.4 \text{ g} \angle 45 \text{ deg}$$

the corresponding vibration vectors became

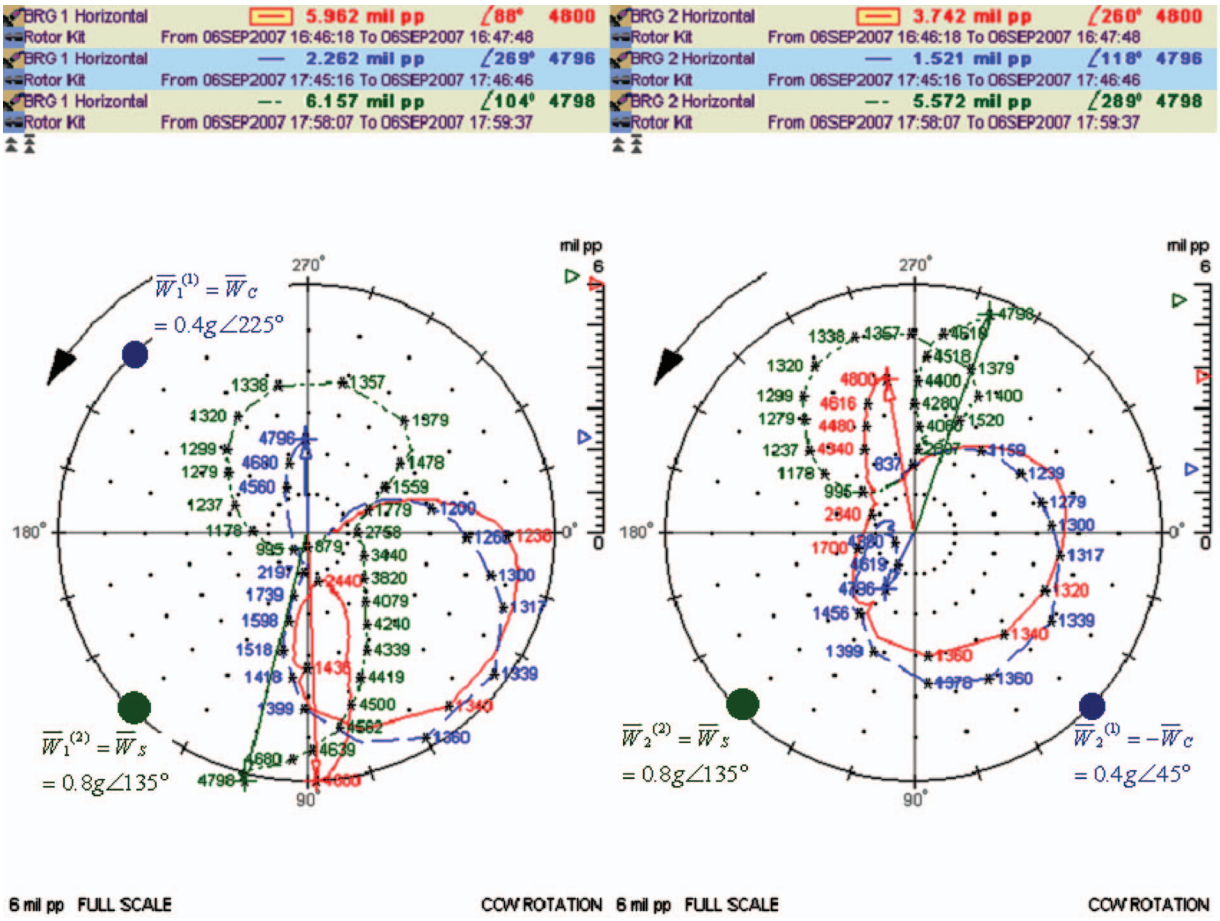


Fig. 4 Polar plots and vibration vectors at 4800 rpm or so for initial run, and first and second trial runs with weight placements using Bently Nevada ADRE® SXP software and 408 DSPi data acquisition system

Downloaded 02 Jun 2010 to 171.66.16.109. Redistribution subject to ASME license or copyright; see http://www.asme.org/terms/Terms_Use.cfm

$$\vec{A}_1^{(1)} = 2.262 \text{ mils pp} \angle 269 \text{ deg}$$

$$\vec{A}_2^{(1)} = 1.521 \text{ mils pp} \angle 118 \text{ deg}$$

Placing the following two 0.8 g weights at planes 1 and 2 (see Fig. 4) after removing the above two 0.4 g weights

$$\vec{W}_1^{(2)} = 0.8 \text{ g} \angle 135 \text{ deg}, \quad \vec{W}_2^{(2)} = 0.8 \text{ g} \angle 135 \text{ deg}$$

corresponded to the following vibration vectors:

$$\vec{A}_1^{(2)} = 6.157 \text{ mils pp} \angle 104 \text{ deg}$$

$$\vec{A}_2^{(2)} = 5.572 \text{ mils pp} \angle 289 \text{ deg}$$

Figure 4 shows polar plots and vibration vectors at 4800 rpm or so for three different runs as well as two sets of weight placement.

Using Eq. (2), the influence coefficient matrix for the multiplane method is computed as

$$\begin{bmatrix} \vec{h}_{11} & \vec{h}_{12} \\ \vec{h}_{21} & \vec{h}_{22} \end{bmatrix} = \begin{bmatrix} 11.3405 \angle 43 \text{ deg} & 9.2189 \angle 223 \text{ deg} \\ 7.8777 \angle 218 \text{ deg} & 4.8643 \angle 58 \text{ deg} \end{bmatrix} \text{ mils pp/g}$$

Assuming that synchronous vibration vectors are linearly proportional to applied balance weights, arbitrary two weight placement sets (as long as its weight matrix is not ill conditioned or singular) should yield the same influence coefficient matrix for this multiplane method at this running speed. Actually the other two sets of weight placement (placing only one weight at one time at one plane followed by the other plane) were tried, which produced the results very close to the above ones. Thus the above four values within the matrix are the influence coefficients for the multiplane method at this running speed.

It is noted that the above two sets of weight placement were also just for couple and static weights, respectively. Therefore the influence coefficients for static-couple method can be directly computed. Using Eq. (3), static and couple vibration vectors for the initial run without weight placement, the first trial run with couple weights

$$\vec{W}_C = 0.4 \text{ g} \angle 225 \text{ deg}$$

and the second trial run with static weights

$$\vec{W}_S = 0.8 \text{ g} \angle 135 \text{ deg}$$

can be computed, respectively, as follows:

$$\vec{S}^{(0)} = 1.158 \text{ mils pp} \angle 101 \text{ deg}$$

$$\vec{C}^{(0)} = 4.841 \text{ mils pp} \angle 85 \text{ deg}$$

$$\vec{S}_C^{(1)} = 0.594 \text{ mil pp} \angle 230 \text{ deg}$$

$$\vec{C}_C^{(1)} = 1.834 \text{ mils pp} \angle 281 \text{ deg}$$

$$\vec{S}_S^{(2)} = 0.388 \text{ mil pp} \angle 65 \text{ deg}, \quad \vec{C}_S^{(2)} = 5.859 \text{ mils pp} \angle 106 \text{ deg}$$

Note that

$$\Delta\vec{S}_S = \vec{S}_S^{(2)} - \vec{S}^{(0)}, \quad \Delta\vec{C}_S = \vec{C}_S^{(2)} - \vec{C}^{(0)}$$

$$\Delta\vec{S}_C = \vec{S}_C^{(1)} - \vec{S}^{(0)}, \quad \Delta\vec{C}_C = \vec{C}_C^{(1)} - \vec{C}^{(0)}$$

and

$$\Delta\vec{A}_{1,S} = \vec{A}_1^{(2)} - \vec{A}_1^{(0)}, \quad \Delta\vec{A}_{2,S} = \vec{A}_2^{(2)} - \vec{A}_2^{(0)}$$

$$\Delta\vec{A}_{1,C} = \vec{A}_1^{(1)} - \vec{A}_1^{(0)}, \quad \Delta\vec{A}_{2,C} = \vec{A}_2^{(1)} - \vec{A}_2^{(0)}$$

The influence vectors due to static and couple weights placed at two ends are computed directly from their definition, as shown in the right column of Table 1.

The left column of Table 1 shows calculated results, using Eqs. (23), (24), (27), (28), and (37)–(40), based on known $\vec{h}_{11}$, $\vec{h}_{12}$, $\vec{h}_{21}$, and $\vec{h}_{22}$ values from the multiplane method. It is found that the results in the left column are the same as those in the right column (little difference appears just due to rounding errors during computations).

It is shown from this real example that influence vectors for the static-couple method can be calculated from known influence coefficients $\vec{h}_{11}$, $\vec{h}_{12}$, $\vec{h}_{21}$, and $\vec{h}_{22}$ in a 2×2 matrix for the multiplane method, without having to place trial static or couple weights. Since Eqs. (29)–(32) are equivalent to Eqs. (23), (24), (27), and (28), and Eqs. (33)–(36) are equivalent to Eqs. (37)–(40), Eqs. (29)–(36) also hold true in this example. Therefore, influence coefficients $\vec{h}_{11}$, $\vec{h}_{12}$, $\vec{h}_{21}$, and $\vec{h}_{22}$ can also be obtained from influence vectors for the static-couple method without having to place two sets of trial weights.

In this example, it is found that static weights affect the couple vibration vector ($\vec{H}_{CS}$ is about 2.8 mils pp/g $\angle$ 24 deg) and that couple weights affect the static vibration vectors ($\vec{H}_{SC}$ is about 4.0 mils pp/g $\angle$ 39 deg). These cross-effects are even higher than the direct static influence vector $\vec{H}_{SS}$ (about 1.1 mils pp/g $\angle$ 161 deg). The high influence vector $\vec{H}_{CC}$ (about 16.6 mils pp/g $\angle$ 44 deg) indicates a very sensitive couple weight effect. The phase readings in $\vec{H}_{SS}$ and $\vec{H}_{CC}$ indicate that the rotor kit runs after the first bending resonance speed and before the second bending resonance speed. This is in good agreement with polar plots in Fig. 4.

Using either Eq. (1) for multiplane method or Eq. (4) for static-couple method, required balance weights to offset the initial vibration at two planes can be determined. The former approach yields the following balance weights:

$$\vec{W}_1 = 0.49 \text{ g} \angle 208 \text{ deg}, \quad \vec{W}_2 = 0.18 \text{ g} \angle 112 \text{ deg}$$

The latter approach yields the following weights:

$$\vec{W}_S = 0.25 \text{ g} \angle 187 \text{ deg}, \quad \vec{W}_C = 0.27 \text{ g} \angle 228 \text{ deg}$$

Note that

$$\vec{W}_1 = \vec{W}_S + \vec{W}_C, \quad \vec{W}_2 = \vec{W}_S - \vec{W}_C$$

The above two sets of weights are identical. Among available weights and holes, the final weights and their orientations were chosen as follows:

$$\vec{W}_1 = 0.5 \text{ g} \angle 202.5 \text{ deg}, \quad \vec{W}_2 = 0.2 \text{ g} \angle 112.5 \text{ deg}$$

Figure 5 shows synchronous orbits before and after the balance with the above weights. Synchronous vibration level has been reduced from around 6 mils to less than 1 mil after placing the above weights.

6 Real Example Two (Application)

The second example is to demonstrate how to apply the developed conversion between the two methods when an influence coefficient matrix for the multiplane method is known. In this example, high synchronous vibration due to unbalance was observed via proximity probes on a 66 MW hydrogen-cooled generator driven by a steam turbine, as shown in Fig. 6. The machine with a two-pole generator was run at 3600 rpm and rotated clockwise when viewed from the turbine to the generator. The two generator bearings were named as bearing Nos. 5 (drive-end) and 6 (non-drive-end). A pair of *X-Y* probes was installed at 45 deg left and

Downloaded 02 Jun 2010 to 171.66.16.109. Redistribution subject to ASME license or copyright; see http://www.asme.org/terms/Terms_Use.cfm

Table 1 Verification of influence coefficient conversion between multiplane and static-couple methods on a real example

Equation No.	Calculated from multiplane method (mil pp/g)		Directly calculated by placing static/couple weights (mil pp/g)	
(23)	$\frac{1}{2}(\vec{h}_{11}+\vec{h}_{22}+\vec{h}_{12}+\vec{h}_{21})$	$1.0905\angle 161$ deg	$\vec{H}_{SS}\left(=\frac{\Delta\vec{S}_S}{\vec{W}_S}\right)$	$1.0905\angle 161$ deg
(24)	$\frac{1}{2}(\vec{h}_{11}-\vec{h}_{22}+\vec{h}_{12}-\vec{h}_{21})$	$2.7863\angle 24$ deg	$\vec{H}_{CS}\left(=\frac{\Delta\vec{C}_S}{\vec{W}_S}\right)$	$2.7863\angle 24$ deg
(27)	$\frac{1}{2}(\vec{h}_{11}-\vec{h}_{22}-\vec{h}_{12}+\vec{h}_{21})$	$4.0089\angle 39$ deg	$\vec{H}_{SC}\left(=\frac{\Delta\vec{S}_C}{\vec{W}_C}\right)$	$4.0090\angle 39$ deg
(28)	$\frac{1}{2}(\vec{h}_{11}+\vec{h}_{22}-\vec{h}_{12}-\vec{h}_{21})$	$16.5617\angle 44$ deg	$\vec{H}_{CC}\left(=\frac{\Delta\vec{C}_C}{\vec{W}_C}\right)$	$16.5618\angle 44$ deg
(37)	$\vec{h}_{11}+\vec{h}_{12}$	$2.1221\angle 44$ deg	$\vec{h}_{1,S}\left(=\frac{\Delta\vec{A}_{1,S}}{\vec{W}_S}\right)$	$2.1221\angle 44$ deg
(38)	$\vec{h}_{21}+\vec{h}_{22}$	$3.6610\angle 192$ deg	$\vec{h}_{2,S}\left(=\frac{\Delta\vec{A}_{2,S}}{\vec{W}_S}\right)$	$3.6609\angle 192$ deg
(39)	$\vec{h}_{11}-\vec{h}_{12}$	$20.5594\angle 43$ deg	$\vec{h}_{1,C}\left(=\frac{\Delta\vec{A}_{1,C}}{\vec{W}_C}\right)$	$20.5594\angle 43$ deg
(40)	$\vec{h}_{21}-\vec{h}_{22}$	$12.5713\angle 226$ deg	$\vec{h}_{2,C}\left(=\frac{\Delta\vec{A}_{2,C}}{\vec{W}_C}\right)$	$12.5713\angle 226$ deg

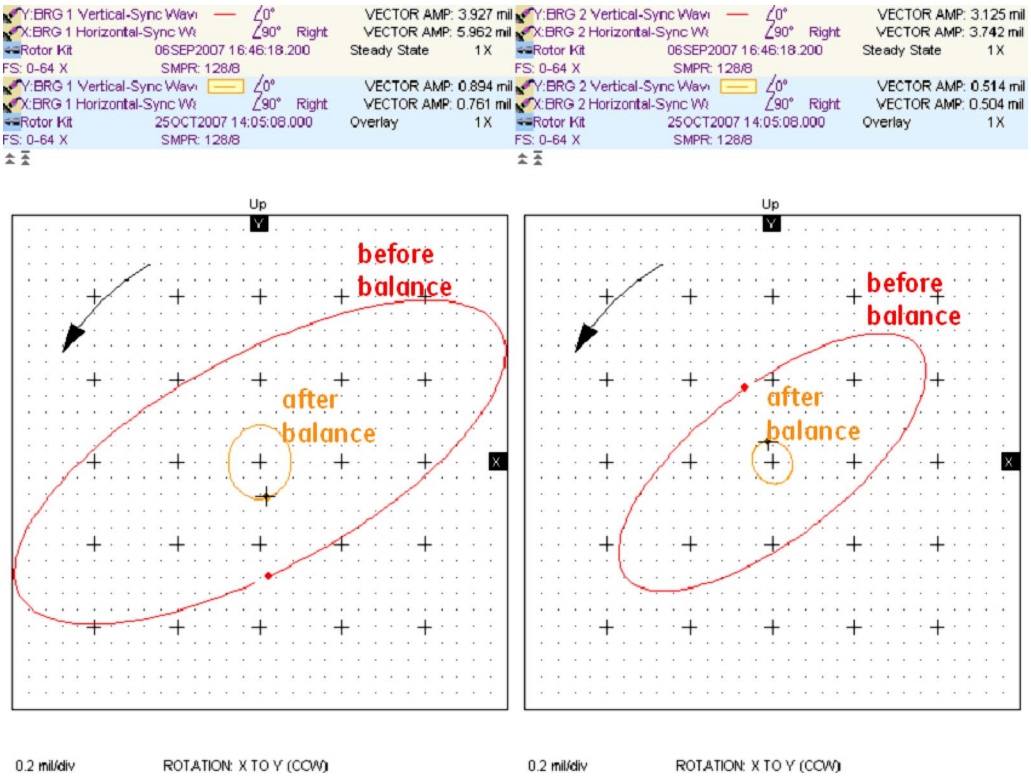


Fig. 5 Synchronous orbits before and after balance at bearing Nos. 1 and 2 using Bently Nevada ADRE SXP software and 408 DSPi data acquisition system

Downloaded 02 Jun 2010 to 171.66.16.109. Redistribution subject to ASME license or copyright; see http://www.asme.org/terms/Terms_Use.cfm

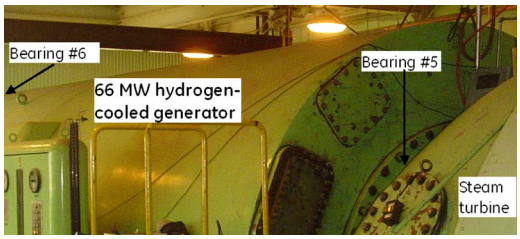


Fig. 6 Generator rotor balance as real example

right at bearing No. 5 while another pair of *X*-*Y* probes was installed at 60 deg left and 30 deg right at bearing No. 6.

Synchronous vibration amplitudes were higher on *Y*-probes than on *X*-probes at the two bearings on the generator. Balance calculations were therefore conducted on *Y*-probes only. In order to use the same nomenclature and subscripts for the equations developed earlier, probes and weight plane at bearing No. 5 are denoted as 1 while those at bearing No. 6 are denoted as 2. As shown in Fig. 7, *Y*-probe readings at bearing Nos. 5 and 6 were

$$\vec{A}_1^{(0)} = 4.02 \text{ mils pp} \angle 301 \text{ deg}$$

$$\vec{A}_2^{(0)} = 2.066 \text{ mils pp} \angle 115 \text{ deg}$$

The previous influence coefficients used for the multiplane method were given by

Table 2 Calculated influence vectors in static and couple methods from the known influence vectors in the multiplane method, without placing static or couple trial weights

Conversion equation	Results (mils pp/g)
$\vec{H}_{SS}\left(=\frac{1}{2}(\vec{h}_{11}+\vec{h}_{22}+\vec{h}_{12}+\vec{h}_{21})\right)$	$0.0010 \angle 157$ deg
$\vec{H}_{CS}\left(=\frac{1}{2}(\vec{h}_{11}-\vec{h}_{22}+\vec{h}_{12}-\vec{h}_{21})\right)$	$0.0022 \angle 136$ deg
$\vec{H}_{SC}\left(=\frac{1}{2}(\vec{h}_{11}-\vec{h}_{22}-\vec{h}_{12}+\vec{h}_{21})\right)$	$0.0024 \angle 131$ deg
$\vec{H}_{CC}\left(=\frac{1}{2}(\vec{h}_{11}+\vec{h}_{22}-\vec{h}_{12}-\vec{h}_{21})\right)$	$0.0111 \angle 131$ deg
$\vec{h}_{1,S}(=\vec{h}_{11}+\vec{h}_{12})$	$0.0032 \angle 143$ deg
$\vec{h}_{2,S}(=\vec{h}_{21}+\vec{h}_{22})$	$0.0013 \angle 301$ deg
$\vec{h}_{1,C}(=\vec{h}_{11}-\vec{h}_{12})$	$0.0135 \angle 131$ deg
$\vec{h}_{2,C}(=\vec{h}_{21}-\vec{h}_{22})$	$0.0087 \angle 310$ deg

$$\begin{bmatrix} \vec{h}_{11} & \vec{h}_{12} \\ \vec{h}_{21} & \vec{h}_{22} \end{bmatrix} = \begin{bmatrix} 0.0083 \angle 133 \text{ deg} & 0.0052 \angle 307 \text{ deg} \\ 0.0052 \angle 294 \text{ deg} & 0.0037 \angle 117 \text{ deg} \end{bmatrix} \text{ mil pp/g}$$

where $\vec{h}_{11}$, $\vec{h}_{12}$, $\vec{h}_{21}$, and $\vec{h}_{22}$ were applied to Eq. (1) in which synchronous vibration vectors were defined as original ones from the two *Y*-probes (1 was referenced to 45 deg left and 2 was referenced to 60 deg left) while weights at both ends were all referenced to 45 deg left. The balance plane radius where weights

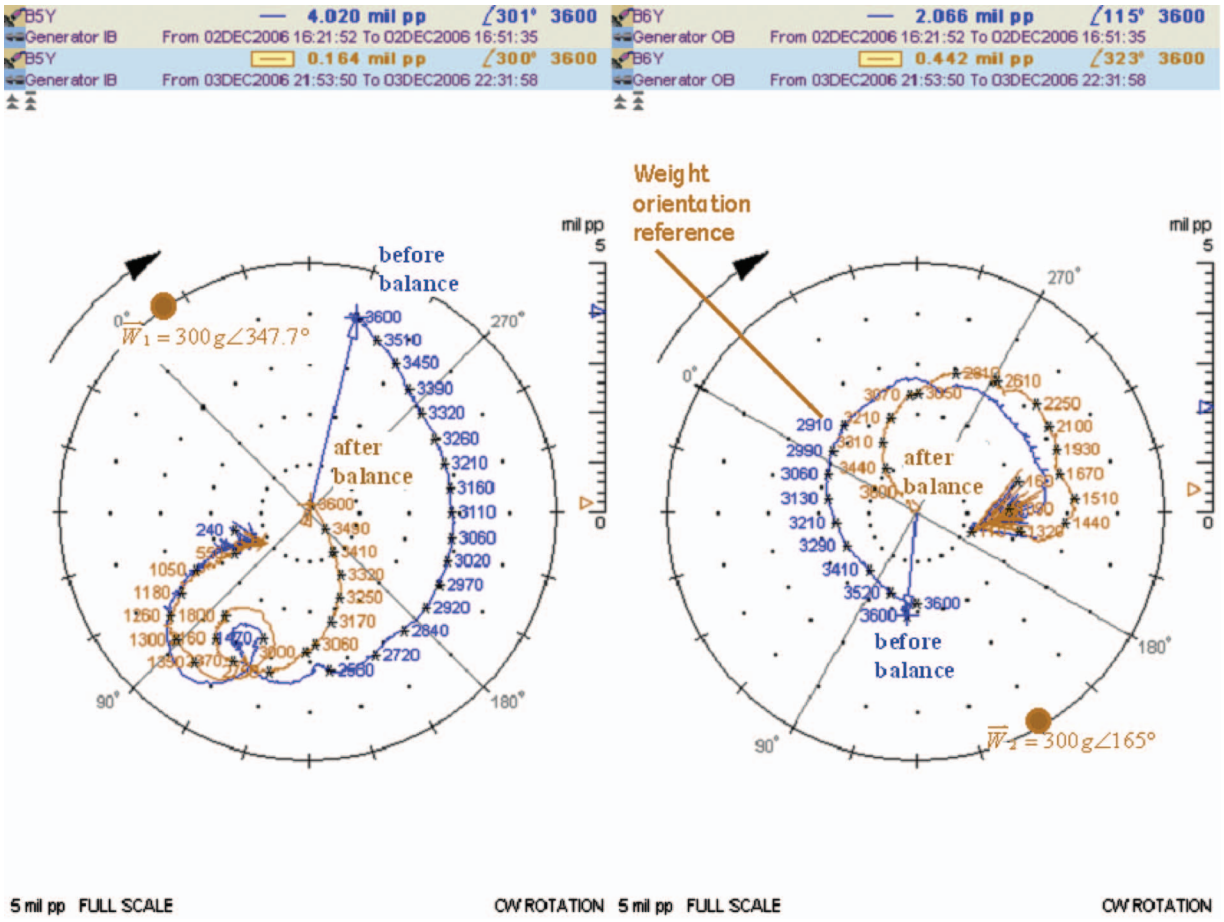


Fig. 7 Polar plots and vibration vectors at 3600 rpm before and after balance

Downloaded 02 Jun 2010 to 171.66.16.109. Redistribution subject to ASME license or copyright; see http://www.asme.org/terms/Terms_Use.cfm

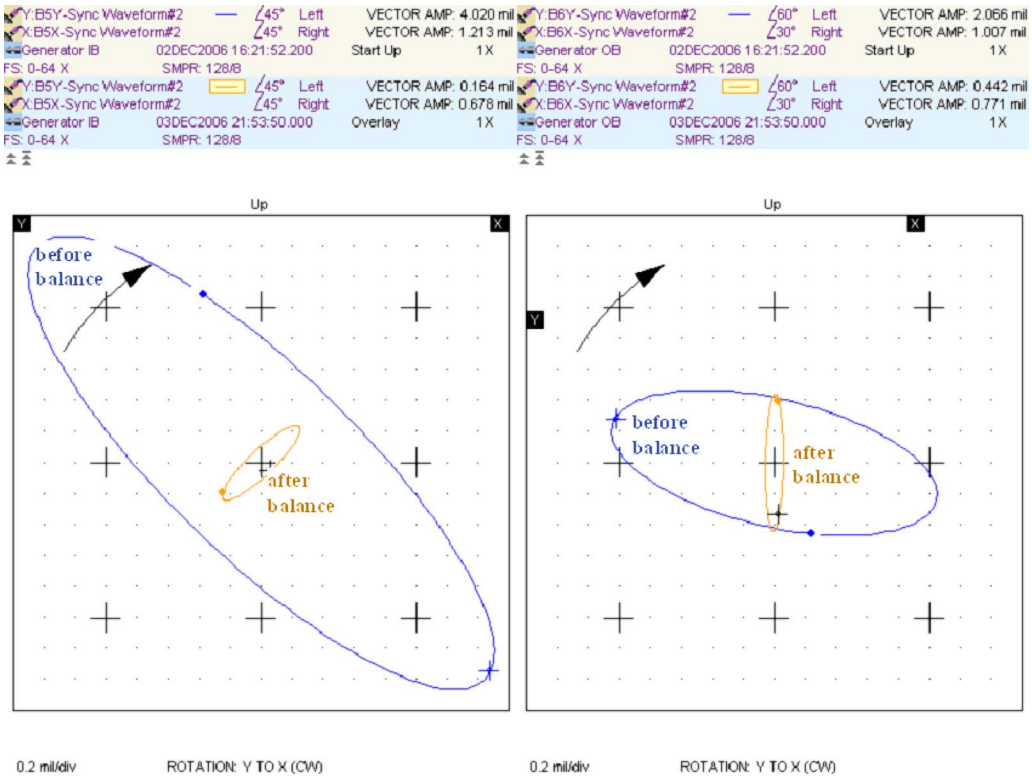


Fig. 8 Synchronous orbits at 3600 rpm before and after balance

were placed was about 0.254 m (10 in.) with the one at bearing No. 5 slightly larger than that at bearing No. 6 (about 1% difference). Note that the radius difference between the two weight planes would not affect the validity of all the equations developed in the paper. Weight planes at bearing Nos. 5 and 6 had 44 and 36 holes for weight placement, respectively. Their weight sizes were also different between two planes.

Using Eq. (1), the required balance weights at two planes appeared to be

$$\vec{W}_1 = 653 \text{ g} \angle 299 \text{ deg}, \quad \vec{W}_2 = 794 \text{ g} \angle 259 \text{ deg}$$

These large amounts of weight at two planes were unable to be placed into empty holes or achieved by adjustment of existing weights. The alternative needed to be found. The study of influence data was then performed.

Influence coefficients for static and couple weights were calculated based on known $\vec{h}_{11}$, $\vec{h}_{12}$, $\vec{h}_{21}$, and $\vec{h}_{22}$ values without placing static or couple trial weights. Note that the *Y*-probe at bearing No. 6 was not parallel to the *Y*-probe at bearing No. 5. In order to evaluate static and couple effects better, the synchronous vector at bearing No. 6, as though it was measured by a proximity probe at 45 deg left, needed to be known, and $\vec{h}_{11}$, $\vec{h}_{12}$, $\vec{h}_{21}$, and $\vec{h}_{22}$ needed to be applicable to this change. Although the above-mentioned synchronous vector at bearing No. 6 could be determined by using vectors from both *X* and *Y* probes, $\vec{h}_{11}$, $\vec{h}_{12}$, $\vec{h}_{21}$, and $\vec{h}_{22}$ might not fit the new defined vector. Therefore, the original vector was used as the new vector except its phase being lagged 15 deg more. Thus the two vibration vectors referenced to 45 deg left became

$$\vec{A}_1^{(0)} = 4.02 \text{ mils pp} \angle 301 \text{ deg}$$

$$\vec{A}_2^{(0)} = 2.066 \text{ mils pp} \angle 115 \text{ deg} + 15 \text{ deg}$$

and the influence matrix with both vibration and weight vectors referenced to 45 deg left became

$$\begin{bmatrix} \vec{h}_{11} & \vec{h}_{12} \\ \vec{h}_{21} & \vec{h}_{22} \end{bmatrix} = \begin{bmatrix} 0.0083 \angle 133 \text{ deg} & 0.0052 \angle 307 \text{ deg} \\ 0.0052 \angle 294 \text{ deg} + 15 \text{ deg} & 0.0037 \angle 117 \text{ deg} + 15 \text{ deg} \end{bmatrix} \text{ mil pp/g}$$

Table 2 shows calculated influence vectors for static and couple weights from known influence vectors $\vec{h}_{11}$, $\vec{h}_{12}$, $\vec{h}_{21}$, and $\vec{h}_{22}$ used for the multiplane method, without having to place static or couple trial weights. The direct couple influence vector $\vec{H}_{CC}$ was the most sensitive one (0.0111 mil pp/g$\angle$131 deg), indicating that appropriate couple weights would effectively reduce the current synchronous vibration level, especially to bearing No. 5 ($\vec{h}_{1,C}$=0.0135 mil pp/g$\angle$131 deg). Static weights appeared not to be sensitive to synchronous vibration vectors at the running speed for this generator, as shown in Table 2. The current static and couple vibration vectors were as follows:

$$\vec{S}^{(0)} = 1.003 \text{ mils pp} \angle 292 \text{ deg}$$

Downloaded 02 Jun 2010 to 171.66.16.109. Redistribution subject to ASME license or copyright; see http://www.asme.org/terms/Terms_Use.cfm

$$\vec{C}^{(0)} = 3.035 \text{ mils pp} \angle 304 \text{ deg}$$

Using Eq. (4) by setting $\vec{W}_S=0$ and neglecting $\vec{H}_{SC}$ effect, the required couple weights were calculated as follows:

$$\vec{W}_C = 273 \text{ g} \angle 353 \text{ deg}$$

or

$$\vec{W}_1 = 273 \text{ g} \angle 353 \text{ deg}, \quad \vec{W}_2 = 273 \text{ g} \angle 173 \text{ deg}$$

Based on available weights and holes on the two balance planes as well as the above estimation, the following chosen weights

$$\vec{W}_1 = 300 \text{ g} \angle 347.7 \text{ deg}, \quad \vec{W}_2 = 300 \text{ g} \angle 165 \text{ deg}$$

would yield synchronous vibration vectors of about 0.2 mil pp and 0.7 mil pp at bearing Nos. 5 and 6, predicted from the original multiplane influence coefficient matrix.

After placing the above weights, synchronous vibrations at bearing Nos. 5 and 6 were reduced to 0.2 mil pp and 0.4 mil pp, respectively, as shown in Figs. 7 and 8.

7 Conclusions

Based on both analytical and real case studies presented in this paper, the following conclusions are stated regarding influence vectors using static-couple and multiplane methods for two-plane balancing.

(1) For the static-couple method, cross-effects between static weights and couple response as well as between couple weights and static response can be included so that a good combination of static and couple weights can be applied to offset synchronous vibration more effectively.
(2) Conversion equations of influence vectors between the static-couple and multiplane methods are given in this paper. Equations (23), (24), (27), and (28) are used for conversion from multiplane format to static-couple format and Eqs. (29)–(32) are used for conversion from static-couple format to multiplane format.
(3) Individual probe influence vectors due to static or couple weights can be vital information. Static and couple influence vectors as well as cross-effects can be evaluated from them by using Eqs. (13)–(16) and multiplane influence vectors can be evaluated from them by using Eqs. (33)–(36).
(4) The above analytical findings have been confirmed by experimental results.
(5) The analytical findings can be applied to real rotating machinery balance as shown in this paper. Effective balance weights can be best evaluated by using conversion equations of influence vectors between multiplane and static-couple formats. Knowing influence vectors in both formats can also help troubleshoot unbalance changes as well as running modes.

Acknowledgment

The author is grateful to Robert C. Eisenmann, Sr. of GE Energy for his support and comments on the current work.

Nomenclature

$\vec{A}_1$ = synchronous vibration vector measured by probe 1
$\vec{A}_2$ = synchronous vibration vector measured by probe 2
$\vec{C}$ = couple vibration vector
$\vec{C}_C$ = couple vibration vector with couple weights
$\vec{C}_S$ = couple vibration vector with static weights
$\vec{H}_{CC}$ = couple vibration influence vector due to couple weights
$\vec{H}_{CS}$ = couple vibration influence vector due to static weights (cross-effect)
$\vec{H}_{SC}$ = static vibration influence vector due to couple weights (cross-effect)
$\vec{H}_{SS}$ = static vibration influence vector due to static weights
$\vec{h}_{11}$ = probe 1 vibration influence vector due to plane 1 weight
$\vec{h}_{12}$ = probe 1 vibration influence vector due to plane 2 weight
$\vec{h}_{21}$ = probe 2 vibration influence vector due to plane 1 weight
$\vec{h}_{22}$ = probe 2 vibration influence vector due to plane 2 weight
$\vec{h}_{1,C}$ = probe 1 vibration influence vector due to couple weights
$\vec{h}_{2,C}$ = probe 2 vibration influence vector due to couple weights
$\vec{h}_{1,S}$ = probe 1 vibration influence vector due to static weights
$\vec{h}_{2,S}$ = probe 2 vibration influence vector due to static weights
$\vec{S}$ = static vibration vector
$\vec{S}_C$ = static vibration vector with couple weights
$\vec{S}_S$ = static vibration vector with static weights
$\vec{W}_1$ = weight vector at balance plane 1
$\vec{W}_2$ = weight vector at balance plane 2
$\vec{W}_C$ = couple weight vector
$\vec{W}_S$ = static weight vector
$\Delta\vec{A}_{1,C}$ = $\vec{A}_1$ with couple weights initial $\vec{A}_1$
$\Delta\vec{A}_{2,C}$ = $\vec{A}_2$ with couple weights initial $\vec{A}_2$
$\Delta\vec{A}_{1,S}$ = $\vec{A}_1$ with static weights initial $\vec{A}_1$
$\Delta\vec{A}_{2,S}$ = $\vec{A}_2$ with static weights initial $\vec{A}_2$
$\Delta\vec{C}_C$ = $\vec{C}$ with couple weights initial $\vec{C}$
$\Delta\vec{C}_S$ = $\vec{C}$ with static weights initial $\vec{C}$
$\Delta\vec{S}_C$ = $\vec{S}$ with couple weights initial $\vec{S}$
$\Delta\vec{S}_S$ = $\vec{S}$ with static weights initial $\vec{S}$

Greek

α_1 = phase lag of $\vec{A}_1$
α_2 = phase lag of $\vec{A}_2$
β_1 = phase lag of $\vec{W}_1$
β_2 = phase lag of $\vec{W}_2$

Superscripts

(0) = initial status without weights
(1) = status with weights or with first trial weights
(2) = status with second trial weights

References

[1] Ehrich, F. F., 1999, *Handbook of Rotordynamics*, Krieger, Malabar, FL.
[2] Foiles, W. C., Allaire, P. E., and Gunter, E. J., 1998, "Review: Rotor Balancing," Shock Vib., **5**, pp. 325–336.
[3] Everett, L. J., 1987, "Two-Pane Balancing of a Rotor System Without Phase Response Measurements," Trans. ASME, J. Vib., Acoust., Stress, Reliab. Des., **109**, pp. 162–167.
[4] Foiles, W. C., and Bently, D. E., 1988, "Balancing With Phase Only (Single-

Downloaded 02 Jun 2010 to 171.66.16.109. Redistribution subject to ASME license or copyright; see http://www.asme.org/terms/Terms_Use.cfm

Plane and Multiplane)," Trans. ASME, J. Vib., Acoust., Stress, Reliab. Des., **110**, pp. 151–157.
[5] Thearle, E. L., 1934, "Dynamic Balancing of Rotating Machinery in the Field," Trans. ASME, **56**, pp. 745–753.
[6] Wowk, V., 1995, *Machinery Vibration: Balancing*, McGraw-Hill, New York.
[7] Eisenmann, R. C., Sr., and Eisenmann, R. C., Jr., 1997, *Machinery Malfunction Diagnosis and Correction: Vibration Analysis and Troubleshooting for the Process Industries*, Prentice-Hall, Englewood Cliffs, NJ.

Downloaded 02 Jun 2010 to 171.66.16.109. Redistribution subject to ASME license or copyright; see http://www.asme.org/terms/Terms_Use.cfm

The Lean Mixture Operational Limits of a Spark Ignition Engine When Operated on Fuel Mixtures

Hailin Li

Ghazi A. Karim
e-mail: karim@enme.ucalgary.ca

A. Sohrabi

Department of Mechanical and Manufacturing Engineering,
The University of Calgary,
Calgary, AB, T2N 1N4, Canada

The operation of spark ignition (SI) engines on lean mixtures is attractive, in principle, since it can provide improved fuel economy, reduced tendency to knock, and extremely low NO_x emissions. However, the associated flame propagation rates become degraded significantly and drop sharply as the operating mixture is made increasingly leaner. Consequently, there exist distinct operational lean mixture limits beyond which satisfactory engine performance cannot be maintained due to the resulting prolonged and unstable combustion processes. This paper presents experimental data obtained in a single cylinder, variable compression ratio, SI engine when operated in turn on methane, hydrogen, carbon monoxide, gasoline, iso-octane, and some of their binary mixtures. A quantitative approach for determining the operational limits of SI engines is proposed. The lean limits thus derived are compared and validated against the corresponding experimental results obtained using more traditional approaches. On this basis, the dependence of the values of the lean mixture operational limits on the composition of the fuel mixtures is investigated and discussed. The operational limit for throttled operation with methane as the fuel is also established. [DOI: 10.1115/1.2978998]

Keywords: lean operational limits, SI engine combustion, fuel mixtures

1 Introduction

The use of alternative fuels in transport and industrial power production applications has been increasing steadily in recent years. This is prompted not only by the need to diversify the fuels used, ensure continued adequate supplies, and cut costs but often also to utilize whenever possible locally available fuel resources. Some of these fuels have been shown to have distinct superior merits to those of conventional liquid fuels in applications of spark ignition engines [1]. Most of these fuels can produce favorable exhaust emission characteristics that can meet the ever increasingly stringent emission regulations combined with enhanced power production efficiency and improved engine operational life. For example, gaseous fuels tend to show superior combustion characteristics over liquid fuels in mixture preparation, combustion stability, and tolerance to lean mixtures or the presence of diluents [2,3].

The most common alternative fuel is natural gas, which is usually made available after processing. It is supplied normally either as pipeline natural gas for numerous applications, including power production in large stationary engines, or as compressed natural gas (CNG) and occasionally in its cryogenic liquid form (LNG) for mobile vehicle applications. The composition of natural gas in its raw state can vary widely depending on its source, treatment, and local conditions. However, following its processing for transport to its ultimate consumption points, it becomes made up mostly of methane [3]. Accordingly, much of the work and information available relating to natural gas as an engine fuel consider methane to be an adequate representation of the whole fuel. Such gas has been demonstrated to be well suited for internal combustion engine applications, especially in reducing exhaust emissions and extending the lean operational region.

Hydrogen has long been recognized as a fuel having some unique and highly desirable combustion properties for applications in SI engines, such as a wide flammable mixture range, low ignition energy, and very fast flame propagation rates [4,5]. These features make H_2 an excellent potential fuel for SI engine applications whether on its own or in combination with other fuels. The burning of H_2 in a SI engine produces mainly H_2O, some NO_x with negligible amounts of CO, unburned hydrocarbon (UHC), and CO_2, which originate from the burning of the small amounts of lubrication oil [6–8]. The authors also demonstrated that the application of H_2 as a SI engine fuel can display superior performance features to those of conventional fuels, yielding high power production efficiency combined with extremely low NO_x emissions under a lean operation [9]. Moreover, the addition of H_2 to other traditional relatively slow burning fuels with a narrow operational range has been demonstrated to accelerate significantly the flame propagation rates and to extend the lean operational range [10,11]. The addition of hydrogen to fossil fuels also reduces the emissions of CO_2, CO, and UHC due to the less fractional burning of the hydrocarbon fuels. These features make H_2-enrichment an attractive approach for improving SI engine performance.

Hydrogen-rich gases containing CO, CH_4, CO_2, H_2O, and N_2 can be produced through steam or gas reforming of traditional liquid and gaseous fuels [12,13]. Such mixtures were demonstrated to have H_2-like desirable combustion properties such as fast flame propagation rate combined with a wide lean operational mixture region [14,15]. For example, the application of such H_2-rich gases should permit a SI engine operation either under ultralean or with a high level of exhaust gas recirculation (EGR) to enhance the work production efficiency and reduce engine-out NO_x emissions.

Much work has been done in examining the lean operational limits of common gaseous and liquid fuels such as natural gas, liquefied petroleum gas (LPG), and gasoline [16,17]. Recently, there is increasing interest to burn mixtures of H_2-rich gases with conventional liquid and gaseous fuels such as gasoline or natural gas in SI engines to improve the combustion stability when operated under lean or diluents containing mixtures [13,15,18–21].

Contributed by the Internal Combustion Engine Division of ASME for publication in the JOURNAL OF ENGINEERING FOR GAS TURBINES AND POWER. Manuscript received February 6, 2007; final manuscript received October 22, 2007; published online November 20, 2008. Review conducted by Thomas W. Ryan III. Paper presented at the 2005 Spring Conference of the ASME Internal Combustion Engine Division (ICES2005), Long Beach, CA, April 5–7, 2005.

Copyright © 2009 by ASME

Downloaded 02 Jun 2010 to 171.66.16.109. Redistribution subject to ASME license or copyright; see http://www.asme.org/terms/Terms_Use.cfm

For example, Andreatta and Dibble [20] and Bromberg et al. [13] examined the performance of SI production engines operated on the reformed products of natural gas prepared by a plasma fuel reformer. Søgaard et al. [21] also investigated exhaust emissions of UHC and cyclic variations in SI engines fueled with a mixture of natural gas and its reforming products. Quader et al. [15] examined the performance and exhaust emissions of a SI engine operated at around the operational limits of reformed gases while employing a large amount of EGR. However, much of the results of research on such gaseous fuel mixtures reported in the open literature appear to have been focused mainly on engine performance, such as power production, thermal efficiency, and exhaust emissions under relatively limited operating conditions and fuel mixture composition. Information about the lean operational limits of fuel mixtures of CH_4, CO, H_2, diluents, and liquid fuels tends in comparison to be quite limited. Also, the operational data reported appear to have been mainly obtained for fully open throttle operating conditions.

2 Lean Operational Limits

The lean operational limits of SI engines when operated on liquid or gaseous fuels have been established in a variety of engines. For a production engine with a variety of auxiliary devices, such as alternator, cooling fans, water pump, and air conditioning system, a limit occurs mainly due to insufficient mechanical power output that is produced to drive the auxiliary devices. The limit then depends mainly on the energy needed to power these devices, which may vary significantly from engine to engine. The results reported in the literature tend to be inconsistently varied and may not demonstrate accurately the lean operation capability of the fuel or fuel mixtures examined. However, when examining the combustion characteristics of a range of fuels in a research engine with the minimum of such auxiliary devices fitted, the operational limits derived would then depend mainly on the minimum energy needed to overcome frictional losses and maintain continued engine running. Accordingly, values for the operational limit derived in this way will be governed by the combustion process and could provide fundamental information about the corresponding limit values under other operating conditions and engines.

The irregular flame propagation associated with extremely lean or diluted mixtures will result in prolonged combustion, partial burning, and even occasional misfire. These may lead to increased emissions of unburned fuel, deteriorated thermal efficiencies, and unacceptably high cyclic variations accompanied by an abrupt drop in the exhaust temperature and the observation of specific noise associated with occasional misfiring. These combustion characteristics of the lean or diluents containing mixture were traditionally adopted as approaches to detect the operational limits.

Over the years, a number of different approaches have been developed and employed to determine such limits. For example, they can be based on the equivalence ratio at which a first engine misfire occurs [22], a selected frequency of total misfires [23], attaining a specific cylinder peak pressure value [24], a specific amount of HC or CO emission in the exhaust gas, specific values of cyclic variations in the indicated mean effective pressure (imep) [17,25], a dramatic brake power loss [11], or specific noise associated with a misfire [16]. The choice of any particular approach is often dictated by the specific needs of the application and, to a large extent, also by the availability of the specific experimental facilities needed. For example, in experiments involving a homogeneous mixture of fuel and air, the operational limits were determined while monitoring continuously the cylinder pressure development and/or detecting the typical specific noise associated with a misfire following a reduction in the fuel flow rate gradually until a misfire was detected [16]. This approach was widely adopted to determine the misfire limits of common liquid and gaseous fuels in SI engine applications. However, such a qualitative approach, which requires extensive experience, incorporates too much reliance on human factors and may produce inconsistent results. Moreover, it is very difficult to detect the misfire limits by this approach in some experimental cases, such as when operating on H_2 or for a highly throttled operation. In these cases, the specific noise associated with a misfire tends to be too weak to be detected compared with the mechanical noise, such as that associated with the opening and closing of the intake and exhaust valves. Also, the pressure variation is found to display minor differences due to the low energy release rate arising from the slow flame propagation rates combined with the low energy density of ultralean or diluted fuel-air mixtures or a low volumetric efficiency. Therefore, it would be beneficial to establish a quantitative approach that can determine and evaluate the operational limits accurately with good repeatability and applicability to a wide range of fuels and operating conditions.

This paper describes an experimental approach for determining quantitatively the operational limit of SI engines. In this contribution, the "knock limit" corresponds to a borderline knock, and it is defined in terms of the equivalence ratio (i.e., fuel-air ratio relative to the stoichiometric value) at a specific compression ratio and a set of operating conditions [26]. In comparison, the lean operational limit, which is the focus of this research, is defined in terms of the operating conditions associated with the first appearance of a cycle with a negative indicated work among a large number of cycles (at least 250 consecutive cycles) monitored as the operating mixture is leaned gradually. This approach is to be validated against the limit values derived by other experimental approaches for CH_4 and $70\%CH_4+30\%H_2$ operations. On this basis, the lean operational limits of CH_4, H_2, CO, gasoline, isooctane, and some of their binary mixtures are experimentally determined. The dependence of these values on the composition of the fuel mixtures is investigated and discussed. Moreover, the effect of throttling on the limits is also experimentally determined while operating on CH_4.

3 Experimental Setup and Procedure

A single cylinder, four stroke spark ignition CFR engine of 82.6 mm bore and 114 mm stroke was used while operating unthrottled under the prevailing local atmospheric pressure conditions (around 88 kPa). The engine is of variable compression ratio (from 4.5:1 to 16:1) and spark timing (up to 40 deg CA (crank angle) before and after the top dead center). Figure 1 shows a schematic diagram of the experimental engine setup. The engine was maintained at a constant engine speed of 900 rpm. The dynamometer could absorb the generated engine brake power or motor, the engine promptly maintaining a constant operational speed throughout even when combustion becomes severely unstable. The induction system was modified to permit the admission of either single or multifuels simultaneously involving both gaseous and liquid fuels. The gaseous fuels employed were supplied from a set of high-pressure cylinders and metered individually using a series of calibrated choked nozzles. The liquid fuel was gravity fed from a fuel tank and metered by examining the time needed for a specific volume of fuel to be consumed. Different fuel mixtures were prepared by precisely controlling the flow rates of the pure fuels and mixing them with the air into the intake manifold just before entry into the cylinder. The flow rate of the air was determined using a laminar flow air meter. Thermocouples were employed to measure the temperatures of intake mixture and exhaust gas. The intake mixture temperature could be varied through adjusting the power of the electric heater.

The in-cylinder pressure was measured with a high-frequency-response, water-cooled piezoelectric type transducer that was mounted flush with the pan-shaped cylinder head and connected to a charge amplifier. An electric encoder fitted to the end of the crank shaft can recognize equally 1000 points in each 360 deg CA. The pressure-time variation signal was recorded with a data acquisition system and processed in a computer to obtain the

Downloaded 02 Jun 2010 to 171.66.16.109. Redistribution subject to ASME license or copyright; see http://www.asme.org/terms/Terms_Use.cfm

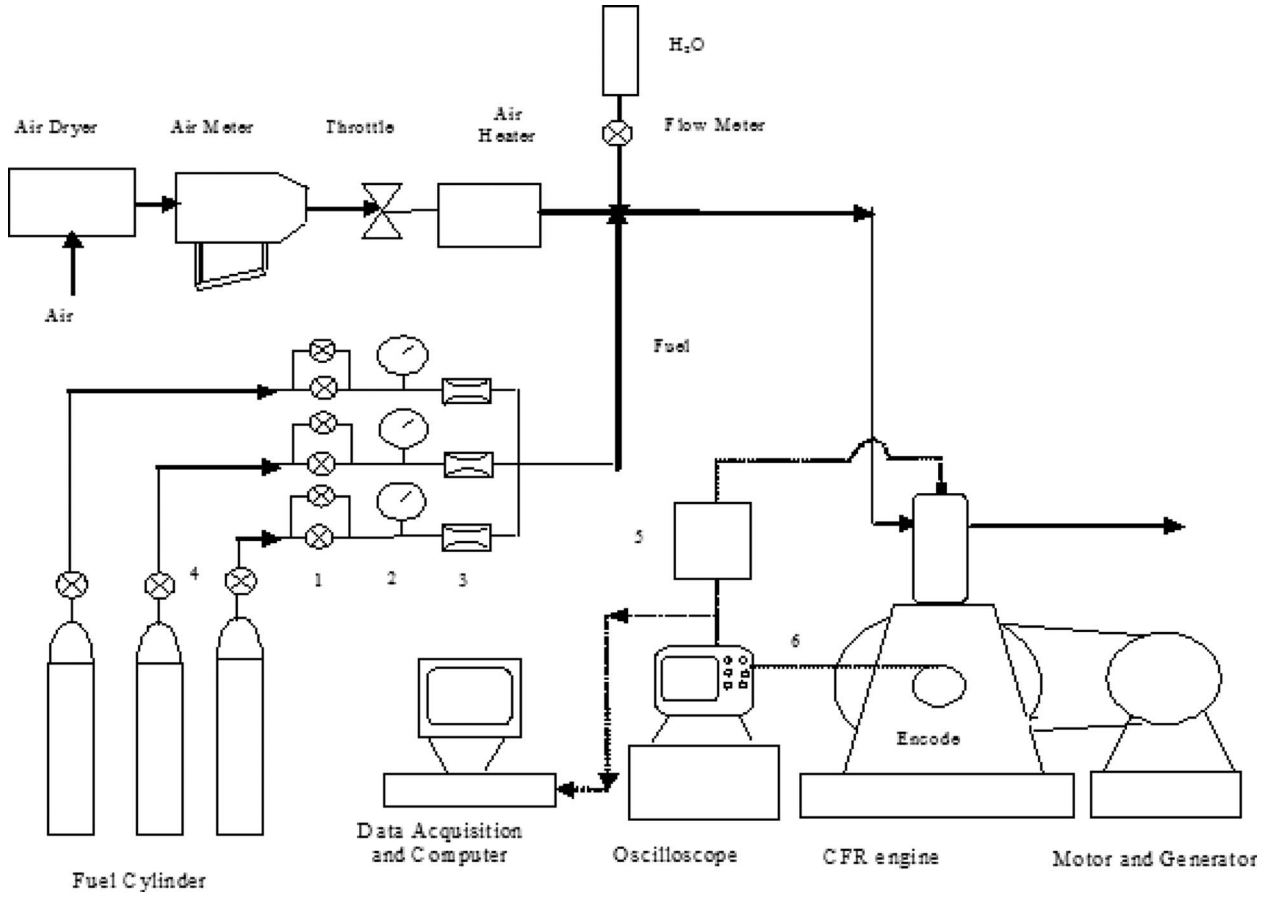


Fig. 1 Schematic diagram of the experimental engine setup

pressure-crank angle diagram, maximum pressure, indicated work production, and other combustion parameters such as the combustion duration, ignition lag time, and energy release rate. Consecutive pressure-crank angle diagrams could be further processed to examine the cyclic variation under various operating conditions. An oscilloscope was also installed in parallel to visually monitor simultaneously the pressure temporal variation.

The engine was warmed up on CH_4, and later on the test fuel or fuel mixture was fed to the engine continuously. At each operating condition, the engine was run until the engine operation stabilized (for at least 5 min) before sampling experimental data while continually monitoring the main parameters such as intake pressure, temperature, fuel flow rate, and exhaust temperature and emissions. To determine the lean operational limits, the fuel-air mixture components were leaned gradually until a misfire was first encountered, while other operating parameters such as the compression ratio, spark timing, and intake mixture and water jacket temperatures were kept constant. Unless otherwise specified, the operational limits for the different fuels were determined for a fixed spark timing of 15 deg CA BTDC, a compression ratio of 8.5:1, an intake temperature of 22°C, and fully open throttle operating conditions. The commercial CH_4 employed was processed pipeline natural gas that had the following average volumetric composition: 93.07%CH_4, 5.74%C_2H_6, 0.16%CO_2, and 1.03%N_2. The purity of CO, H_2, and iso-octane was over 99.5% by volume. The commercial gasoline used had an average octane number (0.5 MON+0.5 RON) of 92. For gaseous fuels the composition was evaluated on a molar basis. However, for fuel mixtures involving both gaseous and liquid fuels, the composition was evaluated through their fractional contributions to the total equivalence ratio defined as

$$f_{\mathrm{ER},i} = \frac{\mathrm{ER}_i}{\mathrm{ER}_{\mathrm{total}}} \tag{1}$$

where ER_i is the apparent equivalence ratio of species i defined as

$$\mathrm{ER}_i = \left(\frac{\dot{m}_{\mathrm{fuel},i}}{\dot{m}_{\mathrm{air,total}}}\right)\left(\frac{\dot{m}_{\mathrm{air}}}{\dot{m}_f}\right)_{i,\mathrm{stoichio}} \tag{2}$$

$\mathrm{ER}_{\mathrm{total}}$ is the total equivalence ratio defined as

$$\mathrm{ER}_{\mathrm{total}} = \sum_{i=1}^{n} \mathrm{ER}_i \tag{3}$$

Such a ratio represents also approximately the contributions of the specific individual fuel components to the total energy to be released due to the fact that the heating value of most fuels are fairly comparable at the same equivalence ratio.

4 The Determination of the Lean Operational Limits

The emissions of the incomplete combustion products, CO and unburned fuel, are important tracers to any incomplete combustion especially when occasional misfire may occur while increased cyclic variation tends to reflect more the occurrence and severity of any unstable combustion. Figure 2 shows the case when methane is the fuel and the variations in the concentrations of the exhaust emissions of CO and relative emissions of unburned CH_4, together with the development of cyclic variation evaluated in terms of the coefficient of variation (COV) in the imep. The value of COV in imep is observed to increase significantly accompanied by a relatively substantial increase in CO emissions as the operating mixture is leaned. Unacceptably high emission of unburned

Downloaded 02 Jun 2010 to 171.66.16.109. Redistribution subject to ASME license or copyright; see http://www.asme.org/terms/Terms_Use.cfm

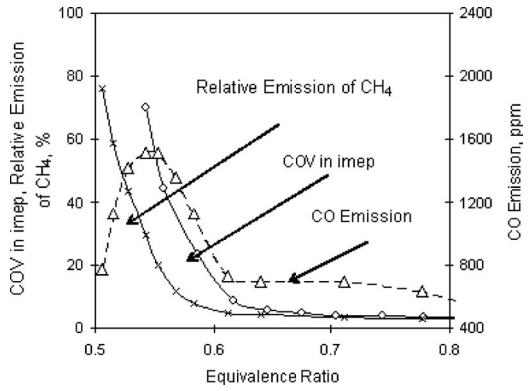


Fig. 2 Comparison of the variation in the trends of COV in imep, CO emissions, and relative emissions of CH_4 with leaning operation, fuel: CH_4, CR=8.5, T_{in}=22°C, ST=15° CA BTDC, and fully open throttle

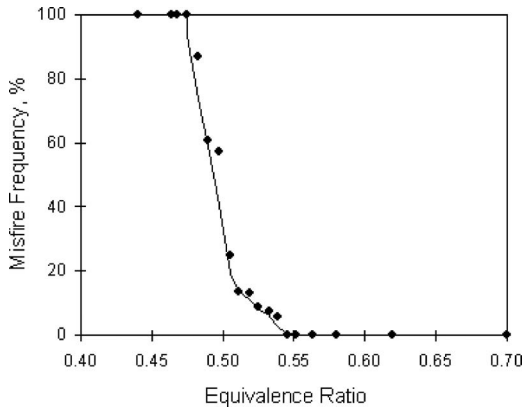


Fig. 4 Variation of the misfire frequency with leaning operation; fuel: CH_4. CR=8.5, T_{in}=22°C, ST=15° CA BTDC, and fully open throttle.

CH_4 was found mainly at leaner mixtures when a significant cyclic variation was observed. This would indicate that work is much more sensitive to the deterioration in the combustion process as it is affected directly by the heat release rate and, correspondingly, the pressure-time history.

Figure 3 shows the value of the indicated work of 20 consecutive cycles when examined experimentally over a wide range of equivalence ratios for CH_4 operation. The indicated work decreases and varies increasingly with leaning mixture operation until its minimum value drops from a relatively large positive value down to a negative with a small change in equivalence ratio when the specific noise of an obvious misfire was detected. Such specific characteristics make the value of the indicated work a suitable quantitative criterion for establishing the operational limit of SI engines. Accordingly, the lean operational limit is defined as the operating condition associated with the first observation of a working cycle among many with a negative indicated work when the mixture is being leaned, as shown in Fig. 3.

The "misfire frequency," defined as the ratio of the number of misfired cycles relative to the total number of cycles consecutively examined, is shown in Fig. 4 for CH_4 operation while the speed maintained constant throughout. It can be seen that misfire was first encountered at an equivalence ratio of 0.548. Any further leaning of the operational mixture increases the misfire frequency rapidly until a value of unity was approached at an equivalence ratio of 0.475. This value can be considered to be the operational limit for "first fire," which had been determined by Karim and Klat [27], and it is of more significance for engine starting. As shown in Fig. 5, misfire occurred at much leaner mixtures associated with substantial cyclic variation and exhaust emissions of the unburned CH_4. Such a difference reflects progress from partial burning to a total misfire. The slow propagating flame was quenched increasingly by the rapidly expanding combustion chamber volume.

Other traditional approaches for establishing the lean operational limits were also examined through measures that included the variations in the values of exhaust temperature, averaged indicated power production efficiency, COV in imep, and the specific noise associated with the occurrence of a misfire when operated on CH_4 and $70\%CH_4+30\%H_2$. For example, Fig. 6 shows the variation in the exhaust temperature with changes in equivalence ratio for operation with the two fuels. The exhaust temperature was shown to undergo a sudden and abrupt drop at a sufficiently lean mixture. The corresponding values of equivalence ratio for the occurrence of this sudden drop in temperature were found to be 0.553 and 0.460 for CH_4 and $70\%CH_4+30\%H_2$ operations, respectively. These values are comparable to 0.548 and 0.465 obtained on the basis of the *negative indicated work* approach.

The variation in the averaged indicated power production efficiency with leaning operation is shown in Fig. 7. The abrupt drop in the value of efficiency is shown when operating on a sufficiently lean mixture. The corresponding mixture limits are 0.62 and 0.54 for CH_4 and $70\%CH_4+30\%H_2$, respectively. Figure 8

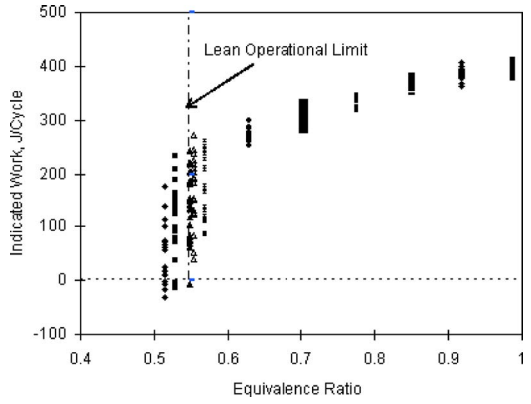


Fig. 3 Variation of the indicated work with changes in equivalence ratio for 20 consecutive cycles; fuel: CH_4. The vertical chained line shows the lean operational limit derived in this research. CR=8.5, T_{in}=22°C, ST=15° CA BTDC, and fully open throttle.

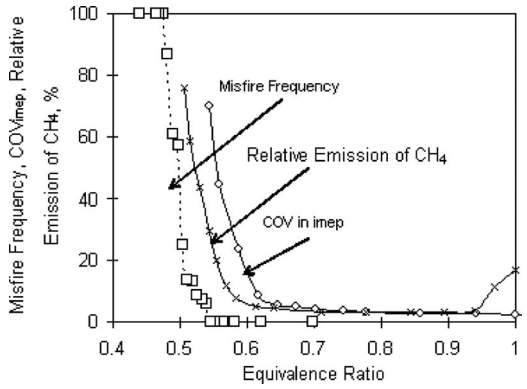


Fig. 5 Comparison of the variation trends of the COV in imep, relative emissions of CH_4, and development of misfire frequency with leaning operation; fuel: CH_4. CR=8.5, T_{in}=22°C, ST=15° CA BTDC, and fully open throttle.

Downloaded 02 Jun 2010 to 171.66.16.109. Redistribution subject to ASME license or copyright; see http://www.asme.org/terms/Terms_Use.cfm

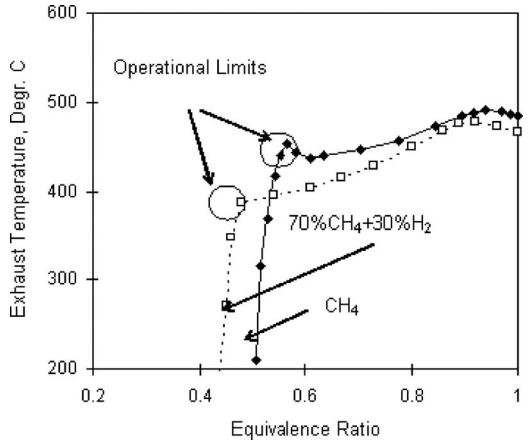


Fig. 6 Variation in the exhaust temperature with changes in equivalence ratio for CH_4 and $70\%CH_4+30\%H_2$ operations. CR =8.5, T_{in}=22°C, ST=15° CA BTDC, and fully open throttle.

shows the corresponding variations of COV in imep with changes in equivalence ratio when operated on lean mixtures of CH_4 and $70\%CH_4+30\%H_2$. The equivalence ratios corresponding to the occurrence of the sudden increase in COV in imep are 0.61 and 0.54, respectively, under the same operating conditions. A comparison of the operational limit values when derived using these various approaches for the two fuels is shown in Table 1. It can be seen that approaches on the basis of the *averaged indicated power production efficiency* and *cyclic variation* produce comparable operational limit values. The negative indicated work approach yields a similar operational limit to that of the *exhaust temperature*. Both correspond to leaner equivalence ratios than those determined by the cyclic variation and averaged indicated power production efficiency approaches since they represent operating conditions when the combustion process starts to become increasingly unstable but without encountering misfire. The value of the limit when based on the *specific noise* associated with a misfire was found to be located between those reported for these two groups of approaches and to reflect qualitatively the unstable nature of the combustion process.

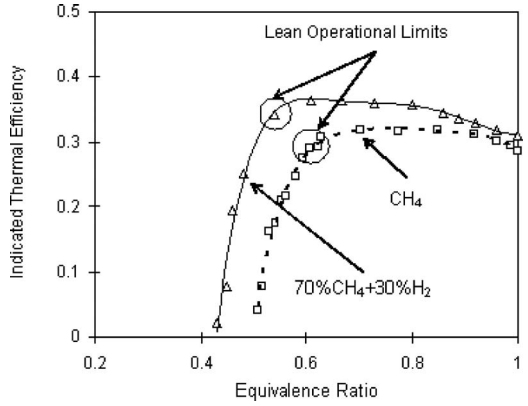


Fig. 7 Comparison of the variation in the indicated power production efficiency with changes in equivalence ratio for CH_4 and $70\%CH_4+30\%H_2$ operations. CR=8.5, T_{in}=22°C, ST=15° CA BTDC, and fully open throttle.

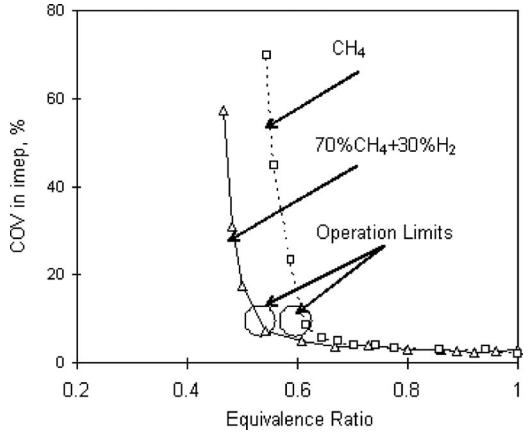


Fig. 8 Variation in the COV in imep with changes in equivalence ratio for CH_4 and $70\%CH_4+30\%H_2$ operations. CR=8.5, T_{in}=22°C, ST=15° CA BTDC, and fully open throttle.

Table 1 Comparison of the lean operational limits determined according to different approaches

Approach	CH_4	$70\%CH_4+30\%H_2$
Negative indicated work	0.548	0.465
Sudden and dramatic drop in exhaust temperature	0.553	0.460
Misfire occurrence	0.58	0.50
Sudden drop in averaged indicated power production efficiency	0.62	0.54
Sudden and dramatic increase in COV in imep	0.61	0.54

5 Lean Operational Limits of Fuel Mixtures

The negative indicated work approach was employed to establish experimentally the lean operational limits for CH_4, H_2, CO, gasoline, iso-octane, and some of their mixtures. For example, the lean operational limits for the binary fuel mixtures of CH_4 with H_2 vary approximately linearly with the changes in fuel composition, as shown in Fig. 9. The addition of H_2 to CH_4 extends gradually the lean operational limits of the resulting binary fuel mixtures. Also, the addition of CO to CH_4 extends the lean operational region but to a lesser extent than with hydrogen addition. This is mainly due to the relatively superior lean operation properties of pure CO to that of CH_4.

It has been reported earlier that the addition of a small amount of H-bearing species such as H_2 or CH_4 to dry CO enhances greatly the oxidation reactions. Such effects were demonstrated to be very important in influencing the laminar flame velocity [28], the knock limits, and the combustion durations of the resulting binary mixtures [26]. Figure 10 shows the effect of adding CH_4 or

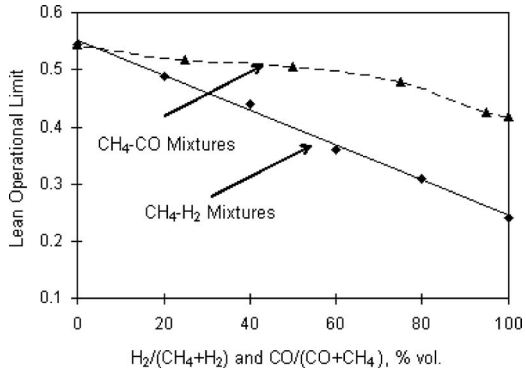


Fig. 9 Variation in the lean operation limited equivalence ratio with the changes in composition of the binary mixture of H_2 with CH_4 and CO with CH_4. CR=8.5, T_{in}=22°C, ST=15° CA BTDC, and fully open throttle.

Downloaded 02 Jun 2010 to 171.66.16.109. Redistribution subject to ASME license or copyright; see http://www.asme.org/terms/Terms_Use.cfm

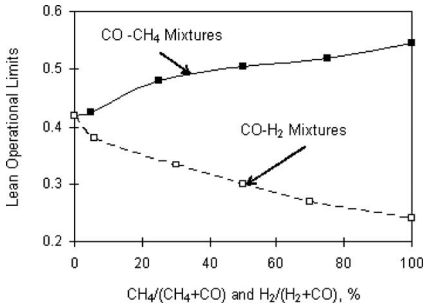


Fig. 10 Comparison of the variation in the lean limits with changes in compositions of the corresponding binary fuel mixtures of CO with CH_4 and CO with H_2. CR=8.5, T_{in}=22°C, ST =15° CA BTDC, and fully open throttle.

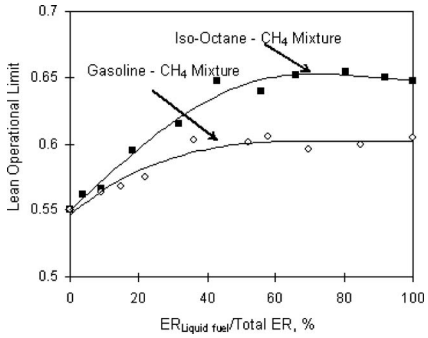


Fig. 12 Variations in the lean operation limited equivalence ratio with changes in composition of the binary mixture of CH_4 with gasoline and CH_4 with iso-octane. CR=10, ST=19° CA BTDC, T_{in}=38°C, N=900 rpm, and fully open throttle.

H_2 to pure CO on the lean operational limits of the resulting binary mixtures. The limit was found to decrease at a significant rate when adding small amounts of H_2 to CO. However, a further increase in the amount of H_2 added decreases the lean operational limits at a relatively lower rate to approach gradually the eventual value of the corresponding limit for pure H_2. In comparison, the addition of a small amount of CH_4 to CO tends not to change the lean operational limit markedly. However, the increased addition of CH_4 tends to increase the lean limit of the resulting mixtures, reflecting the narrow operational range of CH_4 under the same operating conditions.

These trends reflect in general the composite effects of the enhancement of the flame propagation rates with the addition of these H-bearing species to the CO and the values of the operational limits of these fuels on their own. Also, the effects of the presence of some H-bearing species with the dry CO produce relatively less changes in the operational limits than the corresponding effects found for the knock limits, as shown in Fig. 11 reported earlier [26]. Obviously, this is mainly due to the different mechanisms of knock and combustion failure. The onset of knock with these fuels is strongly controlled kinetically, while the misfire phenomenon is dominated by flame propagation instabilities and failure that are also governed by the transport and thermodynamic properties of the fuel-air mixture.

The lean operational limits of the fuel mixtures of CH_4 with liquid fuels, such as gasoline and iso-octane, are shown in Fig. 12. These mixture limits appear to increase rapidly as some gasoline vapor is added to CH_4, reflecting the narrow operational range of the liquid fuels involved. Such a trend continues until about 35% gasoline is added when the lean operational limit of gasoline at an equivalence ratio of 0.60 is approached. A further increase in the proportion of gasoline in the fuel mixture results in insignificant changes in these limit values. Such a trend is somewhat different from those of the operational limits of gaseous fuel mixtures discussed earlier.

A similar trend was also found with the addition of iso-octane to CH_4. The lean operational limits of the resulting mixtures approach that of iso-octane when around 40% iso-octane is added, as shown in Fig. 12. Also, the limits for iso-octane-methane mixtures tend to be richer than those for gasoline addition under the same operating condition, reflecting the relatively narrow operational regions of iso-octane, as shown in Fig. 13. The specific physical properties of the monocomponent fuel and the relatively high energy needed to ignite iso-octane could have contributed to these trends.

The energy density is reduced increasingly with throttling due to the reduction in the mass of the fresh charge in combination with an increased residual gas ratio, which results in the deterioration of the flame propagation rates. The significant effect of throttling on the operational limit values was evaluated in terms of the corresponding changes to the volumetric efficiency for CH_4 operation. As shown in Fig. 14, the lean operational limit is observed at an equivalence ratio of 0.66 for a volumetric efficiency of 0.50, which is a much higher value than that for fully open throttle operation corresponding to a volumetric efficiency of 0.81. Such increases in the limit with the intensity of throttling can approach the stoichiometric value, should the intake mixture be sufficiently throttled, as shown in Fig. 15. It is evident that excessive throttling can lead eventually to operational failure of a spark ignition engine even for a stoichiometric operation. This is mainly due to the associated deterioration in flame propagation

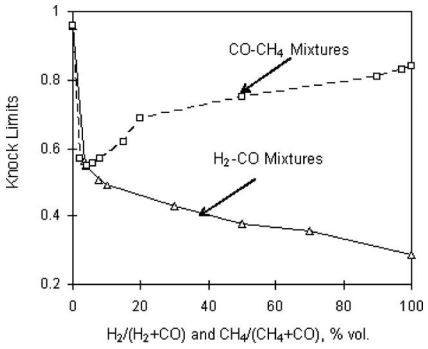


Fig. 11 Variations in the knock limited equivalence ratio with changes in the composition of the binary fuel mixtures of CO with CH_4 and CO with H_2. CR=12, ST=12° CA BTDC, T_{in} =38°C, N=900 rpm, and fully open throttle.

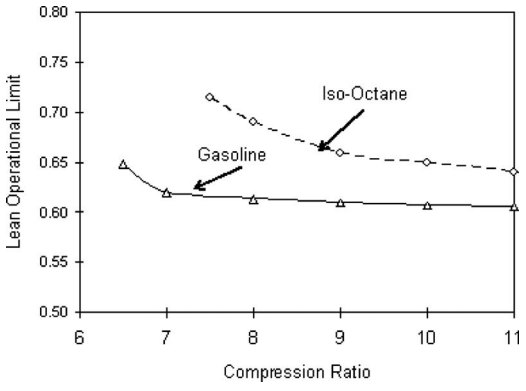


Fig. 13 Variations in the lean operation limits with changes in compression ratio for gasoline and iso-octane operations. Spark timing varies with compression ratio, as shown in literature (Li et al. [26]), T_{in}=38°C, N=900 rpm, and fully open throttle.

Downloaded 02 Jun 2010 to 171.66.16.109. Redistribution subject to ASME license or copyright; see http://www.asme.org/terms/Terms_Use.cfm

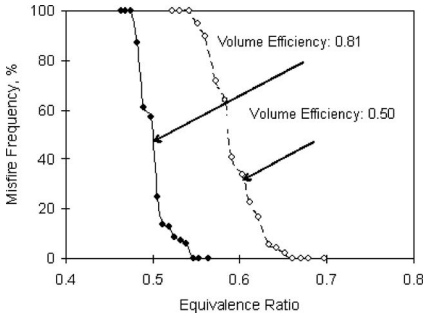


Fig. 14 Comparison of variations in the misfire frequency with leaning operations for fully and partially open throttles. Fuel: CH_4, CR=8.5, ST=15° CA BTDC, T_{in}=22°C, and N=900 rpm.

rates together with the reduction in the total energy released associated with increases in dilution by the presence of residual gases.

6 Conclusion

A quantitative approach for determining the lean operational limits of SI engines is proposed. In this approach, when leaning the operating mixture gradually, the operational limit is defined in terms of the operating conditions associated with the first appearance of a cycle with a negative indicated work among a large number of cycles (250 cycles) monitored. On this basis, the dependence of the values of the lean mixture operational limits on the composition of the fuel mixtures and volumetric efficiency was investigated. Based on the experimental results presented, the following conclusions can be drawn:

- The gradual addition of H_2 or CO to CH_4 tends to extend the lean operational limit to approach eventually those measured for the pure H_2 and CO operation, reflecting the wider operational mixture regions of H_2 and CO than that of CH_4.
- The addition of small amounts of H_2 to pure dry CO reduces the lean operational limits significantly. However, a continued increase in the amount of H_2 addition decreases the lean operational limits at a relatively much lower rate to approach gradually the eventual value of the lean operational limit of H_2 on its own.
- The addition of liquid fuels to CH_4 resulted in big increases in the lean operational limits until reaching values comparable to those of liquid fuels on their own. A further increase in the presence of the liquid fuels beyond that range did not affect significantly the lean operational limit values of the resulting fuel mixtures.
- The lean operational limit tends to increase with throttling. Excessive throttling can lead eventually to operational failure of the SI engines even with a stoichiometric mixture operation.

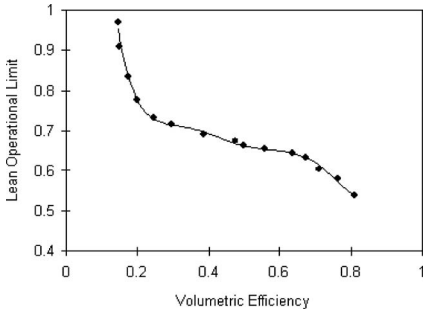


Fig. 15 Variation in the lean operational limits with throttling noted as volumetric efficiency. Fuel: CH_4, CR=8.5, ST=15° CA BTDC, T_{in}=22°C, and N=900 rpm.

Acknowledgment

The financial support of the Natural Science and Engineering Research Council of Canada (NSERC) and the University of Calgary is gratefully acknowledged.

References

[1] Keith, O., and Coley, T., 1995, *Automotive Fuels Reference Book*, 2nd ed., Society of Automotive Engineers, Warrendale, PA.
[2] Nellen, C., and Boulouchos, K., 2000, "Natural Gas Engines for Cogeneration: Highest Efficiency and Near-Zero-Emissions Through Turbocharging, EGR and 3-Way Catalytic Converter," SAE Paper No. 2000-01-2825.
[3] Weaver, C. S., 1989, "Natural Gas Vehicle: A Review of the State of Art," SAE Paper No. 892133.
[4] Furuhama, S., 1983, "State of the Art and Future Trends in Hydrogen-Fuelled Engines," Int. J. Veh. Des., **4**, pp. 359–385.
[5] Karim, G. A., 2003, "Hydrogen as a Spark Ignition Engine Fuel," Int. J. Hydrogen Energy, **28**, pp. 569–577.
[6] Furuhama, S., and Hiruma, M., 1978, "Some Characteristics of Oil Consumption Measured by Hydrogen Fuelled Engine," Lubr. Eng., **34**, pp. 665–675.
[7] Tang, X., Kabat, D. M., Natkin, R. J., Stockhausen, W. F., and Heffel, J. W., 2002, "Ford P2000 Hydrogen Engine Dynamometer Development," SAE Paper No. 2002-01-0242.
[8] Li, H. L., Karim, G. A., and Sohrabi, A., 2004, "Examination of the Oil Combustion in a S.I. Hydrogen Engine," SAE Paper No. 2004-01-2916.
[9] Li, H. L., and Karim, G. A., 2005, "Emissions From a Gas Fuelled S.I. Engine," Int. J. Green Energy, **2**(1), pp. 129–145.
[10] Karim, G. A., Wierzba, I., and Al-Alousi, Y., 1996, "Methane-Hydrogen Mixtures as Fuels," Int. J. Hydrogen Energy, **21**, pp. 625–631.
[11] Bauer, C. G., and Forest, T. W., 2001, "Effect of Hydrogen Addition on the Performance of Methane-Fueled Vehicles, Part I: Effect on S.I. Engine Performance," Int. J. Hydrogen Energy, **26**, pp. 55–70.
[12] Jamal, Y., and Wyszynski, M. L., 1994, "On-Board Generation of Hydrogen-Rich Gaseous Fuels: A Review," Int. J. Hydrogen Energy, **19**, pp. 557–572.
[13] Bromberg, L., Cohn, D. R., Rabinnovich, A., and Heywood, J. B., 2001, "Emissions Reductions Using Hydrogen From Plasmatron Fuel Converters," Int. J. Hydrogen Energy, **26**, pp. 1115–1121.
[14] Shudo, T., Nakajima, Y., and Tsuga, K., 2001, "Combustion Characteristics of H_2–CO–CO_2 Mixture in an IC Engine ," SAE Paper No. 2001-01-0252.
[15] Quader, A. A., Kirwan, J. E., and Grieve, M. J., 2003, "Engine Performance and Emissions Near the Dilute Limit With Hydrogen Enrichment Using an on-Board Reforming Strategy," SAE Paper No. 2003-01-1356.
[16] Bade Shrestha, S. O., Karim, G. A., and Wierzba, I., 2000, "Examination of Operational Limits in Gas Fuelled Spark Ignition Engines," SAE Paper No. 2000-01-1944.
[17] Gupta, M., Bell, S. R., and Tillman, S. T., 1996, "An Investigation of Lean Combustion in a Natural Gas-Fuelled Spark-Ignited Engine," ASME J. Energy Resour. Technol., **118**, pp. 145–151.
[18] Kirwan, J. E., Quader, A. A., and Grieve, M. J., 1999, "Advanced Engine Management Using On-Board Gasoline Partial Oxidation Reforming for Meeting Super-ULEV (SULEV) Emissions Standards," SAE Paper No. 1999-01-2927.
[19] Allenby, S., Chang, W. C., Megaritis, A., and Wyszynski, M. L., 2001, "Hydrogen Enrichment: A Way to Maintain Combustion Stability in a Natural Gas Fuelled Engine With Exhaust Gas Recirculation, the Potential of Fuel Reforming," Proc. Inst. Mech. Eng., Part D (J. Automob. Eng.), **215**(3), pp. 405–418.
[20] Andreatta, D., and Dibble, R. W., 1996, "An Experimental Study of Air-Reformed Natural Gas in S.I. Engines," SAE Paper No. 960852.
[21] Søgaard, C., Schramm, J., and Jensen, T. K., 2000, "Reduction of UHC-Emissions From Natural Gas Fired SI Engine-Production and Application of Steam Reformed Natural Gas," SAE Paper No. 2000-01-2823.
[22] Tanuma, T., Sasaki, K., Kaneko, T., and Kawasaki, H., 1971, "Ignition, Combustion, and Exhaust Emission of Lean Mixtures in Automotive S.I. Engine," SAE Paper No. 710159.
[23] Quader, A. A., 1974, "Lean Combustion and the Misfire Limit in S.I. Engine," SAE Paper No. 741055.
[24] Ryan, T. W., Lestz, S. S., and Meyer, E., 1974, "Extension of the Lean Misfire Limit and Reduction of Exhaust Emission of a S.I. Engine by Modification of Ignition and Intake Systems," SAE Paper No. 740105.
[25] Barton, R. K., Lestz, S. S., and Meyer, W. E., 1971, "An Empirical Model for Correlating Cycle-to-Cycle Cylinder Gas Motion and Combustion Variations of a S.I. Engine," SAE Paper No. 710136.
[26] Li, H. L., Karim, G. A., and Sohrabi, A., 2003, "Knock and Combustion Characteristics of CH_4, CO, H_2 and Their Binary Mixtures," SAE Paper No. 2003-01-3088.
[27] Karim, G. A., and Klat, S. R., 1966, "Knock and Auto-Ignition Characteristics of Some Gaseous Fuels and Their Mixtures," J. Inst. Fuel, **39**, pp. 109–119.
[28] Mclean, I. C., Smith, D. B., and Taylor, S. C., 1994, "The Use of Carbon Monoxide/Hydrogen Burning Velocities to Examine the Rate of the CO+OH Reaction," *Proceedings of the 25th Symposium (International) on Combustion*, Irvine, CA, Jul. 31–Aug. 5, Combustion Institute, Pittsburgh, PA, pp. 749–757.

Downloaded 02 Jun 2010 to 171.66.16.109. Redistribution subject to ASME license or copyright; see http://www.asme.org/terms/Terms_Use.cfm

Three–Dimensional Transient Elastic Thermal Stress Field During Diesel Particulate Filter Regeneration

Zhenhua Guo

Zhaoyan Zhang
e-mail: zzhang5@unl.edu.

Biqing Sheng

Wen Peng

Department of Mechanical Engineering,
University of Nebraska-Lincoln,
Lincoln, NE 68588

A displacement based 3D finite element model is developed to simulate thermal stress induced by high temperature and temperature gradient during diesel particulate filter (DPF) regeneration. The temperature field predicted by 3D regeneration model from previous work is used as input. This finite element model agrees well with commercial software. It is a self-contained package capable of implementing meshing body, assembling global stiffness matrix and solving final equilibrium equations. Numerical simulation indicates that it is peak temperature rather than temperature gradient that leads to higher compressive thermal stress during regeneration. The maximum stress always appears at the channel corner located at the end of DPF. Parametric studies are performed to investigate the effects of DPF design on pressure drop, regeneration temperature, and thermal stress. This model provides insights into the complicated DPF working mechanism, and it can be used as design tools to reduce filter pressure drop while enhance its short term and long term durability. [DOI: 10.1115/1.2979000]

Keywords: diesel particulate filter, thermal stress, regeneration

1 Introduction

Diesel engines are known for their reliability, high fuel economy, and low operating cost. They have dominated the market of heavy-duty vehicles and have been growing in the market of light-duty vehicles due to these qualities. In contrast to these benefits, diesel engines operate on diffusion combustion base, producing a considerable amount of particulate matter (PM). On December 21, 2000, the U.S. Environmental Protection Agency (EPA) signed very stringent PM emission standard of 0.01 g/bhp h for model year 2007 and later heavy-duty highway diesel engines. On May 11, 2004, the EPA signed the final regulation introducing Tier 4 emission standards for nonroad diesel engines, which are to be phased-in over the period of 2008–2015. The diesel particulate filter (DPF) technology, developed in the 1980s, is nowadays deemed as a substantially applicable solution to reduce PM emission to meet stringent EPA regulations.

The most common design of DPF is the wall-flow monolith. It is constructed from an extruded square cell ceramic porous media, in which every channel is plugged at the alternate ends. Exhaust gases enter the filter from inlet channels and pass through the porous wall into the contiguous outlet channels. During this process, the particulate matter is captured inside the porous wall and a particulate layer is formed above the wall as well. These collected particles cause the pressure drop across the DPF to increase. Excess pressure drop affects engine performance and penalizes fuel economy. DPF thus has to be regenerated periodically to remove particulate matter by oxidation. The regeneration of DPF is initiated by ramping up engine load while applying brake simultaneously. Increased engine load increases the exhaust gas temperature to trigger the oxidation of particulate matter. Typically, the particulate matter begins to oxidize when the filter is sufficiently loaded and the inlet exhaust temperature exceeds 550°C.

Manuscript received April 17, 2007; final manuscript received May 20, 2008; published online November 20, 2008. Review conducted by Christopher J. Rutland. Paper presented at the SAE World Congress 2007.

The major challenge with DPF is the uncertainty of the regeneration processes. Since the accumulated particulate matter consists mainly of carbonaceous matter, its heating value is very high and a given mass of particulate matter at the time of regeneration will release large amounts of energy. If this energy is not removed sufficiently from DPF, considerably high temperature and thermal stress will occur and this may lead to melting and cracking of the filter. In addition to this type of filter failure subject to occasionally high exposure, repeated regeneration of DPF leads to strength loss called thermal fatigue, which may causes iterative damage instead of immediate failure [1]. Cordierite and silicon carbide (SiC) are two widely used materials in commercialized DPF. Cordierite is characterized by good thermal stress resistance and lower cost, but it has lower melting temperature. On the other hand, SiC has higher operating temperature limit but lower thermal stress resistance, which makes it susceptible to cracking. In this article, thermal stress analysis will be carried out on both of these DPFs.

Two basic approaches are extensively used to study DPF performance in the literature. The first approach, single channel model, is based on the assumption that all channels behave the same. The solutions of the mass, momentum and energy balance equations for representative channels can be applied to other channels. The research work presented in this article falls into this category. Whole scale model, on the contrary, simulates the whole DPF or part of it as continuous structure with effective material properties.

1.1 Single Channel Model. Significant progress toward understanding the complicated transport and regeneration processes was gained by the pioneering work of Bissett [2–4]. He provided a complete DPF regeneration model with an application of fundamental conservation laws to filter channel. Flow resistance across the wall was expressed with Darcy's law to account for pressure drop from inlet channel to outlet channel. Majority of research works on DPF pressure drop and regeneration thereafter followed Bissett's approach but with more complicated transport mechanisms involved. Based on Bissett's model, Konstandopoulos and Johnson [5] derived a one-dimensional analytical flow field solu-

Copyright © 2009 by ASME

Downloaded 02 Jun 2010 to 171.66.16.109. Redistribution subject to ASME license or copyright; see http://www.asme.org/terms/Terms_Use.cfm

tion for clean DPF with pressure loss components attributed to channel frictional flow and wall-flow. With the assumption that the porous wall was a collection of spherical collectors, they employed diffusion and interception mechanisms to describe clean DPF filtration characteristics. Since the DPF open frontal area was significantly shrunk considering the fact of alternately plugged channels and wall thickness, initial loss due to the contraction and expansion of the flow as it entered and left the filter channel could not be neglected, especially with high exhaust flow rate operating conditions. Konstandopoulos [6] presented a comprehensive understanding on DPF pressure drop and summarized experimental setup and data analysis methods to determine flow resistance descriptor, namely, filter wall permeability and inlet/outlet loss coefficient. The content of this article has been widely used in the industry to predict DPF pressure drop to design aftertreatment system. With deeper understanding on DPF regeneration, numerical simulation becomes a cost-effective way to refine regeneration strategy and to enhance filter mechanical integrity. Opris and Johnson [7,8] developed a 2D computational model to study the flow, heat transfer, and regeneration behaviors of DPF. By neglecting nonlinear terms in Navier–Stokes equations, an analytical solution for the flow field was derived. The filter temperature profile was determined by numerically solving the 2D unsteady energy equation including the convection, conduction, and viscous dissipation terms. One-dimensional models were developed by Haralampous and Koltsakis [9,10] to account for oxygen diffusion and NO_2 back-diffusion on DPF regeneration. The role of oxygen diffusion was shown to be important in uncontrolled regenerations, which can cause high peak temperature. The contribution of NO_2 back-diffusion was responsible for about one-third of the total regeneration rate for catalyst coated filter. A multidimensional numerical model was developed by Guo and Zhang [11] to study the loading and regeneration characteristics of DPF. It was found that the instant when maximum temperature occurred usually lagged behind the instant when peak temperature gradient occurred. This delay became negligible for high particulate loading. These two instants are critical to the reliability of a DPF due to the effects of thermal stress. In addition to numerical simulation, various testing approaches were applied to DPF studies as well. Suresh et al. [12] performed experiments with several commonly used DPF to determine the regeneration efficiency of these filters at different loading conditions. The temperatures inside the DPF were constantly monitored during the experimental runs by using thermocouples, which were inserted from the outlet channels to the desired positions. Yezerets et al. [13] applied several complementary experimental techniques to investigate kinetics of diesel soot oxidation by O_2 in an attempt to provide accurate data for the modeling of the DPF regeneration process. A good mathematical description of the results was obtained using the hypothesis that reaction order with respect to soot mass is close to unity. Hanamura et al. [14] clarified the combustion mechanism in the regeneration of a DPF through a visualization experiment using a half-cylindrical wall-flow DPF covered by a quartz glass plate.

1.2 Whole Scale Model. The problem of scaling up from a single channel to the entire DPF was dealt with in the literature using several different approaches. One line of approach was to discretize the cylindrical DPF in the radial direction with axisymmetric radial sectors [15,16]. Assuming that all channels in the same radial sector behaved the same, a representative channel for each sector was solved. The sector interactions were not treated in a rigorous way, hence the heuristic aspect of this approach. In addition, considering the tremendous computation tasks, a 1D model was usually employed to depict a representative channel in each sector. Recently, a 3D model for the regeneration of the SiC DPF has been developed by Pontikakis and Stamatelos [17]. The 3D whole scale modeling was achieved by interfacing an existing 1D single channel model to a commercial finite element method software ANSYS for the computation of the 3D temperature field within the whole filter assembly. The numerical results can be used as input data for thermal stress model.

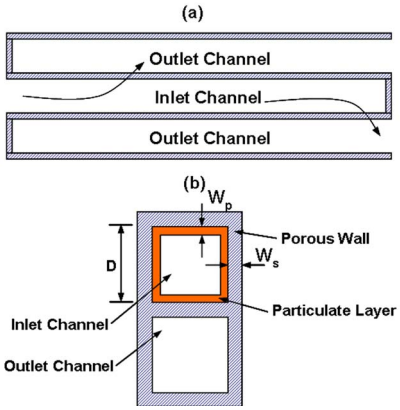


Fig. 1 Schematic of DPF channels: (*a*) side view and (*b*) front view

An alternative way to deal with the scale-up problem was to employ a continuum model of the honeycomb structure. The continuum approach for the wall-flow honeycomb structure was first introduced by Aris [18] who showed the equivalence between the continuum and the discrete channel solutions as the disparity was increased. The most apparent and important usage of the continuum model was to analyze thermal stress, which contributed to the majority of DPF failures. Kuki et al. [19] developed a strategy to efficiently perform thermal stress analysis for the entire DPF through finite element method. The temperature at each node, treated as external loads to DPF, was obtained by interpolating/extrapolating thermocouple readings. All the above whole scale models involve considerable simplifications as they did not simulate the thermal stress field of DPF rigorously.

In this article a 3D finite element model is developed to investigate transient elastic thermal stress during DPF regeneration. This thermal stress model is self-contained and independent of external commercial package. It, together with temperature and pressure drop models, can be used as design tools to optimize DPF performance.

2 Mathematical Models and Numerical Approaches

The schematics of a DPF are shown in Fig. 1. Exhaust gas flows along the inlet channel and passes to the outlet channel through the porous wall. The particulate matter is collected both inside and above the porous wall during this process.

2.1 Temperature Field. The modeling of 3D flow and temperature field in DPF has been discussed in previous work [11], which is based on the solution of mass, momentum, and energy balance equations. 3D Navier–Stokes equations are simplified to a set of 1D conservation equations by employing order of magnitude analysis and integral method. They are then solved by combining the shooting method and the Runge–Kutta method. The 3D flow field is recovered by using the 1D solution and parabolic velocity profile. A filtration model based on the "unit collector" theory is used to determine the transient filtration behaviors of the porous wall. The total pressure drop as exhaust gas passes through DPF is comprised by the pressure drop through porous wall and channels, while the pressure drop through the porous wall obeys Darcy's law. 3D transient conservation of energy is then solved using a modified alternating direction implicit (ADI) method. A brief description of the governing equations of the temperature field in DPF is given below.

Due to the symmetry of the DPF structure, the computational domain for the temperature field can be reduced to the brick element shown in Fig. 2. Three conservation of energy equations are

Downloaded 02 Jun 2010 to 171.66.16.109. Redistribution subject to ASME license or copyright; see http://www.asme.org/terms/Terms_Use.cfm

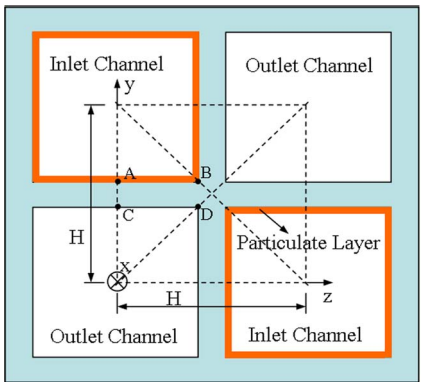


Fig. 2 Computational domain for temperature field

used to describe the temperature field in DPF. The energy equation for the channel flow in both inlet and outlet channels is expressed by

$$\rho_f c_{p,f}\frac{\partial T}{\partial t} = \lambda_f\left(\frac{\partial^2 T}{\partial x^2} + \frac{\partial^2 T}{\partial y^2} + \frac{\partial^2 T}{\partial z^2}\right) - \rho_f c_{p,f}\left(u\frac{\partial T}{\partial x} + v\frac{\partial T}{\partial y} + w\frac{\partial T}{\partial z}\right) \tag{1}$$

The energy equation for the porous wall is expressed by

$$\rho_s c_{p,s}\frac{\partial T}{\partial t} = \lambda_s\left(\frac{\partial^2 T}{\partial x^2} + \frac{\partial^2 T}{\partial y^2} + \frac{\partial^2 T}{\partial z^2}\right) - \rho_f c_{p,f}\left(u\frac{\partial T}{\partial x} + v\frac{\partial T}{\partial y} + w\frac{\partial T}{\partial z}\right) + \mathrm{ST} \tag{2}$$

Special attention should be paid to the interface between the channel flow and the porous wall to take into account the different exhaust gas and porous wall properties.

Due to the particulate oxidation during regeneration, a source term (ST) should be considered in the conservation of energy equation for the porous wall. The particulate oxidation process during regeneration phase is quite complicated. A simplified one-step global reaction is assumed to take place and can be expressed as

$$\mathrm{C} + \mathrm{O_2} \rightarrow \mathrm{CO_2} \tag{3}$$

Both thermal and catalytic oxidation mechanisms are considered. They are modeled using an Arrhenius equation. The overall reaction rate (RR) can be written as the sum of thermal and catalytic reaction rates

$$\mathrm{RR_{ov}} = \mathrm{RR}_t + \mathrm{RR}_c = A_t[\mathrm{O_2}]\exp(-E_t/R_uT) + A_c[\mathrm{O_2}]\exp(-E_c/R_uT) \tag{4}$$

The particulate mass oxidation rate is related to the retained particulate mass and reaction rate by

$$dm_p/dt = -m_p \cdot \mathrm{RR_{ov}} \tag{5}$$

The rate of energy released from particulate oxidation is the product of mass oxidation rate and enthalpy of formation of the aforementioned global chemical reaction. Therefore, the source term in Eq. (2) can be written explicitly as

$$\mathrm{ST} = \rho_{p,\mathrm{effe}}\mathrm{RR_{ov}}H_{\mathrm{reac}} \tag{6}$$

where $\rho_{p,\mathrm{effe}}$ is the effective particulate mass density with respect to the small control volume in the finite difference method.

2.2 Thermal Stress. Several assumptions can be made for the thermal stress field in a porous wall.

(a) The porous wall is a linear elastic isotropic material. Its material properties are temperature independent.
(b) Displacement is small quantity and large deformation is not allowed. The derivative relations between displacement and strain hold over the entire body.
(c) Heat transfer is unaffected by thermal expansion. Temperature field in DPF is obtained from heat transfer code followed by thermal stress simulation.
(d) No external body forces are applied to the part. Stresses occur only due to thermal expansion or contraction.
(e) Inertial effects are negligible during thermal stress development.

The high temperature and temperature gradient that occur during DPF regeneration result in large localized thermal expansion. This thermal expansion, in turn, causes large thermal stress in the porous wall. Theoretically, stress distribution under given temperature field and geometry can be determined using a commercial finite element package. However, the extreme large dimension ratio between DPF length and wall thickness necessitates substantial elements to mesh structure in commercial package. This precludes the use of such commercial package in personal computer (PC) with limited memory capacity.

Assuming body forces are negligible and the part is motionless, the conservation of linear momentum can be expressed as [20]

$$\sigma_{ij,j} = 0, \quad i = 1,2,3 \tag{7}$$

For linear elastic isotropic material, the stress-strain relations come from the generalized Hooke's law

$$\boldsymbol{\sigma} = [D](\boldsymbol{\varepsilon} - \boldsymbol{\varepsilon}_0) \tag{8}$$

where $\boldsymbol{\sigma} = [\sigma_{xx}, \sigma_{yy}, \sigma_{zz}, \sigma_{xy}, \sigma_{yz}, \sigma_{zx}]^T$ is the stress vector. $\boldsymbol{\varepsilon} = [\varepsilon_{xx}, \varepsilon_{yy}, \varepsilon_{zz}, \varepsilon_{xy}, \varepsilon_{yz}, \varepsilon_{zx}]^T$ is the strain vector. $\boldsymbol{\varepsilon}_0 = \alpha\Delta T[1\ 1\ 1\ 0\ 0\ 0]^T$ is the initial strain vector caused by temperature rise with respect to reference temperature. $[D]$ is the symmetric material matrix.

Under the assumption of small deformation, the relation between strain and displacement can be expressed as

$$\boldsymbol{\varepsilon} = \left[\frac{\partial \underline{u}}{\partial x}, \frac{\partial \underline{v}}{\partial y}, \frac{\partial \underline{w}}{\partial z}, \frac{\partial \underline{u}}{\partial y} + \frac{\partial \underline{v}}{\partial x}, \frac{\partial \underline{v}}{\partial z} + \frac{\partial \underline{w}}{\partial y}, \frac{\partial \underline{w}}{\partial x} + \frac{\partial \underline{u}}{\partial z}\right]^T \tag{9}$$

Inserting Eqs. (8) and (9) into Eq. (7) gives three equations in terms of displacements, from which the stress distribution of the entire part can be determined. The three equations can be expressed in a compact format as [20]

$$\underline{u}_{i,kk} + \frac{1}{1-2\nu}\underline{u}_{k,ki} - \frac{2\alpha(\nu+1)}{1-2\nu}T_i = 0, \quad i = 1,2,3 \tag{10}$$

2.3 Finite Element Analysis. Equation (10) contains three displacement unknowns in partial derivative format with respect to space. Finite element method is employed in this study and the solution steps are summarized as follows:

(a) The porous wall is meshed with brick element.
(b) Temperature interpolation is carried out to find temperature distribution at element nodes based on temperature prediction from previous work [11].
(c) After a coordinate transformation from global to isoparametric coordinates, the local stiffness matrix and force vector of each element is calculated with Gaussian quadrature numerical integration method.
(d) Through assembling local stiffness matrix and force vector, the final equilibrium equation is expressed as

$$[K]_{3n\times 3n}\boldsymbol{Q}_{3n\times 1} = \boldsymbol{F}_{3n\times 1} \tag{11}$$

(e) Penalty method is used to incorporate boundary conditions into Eq. (11) to make it solvable.

The computational domain for 3D temperature field in Fig. 2 can be divided into four equivalent parts using two diagonals. The porous wall in each part has the same

Downloaded 02 Jun 2010 to 171.66.16.109. Redistribution subject to ASME license or copyright; see http://www.asme.org/terms/Terms_Use.cfm

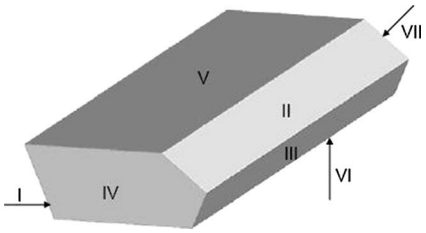


Fig. 3 Geometry of porous wall for 3D thermal stress analysis

geometry, temperature distribution, and boundary conditions. Thus, only one-quarter, shown in Fig. 3, needs to be considered in thermal stress analysis.

Since the body forces are neglected for simplification, only displacement boundary conditions are involved. There are no displacement along normal directions for Surfaces I, II, and III due to symmetric geometry and temperature distributions. There are no displacement constraints at the other two degrees of freedom for these three surfaces. Similarly, Surfaces IV, V, VI, and VII are associated with free expansion conditions, namely, no displacement constraints at all three degrees of freedom.

(f) Considering global stiffness is a highly sparse banded matrix, a modified Gaussian elimination algorithm is employed to solve the equilibrium equation.

(g) Once the displacement field is solved, the strain and stress fields are easily obtained using Eqs. (9) and (8).

It is well established that the elastic properties of porous materials depend on its porosity. There have been several published approaches to derive the property-porosity relations for ceramics, e.g., micromechanics method [21], semiempirical correction, and actual rupture experiment [22]. An empirical relations proposed by Coble and Kingery [23] is used in this article due to their satisfactory prediction against actual measurement

$$\frac{\sigma_{c,\mathrm{po}}}{\sigma_{c,\mathrm{np}}} = \exp(-4.9\beta_0) \tag{12}$$

$$\frac{E_{\mathrm{po}}}{E_{\mathrm{np}}} = \frac{1-\beta_0}{1+4\beta_0} \tag{13}$$

3 Model Validation

To validate this 3D thermal stress model, a simple simulation for a DPF porous wall with uniform temperature at 900 K was performed and compared to results from a widely used commercial finite element package—ANSYS. Input parameters are listed in Table 1, among which, Young's modulus, Poisson's ratio, thermal expansion coefficient, and reference temperature are valid for cordierite throughout this article. It should be noted that the DPF length for current simulation is 5 mm instead of the actual value. This primarily aims to diminish the considerable dimension difference between DPF length and porous wall thickness, which precludes the use of commercial package.

Table 1 Input data of cordierite DPF

Porous wall material	Cordierite
DPF length	5.0 mm
Channel width	2.0 mm
Porous wall thickness	0.43 mm
Young's modulus	17.09 GPa
Poisson's ratio	0.21
Thermal expansion coefficient	$3.57\times10^{-7}/^{\circ}\mathrm{C}$
Compressive strength	13.4 MPa
Uniform temperature	900 K
Reference temperature	25°C

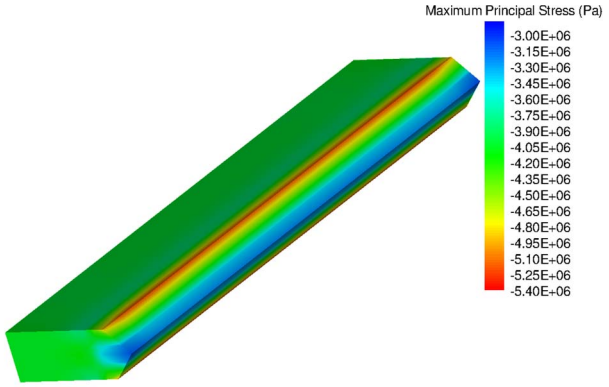


Fig. 4 Thermal stress predicted by 3D model

The contours of maximum principal thermal stress obtained from 3D model and ANSYS are presented in Figs. 4 and 5, respectively. Since the expansion of porous wall, induced by the increase in temperature with respect to reference temperature, is constrained by boundary conditions; the whole part is under compression with negative stress by convention. The maximum compressive thermal stress is distributed along the channel corner, and the minimum thermal stress is found in the middle of the channel width. It can be seen that these two thermal stress contours are very similar to each other in terms of distribution and magnitude of the thermal stress marked in the legend. Further quantitative validation is performed through exporting nodal solutions from ANSYS and comparing to those from this 3D model. The contour of relative stress deviation at the end of the DPF is presented in Fig. 6. It shows that the maximum relative stress deviation is within 3% across the whole area. These results indicate that the thermal stress model is developed properly. This model can predict thermal stresses in DPF with various geometric dimensions as long as sufficiently fine meshes are used.

4 Results and Discussions

It has been well documented that high localized temperature and temperature gradient incurred during regeneration may lead to cracking of the DPF. High temperature causes expansion of the porous wall and consequently high thermal stress when the expansion is restricted. The sharp temperature gradient causes the porous wall to expand unevenly and further increases the thermal stress. Therefore, two quantities are of interest to DPF designers. Based on the simulation results of 3D temperature field, it was found that the maximum temperature always occurs at the downstream of the DPF. Therefore, four points at the end of DPF (*A*, *B*, *C*, and *D*), marked in Fig. 2, are chosen to show the magnitude of temperature and temperature gradient. During cordierite DPF regeneration, maximum temperature usually occurs at Point A and maximum temperature gradient usually along the A–C direction. This is primarily due to low thermal conductivity of cordierite, which is less efficient for dispersing heat generated from exothermal soot oxidation. On the other hand, the maximum temperature gradient for SiC DPF appears along the *A*-*B* direction, which is due to high thermal conductivity of SiC and low convection at the corner of the channel [11].

Comparisons of thermal stresses in cordierite DPF between two instants when maximum temperature and temperature gradient occur are investigated for two initial particulate loadings at 220 g (9.25 g/l) and 240 g (10.09 g/l). The specifications of cordierite DPF geometry are listed in Table 2. The mesh density is determined by the convergence requirement of the finite element method and aspect ratio of hexahedral element. For a typical DPF

Downloaded 02 Jun 2010 to 171.66.16.109. Redistribution subject to ASME license or copyright; see http://www.asme.org/terms/Terms_Use.cfm

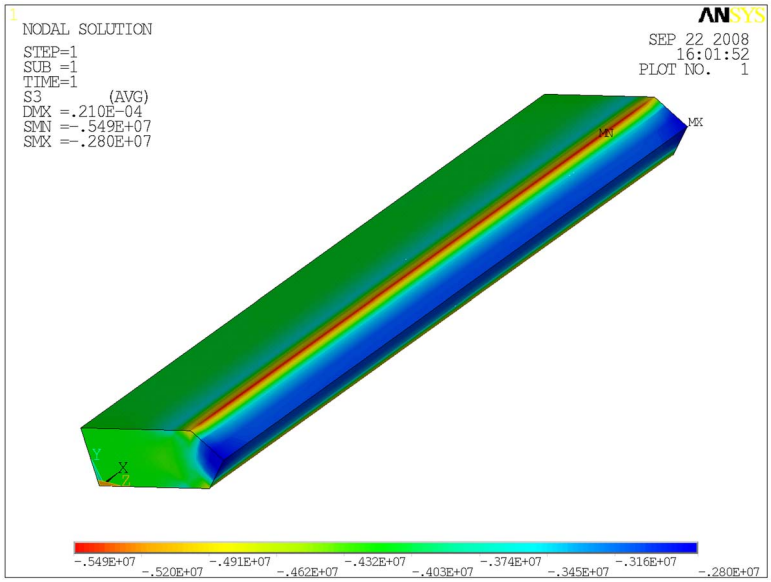


Fig. 5 Thermal stress predicted by ANSYS

with a channel length of 0.36 m, channel width of 2 mm, and wall thickness of 0.43 mm, the number of element divisions along each dimension are 1200, 10, and 6, respectively. The CPU time is approximately 1.5 h for each thermal stress simulation on a PC with Pentium 3.0 GHz processor and 3.0 GByte memory.

The soot regeneration strategy discussed in previous publication [11] is used throughout the remaining part of this article. Based on the simulation results on cordierite DPF, the maximum principal stress contours for 220 g are shown in Figs. 7 and 8, and the maximum principal stress contours for 240 g are shown in Figs. 9 and 10. Different scales for DPF length, channel width, and wall thickness are used in postprocessing to make it possible to put entire structure in one figure. Since the expansion of porous wall is constrained at boundaries, compressive thermal stress is exerted throughout the solid wall. The maximum compressive stress for each cross section along the DPF length is always found at the channel corner. This is primarily attributed to abrupt geometry change without connecting fillet between two channel walls. In addition, since the most severe regeneration takes place at the end of DPF, the maximum compressive stress throughout the entire structure is found at the channel corner, which is located at the end of DPF. Those four figures also show that the maximum thermal stresses for the cases when maximum temperature occurs are larger than those when maximum temperature gradient occurs. Therefore, maximum wall temperature rather than temperature gradient leads to highest thermal stress during DPF regeneration. Unless stated otherwise, the thermal stress analyses in the remaining part of this article correspond to thermal stresses at the instant when maximum temperature occurs.

Comparison of the thermal stresses in cordierite DPF and SiC DPF when maximum temperature occurs at 240 g soot loading are carried out. Input parameters for SiC DPF are listed in Table 3, while the geometry is the same as that of cordierite DPF. The maximum principal stress contours for SiC DPF at 240 g soot

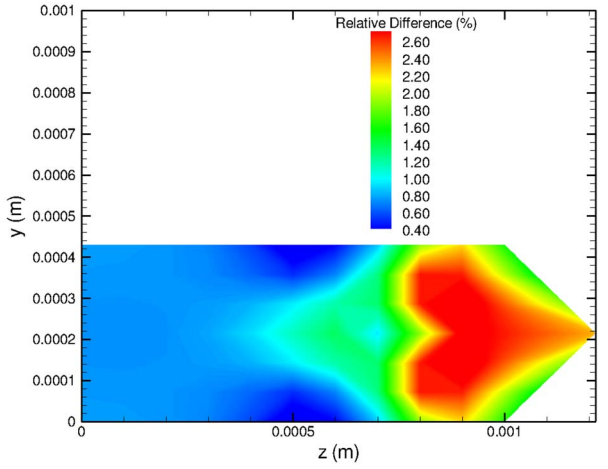


Fig. 6 Comparison of thermal stress at the end of DPF between 3D model and ANSYS

Table 2 Specifications of DPF geometry

DPF length	0.36 m
Channel width	2.0 mm
Porous wall thickness	0.43 mm
DPF diameter	0.29 m
Cell density	100 cpsi

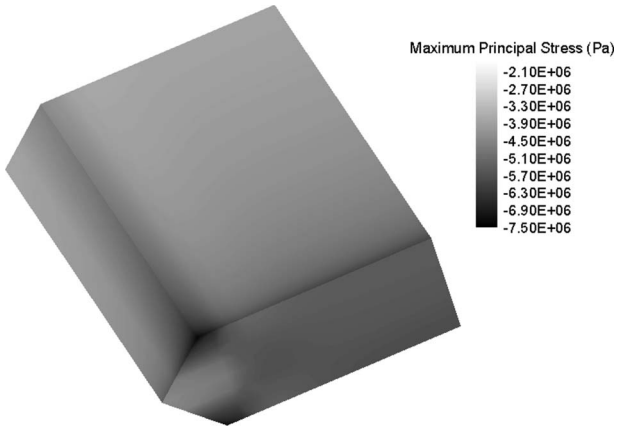


Fig. 7 Back view of thermal stress in cordierite DPF when maximum temperature gradient occurs for initial soot loading at 220 g

Downloaded 02 Jun 2010 to 171.66.16.109. Redistribution subject to ASME license or copyright; see http://www.asme.org/terms/Terms_Use.cfm

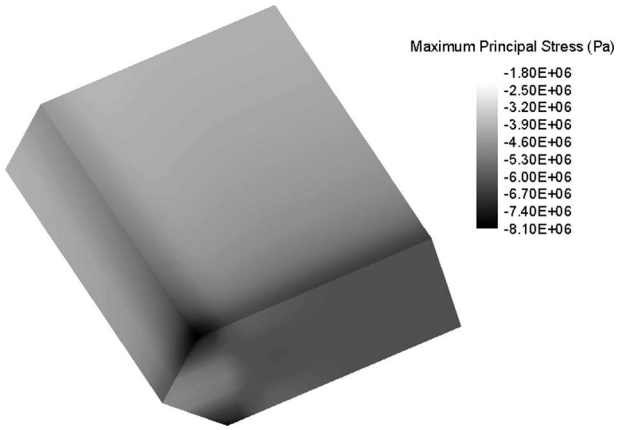


Fig. 8 Back view of thermal stress in cordierite DPF when maximum temperature occurs for initial soot loading at 220 g

loading are shown in Fig. 11. It can be found that the maximum compressive thermal stress in cordierite DPF is around 8.8 MPa, which is lower than the compressive strength of porous cordierite (13.4 MPa). However, the maximum compressive thermal stress in SiC DPF is around 180 MPa, which is higher than the compressive strength of porous SiC (171.32 MPa). This is primarily attributed to the large Young's modulus and large thermal expansion coefficient of the porous SiC. Therefore, cordierite DPF, unlike SiC DPF, is less prone to failure due to cracking caused by thermal stresses.

Table 3 Input data of SiC DPF

Porous wall material	Silicon carbide
Young's modulus	84.77 GPa
Poisson's ratio	0.19
Thermal expansion coefficient	$1.5\times10^{-6}/^{\circ}\mathrm{C}$
Compressive strength	171.32 MPa
Reference temperature	25°C

The effect of initial soot mass loading on thermal stress is studied using this 3D model. The variation of maximum compressive thermal stress with soot loading is presented in Fig. 12. It can be found that the maximum thermal stress increase very much linearly with soot loading. This, in essence, indicates that interpolation and extrapolation is acceptable in obtaining maximum thermal stress under other initial soot loading if DPF geometry and regeneration strategy are kept unchanged.

In practice, the geometric parameters of DPF need to be changed to make it work seamlessly with different diesel engines, vehicle layouts, and other aftertreatment devices. It is cost effective to quantitatively investigate the impacts of DPF geometry on its performance before putting it to mass production. In this section, thermal stresses of different DPF design will be evaluated

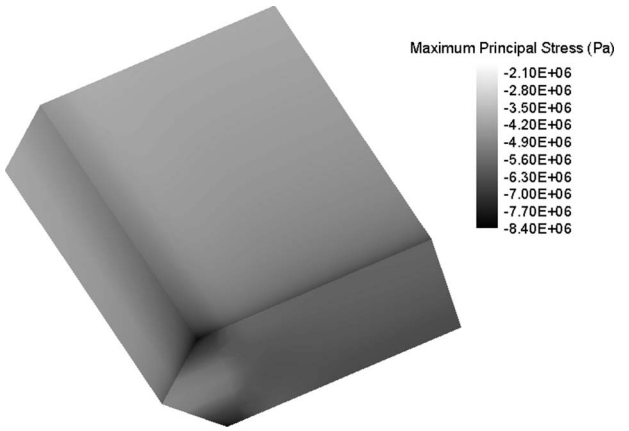


Fig. 9 Back view of thermal stress in cordierite DPF when maximum temperature gradient occurs for initial soot loading at 240 g

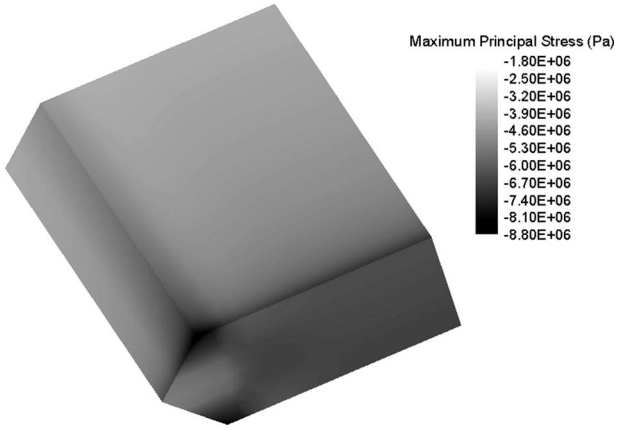


Fig. 10 Back view of thermal stress in cordierite DPF when maximum temperature occurs for initial soot loading at 240 g

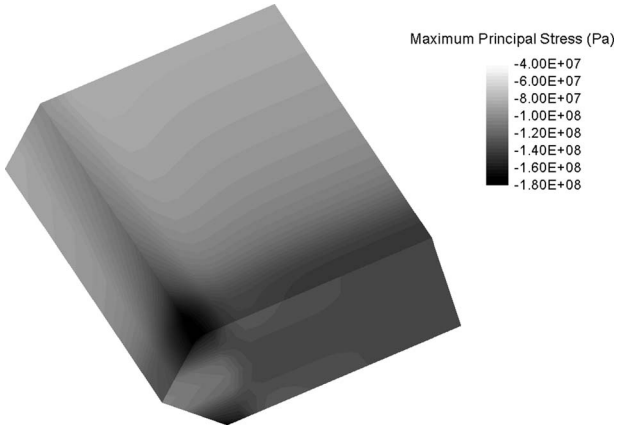


Fig. 11 Back view of thermal stress in SiC DPF when maximum temperature occurs for initial soot loading at 240 g

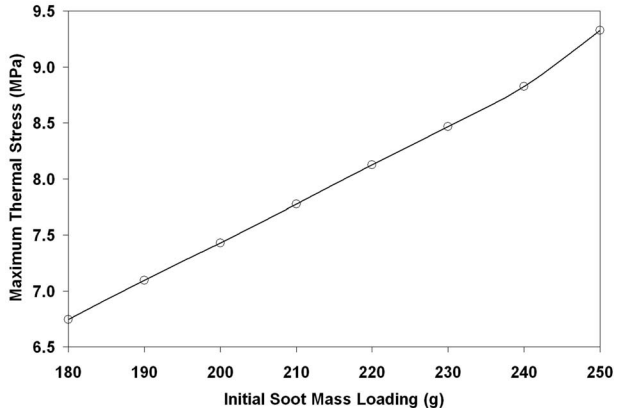


Fig. 12 Variation of maximum compressive thermal stress with initial soot mass loading

Downloaded 02 Jun 2010 to 171.66.16.109. Redistribution subject to ASME license or copyright; see http://www.asme.org/terms/Terms_Use.cfm

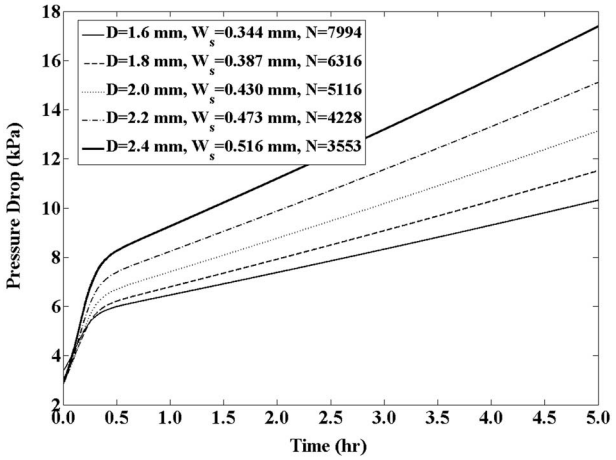


Fig. 13 Pressure drops during particulate loading for five different DPF geometries with constant filtration volume

numerically. To make simulation results comparable to each other, the total soot loading is 155 g (6.5 g/l) for all cases. The parametric studies are carried out in two categories.

4.1 Constant Filtration Volume. In this study, the DPF length L and diameter D_t are kept constant, while channel width D, porous wall thickness W_s, and inlet channel number N varies to keep the filtration volume constant. The channel width D, porous wall thickness W_s, and number of inlet channels N should satisfy the following relations.

$$\frac{(D+W_s)^2}{2W_s^2+4DW_s}=\text{const}, \quad N\cdot(D+W_s)^2=\text{const}$$

These relations imply that DPF with larger channel width has larger porous wall thickness but lower number of inlet channels. Numerical simulations for five different geometries were carried out. The pressure drops as function of time during DPF loading are plotted in Fig. 13. The initial pressure drops for all five cases are about the same. However, the DPF with larger porous wall thickness has greater rate of increase in pressure drop. Figure 14 shows the history of wall temperature at the end of DPF. It can be seen that DPF with larger channel width reaches higher peak temperature during regeneration. The predicted maximum compressive thermal stresses during regeneration for five geometries are shown in Fig. 15. The DPF with larger channel width has higher thermal stress, which is consistent with the temperature trend in Fig. 14. This further validates the conclusion drawn already that higher temperature leads to higher thermal stress during DPF regeneration. Therefore, for DPFs with the same filtration volume, smaller channel width and porous wall thickness result in lower values in the rate of increase in pressure drop, peak temperature, and maximum thermal stress. In practice, however, small channel width and porous wall thickness is limited by manufacturing capability.

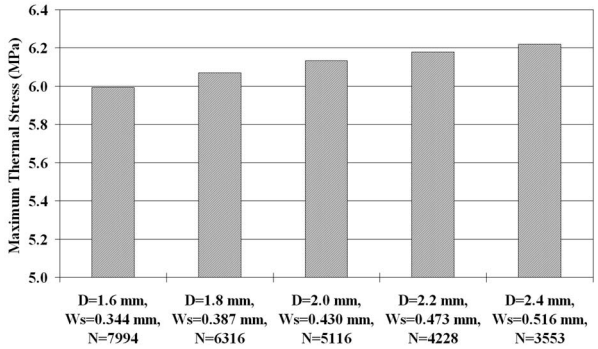


Fig. 15 Maximum compressive thermal stress during regeneration for five different DPF geometries with constant filtration volume

4.2 Constant Cell Density. In this study, the DPF length L, DPF diameter D_t, and inlet channel number N are kept constant while channel width D and porous wall thickness W_s varies to keep the cell density constant. In order to keep the cell density constant, the following relation should be satisfied

$$(D+W_s)=\text{const}$$

The pressure drops versus time for five different geometries during loading are plotted in Fig. 16. It is found that the DPF with larger channel width D and smaller porous wall thickness W_s leads to a smaller initial pressure drop and rate of increase. According to Darcy's law, the pressure drop across the porous wall is directly proportional to the mean wall velocity and wall thickness. The DPF with larger channel width has greater surface area for each channel, which results in smaller mean wall velocity. Larger channel width implies smaller porous wall thickness. Both of these two factors contribute to a low pressure drop. The temperatures versus time during regeneration are plotted in Fig. 17. It can be seen that the peak temperature for DPF with larger channel

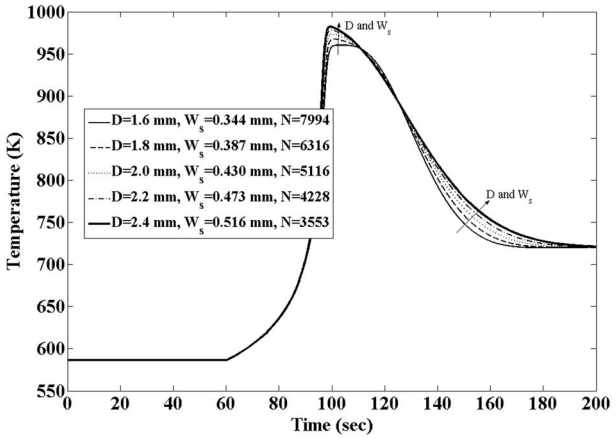


Fig. 14 Porous wall temperatures during regeneration for five different DPF geometries with constant filtration volume

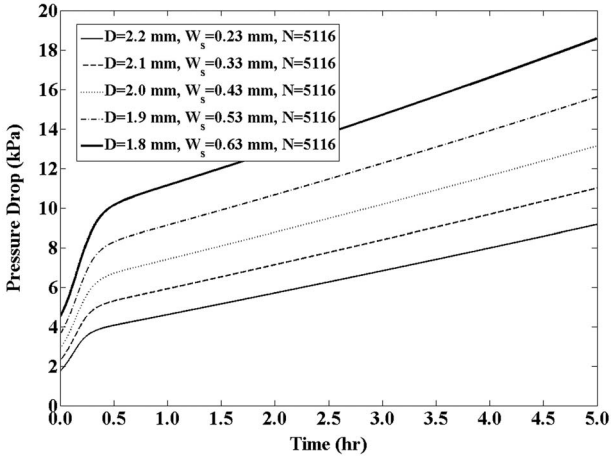


Fig. 16 Pressure drops during particulate loading for five different DPF geometries with constant cell density

Downloaded 02 Jun 2010 to 171.66.16.109. Redistribution subject to ASME license or copyright; see http://www.asme.org/terms/Terms_Use.cfm

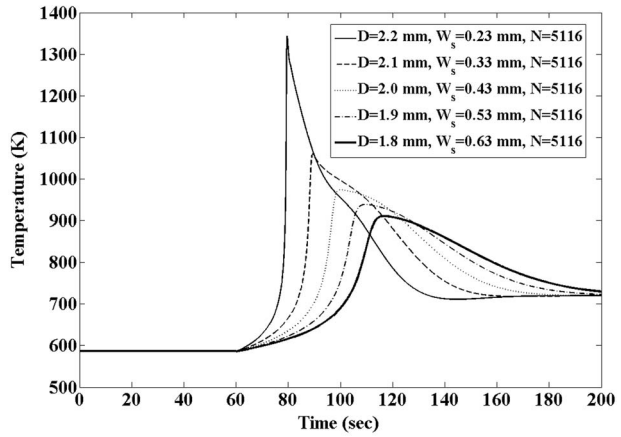


Fig. 17 Porous wall temperatures during regeneration for five different DPF geometries with constant cell density

width can reach more than 1300 K. This can be explained as follows. As the channel width increases, the porous wall thickness decreases. This results in a decrease in total thermal mass of the DPF. Since the particulate masses, therefore energy released, are constant for these five cases, low thermal mass leads to high temperature of DPF. Since the maximum compressive thermal stress is closely related to the maximum temperature during regeneration, the DPF with thinner wall thickness shows higher thermal stress, as shown in Fig. 18. In practice, the channel width and porous wall thickness have to be compromised to provide reasonable pressure drop, peak regeneration temperature, and thermal stress.

5 Conclusion

A 3D linear elastic isotropic finite element model has been developed to predict thermal stress in porous wall during DPF regeneration. The model has been validated by commercial software ANSYS with a uniform temperature field and a small aspect ratio. The main conclusions from this study can be summarized as below:

1. The peak temperature has more significant effects on thermal stress in DPF than peak temperature gradient during regeneration. The maximum compressive thermal stress always appears at the channel corner located towards the end of DPF, where the maximum temperature occurs.
2. As compared to SiC DPF, cordierite DPF is less prone to failure due to cracking induced by thermal stresses.
3. The maximum compressive stress varies very much linearly with initial soot loading. Interpolation and extrapolation in obtaining maximum thermal stress under different initial soot loadings are acceptable when DPF geometry and regeneration strategy are kept unchanged.
4. Parametric studies have been conducted to investigate the effects of DPF geometry on its performance using this numerical model. (a) When the filtration volume is kept constant, the DPF with smaller channel width results in lower values in pressure drop, peak temperature, and maximum thermal stress. However, the DPF with smaller channel width leads to higher initial pressure drop and more frequent regeneration. (b) Under the condition of constant cell density, the DPF with larger channel width leads to smaller pressure drop but much higher peak temperature and thermal stress. By considering these effects, this model, together with previous work [11], can be good DPF design tools to find the best balance for DPF performance.

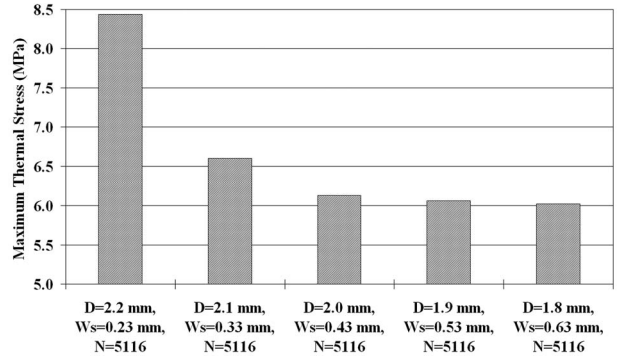


Fig. 18 Maximum compressive thermal stress during regeneration for five different DPF geometries with constant cell density

Nomenclature

Roman

A = pre-exponential factor
D = channel width
D_t = DPF diameter
$[D]$ = symmetric material matrix
E = Young's modulus
E_{act} = activation energy
$\boldsymbol{F}$ = global force vector
H = dimension of computational domain
H_{reac} = enthalpy of formation
$[K]$ = global stiffness matrix
L = DPF length
N = number of inlet channels
$[O_2]$ = oxygen mass concentration
$\boldsymbol{Q}$ = displacement vector
R_u = universal gas constant
T = temperature
W = thickness
m = mass
u,v,w = components of velocity
$\underline{u},\underline{v},\underline{w}$ = components of displacement
x,y,z = coordinates in Cartesian system

Greek

α = linear thermal expansion coefficient
β_0 = porosity of clean porous wall
$\boldsymbol{\varepsilon}$ = strain vector
λ = thermal conductivity
ρ = density
$\boldsymbol{\sigma}$ = stress vector
σ_c = compressive strength
ν = Poisson's ratio

Subscripts

c = catalytic particulate oxidation
f = exhaust gas
i = inlet channel
np = nonporous material
o = outlet channel
p = particulate matter
po = porous material
s = porous wall
t = thermal particulate oxidation

References

[1] Lamon, J., and Pherson, D., 1991, "Thermal Stress Failure of Ceramics under Repeated Rapid Heatings," J. Am. Ceram. Soc., **74**, pp. 1188–1196.
[2] Bissett, E. J., 1984, "Mathematical Model of the Thermal Regeneration of a

Downloaded 02 Jun 2010 to 171.66.16.109. Redistribution subject to ASME license or copyright; see http://www.asme.org/terms/Terms_Use.cfm

Wall-Flow Monolith Diesel Particulate Filter," Chem. Eng. Sci., **39**, pp. 1233–1244.
[3] Bissett, E. J., and Shadman, F., 1985, "Thermal Regeneration of Diesel Particulate Monolithic Filters," AIChE J., **31**, pp. 753–758.
[4] Bissett, E. J., 1985, "Thermal Regeneration of Particle Filters With Large Conduction," Math. Modell., **6**, pp. 1–18.
[5] Konstandopoulos, A. G., and Johnson, J. H., 1989, "Wall-Flow Diesel Particulate Filter-Their Pressure Drop and Collection Efficiency," SAE Trans., **98**, pp. 625–647.
[6] Konstandopoulos, A. G., "Flow Resistance Descriptors for Diesel Particulate Filters: Definitions, Measurements and Testing," SAE Paper No. 2003-01-0846.
[7] Opris, C. N., and Johnson, J. H., 1998, "A 2-D Computational Model Describing the Flow and Filtration Characteristics of a Ceramic Diesel Particulate Trap," SAE Paper No. 980545.
[8] Opris, C. N., and Johnson, J. H., 1998, "A 2-D Computational Model Describing the Heat Transfer, Reaction Kinetics and Regeneration Characteristics of A Ceramic Diesel Particulate Trap," SAE Trans., **107**, pp. 537–544.
[9] Haralampous, O. A., and Koltsakis, G. C., 2004, "Oxygen Diffusion Modeling in Diesel Particulate Filter Regeneration," AIChE J., **50**, pp. 2008–2019.
[10] Haralampous, O. A., and Koltsakis, G. C., 2004, "Back-Diffusion Modeling of NO_2 in Catalyzed Diesel Particulate Filters," Ind. Eng. Chem. Res., **43**, pp. 875–883.
[11] Guo, Z., and Zhang, Z., 2007, "Hybrid Modeling and Simulation of Multidimensional Processes for Diesel Particulate Filter During Loading and Regeneration," Numer. Heat Transfer, Part A, **51**, pp. 519–539.
[12] Suresh, A., Khan, A., and Johnson, J. H., 2000, "An Experimental and Modeling Study of Cordierite Traps-Pressure Drop and Permeability of Clean and Particulate Loaded Traps," SAE Paper No. 2000-01-0476.
[13] Yezerets, A., Currier, N. W., and Eadler, H. A., 2003, "Experimental Determination of the Kinetics of Diesel Soot Oxidation by O_2-Modeling Consequences," SAE Trans., **112**, pp. 537–544.
[14] Hanamura, K., Suzuki, T., and Tanaka, T., 2003, "Visualization of Combustion Phenomena in Regeneration of Diesel Particulate Filter," SAE Trans., **112**, pp. 566–573.
[15] Haralampous, O. C., Koltsakis, G. C., and Samaras, Z. C., 2003, "Partial Regeneration in Diesel Particulate Filters," SAE Paper No. 2003-01-1881.
[16] Konstandopoulos, A. G., Kostoglou, M., Housiada, P., Vlachos, N., and Zarvalis, D., 2003, "Multichannel Simulation of Soot Oxidation in Diesel Particulate Filters," SAE Trans., **112**, pp. 587–604.
[17] Pontikakis, G., and Stamatelos, A., 2006, "Three-Dimensional Catalytic Regeneration Modeling of SiC Diesel Particulate Filters," J. Eng. Gas Turbines Power, **128**, pp. 421–433.
[18] Aris, R., 1979, "De Exemblo Simulacrorum Continuorum Discritalumque," Arch. Ration. Mech. Anal., **70**, pp. 203–209.
[19] Kuki, T., Miyairi, Y., Kasai, Y., Miyazaki, M., and Miwa, S., 2004, "Study on Reliability of Wall-Flow Type Diesel Particulate Filter," SAE Paper No. 2004-01-0959.
[20] Rao, S. S., 2005, *The Finite Element Method in Engineering*, 4th ed., Elsevier Butterworth-Heinemann, Boston, MA.
[21] Hashin, Z., 1983, "Analysis of Composite-Materials—A Survey," ASME J. Appl. Mech., **50**, pp. 481–505.
[22] Roberts, A. P., and Garboczi, E. J., 2000, "Elastic Properties of Model Porous Ceramics," J. Am. Ceram. Soc., **83**, pp. 3041–3048.
[23] Coble, R. L., and Kingery, W. D., 1956, "Effect of Porosity on Physical Properties of Sintered Alumina," J. Am. Ceram. Soc., **39**, pp. 377–385.

Downloaded 02 Jun 2010 to 171.66.16.109. Redistribution subject to ASME license or copyright; see http://www.asme.org/terms/Terms_Use.cfm

Tian Guohong
State Key Laboratory of Automotive Safety and Energy,
Tsinghua University,
Beijing 100084, China;
University of Birmingham,
Edgbaston, Birmingham B15 2TT, UK
e-mail: g.tian@bham.ac.uk

Wang Zhi

Wang Jianxin
e-mail: wangjx@tsinghua.edu.cn

State Key Laboratory of Automotive Safety and Energy,
Tsinghua University,
Beijing 100084, China

Hongming Xu
University of Birmingham,
Edgbaston, Birmingham B15 2TT, UK

Shuai Shijin
State Key Laboratory of Automotive Safety and Energy,
Tsinghua University,
Beijing 100084, China

Effects of Key Factors on the Engine Combustion Mode Switching Between HCCI and SI

A technical strategy for a rapid and smooth switching between spark ignition (SI) mode and homogeneous charge compression ignition (HCCI) mode on a gasoline direct injection engine has been proposed and investigated, which involves an electrohydraulic two-stage cam profile mechanism and special injection strategies. The key factors that affect the HCCI/SI mode switching processes were analyzed on the basis of transient engine tests in terms of combustion parameters and exhaust emissions. It is shown that special care should be taken on the engine functionalities during the mode switching from SI to HCCI, which appears to be more difficult, and simultaneous control of the key parameters such as injection mass, injection timing, and spark timing is required. Various strategies and their general criteria for the mode switching were discussed. An optimized combination of selected control strategies has been demonstrated with a satisfactory switching process completed in ten engine cycles, without any abnormal combustion cycles in between. [DOI: 10.1115/1.2979003]

1 Introduction

Homogeneous charge compression ignition (HCCI) is a promising engine combustion concept with the advantages of high fuel economy and ultralow NO_x emissions. However, applications of this technology are limited by the size of its operating window and the difficulty of the control of auto-ignition timing for various engine speeds and loads. A hybrid combustion system, which combines spark ignition (SI) mode and HCCI mode in different operating regions, is regarded as a practical strategy for a new generation of gasoline direct injection engines. In middle-low load regions, HCCI mode can be used to replace the conventional SI mode, which is associated with high fuel consumption, while in high load and high speed regions the engine returns to the SI mode. Although the HCCI operating range is limited, the benefit of resultant fuel consumption reduction is widely considered attractive due to the ever increasing demand to reduce CO_2 emissions.

One major challenge for such a hybrid mode engine is the necessity to perform the mode switching between SI and HCCI. When combustion mode switching is required, engine functionalities have to be changed, because HCCI combustion must be enabled by certain methods such as intake heating, high compression ratio, or negative valve overlap (NVO). This implies that a mode switching mechanism must be set up and the engine in-cylinder process must be precisely controlled during the mode switching process in order to avoid misfiring or knocking.

The HCCI and SI mode switching can be realized by variable compression ratio (VCR) or fully variable valve timing (FVVT) systems. VCR, due to its slow response and difficulty to secure a precise control in its operation, was hardly used for the combustion mode switching [1]. FVVT was shown by several research groups [2,3] to be able to achieve desirable results, but the cost is very high, which limits its applications. As a compromise, a two-stage cam profile mechanism is considered a promising solution [4–6]. Because cam profile switching occurs within only one engine cycle, the control of combustion during this very short but rapid transient process will be critical for a smooth transition between HCCI and SI operating modes.

In the present study, an electrohydraulic two-stage cam profile mechanism was designed for a gasoline direct injection (GDI) engine, and the switching between the HCCI and SI combustion modes is enabled by switching the cam profile between the conventional positive and the special negative overlaps. Several key factors affecting the switching process were studied, and optimized strategies with general criteria for the mode switching control were proposed.

2 Experimental Setup

The experiments were carried out on a two-cylinder GDI engine with the specifications listed in Table 1.

The two-stage cam mechanism has two pairs of cam profile for different valve timings, with typical values given in Table 2. It can be switched from one cam profile to the other within one engine cycle. Figure 1 presents the basic mode switching strategy.

The injection system was controlled by a computing code programed in C language, which allowed three split injections per cycle. A high pressure swirl injector adopted by Mitsubishi was used and it operates with 5 MPa injection pressure. The spark ignition system was controlled by the Delphi PC-HUD system.

Contributed by the International Gas Turbine Institute (IGTI) of ASME for publication in the JOURNAL OF ENGINEERING FOR GAS TURBINES AND POWER. Manuscript received July 10, 2007; final manuscript received June 30, 2008; published online November 20, 2008. Review conducted by Christopher J. Rutland.

Copyright © 2009 by ASME

Downloaded 02 Jun 2010 to 171.66.16.109. Redistribution subject to ASME license or copyright; see http://www.asme.org/terms/Terms_Use.cfm

Table 1 Engine specifications

Type	Two-cylinder in-line, four-stroke, DI
No. of valves	two per cylinder
Bore	95 mm
Stroke	115 mm
Connecting rod	210 mm
Compression ratio	11.3
Throttle	WOT
Intake temperature	Ambient
Fuel	Gasoline (RON90)
Injector	High pressure swirl injector
Injection pressure	5 MPa
Intake port	Helical

The two-stage cam system was controlled by a high speed solenoid valve with a response time of 5 ms. The time delay of the valve action was compensated by the control system programming.

A Kistler 6125B pressure transducer with a Kistler 5011 charge amplifier was used to measure the in-cylinder pressure, and the data were acquired with a high speed data acquisition system. Air/fuel ratio was measured through exhausted gas by a NTK ABM-10 air/fuel booster. Gaseous exhaust emissions were measured by an AVL CEB-II exhaust gas analyzer.

The engine was started in SI mode until its coolant temperature reached 75°C, and the SI/HCCI mode switching was then carried out. Spark assistance was used throughout all the HCCI operation and the mode switching.

3 Test Results and Analysis

3.1 Switching Strategy and Time Scale Analysis. Several control parameters are varied during the mode switching process, and this involves injection strategy, cam profile, and throttle position. In the SI mode, the engine throttle is 5% open, with the cam profile having positive valve overlap. The split injection strategy is used with the main injection occurring in the intake stroke and the second injection in the compression stroke. The overall air/fuel ratio is higher than stoichiometric, but due to the stratified charge produced by the second injection, the mixture can be ignited [7]. In the HCCI mode, the cam is switched to the NVO profile and the throttle is wide open, whereas the injection strategy

Table 2 Cam profiles

	SI	HCCI
IVO/°CA BTDC	10	−56.4
IVC/°CA ABDC	50	34.8
EVO/°CA BBDC	56	39.8
EVC/°CA ATDC	10	−61.4

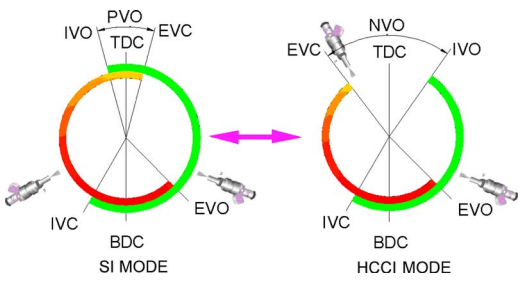


Fig. 1 Cam profiles for the HCCI and SI modes

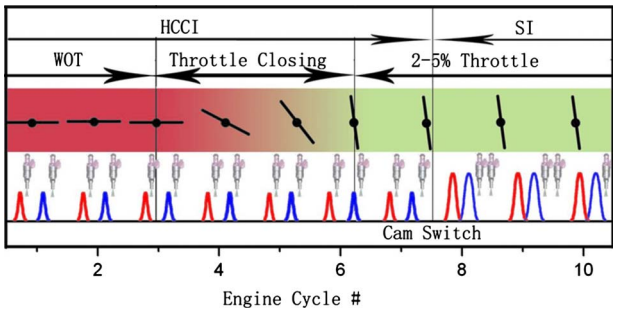


Fig. 2 SI/HCCI stepped switching

depends on the engine load condition [8].

The investigation on an electronically operated butterfly valve has shown that the transient response times for the throttle are as follows:

closed to WOT (i.e., opening), 120 ms(max)

WOT to closed (i.e., closing), 140 ms(max)

At the engine speed of 1500 rpm, for instance, the time required to complete one engine cycle is 80 ms. As the throttle position varies between 5% to fully open, the response time is slightly less than the above. The throttle operation time in terms of engine cycle at 1500 rpm will approximately be as follows:

SI to HCCI (i.e., opening), 1.25 engine cycles

HCCI to SI (i.e., closing), 1.5 engine cycles

For the two-stage cam profile mechanism, the limitation placed on the switching event is that it must occur when the valve lift is zero. Immediately after this point the new profile is then implemented. The time windows of cam profile switching from HCCI to SI or the other way around are the same. Corresponding to the cam profiles used in this experiment, the window for switching in one cycle is 250°CA. When the engine speed is under 4000 rpm, which is the highest for the HCCI operation region, the cam profile can be switched successfully and reliably within one cycle.

Clearly, in the three actions mentioned above concerning the mode switching process, the change of injection strategy can also be finished within one engine cycle, but the throttle has the slowest response and cannot move in a speed exceeding certain limits. Abnormal combustion may occur during the switching process if these parameters do not match well.

Therefore, a stepped switching strategy is put forward in the present study. The throttle movement is separated from the cam profile and injection strategy switching. When the cam profile and injection are being switched, at the start of the combustion mode switching, the throttle position remains unchanged initially. This may loose the benefit of high fuel economy of HCCI operation but gain the smoothness in the switching process. The schematic of stepped switching is shown in Fig. 2. More details about this stepped switching can be found in literature [4,9]

3.2 Mode Switching From HCCI to SI. During a stepped switching from HCCI to SI, the throttle position was kept at 5% opening. Engine speed was kept constantly at 1000 rpm and IMEP was maintained at about 0.3 MPa. The switching process recorded in the experiment is presented in Fig. 3, and the pressure traces during the switching are shown in Fig. 4.

Before the switching, HCCI combustion was stable with the NVO cam profile and a single fuel injection at 100°CA ATDC in the intake stroke. After the switching, the air/fuel ratio increased because the cam lift is higher, which results in a higher airflow rate. The injection was then switched into a two-stage injection strategy, one in the intake stroke with 3/4 of the total fuel mass for the cycle and the other in the compression stroke with 1/4 of the

Downloaded 02 Jun 2010 to 171.66.16.109. Redistribution subject to ASME license or copyright; see http://www.asme.org/terms/Terms_Use.cfm

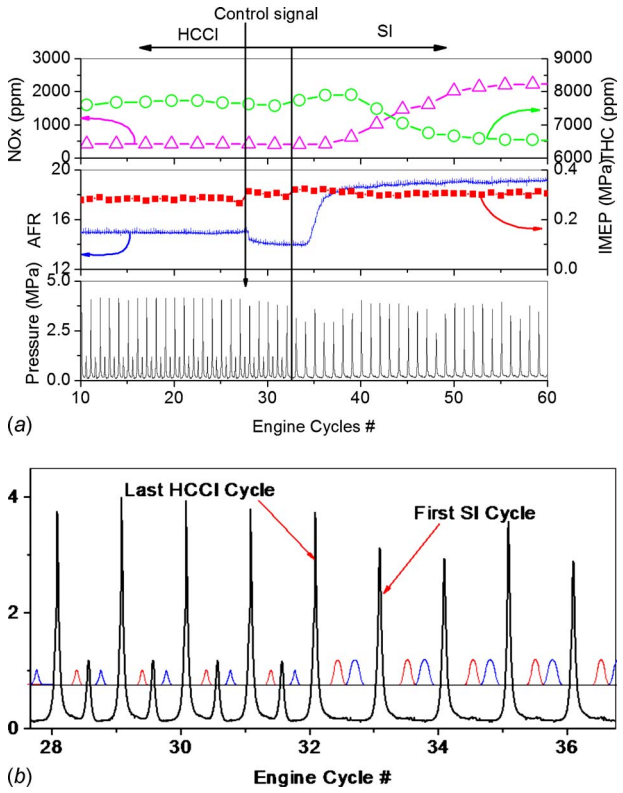


Fig. 3 Mode switching from HCCI to SI

fuel mass. The split injection generated a rich zone near the spark plug and ensured a stable SI combustion process, while the IMEP was unchanged. The pressure traces of the last five HCCI cycles before switching were noticeable. The injection strategy switching was instant but the cam switching was delayed approximately 400 ms due to the need to establish the oil pressure to trigger the cam switching mechanism. Therefore when the switching control signals were sent from the controller to the concerned engine actuator, the injection strategy was changed, but the valves were still operating with the HCCI cam profiles. It was a little surprising that the combustion remained stable and only the THC emission increased slightly. However, this delay did not affect the mode switching process.

The pressure traces and heat release rated in Fig. 4 provide the detail of the switching process for analysis. Before the switching, the HCCI combustion was stable with a high pressure raise rate and peak pressure, and the combustion duration was short. After the switching, the heat release rate was lower, and the peak pressure and pressure raise rate decreased, which indicates the typical

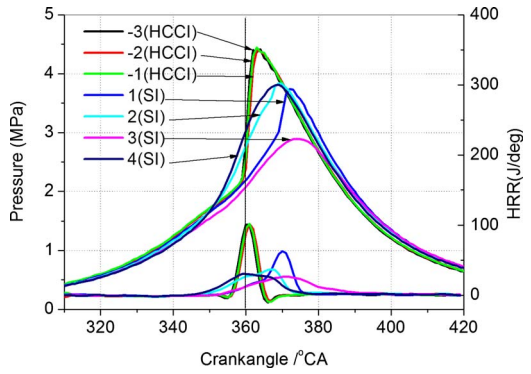


Fig. 4 Pressure trace from HCCI to SI

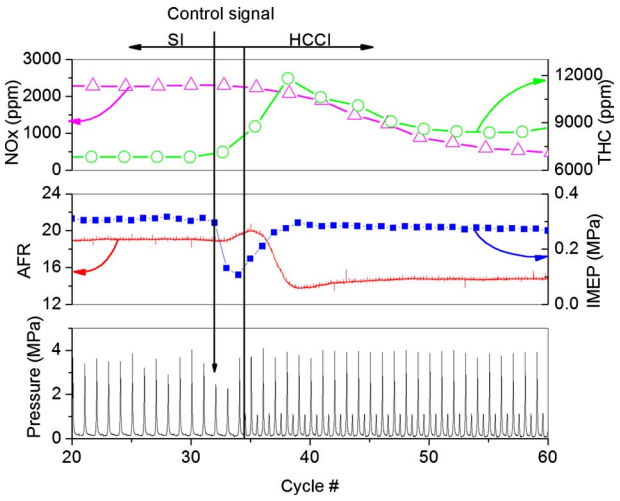


Fig. 5 Failed switching from SI to HCCI

SI combustion. In the SI mode, the spark controls the ignition timing from a single point. The combustion development depends largely on the mixture property and distribution around the spark plug when the spark occurs. This explains the higher cycle-by-cycle variations of the SI combustion than the HCCI case. Nevertheless, the transition from HCCI to SI seems to be straightforward and there is no obvious instability involved in the switching process.

3.3 Mode Switching From SI to HCCI. The mode switching from SI to HCCI is investigated at the same operation point and the process is shown in Fig. 5. Totally different from the case of switching from HCCI to SI, the last two SI cycles combustion failed during the process. As mentioned before, releasing the oil pressure of the cam switching mechanism takes approximately 150 ms time, which corresponds to about two engine cycles, and thus a desynchronized switching for the cam profiles and injection has occurred. This did not cause any serious failure during the HCCI-SI switching; however, in the reversed process, it does result in a problem. In the last two SI cycles, the injection was already switched to the HCCI strategy, while the valve operation still remained on the SI profile. Because there was no ignitable mixture around the spark plug, flame failed to propagate. The failure of the last two SI cycles caused an obvious peak of THC emissions, and the IMEP dropped sharply during the switching. Although the combustion mode was at last switched into the HCCI mode after several cycles, this is still considered an undesirable switching because of the penalty in engine operation stability and emissions.

By retarding the injection switching command, the cam switching and injection switching can be synchronized. However, it was found that a switching as such was also not satisfactory, as shown in Fig. 6 with the pressure traces and heat release rate of six cycles after the switching. The injection strategy consists of a main injection in the intake stroke for 80% of the total fuel mass for the cycle and a second injection in the NVO period for 20% of the fuel mass. The purpose of NVO injection is to generate radicals, which enhance the ignitability of the mixture [8]. The experimental data show that the first HCCI cycle had a very advanced combustion with a very high peak pressure and a pressure rise rate. This can be explained by the fact that because the combustion temperature of the SI combustion is higher than that of the HCCI combustion, the temperatures of the trapped EGR by NVO for the first HCCI cycle are higher than the normal HCCI combustion. The fuel injected in the NVO period was mixed and burned with the high temperature EGR, illustrated on the expanded figure on the top right corner, Fig. 6. The heat release in the NVO period

Downloaded 02 Jun 2010 to 171.66.16.109. Redistribution subject to ASME license or copyright; see http://www.asme.org/terms/Terms_Use.cfm

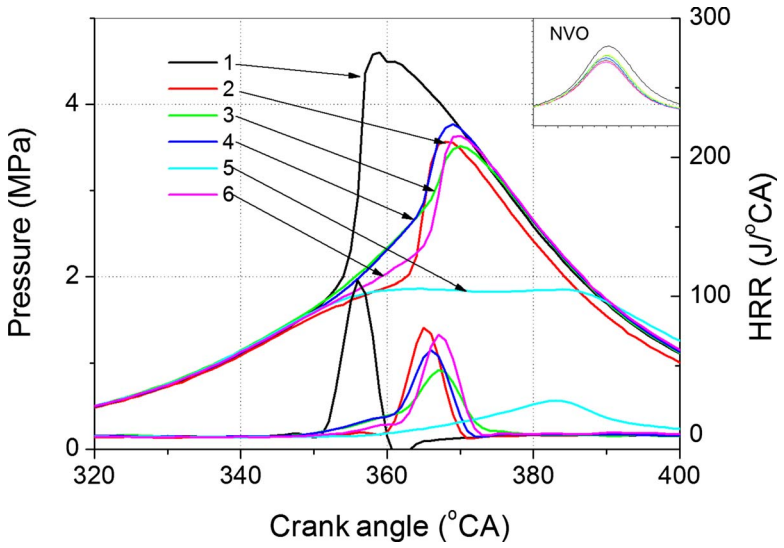


Fig. 6 SI to HCCI switching without optimization

caused the in-cylinder temperature to increase and led to an advanced and violent combustion cycle before the TDC. Impacted by the very abnormal first HCCI cycle, the following several cycles of combustion fluctuated, with one cycle nearly misfired. This result indicates that the switching from SI to HCCI is much more difficult than the reversed process. The reason is that after switching, there is no direct combustion trigger, and the development of the in-cylinder process is mainly in the hand of charge conditions, including temperature, mixture concentration, and species, which is difficult to control during an extremely dynamic period. Clearly, the switching process from SI to HCCI has to be optimized very carefully, and the first HCCI cycle is the key step for the optimization.

3.4 Optimization of Switching From SI to HCCI. For the first HCCI cycle that has to be optimized in the switching from SI, optimization parameters include injection mass, injection timing, and spark timing. The optimizing objectives are (1) relatively late combustion, (2) low peak pressure, (3) low pressure rise rate, and (4) low IMEP fluctuations.

Based on the earlier analysis, it appears that although the NVO injection enhances the HCCI combustion stability, it may not be suitable for the first HCCI cycle during mode switching. Therefore, the injection strategy of one-stage injection is adopted for the first HCCI cycle, instead of the two-stage injection used for normal HCCI combustion.

To achieve lower peak pressure while keeping the IMEP constant in the first HCCI cycle, varied injection quantities, from 60% to 110% of the normal injection mass, have been tested and the experimental results are presented in Fig. 7. With all the different injection quantities tested, the mode switching has been successful and the engine behaved as follows. The IMEP decreased in the first HCCI cycle, but recovered soon after a few cycles. The air/

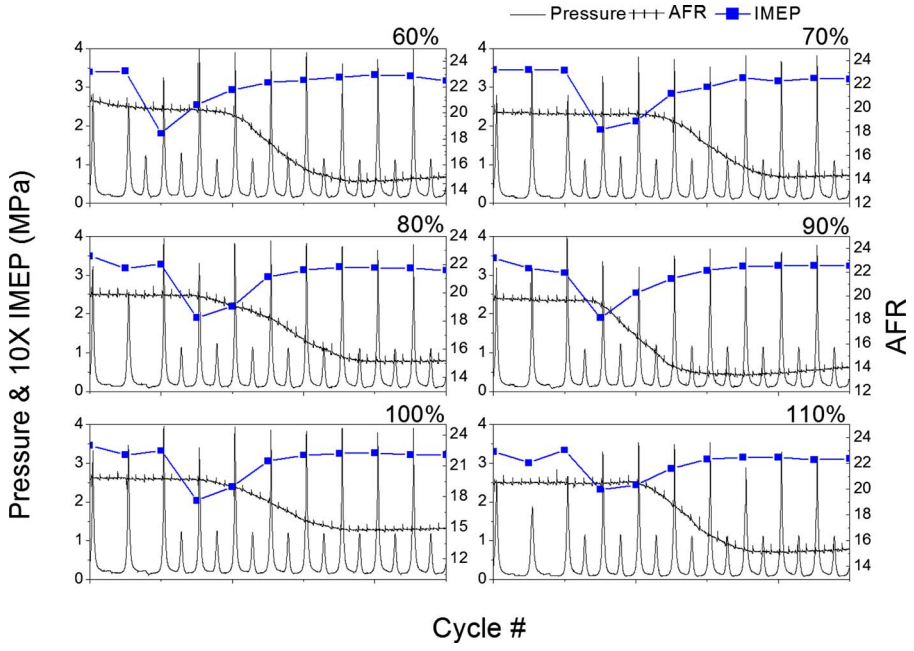


Fig. 7 SI to HCCI switching with different injection masses

Downloaded 02 Jun 2010 to 171.66.16.109. Redistribution subject to ASME license or copyright; see http://www.asme.org/terms/Terms_Use.cfm

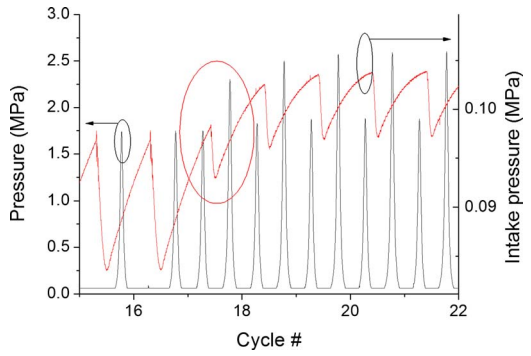


Fig. 8 Intake pressure trace of SI to HCCI switching

fuel ratio decreased after the switching from the SI mode to the HCCI mode, apparently because the valve timing of the HCCI mode has reduced the intake air mass while the throttle position was unchanged. The dip of the IMEP for the first HCCI cycle cannot be prevented by increasing the fuel injection mass. The AFR value decreased to lower than 14.5 and then slightly recovered when the first cycle injection mass was higher than 90% of the normal mass. The reasons for the decrease in the IMEP in the first two HCCI cycles need some explanation, although the effect of the decrease in the engine torque output will be negligible.

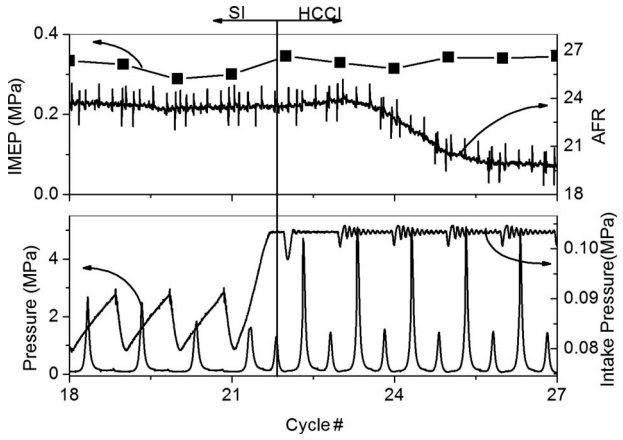


Fig. 9 SI to HCCI switching with synchronized throttle opening

The intake manifold pressure trace along with the inclined pressure trace in Fig. 8 seems to give some explanation to the IMEP dip in the first HCCI cycle. When the throttle is partially opened during the early stage of the transition, the vacuum level in the intake pipe was higher for the SI mode due to a less restriction of the flow rate through the intake valves with the SI cam profile, and therefore the peak pressure in the intake manifold was lower than that in a normal HCCI mode operation. When the cam was switched to the HCCI profile, while the intake manifold pressure was the same as that of the SI mode when the intake valve was opened (see the marked area in Fig. 8), the valve open duration was, however, shorter, which made the intake mass of the first HCCI cycle lower than normally required. This reduced airflow in the first cycle after switching has limited the maximum output of the HCCI cycle with the stoichiometric air-fuel ratio and thus cannot be compensated by simply increasing the fuel mass during the transition. In the subsequent tests, the injection mass for the first HCCI cycle was set to 80% of the normal quantity.

Alternatively, opening the throttle synchronized with the mode switching has been tested a number of times and demonstrated to be promising to correct this problem, as shown in Fig. 9. During the tests, the throttle was opened right after the last SI cycle, indicated by the intake pressure trace. From the first HCCI cycle, the peak pressure in the intake manifold was thus much higher than that for the SI mode, in contrast with the result obtained with the fixed throttle position associated with Fig. 7. The IMEP displayed a much improved curve during the whole switching process and the sharp dip was eliminated. Clearly an electronic throttle is necessary for the synchronization control.

The injection timing strategy for the first HCCI cycle during

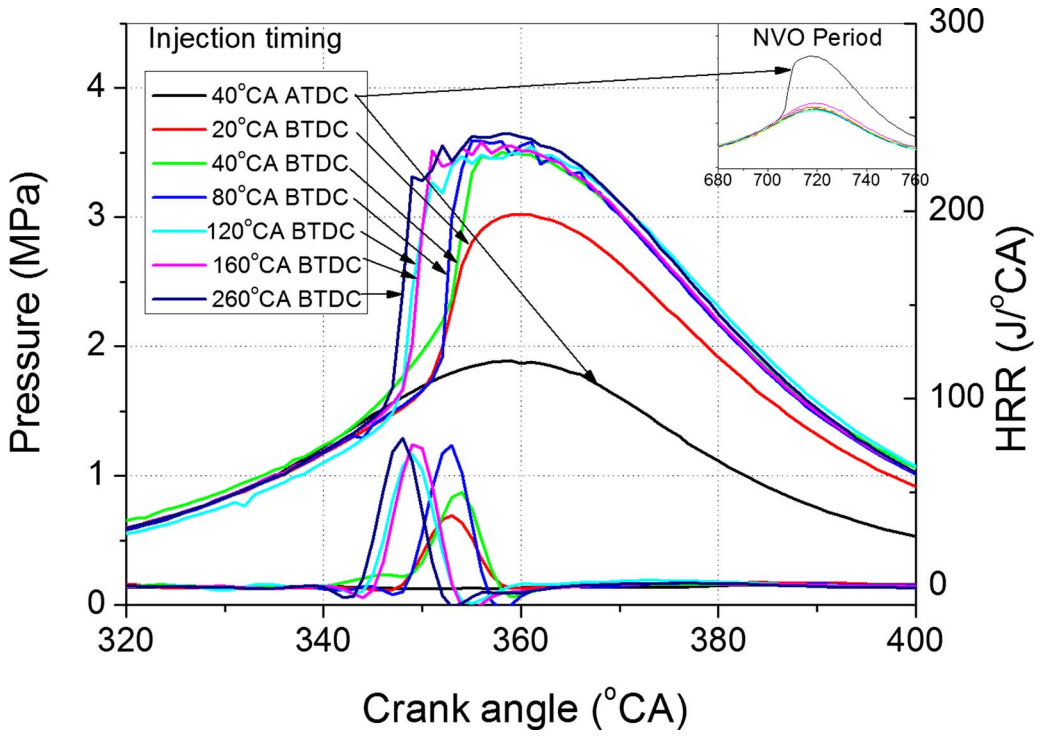


Fig. 10 Pressure traces of the first HCCI cycle for different injection timings

Downloaded 02 Jun 2010 to 171.66.16.109. Redistribution subject to ASME license or copyright; see http://www.asme.org/terms/Terms_Use.cfm

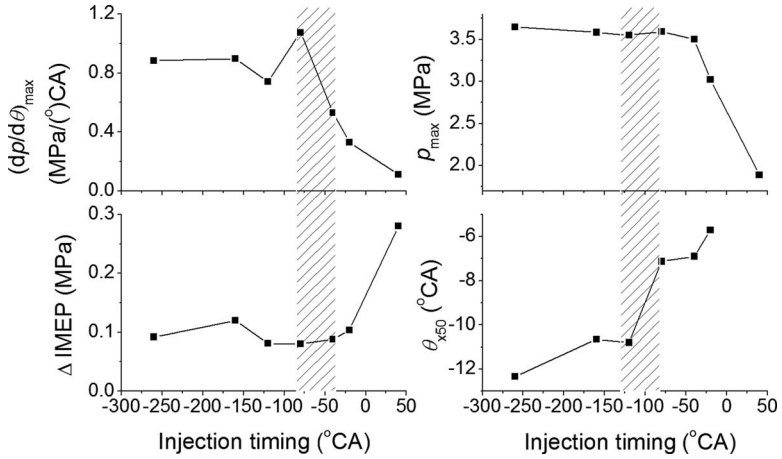


Fig. 11 Combustion properties of the first HCCI cycle for varied injection timing

mode switching has also been investigated and the test result presented in Fig. 10 is on the same operation point discussed above. The injection mass for the first HCCI cycle was 80% of the normal as explained earlier and the injection timing was varied between 260°CA BTDC and 40°CA ATDC. The pressure traces and heat release rates of the first HCCI cycle for different injection timings, Fig. 10, show that the combustion phasing was retarded with the retarded injection timing. When the injection took place after TDC, which was too late, the engine misfired and prolonged in-cylinder chemical reactions resulted in the heat release of the unburned mixture during the recompression process in the NVO period, shown by the top right corner of the figure. This very late injection should be avoided during the mode switching.

As mentioned earlier, the preferred first HCCI cycle during the mode switching should have a relatively late combustion, lower peak pressure, lower pressure raise rate, and minimized IMEP perturbation. The combustion properties with the varied injection timing investigated are shown in Fig. 11, where CA50 (the timing of the 50% burned mass) is used to indicate the combustion phasing. It was found that the switching result varies each time as it is an extremely dynamic process, perhaps as expected. However, there is a clear trend presented by the typical data in Fig. 11. The pressure rise rate decreased with retarded injection. The mostly affected parameter is CA50, which retarded sensitively with late injection until the misfire occurred with the injection at 40°CA ATDC. For the optimization goal, the preferable injection timing appears to be between 80°CA BTDC and 40°CA BTDC, marked with the shaded areas.

Spark timing is another interesting parameter for the mode switching process, which should be investigated. Several research groups have published recently about spark assisted HCCI [10,11] and it is shown that spark has influence on the HCCI combustion. Because spark plays a key role in controlling SI combustion phasing whereas the first HCCI cycle is affected significantly by trapped EGR and wall temperature, spark timing is expected to be effective in assisting the mode switching process.

The switching processes with varied spark timing from 27°CA BTDC to 10°CA BTDC are presented in Fig. 12. For each switching process, spark timing was kept constant and the operation point was the same as before. In the SI mode, an overearly spark ignition or overlate spark ignition timing will lead to knocking or unstable combustion, respectively. Since the same spark timing is used for both of the combustion modes, an optimized setting should be found. When the spark was too early such as 30°CA BTDC in Fig. 12, combustion was unstable with knocking and misfiring alternately. With the spark timing between 27°CA BTDC and 17°CA BTDC, the SI mode combustion was stable. Further retarding the spark timing made the SI combustion unstable again, with misfiring occasionally and larger combustion variability. However, irrespective of the situation in the SI combustion, when the mode was switched, the combustion was always able to switch into the HCCI mode successfully without any misfiring. The continuous pressure traces show that there was no obvious difference in the switching process with different spark timings. Taking both of the combustion modes into consideration, the switching process was acceptable when the spark timing was between 27°CA BTDC and 17°CA BTDC.

The mechanism of the effect of spark on the switching process needs to be discussed further. The influence can be separated into two parts: one is on the HCCI combustion and the other is on the SI combustion, which then in turn affect the first HCCI cycle by trapped EGR.

Generally speaking, spark timing does affect the HCCI combustion slightly [11] and the present study confirms that combustion phase can be retarded by retarded spark timing. The influence of spark timing on stable HCCI combustion is shown in Fig. 13. Since it was a dynamic process, the eighth HCCI cycle was regarded as settled and stable combustion in new balance. The corresponding heat release rate was higher and the combustion duration was shorter. However, the effect is not significant, and, in fact, for certain engine conditions, the spark timings may almost have no influence on combustion. Figure 13 indicates that when the spark timing was earlier than −17°CA, there was an obvious triggering effect. The combustion phase was later than −17°CA, with the case for an ignition later than −10°CA. This means the spark at this time had little influence on combustion in this case. Although the spark timing varied by 20°CA for these seven cases, the difference in the combustion starting position was less than 5°CA.

Unexpectedly, the influence of spark timing on the first HCCI cycle was insignificant, which can be seen from Fig. 14. With the spark timing varied by 20°CA, the combustion phase of the first HCCI cycle was changed by less than 5°CA too. Compared with the eighth HCCI cycle presented in Fig. 13, all the first cycles with varied spark timing have advanced ignition. However, comparing all the first HCCI cycles with different spark timings, the combustion phase difference between them is negligible. The investigated spark timing had no significant effect on the SI-HCCI mode switching.

HCCI combustion is affected by the previous cycle through the trapped EGR and wall temperature. This implies that based on the in-cylinder condition of the present cycle, it is possible to predict the next cycle if a well established simulation model is made available. The test results presented earlier have shown that spark

Downloaded 02 Jun 2010 to 171.66.16.109. Redistribution subject to ASME license or copyright; see http://www.asme.org/terms/Terms_Use.cfm

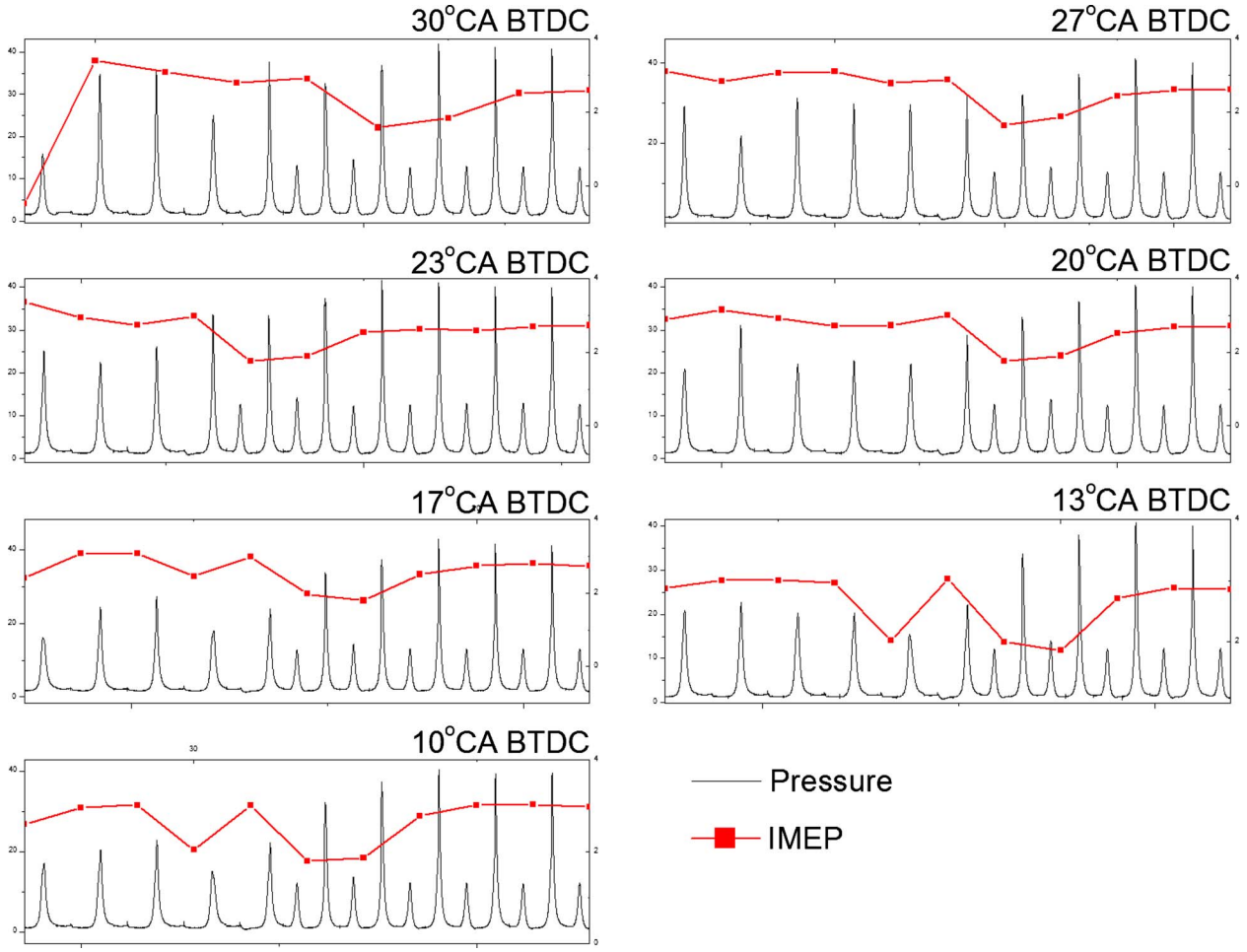


Fig. 12 Switching process for different spark timings

timing influences the last SI cycle significantly but has no obvious effect on the first HCCI cycle. Figure 15 presents the exhaust temperature and NO_x emissions as functions of ignition timing, both of which have a promotion effect on the HCCI combustion [12]. With higher exhaust temperature, the trapped EGR was hotter, which would accelerate the first HCCI cycle combustion. NO_x also has a speedup effect on self-ignition, thus the higher concentration of NO_x would accelerate the first HCCI cycle too. It can be seen from Fig. 15 that with retarded spark timing, NO_x emissions decreased, but exhaust temperature increased due to later combustion. The reversed trends of the two parameters offset their influences on the HCCI combustion. This may partially explain why spark timing has no obvious effect on the first HCCI cycle. Furthermore, as long as misfiring does not occur in the last SI cycle, the combustion mode will always be successfully switched into HCCI, as shown in Fig. 12.

Special care needs to be taken when considering the spark timing at −30°CA ATDC. Both the exhaust temperature and NO_x emissions are low, but the combustion phase of the first HCCI cycle was the most advanced. The reason is that the SI combustion cycles with this spark timing were not stable, with misfiring and knocking alternately. The NO_x emission level is an averaged value for 10 s, but in some knocking cycles, the NO_x emission level is expected to be high. Therefore, when the SI combustion is

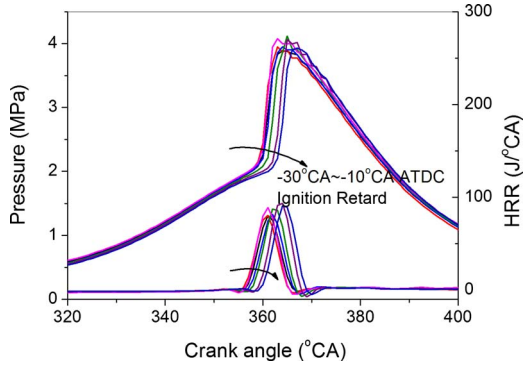


Fig. 13 The eighth HCCI cycle after switching with different spark timings

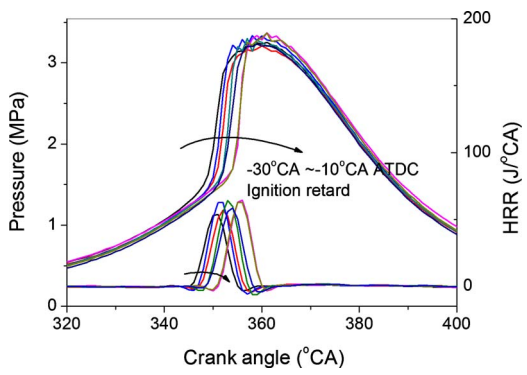


Fig. 14 The first HCCI cycle for different spark timings

Downloaded 02 Jun 2010 to 171.66.16.109. Redistribution subject to ASME license or copyright; see http://www.asme.org/terms/Terms_Use.cfm

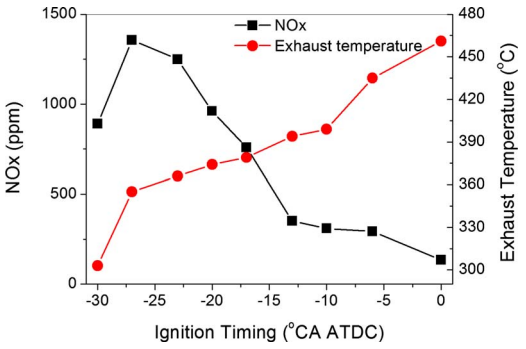


Fig. 15 NO_x and exhaust temperature with different spark timings

unstable the mode switching process depends strongly on the last SI cycle before switching and the process can be highly stochastic with little regularity.

At the same time, spark timing during the mode switching process should first meet the demand of the SI combustion. Because the changing trends of exhaust temperature and NO_x emissions are opposite, the influence of the two factors was partly offset. For this research engine, spark timing between −17°CA ATDC and −23°CA ATDC has been shown to lead to satisfactory effect.

3.5 Mode Switching Control Criteria. Based on the experimental results discussed above, some control criteria have been proposed as follows.

1. *SI mode priority criteria*. As the test results show, if the switching processes of fuel injection and gas flow are not synchronized in the SI mode, misfiring will occur; however, if the problem is in the HCCI mode, no abnormal combustion cycle will appear. Lean burn SI mode combustion is even more sensitive to the mixture distribution than the HCCI mode. It depends strongly on the rich mixture near the spark plug when sparking. Once the concentration is not robust for spark ignition, misfiring will occur. HCCI combustion does not depend on one point situation at desired ignition time, and thus if only part of the mixture reaches the desired condition, compression ignition will still proceed. From this point of view, a less homogeneous charge is easier to be ignited, and the randomness in HCCI combustion development is lower than the SI combustion. Therefore, when combustion mode is switched, the SI mode should be ensured by a correct mixture distribution first. The adjustment actions that influence the combustion stability should be taken in the HCCI mode.
2. *Intake flow rate priority criteria*. Intake flow rate is controlled by the throttle position. In the mode switching process toward either direction, the demand of the throttle position has to be met; otherwise, misfiring may occur.
3. *Injection and cam profile synchronization criteria*. The injection strategy and cam profile should be switched with synchronization. However, if this demand cannot be met somehow, criteria No. 1 must be taken.

4 Conclusions

SI/HCCI mode switching has been performed in both directions on a GDI-HCCI research engine using a two-stage cam profile mechanism. The factors that influence the mode switching process have been examined to optimize the process. The conclusions are as follows.

1. Mode switching from HCCI to SI is relatively straightforward, but the process in the opposite direction is more challenging and must be optimized. The optimization should be focused on the first HCCI cycle.
2. The NVO injection in the first HCCI cycle has to be reduced in quantity in order to avoid an advanced combustion.
3. The injection timing in the first HCCI cycle affects the switching process. Retarding the injection timing to a certain extent makes the switching smoother. The suitable injection timing for this research engine is −80°CA ATDC to −40°CA ATDC.
4. Spark timing has a little influence on the mode switching. According to the demand for both modes, the preferable spark timing range for this engine is −17°CA ATDC to −23°CA ATDC.
5. Based on the SI/HCCI switching results, general control criteria for the mode switching proposed above should be observed.

Acknowledgment

This research work is supported by the National Key Basic Research Plan ("973" Plan), under Grant No. 2007CB210005 and the National Natural Science Foundation projects, under Grant No. 50606019.

Nomenclature

AFR	=	air fuel ratio
ATDC	=	after top dead center
BTDC	=	before top dead center
CA	=	crank angle
EGR	=	exhaust gas recirculation
EVC	=	exhaust valve close
EVO	=	exhaust valve open
IMEP	=	indicated mean effective pressure
IVC	=	intake valve close
IVO	=	intake valve open
NO_x	=	nitrogen oxides
RON	=	research octane number
TDC	=	top dead center
THC	=	total hydrocarbon
WOT	=	wide open throttle
θ_{x50}	=	crank angle of 50% mass burned

References

[1] Hyvonen, J., 2005, "Operating Conditions Using Spark Assisted HCCI Combustion During Combustion Mode Transfer to SI in a Multi-Cylinder VCR-HCCI Engine," SAE Paper No. 2005-01-0109.
[2] Santoso, H., Matthews, J., and Cheng, W. K., 2005, "Managing SI/HCCI Dual-Mode Engine Operation," SAE Paper No. 2005-01-0162.
[3] Milovanovic, N., Blundell, D., and Gedge, S., 2005, "Cam Profile Switching and Phasing Strategy Versus Fully Variable Valve Train Strategy for Transitions Between Spark Ignition and Controlled Auto Ignition Modes," SAE Paper No. 2005-01-0776.
[4] Xu, H., Rudolph, S., and Liu, Z., 2004, "An Investigation Into the Operating Mode Transitions of a Homogeneous Charge Compression Ignition Engine Using EGR Trapping," SAE Paper No. 2004-01-1911.
[5] Herrmann, H.-O., Herweg, R., and Karl, G., 2005, "Regelungskonzepte in Ottomotoren Mit Homogen-Kompressionsgezündeter Verbrennung," Congress Haus der Technik, Controlled Auto Ignition, Essen, Oct.
[6] Fritz, D., 2007, "GM Moves Closer to Market With HCCI," Automot. Eng. Int., **2**, pp. 22–24.
[7] Yanjun, W., Xiaohu, L., Jianxin, W., Xiao-Hu, L., and Xin-Liang, A., 2005, "Study of Injection Strategies of Two-Stage Gasoline Direct Injection (TSGDI) Combustion System," SAE Paper No. 2005-01-0107.
[8] Guohong, T., Zhi, W., Jianxin, W., Shijin, S., and Xin-Liang, A., 2006, "HCCI Combustion Control by Injection Strategy with Negative Valve Overlap in a GDI Engine," SAE Paper No. 2006-01-0415.
[9] Tian, G., Wang, Z., Ge, Q., Wang, J., and Shuai, S., 2007, "Mode Switch of SI-HCCI Combustion on a GDI Engine," SAE Paper No. 2007-01-0195.
[10] Bunting, B. G., 2006, "Combustion, Control, and Fuel Effects in a Spark Assisted HCCI Engine Equipped with Variable Valve Timing," SAE Paper No. 2006-01-0872.
[11] Zhi, W., Jianxin, W., Shijin, S., and Guo-hong, T., 2006, "Study of Spark Ignition on Gasoline HCCI Combustion," Proc. Inst. Mech. Eng., Part D (J. Automob. Eng.), **220**(6), pp. 817–825.
[12] Risberg, P., Johansson, D., Andrae, J., Kalghatgi, G., Bjornbom, P., and Angstrom, H. E., 2006, "The Influence of NO on the Combustion Phasing in an HCCI Engine," SAE Paper No. 2006-01-0416.

Downloaded 02 Jun 2010 to 171.66.16.109. Redistribution subject to ASME license or copyright; see http://www.asme.org/terms/Terms_Use.cfm

Three-Dimensional Computational Fluid Simulation of Diesel and Dual Fuel Engine Combustion

Chengke Liu

G. A. Karim
e-mail: karim@ucalgary.ca

Department of Mechanical and Manufacturing Engineering,
University of Calgary,
2500 University Drive,
Northwest Calgary, AB, T2N 1N4, Canada

A 3D computational fluid dynamics model with a reduced detailed chemical kinetics of the combustion of diesel and methane fuels is developed while considering turbulence during combustion to simulate the mixture flow, formation, and combustion processes within diesel and diesel/methane dual fuel engines having swirl chambers. The combustion characteristics of the pilot injection into a small prechamber are also investigated. Modeled results were validated by a group of corresponding experimental data. The spatial and temporal distributions of the mixture temperature, pressure, and velocity under conditions with and without liquid fuel injection and combustion are compared. The effects of engine speed, injection timing, and the addition of carbon dioxide on the combustion process of dual fuel engines are investigated. It is found that in the absence of any fuel injection and combustion, the swirl center is initially formed at the bottom-left of the swirl chamber, and then moved up with continued compression in the top-right direction toward the highest point. The swirling motion within the swirl and main combustion chambers promotes the evaporation of the liquid pilot and the combustion processes of diesel and dual fuel engines. It was observed that an earlier autoignition can be obtained through injecting the pilot fuel into the small prechamber compared with the corresponding swirl chamber operation. It is to be shown that reduced engine emissions and improved thermal efficiency can be achieved by a two-stage homogenous charge compression ignition combustion. [DOI: 10.1115/1.2981175]

Keywords: dual fuel engine, swirl chamber, small prechamber, autoignition

1 Introduction

In order to satisfy the requirements of the ever stricter regulations for emissions all over the world, engines with swirl chambers have been widely used in transport and utility power applications due to their advantages of relatively low NO_x emissions, low noise, and good adaptability to changes in engine speed. However, to improve the specific fuel consumption and starting performance at low ambient temperature remain a challenge. Natural gas, which is considered to be a clean fuel, having the potential to produce lower CO_2 emission and higher thermal efficiency values than liquid fuels, is being widely used as an engine fuel to reduce NO_x emissions and particulates. It is found that for engines with cylinder bores of more than 150 mm, diesel/natural gas dual fuel engines with prechamber micropilot (PCMP) systems have the potential to combine high power density with low NO_x emissions and excellent efficiencies where stable and fast combustion can be achieved [1]. However, it remains a challenge to improve the performance and emissions of such smaller size engines.

With the continued development of computing power, multidimensional modeling has become an increasingly feasible and economical tool in engine design and development processes [2]. Good computer models may be used to achieve a better understanding of the combustion process within engines, finding effective measures to overcome operational problems, evaluating new design concepts, and reducing hardware prototype and development costs. Compared with the extensive research on the modeling of diesel engines, there are only a few references on the computational fluid dynamics (CFD) simulation of dual fuel engines. This is mainly due to the complexity of the combustion processes while most of these are related to direct injection dual fuel engines. The combustion modeling of dual fuel engines with a prechamber or swirl chamber tends to be at the initial stages of development due to the increased complexity of both the geometry of the combustion chamber and the combustion processes involved. Therefore, there is a need to develop a 3D-CFD modeling with detailed chemical kinetics to simulate comprehensively the combustion processes of this kind of engines.

In the present contribution, a 3D-CFD model developed with a reduced detailed chemical kinetics of diesel fuel and methane is described while considering the turbulence function to simulate the combustion processes of a diesel/methane dual fuel engine with a swirl chamber. The combustion characteristics of pilot injection into a small prechamber are also investigated.

2 The Engine

An existing diesel engine test facility was modified to render it suitable for the present investigation, and new data acquisition and control systems were developed. The three cylinder, 4 cycle diesel engine is water-cooled, normally aspirated, of indirect injection, and with inline swirl chamber type. The Isuzu 3KC1 engine, which has a compression ratio (CR) of 23:1, a 74 mm bore, and 76 mm stroke, was coupled with an electric dynamometer and could operate over the speed range of 800-3600 rpm. The engine when operating as a diesel at sea level had a declared maximum torque of 57.8 N m at 2000 rpm and a maximum power of 16.1 kW at 3000 rpm. The diesel fuel employed was of around 47

Contributed by the Internal Combustion Engine Division of ASME for publication in the JOURNAL OF ENGINEERING FOR GAS TURBINES AND POWER. Manuscript received February 19, 2008; final manuscript received July 25, 2008; published online November 20, 2008. Review conducted by Christopher J. Rutland. Paper presented at the 2007 Fall Conference of the ASME Internal Combustion Engine Division (ICEF2007), Charleston, SC, October 14–17, 2007.

Copyright © 2009 by ASME

Downloaded 02 Jun 2010 to 171.66.16.109. Redistribution subject to ASME license or copyright; see http://www.asme.org/terms/Terms_Use.cfm

cetane number injected at 12 before top dead center (BTDC) into the prechamber. Dual fuel engine operation was produced by introducing small metered amounts of methane into the intake system from compressed natural gas cylinders. The high-pressure methane supplied was metered by small size calibrated choked nozzles, and the air was metered by a calibrated laminar air flow meter. Mainly commercial methane of around 95% purity was used. In these tests, the engine speed was kept fixed so that a certain diesel fuel flow rate would be associated with essentially a fixed value of pilot diesel equivalence ratio (EQ).

The cylinder pressure was measured using a piezoelectric pressure transducer fitted into the glow plug aperture of one of the cylinders. The crank angle position signal was produced by an encoder and was fed to a computer to trigger the capture of the pressure data. Continuous analysis of the composition of the exhaust gases was also made.

3 The Model

CFD has been shown to be an effective tool for design as well as improved understanding of actual combustion systems behavior. There are a number of commercial CFD-three dimensional program packages available on the market, including KIVA, which has been widely used for engine simulations. The original version of the model employed only global type combustion reaction kinetics. It needs to be suitably modified to consider the homogenous charge compression ignition (HCCI) and the dual fuel combustion applications and to simulate more reliably the details of the important complex chemical processes leading to autoignition and subsequent combustion. To do this suitably reduced detailed chemical kinetics for the fuel systems, including hydrogen, *n*-heptane and diesel fuel were incorporated into the modified code. The solving of the comprehensive kinetic scheme reaction rates equations with the perfectly stirred reactor (PSR) assumption will show the changes in the concentrations of the different species over the time increment represented by the corresponding residence time. Such calculated changes are entirely kinetically based. The use of kinetics-controlled reaction rates usually results in very fast combustion rates [3]. The fuel, oxidizer, and intermediate products may not have enough time then to mix down to the molecular level in the actual engine environment. Also, the presence of combustion products with the air-fuel mixture may result in the reactions to be partly controlled by the breakup of turbulent eddies that can produce correspondingly slower reaction rates. Accordingly, both chemical kinetics and turbulence influence the course of the combustion processes in practical engines requiring suitable modeling of this interaction [4,5]. Therefore, a turbulence-chemistry combustion model, based on a partially stirred combustion model, was developed [5] and incorporated into the code.

A more realistic representation, which takes into account the additional contribution of turbulent mixing, considers that for a small incremental change in concentrations the corresponding time increment can be viewed to be made up of two segments: a chemical time increment on the basis of the perfectly stirred reactor assumption and a physical part due to the contribution of turbulent mixing effects.

To predict satisfactorily the changes in species concentrations during the course of a reaction, it is necessary to ensure that any finite time increment chosen during the solution is sufficiently small, and no species among the many in the reacting mixture displays an unrealistic overestimate of the change in its concentration. Accordingly, the solution procedure adopted during the course of combustion incorporated a method of selecting an appropriately small time increment that could not produce in any of the many reacting species a depletion in concentration that is in excess of the corresponding value at the beginning of the time increment. The instantaneous concentrations of all the species involved were examined at the end of a time increment and a species described as a "reference" identified, such that over the following time step its concentration may become depleted to a sufficiently negligible value without becoming negative. This following chemical time step was then modified by accounting for the associated physical turbulent mixing part. This way the identified reference species can vary over the course of the combustion process.

In addition to the general chemical kinetic equations included in KIVA3 [6,7], a modified formulation was employed that accounted for a partially stirred reactor approach according to the following form [5]:

$$\frac{\Delta c_m}{\Delta t} = \frac{c_m^k - c_m^0}{\tau} = \dot{\omega}_r(c_m^k)\frac{\tau_{\text{chem}}}{\tau_{\text{chem}} + \tau_{\text{mix}}} = \frac{c_s^0[\dot{\omega}]_{sr}^0}{c_s^0 + R_D^0 - [\dot{\omega}]_{sr}^0 \tau_{\text{mix}}} \quad (1)$$

where c_m^0 and c_m^k are the mean molar concentrations of any species m at the beginning and end of each computational reaction step, τ is the residence time scale (or the Lagrangian integration time step as used in KIVA3), and $\dot{\omega}_r(c_m^k)$ is the reaction rate of species m in terms of the PSR assumption. c_s^0 is the initial concentration of a reference species, which has the lowest concentration in the computational time increment being considered. $[\dot{\omega}]_{sr}^0$ is the reaction rate of this reference species s at the beginning of the computational reaction step, calculated for the corresponding kinetic scheme using the following formulation:

$$[\dot{\omega}]_{sr}^0 = (b_{sr} - a_{sr})\left[\kappa_{fr}\prod_m \left(\frac{\rho_m}{W_m}\right)^{a'_{mr}} - \kappa_{br}\prod_m \left(\frac{\rho_m}{W_m}\right)^{b'_{mr}}\right] \quad (2)$$

where a_{sr} and b_{sr} are the integral stoichiometric coefficients of the s reference species on the left and right hand sides of the reaction. r, a'_{mr} and b'_{mr} are the reaction orders, W_m is the molecular weight, and ρ_m is the mass density of species m. k_{fr} and k_{br} are the coefficients of the forward and backward reactions in the generalized Arrhenius form.

For the above formulations, the production or positive term R_C^0 and the consumption or negative term R_D^0 can be as follows:

$$R_C^0 = a_{sr}\kappa_{br}\prod_m \left(\frac{\rho_m}{W_M}\right)^{b'_{mr}} + b_{sr}\kappa_{fr}\prod_m \left(\frac{\rho_m}{W_m}\right)^{a'_{mr}} \quad (3)$$

$$R_D^0 = b_{sr}\kappa_{br}\prod_m \left(\frac{\rho_m}{W_M}\right)^{b'_{mr}} + a_{sr}\kappa_{fr}\prod_m \left(\frac{\rho_m}{W_m}\right)^{a'_{mr}} \quad (4)$$

The chemical kinetic time scale (τ_{chem}) is defined as the time assumed to be needed for a species to reach its effective equilibrium state under perfectly homogeneous conditions. For a "fast" combustion step, the chemical time scale can be defined as the consumption time of the fuel or oxidants. For complex chemistry, the definition of the chemical time scale of each reversible elementary reaction relies on the reference species of the reaction, which is expressed by [5,8]

$$\tau_{\text{chem}}^{-1} = -[\dot{\omega}]_{sr}^0/(c_s^0 + R_D^0\tau) \quad (5)$$

The turbulence time scale is defined as the time of eddy breakup in order to mix the fuel, oxidizer, and hot combustion products assuming that an inhomogeneity exists in the mixture, which is generally symbolized by

$$\tau_{\text{mix}} = ck/\varepsilon \quad (6)$$

where k is the turbulence kinetic energy, ε is k's dissipation rate, and c is a constant taken to be around 0.01 for diesel engine combustion [5]. When $\tau_{\text{mix}} \to 0$, the model reduces to the perfectly stirred reactor approach. If the term $\dot{\omega}_{sr}^0\tau_{\text{mix}}$ dominates, the expression reproduces the eddy breakup rate $-c_s^0/\tau_{\text{mix}}$.

In order to make sure that the initiation of combustion relies exclusively on chemistry–with turbulence having influence only after reactive events have already been taking place–the delay coefficient f was used in the simulation of the combustion pro-

Downloaded 02 Jun 2010 to 171.66.16.109. Redistribution subject to ASME license or copyright; see http://www.asme.org/terms/Terms_Use.cfm

cesses of diesel and dual fuel engines. This delay coefficient was originally calculated based on a global reaction to describe the oxidation of diesel fuel at high temperature [9]. For the present work, the delay coefficient f in the following equation

$$\frac{c_m^k - c_m^0}{\tau} = \dot{\omega}(c_m^k)\frac{\tau_{\text{chem}}}{\tau_{\text{chem}} + f\tau_{\text{mix}}} = \frac{c_s^0[\dot{\omega}]_{sr}^0}{c_s^0 + R_D^0\tau - f[\dot{\omega}]_{sr}^0\tau_{\text{mix}}} \tag{7}$$

was calculated based on the detailed chemical kinetics using the following formulation:

$$f = \frac{1 - e^{-\gamma}}{1 - e^{-1}}, \quad \gamma = \frac{Y_{\text{CO}_2} + Y_{\text{H}_2\text{O}} + Y_{\text{CO}} + Y_{\text{H}_2} + Y_{\text{CHO}}}{1 - Y_{\text{N}_2}} \tag{8}$$

where Y is the molar fraction of the different species, and γ indicates the extent of completeness of combustion in a particular region with its value varying from 0 for no combustion to 1 when consumption of the fuel and oxygen is completed. On this basis, the delay coefficient f changes from 0 to 1 depending on the local progress of combustion [9].

Practical diesel fuels consist of a great number of compounds, mainly of the aliphatic and aromatic types. It is not possible at present to model its combustion reactions effectively using a sufficiently comprehensive chemical mechanism due to the very complex and varying combustion reactions of such compounds. A practical approach is to propose a surrogate fuel with a very few components of relatively known reaction schemes that can be used instead in the numerical simulations [10]. The aliphatic part of the diesel fuels can be represented by *n*-heptane (C_7H_{16}), since its cetane number is close to that of conventional diesel fuels, and its reaction kinetics can be simulated while the aromatic part of diesel fuel can be expressed by toluene (C_7H_8) of also relatively known kinetics. The overall equivalent molecule of the No. 2 diesel fuel was assumed to be approximated by $C_{14}H_{28}$ with its thermodynamic properties represented by polynomial functions. The detailed reduced chemical kinetic scheme of the fuel was validated and made up of 291 reactions and 79 species [3,8,10], which included the following overall reactions:

$$C_{14}H_{28} + 2H_2O \rightarrow 2C_7H_{16} + O_2 \tag{9}$$

$$C_{14}H_{28} + 3O_2 \rightarrow 2C_7H_8 + 6H_2O \tag{10}$$

When the reaction rates in Eqs. (9) and (10) are the same, the ratio of *n*-heptane to toluene is 75/25 since the reaction becomes

$$2C_{14}H_{28} \rightarrow 3C_7H_{16} + C_7H_8$$

There are chemical reaction atom conservation equations in the KIVA3 code and the developed program in this contribution ensured throughout that the atom conservation for the different chemical reactions were satisfied. Moreover, since a sufficiently comprehensive chemical kinetics scheme was used to model the reactions activity in the dual fuel engine, all phases of the combustion processes, including those associated with ignition, were predicted and no empirical model for ignition was needed [11].

4 Validation of the 3D Model

An example of the mesh employed for the engine is shown in Fig. 1. The mesh size was selected based on a compromise between accuracy and the time required to finish the calculation. Variable mesh sizes were employed. The mesh size in the main combustion chamber is sufficiently small (around 1 mm $\times$1 mm$\times$ variable height) while that in the passage between the swirl and main combustion chambers and inside the swirl chamber are very much finer. More than 24 h were needed for a single case on a work station. The calculated and experimental cylinder pressure-time curves for an operational condition of a relatively large equivalence ratio of diesel fuel combustion showed generally good agreement with the corresponding predicted values. It was found during this research and also from reference to the literature [12] that there exists a certain small difference between

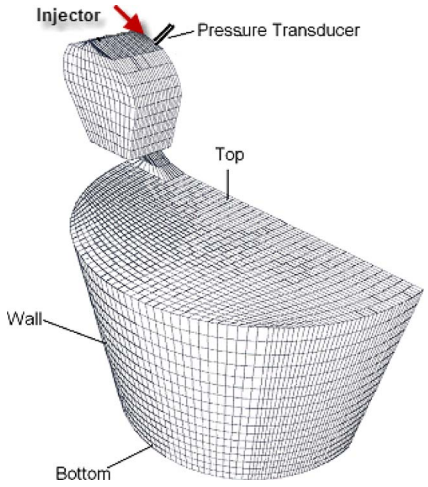


Fig. 1 An example of the 3KC1 engine 3D mesh for calculation purposes (CA=−146°CA)

results calculated with the KIVA fuel spray model and those obtained by experiment when injecting a relatively small quantity of liquid fuel. This is mainly because the characteristics of the spray then may become changed from that assumed by KIVA for around high load diesel operation, e.g., changes to the quality of spray distribution within the space, the occurrence of big droplets, and different thermal loads.

Figure 2 shows a comparison of results obtained by calculation and experiment for diesel/methane dual fuel operation. Although some differences between the two values appear to exist, they are qualitatively in good agreement. A likely reason contributing to the difference may be that the experimental values were obtained by measuring the pressure value in the swirl chamber and assumed to be also applicable to the averaged pressure values of the whole cylinder chamber. Further analyses indicated the existence of a slight difference between the pressure values within the swirl chamber and the main combustion chamber as well as the inevitable contribution of cyclic variation associated with experimentally observed pressure development values.

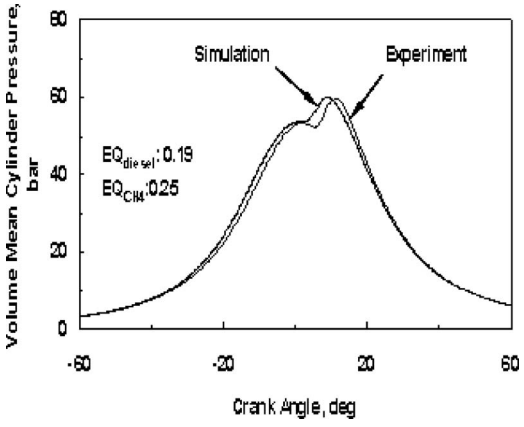


Fig. 2 A comparison of experimental results with the calculated ones for dual fuel operation under small pilot conditions (P_{in}=88.23 kPa, T_{in}=18.7°C, n=1800 rpm, T_{oil}=85°C, m_{diesel}=0.00387 g/cycle, T_{inj}=−6.0°CA (input), and D_{inj}=10.0°CA)

Downloaded 02 Jun 2010 to 171.66.16.109. Redistribution subject to ASME license or copyright; see http://www.asme.org/terms/Terms_Use.cfm

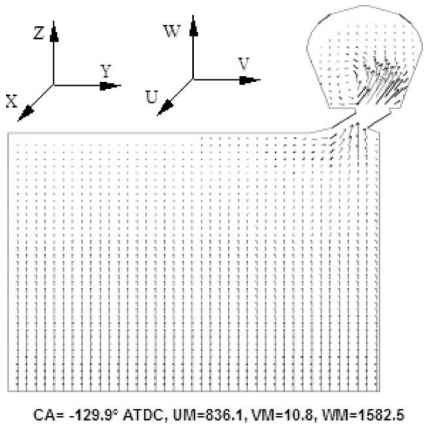


Fig. 3 Velocity distribution (cm/s) at Y=0.01 plane and CA= −129.9° CA ATDC, where the initial swirl center is formed (CR = 23, P_{in}=80.0 kPa, T_{in}=292.5 K, n= 1800 rpm, and T_{wall}=350 K)

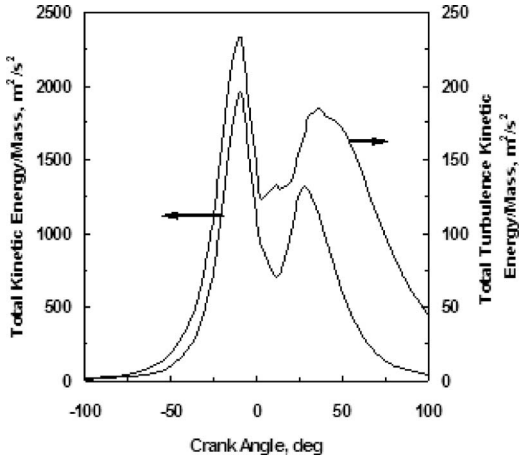


Fig. 5 Variations of total kinetic energy/mass (K_t) and total turbulence kinetic energy/mass (K_t) with crank angle under the motored condition (CR= 23, P_{in}=80.0 kPa, T_{in}=292.5 K, n =1800 rpm, and T_{wall}=350 K)

5 Simulation Results

5.1 Variations in the Distribution of Mixture Velocity, Pressure, and Temperature in the Absence of Fuel Injection and Combustion. The calculation began at a crank angle of −146.0° CA after top dead center (ATDC) when the intake valve just closed, and it was assumed that the cylinder pressure and temperature are uniform then. Through analyses of the variations in velocity distribution at every crank angle within the compression and expansion, it was found that the swirl center for an engine speed of 1800 rpm was formed initially at the left side of the swirl chamber at a crank angle of around −130.0° CA ATDC, as shown in Fig. 3. The swirl center moved toward the top-right direction up to a highest point with continued compression. During the expansion stroke, the swirl center moved down-leftward until it disappeared. Figure 4 shows examples of the velocity distribution at typical crank angles. It can be seen that the swirl can be formed not only in the swirl chamber but also in the main combustion chamber. It can be also formed in the horizontal cross section at some crank angles.

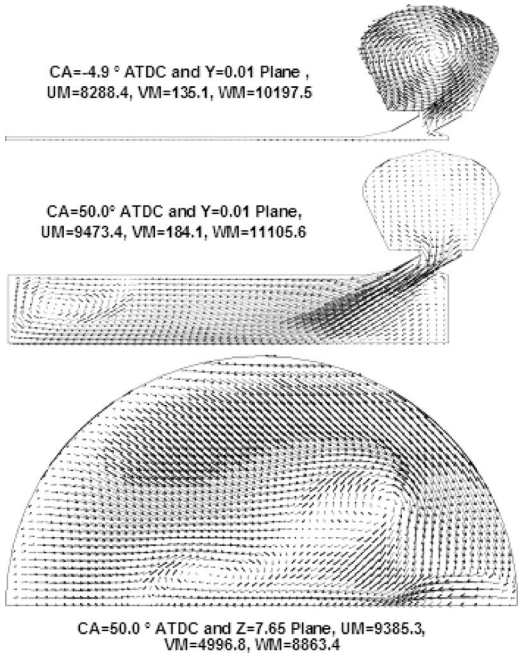


Fig. 4 Velocity distribution (cm/s) at Z=7.65 plane under the motored condition (CR= 23, P_{in}=80.0 kPa, T_{in}=292.5 K, n =1800 rpm, and T_{wall}=350 K)

The velocity in every cell was calculated and then the total kinetic energy/mass (K_t) and turbulence kinetic energy/mass (k_t) were derived using the following formulations:

$$K_t = \frac{\Sigma_i 0.5 m_i (U_i^2 + V_i^2 + W_i^2)}{\Sigma_i m_i} \tag{9'}$$

$$k_t = \frac{\Sigma_i 0.5 m_i (U_i'^2 + V_i'^2 + W_i'^2)}{\Sigma_i m_i} \tag{10''}$$

where U, V, and W are the velocities in the radial, tangential, and axial directions, and U', V', and W' are the velocity fluctuation components in the radial, tangential, and axial directions. The variations in K_t and k_t with crank angle are shown in Fig. 5. It can be seen that K_t increases with the upward movement of the piston from the bottom to the top dead center positions and achieves a maximum value at a crank angle of −10.0° CA ATDC. Around top dead center and during expansion, K_t reduces down to a minimum value at a crank angle of around 12.0° CA ATDC. It then increases up to another maximum value at a crank angle of 36° CA ATDC to decrease later on gradually for the remaining part of the expansion stroke. Variations in k_t values with crank angle have similar trends to those of K_t, but the corresponding crank angles to achieve the maximum and minimum values are slightly different.

Diagrams of the distribution of cylinder pressure and temperature at every crank angle were produced and analyzed. Samples of these sets of values are shown in Fig. 6. It is found that the cylinder pressure in the main combustion chamber is slightly higher than that in the swirl chamber during the compression stroke. In the part around top dead center and during the expansion stroke, the cylinder pressure within the swirl chamber is higher than that in the main combustion chamber. Variations in the maximum and minimum values of cylinder pressure and temperature with the crank angle are shown in Fig. 7. It can be seen that the difference between the two sets of values are relatively small and vary following the corresponding variations of K_t. The differences between the maximum and minimum cylinder temperatures shows only little changes within the compression stroke but change much more during the expansion stroke due to the variations in the values of K_t, k_t, and heat loss.

Downloaded 02 Jun 2010 to 171.66.16.109. Redistribution subject to ASME license or copyright; see http://www.asme.org/terms/Terms_Use.cfm

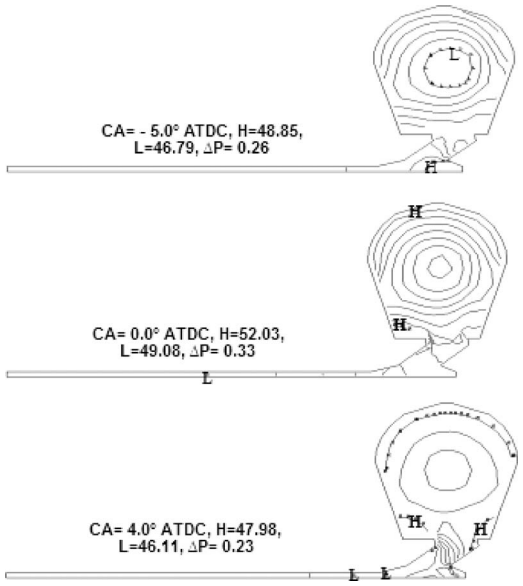


Fig. 6 Pressure distribution (bar) at Y=0.0 plane under the motored condition (CR= 23, P_{in}=80.0 kPa, T_{in}=292.5 K, n =1800 rpm, and T_{wall}=350 K)

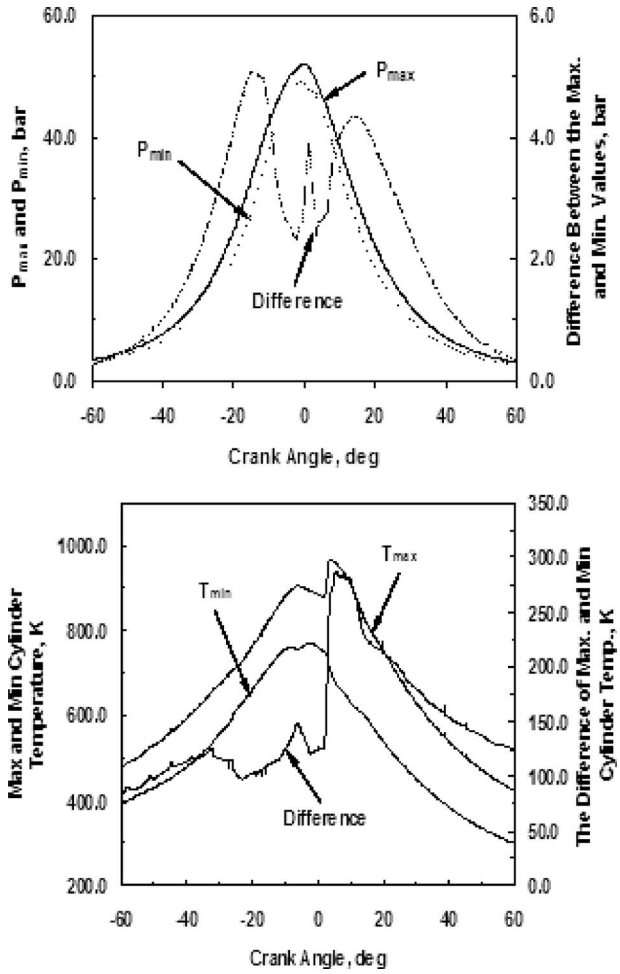


Fig. 7 A comparison of maximum and minimum cylinder pressures and temperatures under the motored condition (CR= 23, P_{in}=80.0 kPa, T_{in}=292.5 K, n=1800 rpm, and T_{wall}=350 K)

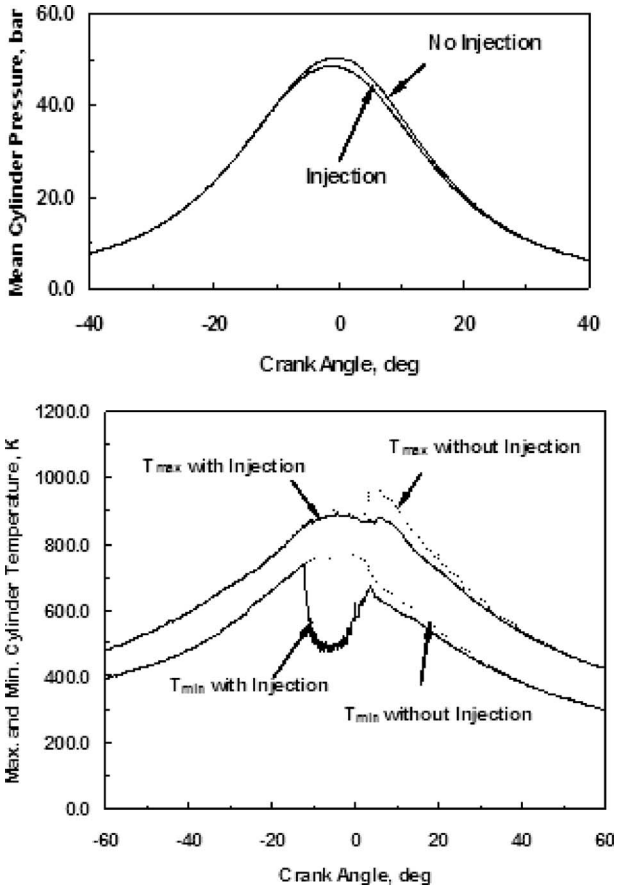


Fig. 8 A comparison of the mean cylinder pressure and maximum and minimum cylinder temperature in the operations with and without pilot injection under the motored condition (CR= 23, P_{in}=80.0 kPa, T_{in}=292.5 K, n=1800 rpm, T_{wall}=350 K, T_{inj} =−12.5°CA ATDC, D_{inj}=−12.5°CA, and m_{inj}=7.2 mg/2 cycle)

5.2 Pilot Injection, Evaporation, and Mixing Characteristics in the Absence of Combustion. In order to investigate the liquid fuel injection spray characteristics, the combustion model was artificially closed and some parameters were used as input to the modified program. Figure 8 shows the calculated results of the variations in the mean cylinder pressure and maximum and minimum cylinder temperatures with crank angle then. It can be seen that the minimum cylinder temperature displays a big reduction during pilot injection presumably due to the evaporation of the liquid fuel. Both the maximum and minimum cylinder temperatures during operation with liquid fuel injection are lower than without during most of the expansion stroke, mainly due to the evaporation and mixing of the liquid diesel fuel with air. Also, the mean cylinder pressure with pilot injection is lower than without during the injection period and for much of the expansion stroke due to the corresponding temperature reduction.

Analyses of the diagrams of the calculated distributions of the values of liquid fuel droplets, mass fraction, mixture charge temperature, velocity, and Sauter droplet mean radius (SMR) at each crank angle showed that the injected liquid particles move from the top-left to the center of the bottom of the chamber, and move to the top-right with the strong swirling flow. The areas with high concentrations of diesel fuel also move from the top-left region to the region of the bottom of the swirl chamber, and then move up to the top region again with the swirling flow. Similarly, the areas with low mixture temperature are around the top-left area of the swirl chamber during the injection period since more evaporation and mixing take place around the corresponding area with the high concentrations of diesel fuel. The low temperature zone

Downloaded 02 Jun 2010 to 171.66.16.109. Redistribution subject to ASME license or copyright; see http://www.asme.org/terms/Terms_Use.cfm

moves to the center of the bottom of the swirl chamber at a crank angle of 1.1°CA ATDC and moves back to the top of the swirl chamber again following the high concentration zone of diesel fuel movement at a crank angle of 7.1°CA ATDC. The distributions of mixture velocity with and without pilot injection indicate that the pilot injection can slightly affect the velocity distribution in some areas, with relatively higher maximum velocities in the radial, tangential, and axial directions are achieved. However, pilot injection appeared not to change the bulk of the swirl motion pattern.

5.3 Combustion Characteristics of Diesel and Dual Fuel Engines With a Swirl Chamber. The combustion characteristics of the water-cooled, normally aspirated variable speed ISUZU 3KC1 indirect injection diesel engine with the swirl chamber used were examined using the developed combustion model incorporating detailed chemical kinetics [13]. Figure 10 shows the corresponding variations in the heat release rate and values of the maximum and minimum cylinder pressures and temperatures with crank angle. It can be observed that the differences between the cylinder pressure values are bigger during the combustion duration. It can be seen also that very big temperature differences exist. Also, the heat release rates are lower than values obtained for a direct injection diesel engines of similar size and speed. However, it should be noted that the differences between the maximum and minimum cylinder pressure values are only for some very specific points. The mean cylinder pressure values between the swirl and main combustion chambers do not have big differences since the mean cylinder pressure values are very close to the maximum cylinder pressure values, as shown in Fig. 9.

Formaldehyde CH_2O is an important intermediate product during the oxidation of hydrocarbon fuels, and variations in its mass fraction can indicate the extent of the progress in the combustion processes. Figures 10 and 11 show the corresponding distributions of the values of the concentration of CH_2O and cylinder temperature. In the initial phase of combustion, the higher concentrations of CH_2O zone represent the relatively extensive reaction zone with high temperatures. However, much of the CH_2O will be oxidized with the further high temperature reactions. Therefore, the low concentrations of CH_2O represent an extensive reaction zone with high temperatures in the middle and later phases of combustion. Also, it can be seen from Figs. 10 and 11 that the relatively extensive reaction zone with high temperature initially occurs at the bottom-left region of the swirl chamber at a crank angle of −8.0°CA ATDC. This extensive reaction zone moves to the center-right region of the swirl chamber following the very strong swirl at the crank angle of −4.0°CA ATDC with the area of the reaction zone enlarged. The extensive reaction zone moves further to the center of the swirl chamber and combustion spreads to most of it when the piston moves toward the top dead center. Both the low and high CH_2O mass fraction zones appear in the central regions of the swirl chamber at the crank angle of 3.0°CA ATDC. The low mass fraction zone is included in the high temperature region, as shown in Fig. 11, where extensive high temperature reactions are taking place. The high mass fraction CH_2O zone corresponds to the extensive initial reaction zone. The combustion products are moved to the center of the swirl chamber and the unburned fuels moved to the wall of the swirl chamber under the influence of the strong swirl. The central area of the swirl chamber becomes the high temperature zone at the crank angle of 6.1°CA ATDC with most of the fuel in the swirl chamber burned and the combustion moved to the main chamber. At the crank angle of 8.0°CA ATDC, the flame spread to more than half of the main chamber

Figure 12 shows the effects of injection timing (IT) on combustion for the case of a very small pilot injection. It can be seen that the cylinder pressure appears to become reduced during combustion and the expansion when the injection timing was changed from −6.0°CA to 0.0°CA ATDC. The cylinder pressure curves

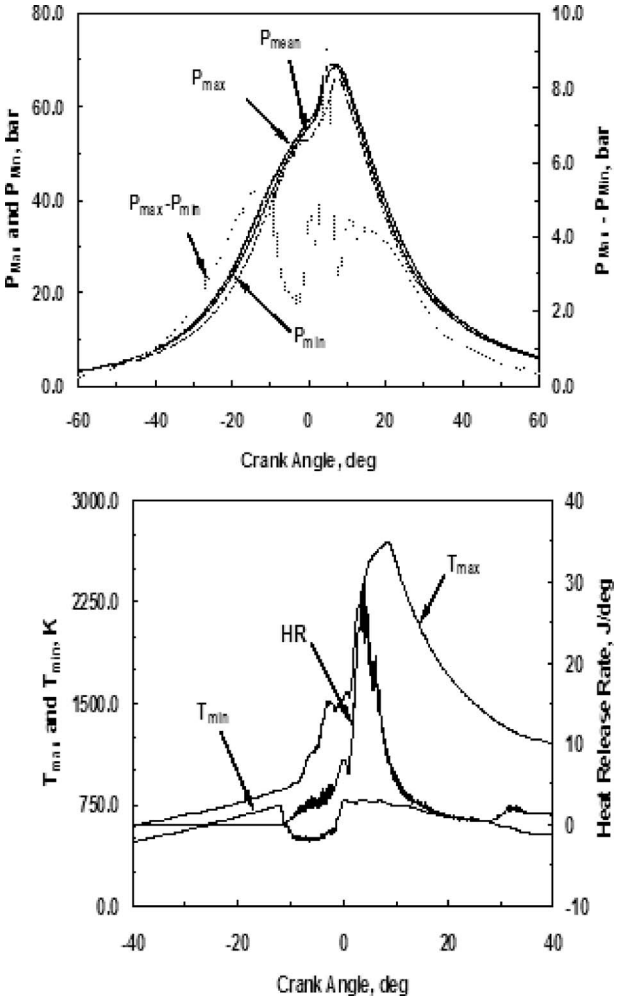


Fig. 9 Variations in calculated heat release rate and maximum and minimum values of cylinder pressure and temperature with crank angle for the 3KC1 diesel engines with a swirl chamber (CR= 23, n=1800 rpm, P_{in}=87.67 kPa, T_{in}=290 K, T_{wall}=350 K, and EQ_{diesel}=0.324)

are nearly the same when the injection timing is equal to or greater than 10°CA ATDC since the pilot fuel is hardly burned after injection. When the injection timing is advanced to −12.0°CA ATDC, the combustion process is advanced with the highest cylinder pressure value achieved. When the injection timing is advanced much further to −30°CA and −40°CA ATDC, different extents of prereaction activity take place; but much of the fuel is not burned. The cylinder pressure-time curves are almost the same with injection timing earlier than −60.0°CA ATDC due to the very small extent of prereactions at the corresponding low temperatures.

Figure 13 shows variation in the values of the maximum and minimum cylinder pressure and temperature and heat release rate with crank angle for a dual fuel operational condition with a relatively large pilot mass injection. It can be seen that the mean cylinder pressure values are very near to those of the maximum cylinder pressure. Therefore, the mean cylinder pressure difference between the swirl chamber and the main combustion chamber is not very big for large pilot quantity operation. It can also be noted that the difference between the maximum and minimum cylinder temperatures is still very big even for dual fuel operation with the duration of heat release becoming longer.

It can be noted from Fig. 14 that changing the engine speed is also an effective method for controlling combustion in dual fuel

Downloaded 02 Jun 2010 to 171.66.16.109. Redistribution subject to ASME license or copyright; see http://www.asme.org/terms/Terms_Use.cfm

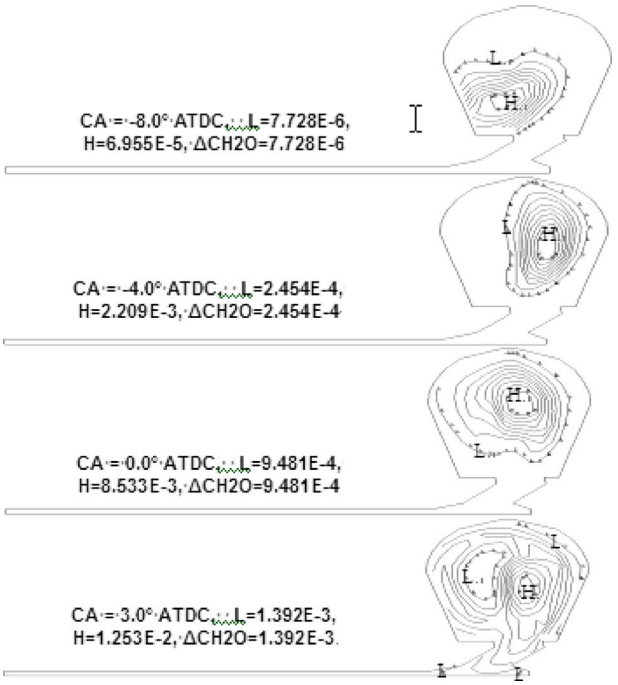


Fig. 10 CH_2O mass fraction distribution across $Y=0$ plane for the 3KC1 diesel engine with a swirl chamber (CR= 23, n =1800 rpm, P_{in}=87.67 kPa, T_{in}=290 K, EQ_{diesel}=0.324, T_{inj}= −12.0°CA ATDC, and D_{inj}=12.0°CA)

engines. For a constant injection timing, reducing engine speed can make combustion take place earlier with more complete methane oxidation due to the longer time provided for the oxidation

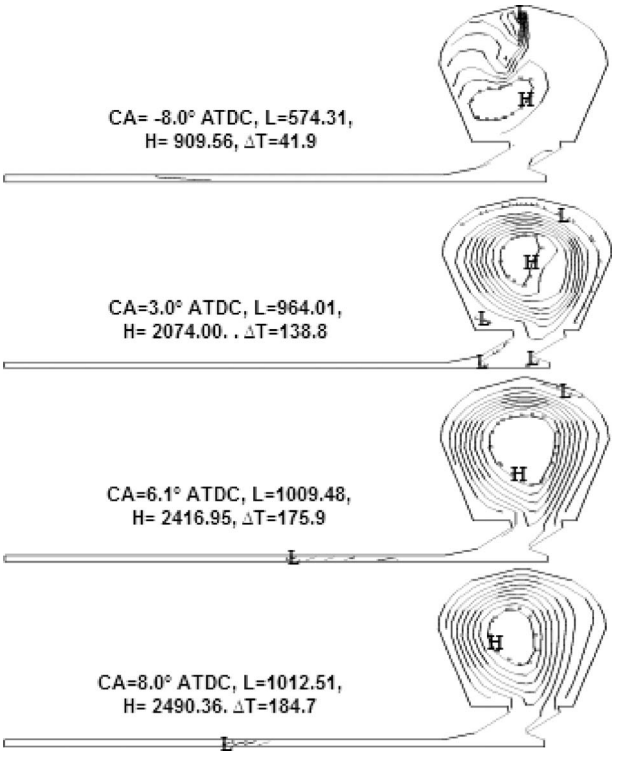


Fig. 11 Cylinder temperature (K) distribution across $Y=0.0$ plane for the 3KC1 diesel engine with a swirl chamber (CR= 23, n=1800 rpm, P_{in}=87.67 kPa, T_{in}=290 K, EQ_{diesel}=0.324, T_{inj}= −12.0°CA ATDC, and D_{inj}=12.0°CA)

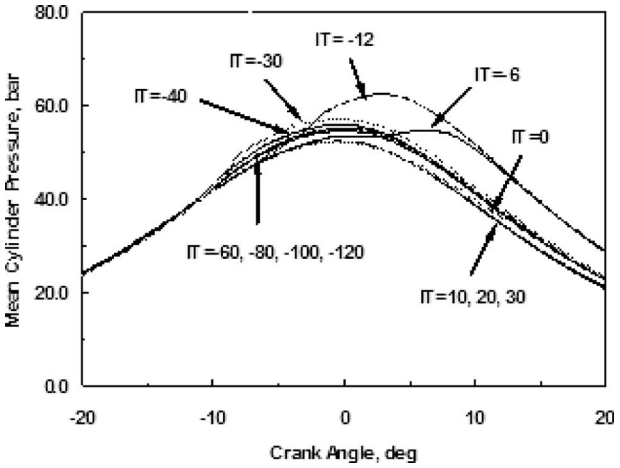


Fig. 12 Effects of IT on the variations of mean cylinder pressure under small pilot conditions (P_{in}=88.23 kPa, T_{in}=18.7°C, n=1800 rpm, CR=23, T_{wall}=350 K, m_{diesel}=0.00387 g/cycle, and D_{inj}=10.0°CA)

processes. Figure 15 shows the effects of adding carbon dioxide on the combustion processes of the dual fuel engine. It can be seen that increasing the carbon dioxide can effectively delay and reduce the intensity of the combustion processes. Introducing carbon dioxide by using exhaust gas recirculation (EGR) is probably an effective method to reduce the combustion intensity and knock

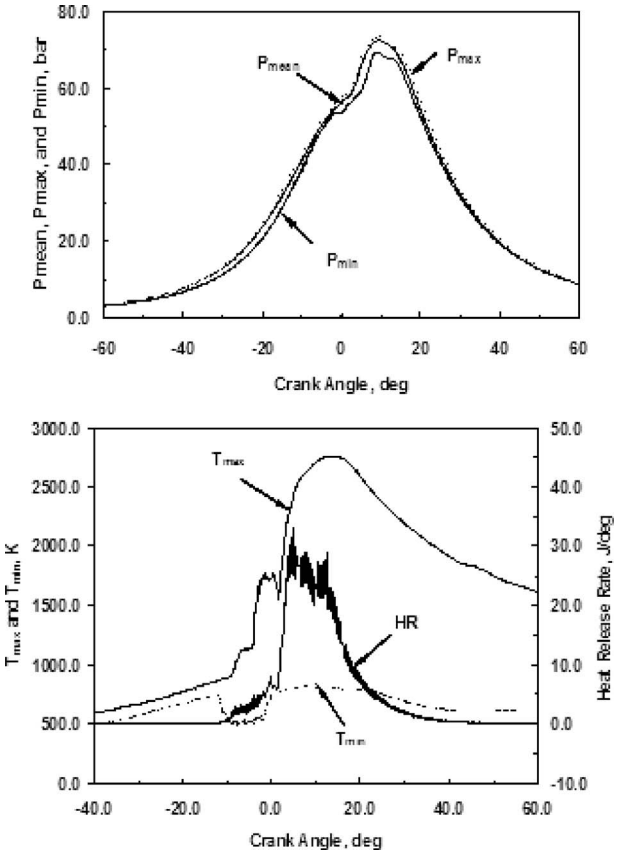


Fig. 13 Variations in maximum and minimum cylinder pressures and temperatures and heat release rates with crank angle for dual fuel engine operation (n=1800 rpm, P_{in}=87.67 kPa, T_{in}=290 K, EQ_{diesel}=0.324, EQ_{CH_4}=0.4 T_{inj}=−12.0°CA ATDC, D_{inj}=12.0°CA, and T_{wall}=450−500 K)

Downloaded 02 Jun 2010 to 171.66.16.109. Redistribution subject to ASME license or copyright; see http://www.asme.org/terms/Terms_Use.cfm

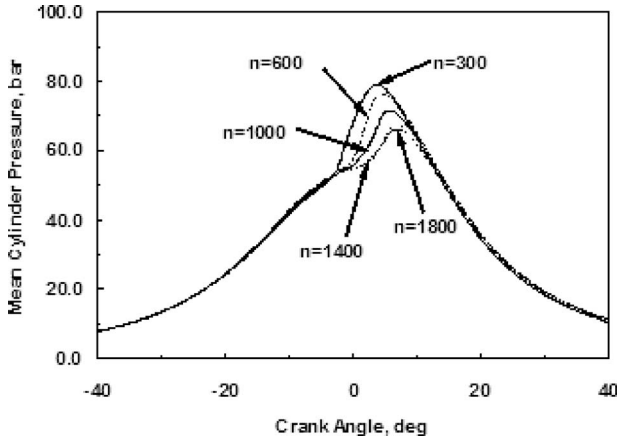


Fig. 14 Effects of engine speed on combustion in the dual fuel engine with a swirl chamber (P_{in}=88.23 kPa, T_{in}=18.7°C, n=1800 rpm, CR=23, T_{wall}=425 K, m_{diesel}=0.00387 g/cycle, EQ_{diesel}=0.19, EQ_{CH_4}=0.25, T_{inj}=−6.0°CA, and D_{inj}=10.0°CA)

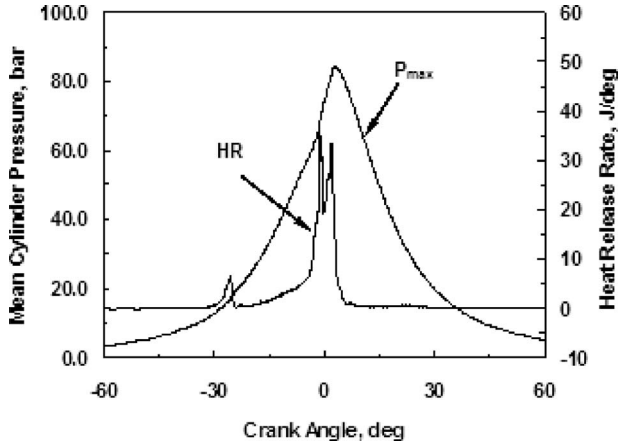


Fig. 16 HCCI combustion achieved by early pilot fuel injection in the dual fuel engine with a swirl chamber (P_{in}=83.0 kPa, T_{in}=118.7°C, n=600 rpm, T_{wall}=520 K, m_{diesel}=0.0022 g/cycle, EQ_{diesel}=0.14, EQ_{CH_4}=0.30, T_{inj}=−40.0°CA, and D_{inj}=10.0°CA)

occurrence in dual fuel combustion.

Through analysis of the combustion process in the main combustion chamber, it is found that there are still some areas near the cylinder wall and far from the passage where no complete combustion appears to take place [13,14]. In order to reduce the quantity of the unburned methane within these areas, some effective remedial measures need to be adopted. Figure 16 shows an example of a HCCI type combustion achieved by injecting a certain amount of diesel fuel into the swirl chamber earlier than normal while introducing a certain amount of gaseous fuel into the intake. It is found through analysis of the component variations during these processes that the diesel fuel is initially oxidized into the intermediate products after it is injected into the cylinder at a crank angle of −40.0°CA ATDC. Intensive combustion takes place at −4.0°CA ATDC and finishes near to 7.0°CA ATDC. However, it is also found that there is still a certain amount of unburned methane in the exhaust. In actual engine operation, some effective measures, e.g., using hot EGR and increasing the wall surface temperature of the combustion chamber, can be used to reduce the quantity of unburned methane [11].

5.4 The Combustion of Pilot Fuel Injected Into a Small Prechamber. A 3D mesh developed to investigate the combustion characteristics of pilot fuel injection into a small prechamber is shown in Fig. 17. The prechamber volume is around 15% of the total clearance volume. A comparison of mean cylinder pressure-time curves for the diesel engine with a swirl chamber and a prechamber both without and with combustion are shown in Fig. 18. It can be seen that the calculated cylinder pressure-time curves are almost the same for the condition without combustion. The pilot injection into a small prechamber can provide a relatively earlier autoignition than the corresponding swirl chamber operation, but the maximum cylinder pressure for the prechamber operation is lower than that for the swirl chamber since a larger throttling loss could be produced when the diesel fuel moves from the small prechamber into the main combustion chamber.

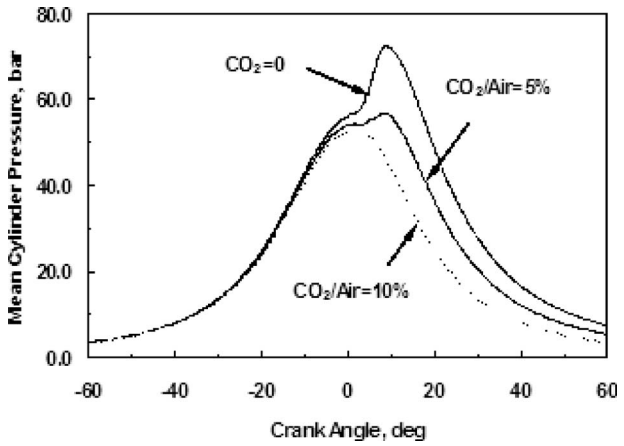


Fig. 15 Effects of adding CO_2 on combustion in the dual fuel engine with a swirl chamber (P_{in}=88.23 kPa, T_{in}=18.7°C, n=1800 rpm, m_{diesel}=0.00387 g/cycle, EQ_{diesel}=0.19, EQ_{CH_4}=0.25, T_{inj}=−6.0°CA ATDC, D_{inj}=10.0°CA, and T_{wall}=425 K)

6 Conclusion

In the absence of any combustion, with the engine motored, the swirl center is initially formed at the bottom-left of the swirl chamber and then moved in the top-right direction up toward the highest point with continued compression. The swirl center moves down until it disappears during the expansion stroke.

The variations in cylinder pressure and temperature are affected by the total kinetic energy variations following piston movement, with a slight pressure difference existing between the swirl and the main combustion chambers. Injection of the pilot fuel into a swirl chamber will reduce the volumetric mean cylinder pressure

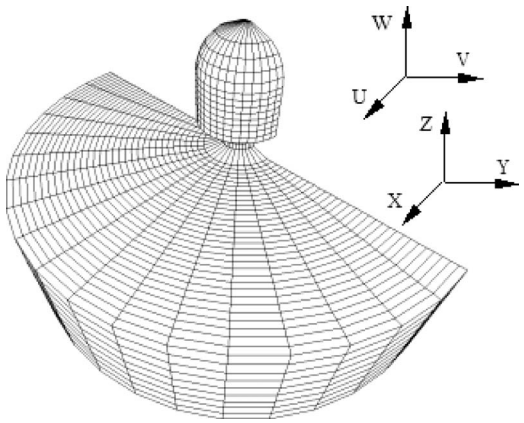


Fig. 17 A 3D mesh of a diesel engine with a small prechamber (CA=−50.0°CA)

Downloaded 02 Jun 2010 to 171.66.16.109. Redistribution subject to ASME license or copyright; see http://www.asme.org/terms/Terms_Use.cfm

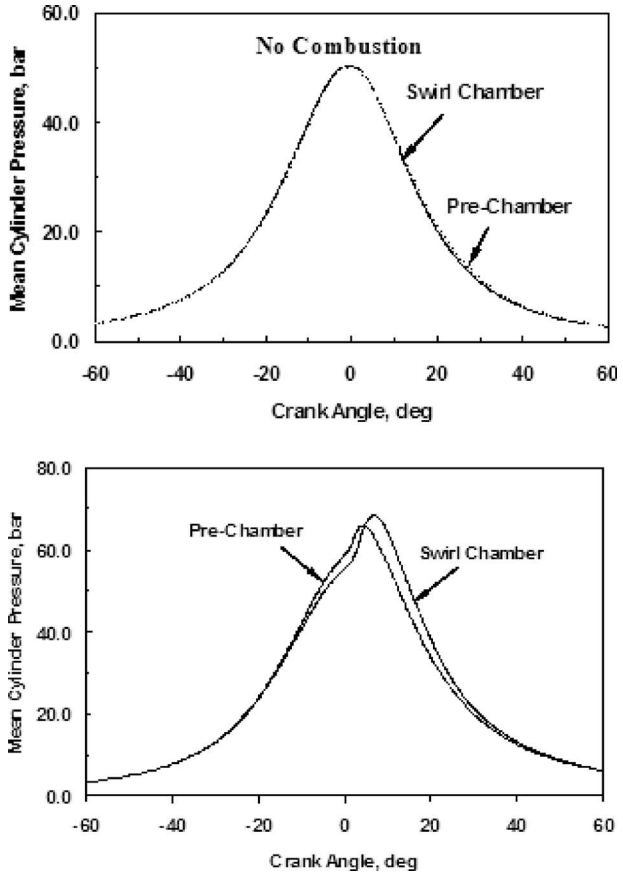


Fig. 18 A comparison of calculated mean cylinder pressures for diesel engines with a prechamber and a swirl chamber (CR =23, n=1800 rpm, T_{inj}=−12°CA, D_{inj}=12°CA, P_{in}=87.67 kPa, T_{in}=292.5 K, EQ=0.324 g/cycle or 0.00666 g/cycle)

and the minimum temperature within the combustion chamber when compared with engine motoring operation without pilot injection.

The swirl motion within the swirl and the main combustion chambers promotes the evaporation of the pilot and the combustion processes of diesel and dual fuel engines. Reducing engine speed can advance the autoignition and combustion.

There exists optimum injection timing for a specific diesel and dual fuel operation. Overadvancing or delaying the injection timing will lead to incomplete combustion.

Adding carbon dioxide into the intake can reduce effectively the intensity of combustion and delay the occurrence of autoignition.

HCCI combustion can be achieved by injecting a small amount of pilot fuel into a swirl chamber with a very relatively early injection timing and low engine speed.

Earlier autoignition can be achieved by injecting a pilot fuel into a small prechamber compared with the corresponding swirl chamber operation.

Acknowledgment

The financial support of Canadian Natural Science and Engineering Research Council (NSERC), Westgrid, and University of Calgary is gratefully acknowledged. The contributions of Dr. Fuming Xiao, Dr. Sohrabi, and Mr. J. McNeely to the experimental part and of Dr. D. G. Phillips in the running of the code are greatly appreciated.

Nomenclature

a, b = stoichiometric coefficient
a', b' = reaction order
C = molar concentration
CR = compression ratio
EGR = exhaust gas recirculation by volume
EQ = equivalence ratio
f = delay coefficient
k = reaction coefficient, turbulence K.E
m = any species
n = engine speed, rpm
P_{in} = initial intake pressure
P_{max} = maximum cylinder pressure
R = reaction rate
s = reference species
T_{in} = intake temperature
T_{inj} = injection timing
U, V, W = velocity components
W = molar mass
$\hat{w}$ = reaction rate
ρ = density
τ = residence time
ε = dissipation rate

References

[1] Ludu, A., and Baufeld, T., 2005, "Micro-Pilot and Spark Ignition Tests on the Same 5 L/Cylinder Displacement Engine," ASME Paper No. ICES2005-1094.
[2] He, Y., and Rutland, C. J., 2002, "Modeling of a Turbocharged DI Diesel Engine Using Artificial Neural Networks," SAE Paper No. 2002-01-2772.
[3] Khalil, E. B., and Karim, G. A., 2002, "A Kinetic Investigation of the Role of Changes in the Composition of Natural Gas in Engine Applications," Trans. ASME: J. Eng. Gas Turbines Power, **124**, pp. 404–411.
[4] Kong, S. C., Marriott, C. D., and Reitz, R. D., 2001, "Modelling and Experiments of HCCI Engine Combustion Using Detailed Chemical Kinetics With Multidimensional CFD," SAE Paper No. 2001-01-1026.
[5] Rente, T., Golovichev, V. I., and Denbratt, I., 2001, "Effect of Injection Parameters on Auto-Ignition and Soot Formation in Diesel Sprays," SAE Paper No. 2001-01-3687.
[6] Amsden, A. A., O'Rourke, P. J., and Butler, T. D., 1989, "KIVA-II: A Computer Program for Chemically Reactive Flows With Sprays," Los Alamos National Laboratory, Report No. LA-11560-MS.
[7] Liu, C., and Karim, G. A., 2005, "A Simulation of the Combustion of N-Heptane Fueled HCCI Engines Using a 3D Model With Detailed Chemical Kinetics," ASME Paper No. ICEF05-1220.
[8] Golovitchev, V. I., Nordin, N., Jarnicki, R., and Chomiak, J., 2000, "3D Diesel Spray Simulation Using a New Detailed Chemistry Turbulent Combustion Model," SAE Paper No. 2000-01-1891.
[9] Kong, S. C., Han, Z., and Reitz, R. D., 1995, "The Development and Application of a Diesel Ignition and Combustion Model for Multidimensional Engine Simulation," SAE Paper No. 950278.
[10] Golovitchev, V. I., Atarashiya, K., Tanaka, T., and Yamada, S., 2003, "Towards Universal EDC-Based Combustion Model for Compression-Ignited Engine Simulations," SAE Paper No. 2003-01-1849.
[11] Karim, G. A., 2003, "Combustion in Gas Fuelled Compression Ignition Engines of the Dual Fuel Type," Trans. ASME: J. Eng. Gas Turbines Power, **125**, pp. 827–836.
[12] Dong, Y., 1996, "The Multi-Dimensional Model of Diesel Spray and Combustion and Comparison it With Data of PDPA and Experimental Results of ICIS," Ph.D. thesis, University of Jilin Industry, Changchun.
[13] Liu, C., Karim, G. A., and Xiao, F., and Soharabi, A., "An Experimental and Numerical Investigation of the Combustion Characteristics of a Dual Fuel Engine With a Swirl Chamber," SAE Paper No. 2007-01-0615.
[14] Liu, C., 2006, "An Experimental and Analytical Investigation Into the Combustion Characteristics of HCCI and Dual Fuel Engines With Pilot Injection," Ph.D. thesis, University of Calgary, Canada.

Downloaded 02 Jun 2010 to 171.66.16.109. Redistribution subject to ASME license or copyright; see http://www.asme.org/terms/Terms_Use.cfm

Maria Naidin
e-mail: maria.naidin@mycampus.uoit.ca

Sarah Mokry
e-mail: sarah.mokry@mycampus.uoit.ca

Farina Baig
e-mail: farina.baig@gmail.com

Yevgeniy Gospodinov
e-mail: yevgeniy.uoit@gmail.com

Faculty of Energy Systems and Nuclear Science,
University of Ontario Institute of Technology,
2000 Simcoe Street North,
Oshawa, ON, L1K 7K4, Canada

Udo Zirn
Hitachi Power Systems America, Ltd.,
645 Martinsville Road,
Basking Ridge, NJ 07920
e-mail: udo.zirn@hal.hitachi.com

Igor Pioro
Faculty of Energy Systems and Nuclear Science,
University of Ontario Institute of Technology,
2000 Simcoe Street North,
Oshawa, ON, L1K 7K4, Canada
e-mail: igor.pioro@uoit.ca

Greg Naterer
Faculty of Engineering and Applied Science,
University of Ontario Institute of Technology,
2000 Simcoe Street North,
Oshawa, ON, L1K 7K4, Canada
e-mail: greg.naterer@uoit.ca

Thermal-Design Options for Pressure-Channel SCWRS With Cogeneration of Hydrogen

Currently there are a number of Generation IV supercritical water-cooled nuclear reactor (SCWR) concepts under development worldwide. The main objectives for developing and utilizing SCWRs are (1) to increase the gross thermal efficiency of current nuclear power plants (NPPs) from 33–35% to approximately 45–50% and (2) to decrease the capital and operational costs and, in doing so, decrease electrical-energy costs (approximately US$ 1000/kW or even less). SCW NPPs will have much higher operating parameters compared to current NPPs (i.e., pressures of about 25 MPa and outlet temperatures of up to 625°C). Additionally, SCWRs will have a simplified flow circuit in which steam generators, steam dryers, steam separators, etc. will be eliminated. Furthermore, SCWRs operating at higher temperatures can facilitate an economical cogeneration of hydrogen through thermochemical cycles (particularly, the copper-chlorine cycle) or direct high-temperature electrolysis. To decrease significantly the development costs of a SCW NPP and to increase its reliability, it should be determined whether SCW NPPs can be designed with a steam-cycle arrangement that closely matches that of mature supercritical (SC) fossil power plants (including their SC turbine technology). On this basis, several conceptual steam-cycle arrangements of pressure-channel SCWRs, their corresponding T-s diagrams and steam-cycle thermal efficiencies are presented in this paper together with major parameters of the copper-chlorine cycle for the cogeneration of hydrogen. Also, bulk-fluid temperature and thermophysical properties profiles were calculated for a nonuniform cosine axial heat-flux distribution along a generic SCWR fuel channel, for reference purposes. [DOI: 10.1115/1.2983016]

1 Introduction

Prior to a discussion of the conceptual steam-cycle arrangements of a SCW NPP, it is important to describe the general features of the various types of SCWRs that are currently investigated. This section also includes a review of the modern SC turbines and their parameters to ensure that current technology can match the pressure and temperature parameters proposed.

1.1 SCWR Concepts. Currently there are a number of Generation IV SCWR concepts under development worldwide [1]. The main objectives for developing and utilizing SCWRs are (1) to increase the thermal efficiency of current NPPs from 33–35% to approximately 45–50% and (2) to decrease the capital and operational costs and, in doing so, decrease electrical-energy costs (approximately US$ 1000/kW or even less).

SCW NPPs will have much higher operating parameters compared to current NPPs (i.e., pressures of about 25 MPa and outlet temperatures of up to 625°C) (for details, see Fig. 1). Additionally, SCWRs will have a simplified flow circuit in which steam generators, steam dryers, steam separators, etc. will be eliminated. Furthermore, SCWRs operating at higher temperatures can facilitate an economical production of hydrogen through thermochemical cycles or direct high-temperature electrolysis.

The SCWR concepts [1] follow two main types: (a) a large reactor pressure vessel (PV) with a wall thickness of about 0.5 m to contain the reactor core (fueled) heat source, analogous to conventional LWRs or (b) distributed pressure channels (PChs) or tubes analogous to conventional heavy water reactors (HWRs).

Within those two main classes (PV and PCh) [1], pressure-channel reactors are designed to be more flexible to flow, flux, and density changes than the PV reactors. This makes it possible to use the experimentally confirmed better solutions developed for these reactors. The main ones are fuel reloadings and channel-specific flow-rate adjustments or regulations. A design whose basic element is a channel or tube, which carries a high pressure, has an inherent advantage of greater safety than large vessel structures at supercritical (SC) pressures. (For reference purposes, the bulk-fluid temperature and thermophysical properties profiles in a generic PCh SCWR fuel channel can be found in the Appendix.)

Atomic Energy of Canada Limited (AECL) and the Research and Development Institute of Power Engineering (RDIPE or NIKIET in Russian abbreviations) [1,3] are currently developing concepts of the PCh SCWRs (see Table 1). Table 2 lists the critical parameters of water.

Manuscript received June 17, 2008; final manuscript received June 23, 2008; published online October 1, 2008. Review conducted by Dilip R. Ballal. Paper presented at the 16th International Conference on Nuclear Engineering (ICONE16), Orlando, FL, May 12–15, 2008.

Copyright © 2009 by ASME

Downloaded 02 Jun 2010 to 171.66.16.109. Redistribution subject to ASME license or copyright; see http://www.asme.org/terms/Terms_Use.cfm

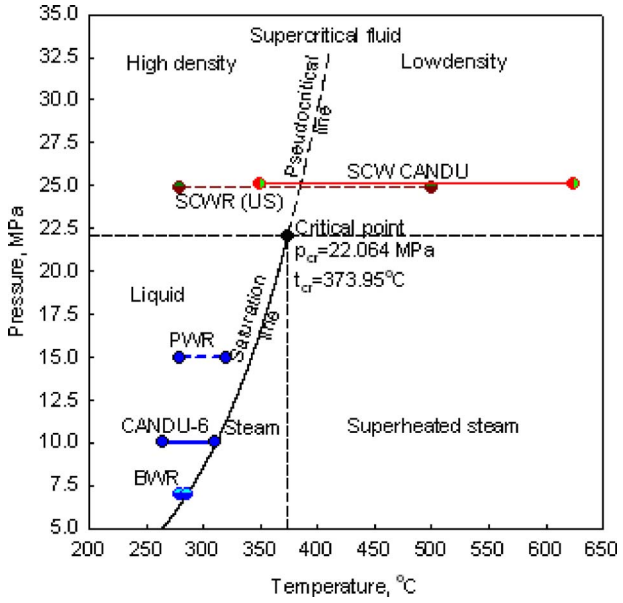


Fig. 1 Pressure-temperature diagram of water for typical operating conditions of SCWRs and modern reactors [2]

To decrease significantly the development costs of a SCW NPP and to increase its reliability, it should be determined whether SCW NPPs can be designed with a steam-cycle arrangement that closely matches that of SC fossil power plants (including their SC turbine technology) that have been used extensively in existing thermal power plants for the last 50 years.

Previous publications have been mainly devoted to a general development of SCWR concepts [1]. However, very few publications were dedicated to developments of a general steam-cycle arrangement of a SCW NPP [4].

Therefore, the first objective of this paper is a literature review of modern SC turbines and their major steam parameters.

Table 1 Major parameters of PCh SCW CANDU® (Canada deuterium uranium is a registered trademark of AECL) and KP-SKD nuclear reactors concepts [1]

Parameters	SCW CANDU	KP-SKD
Reactor spectrum	Thermal	
Coolant	Light water	
Moderator	Heavy water	
Thermal power (MW)	2540	1960
Electric power (MW)	1220	850
Thermal efficiency (%)	48	42
Pressure (MPa)	25	25
Inlet temperature (°C)	350	270
Outlet temperature (°C)	625	545
Flow rate (kg/s)	1320	922
No. of fuel channels	300	653
No. of fuel elements in bundle	43	18
Length of bundle string (m)	6	—
Maximum cladding temperature (°C)	850	700

Table 2 Critical parameters of water [5]

Parameter	Unit	Water
Critical pressure	MPa	22.064
Critical temperature	°C	373.95
Critical density	kg/m^3	322.0

Table 3 No-reheat cycle heat-transfer rates

Main steam temperature (°C)		625
Mass flow rate (kg/s)		765
Stage	ΔH (kJ/kg)	Q MW_{th}
Pumps	25	19
Preheater	1438	1100
Reactor	1943	1485
Turbine	−1570	−1200
Condenser	−1837	−1405
Efficiency (%)		46.1

1.2 Review of Modern Supercritical Turbines and Their Major Parameters. SC "steam" turbines of medium and large capacities (450–1200 MW) (for details, see Ref. [1]) have been used very successfully in many fossil power plants worldwide for more than 50 years. The steam-cycle thermal efficiencies have reached nearly 54%, which is equivalent to a net-plant efficiency of approximately 40–43% on a HHV basis. It should be noted that the absolute leaders among large-scale power plants in terms of thermal efficiencies are combined-cycle (i.e., tandem arrangement of gas turbine and subcritical-pressure steam turbine) gas-fired power plants with net-plant efficiencies of up to 54% on a HHV basis (or approximately 60% on a LHV basis).

An analysis of the SC turbine data showed the following.

- The vast majority of the modern SC turbines are single-reheat-cycle turbines.
- Major steam inlet parameters of these turbines are the main or primary SC steam—a pressure of 24–25 MPa and a temperature of 540–600°C—and the reheat or secondary subcritical-pressure steam—a pressure of 3–5 MPa and a temperature of 540–600°C.
- Usually, the main steam temperatures and the reheat steam temperatures are the same or very close (for example, 538/538°C, 566/566°C, and 600/600°C, or 538/566°C, 566/593, and 600/620°C).
- Only very few double-reheat-cycle turbines were manufactured. The market demand for double-reheat turbine disappeared due to economic reasons after the first few units were built.

2 Comparison of Potential Steam-Cycle Arrangements for SCW NPP

In general, the major SCW CANDU reactor parameters, such as the outlet pressure and temperature and the capacity (for details, see Table 1), are the same or close to the corresponding parameters of the most advanced SC turbines.

Therefore, the second objective of this paper is to introduce the most common steam-cycle arrangements used in existing fossil power plants and to evaluate conceptually their complexity and adaptability to current SCW NPP concepts.

The following analysis provides a thermodynamic comparison of the most common steam-cycle arrangements used in existing thermal power plants: (1) the no-reheat cycle, (2) the single-reheat cycle, and (3) the double-reheat cycle. Moreover, the thermodynamic benefit of regenerative heating is presented based on the single-reheat cycle.

All of the steam-cycle arrangements considered are based on the Rankine cycle, and all of the cycles are based on the main steam pressure and temperature of 25 MPa and 625°C, respectively. Where reheat is present, the reheat temperature was assumed to be 625°C or 700°C as indicated. All cycles are based on a condensing pressure of 6.77 kPa. The amount of cycle heat input (Q), illustrated in Tables 3–7, is based on a cycle with a

Downloaded 02 Jun 2010 to 171.66.16.109. Redistribution subject to ASME license or copyright; see http://www.asme.org/terms/Terms_Use.cfm

Table 4 Single-reheat cycle heat-transfer rates

Steam temperature main/reheat (°C)	625/625		625/700	
Mass flow rate (kg/s)	613		579	
Stage	ΔH (kJ/kg)	Q (MW_{th})	ΔH (kJ/kg)	Q (MW_{th})
Pump	25	15	25	14
Preheater	1438	882	1438	832
Reactor	1943	1191	1943	1124
HP turbine	−506	−310	−506	−293
Reheater	665	408	840	486
LP turbine	−1451	−890	−1568	−907
Condenser	−2114	−1296	−2172	−1257
Efficiency (%)	48.1		48.8	

total useable work ("thermal output") of 1200 MW_{th}.

It is to be noted that the thermal-cycle efficiencies stated in Tables 3–7 are based on a reversible thermodynamic cycle and do not account for any irreversibility that would occur in an actual steam cycle. For example, all compression and expansion processes are assumed isentropic and piping pressure drops are neglected. For illustration purposes, the *T-s* diagrams show irreversible compression and both the reversible (dashed line) and irreversible (solid line) expansion.

Table 5 Double-reheat cycle heat-transfer rates

Steam temperature main/reheat/reheat (°C)	625/625/625	
Mass flow rate (kg/s)	554	
Stage	ΔH (kJ/kg)	Q (MW_{th})
Pump	25	14
Preheater	1438	797
Reactor	1943	1076
HP Turbine	−387	−214
Reheater 1	526	291
IP Turbine	−423	−234
Reheater 2	463	256
LP Turbine	−1356	−751
Condenser	−2228	−1234
Efficiency (%)	49.3	

Table 6 Mass-flow and heat-transfer rates through system components

Steam temperature main/reheat (°C)	625/625		625/700	
Stage	m (kg/s)	Q (MW_{th})	m (kg/s)	Q (MW_{th})
Pumps (total)	N/A	26	N/A	24
Deaerator (2-3)	571	1556	541	1474
Reactor (4-5)	1030	2002	976	1896
HP turbine (5-6)	1030	−372	976	−352
Reheater (6-7)	571	380	541	454
LP turbine (7-8)	571	−829	541	−848
Condenser (8-1)	571	−1207	541	−1175
Efficiency (%)	49.9		50.5	

Table 7 Mass-flow and heat-transfer rates through system components

Steam temperature main/reheat (°C)	625/625	
Stage	m (kg/s)	Q (MW_{th})
Pumps (total)	N/A	27
Feedwater heater (HX1)	650	444
Deaerator	650	199
Feedwater heater (HX2)	937	416
Reactor	937	1821
HP turbine	937	−404
Reheater	749	428
LP turbine	650	−796
Condenser	508	−1076
Efficiency (%)	52.7	

2.1 Cycles Without Heat Regeneration. The three basic steam-cycle arrangements in fossil power plants are (1) the no-reheat cycle, (2) the single-reheat cycle, and (3) the double-reheat cycle.

2.1.1 No-Reheat Cycle. The most basic steam-cycle configuration that could be used in a SCW NPP is the no-reheat cycle without heat regeneration.

A simplified cycle and the corresponding *T-s* diagram of the no-reheat cycle are presented in Figs. 2(*a*) and 2(*b*). The corresponding heat-transfer rates are listed in Table 3.

The water/steam properties were calculated using the WINSTEAM 3.1 software, which is based on the 1997 formulations published by the IAPWS-IF97.

Saturated feedwater (i.e., condensate) from a condenser (Point 1: pressure of 6.77 kPa and a temperature of 38.3°C) enters a pump, which compresses the condensate (water) to a supercritical operating pressure (Point 2: pressure of 25 MPa and a temperature of 39.1°C). After that, the supercritical water is heated in a preheater (for simplification purposes the preheater is considered to be a part of the reactor) between Points 2 and 3 from 39.1°C to 350°C at a pressure of 25 MPa. Further on, the supercritical water continues to flow through the steam generator (reactor), being heated from 350°C to 625°C at the same operating pressure of 25 MPa (Points 3 and 4).

In the next step, the supercritical water (here it is better to say supercritical steam because this actually incorrect term suits better in connection with SC turbines) at the pressure of 25 MPa and temperature of 625°C (Point 4) enters the turbine where it expands and produces mechanical work by rotating the turbine shaft connected to an electrical-generator rotor. Inside the turbine, the pressure and temperature drop and saturated steam at a low pressure leaves the turbine at Point 5 (pressure of 6.77 kPa and a temperature of 38.3°C).

The steam is condensed at a pressure of 6.77 kPa and at a saturation temperature of 38.3°C inside a condenser (Points 5 and 1). The condenser is basically a heat exchanger that uses water from a cooling tower, river, or lake as cooling medium. The water (condensate) leaves the condenser as a saturated liquid (in reality it would be slightly subcooled) and enters the pump (Point 1), thus completing the thermodynamic cycle.

The difference between the energy added to the cycle (energy added to the reactor plus the energy added by the pumps) and the heat rejected through the condenser represents the useful work generated by this configuration. The efficiency of cycle is the ratio of the total useful work and heat added to the cycle.

As per Table 3, the total thermal energy added to the cycle is 3406 kJ/kg. The energy lost through the condenser is 1837 kJ/kg.

Downloaded 02 Jun 2010 to 171.66.16.109. Redistribution subject to ASME license or copyright; see http://www.asme.org/terms/Terms_Use.cfm

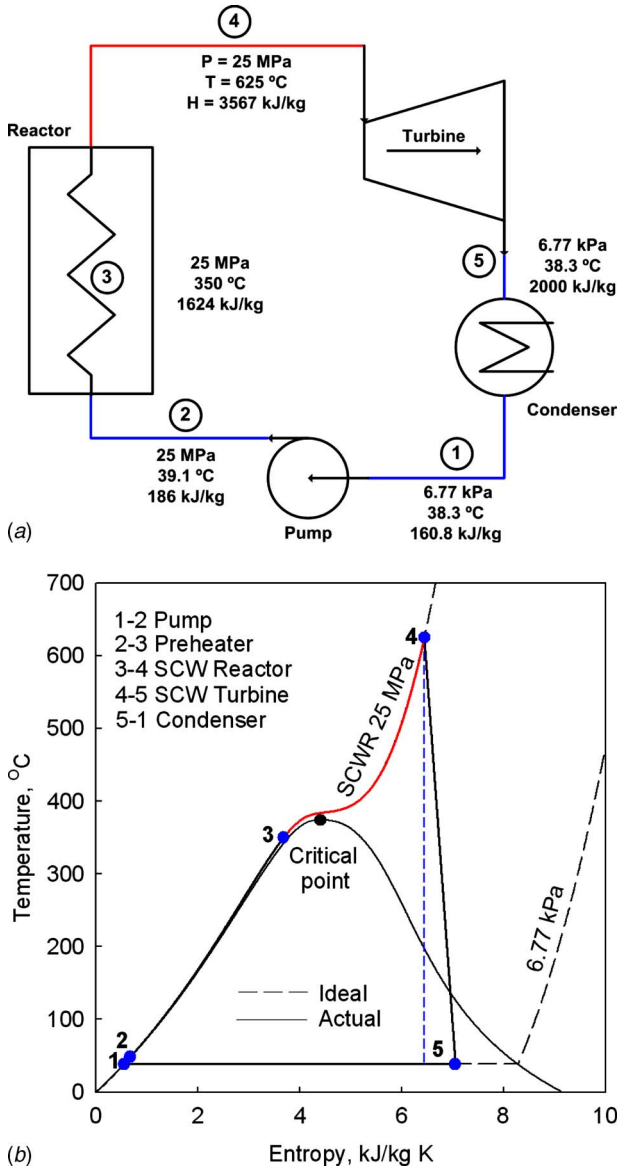


Fig. 2 No-reheat cycle layout (*a*) and the corresponding *T-s* diagram (*b*)

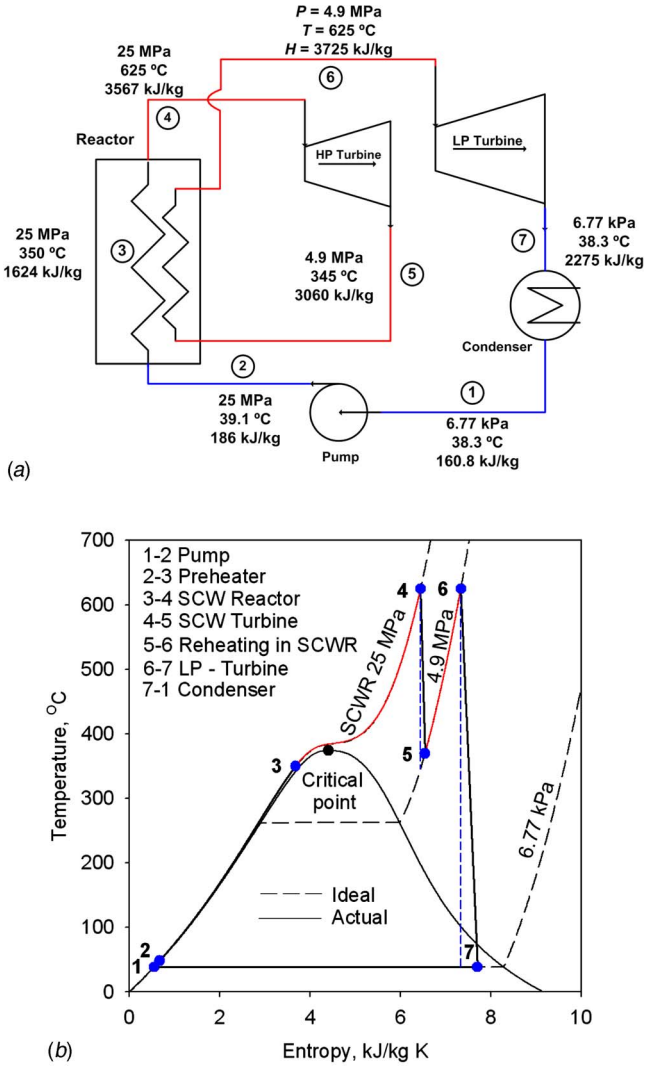


Fig. 3 Single-reheat cycle layout (*a*) and the corresponding *T-s* diagram (*b*)

Therefore, the thermal efficiency of the cycle is 46.1%.

Advantages of this no-reheat cycle for a SCW NPP are:

(1) a simplified general SCW NPP layout that lowers the capital costs associated with the design, construction, and operation of a NPP and
(2) a simplified SCWR design, which can be PCh or PV type.

2.1.2 Single-Reheat Cycle. A single-reheat steam-cycle arrangement is illustrated in Fig. 3(*a*). The corresponding *T-s* diagram and heat-transfer rates are illustrated in Fig. 3(*b*) and Table 4, respectively.

Compared to the no-reheat cycle the single-reheat cycle uses two turbine sections or cylinders: a high-pressure (HP) turbine and an intermediate-pressure (IP) or/and low-pressure (LP) turbine(s) (for details, see Table 4). Moreover, a steam reheat is added to the cycle.

For that reason, the vast majority of SC thermal power plants operating around the world employ SC steam generators and turbines with a single-reheat cycle (for details, see Sec. 1.2).

The SC steam from the reactor is expanded inside the HP turbine from a supercritical pressure of 25 MPa and a temperature of 625°C (Point 4) to an intermediate pressure of 4.9 MPa and a temperature of 345°C (Point 5). The subcritical-pressure steam leaves the HP turbine in a superheated state and is sent back to the reactor where it is reheated from 345°C to 625°C at an approximately constant pressure of 4.9 MPa (Point 6). After the reactor, the superheated steam is expanded in the IP/LP turbine(s) to a subatmospheric pressure of 6.77 kPa and a temperature of 38.3°C (Point 7), at which it is condensed in the condenser.

For this cycle, the total heat energy added to the cycle is approximately 4071 kJ/kg, and the energy rejected through the condenser is 2114 kJ/kg. Thus, the thermal efficiency of the cycle is around 48.1%. If a higher steam reheat temperature is achieved, for example 700°C, the thermal efficiency would rise by about 0.7%. However, this increase in temperature may be very expensive accounting on special materials to be used inside the reactor. Therefore, on the current level of technology, this option may not be viable in spite of the slightly increased thermal efficiency.

In order to maximize the thermal-cycle efficiency of SCW NPPs, it would be beneficial to include nuclear-steam reheat, similar to the reheat cycle of fossil power plants. This nuclear-steam reheat is easier to implement inside PCh reactors compared to PV reactors.

2.1.3 Double-Reheat Cycle. The double-reheat cycle arrangement and the corresponding *T-s* diagram are illustrated in Fig. 4.

Downloaded 02 Jun 2010 to 171.66.16.109. Redistribution subject to ASME license or copyright; see http://www.asme.org/terms/Terms_Use.cfm

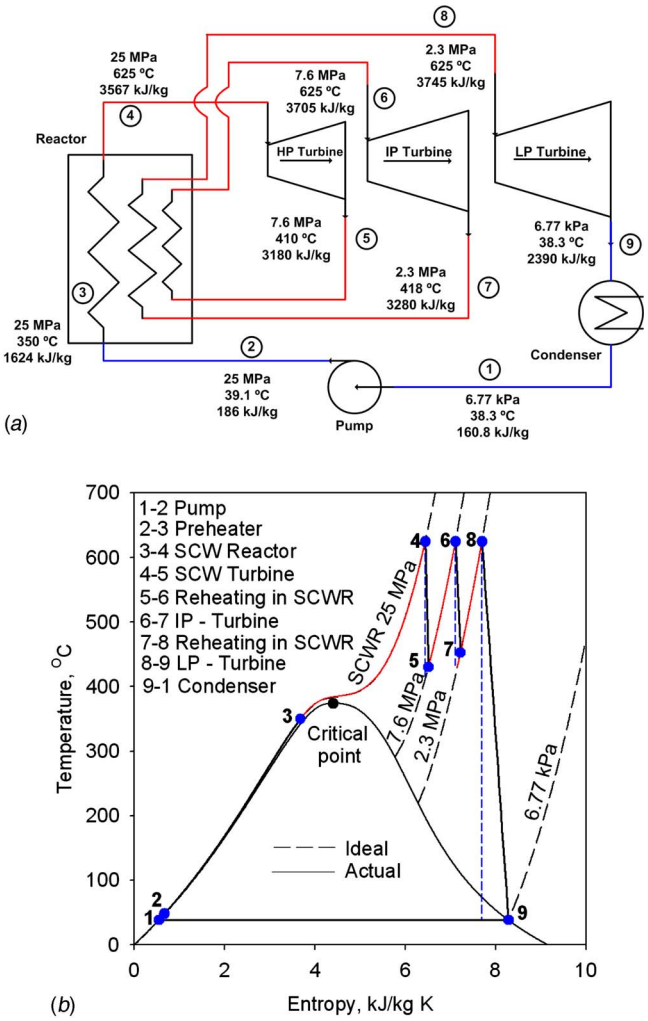


Fig. 4 Double-reheat cycle layout (*a*) and the corresponding *T-s* diagram (*b*)

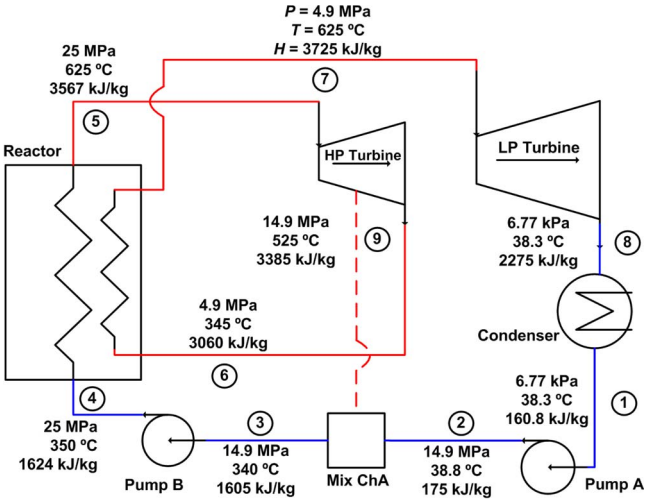


Fig. 5 Single-reheat cycle with heat regeneration through a single deaerator

The corresponding heat-transfer rates are listed in Table 5.

In comparison to the single-reheat cycle (for details, see Sec. 2.1.2) the double-reheat cycle has three turbine sections: a HP turbine, IP turbine(s), and LP turbine(s); moreover, the second steam reheat is added to the reactor.

The SC steam from the reactor is expanded inside the HP turbine from a supercritical pressure of 25 MPa and a temperature of 625°C (Point 4) to an intermediate pressure of 7.6 MPa and a temperature of 410°C (Point 5). The subcritical-pressure steam leaves the HP turbine in a superheated state and is sent back to the reactor where it is heated from 410°C to 625°C at an approximately constant pressure of 7.6 MPa (Point 6). After the reactor, the superheated steam is expanded in the IP turbine(s) to a pressure of 2.3 MPa and a temperature of 418°C (Point 7). The subcritical-pressure steam leaves the IP turbine in a superheated state and is sent back to the reactor where it is heated from 418°C to 625°C at an approximately constant pressure of 2.3 MPa (Point 8). After the reactor, the superheated steam is expanded in the LP turbine(s) to a subatmospheric pressure of 6.77 kPa and a temperature of 38.3°C (Point 9) and is condensed in the condenser.

For this cycle, the total heat energy added to the cycle is 4395 kJ/kg and the energy rejected through the condenser is 2228 kJ/kg. Thus, the thermal efficiency is around 49.3%.

The only advantage of the double-reheat cycle is the higher thermal efficiency compared to that of the no-reheat and single-reheat cycles.

2.2 Cycles With Heat Regeneration. It has been well established that an increased feedwater temperature leads to an improvement in the efficiency of the cycle the if heat from within the steam cycle is used to preheat the feedwater. A practical regeneration process can be accomplished by extracting steam from the turbine at various points. Although this steam could have been expanded inside the turbine to produce more useful work, it is used to preheat the feedwater instead.

Figure 5 illustrates a very simple regenerative single-reheat cycle where the feedwater heater is an open type, and the extraction steam is taken from the HP turbine. It is to be noted that using just one deaerator is a very inefficient way of heat regeneration and, moreover, would result in a very large deaerator. However, a single heater is sufficient for the purpose of this illustration of thermal efficiency improvements.

It is difficult to show the benefit of the regenerative-feedwater heating in a *T-s* diagram, because the flow rates at the various points in the cycle are not the same and hence, the areas within the T-s diagram do not represent the total work and heat rejection of the cycle. For the same reason, it is not meaningful to show the heat sources and sinks in Tables 6 and 7 on the basis of energy per unit mass (kJ/kg). As for Tables 3–5, Tables 6 and 7 are based on a total useful heat of 1200 MW_{th}.

The total energy added to the single-reheat cycle with a single-feedwater heater (see Table 6) is approximately 2407 MW_{th}, while the heat rejected in the condenser is around 1207 MW_{th}. Thus, the thermal efficiencies of the cycle have been determined to be around 49.9% for the main/reheat steam temperatures of 625/625°C and to be around 50.5% for the main/reheat steam temperatures of 625/700°C.

The single-reheat configuration with one feedwater heater (see Fig. 5 and Table 6) employs a single open feedwater heater (deaerator). The arrangement analyzed below involves three feedwater heaters: one LP heater, one deaerator, and one HP heater (for details, see Fig. 6 and Table 7). Figure 6 shows the general arrangement of this system and illustrates major pressure and temperature parameters. Steam is extracted from the HP turbine and is used to heat the feedwater flowing through heat exchanger (HX3) (closed-type feedwater heater). The LP turbine supplies extraction steam for the LP feedwater heater (HX1). Also, a fraction of the steam exhausted from the HP turbine is diverted to heat the water in the deaerator (HX2).

Downloaded 02 Jun 2010 to 171.66.16.109. Redistribution subject to ASME license or copyright; see http://www.asme.org/terms/Terms_Use.cfm

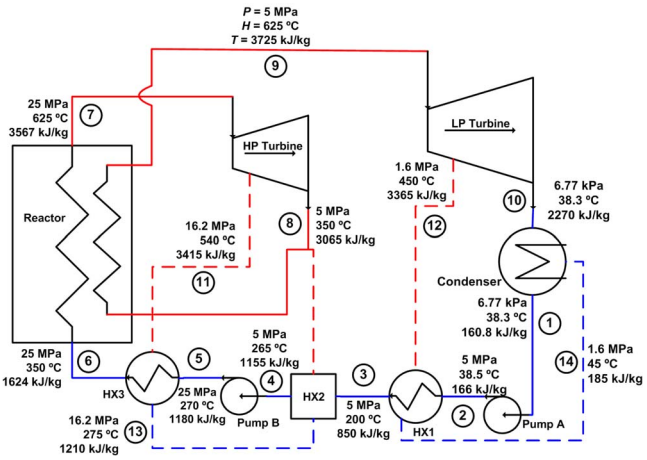


Fig. 6 Single-reheat cycle with heat regeneration through a single deaerator and two feedwater heaters

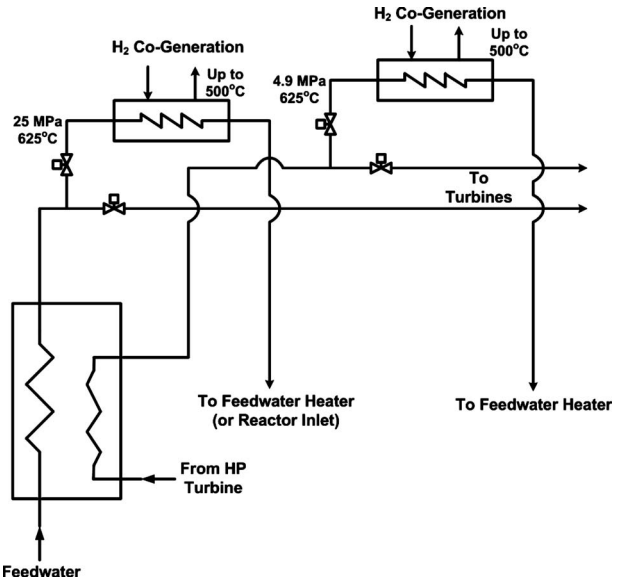


Fig. 7 Single-reheat cycle with heat regeneration and cogeneration of hydrogen (shown only the part related to hydrogen cogeneration)

Table 7 summarizes the calculated values for flow rates and the thermal efficiency associated with this cycle (see Fig. 6). The calculations were again based on a thermal output (i.e., useful work) of 1200 MW_{th}. The total heat added to the cycle is approximately 2276 MW_{th}. At the same time, the heat rejected in the condenser is approximately 1076 MW_{th}. Thus, the thermal efficiency of the system is determined to be around 52.7%.

As can be seen from Tables 4, 6, and 7, the thermal efficiencies of the regenerative single-reheat cycles are significantly higher than those for the single-reheat cycles without regeneration, and it increases proportionally with the number of feedwater heaters used. The optimum number of feedwater heaters would have to be determined through a cost-benefit analysis.

The regenerative cycles presented in this section represent a viable basis for a future SCW NPP. The optimum number of regenerative heaters should be investigated—it is likely going to be higher than what was presented herein for the the illustration of efficiency trends. However, it is clear that the calculated thermal efficiencies with regenerative heating are significantly higher than currently operating NPPs. The increase in efficiency is high enough to justify the increased costs associated with the design, construction, and operation of this new type of SCW NPP.

3 Cogeneration of Hydrogen at SCW NPP

SCWRs operating at higher temperatures (550–625°C) can facilitate an economical cogeneration of hydrogen through thermochemical cycles (particularly, the copper-chlorine cycle) or direct high-temperature electrolysis. In general, a SCW NPP with the cogeneration of hydrogen should operate at an invariable maximum power, which will be independent of an electrical load through a day or year. With the electrical load decrease, the SCW NPP will produce more hydrogen and vice versa. Thus, SCW NPPs with hydrogen cogeneration will operate at the most efficient level.

Currently, University of Ontario Insititute of Technology (UOIT) in collaboration with AECL is developing the copper-chlorine cycle with the maximum temperature in the cycle of up to 500°C (Table 8). Therefore, using the high-temperature heat from a SCWR to heat water in the hydrogen-production loop is a viable option. Heat exchangers of a recuperator-type have to be used for this purpose (Fig. 7). The layout of a SCW NPP with hydrogen cogeneration is more complicated than the regular SCW NPP cycle. Currently, UOIT is analyzing various configurations for the cogeneration of electricity and hydrogen.

4 Conclusions

The following conclusions can be made.

1. The vast majority of the modern SC turbines are single-reheat-cycle turbines and their major parameters are the main or primary SC steam—pressure of 24–25 MPa and a

Table 8 Chemical reaction steps and basic parameters of the copper-chlorine cycle

Step	Reaction	Temperature range (°C)		Feed/output
1	$2Cu(s)+2HCl(g)\rightarrow CuCl(l)+H_2(g)$	430–475	Feed:	Electrolytic Cu+dry HCl+Q
			Output:	H_2+CuCl(l) salt
2	$2CuCl(s)\rightarrow 2CuCl(aq)$ $\rightarrow CuCl_2(aq)+Cu(s)$	Ambient (electrolysis)	Feed:	Powder/granular CuCl and HCl+V
			Output:	Cu and slurry containing HCl and $CuCl_2$
3	$CuCl_2(aq)\rightarrow CuCl_2(s)$	<100	Feed:	Slurry containing HCl and $CuCl_2$+Q
			Output:	Powder/granular $CuCl_2+H_2O$/HCl vapors
4	$2CuCl_2(s)+H_2O(g)\rightarrow$ $CuO*CuCl_2(s)+2HCl(g)$	400	Feed:	Powder/granular $CuCl_2+H_2O(g)+Q$
			Output:	Powder/granular $CuO*CuCl_2+2HCl(g)$
5	$CuO*CuCl_2(s)\rightarrow 2CuCl(l)+1/2O_2(g)$	500	Feed:	Powder/granular $CuO*CuCl_2(s)+Q$
			Output:	Molten CuCl salt+oxygen

Q, thermal energy; V, electrical energy

Downloaded 02 Jun 2010 to 171.66.16.109. Redistribution subject to ASME license or copyright; see http://www.asme.org/terms/Terms_Use.cfm

temperature of 540–600°C—and the reheat or secondary subcritical-pressure steam—temperature is within the 540–600°C range.
2. Although the no-reheat cycle offers a simplified SCW NPP layout, contributing to lower capital costs, the efficiency of this cycle was calculated to be around 46%, which is the lowest of all the considered configurations.
3. In order to maximize the thermal-cycle efficiency of SCW NPPs it would be beneficial to include nuclear-steam reheat. Advantages of a single-reheat cycle in application to SCW NPPs are as follows

   - high thermal efficiency (approximately 48%), which is the current level for SC thermal power plants and is close to the maximum thermal efficiency achieved in the power industry at combined-cycle power plants (up to 60%),
   - proven state-of-the-art turbine technology, and
   - reduced development costs accounting to a wide variety of SC turbines manufactured by companies worldwide.

The major disadvantage of the implementation of a single-reheat cycle in SCW NPPs is significant changes required to a reactor core design with an addition of the nuclear-steam reheat at lower pressures.

4. The double-reheat configuration has the advantage of high efficiency (around 49%), but the complicated nuclear-steam reheat configuration would significantly increase the costs associated with the design and construction of such a facility.
5. The thermal efficiencies of the regenerative single-reheat cycles are significantly improved (up to 52.7%) when compared to those of the single-reheat cycles without regeneration, and it increases proportionally with the number of feedwater heaters used. The optimum number of feedwater heaters shall be determined through a cost-benefit analysis.
6. Based on the abovementioned analysis the single-reheat cycle with heat regeneration and the corresponding layout were chosen as a basis for a SCW NPP with the cogeneration of hydrogen.

Acknowledgment

Financial support from the Ontario Research Excellence Fund, AECL, and NSERC Discovery Grant is gratefully acknowledged.

Nomenclature

c_p = specific heat at constant pressure (J/kg K)
$\bar{c}_p$ = average specific heat within range of $(T_w - T_b)$; $(H_w - H_b / T_w - T_b)$ (J/kg K)
D_{hy} = hydraulic-equivalent diameter (m)
G = mass flux (kg/m^{2}s)
H = specific enthalpy (J/kg)
k = thermal conductivity (W/m K)
m = mass-flow rate (kg/s)
P, p = pressure (MPa)
Q = power or heat-transfer rate (W)
q = heat flux (W/m)
s = specific entropy (J/kg K)
T, t = temperature (°C)
V = specific volume (m^3/kg)

Greek Symbols

Δ = difference
μ = dynamic viscosity (Pa s)

Nondimensional Numbers

Pr = Prandtl number, $(\mu_b c_{pb} / k_b)$
$\overline{\mathrm{Pr}}$ = average Prandtl number; $(\mu_b \bar{c}_p / k_b)$

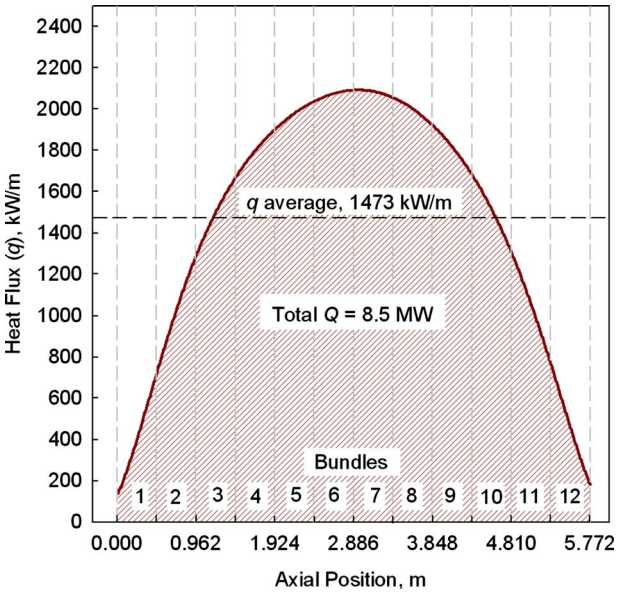


Fig. 8 Axial heat flux distribution along the SCWR heated channel

Subscripts

ave = average
b = bulk
in = inlet
out = outlet
pc = pseudocritical
th = thermal
w = wall

Acronyms

AHFD = axial heat flux distribution
BWR = boiling water reactor
CANDU = Canada deuterium uranium (reactor)
HHV = higher heating value
IAPWS = International Association for the Properties of Water and Steam
LHV = lower heating value
LWR = light water reactors
Mix Ch = mixing chamber (deaerator)
PWR = pressurized water reactor
SCW = supercritical water

Appendix

Temperature and Thermophysical Properties Profiles in Generic PCh SCWR Fuel Channel for the Main SCW Loop

In general, any SCWR will have fuel channels for the main supercritical water heating of up to 625°C. Therefore, it is important to determine the bulk-fluid temperature and thermophysical properties profiles along a generic SCWR fuel channel, for reference purposes. In previous studies [2], an average linear heat flux was used along the fuel channel. However, an actual AHFD in various reactors is close to a cosine-type profile [6].

Therefore, the following parameters were used in these thermalhydraulic calculations: $P=25$ MPa, $T_{in}=350$°C, $T_{out}=625$°C, $G=1300$ kg/m^2 s; fuel channel power=8.5 MW, and a nonuniform cosine AHFD (see Fig. 8). A generic SCWR fuel-bundle string is about 6-m long and has $D_{hy}=7.5$ mm.

Downloaded 02 Jun 2010 to 171.66.16.109. Redistribution subject to ASME license or copyright; see http://www.asme.org/terms/Terms_Use.cfm

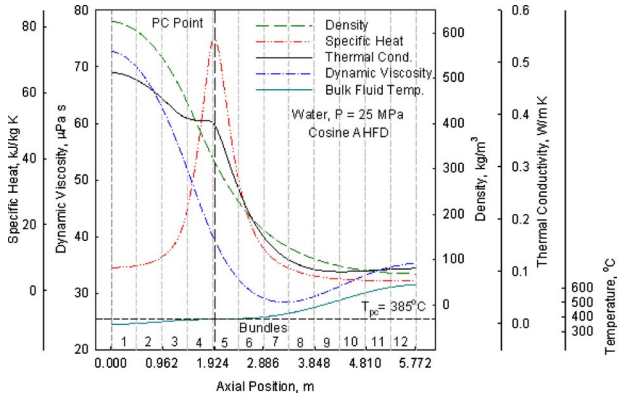


Fig. 9 Bulk-fluid temperature and thermophysical properties profiles for water along the heated length of the fuel channel

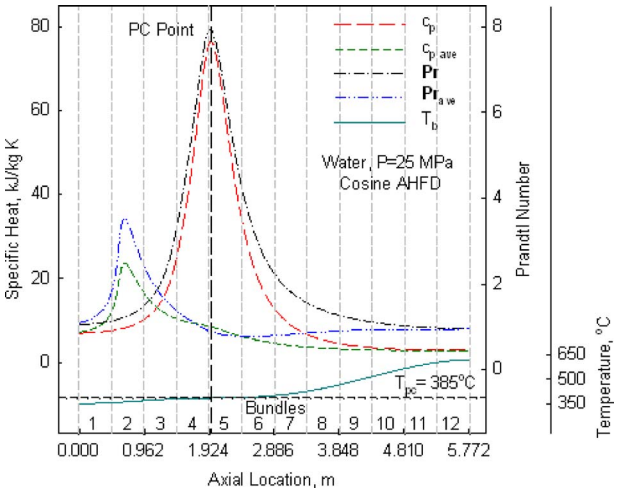


Fig. 10 Prandtl number and specific heat profiles for water along the heated length of the fuel channel

It is well established that thermophysical properties of any fluid including water experience significant changes within critical and pseudocritical regions (for details, see Ref. [1]). In this paper, the coolant pressure used in the calculations is 25 MPa, and thus the *pseudocritical temperature*, which corresponds to this pressure, is 384.9°C. The NIST REFPROP [5] software was used to determine values of the thermophysical properties based on a pressure and bulk-fluid temperature. The bulk-fluid temperature was calculated based on the method of heat balances.

A comparison of selected thermophysical properties profiles for water along the fuel channel heated length at the nonuniform cosine AHFD are shown in Figs. 9 and 10. The following bulk-fluid thermophysical properties were calculated: (*a*) density, (*b*) specific heat, (*c*) thermal conductivity, (*d*) dynamic viscosity, and Prandtl number. In addition to the regular bulk-fluid properties, the cross-section average specific heat and the corresponding average Prandtl number, which are used in various supercritical heat-transfer correlations (for details, see Ref. [1]), were shown in Fig. 10 for comparison purposes.

Figures 9 and 10 show that the pseudocritical region occurs within Bundles 4 and 5. It can be observed in Fig. 9 that in general, properties such as density, thermal conductivity, and dynamic viscosity undergo a significant drop along the heated channel. Dynamic viscosity has a minimum value within Bundles 7 and 8, beyond which, it is slightly increasing. The specific heat, Prandtl number, and thermal conductivity all have peaks near the pseudocritical point.

The cross section average specific heat and Prandtl number (see Fig. 10 and their definitions as listed in the Nomenclature) have significantly lower peaks compared to those based on the bulk-fluid temperature only, which are shifted upstream of the pseudocritical point.

References

[1] Pioro, I. L., and Duffey, R. B., 2007, *Heat Transfer and Hydraulic Resistance at Supercritical Pressures in Power Engineering Applications*, ASME, New York, NY.

[2] Gopaul, S., Hopps, V., Jacobs, Ch., Khan, M., Patkunam, R., and Pioro, I. L., 2007, "Some Design Features of SCW Pressure-Tube Nuclear Reactor," *Proceedings of the 15th International Conference on Nuclear Engineering*, ICONE15-10829, Nagoya, Japan, Apr. 22–26.

[3] Duffey, R. B., Pioro, I. L., and Kuran, S., 2008, "Advanced Concepts for Pressure-Channel Reactors: Modularity, Performance and Safety," JSME J. of Power and Energy Systems, **2**(1).

[4] Duffey, R. B., and Pioro, I. L., 2006, "Advanced High Temperature Concepts for Pressure-Tube Reactors, Including Co-Generation and Sustainability," *Proceedings of the 3rd International Topical Meeting on High Temperature Reactor Technology*, Johannesburg, South Africa, Oct. 1–4.

[5] Lemmon, E. W., McLinden, M. O., and Huber, M. L., 2000, NIST Reference Fluid Thermodynamic and Transport Properties—REFPROP, NIST Standard Reference Database 23, Ver. 7.0, National Institute of Standards and Technology, Department of Commerce, Boulder, CO.

[6] Hwang, D. H., Seo, K. W., and Lee, C. C., 2006, "Critical Heat Flux in Square- and Nonsquare-Array Rod Bundles for Advanced Light Water Reactors," Nucl. Technol., **158**, pp. 219–228.

Downloaded 02 Jun 2010 to 171.66.16.109. Redistribution subject to ASME license or copyright; see http://www.asme.org/terms/Terms_Use.cfm

Effect of Hydrated Salt Additives on Film Boiling Behavior at Vapor Film Collapse

Takahiro Arai
e-mail: t-araj@criepi.denken.or.jp

Masahiro Furuya

Nuclear Technology Research Laboratory,
Central Research Institute of Electric Power Industry,
2-11-1, Iwado Kita, Komae-shi,
Tokyo 201-8511, Japan

A high-temperature stainless steel sphere was immersed into various salt solutions to investigate film boiling behavior at vapor film collapse. The film boiling behavior around the sphere was observed with a high-speed digital-video camera. Because the salt additives enhance the condensation heat transfer, the observed vapor film was thinner. The surface temperature of the sphere was measured. Salt additives increased the quenching (vapor film collapse) temperature because the frequency of direct contact between the sphere surface and the coolant increased. Quenching temperature increases with increased salt concentration. The quenching temperature, however, approaches a constant value when the salt concentration is close to its saturation concentration. The quenching temperature is well correlated with ion molar concentration, which is a number density of ions, regardless of the type of hydrated salts. [DOI: 10.1115/1.2983056]

Keywords: vapor film, hydrated salt, film boiling, quenching temperature

1 Introduction

In recent years, amorphous metals are widely used in the fields of semiconductors, magnetic materials, and metal materials. Amorphous metals are metals with atoms in an irregular array. They have outstanding characteristics such as high toughness, corrosion resistance, and soft magnetism.

The authors have proposed a rapid cooling and liquid atomizing process called the cooling and atomizing based on noble process utilizing steam explosion (CANOPUS) method. The CANOPUS method uses a sustainable small-scale vapor explosion. The cooling rate is up to 1.5×10^8 K/s, more than 280 times faster than that of conventional methods. The CANOPUS method should lead to the production of new functional amorphous metals.

Vapor explosions have been considered industrial accidents in fields such as nuclear power, metallurgy, and the paper industry. A great deal of experimental and theoretical researches has therefore been conducted since the 1960s in order to predict and prevent vapor explosions. A large-scale vapor explosion is generally considered to involve the following four stages [1].

Figure 1 shows a schematic of the basic process of a large-scale vapor explosion. A high-temperature liquid, such as molten metal, is dispersed into a low-temperature volatile liquid such as water. A vapor film separates these two liquids (premixing). The vapor film destabilizes spontaneously or because of an outside trigger, the high-temperature liquid directly contacts the low-temperature liquid, and a pressure wave is generated (triggering). The pressure wave propagates to the entire premixing region, contributing to rapid heat transfer, vapor generation, and fragmentation of the high-temperature liquid (propagation). Expansion of the high-pressure region causes the release of kinetic energy (expansion).

Figure 2 shows a schematic of the triggering process of vapor explosions. A vapor film covers a molten metal droplet. The vapor film collapses due to some cause. When spontaneous nucleation on the liquid-liquid contact interface occurs, the interface becomes unstable leading to the atomization of the molten metal. A new contact interface forms and spontaneous nucleation reoccurs, creating positive feedback [2].

Manuscript received July 14, 2008; final manuscript received July 28, 2008; published online October 1, 2008. Review conducted by Dilip R. Ballal. Paper presented at the 16th International Conference on Nuclear Engineering (ICONE16), Oriando, FL, May 12–15, 2008.

Most practical metals have a relatively high melting point. In order to generate vapor explosions, it is therefore necessary to collapse a vapor film at high-temperature. There are two ways to facilitate vapor film collapses: application of mechanical external force or enhancement of condensation heat transfer. This research concentrated on the latter method of promoting vapor film collapse. Experiments have been conducted with metal wires and spheres [3–8] to investigate facilitation of vapor film collapse at high-temperature. Experimentation has found that adding hydrated salt to water raises the temperature at which vapor film collapses. Most of these experiments, however, used $CaCl_2$ or NaCl, knowledge of other hydrated salts is limited. Furthermore, there is insufficient knowledge regarding the detailed mechanism of vapor film collapse in a high degree of superheat.

This study clarifies the mechanism of vapor film collapse and quantitatively evaluates the effects of types and concentrations of hydrated salt additives.

2 Vapor Film Collapse Experiments

2.1 Experimental Apparatus and Procedure. Figure 3 depicts the experimental apparatus. The current experimental apparatus and procedure are the same as in the previous report [9]. In order to improve the controllability and homogeneity of the coolant pool temperature, the conventional sheathed heater was replaced with a hot stirrer. The apparatus consists of a heating furnace and a coolant pool. The heating furnace is a cylindrical electric furnace of 40 mm in internal diameter. A solid sphere of type 304 stainless steel is air-heated in the electric furnace. *K*-type grounded sheathed thermocouples are inserted into the center of the test sphere. These thermocouples are used to hold the sphere. The test sphere is raised and lowered by a motor located at the top of the electric furnace.

Figure 4 shows a detailed view of the stainless steel sphere. The stainless steel test sphere is 30 mm in diameter. In order to measure the surface temperature of the stainless steel sphere, *K*-type grounded sheathed thermocouples are inserted into the center of the sphere. The sheathed thermocouples are 1.6 mm in diameter. The time constant of the thermocouple is about 0.1 s. The tips of the thermocouples are TIG welded to the bottom surface of the sphere. The welding points are buffed to minimize irregularities so they will not become bubble nucleuses that could affect the vapor film collapse. The thermocouples inserted into the sphere

Copyright © 2009 by ASME

Downloaded 02 Jun 2010 to 171.66.16.109. Redistribution subject to ASME license or copyright; see http://www.asme.org/terms/Terms_Use.cfm

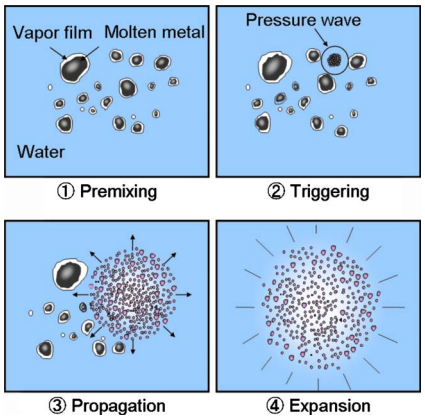


Fig. 1 Schematic of the basic process on a large scale vapor explosion

are also used to control the location of the sphere. The data logger (Graphtec Co., Ltd., GL400) is used to measure the surface temperature of the sphere. The measuring interval is set to 0.1 s. The *K*-type grounded sheathed thermocouples are JIS Class 1. The tolerance is ±0.4% of the measurement temperature. The measurement error of the GL400 data logger is ±(0.05% +1.5°C) of reading. Therefore, the measuring error of the surface temperature of the sphere is a maximum of ±3.7 K.

The experimental procedure was as follows. First, the stainless steel sphere was heated in the electric furnace. After the sphere was kept at a specific temperature, the sphere was slowly immersed into the coolant by motorized equipment. The surface temperature of the sphere was measured by thermocouples inserted into it. The boiling behavior around the sphere was observed with a digital-video camera (Panasonic Co. SDR-S100). The test section was illuminated by metal halide lights (Sumita Optical Glass Company, LS-M250). The digital-video camera had a frame rate of 30 frames per second with a shutter speed of 1/8000 s.

The immersion depth of the sphere was 15 mm, one-half the sphere's diameter. In order to maintain the purity of the sphere's

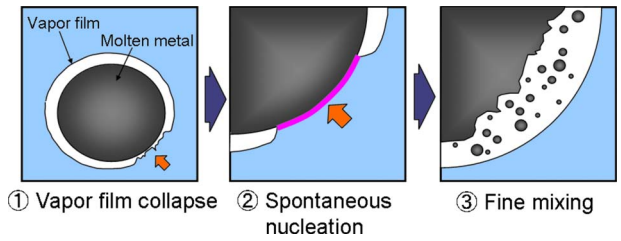


Fig. 2 Schematic of the triggering process on vapor explosion

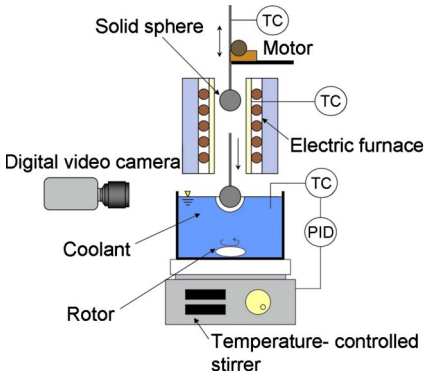


Fig. 3 Schematic of experimental apparatus

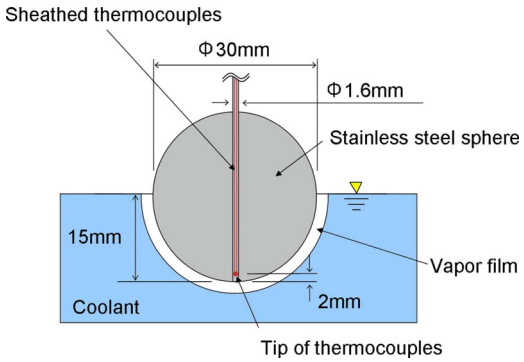


Fig. 4 Schematic of the stainless steel sphere

surface condition, it was degreased with ethanol before the experiment. The sphere was replaced for every experiment.

2.2 Experimental Conditions. Table 1 shows the experimental conditions. The experimental parameters are solute and concentration of solution. The initial temperature of the stainless steel sphere, the initial temperature of the coolant, and the immersion depth of the sphere are constant. In order to minimize oxidation, the initial temperature of the sphere was 800°C.

The thermodynamic properties among the salt solutions are not significantly different with that of water. For instance 30 wt % calcium chloride aqueous solution has higher boiling point by 6 K and smaller thermal conductivity by 7%.

2.3 Measurement of Vapor Film Thickness. In order to quantitatively evaluate vapor film behavior during film boiling, a vapor film thickness was calculated using image-processing of a series of observation images in which the vapor film around the sphere was observed with a high-speed digital-video camera.

Figure 5 shows the result of the image-processing. The image-processing procedure is as follows. First, the stainless steel sphere and the background are removed from the original images, and the images are digitized so that only the vapor film remains. Finally, the vapor film thickness is estimated as the average thickness across approximately 120 deg at the bottom of the sphere.

When the behavior of the vapor film is observed, two factors affecting the measurement of the vapor film thickness are considered. They are oscillation of the sphere and axial fluctuation of the sphere. In order to control oscillation of the sphere, sheathed thermocouples that support the sphere were fixed above the pool after immersion. Fluctuation of the sphere is produced by thermal expansion of the support rods. The relative displacement by thermal expansion was measured before the experiment in order to compensate.

2.4 Experimental Results and Discussion. Figure 6 shows a series of observation images in which the stainless steel sphere at 700°C was immersed into water with 20 wt % $CaCl_2$ solution. The time when the surface temperature of the sphere reached 800°C is 0.0 s. Coolant temperature was 80°C.

In the case of water, Image A at 0.00 s shows that a vapor film

Table 1 Experimental conditions

Solute	$CaCl_2$, LiCl, NaCl $MgCl_2$, KCl, $LiNO_3$, $NaNO_3$, Li_2SO_4, $MgSO_4$
Concentration of solution (wt %)	0, 10, 20, 30, 40
Initial temperature of coolant	80°C
Initial temperature of stainless steel sphere	700°C
Immersion depth	0.5D (=15 mm)

Downloaded 02 Jun 2010 to 171.66.16.109. Redistribution subject to ASME license or copyright; see http://www.asme.org/terms/Terms_Use.cfm

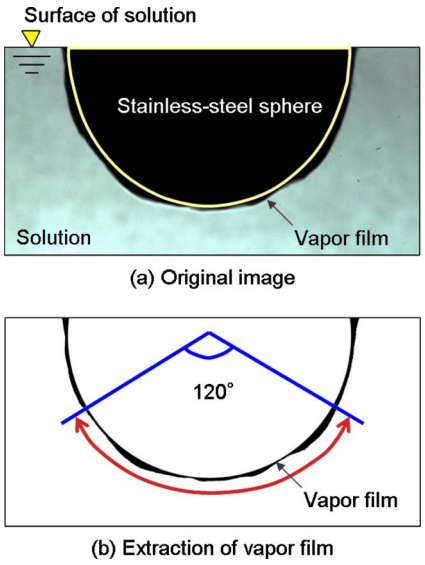


Fig. 5 Extraction of vapor film with image-processing

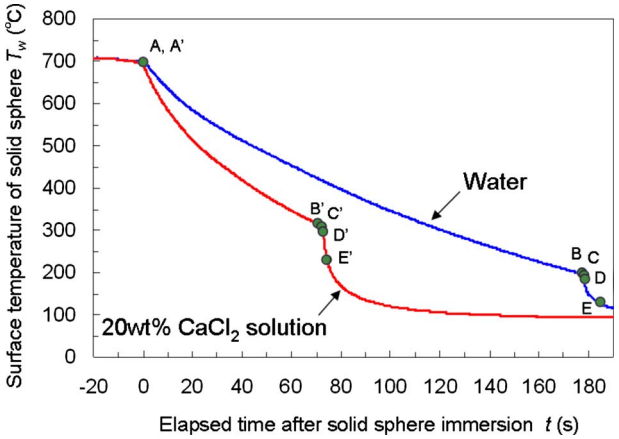


Fig. 7 Effect of hydrated salt on quenching curve

stably formed around the sphere. Because a large amount of vapor was generated locally, however, the surface of the vapor film oscillated. Image B at 178.27 s confirms the formation of a stable vapor film. Although there is oscillation, the fluctuation amplitude of the vapor film surface decreased along with the surface temperature of the sphere. Image C at 178.30 s shows the beginning of vapor film collapse. Image D at 178.39 s shows that the vapor film collapse propagating across the sphere and numerous vapor bubbles forming. Image E at 180.00 s shows nucleate boiling around the sphere. The quenching temperature is defined as the surface temperature of the sphere at which temperature begins rapidly decreasing. The quenching temperature was 194°C when water was the coolant.

In the case of 20 wt % $CaCl_2$ solution, a vapor film stably formed around the sphere from Image A′ at 0.00 s to Image B′ at 72.67 s. Compared with water, however, the vapor film was thin, with a smaller fluctuation amplitude of the vapor film surface. Vapor film collapse was much faster than with water beginning at 72.70 s, as shown in Image C′. The vapor film began to collapse and propagate to the entire lower hemisphere. The quenching temperature was 308°C. Image D′ at 72.73 s shows that the vapor film expanded due to rapid generation of a large amount of vapor. Image E at 74.00 s shows nucleate boiling around the sphere. When the film boiling state transitioned to a nucleate boiling state, the minute vapor bubbles separated from the surface of the sphere, and the $CaCl_2$ solution became cloudy.

Figure 7 shows the cooling curves of the stainless steel sphere. After the surface temperature of the sphere was maintained at about 700°C, the sphere was immersed into a coolant, with 0.0 s as the time when the temperature of the stainless steel sphere reached 700°C. Each line represents water case and 20 wt % $CaCl_2$ solution case. The surface temperature of the sphere at vapor film collapse—the so-called quenching temperature—is defined as an intersection of the cooling curves of a film boiling state and a nucleate boiling state.

In the case of water, after the sphere was immersed into water, it cooled relatively slowly, maintaining a film boiling state. Although the cooling rate was 9.0 K/s just after immersion, it decreased to 1.5 K/s immediately before vapor film collapse. Vapor film collapse began at 178.30 s, and the quenching temperature was 194°C. After vapor film collapse, the boiling state shifted to nucleate boiling from transition boiling, and the surface temperature of the sphere descended rapidly.

In the case of 20 wt % $CaCl_2$ solution, as with water, after immersion, the sphere cooled slowly while maintaining a film boiling state. Although the cooling rate was 13.0 K/s just after immersion, it decreased to 2.6 K/s just before vapor film collapse. The cooling rate in the case of $CaCl_2$ solution was about 1.5 times as fast as with water. Vapor film collapse began at 72.70 s, and the

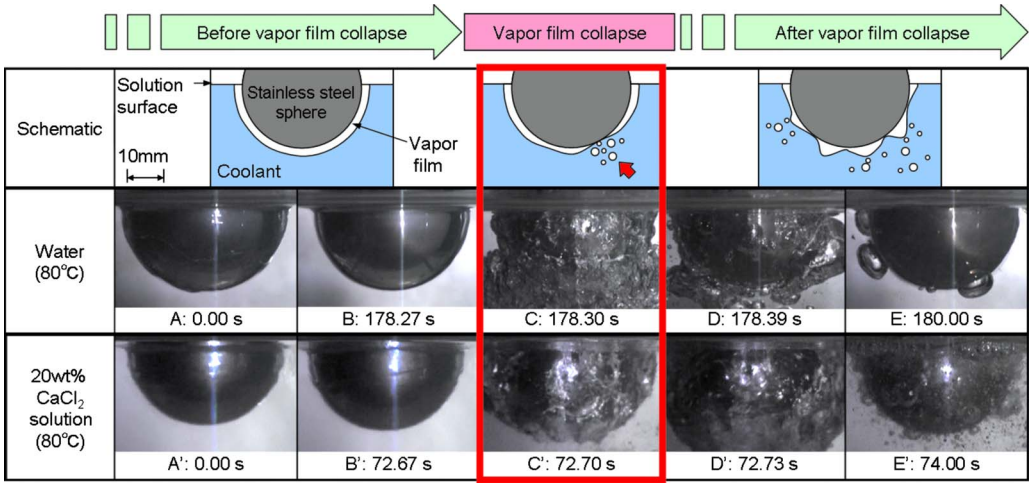


Fig. 6 Effect of salt additives on vapor film collapse

Downloaded 02 Jun 2010 to 171.66.16.109. Redistribution subject to ASME license or copyright; see http://www.asme.org/terms/Terms_Use.cfm

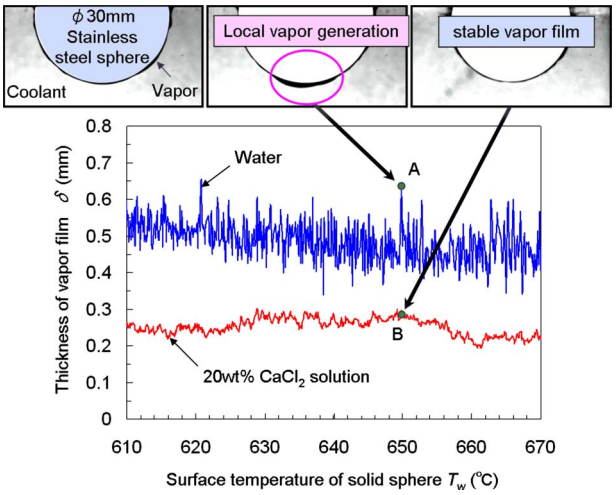


Fig. 8 Effect of salt additives on vapor film collapse

quenching temperature was 308°C. The surface temperature of the sphere subsequently fell rapidly while the boiling state shifted from transition boiling to nucleate boiling.

Based on the above visual observation results and cooling curves, the addition of hydrated salt additives improves film boiling heat transfer and increases quenching temperature. In order to evaluate differences in the process from film boiling to quenching, the behavior of the vapor film was observed with a high-speed digital-video camera. As shown in Fig. 7, the film boiling state was stable in both water and 20 wt % $CaCl_2$ solution at 610–670°C. Image-processing was applied to the images obtained to estimate vapor film thickness and evaluate it over time.

Figure 8 shows the vapor film thickness on a superheated surface. In the case of water, a large amount of vapor was locally generated in various locations on the sphere's surface. The fluctuation amplitude of the vapor film surface was large, and the average vapor film thickness was about 0.5 mm. Point A indicates typical vapor film behavior, showing maximum vapor film thickness. Vapor was generated locally in large quantities and vapor film thickness increased. Since vapor moved toward the water surface through the inside of the vapor film, fluctuation of the vapor film surface propagated toward the water surface. In the case of 20 wt % $CaCl_2$ solution, the average of the vapor film thickness was relatively thin. Point B shows typical vapor film behavior. The thickness of the vapor film was seldom changed and the fluctuation amplitude of the vapor film surface was very small compared with water.

Figure 9 shows the boiling curves of the sphere derived from

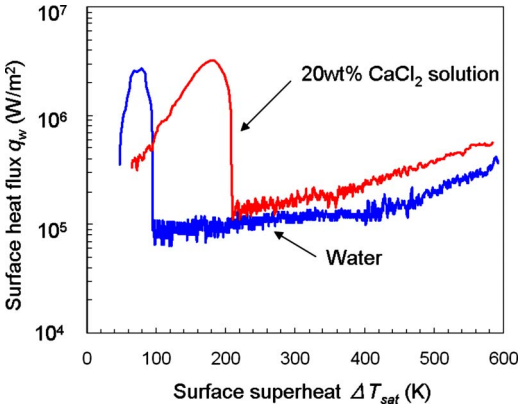


Fig. 9 Effect of hydrated salt on boiling curve

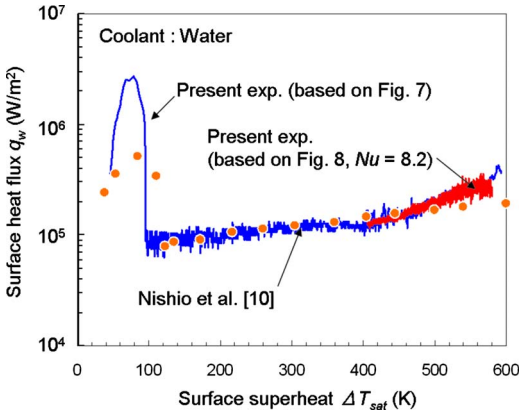


Fig. 10 Comparison of boiling curves

the cooling curves shown in Fig. 7. The influence of a measuring noise was removed by taking the moving average of every two points. A film boiling state formed in the superheat range of 500 K and above. Surface heat flux decreased as surface superheat became smaller. Vapor film collapsed near the minimum heat flux point. The surface heat flux rapidly increases when the sphere surface directly contacts a coolant. The boiling state shifted to nucleate boiling through transition boiling. The 20 wt % $CaCl_2$ solution showed similar trends, but both of the surface heat flux during film boiling and the maximum heat flux were larger than with water.

Figure 10 shows a comparison of the boiling curves in the present experiments and the existing previous of Nishio and Vemura [10] when the coolant is water. In terms of the present experiments, there are two boiling curves. The first is derived from the cooling curve shown in Fig. 7. In order to estimate the boiling curve, the experimental system was approximated as a lumped parameter system. The second is estimated by the vapor film thickness shown in Fig. 8.

To estimate surface heat flux based on vapor film thickness, it was assumed that a vapor flow inside the vapor film was a natural convection in a laminar flow zone. Surface heat flux was estimated using the following equation.

$$q_w = \frac{Nu\lambda(T_w - T_{\mathrm{sat}})}{\delta} + \varepsilon\sigma(T_w^4 - T_{\mathrm{sat}}^4) \tag{1}$$

Nusselt number was calculated using the equation of Fujii et al. [11], which was the average heat transfer of a natural convection in laminar flow around a sphere with uniform temperature. When the surface temperature of the sphere was 600°C, Nusselt number was 8.2. Emissivity of the sphere was 0.5. The surface heat flux during film boiling based on the vapor film thickness was in good agreement with that based on the cooling curve.

Comparing the experimental data obtained by the cooling curve of the sphere and existing data from Nishio and Vemura [10], the surface heat flux in the film boiling regime coincide with each other to a certain degree. In contrast to this, the maximum heat flux in the present experiments is higher than that in their experiments though the thermal conductivity of platinum is three times larger than that of the stainless steel. The primary factor of the difference seems to be the location of the thermocouples tip. In the present experiments, the tip of the thermocouples was embedded near the surface of the stainless steel sphere. In the experiments of Nishio and Vemura, the tip of the thermocouples was embedded in the center of the platinum sphere. The closer tip of the thermocouples to a sphere surface is embedded, the larger maximum heat flux is measured.

In order to evaluate condensation characteristics of the vapor film surface during a film boiling state in hydrated salt solutions, condensation heat transfer rate was estimated using surface heat

Downloaded 02 Jun 2010 to 171.66.16.109. Redistribution subject to ASME license or copyright; see http://www.asme.org/terms/Terms_Use.cfm

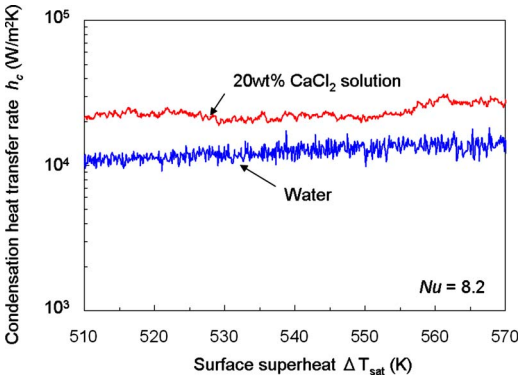


Fig. 11 Effect of hydrated salt on condensation heat transfer rate

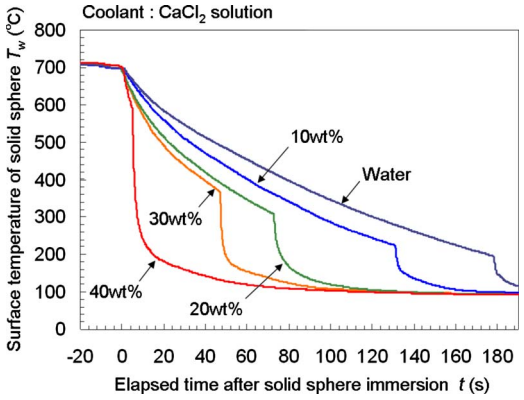


Fig. 12 Effect of solution concentration on quenching curve

flux based on the vapor film thickness shown in Fig. 10.

Figure 11 shows the condensation heat transfer rate to surface superheat. As the degree of superheat decreased, the condensation heat transfer rate also decreased. The condensation heat transfer rate in the superheat range of 510–570 K was 3.5×10^3–4.5×10^3 W/m^2/K with water and 6.3×10^3–8.0×10^3 W/m^2/K with 20 wt % $CaCl_2$ solution. The condensation heat transfer rate was improved twice when hydrated salt was added to water.

The present experimental system is similar to that of natural convection heat transfer from a vapor film surface to water. When the condensation heat transfer rate is estimated using the equation of Fujii et al., which indicates the average heat transfer rate of natural convection in a laminar flow around a sphere, the result was about 10^4 W/m^2/K. There is also another existing knowledge regarding the condensation heat transfer rate during direct contact condensation between a vapor bubble and water. According to condensation experiments with single vapor bubbles by Kamei and Hirata [12], the condensation heat transfer rate is 10^4 W/m^2/K. In other experimental results regarding the condensation of vapor bubbles, the condensation heat transfer rate is about 10^4–10^5 W/m^2/K. Therefore, the condensation heat transfer rate of the present experiments gave close agreement with the existing experiments.

The following conclusions were obtained based on the above experimental results. Adding hydrated salt decreases fluctuation of the vapor film surface and causes formation of a thin vapor film. As the amount of vapor generation decreases, the amount of vapor that moves toward the water surface through the inside of the vapor film also decreases. Vapor film thickness also decreases. Since there are smaller amounts of vapor to form a film boiling state, both film boiling heat transfer and condensation heat transfer on the interface between vapor and coolant is improved. When the film boiling vapor film becomes thinner, the frequency with which the sphere directly contacts with the coolant increases, and the vapor film collapses at a higher sphere temperature.

Next, we discuss the effects of solution concentrations types of hydrated salt. Figure 12 depicts the cooling curves of water, 10 wt % $CaCl_2$ solution, 20 wt % $CaCl_2$ solution, and 30 wt % $CaCl_2$ solution. The time when the sphere is immersed into the solution is 0.0 s, and the temperature of the sphere at 0.0 s is 700°C. The temperature of the sphere descended by 9.0 K/s immediately after immersion. Just before the vapor film collapsed, the cooling rate decreased to 1.5 K/s. Vapor film collapse began at 178.3 s, and the quenching temperature was 194°C. In the case of 10 wt % $CaCl_2$ solution, the surface temperature of the sphere began to decrease at 10.0 K/s, keeping the film boiling. The cooling rate fell to 1.8 K/s just before vapor film collapse. The vapor film collapsed at 131.1 s, and the quenching temperature was 220°C. In the case of 20 wt % $CaCl_2$ solution, the surface temperature of the sphere began to fall at 12.8 K/s, maintaining film boiling. The cooling rate fell to 2.4 K/s just before vapor film collapse. The vapor film collapsed at 72.7 s, and the quenching temperature was 308°C. In the case of 30 wt % $CaCl_2$ solution, the surface temperature of the sphere began to fall at 20.4 K/s, maintaining film boiling. The cooling rate fell to 3.8 K/s just before vapor film collapse. The vapor film collapsed at 47.0 s, and the quenching temperature was 368°C. In the case of 40 wt % $CaCl_2$ solution, the surface temperature of the sphere began to decrease at 31.0 K/s, maintaining film boiling. The cooling rate fell to 18.2 K/s just before vapor film collapse. The vapor film collapsed at 4.9 s, and the quenching temperature was 588°C. As solution concentration, increased the film boiling heat transfer improved and the quenching temperature increased. Other hydrated salts also displayed a similar tendency. When solubility is low, however, quenching temperature has difficulty increasing as solution concentration nears saturation. When a solution concentration has a sufficient margin until saturation, quenching temperature increases with an increase in solution concentration. In order to collapse vapor films at higher temperatures, it is necessary to use hydrated salts with high solubility.

In order to evaluate the effect of each salt on quenching temperature, hydrated salts were classified by type of anion and cation.

Figure 13 shows the quenching temperature of ion mole concentrations for each anion of hydrated salts. Figure 14 shows quenching temperature to ion molar concentration for each cation of hydrated salt. Ion molar concentration was defined as a product of the volume mole-concentration of solution and the total number of valence electrons. The quenching temperature correlates positively with the ion molar concentration. The results indicate that only the ion molar concentration contributes to the quenching temperature regardless of the type of hydrated salts.

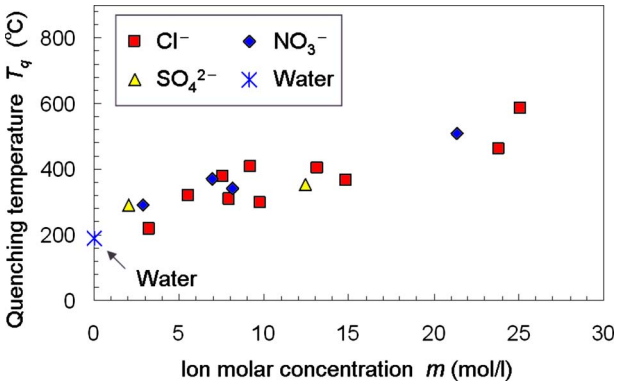


Fig. 13 Effect of anion on quenching temperature

Downloaded 02 Jun 2010 to 171.66.16.109. Redistribution subject to ASME license or copyright; see http://www.asme.org/terms/Terms_Use.cfm

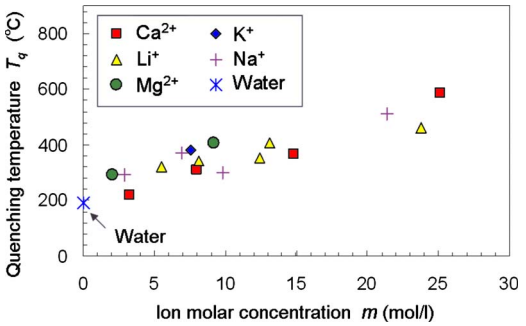


Fig. 14 Effect of cation on quenching temperature

3 Conclusion

The vapor film collapse experiments were conducted to clarify the mechanism by which vapor films collapse at higher temperature by adding hydrated salt into water. A high-temperature stainless steel sphere was immersed into a hydrated salt solution pool. The cooling curve of the sphere was measured, and the behavior of film boiling was observed with a high-speed digital-video camera to evaluate vapor film thickness using image-processing. The conclusions obtained are as follows.

(1) Measurement of the surface temperature of the sphere and observation image of film boiling behavior suggest that hydrated salt additions enhanced condensation heat transfer. Enhanced condensation heat transfer made the vapor film thinner. Without the salt addition, vapor bubbles were generated and moved toward the pool surface through the vapor layer. The vapor layer fluctuated due to an insufficient condensation heat transfer rate.
(2) Evaluation of vapor film thickness using image-processing suggests that the hydrated salt additions made the vapor film during film boiling thin. When the vapor film became thin, direct-contact frequency between the sphere and the solution increased and quenching temperature also increased.
(3) Quenching temperature increases with increased salt concentration. When solubility is low, however, quenching temperature has difficulty increasing as solution concentration nears saturation.
(4) Quenching temperature is well correlated with ion molar concentration, which is a number density of ions, regardless of the type of hydrated salts.

Acknowledgment

The authors would like to thank Mr. Takeo Yoshioka and Mr. Yoshihiro Saito of CERES Inc. and Mr. Hirokazu Kamata and Mr. Kunihiko Nishiyama of Electric Power Engineering Systems Co., Ltd., for their assistance with these experiments.

Nomenclature

D = diameter of stainless steel sphere (mm)
h = heat transfer rate ($W/m^2/K$)
h_c = condensation heat transfer rate ($W/m^2/K$)
m = ion molar concentration (mol/l)
Nu = Nusselt number (-)
q_w = surface heat flux (W/m^2)
t = elapsed time after immersion of sphere (s)
T_{sat} = saturation temperature (°C)
T_q = quenching temperature (°C)
T_w = surface temperature of stainless steel sphere (°C)
x = weight percent concentration (wt %)
δ = vapor film thickness (mm)
ε = emissivity (-)
ΔT_{sat} = surface superheat (K)
λ = thermal conductivity (W/m/K)
σ = Stefan–Boltzmann constant ($W/m^2/K^4$)

References

[1] Furuya, M., 2002, "Development of Novel Rapid Cooling and Atomization Process Making the Best Use of Vapor Explosion Phenomenon," *Proceedings of the 12th International Heat Transfer Conference*, pp. 705–709.
[2] OECD/NEA, 1993, "Meeting Summary," *Proceedings of the CSNI Specialists Meeting on Fuel-Coolant Interactions*, NUREG/CP-0127, NEA/CSNI/R 98-8, MS-1-MS-11.
[3] Tagaya, M., and Tamura, I., 1952, "Studies on the Quenching Media (4th Report) The Cooling Abilities of Water and Aqueous Liquids," J. Jpn. Inst. Met., **B-16-2**, pp. 107–111. (in Japanese).
[4] Tagaya, M., and Tamura, I., 1952, "Studies on the Quenching Media (6th Report) Cooling Ability of Concentrated Salts Solutions," J. Jpn. Inst. Met., **B-16-2**, pp. 652–655.
[5] Ohnaka, I., Fukusako, T., Ohmichi, T., Masumoto, T., Inoue, A., and Hagiwara, M., 1981, "Production of Amorphous Filament by In-Rotating-Liquid Spinning Method," *Proceedings of the Fourth International Conference on Rapidly Quenched Metals*, pp. 31–34.
[6] Honda, H., Takamatsu, H., Yamashiro, H., and Matsuo, H., 1992, "Heat Transfer Characteristics During Rapid Quenching of Thin Platinum Wire," Trans. Jpn. Soc. Mech. Eng., Ser. B, **58–554**, pp. 3135–3140.
[7] Matsumura, K., Furuya, M., and Kaminaga, F., 2003, "Study on the Quenching Characteristics of Solid Sphere (Effect of Salt Additive to a Coolant)," *Proceedings of the 40th National Heat Transfer Symposium of Japan*, D143, pp. 139–140.
[8] Takigahira, Y., Sugiyama, K., and Ishikawa, M., 1997, "Spontaneous Vapor Explosion of Molten Materials in Salt Solutions," *Proceedings of the 5th International Conference on Nuclear Engineering (ICONE5)*, 2307, pp. 1–5.
[9] Arai, T., and Furuya, M., 2006, "Effect of Salt Additives to Water on the Triggering of Vapor Explosions and on the Collapse of Vapor Film," *Proceedings of the 12th International Symposium on Flow Visualization (ISFV12)*, pp. 1–10.
[10] Nishio, S., and Uemura, M., 1986, "Study on Film Boiling Heat Transfer and Minimum Heat Flux Condition for Subcooling Boiling," Trans. Jpn. Soc. Mech. Eng., Ser. B, **52–476**, pp. 1811–1816.
[11] Fujii, T., Honda, T., and Fujii, M., 1984, "A Numerical Analysis of Laminar Free Convection Around an Isothermal Sphere: Finite-Difference Solution of the Full Navier-Stokes and Energy Equations Betwen Concentric Spheres," Numer. Heat Transfer, **7**, pp. 103–111.
[12] Kamei, S., and Hirata, M., 1988, "Study on Condensation of a Single Vapor Bubble into Subcooled Water," Trans. Jpn. Soc. Mech. Eng., Ser. B, **54–53**, pp. 1791–179.

Downloaded 02 Jun 2010 to 171.66.16.109. Redistribution subject to ASME license or copyright; see http://www.asme.org/terms/Terms_Use.cfm

Effects of Surface Tension on Two-Phase Void Drift Between Triangle Tight Lattice Subchannels

Akimaro Kawahara
Michio Sadatomi
Tatsuya Higuchi

Department of Mechanical System Engineering,
Graduate School of Science and Technology,
Kumamoto University,
Kumamoto City 860-8555, Japan

In this study, void drift phenomena, which are one of three components of the intersubchannel fluid transfer, have been investigated experimentally and analytically. In the experiments, data on flow and void redistributions were obtained for hydraulically nonequilibrium flows in a multiple channel consisting of two subchannels simplifying a triangle tight lattice rod bundle. In order to know the effects of the reduced surface tension on the void drift, water and water with a surfactant were used as test liquids. In addition, data on the void diffusion coefficient, $\tilde{D}$, needed in a void drift model, have been obtained from the redistribution data. In the analysis, the flow and the void redistributions were predicted by a subchannel analysis code based on a one-dimensional two-fluid model. From a comparison between the experiment and the code prediction, the present analysis code was found to be valid against the present data if newly developed constitutive equations of wall and interfacial friction were incorporated in to the model to account for the reduced surface tension effects. [DOI: 10.1115/1.2983083]

Keywords: gas-liquid two-phase flow, tight lattice subchannel, void drift, surface tension

Introduction

As a next generation nuclear reactor, a high-conversion boiling water nuclear reactor (BWR) is being planned [1,2]. A higher conversion ratio will be realized by narrowing the flow area among the fuel rods in the reactor since the moderation of neutron decreases with the area. Thus, a triangle tight lattice array of the rods will be adopted for the fuel assembly, and the spacing between the rods will be narrowed to about 1 mm to get a conversion ratio higher than unity. In the development of such a reactor, an accurate prediction of critical power is essential because a deterioration of the cooling performance is apprehended compared with a conventional BWR fuel rod bundle. For predicting the critical power in a conventional BWR fuel rod bundle, a subchannel analysis code is usually used [3]: the use of the code in a tight lattice fuel rod bundle is under consideration [4]. In order to validate the code for such a bundle, experimental data, say [5], are necessary. However, the data are few especially on the intersubchannel fluid transfer, which is one of key parameters in the subchannel analysis.

In a gas-liquid two-phase flow system, the intersubchannel fluid transfer has been modeled as three independent components [3,6,7]: turbulent mixing, void drift, and diversion cross-flow. Therefore, an experimental program was performed at Kumamoto University for collecting the data on each fluid transfer component [8–13], using a vertical test channel that consisted of two subchannels simplifying a triangle tight lattice rod bundle. Following our previous study [8,9] on air-water flow redistribution due to the void drift, in the present study, the void drift phenomena in the same test channel were investigated experimentally and analytically. In the present experiment, in order to know the effects of the reduced surface tension on the void drift, experiments were conducted for both the air-water system and the air-water with a surfactant system in which the surface tension was about 0.6 times of that for the air-water system. Why the effects of reduced surface tension was studied is that the surface tension of steam water at a high-temperature and high-pressure in an actual rod bundle is much lower than that for the air-water system. In the analysis, a subchannel analysis code based on a one-dimensional two-fluid model was used to predict the flow redistribution. In the code, newly developed constitutive equations of wall and interfacial friction in the two-fluid model [13] were incorporated to take into account the reduced surface tension effects. The results of the experiments and the analysis have been presented in this paper.

Manuscript received July 18, 2008; final manuscript received July 18, 2008; published online October 2, 2008. Review conducted by Dilip R. Ballal. Paper presented at the 16th International Conference on Nuclear Engineering (ICONE16), Orlando, FL, May 12–15, 2008.

Experiment

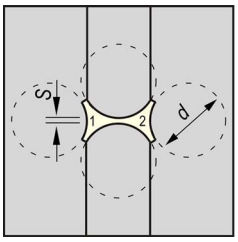
Method for Estimating Void Drift Phenomena. Figure 1 shows the cross section used in our previous [8–13]. The channel consisted of two identical subchannels, each surrounded by three partial rods in a triangular array. In order to get hydraulically smooth inner walls and to observe a flow, the test channel was machined from transparent acrylic slabs and polished quite well. No spacer was inserted in the channel.

Figure 2 shows an explanatory diagram of flow and pressure redistributions in a hydrodynamic equilibrium flow without pressure difference between subchannels [6,8]. This figure (*a*) illustrates the arrangement of the test channel, (*b*) illustrates the axial pressure profile in each subchannel, and (*c*) the axial profiles of volume flow rates of both phases in each subchannel. The channel can be divided into three sections from the bottom to the top: an entry section, a test section, and a discharge section. The cross-sectional shape of these sections is the same except for the gap portion. In the entry and the discharge sections, as seen in the left in Fig. 2, a 1 mm thick partition in the gap portion completely blocked the movement of the fluids between the subchannels. Intersubchannel fluid transfer thus could occur only in the test section.

In order to prevent the diversion of cross-flow due to a lateral pressure difference between the subchannels, the following two conditions were imposed.

Copyright © 2009 by ASME

Downloaded 02 Jun 2010 to 171.66.16.109. Redistribution subject to ASME license or copyright; see http://www.asme.org/terms/Terms_Use.cfm



Gap clearance: S = 1.0 mm
Rod diameter: d = 12.0 mm
Rod to rod pitch: p = 13.0 mm
Pitch/rod diameter: p/d = 1.083
Hydraulic diameter: D_h = 3.19 mm
Flow area of one subchannel: A_1 = 16.6 mm^2

Fig. 1 Cross section of the test channel

(I) In the entry section, the pressure gradient in each subchannel had to be the same, as shown in Fig. 2(*b*).

$$(dP/dZ)_1 = (dP/dZ)_2 \tag{1}$$

(II) At both the inlet and the outlet ends of the test section, the pressure had to be identical between the subchannels as time-averaged values.

$$P_1(0) = P_2(0), \quad P_1(Z) = P_2(Z) \tag{2}$$

In addition, the gas and the liquid flow rates in each subchannel at the inlet were set to be dissimilar to those for the equilibrium flow in order to obtain flow redistribution data due to the void drift, i.e., $\mathcal{Q}_{G1}(0) > \mathcal{Q}_{G1}(Z_{eq})$ and $\mathcal{Q}_{L1}(0) < \mathcal{Q}_{L1}(Z_{eq})$. Under a fixed condition of the above inlet flow rates, the outlet flow rates of both phases in each subchannel were measured by changing the communication length Z, the length of the test section, systematically from 0.11 m to 1.28 m. Thus, the data on the flow redistribution due to the void drift were obtained, as shown in Fig. 2(*c*). Of course, the turbulent mixing occurs even when the void drift takes place. However, the turbulent mixing induces neither net mass nor net volume exchanges between the subchannels [7,14,15].

Test Conditions. Air at room temperature and at near atmospheric pressure was used as the test gas, while water with a surfactant called polyoxyethylene laury ether (PLE for short) and water were the test liquids. Table 1 lists properties of the present test liquids at 20°C. PLE as used to study the effects of the reduced surface tension on the void drift phenomena. The table shows that the surface tension of PLE is about 60% of that of water, but the density and viscosity are almost the same between them.

Table 2 summarizes the experimental conditions. The data listed are the number of test runs, the ranges of the volumetric fluxes of the liquid, and the air for the whole channel, j_L and j_G, and the void fraction in the whole channel, α. Flow patterns observed were slug or churn flow and annular flow.

Table 1 Properties of test liquids at 20°C

Liquids	σ (N/m)	ρ (kg/m^3)	μ (mPa s)
Water	0.072	998.2	1.002
PLE	0.042	998.2	0.981

Experimental Results

Flow and Void Redistribution Data. Figures 3(*a*) and 4(*a*), respectively, show typical flow redistribution data on both gas and liquid phases for the slug or churn flow at j_L=1.0 m/s and j_G=6.0 m/s and the annular flow at j_L=0.2 m/s and j_G=20 m/s. The ordinate indicates the volume flow rate ratio of Ch. 1 to the whole channel in each phase, $\mathcal{Q}_{k1}/\mathcal{Q}_k$ (k=G for gas phase and k=L for a liquid one). The abscissa indicates the distance from the inlet of the test section, Z. In each figure, j_L and j_G are the volumetric fluxes of the liquid and the gas for the whole channel. Circular and triangular symbols indicate the experimental data of the gas and the liquid, respectively. Furthermore, open symbols represent the data for the air-water system, while solid symbols for the air-water with a surfactant system, i.e., air-PLE one. The points at Z=Z_{eq} indicate those in the equilibrium flow. The gas and the liquid data in Figs. 3(*a*) and 4(*a*) approach those in the equilibrium flow as going downstream irrespective of the liquid employed. This means that the net transfer of the gas and the liquid due to the void drift occurs between the subchannels in these experiments. No diversion cross-flow occurs in the present experiment because the time-averaged value of the pressure difference between the subchannels was set at zero.

Figures 3(*b*) and 4(*b*) show the axial variation data on the void fraction in each subchannel for the same flow conditions as those in Figs. 3(*a*) and 4(*a*). Diamond symbols correspond to Ch. 1 and square ones to Ch. 2. The void fraction in each subchannel at any axial point, $\alpha_1(Z)$ or $\alpha_2(Z)$, is evaluated through the following steps. (1) Volumetric fluxes of both phases in, say, Ch. 1, $j_{G1}(Z)$ and $j_{L1}(Z)$, were calculated by substituting the experimental data on the flow rate ratio, $\mathcal{Q}_{k1}(Z)/\mathcal{Q}_k$, into continuity equations for the respective phases. (2) The subchannel void fraction, $\alpha_1(Z)$, was calculated by substituting $j_{G1}(Z)$ and $j_{L1}(Z)$ into an empirical correlation. The correlation was based on the measured void fraction data with the well-known quick shut valve method for various air

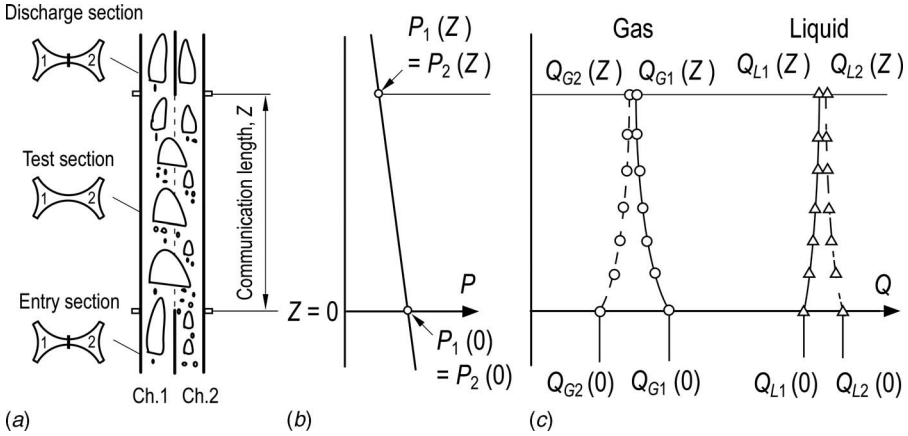


Fig. 2 Explanatory diagram of the experimental method for determining the flow redistribution due to void drift: (*a*) flow and channel arrangement, (*b*) pressure distributions, and (*c*) flow distributions

Downloaded 02 Jun 2010 to 171.66.16.109. Redistribution subject to ASME license or copyright; see http://www.asme.org/terms/Terms_Use.cfm

Table 2 Test conditions

Flow system	No. of runs	j_L (m/s)	J_G (m/s)	α
Air-water	18	0.1–2.0	0.75–20	0.35–0.84
Air-PLE	13	0.1–2.0	1.5–30	0.31–0.95

and liquid flow rates under hydraulically equilibrium flow conditions in the same channel [12]. The accuracy of the void fraction measurement was ± 0.03 as an averaged value (± 0.07 as a maximum value). From Figs. 3(*b*) and 4(*b*), the following can be seen.

- The void fraction difference between the subchannels approaches zero due to the void drift.
- The void fraction in each subchannel is higher for the air-PLE system than the air-water one because of the thinner liquid film around large gas bubbles and the gas core for the air-PLE system [12].

Void Diffusion Coefficient Data. In order to evaluate the net transfer of the gas phase mass flux from subchannel i to j due to the void drift, G_{Gij}, the following void settling model [3,16] has been widely used [4,17,18]:

$$G_{Gij} = \rho_G \tilde{D} \lfloor (\alpha_i - \alpha_j) - (\alpha_i - \alpha_j)_{\text{eq}} \rfloor / S_{ij} \tag{3}$$

Here, ρ_G is the gas phase density, $\tilde{D}$ is the void diffusion coefficient, which must be determined experimentally, $(\alpha_i - \alpha_j)$ is the void fraction difference between subchannels, and S_{ij} is the gap clearance between subchannels. The subscript eq denotes the hydrodynamic equilibrium state. For a channel consisting of identical subchannels, as seen in the present channel, Eq. (3) is reduced to

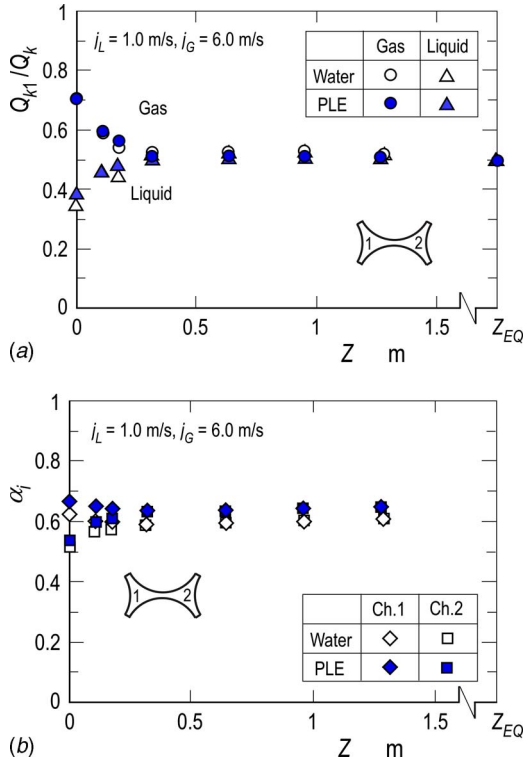


Fig. 3 Redistribution data for the slug or churn flow: (*a*) flow rate ratios for both phases and (*b*) the subchannel void fraction

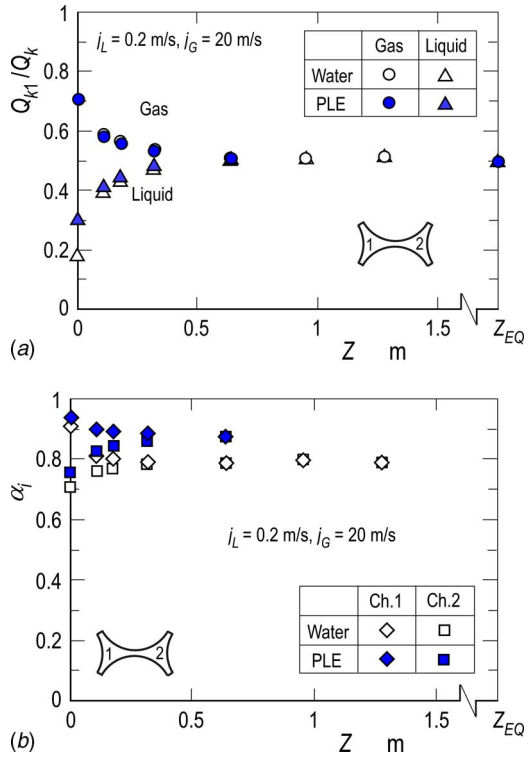


Fig. 4 Redistribution data for the annular flow: (*a*) flow rate ratios for both phases and (*b*) the subchannel void fraction

$$G_{Gij} = \rho_G \tilde{D} (\alpha_i - \alpha_j) / S_{ij} \tag{4}$$

since $(\alpha_i - \alpha_j)_{\text{eq}}$ must be zero. By fitting the axial redistribution data on the void fraction and flow rate of the gas phase into Eq. (4), we determined the void diffusion coefficient, $\tilde{D}$. Figure 5 shows the $\tilde{D}$ values determined from the present redistribution

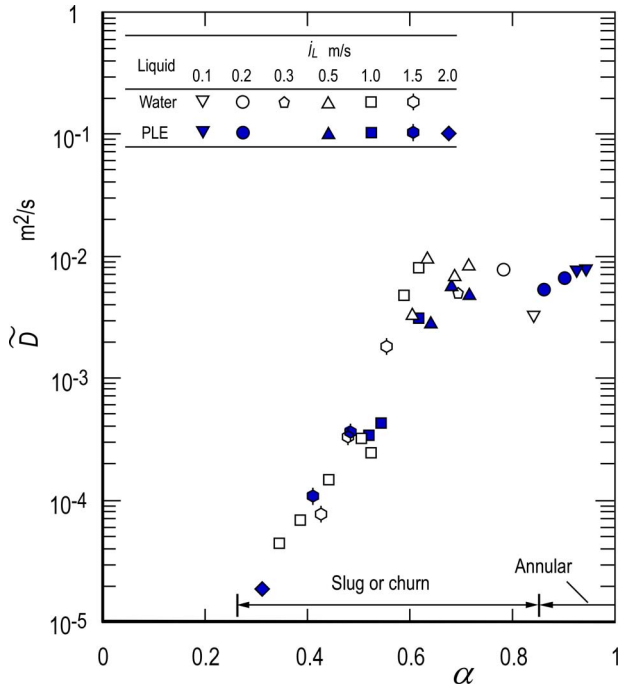


Fig. 5 Void diffusion coefficient data: effects of the surface tension

Downloaded 02 Jun 2010 to 171.66.16.109. Redistribution subject to ASME license or copyright; see http://www.asme.org/terms/Terms_Use.cfm

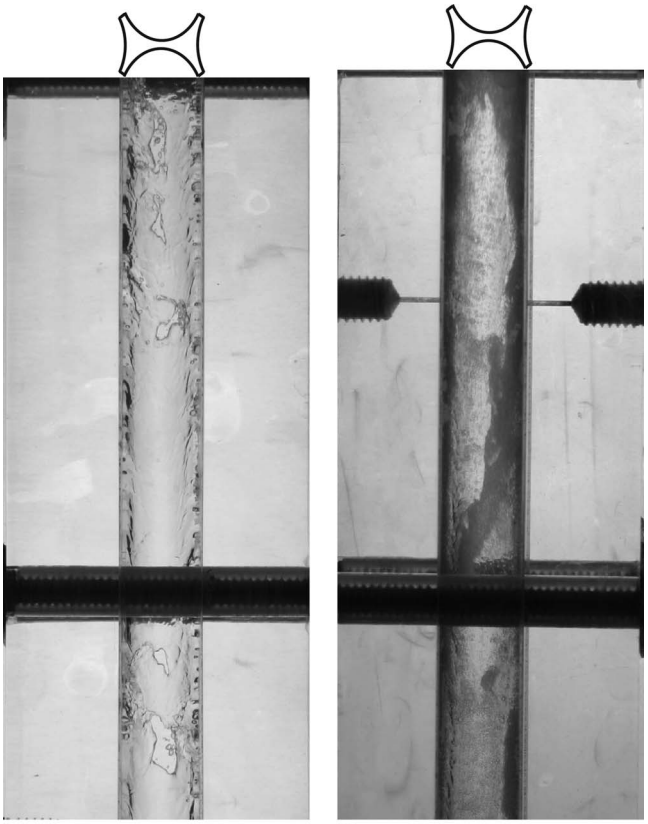


Fig. 6 Flow in the tight lattice subchannel under a flow condition of j_L=1.0 m/s and j_G=6.0 m/s: (*a*) air-water and (*b*) air-PLE

data for both air-water and air-PLE systems. The abscissa is the mean void fraction of the two subchannels, and the parameters are the liquid volumetric flux, j_L, and the liquid types. Data trend against the void fraction are similar between the air-water and the air-PLE systems. That is, the void diffusion coefficient increases exponentially with the void fraction of up to $\alpha=0.7$ and is nearly constant or increases a little with the void fraction in $\alpha>0.7$. As for the surface tension effects, we can see that the void diffusion coefficient is a little smaller for the air-PLE system than the air-water one in $0.5<\alpha<0.7$. As seen in Fig. 6, the bubbles in the liquid phase became smaller and more for the air-PLE system than the air-water system due to the reduced surface tension effects. These smaller bubbles are considered to be difficult to move from one subchannel to the other, thus the void diffusion coefficient became smaller for the air-PLE system than the air-water one.

Analysis

The present analysis code was developed in order to predict flow redistribution phenomena due to the void drift in a vertical multiple channel consisting of two subchannels. For the development, the following assumptions were made by accounting for the experimental conditions.

(1) The flow in each subchannel is a one-dimensional steady state adiabatic two-component two-phase flow.
(2) The flow is a hydraulically nonequilibrium two-phase flow without pressure difference between the subchannels as a time-averaged value. In such a flow, the void drift and the turbulent mixing are independently coexistent [7].
(3) The cross-sectional area of each subchannel is uniform along the channel axis.

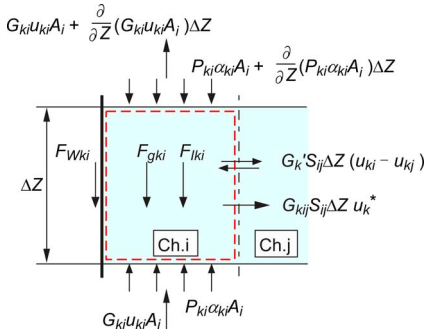


Fig. 7 Control volume for deriving an axial momentum equation based on the two-fluid model

Basic Equations. The basic equations are based on a two-fluid model [19] and are conservation equations for mass and momentum in the axial direction in subchannel-*i* (Ch. *i*) and subchannel-*j*.

The mass conservation equations for Ch. *i* and Ch. *j* are expressed by

$$\frac{\partial G_{ki}}{\partial Z} + \frac{G_{kij}S_{ij}}{A_i} = 0 \tag{5}$$

and

$$\frac{\partial G_{kj}}{\partial Z} - \frac{G_{kij}S_{ij}}{A_j} = 0 \tag{6}$$

Here, G_{ki} and A_i are, respectively, the mass flux of the k-phase and flow area for Ch. i, G_{kij} is the lateral mass flux due to the void drift from Ch. i to Ch. j, and S_{ij} is the gap clearance between the subchannels.

The axial momentum conservation equation in Ch. i was derived for the control volume shown in Fig. 7. The results for Ch. i and Ch. j are as follows:

$$\frac{dP_{ki}}{dZ} = -\frac{1}{\alpha_{ki}}\left[(F_{Wki} + F_{gki} + F_{Iki}) + \frac{S_{ij}}{A_i}\{G_k'(u_{ki} - u_{kj}) + G_{kij}u_k^*\} + \frac{d}{dZ}(G_{ki}u_{ki})\right] \tag{7}$$

$$\frac{dP_{kj}}{dZ} = -\frac{1}{\alpha_{kj}}\left[(F_{Wkj} + F_{gkj} + F_{Ikj}) - \frac{S_{ij}}{A_j}\{G_k'(u_{ki} - u_{kj}) + G_{kij}u_k^*\} + \frac{d}{dZ}(G_{kj}u_{kj})\right] \tag{8}$$

Here, dP_{ki}/dZ is the pressure gradient for the k-phase in Ch. i. F_{wki}, F_{gki}, and F_{Iki}, respectively, represent the wall friction, gravity, and interfacial shear forces per unit volume. G_k' is the lateral mass flux due to the turbulent mixing for the k-phase. u_{ki} and α_{ki} are the velocity and the volume fraction of k-phase in Ch. i. A characteristic velocity, u_k^*, in Eqs. (7) and (8) is taken as $u_k^*=u_{ki}$ if $G_{kij}>0$ and $u_k^*=u_{kj}$ if $G_{kij}<0$.

As for pressure gradients in Eqs. (7) and (8), the following one-pressure model in each subchannel is applied since the flow under consideration is a vertical upward two-phase flow:

$$\frac{dP_{Gi}}{dZ} = \frac{dP_{Li}}{dZ}, \quad \frac{dP_{Gj}}{dZ} = \frac{dP_{Lj}}{dZ} \tag{9}$$

Furthermore, according to the assumption (2) mentioned before, the time-averaged pressure difference does not exist between the subchannels. Therefore, the equal pressure gradient between the subchannels holds.

Downloaded 02 Jun 2010 to 171.66.16.109. Redistribution subject to ASME license or copyright; see http://www.asme.org/terms/Terms_Use.cfm

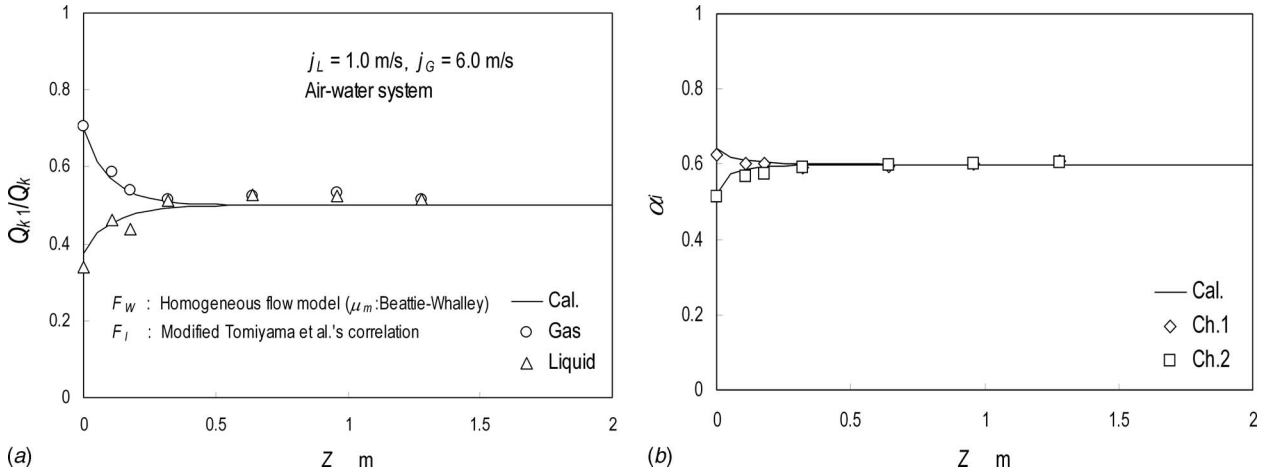


Fig. 8 Comparison of the axial variation in flow parameters between the experiment and calculation for a typical slug or churn flow for air-water system: In the calculation, the homogeneous flow model with Beattie–Whalley's viscosity model is used for F_W and the modified correlation of Tomiyama et al. for F_I. (*a*) Flow rate ratios for both phases and (*b*) the subchannel void fraction.

$$\frac{dP_{ki}}{dZ} = \frac{dP_{kj}}{dZ} \tag{10}$$

Constitutive Equations

Intersubchannel Fluid Transfer. As for the mass flux due to the turbulent mixing, G'_k, we used measured data in our previous experiment [10]. For the net lateral mass flux of gas phase due to the void drift, G_{Gij}, we calculated from the void settling model, Eq. (3), by substituting the experimentally determined void diffusion coefficient shown in Fig. 5. Regarding the lateral mass flux of the liquid phase, G_{Lij}, we did not need any constitutive equation and/or experimental data because the flux was automatically calculated from Eq. (10).

Wall and Interfacial Friction Forces. In our previous study [13], experimental data on wall and interfacial friction forces, F_W and F_I, for both the air-water and air-PLE systems were obtained for a hydrodynamic equilibrium two-phase flow in the same test channel. In addition, the respective data were compared with the predicted values by the existing correlations, and modified one of them to improve its accuracy against the data. As a result, the following correlations were recommended, respectively, for the wall and the interfacial friction forces in the present test channel.

Wall Friction Force for Liquid, F_{WL}. The homogeneous flow model with Beattie–Whalley's mixture viscosity model [20] together with the Lockhart–Martinelli model [21] with a modified *C*-value correlation accounting for the reduced surface tension effects are suitable irrespective of two-phase flow regimes and the liquid in the present gas-liquid systems. It should be noted here that the wall friction force for the gas phase, F_{WG}, was taken to be zero because the channel wall was kept in contact with the liquid in the present experimental ranges. Hereafter, thus, wall friction force, F_W, means that for the liquid phase, i.e., $F_W = F_{WL}$.

Interfacial Friction Force, F_I. The suitable correlation was different depending on the flow regime and/or the void fraction. For $\alpha < 0.7$ in both the air-water and the air-PLE systems, the correlation of Tomiyama et al. [22] with some modifications accounting for the effects of the reduced surface tension, channel size, and channel geometry. For $\alpha > 0.8$ in both systems, the correlation of Fukano–Furukawa [23] with some modifications accounting for the effects of the reduced surface tension, and for the air-PLE system, the correlation of Wallis [24]. For $0.7 < \alpha < 0.8$ in both flow systems, an interpolation equation with the modified versions of Tomiyama et al. and Fukano–Furukawa.

Coupled F_I and F_W correlations from the above ones were incorporated in turn into the present analysis code. In addition, the separated flow model [25], which is valid for the calculation of the two-phase frictional pressure drop in a narrow channel [26], was tested for F_W. For F_I, on the other side, correlations used in the two-fluid model based thermal-hydraulic analysis codes, TRAC-PF1/MOD1 [27], RELAP5/MOD2 [28], NASCA [29], and TRACE [30], were also tested.

Comparison Between Data and Code Prediction. In slug or churn flow regime in a void fraction range of $0.4 < \alpha < 0.7$, good agreements were obtained between the calculation and the experiment when the modified correlation of Tomiyama et al. was used for evaluating the interfacial friction force, F_I, and when Beattie–Whalley's homogeneous flow model was used for evaluating the wall friction force, F_W. Figures 8 and 9 show typical examples of the comparisons, respectively, for the air-water and air-PLE systems. The solid curves are calculated results by the present code. Similar agreements were also obtained for other test runs for both the air-water and air-PLE systems.

Figure 10 shows an example of the comparison when the TRAC-PF1/MOD1 correlation [27] was used for F_I instead of the modified correlation of Tomiyama et al. The experimental condition is the same as that in Fig. 9. The agreement between the calculation and experiment in Fig. 10 is inferior to that in Fig. 9, and the calculation in Fig. 10(*b*) remarkably overpredicts the data in both subchannels. Poor agreements were also seen for both air-water and air-PLE systems when RELAP5/MOD2 [28], NASCA [29], and TRACE [30] correlations were used for F_I.

From the comparisons in the annular flow regime of $\alpha > 0.8$, it was found that the following modified correlation of Fukano–Furuakawa is more suitable for evaluating F_I:

$$F_I = K_S F_{IFF} \text{ and } K_S = 0.60(\sigma_W/\sigma)^{0.30} \tag{11}$$

Here, F_{IFF} is F_I calculated by the correlation of Fukano–Furukawa [23], σ and σ_W are the surface tensions of the working liquid and the water at 20°C. Figure 11 shows an example of the comparison for an annular flow in the air-PLE system. If K_S in Eq. (11) is multiplied by F_I calculated by the correlation of Wallis instead of the correlation of Fukano–Furukawa, the second best agreements were obtained.

In a transition region from the churn flow to the annular flow of $0.7 < \alpha < 0.8$, similar to Ref. [31], the following interpolation equation [13,32] was adopted for F_I:

Downloaded 02 Jun 2010 to 171.66.16.109. Redistribution subject to ASME license or copyright; see http://www.asme.org/terms/Terms_Use.cfm

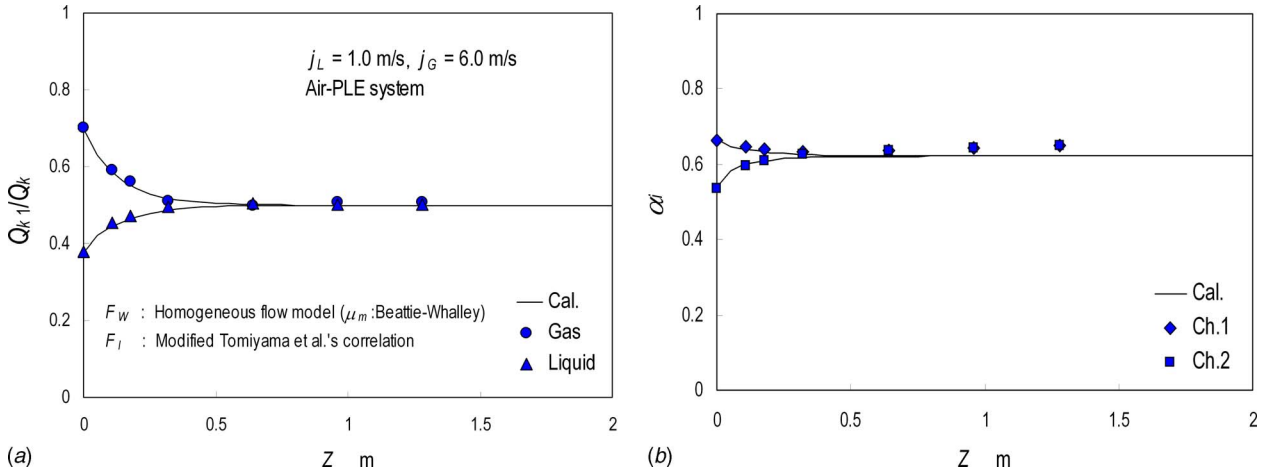


Fig. 9 Comparison of the axial variation in flow parameters between the experiment and calculation for a typical slug or churn flow for the air-PLE system: In the calculation, the homogeneous flow model with Beattie–Whalley's viscosity model is used for F_W and the modified correlation of Tomiyama et al. for F_I. (*a*) Flow rate ratios for both phases and (*b*) the subchannel void fraction.

$$F_I = (1-n)F_{I07} + nF_{I08}, \quad \text{where } n = 10\alpha - 7 \tag{12}$$

Here, F_{I07} is F_I calculated by the modified correlation of Tomiyama et al. at α=0.7, F_{I08} by the modified correlation of Fukano–Furukawa et al. at α=0.8. Figure 12 shows an example of the comparison in this region, and shows good agreement. Similar agreements were obtained for other runs. In addition, if the correlation of Wallis modified by K_S in Eq. (11) was used for the calculation of F_{I08} in Eq. (12), the second best results were obtained.

Conclusions

Void drift phenomena in the test channel simulating a tight lattice rod array bundle were investigated experimentally and analytically. In the experiments, data on the flow and void redistributions due to the void drift were obtained under relatively wider gas-liquid two-phase flow conditions. In order to know the effects of the reduced surface tension on the void drift phenomena, water with a surfactant (PLE for short) and water were used as test liquids. In the analysis, a subchannel analysis code based on a one-dimensional two-fluid model was used to predict the flow and the void redistributions. The following are our main findings.

- The void diffusion coefficient, $\tilde{D}$, obtained for both the air-PLE and the air-water systems increased with the void fraction up to α=0.7 and was nearly constant and/or increases a little in $\alpha > 0.7$.
- As for the reduced surface tension effects, the void diffusion coefficient was a little smaller for the air-PLE system than the air-water one in $0.5 < \alpha < 0.7$.
- Validation tests of the present subchannel analysis code showed that the validity depends on the selection of the constitutive equations for wall and interfacial friction forces.
- For the constitutive equation of the wall friction force, a homogeneous flow model with Beattie–Whalley's viscosity model is the best irrespective of flow patterns and also air-PLE and air-water systems.
- For the constitutive equation of the interfacial friction force, a modified correlation of Tomiyama et al. is the best in $0.4 < \alpha < 0.7$, in an interpolation equation with the modified correlations of Tomiyama et al. and Fukano–Furukawa (or Wallis) in $0.7 < \alpha < 0.8$, and in the modified correlations of Fukano–Furukawa and Wallis in $\alpha > 0.8$.

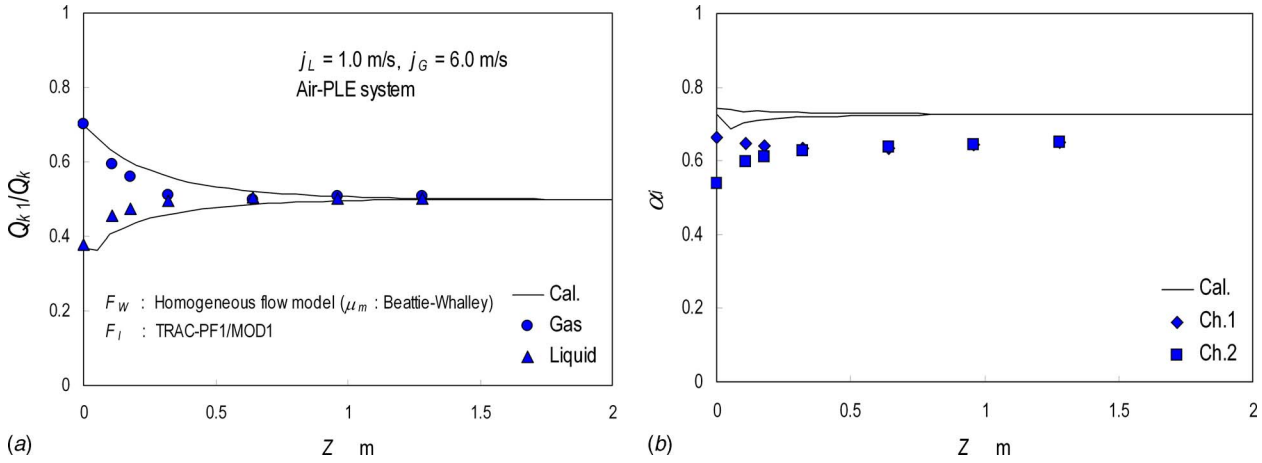


Fig. 10 Comparison of the axial variation in flow parameters between the experiment and calculation for a typical slug or churn flow for the air-PLE system: In the calculation, the homogeneous flow model with Beattie–Whalley's viscosity model is used for F_W and the TRAC-PF1/MOD1 correlation for F_I. (*a*) Flow rate ratios for both phases and (*b*) the subchannel void fraction.

Downloaded 02 Jun 2010 to 171.66.16.109. Redistribution subject to ASME license or copyright; see http://www.asme.org/terms/Terms_Use.cfm

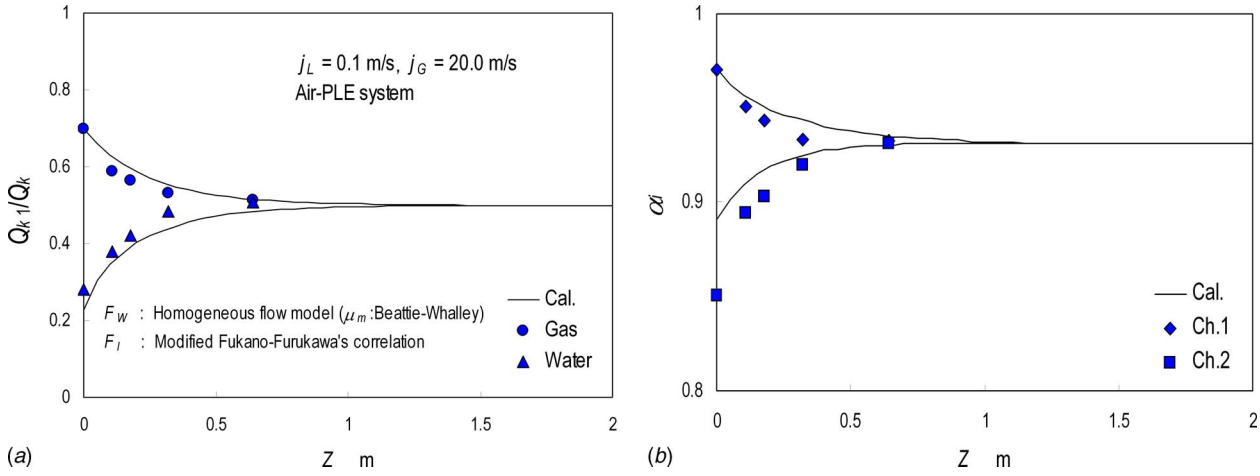


Fig. 11 Comparison of the axial variation in flow parameters between the experiment and calculation for a typical annular flow for the air-PLE system: In the calculation, the homogeneous flow model with Beattie–Whalley's viscosity model is used for F_W and the modified correlation of Fukano–Furukawa for F_I. (*a*) Flow rate ratios for both phases and (*b*) the subchannel void fraction.

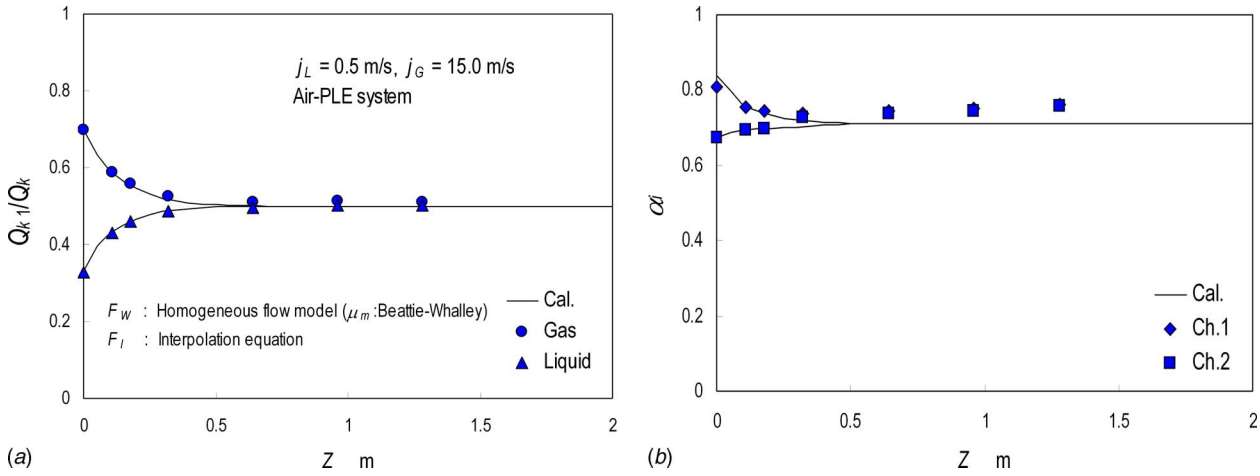


Fig. 12 Comparison of the axial variation in flow parameters between the experiment and calculation for the flow in a churn flow to the annular flow transition region for the air-PLE system: In the calculation, the homogeneous flow model with Beattie–Whalley's viscosity model is used for F_W and an interpolation equation (12) for F_I. (*a*) Flow rate ratios for both phases and (*b*) the subchannel void fraction.

In addition, for some correlations to be valid for the air-PLE system data must be valid also for an actual steam-water flow in a tight lattice subchannel because the surface tension is much smaller in steam-water flows than air-water flows.

Acknowledgment

The authors would like to thank Mr. Y. Sasaki and H. Kudo, who were students at Kumamoto University, for their help in the experiments and the data reduction.

Nomenclature

A = flow area (m^2)
d = rod diameter (m)
D_h = hydraulic diameter (m)
$\tilde{D}$ = void diffusion coefficient (m^2/s)
F_g = gravitational force per unit volume (N/m^3)
F_I = interfacial shear force per unit volume (N/m^3)
F_W = wall friction force per unit volume (N/m^3)
G = mass flux ($kg/m^2\,s$)
G_{ij} = lateral mass flux due to void drift ($kg/m^2\,s$)
G' = lateral mass flux due to turbulent mixing ($kg/m^2\,s$)
g = gravitational acceleration (m/s^2)
j = volumetric flux (m/s)
P = pressure (N/m^2)
p = rod to rod pitch (m)
Q = volume flow rate (m^3/s)
S_{ij} = gap clearance between subchannels (m)
u = mean velocity (m/s)
Z = axial distance (m)

Greek

α = void fraction
μ = dynamic viscosity ($N\,s/m^2$)
ρ = density (kg/m^3)
σ = surface tension (N/m)

Subscripts

EQ = hydrodynamic equilibrium state
G = gas phase
k = phase index

Downloaded 02 Jun 2010 to 171.66.16.109. Redistribution subject to ASME license or copyright; see http://www.asme.org/terms/Terms_Use.cfm

L = liquid phase
$i,j,1,2$ = subchannel identifier.

All the parameters without a subchannel identifier refer to those for the whole channel made up of two subchannels.

References

[1] Iwamura, T., Okubo, T., Kureta, M., Nakatsukasa, T., and Takeda, R., 2002, "Development of Reduced-Moderation Water Reactor (RMWR) for Sustainable Energy Supply," *Proceedings of 13th Pacific Basin Nuclear Conference*, TS-8C-6, Shenzhen, China.

[2] Kureta, M., Yoshida, H., Ohnuki, A., and Akimoto, H., 2003, "Experimental Study on Void Fraction in Tight-Lattice Rod Bundles," *Proceedings of the Tenth International Topical Meeting on Nuclear Reactor Thermal Hydraulics (NURETH 10)*, Seoul, Korea.

[3] Lahey, R. T., Jr., and Moody, F. J., 1993, *The Thermal-Hydraulics of a Boiling Water Nuclear Reactor*, 2nd ed., ANS, La Grange Park, pp. 168–184.

[4] Ninokata, H., Sadatomi, M., Okawa, T., Serizawa, A., Mishima, K., Koshizuka, S., Kudo, Y., Hotta, A., Yamamoto, Y., Shirakawa, N., and Nishida, K., 2003, "Development of Generalized Boiling Transition Analysis Methodology Applicable to a Wide Variety of BWR-Type Fuel Bundle Geometery—Master Plan and Status of First Year," *Proceedings of the Tenth International Topical Meeting on Nuclear Reactor Thermal Hydraulics (NURETH 10)*, Seoul, Korea.

[5] Tamai, H., Kureta, M., Ohnuki, A., Sato, T., and Akimoto, H., 2006, "Pressure Drop Experiments Using Tight-Lattice 37-Rod Bundles," J. Nucl. Sci. Technol., **43**(6), pp. 699–706.

[6] Sadatomi, M., Kawahara, A., and Sato, Y., 1994, "Flow Redistribution Due to Void Drift in Two-Phase Flow in a Multiple Channel Consisting of Two Subchannels," Nucl. Eng. Des., **148**(2–3), pp. 463–474.

[7] Sadatomi, M., Kawahara, A., and Sato, Y., 1997, "Treatment of Two-Phase Turbulent Mixing, Void Drift and Diversion Cross-Flow in a Hydraulically Non-Equilibrium Subchannel Flow," *Proceedings of Fourth International Seminar on Subchannel Analysis (ISSCA-4)*, Tokyo, Japan, pp. 87–104.

[8] Kawahara, A., Sadatomi, M., Kano, K., and Sasaki, Y., 2004, "Flow Redistribution Phenomena Due to Void Drift in Triangle Tight Lattice Subchannels," *Proceedings of Fifth International Conference on Multiphase Flow (ICMF'04)*, Yokohama, Japan, May–Jun., 2004.

[9] Kawahara, A., Sadatomi, M., Kano, K., Sasaki, Y., and Kudo, H., 2006, "Void Diffusion Coefficient in Two-Phase Void Drift for Several Channels of Two- and Multi-Subchannel Systems," Multiphase Sci. Technol., **18**(1), pp. 31–54.

[10] Kawahara, A., Sadatomi, M., Kudo, H., and Kano, K., 2006, "Single- and Two-Phase Turbulent Mixing Rate Between Subchannels in Triangle Tight Lattice Rod Bundle," JSME Int. J., Ser. B, **49**(2), pp. 287–295.

[11] Kawahara, A., Higuchi, T., Sadatomi, M., and Kudo, H., 2007, "Single- and Two-Phase Diversion Cross-Flows Between Triangle Tight Lattice Rod Bundle Subchannels—Data on Flow Resistance Coefficient and Interfacial Friction Coefficients for the Cross-Flow," Journal of Power and Energy Systems, **1**(1), pp. 111–122.

[12] Sadatomi, M., Kawahara, A., Kudo, H., and Shirai, H., 2007, "Effects of Surface Tension on Void Fraction in a Multiple-Channel Simplifying Triangle Tight Lattice Rod Bundle—Measurement and Analysis," Journal of Power and Energy Systems, **1**(2), pp. 143–153.

[13] Kawahara, A., Sadatomi, M., and Shirai, H., 2008, "Two-Phase Wall and Interfacial Friction Forces in Triangle Tight Lattice Rod Bundle Subchannel," Journal of Power and Energy Systems, **2**(1), pp. 283–294.

[14] Sadatomi, M., Kawahara, A., and Sato, Y., 1995, "Turbulent Mixing of Both Gas and Liquid Phases Between Subchannels in Two-Phase Hydrodynamic Equilibrium Flows," *Proceedings of International Symposium on Two-Phase Flow Modelling and Experimentation 1995*, G. P. Celeta and R. K. Shah, eds., Rome, Vol. 1, pp. 403–409.

[15] Kawahara, A., Sato, Y., and Sadatomi, M., 1997, "The Turbulent Mixing Rate and the Fluctuations of Static Pressure Difference Between Adjacent Subchannels in a Two-Phase Subchannel Flow," Nucl. Eng. Des., **175**, pp. 97–106.

[16] Gonzalez-Santalo, J. M., and Griffith, P., 1972, "Two-Phase Flow Mixing in Rod Bundle Subchannel," ASME Paper No. 72-WA/NE-19.

[17] Kazimi, M. S., and Kelly, J. E., 1983, "Formulation of a Two-Fluid Model for Mixing in LWR Bundles," *Proceedings of the 2nd International Topical Meeting on Nuclear Reactor Thermal Hydraulics*, Santa Barbara, CA, pp. 433–439.

[18] Tapucu, A., Teyssedou, A., Tye, P., and Troche, N., 1994, "The Effect of Turbulent Mixing Models on the Predictions of Subchannel Codes," Nucl. Eng. Des., **149**, pp. 221–231.

[19] Ishii, M., and Mishima, K., 1984, "Two-Fluid Model and Hydrodynamic Constitutive Relations," Nucl. Eng. Des., **82**, pp. 107–126.

[20] Beattie, D. R. H., and Whalley, P. B., 1982, "A Simple Two-Phase Frictional Pressure Drop Calculation Method," Int. J. Multiphase Flow, **8**(1), pp. 83–87.

[21] Lockhart, R. W., and Martinelli, R. C., 1969, "Proposed Correlation of Data for Isothermal Two-Phase, Two-Component Flow in Pipes," Chem. Eng. Prog., **45**(1), pp. 39–48.

[22] Tomiyama, A., Furutani, N., and Sakaguchi, T., 1993, "Numerical Stability of the One-Pressure Steady Two-Fluid Model," Trans. Jpn. Soc. Mech. Eng., Ser. B, **59**(560), pp. 1071–1078 (in Japanese).

[23] Fukano, T., and Furukawa, T., 1998, "Prediction of the Effects of Liquid Viscosity on Interfacial Shear Stress and Frictional Pressure Drop in Vertical Upward Gas-Liquid Annular Flow," Int. J. Multiphase Flow, **24**(4), pp. 587–603.

[24] Wallis, G. B., 1969, *One-Dimensional Two-Phase Flow*, McGraw-Hill, New York.

[25] Chierici, G. L., Ciucci, G. M., and Sclocchi, G., 1974, "Two-Phase Vertical Flow in Oil Wells—Prediction of Pressure Drop," JPT, J. Pet. Technol., **26**(8), pp. 927–938.

[26] Ali, M., Sadatomi, M., and Kawaji, M., 1993, "Adiabatic Two-Phase Flow in Narrow Channels Between Two Flat Plates," Can. J. Chem. Eng., **71**, pp. 657–666.

[27] Liles, D. R., Spore, J. W., Knight, T. D., Nelson, R. A., Cappiello, M. W., Pasamehmetoglu, K. O., Mahaffy, J. H., Guffee, L. A., Stumpf, H. J., Dotson, P. J., Steinke, R. G., Shire, P. R., Greiner, S. E., and Sherwood, K. B., 1988, "TRAC-PF1/MOD1—Correlations and Methods," Report Nos. NUREG/GR-5069 and LA-11208-MS.

[28] Ransom, V. H. et al., 1985, "RELAP5/MOD2 Code Manual, Volume I, Code Structure, System Models, and Solution Methos," Report Nos. NUREG/CR-4312 and EGG-2796.

[29] Ninokata, H., Aritomi, M., Anegawa, T., Sato, Y., Sadatomi, M., Mishima, K., Nishida, K., Yamamoto, Y., Morooka, S., Yabushita, Y., Sou, A., Kamo, H., and Kusuno, S., 1997, "Development of the NASCA Code for Prediction of Transient BT and Post BT Phenomena in BWR Rod Bundles," *Proceedings of Fourth International Seminar on Subchannel Analysis (ISSCA-4)*, Tokyo, Japan, pp. 231–265.

[30] Welter, K. B., Kelly, J. M., and Bajorek, S. M., 2006, "Assessment of TRACE Code Using Rod Bundle Heat Transfer Mixture Level-Swell Tests," *Proceedings of 14th International Conference on Nuclear Engineering (ICONE14)*, Miami, FL, Paper No. ICONE14-89756.

[31] Mishima, K., and Ishii, M., 1984, "Flow Regime Transition Criteria for Upward Two-Phase Flow in Vertical Tubes," Int. J. Heat Mass Transfer, **27**(5), pp. 723–737.

[32] Kawahara, A., Sadatomi, M., and Iwamoto, K., 2000, "Calculation of Two-Phase Flow Redistribution Due to Void Drift in Two-Interconnected Subchannels by a Two-Fluid Model," *Proceedings of Second Japan-Korea Symposium on Nuclear Thermal Hydraulics and Safety (NTHAS2)*, Fukuoka, Japan, pp. 719–725.

Downloaded 02 Jun 2010 to 171.66.16.109. Redistribution subject to ASME license or copyright; see http://www.asme.org/terms/Terms_Use.cfm

On the Pressure Dependency of Physical Parameters in Case of Heat Transfer Problems of Supercritical Water

Gabor Hazi
e-mail: gah@sunserv.kfki.hu

Istvan Farkas
e-mail: farkasi@sunserv.kfki.hu

MTA KFKI Atomic Energy Research Institute,
H1525 Budapest, Hungary

Studying heat transfer problems of supercritical water, the pressure dependency of thermophysical parameters (density, specific heat, viscosity, and thermal conductivity) and the work done by pressure are often neglected. Here we show that the variations of some physical parameters as functions of pressure have the same order of magnitude than their variations as functions of temperature in supercritical water. Therefore, pressure dependency of physical parameters should be taken into account in heat transfer calculations of supercritical water. It is also pointed out that the work done by pressure should not be neglected in supercritical water since the pressure work term has the same order of magnitude than the convective term near the pseudocritical temperature.
[DOI: 10.1115/1.2983135]

1 Introduction

High temperature nuclear reactor cooled by water at supercritical pressure is among the six, most promising new, innovative reactor concepts selected by the Generation IV International Forum for further study. This concept differs from conventional light water reactor concepts by the use of water at supercritical pressure as coolant.

Above the thermodynamic critical point (critical pressure and temperature) the fluid is in supercritical state, and the distinction between liquid and vapor phases disappears. Nevertheless, significant changes in thermophysical parameters still exist near the pseudocritical line. Although these changes are continuous, they can significantly influence heat transfer mechanisms and as a consequence, accurate prediction of heat transfer at supercritical pressure is still an unresolved problem. According to Pioro et al. [1], no one correlation can predict the magnitude and onset of deteriorated heat transfer, a phenomenon often observed in heat transfer experiments.

In the past few years, computational fluid dynamics (CFD) tools have been used intensively to study heat transfer in supercritical fluids [2–11]. The computational approach is very attractive since the variation of fluid properties and its coupling with fluid velocity can be taken into account in a mechanistic way. However, the use of CFD has shown limited success. Good agreement between measurements and CFD calculations was achieved at high mass flow rates, but CFD predictions gave unreasonable results at high heat and low mass fluxes [6]. A possible reason of this failure might be that significant simplifications have been applied in most CFD calculations, neglecting, for instance, the pressure variation of the thermophysical parameters and the work done by pressure. In the light of some experiments made in microgravity environment and in terrestrial conditions, such simplifications seem to be questionable.

Indeed, heat transfer in supercritical fluid was studied intensively in microgravity environment (e.g., Refs. [12–20]). Those studies brought understanding some details of the physics of heat transfer at near critical state.

As the critical point is approached the isothermal compressibility and isobaric thermal expansion tend to infinity, while the thermal diffusivity tends to zero. Due to these specific material properties an adiabatic process, often called "the piston effect," can play an important role in heat transfer problems near the critical point [18]. Basically, this effect can be explained as follows. By heating the wall of a cell filled with a near critical fluid, a thin thermal boundary layer forms at the wall. Due to the high thermal expansion coefficient of the fluid, the layer can expand very rapidly and like a piston, it can compress the rest of the highly compressible fluid. The compression results in a homogenous temperature rise in the fluid. It was demonstrated in microgravity environment that the heat transfer "speeds up" due to this mechanism, instead of the "critical speeding down" scenario, which had been expected because of the low thermal diffusivity near the critical point [16]. The piston effect has been observed in terrestrial conditions too [15]. Note that the piston effect transfers heat by acoustic waves and although the effect itself might be not relevant in forced convection, the role of acoustic activities on heat transfer in supercritical fluid should be clarified. It is also worth mentioning that pressure oscillations (sometimes called thermoacoustic oscillations) were often observed in large scale test facilities [21], giving us further motivation to answer the question we have recently posed [22]: Can the pressure dependence of thermophysical parameters and the work done by pressure play important role in the case of heat transfer problems in supercritical water?

In the following sections we would like to answer this question.

2 Pressure Dependency of Physical Parameters

Our starting point is the Navier–Stokes equations supplemented by the energy equation:

$$\frac{\partial \rho^*}{\partial t^*} + \frac{\partial (\rho^* u_i^*)}{\partial x_i^*} = 0 \tag{1a}$$

$$\rho^* \left(\frac{\partial u_i^*}{\partial x_i^*} + u_j^* \frac{\partial u_i^*}{\partial x_j^*} \right) = - \frac{\partial p^*}{\partial x_i^*} - \frac{\partial}{\partial x_j^*} \left[\mu^* \left(\frac{\partial u_i^*}{\partial x_j^*} + \frac{\partial u_j^*}{\partial x_i^*} \right) - \frac{2}{3} \delta_{ij} \frac{\partial u_m^*}{\partial x_m^*} \right] \tag{1b}$$

Manuscript received July 19, 2008; final manuscript received July 19, 2008; published online October 2, 2008. Review conducted by Dillip R. Ballal. Paper presented at the 16th International Conference on Nuclear Engineering (ICONE16), Orlando, FL, May 12–15, 2008.

Copyright © 2009 by ASME

Downloaded 02 Jun 2010 to 171.66.16.109. Redistribution subject to ASME license or copyright; see http://www.asme.org/terms/Terms_Use.cfm

$$\rho^* c_p^* \left(\frac{\partial T^*}{\partial x_i^*} + u_j^* \frac{\partial T^*}{\partial x_j^*} \right) = T^* \beta^* u_j^* \frac{\partial p^*}{\partial x_j^*} + \frac{\partial}{\partial x_j^*} \left(k^* \frac{\partial T^*}{\partial x_j^*} \right) + \Phi^*$$

where the thermal expansion coefficient is defined as follows:

$$\beta^* = \frac{1}{\rho^*} \left(\frac{\partial \rho^*}{\partial T^*} \right)_p \tag{2}$$

This equation system is closed by an equation of state (EOS). For analytical studies simple relations such as the van der Waals EOS could be used. However, to give practically relevant answers we need to use more realistic EOS, suitable for water. Therefore the EOS of International Association for Properties of Water and Steam (IAPWS) is used throughout the paper, and the calculations have been performed by the corresponding MS Excel Adds-In.[1]

In the transport equations, all thermophysical quantities are functions of temperature and pressure. In Fig. 1 the temperature dependence of density, specific heat at constant pressure, heat conductivity, and dynamic viscosity of water are shown at three different supercritical pressures (the critical pressure of water is 22.064 MPa). The temperature where the specific heat has its maximum is the so-called pseudocritical temperature, and significant changes of physical parameters can be observed around this point. Note that parameters also depend on the pressure, and our objective is to compare this dependence with the temperature one.

Let us introduce the following nondimensional variables:

$$p = \frac{p^* - p_0^*}{\rho_0^* (u_0^*)^2}, \quad T = \frac{T^* - T_0^*}{T_w^* - T_0^*} = \frac{T^* - T_0^*}{\Delta T_0^*}, \quad \alpha = \alpha^* / \alpha_0^* \tag{3}$$

where the subscript "0" means a reference state, T_w is a reference wall temperature, and α is one of the physical parameters ρ, c_p, k, and μ. The choice of reference variables is not arbitrary, but we shall turn back this problem later on.

Following Herwig and Schafer [23] we expand all thermophysical parameters as Taylor series at the reference state "0" and keep terms up to first order

$$\alpha^* = \alpha_0^* + \left(\frac{\partial \alpha^*}{\partial T^*} \right)_0 (T^* - T_0^*) + \left(\frac{\partial \alpha^*}{\partial p^*} \right)_0 (p^* - p_0^*) \tag{4}$$

Writing terms in nondimensional form

$$\alpha = 1 + \left(\frac{\partial \alpha}{\partial T} \right)_0 T + \left(\frac{\partial \alpha}{\partial p} \right)_0 p \tag{5}$$

and rewriting the coefficients, we obtain

$$\alpha = 1 + \left(\frac{\Delta T_0^*}{\alpha_0^*} \frac{\partial \alpha^*}{\partial T^*} \right)_0 T + \left(\frac{\rho_0^* (u_0^*)^2}{\alpha_0^*} \frac{\partial \alpha^*}{\partial p^*} \right)_0 p \tag{6}$$

Now, let us introduce the sensitivity parameters

$$K_{\alpha T} = \left(\frac{T^*}{\alpha^*} \frac{\partial \alpha^*}{\partial T^*} \right)_0, \quad K_{\alpha p} = \left(\frac{p^*}{\alpha^*} \frac{\partial \alpha^*}{\partial p^*} \right)_0 \tag{7}$$

and rewrite Eq. (6) as follows:

$$\alpha = 1 + \varepsilon_T K_{\alpha T} T + \varepsilon_p K_{\alpha p} p \tag{8}$$

where

$$\varepsilon_T = \Delta T_0^* / T_0^*, \quad \varepsilon_p = \rho_0^* (u_0^*)^2 / p_0^* \tag{9}$$

are small parameters.

In Eq. (8) all thermophysical parameters are expressed as functions of temperature and pressure, and the dependencies can be studied by comparing the coefficients of the state variables. Herwig and Schafer [23] used sensitivity parameters $K_{\alpha T}$ and $K_{\alpha p}$ to justify the negligence of pressure dependence of physical parameters in the case of water at a temperature of 293 K and a pressure of 1 bar. Note that such comparison can be justified only if ε_T and ε_p have the same order of magnitude, so the choice of the reference state is not arbitrary as we have already mentioned. This analysis gives meaningful results only if we ensure that ε_T, ε_p, and P, T have the same order of magnitude, respectively. A good choice comes from boundary layer theory [24], where T_0 and u_0

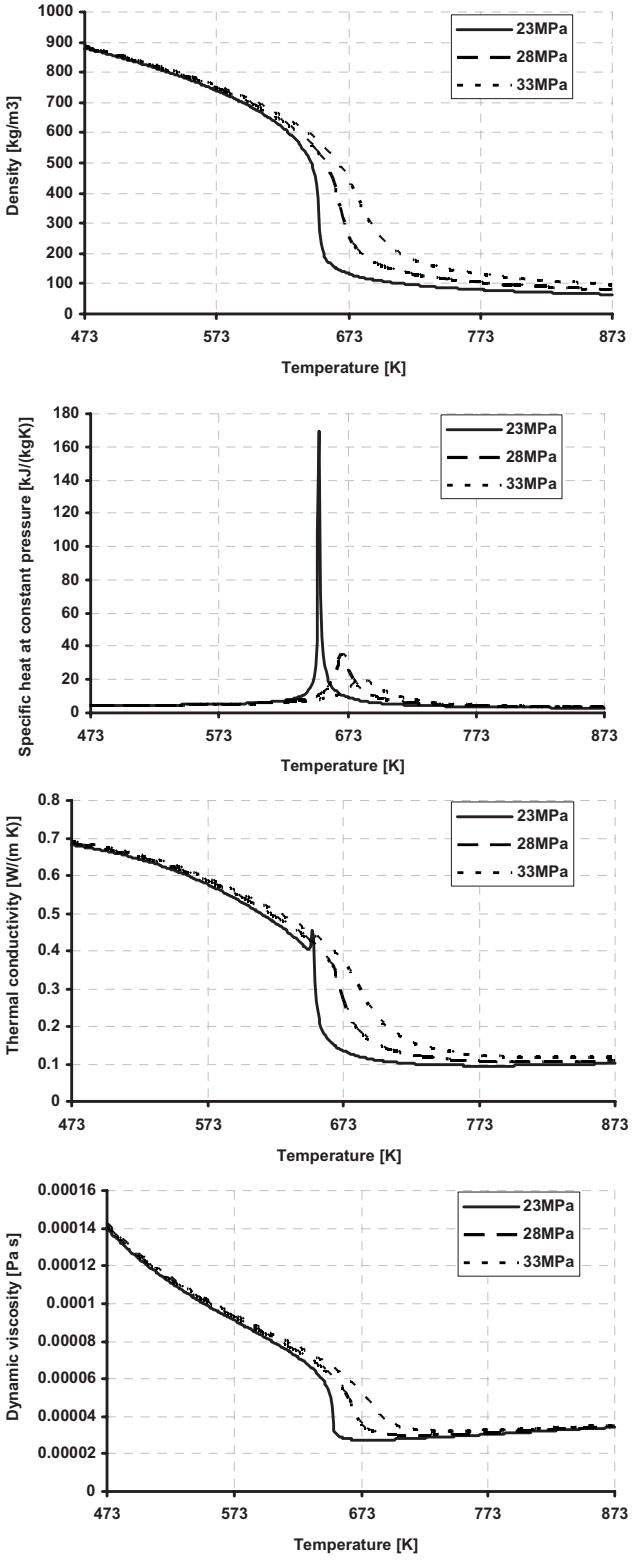


Fig. 1 Density, specific heat at constant pressure, heat conductivity, and dynamic viscosity of water are shown as functions of temperature at three different supercritical pressures

[1] www.iapws.org.

Downloaded 02 Jun 2010 to 171.66.16.109. Redistribution subject to ASME license or copyright; see http://www.asme.org/terms/Terms_Use.cfm

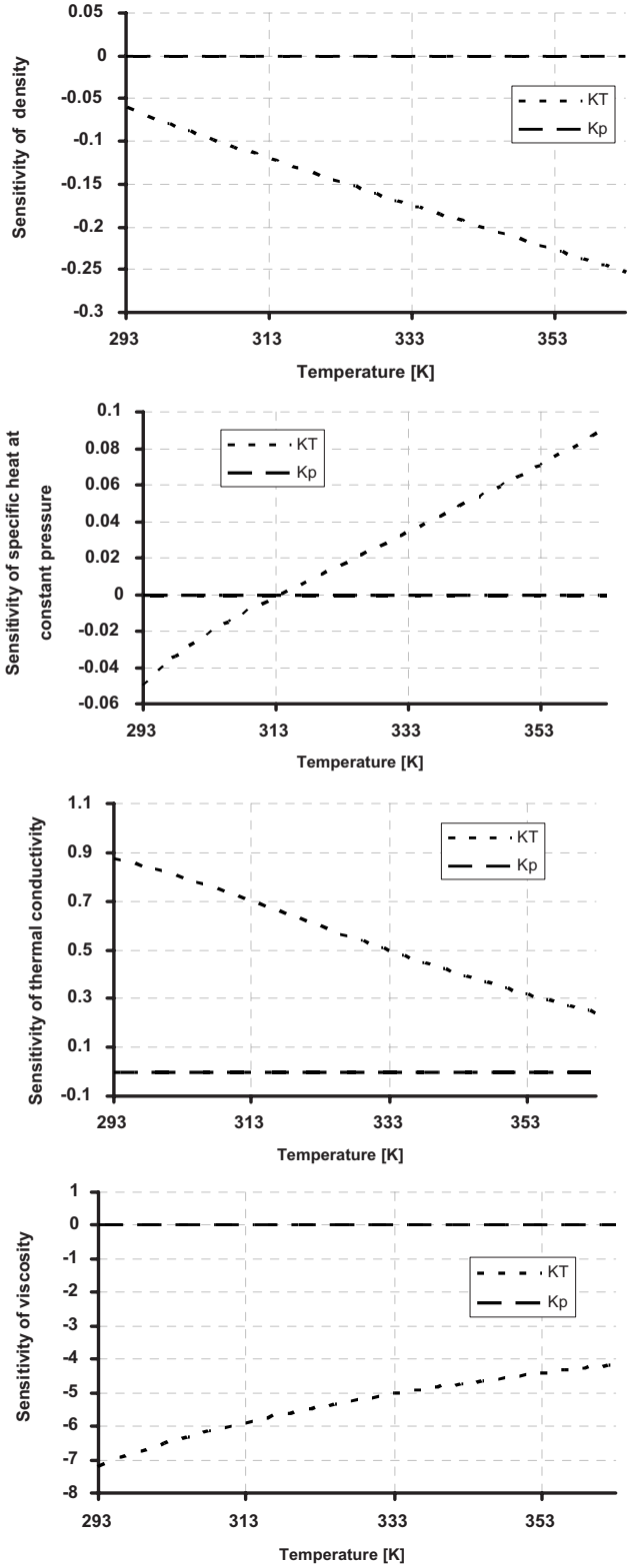


Fig. 2 Sensitivity parameters $K_{\alpha T}$ and $K_{\alpha p}$ as functions of temperature in the range of 293–353 K at a pressure of 1 bar

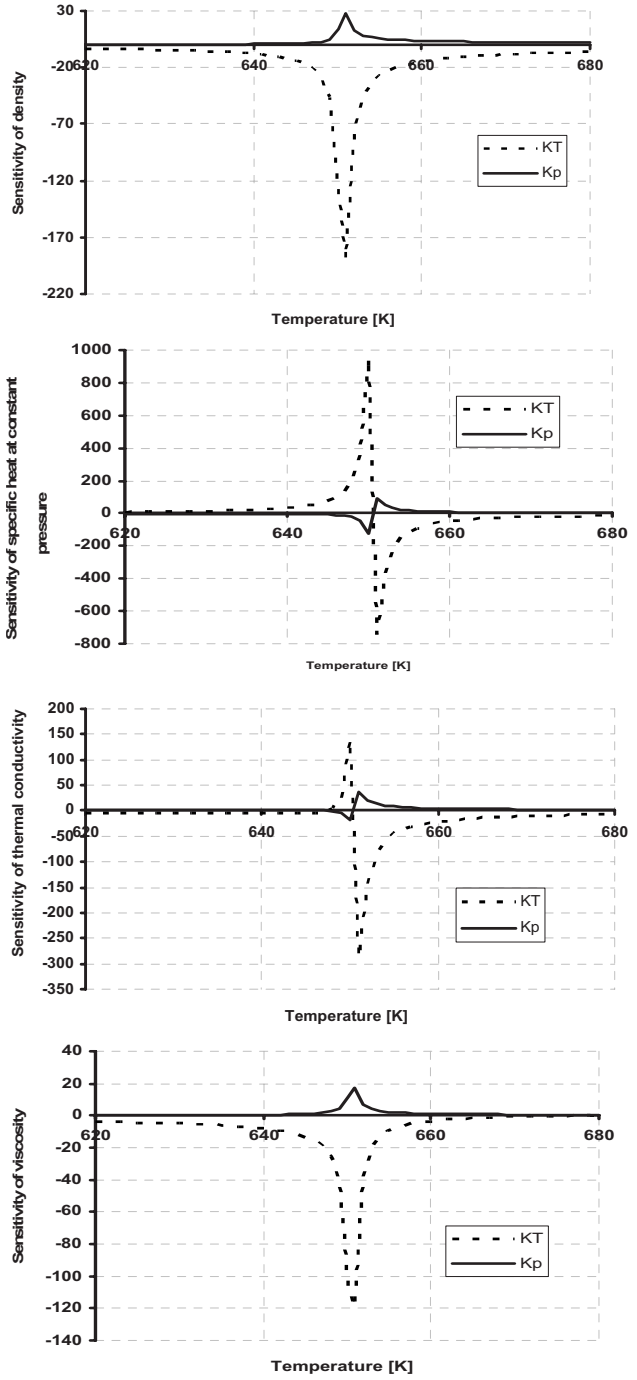


Fig. 3 Sensitivity parameters $K_{\alpha T}$ (dotted) and $K_{\alpha p}$ (solid) as functions of temperature at a supercritical pressure of 23 MPa

are specified as the freestream temperature and velocity, respectively, and p_0 and ρ_0 are given as the nominal pressure and the corresponding density. Figure 2 shows the sensitivity parameters $K_{\alpha T}$ (dotted line) and $K_{\alpha p}$ in the temperature range of 293–353 K at a pressure of 1 bar.

As it is expected, the pressure dependence $K_{\alpha p}$ remains close to zero for each parameter in the given temperature range, i.e., the pressure dependence is negligible. On the other hand, the temperature dependence of viscosity is pretty strong at least compared with other sensitivities. This fact motivated several researchers to take into account the effect of temperature dependent viscosity on heat transfer for calculations with high accuracy (see, e.g., Refs. [25,26]).

The situation is different in the case of supercritical pressure, see Figs. 3 and 4, where the sensitivity parameters are shown at supercritical pressures of 23 MPa and 28 MPa, respectively. In each figure the solid line represents $K_{\alpha p}$ and the dotted line is used for $K_{\alpha T}$.

At supercritical pressure the dominance of temperature depen-

Downloaded 02 Jun 2010 to 171.66.16.109. Redistribution subject to ASME license or copyright; see http://www.asme.org/terms/Terms_Use.cfm

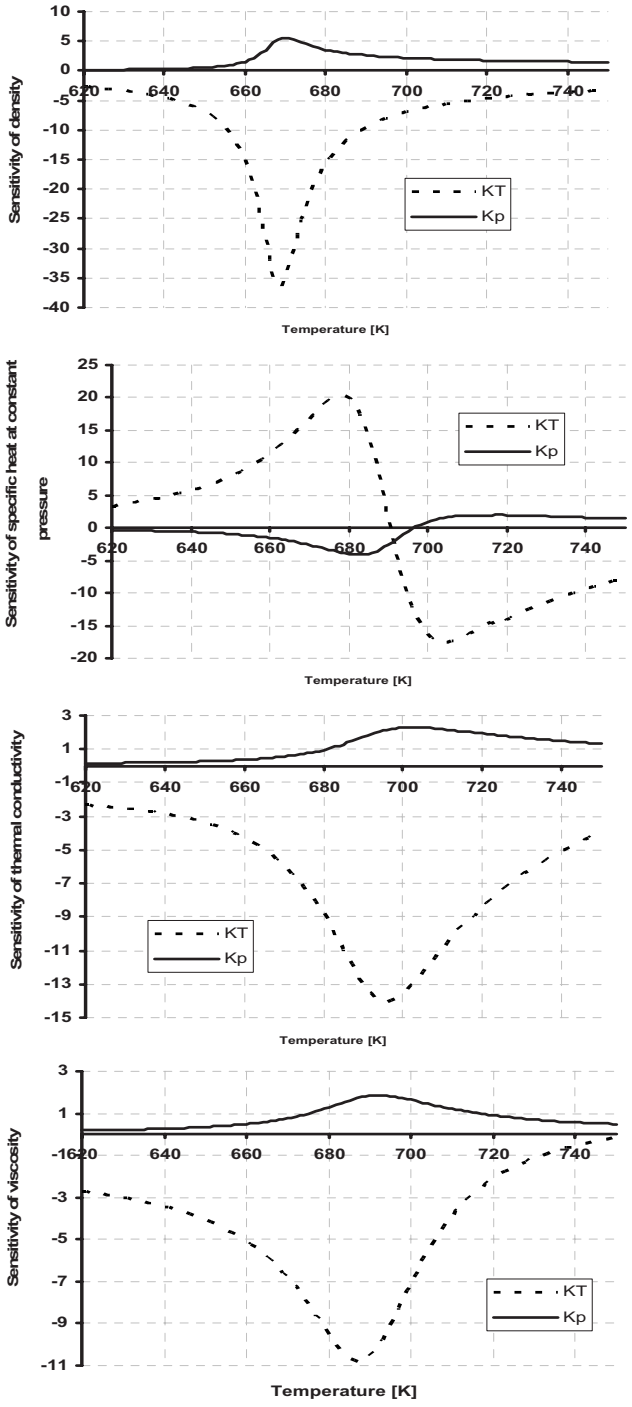


Fig. 4 Sensitivity parameters $K_{\alpha T}$ (dotted line) and $K_{\alpha p}$ (solid line) as functions of temperature at a supercritical of pressure of 28 MPa

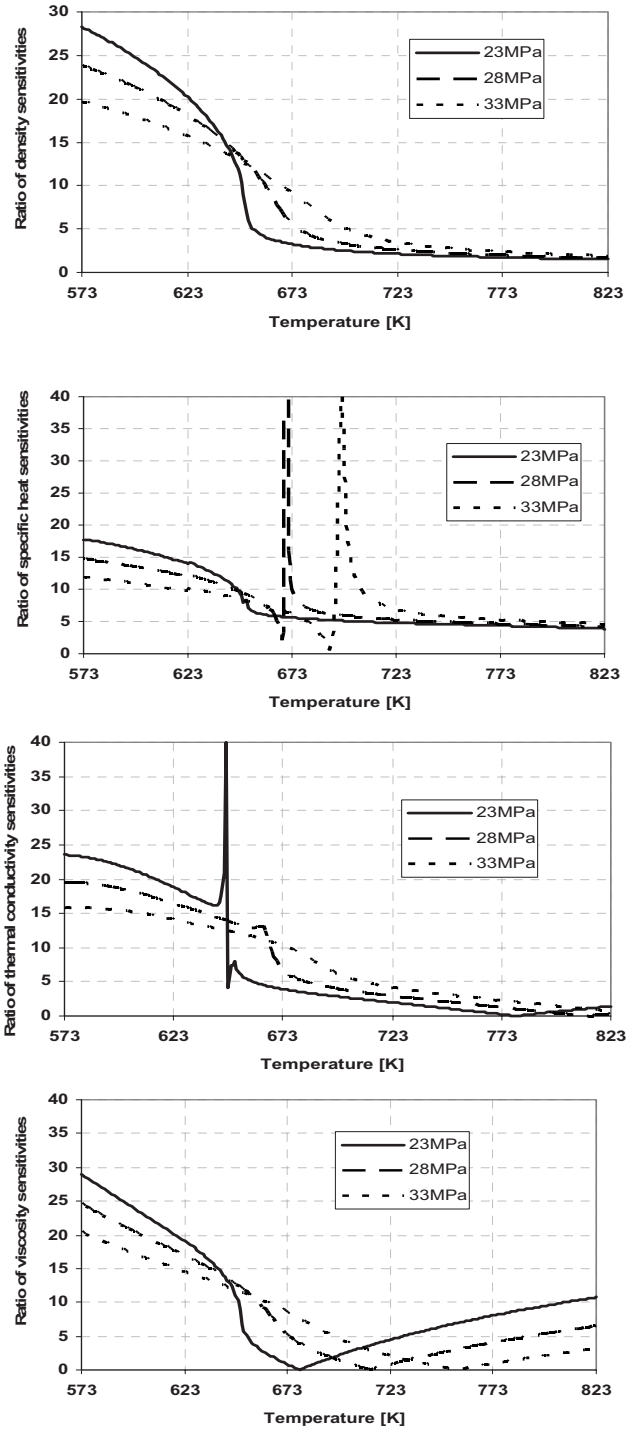


Fig. 5 Ratio of the sensitivity parameters $K_{\alpha T}/K_{\alpha p}$ at 23 MPa (solid), 28 MPa (dashed), and 33 MPa (dotted)

dence is less pronounced. Actually, for several parameters the temperature and pressure sensitivities have the same order of magnitude in certain ranges of temperature, highlighting the relevance of pressure dependence in the case of supercritical water. It is also worth noting that at higher pressures (28 MPa) and above the pseudocritical temperature the pressure sensitivities of some parameters do not converge rapidly to zero.

In order to give a more informative picture about the sensitivities, Fig. 5 shows the ratio of $K_{\alpha T}$ and $K_{\alpha p}$ for supercritical pressures of 23 MPa (solid line), 28 MPa (dashed line), and 33 MPa (dotted line). Roughly speaking, the pressure dependency can be neglected when $K_{\alpha T}/K_{\alpha p} \geq 10$, that is, the temperature dependency is higher with an order of magnitude than the pressure dependency. This condition holds for all parameters below the pseudocritical temperature but not above this temperature.

3 The Pressure Work Term

Now, let us turn our attention to the pressure work. The simple question is can we neglect this term in the energy equation studying heat transfer problems in the case of supercritical pressure?

Downloaded 02 Jun 2010 to 171.66.16.109. Redistribution subject to ASME license or copyright; see http://www.asme.org/terms/Terms_Use.cfm

To clarify this question, we use the energy equation in its dimensional form and compare the magnitude of the convective term with the magnitude of the pressure work term, that is, we estimate

$$R = \frac{\rho c_p u_x \dfrac{\partial T}{\partial x}}{T\beta u_x \dfrac{\partial p}{\partial x}} \tag{10}$$

Here we consider x as the streamwise direction of the given heat transfer problem.

Again, roughly speaking, the work done by pressure might be negligible if $R \geqslant 10$, while in the case of $R < 10$ the pressure work has the same order of magnitude than the convective term, so it should not be neglected.

Let us rewrite R as follows:

$$|R| = \frac{\rho c_p \dfrac{\partial T}{\partial p}\dfrac{\partial p}{\partial x}}{T\dfrac{1}{\rho}\left(\dfrac{\partial \rho}{\partial T}\right)_p \dfrac{\partial p}{\partial x}} = \frac{\rho^2 c_p \dfrac{\partial T}{\partial p}}{T\left(\dfrac{\partial \rho}{\partial T}\right)_p} \tag{11}$$

and use the thermodynamic relation

$$\left(\frac{\partial T}{\partial p}\right)_\rho = -\frac{\dfrac{T}{\rho^2}\left(\dfrac{\partial \rho}{\partial T}\right)_p}{c_p - c_v} \tag{12}$$

Substituting Eq. (12) into Eq. (11) we arrive the simple relation

$$|R| = \frac{c_p}{c_p - c_v} \tag{13}$$

Here we assumed that

$$\frac{\partial T}{\partial p} \cong \left(\frac{\partial T}{\partial p}\right)_\rho \tag{14}$$

is a good approximation, which is certainly true for isochoric systems, but not necessarily for forced convective problems. An alternative way to formulate the problem is to write

$$\frac{\partial T}{\partial x} = \frac{\partial T}{\partial \rho}\frac{\partial \rho}{\partial p}\frac{\partial p}{\partial x} \tag{15}$$

and use the approximations

$$\frac{\partial T}{\partial \rho} \cong \left(\frac{\partial T}{\partial \rho}\right)_p$$

$$\frac{\partial \rho}{\partial p} \cong \left(\frac{\partial \rho}{\partial p}\right)_T \tag{16}$$

Here we need to justify that the isothermal compressibility is a good approximation for $\partial\rho/\partial p$.

Note that the density sensitivity parameter $K_{\rho p}$ is proportional to the isothermal compressibility

$$K_{\rho p} = \left(\frac{p^*}{\rho^*}\frac{\partial \rho^*}{\partial p^*}\right)_0 = \left(\frac{p^*}{\rho^*}\right)_{T_0}\left(\frac{\partial \rho^*}{\partial p^*}\right)_{T_0} \tag{17}$$

therefore in Figs. 3 and 4 (top) we can follow how this parameter changes as a function of temperature. For example, in a heated pipe this parameter increases as the pseudocritical point is approached and then it tends to zero as the temperature increases further. So a "temperature window" is formed in which the fluid is strongly compressible, while out of this window the fluid is incompressible. In the temperature window, the isochoric approximation (14) seems to be reasonable and phenomenon like the piston effect can be effective since the borders of the window detain the expansion of the compressed bulk fluid layer into the streamwise direction and behave like walls of a volume.

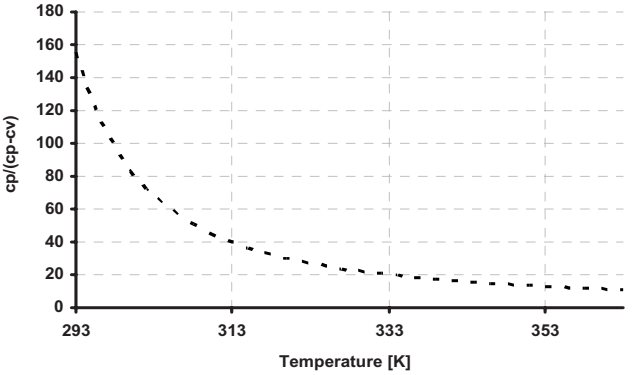


Fig. 6 Ratio of the convective and pressure work terms as a function of temperature at a pressure of 1 bar

Figure 6 shows $|R|$ for water in the temperature range of 293–353 K at a pressure of 1 bar.

As it is expected the convective term highly dominates the pressure work term in this parameter range, but the situation is again different in the case of supercritical pressure (Fig. 7). Here the work done by pressure has almost the same magnitude than the convective term near the pseudocritical temperature. It is even more surprising that the pressure work term has the same order of magnitude in the overall temperature range not only at the pseudocritical temperature. However, we should keep in mind that Eq. (14) is a good approximation only in the vicinity of the pseudocritical point so the compression work is probably the most effective around that temperature.

4 Discussion From CFD Point of View

In the understanding of how the pressure effects can influence on heat transfer processes, CFD can play a major role.

In CFD calculations, the pressure dependencies can be taken into account by using a proper equation of state for water and calculating all thermophysical parameters as functions of pressure and temperature. Using the commercial CFD code FLUENT, such calculations can be carried out by applying its so-called real gas model, which mimics the thermodynamic and transport properties of water in a sufficiently wide range of parameters.

Unfortunately, this model can be applied only with the coupled solver, so its application significantly increases the computational demand; therefore alternative solutions need to be found in the future.

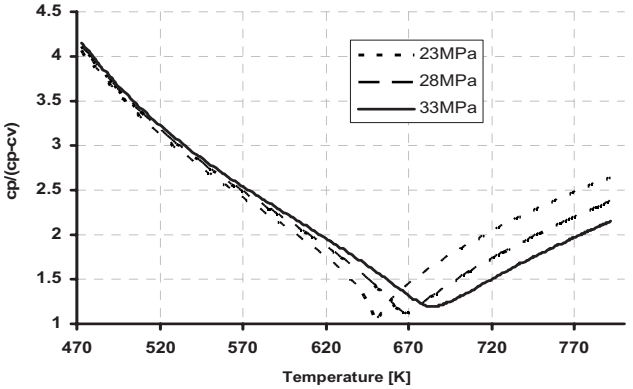


Fig. 7 Ratio of the convective and pressure work terms as a function of temperature at supercritical pressures of 23 MPa (solid line), 28 MPa (dashed line), and 33 MPa (dotted line)

Downloaded 02 Jun 2010 to 171.66.16.109. Redistribution subject to ASME license or copyright; see http://www.asme.org/terms/Terms_Use.cfm

5 Conclusion

Introducing sensitivity parameters we have demonstrated that both the temperature and pressure dependencies of thermophysical parameters have the same order of magnitude above the pseudocritical temperature. We have also shown that the work done by pressure has the same order of magnitude near the pseudocritical temperature than the streamwise convective term in the energy equation. Based on these results we believe that both the pressure dependency of thermophysical parameters and the work done by pressure should be taken into account in heat transfer calculations of supercritical fluids.

It is worth mentioning that by means of the sensitivity analysis presented in Sec. 2, the property ratio method can be used on a solid base [27], and the development of new correlations for supercritical fluid might be feasible.

Acknowledgments

This work has been supported by the Hungarian Academy of Science in the framework of the NUKENERG project.

Nomenclature

c_p = specific heat at constant pressure
c_v = specific heat at constant volume
k = thermal conductivity
p = pressure
t = time
u = velocity
x = space coordinate
K = sensitivity parameter (e.g., $K_{\rho T}$ is the sensitivity of the density ρ with respect to temperature)
T = temperature
α = thermophysical parameter (ρ, k, c_p, μ)
β = thermal expansion coefficient
δ = Kronecker delta
μ = dynamic viscosity
ρ = density
Φ = dissipation function

Subscripts

0 = reference state
w = wall

Superscripts

$*$ = dimensional quantities

References

[1] Pioro, I. L., Khartabil, H. F., and Duffey, R. B., 2004, "Heat Transfer to Supercritical Fluids Flowing in Channels-Empirical Correlations (survey)," Nucl. Eng. Des., **230**, pp. 69–91.

[2] Koshizuka, S., Takano, N., and Oka, Y., 1995, "Numerical Analysis of Deterioration Phenomena in Heat Transfer to Supercritical Water," Int. J. Heat Mass Transfer, **38**, pp. 3077–3084.

[3] Lee, S. H., and Howell, J. R., 1998, "Turbulent Developing Convective Heat Transfer in a Tube For Fluids Near the Critical Point," Int. J. Heat Mass Transfer, **41**, pp. 1205–1218.

[4] Roelofs, F., 2004, "CFD Analysis of Heat Transfer to Supercritical Water Flowing Vertically Upward in a Tube," NRG Report No. 21353/04.60811/P.

[5] Roelofs, F., Lycklama a Nijeholt, J. A., Komen, E. M. J., Löwenberg, M., and Starflinger, J., 2007, "CFD Validation of a Supercritical Water Flow for SCWR Design Heat and Mass Fluxes," International Conference on Advances in Nuclear Power Plants (ICAPP 2007), Nice, France, May 13–18.

[6] Seo, K. W., Kim, M. H., Anderson, M. H., and Corradini, M. L., 2005, "Heat Transfer in a Supercritical Fluid: Classification of Heat Transfer Regimes," Nucl. Technol., **154**, pp. 335–349.

[7] Cheng, X., Kuang, B., and Yang, Y. H., 2006, "Numerical Analysis Of Heat Transfer in Supercritical Water Cooled Flow Channels," Nucl. Eng. Des., **237**, pp. 240–252.

[8] Cheng, X., Laurien, E., and Yang, Y. H., 2005, "CFD Analysis of Heat Transfer in Supercritical Water in Different Flow Channels," *Proceedings of GLOBAL 2005*, Tsukuba, Japan, Oct 9–13, Paper No. 369.

[9] Bae, J. H., Yoo, J. Y., Choi, H., and McEligot, D. M., 2005, "Influence of Fluid-Property Variation on Turbulent Convective Heat Transfer in Vertical Annular Channel Flows," 11th International Topical Meeting on Nuclear Reactor Thermal-Hydraulics (NURETH-11), Avignon, France, Oct. 2–6, Paper No. 018.

[10] Kiss, A., and Aszódi, A., 2007, "Preliminary Calculations of Coolant Flow in a SCWR Fuel Assembly With the Code ANSYS CFX 10.0," *Proceedings of ICAPP 2007 Conference, ICAPP 2007*, Nice, France, May 14–18, Paper No. 7494.

[11] Kiss, A., and Aszódi, A., 2007, "Refined Validation Calculations of Water Coolant Flow in a Supercritical Pressure Test Section Performed With the ANSYS CFX-11 Code," NURETH, Pittsburgh, PA, Sept. 30—Oct. 4.

[12] Amiroudine, S., Bountoux, P., Larroud, P., Gilly, B., and Zappoli, B., 2001, "Direct Numerical Simulation of Instabilities in a Two-Dimensional Near-Critical Fluid Layer Heated From Below," J. Fluid Mech., **442**, pp. 119–140.

[13] Furukawa, A., Meyer, H., and Onuki, A., 2005, "Numerical Simulation Studies of the Convective Instability Onset in a Supercritical Fluid," Phys. Rev. E, **71**, p. 067301.

[14] Házi, G., and Márkus, A., 2008, "Modelling Heat Transfer in Supercritical Fluid Using the Lattice Boltzmann Method," Phys. Rev. E, **77**, p. 026305.

[15] Nakano, A., and Shiraishi, M., 2004, "Numerical Simulation for the Piston Effect and Thermal Diffusion Observed in Supercritical Nitrogen," Cryogenics, **44**, pp. 867–873.

[16] Onuki, A., Hao, H., and Ferrel, R., 1990, "Fast Adibatic Equilibration in a Single-Component Fluid Near the Liquid-Vapor Critical Point," Phys. Rev. A, **41**, pp. 2256–2259.

[17] Straub, J., Eicher, L., and Haupt, A., 1995, "Dynamic Temperature Propagation in a Pure Fluid Near Its Critical Point Observed Under Microgravity During the German Spacelab Mission D-2," Phys. Rev. E, **51**, pp. 5556–5563.

[18] Zappoli, B., Bailly, D., Garrabos, Y., Neindre, B. L., Guenoun, P., and Beysens, D., 1990, "Anomalous Heat Transport by the Piston-Effect in Supercritical Fluids Under Zero Gravity," Phys. Rev. A, **41**, pp. 2264–2267.

[19] Zappoli, B., 1992, "The Response of a Nearly Supercritical Pure Fluid to a Thermal Disturbance," Phys. Fluids A, **4**, pp. 1040–1048.

[20] Zhong, F., and Meyer, H., 1993, "Density Equilibration Near the Liquid-Vapor Critical Point of a Pure Fluid: Single Phase $T > T_c$," Phys. Rev. E, **51**, pp. 3223–3241.

[21] Jackson, J. D., and Hall, W. B., 1979, "Forced Convection Heat Transfer to Fluids at Supercritical Pressure," *Turbulent Forces Convection in Channels and Bundles*, S. Kakac and D. B. Spalding, eds., Hemisphere, Washington, DC.

[22] Házi, G., 2006, "Heat Transfer in Supercritical Fluids," High Perference Light Water Reactor Phase 2 (HPLWR), Kick-Off Meeting, Budapest, Sept. 6.

[23] Herwig, H., and Schafer, P., 1992, "Influence of Variable Properties on the Stability of Two-Dimensional Boundary Layers," J. Fluid Mech., **243**, pp. 1–14.

[24] Schlichting, H., 1979, *Boundary-Layer Theory*, McGraw Hill, New York.

[25] Lin, C. R., and Chen, C. K., 1994, "Effect of Temperature Dependent Viscosity on the Flow and Heat Transfer Over an Accelerating Surface," J. Phys. D: Appl. Phys., **27**, pp. 29–37.

[26] Pinarbasi, A., Ozalp, C., and Duman, S., 2005, "Influence of Variable Thermal Conductivity and Viscosity for Nonisothermal Fluid Flow," Phys. Fluids, **17**, p. 038109.

[27] Herwig, H., 1985, "The Effect of Variable Properties on Momentum and Heat Transfer in a Tube With Constant Heat Flux Across the wall," Int. J. Heat Mass Transfer, **28**, pp. 423–431.

Downloaded 02 Jun 2010 to 171.66.16.109. Redistribution subject to ASME license or copyright; see http://www.asme.org/terms/Terms_Use.cfm

Computational Fluid Dynamics Assessment of the Local Hot Core Temperature in a Pebble-Bed Type Very High Temperature Reactor

Min-Hwan Kim[1]
e-mail: mhkim@kaeri.re.kr

Hong-Sik Lim

Won Jae Lee

Korea Atomic Energy Research Institute,
1045 Daedeokdaero,
Yoseong, Daejeon, 304-353, Republic of Korea

Assessment of the local hot core temperature during normal operation in a pebble-bed type very high temperature reactor has been carried out by using the computational fluid dynamic (CFD) method for which the boundary conditions were obtained from the results of a macroscopic analysis of the core using a system thermal analysis code, GAMMA. Three pebble arrangements are selected, which are simple cubic (SC), body-centered cubic, and face-centered cubic. The results showed that the SC arrangement having the lowest porosity gives the highest fuel temperature of 1237°C but still below the normal operational fuel limit of 1250°C. Comparison of the CFD results with an empirical correlation was made for the pressure drop and Nusselt number. Both results showed a similar tendency that the pressure drop and the Nusselt number increases as the porosity decreases but there were large differences in their absolute values. The benchmark calculation for the pressure drop of the packed particles in a square channel indicated that the correlation for the full core used in the system code is not appropriate for the prediction of a local thermal-fluid behavior in an ordered pebble arrangement.
[DOI: 10.1115/1.2983136]

Introduction

New power plant concepts based on a very high temperature reactor (VHTR) have become of interest for an energy source for hydrogen production [1–3]. The core outlet temperature required for hydrogen production is above 950°C, higher than that of a conventional high temperature gas-cooled reactor (HTGR). An increase in the outlet temperature accompanies an increase in the fuel temperature in the core. Therefore, maintaining the maximum fuel temperature below 1250°C—its steady-state operating limit—is one of the important issues in the VHTR design.

In general, the steady-state fuel temperature in the HTGR core has been evaluated by system thermal-fluid analysis codes using the porous media approach that are not appropriate for a VHTR core with a smaller temperature margin and requiring a detailed analysis. Recently, applications of three dimensional computational fluid dynamic (CFD) codes to the thermal-fluid analysis of the VHTR core have been on the increase [4,5]. A unit-cell approach is a well-known method for predicting the fuel temperature distribution in a prismatic core. Although the unit-cell approach is employed, however, the CFD analysis of a pebble core for its full height requires a large amount of computational resources because of the large number of pebbles, the irregularity of the pebble arrangement, and the high Reynolds number flows. Therefore, a local CFD analysis for a selected hot core region is recommended for a pebble core. The selection of a hot core region can be obtained from the results of a system analysis code.

In this study, analyses are carried out to assess the local hot core temperature of a 400 MW_t pebble-bed reactor (PBR) during steady-state operation by using the CFX-10 [6] commercial CFD code. Three pebble arrangements are selected. The computational results are compared not only with themselves but also with an empirical correlation employed in the system analysis code. In addition, more detailed assessment of the CFD code is performed for an available experiment, which measured the pressure drop through pebble-like packed particles in a square channel.

Local Hot Core Analysis

Computational Method. For the CFD analysis of a local core region, some boundary conditions are required such as the local power of a pebble, the inlet temperature, and so on. To obtain these conditions, the GAMMA system code [7] was employed for a full core analysis of the pebble-bed reactor of which the parameters are shown in Table 1. The core design is the same as that of the pebble-bed modular reactor (PBMR), but the system pressure and core outlet temperature are changed to 70 bars and 950°C, respectively.

The GAMMA core divides the core into 55 meshes consisting of 11 rows and 5 columns in a cylindrical coordinate system, as shown in Fig. 1. According to the GAMMA analysis, the local hot region of the core occurred at the fifth row from the bottom and near to the inner reflector. The results of the GAMMA analysis at the local hot region are presented in Table 2.

The pebble arrangements considered in the CFD analysis are simple cubic (SC), body-centered cubic (BCC), and face-centered cubic (FCC). Because the porosity varies with the arrangement, it is not appropriate to apply an actual helium velocity to all the pebble arrangements. In this study, the mass flow is determined in order to keep the superficial velocity constant regardless of the pebble arrangement as

$$\dot{m}_{CFD} = \dot{m}_{PBR} \times \frac{A_{CFD}}{A_{PBR}} \tag{1}$$

where $\dot{m}_{PBR}$, A_{PBR}, and A_{CFD} are the total core flow in the PBR, the cross-sectional area of the PBR core, and the cross-sectional

[1]Corresponding author.

Manuscript received July 21, 2008; final manuscript received July 28, 2008; published online October 2, 2008. Review conducted by Dilip R. Ballal. Paper presented at the 16th International Conference on Nuclear Engineering (ICONE16), Orlando, FL, May 12–15, 2008.

Copyright © 2009 by ASME

Downloaded 02 Jun 2010 to 171.66.16.109. Redistribution subject to ASME license or copyright; see http://www.asme.org/terms/Terms_Use.cfm

Table 1 Main parameters of pebble core

Reactor power (MW_t)	400
System pressure (bar)	70
Core inlet/outlet temperature (°C)	490/950
Total mass flow (kg/s)	166
Core mass flow (kg/s)	131

area of the CFD model, respectively.

Figure 2 shows the grid systems used for each pebble arrangement. The numbers of nodes are 361,427 for the SC, 872,293 for the BCC, and 1,232,831 for the FCC, respectively. The grid system includes not only the fluid region but also the pebble solid region, which contains the fuel with a diameter of 50 cm and the graphite with a thickness of 5 cm. Although ignoring that the contact heat transfer has an effect on the maximum temperature predicted, a gap size of 0.5 mm between the pebble spheres is assumed not only to avoid the difficulty of a grid generation but also to reduce the computation time.

The temperature variation in the local region is relatively small when compared to that of the full core. Therefore, the physical properties of the coolant and the pebble are independent of the temperature and are listed in Table 3. Although the tristructural-isotropic (TRISO) particles in the fuel region have different conductivities, it is assumed that the conductivity of the fuel region is the same as that of the graphite due to the homogeneous distribution and relatively low density of the TRISO particles.

The mass flow rate obtained from Eq. (1) is fixed at the inlet boundary. At the outlet boundary, the relative static pressure is set

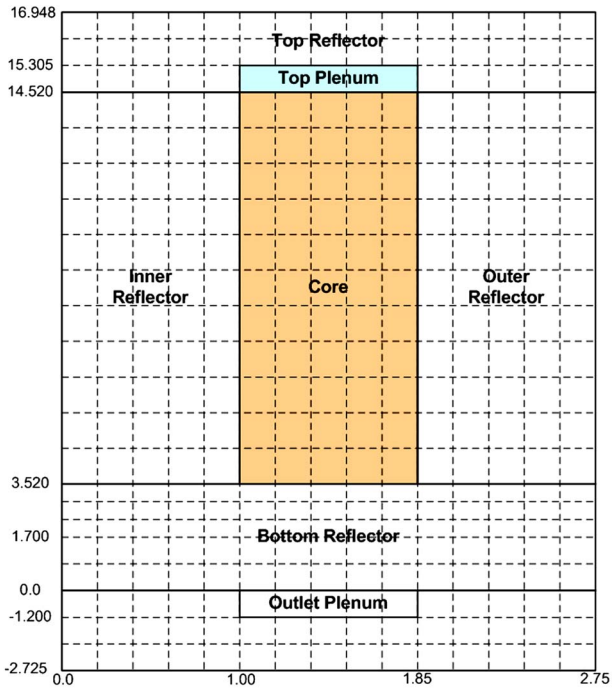


Fig. 1 Pebble core model used in the GAMMA analysis

Table 2 GAMMA results for the local hot region

Radial position (m, Ring 1)	1.112
Vertical position (m, axial Zone 5)	7.846
Local core power density (MW_t/m^3)	9.6
He temperature (°C)	1087
He superficial velocity (m/s)	6.7
Core porosity (ε)	0.39

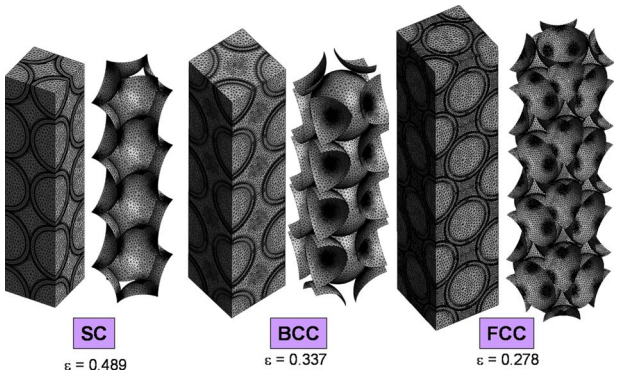


Fig. 2 Computational grid systems

as zero. Periodic condition is imposed on the transverse direction of the fluid region as well as the graphite and the fuel regions. The interface boundaries not only between the fluid and the graphite but also between the graphite and the fuel are treated by using the general grid interface (GGI) method [6] to preserve the momentum and energy flux through them. The Reynolds number based on the inlet superficial velocity and the pebble diameter is 1.84×10^4, which means the flow is turbulent. A standard k-ε model with a wall function method is selected for a turbulence closure. Figure 3 shows the computational domain for the SC arrangement and the applied boundary conditions.

Results and Discussions. To investigate how differently the flow is distributed at each pebble arrangement, their streamlines are compared in Fig. 4. The SC arrangement forms a simple straight flow path so that most of the flow passes without an interaction. However, the BCC and FCC arrangements show complex interactions of the flow with the staggered pebbles, and the interaction is more severe in the FCC arrangement.

Temperature distributions for each pebble arrangement are shown in Fig. 5. The maximum fuel temperature of the SC is 1237°C, which is about 20°C higher than the others but still below the normal operational limit of 1250°C.

Temperature profiles along the vertical and horizontal centerlines of the pebble cross sections are compared in Fig. 6 and 7. The BCC and the FCC represent a similar profile to each other and their temperatures are lower than that of the SC by about 15–20°C. The temperature profile at the vertical centerline is asymmetric. That is, the location of the maximum temperature is below the pebble center, which is more evident in the SC arrangement where a sufficient cooling flow is not supplied to the downstream side of the pebble surface. Temperature distributions at the horizontal centerline are nearly symmetric. A little higher temperature at the horizontal end side of the FCC is due to the fact that the pebbles around it are located more closely than in the BCC.

The validity of the CFD analysis should be accomplished by comparing its results with experimental data, but there are no experimental data available up to now. So, we adopted the correlations used in the GAMMA analysis, which are used for a macroscopic analysis. The correlations for the pressure drop [8] and heat transfer [9] are given as follows;

Pressure drop:

Table 3 Physical properties used in the analysis

Helium density (kg/m^3)	2.5
Helium viscosity ($N\,s/m^2$)	5.6×10^{-5}
Helium conductivity (W/m K)	0.44
Helium capacity (kJ/kg K)	5193
Graphite conductivity (W/m K)	14

Downloaded 02 Jun 2010 to 171.66.16.109. Redistribution subject to ASME license or copyright; see http://www.asme.org/terms/Terms_Use.cfm

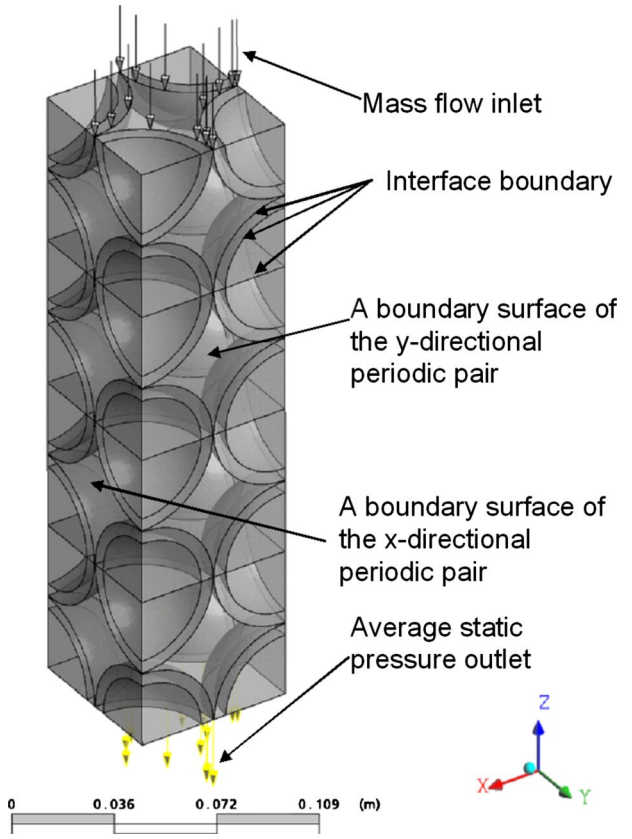


Fig. 3 Computational domain and applied boundary conditions

$$\frac{\Delta P}{\Delta H} = \Psi \frac{1-\varepsilon}{\varepsilon^3} \frac{1}{d_p} \frac{1}{2\rho} \left(\frac{\dot{m}}{A_p} \right)^2 \tag{2}$$

where

$$\Psi = 320/\mathrm{Re}/(1-\varepsilon) + 6/\mathrm{Re}/(1-\varepsilon)^{0.1}$$

Heat transfer:

$$\mathrm{Nu} = 1.27 \frac{\mathrm{Pr}^{1/3}}{\varepsilon^{1.18}} \mathrm{Re}^{0.36} + 0.033 \frac{\mathrm{Pr}^{1/2}}{\varepsilon^{1.07}} \mathrm{Re}^{0.86} \tag{3}$$

where

$$\mathrm{Nu} = \alpha d_p/\lambda, \quad \alpha = Q_s/A_s(T_s - T_f)$$

Table 4 shows a comparison of the pressure drop and Nusselt number. Both the CFD and the correlation results show that the pressure drop and Nusselt number increase as the porosity decreases. However, there are big differences between their absolute values because no pebble arrangement selected in the present study is in the applicable porosity range for the correlation, on average, which is from 0.36 to 0.42. This also implies that the pressure drop correlation for the full core in which the porosity is randomly distributed is not applicable for a local pebble analysis. The CFD results show that the heat transfer in the BCC is better than in the SC but similar to the FCC while the correlation reveals a continued heat transfer enhancement with a decrease in the porosity.

Benchmark Analysis of the Pressure Drop

As shown in the previous section, a direct comparison of the CFD results with the correlation used in the macroscopic analyses is not a proper selection to confirm the CFD validity for a local hot core analysis. Hence, we selected an experiment of Calis et al. [10] as a CFD benchmark problem for a pressure drop prediction. They conducted experiments to obtain pressure drop characteristics over several arrangements of pebble-like catalyst particles packed in a square channel. Here, we selected one of their experi-

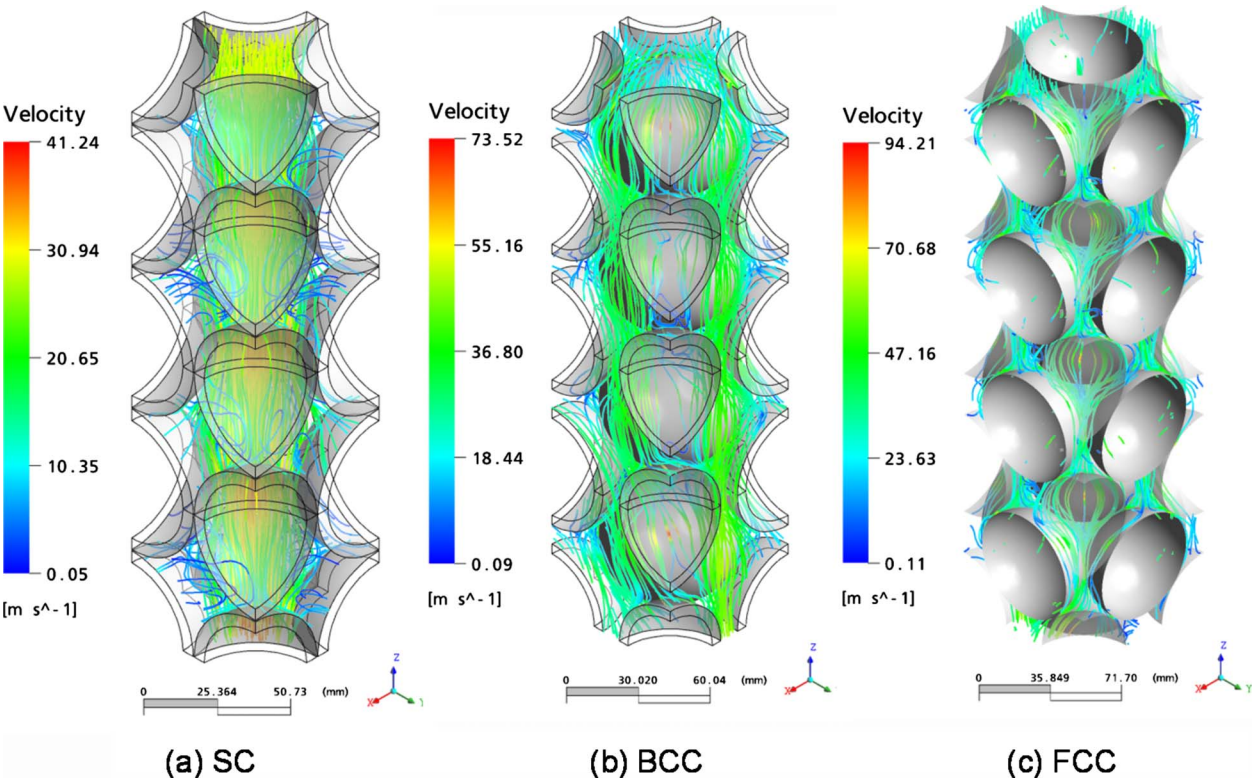


Fig. 4 Streamline distribution

Downloaded 02 Jun 2010 to 171.66.16.109. Redistribution subject to ASME license or copyright; see http://www.asme.org/terms/Terms_Use.cfm

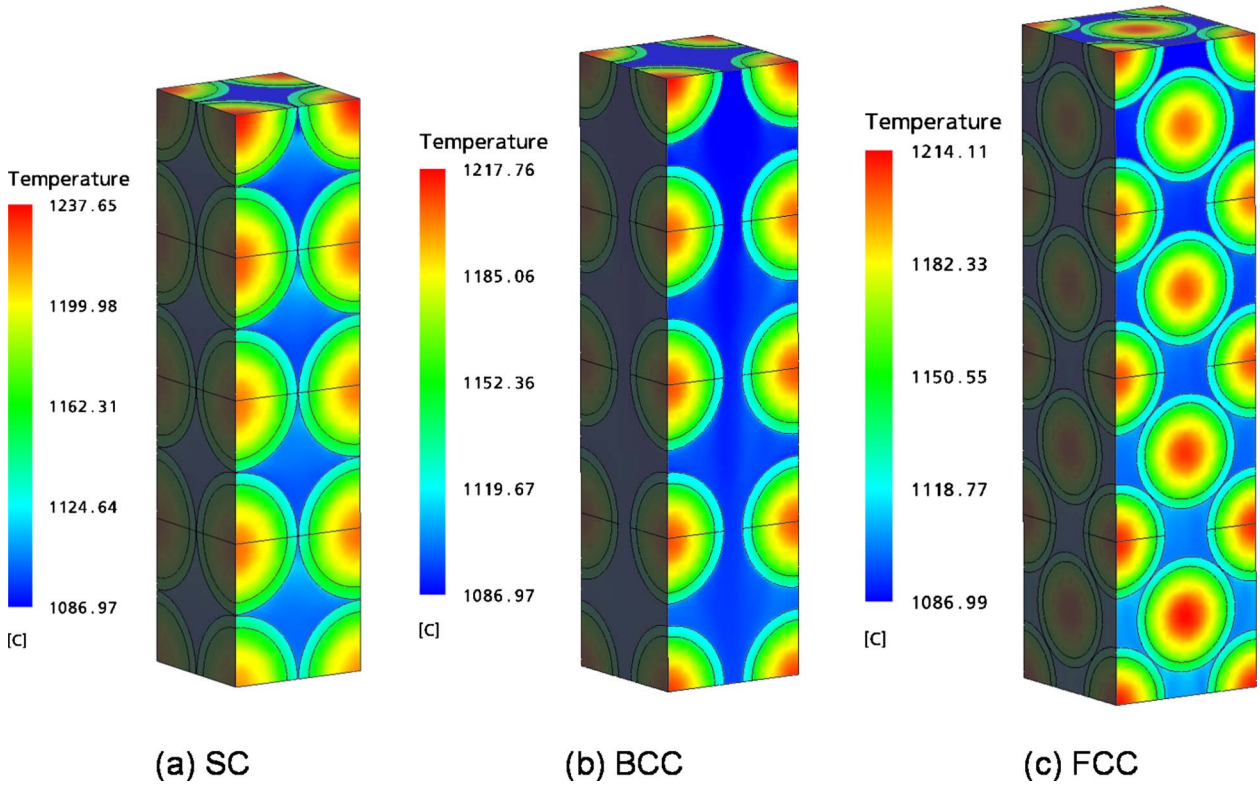


Fig. 5 Temperature distributions

ments as a benchmark problem, which has a channel-to-particle-diameter ratio of 1. The particle diameter is 12.7 mm.

Figure 8 shows the geometry of the problem and its surface grid. It should be noted that this geometry, of which the porosity is 0.476, is similar to the SC arrangement in the previous analysis except that the periodic surfaces are changed to the channel wall. The total number of nodes used is 165 689. Seven Reynolds numbers based on the superficial velocity and hydraulic diameter are selected, which is varied from 1 to 5×10^4 to cover both a laminar and a turbulent flow. A standard k-ε model is employed for a turbulence closure. The velocity that corresponds to the Reynolds number is fixed at the inlet boundary, and the relative static pressure is set to zero at the outlet. A no-slip condition is applied for the wall region.

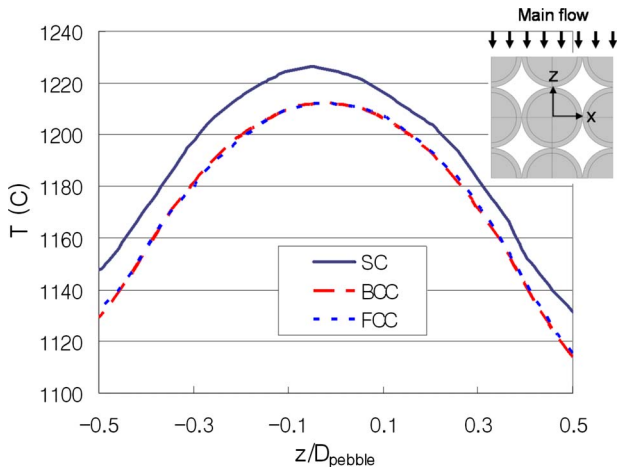


Fig. 6 Comparison of temperature profiles along the vertical direction of the pebble cross section

Figure 9 shows the result of the simulated streamlines for the turbulent flow (Re=5000). It is seen that a similar pattern of the flow is repeated in the downstream flow after passing through the

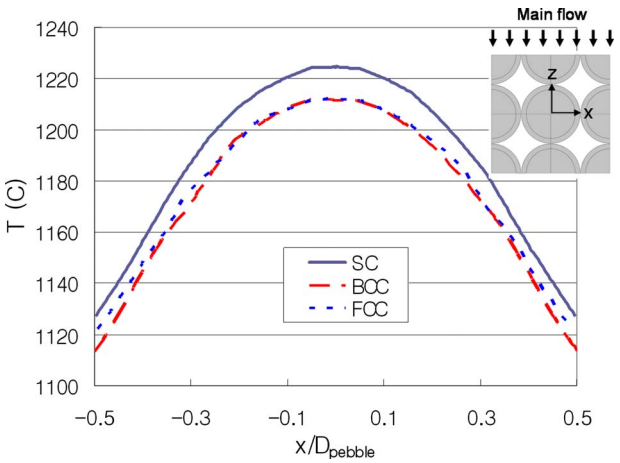


Fig. 7 Comparison of temperature profiles along the horizontal direction of the pebble cross section

Table 4 Comparison of the pressure drop and Nusselt number

Variable		SC	BCC	FCC
Porosity		0.489	0.336	0.277
P/H (kPa/m)	CFD	3.56	14.2	19.9
	Correlation	9.09	37.3	72.9
Nu	CFD	224	386	352
	Correlation	367	553	683

Downloaded 02 Jun 2010 to 171.66.16.109. Redistribution subject to ASME license or copyright; see http://www.asme.org/terms/Terms_Use.cfm

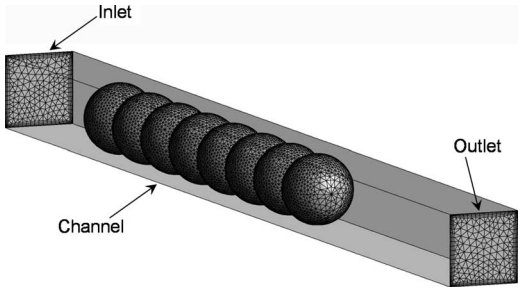


Fig. 8 Geometry and its surface grid for the pressure drop benchmark

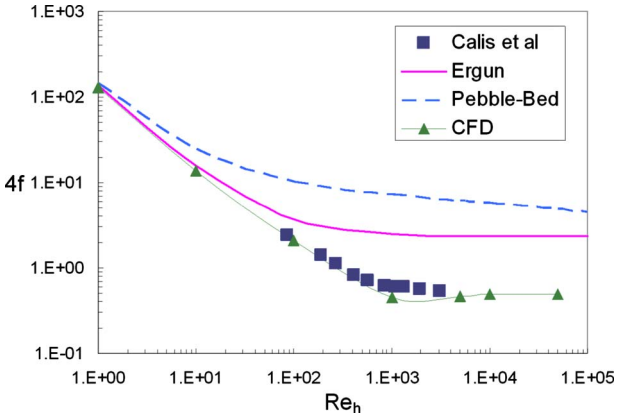


Fig. 10 Comparison of friction factors between experiments, correlation, and CFD results

first particle, which implies that a small number of particles is enough to assess the pressure drop characteristics of the packed particles.

To assess the simulated results, the pressure drop is changed to a friction factor f defined as

$$4f = \frac{2\Delta P}{\rho(u_0/\varepsilon)^2}\left(\frac{d_h}{L}\right) \tag{4}$$

Compared are not only the experiment of Calis et al. but also the well-known Ergun correlation [10] for a pressure drop across a random bed of particles determined from

$$4f = \frac{c_1}{\mathrm{Re}_h} + c_2 \tag{5}$$

where c_1 and c_2 are the empirical parameters, 133 and 2.33, respectively.

Figure 10 shows a comparison of the friction factors from the experimental data, the Ergun correlation, the correlation used for the pebble-bed core, and the CFD results as a function of the Reynolds number. It is seen that the agreements between the CFD results and the experimental data are satisfactory. Some deviation occurs at a Reynolds number of about 1000, which corresponds to a transition region from a laminar flow to a turbulent one, but the difference is not that significant. It is also seen that the correlation describes the friction factor well in the regions of a low Reynolds number but reveals a larger deviation from the experiment. These results support the explanation for the result in the previous section that the experiment correlations obtained from a random packed bed of particles or pebbles has a limitation for describing local flow characteristics.

Conclusion

CFD analyses on a local hot core region in a pebble type VHTR were performed to investigate the local fuel temperature by using the input and boundary data obtained from the result of the GAMMA code analysis for a 400 MW_t PBR of which the inlet and outlet temperatures at the core were 490°C and 950°C, respectively. Three pebble arrangements, which are the SC, the BCC, and the FCC, were selected.

The SC showed the highest fuel temperature among the three pebble arrangements because its main stream is not disturbed by the pebbles so that a cooling flow around their surface is not distributed well. In contrast, the others have zigzagged flow patterns, which supply a sufficient flow around the pebble surfaces and results in an enhancement of the surface cooling effect. It was also found that the maximum fuel temperatures of all the arrangements considered are still below the normal operational limit of 1250°C.

Comparison of the CFD results with the empirical correlation used in a system code was made for the pressure drop and the heat

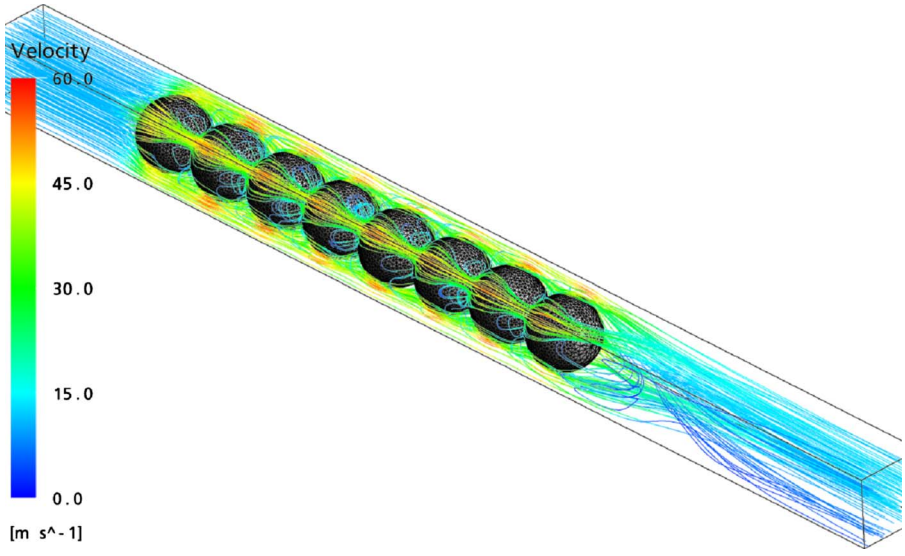


Fig. 9 Simulated streamlines for the turbulent flow (Re=5000)

Downloaded 02 Jun 2010 to 171.66.16.109. Redistribution subject to ASME license or copyright; see http://www.asme.org/terms/Terms_Use.cfm

transfer through the pebble arrangements. Both results showed a similar tendency that the pressure drop and the heat transfer increases as the porosity decreases, but a large difference was observed in their absolute values, which suggests that a direct application of this empirical correlation to a local analysis is not valid. To verify this suggestion, a benchmark calculation for the pressure drop for packed particles in a square channel was performed. The results indicated that the correlation for the full core used in the system code is not valid for the prediction of a local thermal-fluid behavior in an ordered pebble arrangement.

In conclusion, this study showed that the CFD method using the suggested approach could be a possible choice for a local hot core analysis of a PBR core. For this purpose, it is emphasized that detailed benchmark calculations should be performed before applying the CFD approach to a real PBR design, which requires a large number of experimental data for determining the flow and heat transfer characteristics in a pebble core.

Acknowledgment

This study has been carried out under the Nuclear R&D Program by the Korea Ministry of Education, Science and Technology.

Nomenclature

A_{CFD} = cross-sectional area of the CFD model, m^2
A_{PBR} = cross-sectional area of the PBR core, m^2
c_1, c_2 = empirical parameters, dimensionless
c_p = heat capacity, (J/kg K)
d_h = hydraulic diameter, m
d_p = pebble or particle diameter, m
$4f$ = friction factor, dimensionless
L = packing bed length, m
Re = Reynolds number, $(\rho u_o d_p/\mu)$, dimensionless
Re_h = Reynolds number, $(\rho(u_o/\varepsilon)d_h/\mu)$, dimensionless
$\dot{m}_{PBR}$ = total core flow in the PBR, kg/s
Nu = Nusselt number, $(\alpha d_p/\lambda)$, dimensionless
Pr = Prandtl number, $(\mu c_p/\lambda)$, dimensionless
u_o = superficial velocity, m/s
ΔP = pressure drop, Pa
Q_s = heat transferred from the surface, W
ΔH = packing pebble-bed height, m

Greek Letters

α = average heat transfer coefficient, $W/(m^2 K)$
λ = thermal conductivity, W/(m K)
ε = porosity
ρ = density, kg/m^3
μ = viscosity, kg/(m s)
Ψ = pressure drop parameter defined in Eq. (2), dimensionless

References

[1] Chang, J., Kim, Y. W., Lee, K. Y., Lee, Y. W., Lee, W. J., Noh, J. M., Kim, M. H., Lim, H. S., Shin, Y. J., Bae, K. K., and Jung, K. D., 2007, "A Study of a Nuclear Hydrogen Production Demonstration Plant," Nuclear Engineering and Technology—Journal of the Korean Nuclear Society, **39**(2), pp. 111–122.
[2] Oh, C. H., Davis, C., Barner, R., and Sherman, S., 2006, "Design Configurations for Very High Temperature Gas-Cooled Reactor Designed to Generate Electricity and Hydrogen," *Proceedings of International Conference on Nuclear Engineering*, Miami, FL, Jul. 17–20.
[3] Zhang, Z., Wu, Z., Sun, Y., and Li, F., 2006, "Design Aspects of the Chinese Modular High-Temperature Gas-Cooled Reactor HTR-PM," Nucl. Eng. Des., **236**(5–6), pp. 485–490.
[4] Richards, M., Lee, W., Kim, Y., Tak, N., and Reza, M., 2007, "Thermal Hydraulic Optimization of a VHTR Block-Type Core," *Transactions of 15th International Conference on Nuclear Engineering*, Nagoya, Japan, Apr. 22–26.
[5] In, W. K., Chun, T. H., Lee, W. J., and Chang, J. H., 2005, "CFD Analysis of the Fuel Temperature in High Temperature Gas-Cooled Reactors," *Transactions of the Korea Nuclear Society Autumn Meeting*, Busan, Korea, Oct. 27–28.
[6] CFX, Release 10.0, Reference Manual, ANSYS Inc., http://www.ansys.com/cfx (2005).
[7] Lim, H. S., and No, H. C., 2006, "GAMMA Multidimensional Multicomponent Mixture Analysis to Predict Air Ingress Phenomena in an HTGR," Nucl. Sci. Eng., **152**, pp. 87–97.
[8] French, H., 1980, *Heat Transfer and Fluid Flow in Nuclear Systems*, Pergamon, New York, pp. 382–401.
[9] Evaluation of High Temperature Gas Cooled Reactor Performance, IAEA CFP5 Draft 2nd TECDOC, p. 14.
[10] Calis, H. P. A., Nijenhuis, J., Paikert, B. C., Dautzenberg, F. M., and Van den Bleek, C. M., 2001, "CFD Modelling and Experimental Validation of Pressure Drop and Flow Profile in a Novel Structured Catalytic Reactor Packing," Chem. Eng. Sci., **56**, pp. 1713–1720.

Downloaded 02 Jun 2010 to 171.66.16.109. Redistribution subject to ASME license or copyright; see http://www.asme.org/terms/Terms_Use.cfm

Experimental and Numerical Modeling of Transition Matrix From Momentum to Buoyancy-Driven Flow in a Pressurized Water Reactor

Thomas Höhne
e-mail: t.hoehne@fzd.de

Sören Kliem

Roman Vaibar

Forschungszentrum Dresden-Rossendorf (FZD),
Institute of Safety Research,
P.O. Box 510119,
D-01314 Dresden, Germany

The influence of density differences on the mixing of the primary loop inventory and the emergency core cooling (ECC) water in the cold leg and downcomer of a pressurized water reactor (PWR) was analyzed at the Rossendorf coolant mixing (ROCOM) test facility. This paper presents a matrix of ROCOM experiments in which water with the same or higher density was injected into a cold leg of the reactor model with already established natural circulation conditions at different low mass flow rates. Wire-mesh sensors measuring the concentration of a tracer in the injected water were installed in the cold leg, upper and lower part of the downcomer. A transition matrix from momentum to buoyancy-driven flow experiments was selected for validation of the computational fluid dynamics software ANSYS CFX. *A hybrid mesh with* 4×10^6 *elements was used for the calculations. The turbulence models usually applied in such cases assume that turbulence is isotropic, whilst buoyancy actually induces anisotropy. Thus, in this paper, higher order turbulence models have been developed and implemented, which take into account that anisotropy. Buoyancy generated source and dissipation terms were proposed and introduced into the balance equations for the turbulent kinetic energy. The results of the experiments and of the numerical calculations show that mixing strongly depends on buoyancy effects: At higher mass flow rates (close to nominal conditions) the injected slug propagates in the circumferential direction around the core barrel. Buoyancy effects reduce this circumferential propagation with lower mass flow rates and/or higher density differences. The ECC water falls in an almost vertical path and reaches the lower downcomer sensor directly below the inlet nozzle. Therefore, density effects play an important role during natural convection with the ECC injection in PWR and should be also considered in pressurized thermal shock scenarios.* ANSYS CFX *was able to predict the observed flow patterns and mixing phenomena quite well.* [DOI: 10.1115/1.2983137]

Introduction

Density differences between the coolant water and the primary loop inventory can play an important role during loss-of-coolant accidents in nuclear power plants, as the injection of the relatively cold emergency core cooling (ECC) water can induce buoyancy-driven stratification. This stratification can cause high temperature gradients and increased thermal stresses of the reactor pressure vessel (RPV), and these scenarios are called pressurized thermal shock (PTS) scenarios. Moreover, in case of the inadvertent injection of the ECC water with a low boron concentration, a boron dilution transient could be initiated. Grundmann and Rohde [1] has shown that the assumption of a homogeneous distribution (i.e., ideal mixing) of the injected lower borated water at the core inlet of pressurized water reactors (PWRs) does not yield conservative results. The remaining uncertainties are too large to be acceptable for safety analyses: There are for instance numerous postulated accident scenarios in which the reactor core would survive undamaged or would not even reach criticality under the assumption of ideal mixing, whereas incomplete mixing would lead to fuel rod failures. In reality, partial mixing takes place, and the detailed mixing pattern at the core inlet is required to make accurate and realistic predictions about the safety of the reactor. This mixing pattern is the consequence of a complex three-dimensional fluid flow. Recent progress in computer hardware and numerical techniques has made it viable to predict these mixing patterns using CFD codes, see for instance the contributions by Moretti et al. [2], Bieder et al. [3], Prasser et al. [4], Höhne [5], and Cartland-Glover et al. [6]. However, as CFD codes contain more or less empirical models (for instance turbulence models) it is necessary to validate the predicted results using experimental data. This is especially important in case of safety-critical coolant mixing phenomena. There are several test facilities to study the mixing of cold ECC water injected into the cold leg of a PWR, see Refs. [7–10]. In order to examine coolant mixing in the RPV of a German-type PWR, the Rossendorf coolant mixing model (ROCOM) test facility was used in the current work.

A large eddy simulation (LES) formulation was used by Höhne et al. [11] to validate the CFD code TRIO_U for buoyancy-driven flows.

ROCOM Test Facility

The ROCOM test facility [4] consists of a RPV model (Fig. 1) with four inlet and four outlet nozzles. The facility is equipped with four fully operating loops, i.e., it has four circulation pumps, which are driven by motors with computer-controlled frequency transformers. For natural circulation investigations, the pumps are operated at low speed by means of the frequency transformer system. Geometric similarity between the original reactor and

Manuscript received July 21, 2008; final manuscript received July 23, 2008; published online October 2, 2008. Review conducted by Dilip R. Ballal.

Copyright © 2009 by ASME

Downloaded 02 Jun 2010 to 171.66.16.109. Redistribution subject to ASME license or copyright; see http://www.asme.org/terms/Terms_Use.cfm



Fig. 1 Bird's eye view of the ROCOM test facility

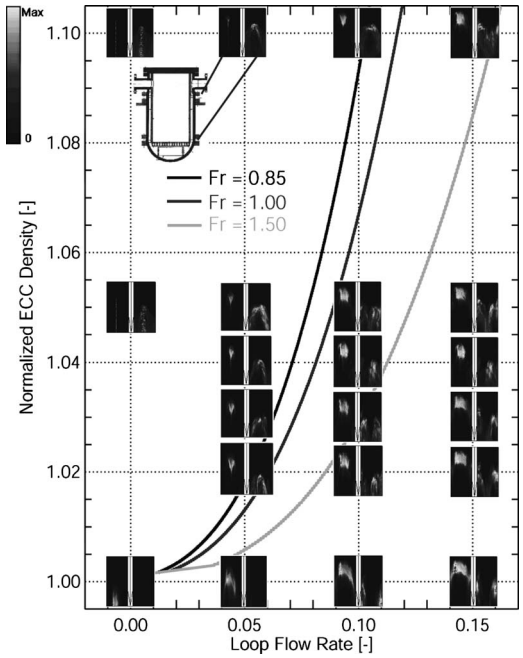


Fig. 2 Test matrix of ECC injection experiments, classification of the ROCOM tests, and isolines of Froude numbers

ROCOM is maintained from the inlet nozzles to the core inlet. The core itself is excluded from the similarity; rather, a core simulator with the same Euler number (pressure drop versus flow head) as in the original reactor is used. The ROCOM reactor model is manufactured from perspex (Fig. 1). The reactor model describes the geometry of the original PWR with respect to the design of the nozzles (diameter, curvature radii, and diffuser parts), the characteristic extension of the downcomer cross section below the nozzle zone, the perforated drum in the lower plenum, and the design of the core support plate with the orifices for the coolant. The flow rate in the loops is scaled according to the transit time of the coolant through the reactor model. Since the geometrical scale of the facility is 1:5, the transit time of the coolant becomes identical to the original reactor when the coolant flow rate is also scaled by 1:5.

From these scaling laws, the nominal flow rate in ROCOM results in 185 m^3/h per loop. The Reynolds numbers in ROCOM are approximately two orders of magnitude smaller than in the original. A factor of 25 results from the downscaling of the geometry and mass flow rates (velocities). The remaining difference comes from operation at room temperature and ambient pressure. At room temperature, the viscosity of water is approximately by a factor of 8 higher than under original reactor conditions.

Since coolant mixing is mainly caused by turbulent dispersion (which is independent of the exact fluid properties) it is possible to use a tracer substance to model differences in boron concentration or coolant temperature. The coolant in the disturbed loop was marked by injecting a sodium chloride solution into the main coolant flow upstream of the reactor inlet nozzle. Magnetic valves controlled the injection process. As the ROCOM facility can not be heated, the higher density of the cold ECC water was simulated by adding sugar (glucose). A sugar solution with a corresponding density of 1100 kg/m^3 has a viscosity, which is by factor of 3 higher than that of pure water. The sugar tracer can therefore still be envisaged as a fluid with low viscosity.

The tracer distribution in the reactor model was measured by electrode-mesh sensors, which sample the distribution of the electrical conductivity over the cross section of the flow path. The development of these sensors was aimed at a direct conductivity measurement between pairs of crossing wires to avoid tomographic reconstruction algorithms [12] and to reach a time resolution of up to 10,000 frames per second [13].

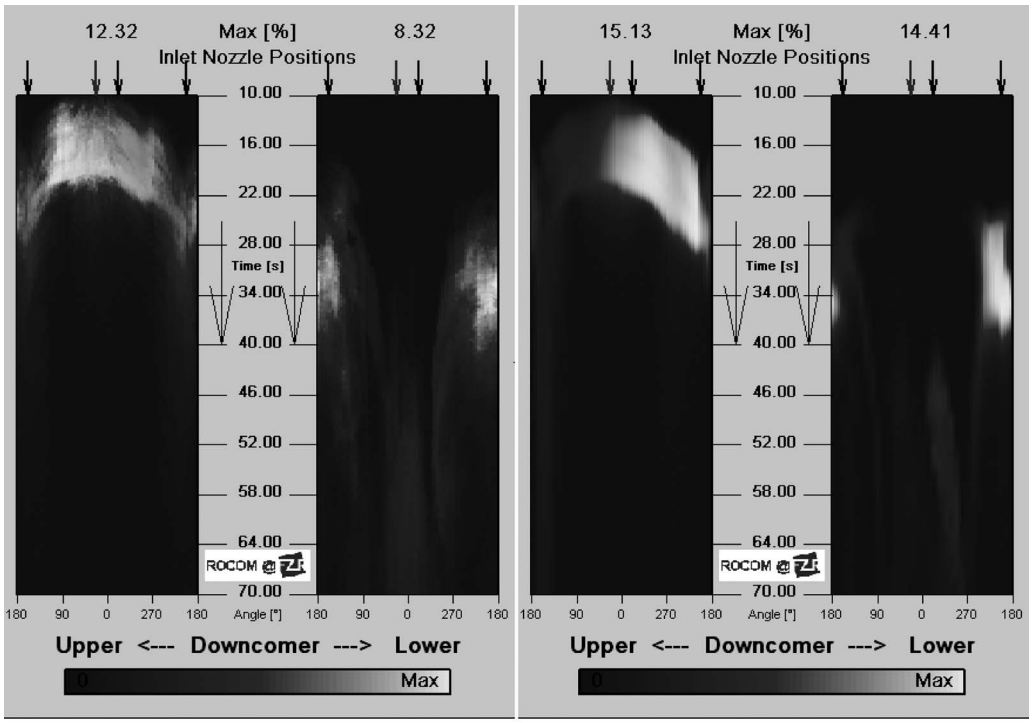
The described mesh sensors are placed at four positions of the flow path. The first sensor is flanged to the reactor inlet nozzle in loop no. 1. It observes the distribution at the reactor inlet. The second and the third sensors are located at the inlet and at the outlet of the downcomer. The downcomer sensors consist of 64 radial fixing rods with orifices for four circular electrode wires. Small ceramic insulation beads separate rods and wires electrically. The rods act as radial electrodes, i.e., each rod corresponds to a circumferential measuring position.

The fourth sensor is integrated into the core support plate. 2×15 electrode wires are arranged such that the wires of the two planes cross in the centers of the coolant inlet orifices of each fuel element. In this way, the tracer concentration is measured at each fuel element inlet. Approximately 1000 measuring points are recorded in total. The measuring frequency is 200 Hz. In most cases ten successive measurements were averaged, and the result was stored with a frequency of 20 Hz because the characteristic frequency of the observed phenomena did not require a higher sampling frequency. The measured local conductivities are then related to reference values. The result is a mixing scalar, which characterizes the instantaneous share of coolant originating from the disturbed loop (i.e., where the tracer is injected) at a given location inside the flow field. This scalar is dimensionless. Assuming similarity between the tracer field and the temperature and boron concentration fields, it can be used to apply the experimental results to the original reactor. The reference values correspond to the unaffected coolant (Index "0") and the coolant at the disturbed reactor inlet nozzle (index "1"). The difference between the two reference values is the magnitude of the perturbation. The mixing scalar Θ is defined as follows:

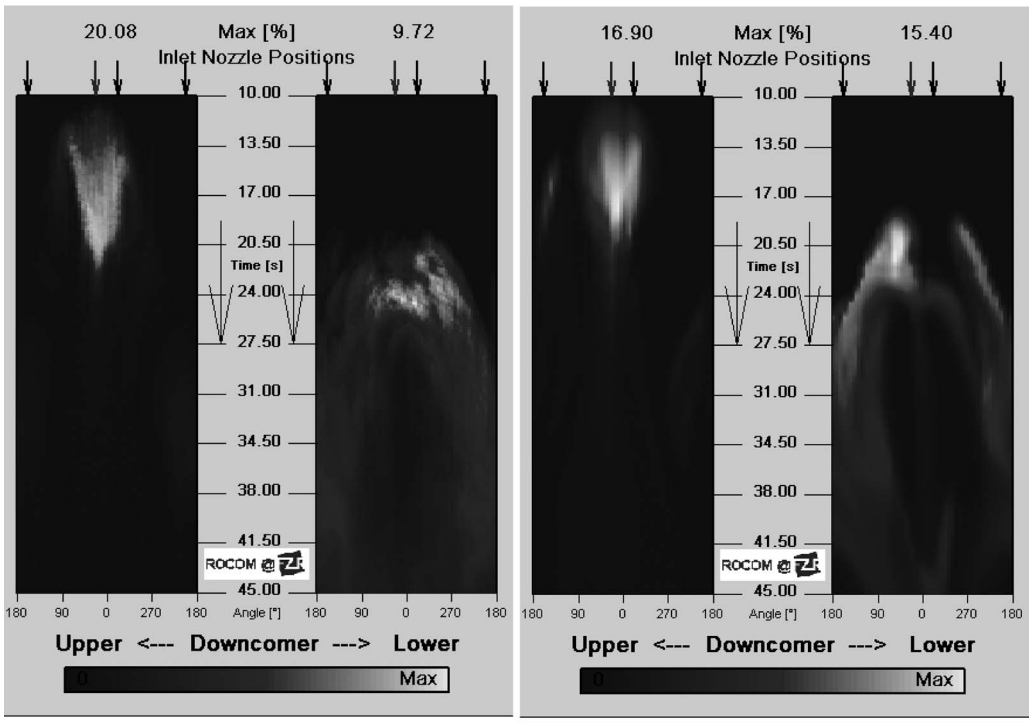


Fig. 3 Flow domain with inlet boundary conditions

Downloaded 02 Jun 2010 to 171.66.16.109. Redistribution subject to ASME license or copyright; see http://www.asme.org/terms/Terms_Use.cfm



(*a*)



(*b*)

Fig. 4 Mixing scalar evolution in the downcomer in ROCOM buoyancy-driven mixing tests (uppercase—no density difference E1 and lowercase—10% density difference E6) and CFX-Experiment

$$\theta_{x,y,z,t} = \frac{\sigma_{x,y,z,t} - \sigma_0}{\sigma_1 - \sigma_0} \cong \frac{T_{x,y,z,t} - T_0}{T_1 - T_0} \cong \frac{C_{B,x,y,z,t} - C_{B,0}}{C_{B,1} - C_{B,0}} \quad (1)$$

Here, σ is the electrical conductivity, T is the temperature, and C_B the boron concentration. Which of the two parameters, the temperature or boron concentration, is represented by the measured mixing scalar depends on the correct choice of reference values and the setup of the boundary conditions in the experiment. Linearity between the tracer concentration and the measured local conductivity is used to transform the conductivity measurements

Downloaded 02 Jun 2010 to 171.66.16.109. Redistribution subject to ASME license or copyright; see http://www.asme.org/terms/Terms_Use.cfm

of the wire mesh sensor into dimensionless scalar concentrations. However, the addition of sugar changes the linear relation between the tracer concentration and conductivity. Therefore, the original correlation for solutions at a low viscosity was replaced by a function, which depends also on the normalized viscosity, which is proportional to the density of the glucose water mixture.

The correlations have been verified by separate mixing tests in which the conductivity was measured for given values of the mixing scalar.

ECC Water Injection With Density Effects

The objective of the experiments was the investigation of the effects of density differences between the primary loop inventory and the ECC water on the mixing in the downcomer. The mass flow rate was varied between 0% and 15% of the nominal flow rate, i.e., it was kept at the same order of magnitude as the natural circulation. The density differences between the ECC and loop water were varied between 0% and 10%. In total, 20 experiments were carried out (mixing pictures in Fig. 2). The analysis of all experiments is presented in Ref. [14]. In that paper, a criterion for the distinction between the momentum driven and density driven flows based on the experimental data has been developed.

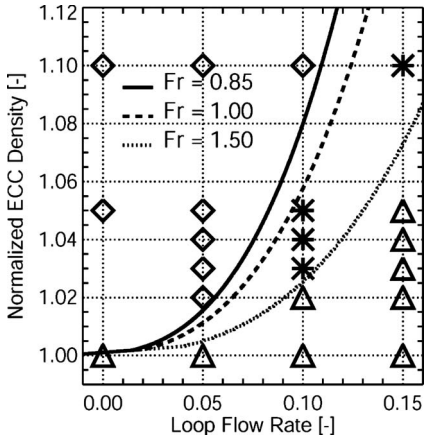


Fig. 5 Classification of ROCOM tests with density differences with respect to the downcomer Froude number (Eq. (2)), calculated cases

Numerical Modeling

The CFD code for simulating the mixing studies was ANSYS CFX [15]. ANSYS CFX is an element-based finite-volume method with second-order discretization schemes in space and time. It uses a coupled algebraic multigrid algorithm to solve linear systems arising from discretization. The discretization schemes and the multigrid solver are scalably parallelized. ANSYS CFX works with unstructured hybrid grids consisting of tetrahedral, hexahedral, prism, and pyramid elements.

Numerical Scheme, Nodalization, Time step size, and Turbulence Modeling. The separation of error components (grid density, discretization method, time step size, iteration error, and the

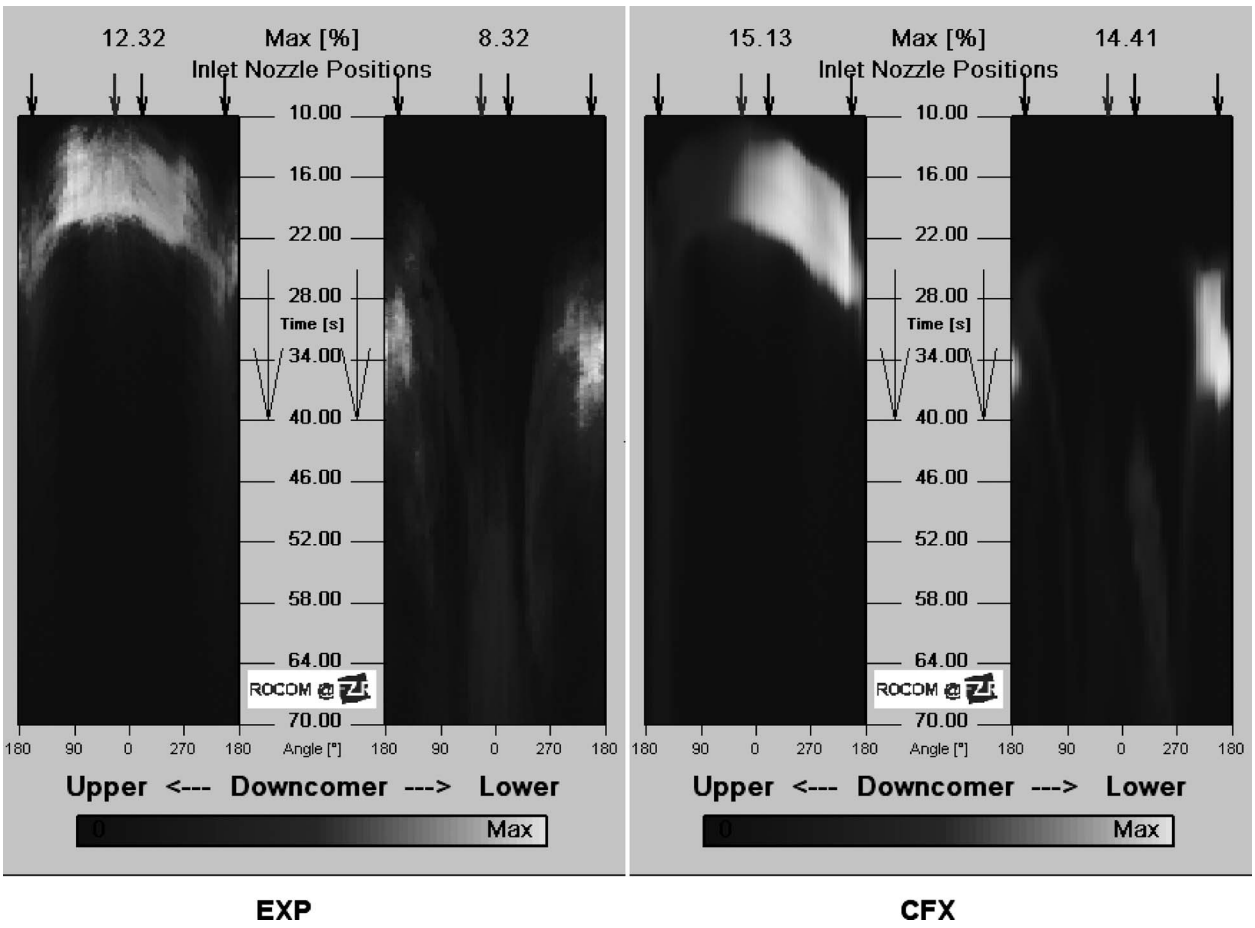


Fig. 6 Upper and lower downcomer—Experiment versus CFX, E1

Downloaded 02 Jun 2010 to 171.66.16.109. Redistribution subject to ASME license or copyright; see http://www.asme.org/terms/Terms_Use.cfm

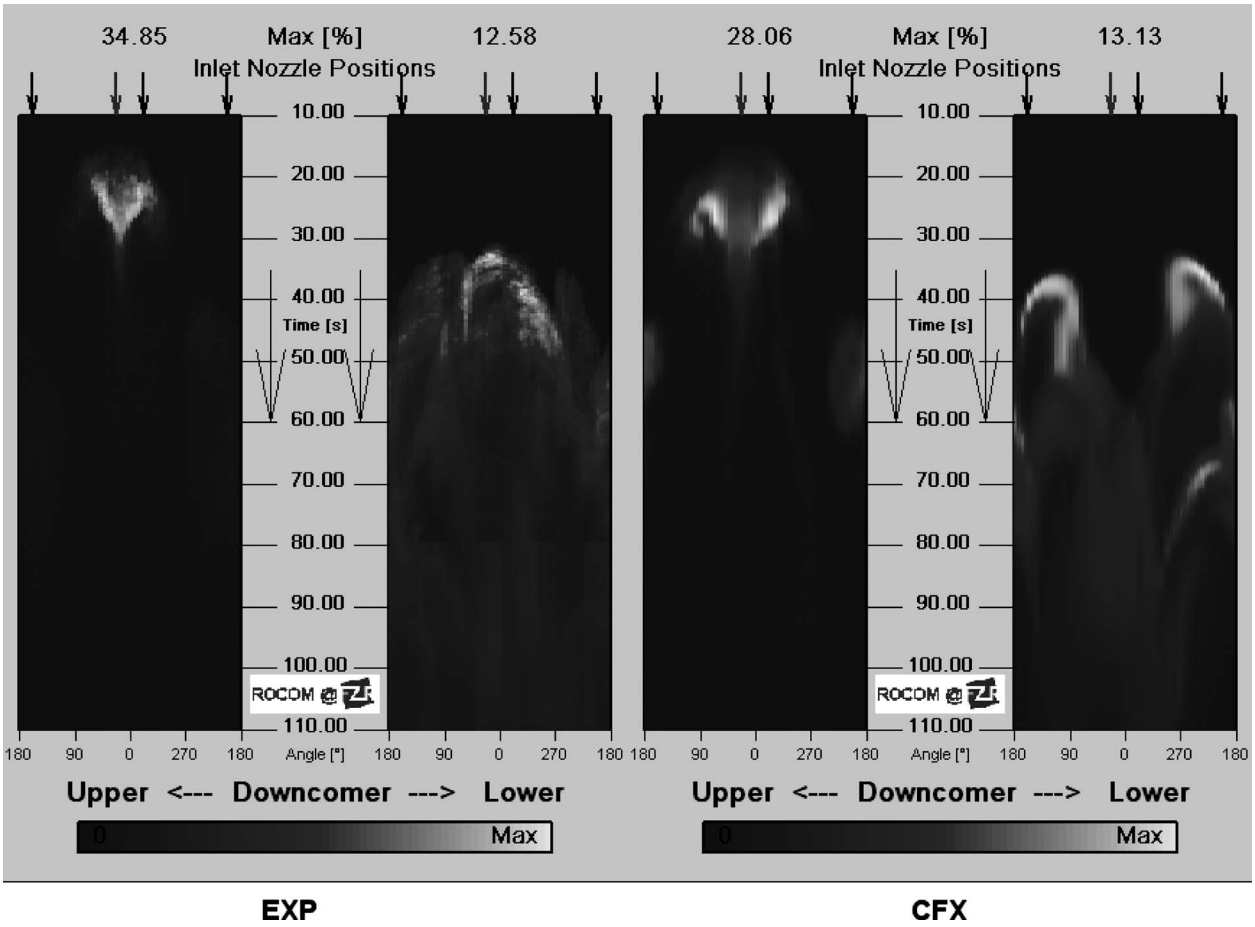


Fig. 7 Upper and lower downcomer—Experiment versus CFX, E2

employed mathematical models) for complex three-dimensional CFD calculation are difficult.

Discretization errors can be reduced by using finer grids, higher order discretization methods, and smaller time step sizes. However, in many practical three-dimensional applications grid- and time step-independent solutions cannot be obtained because of hardware limitations. In these cases, the remaining errors and uncertainties should be quantified as described in the ECORA best practice guidelines (BPGs) by Menter [16].

In the current study, the CFD simulations were performed according to these BPGs [14]. A convergence criterion of 1×10^{-4} was used to ensure negligibly small iteration errors.

In the calculations shown below, the high-resolution (HR) discretization scheme of ANSYS CFX was used to discretize the convective terms in the model equations. A second-order implicit scheme was used to approximate the transient terms. The used time step size was 0.05 s.

The glucose water, which had a higher density, was modeled with the multicomponent model of ANSYS CFX. In a multicomponent flow, the components share the same velocity, pressure, and temperature fields. The properties of multicomponent fluids are calculated on the assumption that the constituent components form an ideal mixture. The glucose water is modeled as a component with a different density and viscosity compared to water. The mass fraction of the glucose water can be directly related to the mixing scalar described in Eq. (1). Six transient calculations were performed on the FZD LINUX cluster (Operating system: Linux Scientific 64 bit, 32 AMD Opteron Computer Nodes, Node configuration: 2×AMD Opteron 285 (2.6 GHz, dual-core), 16 GB Memory) and they took 9 days each to complete. Six processors were used for the above mentioned simulations in a parallel mode with the message passing protocol parallel virtual machine (PVM).

Turbulence Modeling Including Buoyancy. While some commercial CFD codes in general can treat buoyancy, e.g., within the Boussinesq approximation, there are deficiencies in the modeling of buoyancy-driven turbulence. The turbulence models usually applied in such cases assume that turbulence is isotropic, while buoyancy actually induces anisotropy. Thus, higher order turbulence models have been developed that take into account that anisotropy. Buoyancy generated source and dissipation terms were proposed and introduced into the balance equations for the turbulent kinetic energy [17].

Geometrical Simplifications, Local Details. The geometric details of the ROCOM internals have a strong influence on the flow field and on the mixing. Therefore, an exact representation of the cold leg, the inlet nozzle region, the downcomer below the inlet region, and the obstruction of the flow by the outlet nozzles in the downcomer is necessary (see Fig. 3). In the current study, these geometric details were modeled using the ICEM CFD software. The final model included the inlet nozzles with the diffuser part, the orifices of the outlet nozzles, the downcomer extension, the lower plenum, the core support plate, the perforated drum, the core simulator, the upper plenum, and the outlet nozzles. Additionally one cold leg including the ECC injection line was modeled (Fig. 3).

Grid Generation. The mesh was generated with the ICEM CFD software. It consisted of approximately 2×10^{6} nodes and ap-

Downloaded 02 Jun 2010 to 171.66.16.109. Redistribution subject to ASME license or copyright; see http://www.asme.org/terms/Terms_Use.cfm

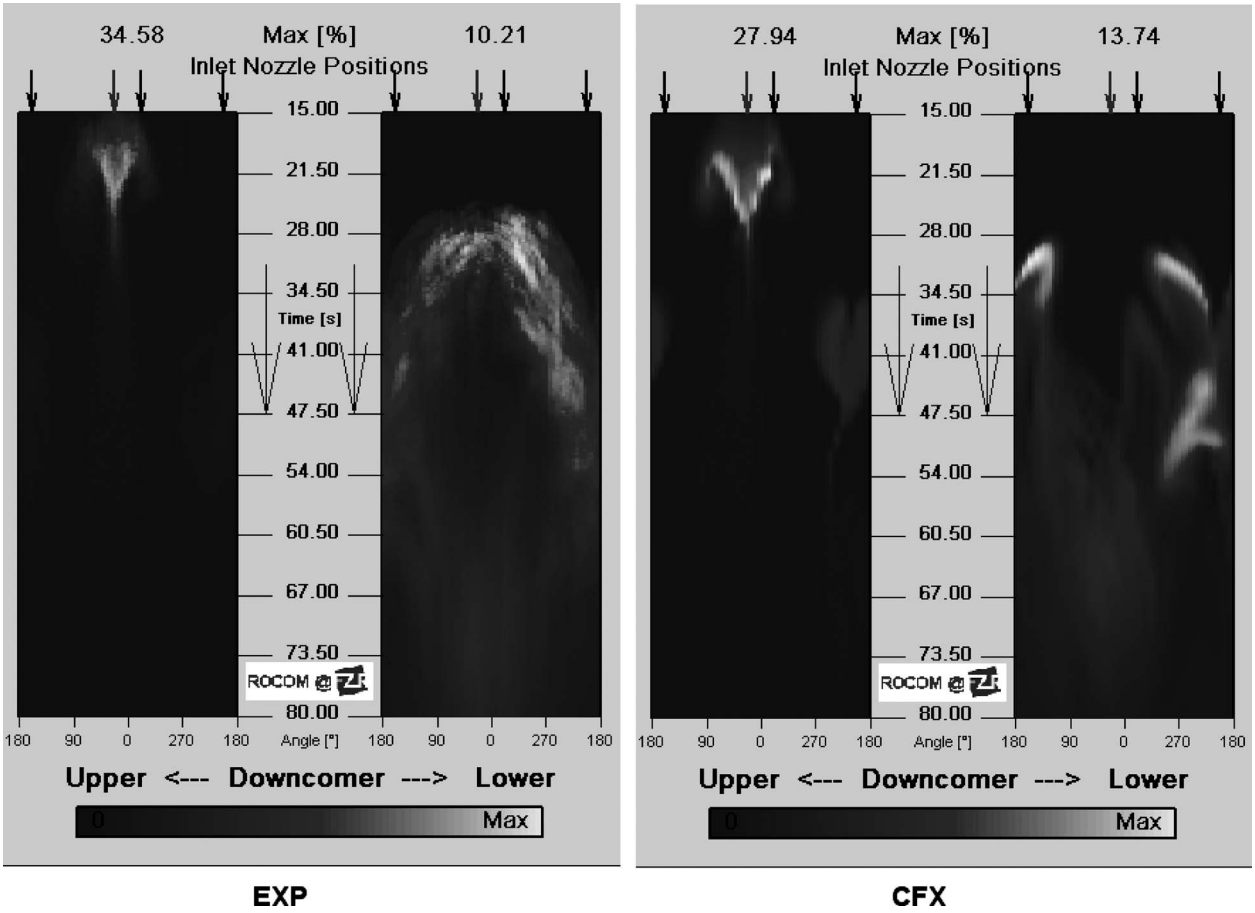


Fig. 8 Upper and lower downcomer—Experiment versus CFX, E6

proximately 4×10^6 hybrid elements (Fig. 3). The mesh was refined at the perforated drum, in the lower support plate, and at the ECC injection line. The downcomer and nozzle regions were discretized with hexahedral cells; tetrahedral elements were used for the lower plenum.

Boundary and Initial Conditions. Inlet boundary conditions were specified at the ECC injection line and after the bend of the cold leg CL1. Constant uniform velocities were used to simulate the one-loop operation for a duration of 10 s. During this period a uniform velocity profile was also defined at the injection line. At all other times the velocities were set to zero. The glucose water mass fraction was set to 1 at the ECC injection line and to 0 at CL1. A zero state initialization was used with a constant loop mass flow rate. The time step selected was $t=0.05$ s and time duration of the flow was specified as $t_{\text{total time}}=150$ s for the cases with the low flow rate (i.e., cases denoted by dxm05). For all other cases, only a $t_{\text{total time}}=100$ s was required. The impulse of the injection of glucose water through the ECC line was defined via a step function.

A constant static pressure was specified at the outlet nozzles. A no-slip boundary condition with automatic linear/logarithmic wall functions was used at all solid walls.

At the cold leg sensor local measurement points (see Fig. 12) 32 circumferential sensor positions in the middle of the upper downcomer sensor plane were selected (Fig. 13) for the comparison of data and numerical predictions.

Results

Altogether 20 experiments have been carried out at the ROCOM test facility. In all experiments, the volume flow rate of the ECC injection line was kept constant at 1.0 l/s. The normalized density (rhoratio) is defined as the ratio between the density of water in the ECC line and density of fluid in the circuit. All other boundary conditions are identical. Due to the observed fluctuations of the flow field in the RPV, each experiment was repeated five times to average over these fluctuations. An error analysis showed that the experimental data have an error range of $\pm3\%$.

The experiments without density effects serve as reference experiments for the comparison. Figure 4 (uppercase) visualizes in unwrapped views the time evolution of the tracer concentration measured at the two downcomer sensors. The downwards directed second arrow from left indicates the position of the loop with the running pump, in that case delivering 15% of the nominal flow rate. No density difference was created (E1). At the upper downcomer sensor, the ECC water appears directly below the inlet nozzle. Due to the momentum created by the pump, the flow entering the downcomer is divided into two streams flowing right and left in a downwards directed helix around the core barrel. At the opposite side of the downcomer, the two streaks of the flow merge together and move down through the measuring plane of the lower downcomer sensor into the lower plenum. Such a flow distribution is typical for a single-loop operation. It is dominated by the momentum insertion due to the operating pump or the high natural circulation flow rate. The maximum tracer concentration of the ECC water in the downcomer is 12% of the injected water concentration at the upper sensor and 8% at the lower sensor.

Figure 4 (lowercase) shows the experiment E6, carried out at 10% of the nominal flow rate, but the density difference between the injected ECC water and the primary loop coolant is now 10%. In that case a streak formation of the water with higher density is

Downloaded 02 Jun 2010 to 171.66.16.109. Redistribution subject to ASME license or copyright; see http://www.asme.org/terms/Terms_Use.cfm

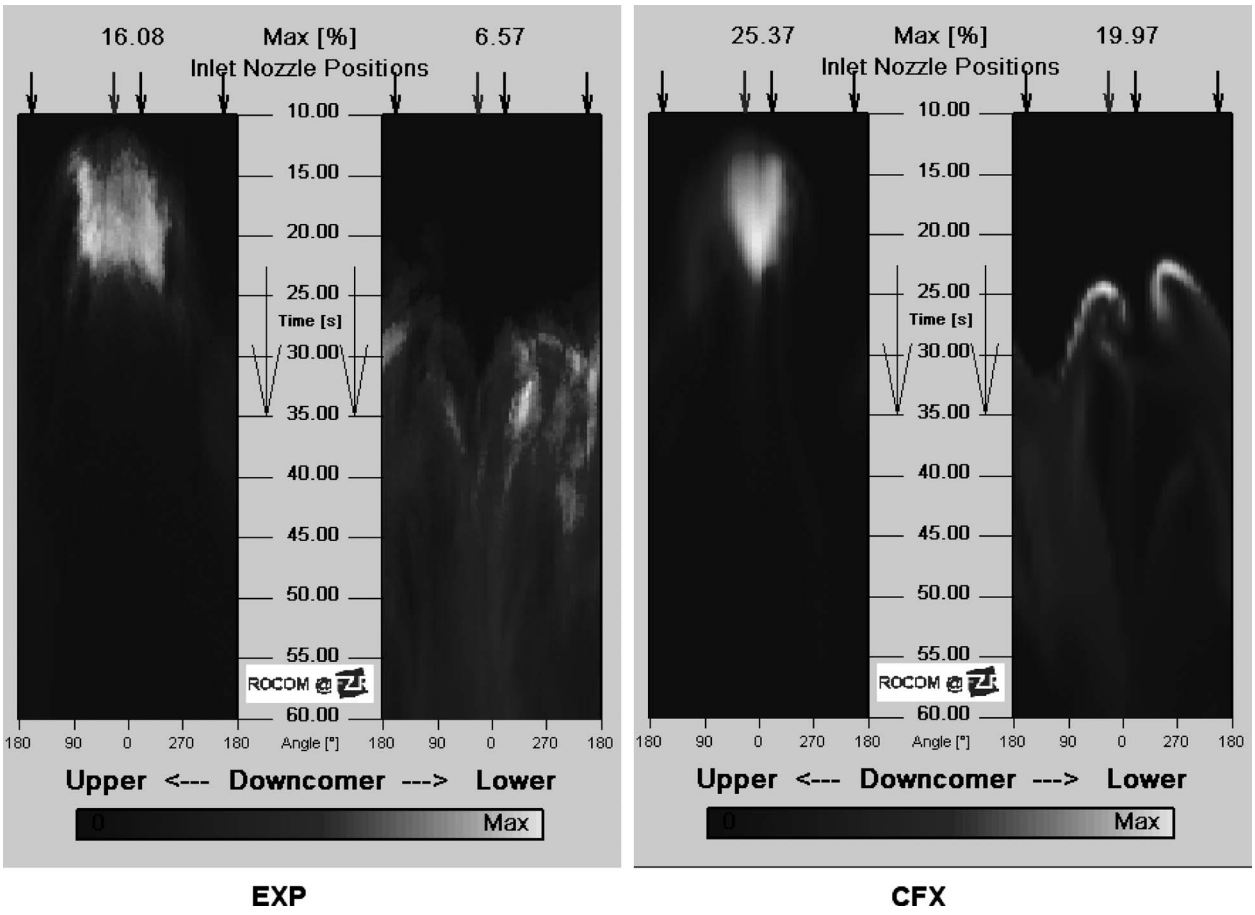


Fig. 9 Upper and lower downcomer—Experiment versus CFX, E4

observed. At the upper sensor, the ECC water covers a much smaller azimuthal sector. The density difference partly suppresses the propagation of the ECC water in horizontal direction. The ECC water falls down in an almost straight streamline and reaches the lower downcomer sensor directly below the affected inlet nozzle. Only later, coolant containing the ECC water appears at the opposite side of the downcomer. The visualizations of the behavior of the ECC water in the downcomer reveals that in case of momentum driven flow, the ECC water covers nearly the whole perimeter of the upper sensor and passes the measuring plane of the lower sensor mainly at the opposite side of the downcomer. When the density effects are dominating, the sector at the upper measuring device covered by the ECC water is very small. The ECC water falls down straightly and passes the sensor in the lower part of the downcomer below the inlet nozzle of the working loop. Furthermore, variations of the density were carried out to identify the transition region between momentum driven and density driven flows.

Based on these observations, the set of experiments conducted was divided into three groups: density dominated flow ($\diamond$), momentum dominated flow (Δ), and the transition region ($*$). The conditions at the inlet into the downcomer were used to calculate Froude numbers of the experiments according to the following formula:

$$\mathrm{Fr}_{\mathrm{DC}} = \frac{v_{\mathrm{in}}}{\sqrt{g \cdot H \cdot \rho_{\mathrm{in}} - \rho_a / \rho_{\mathrm{in}}}} \tag{2}$$

where v_{in} is the velocity at the reactor inlet (combined loop and ECC flow), g is the gravitational acceleration, H is the height of the downcomer, ρ_{in} the density of the incoming flow, calculated with the assumption of homogeneous mixing between the ECC and loop flow, and ρ_a is the density of the ambient water in the downcomer.

Lines of constant Froude numbers calculated by means of this formula are shown in Fig. 5. All experiments, identified as density dominated, are located in the region left of the isoline Fr=0.85 and all momentum dominated points are found right of the isoline Fr=1.5. Therefore, Fr=1 is about the critical Froude number separating the two flow regimes for the ROCOM test facility. Around this critical Froude number a transition region is located.

The flow conditions are defined by a difference in density variable rhoratio and the nominal mass flow rate through the inlet pipe define through the use of the ratio mratio (see also Fig. 5). From the whole set of data the following experiments were selected for the CFD calculations (indicated with an arrow in Fig. 5):

- E1 rhoratio=1.00 mratio=0.15, momentum dominated
- E2 rhoratio=1.02 mratio=0.05, momentum dominated
- E3 rhoratio=1.05 mratio=0.05, density dominated
- E4 rhoratio=1.05 mratio=0.10, transition region
- E5 rhoratio=1.10 mratio=0.15, transition region
- E6 rhoratio=1.10 mratio=0.10, density dominated

Case E1. For Case E1 (Fig. 6) the rhoratio is set to 0 and the Froude number Fr=∞, thus there is no influence of the buoyancy force, either to the global gravity forces or to the turbulence buoyancy force. The flow rate is set to 15% of the nominal mass flow rate of the cold leg, which was the highest flow rate used in the experimental studies. The maximum value of the mixing scalar at the experiment in the upper downcomer is 0.12 (CFX 0.17) and in the lower downcomer is 0.097 (CFX 0.154). In the CFD calculation the poor mixing and stratification in the cold leg causes the slug to be less diffuse, an effect that results in an overprediction

Downloaded 02 Jun 2010 to 171.66.16.109. Redistribution subject to ASME license or copyright; see http://www.asme.org/terms/Terms_Use.cfm

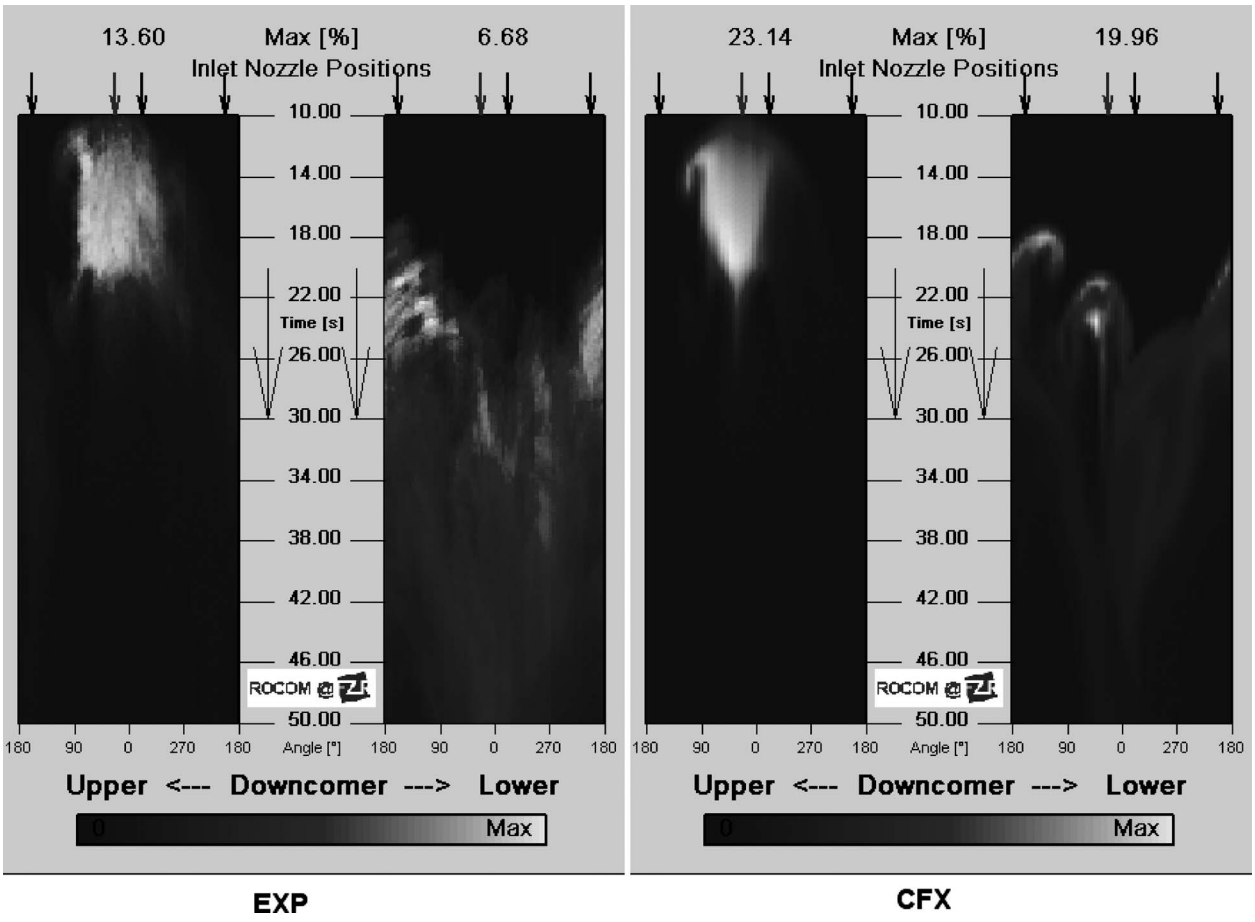


Fig. 10 Upper and lower downcomer—Experiment versus CFX, E3

when compared to the experimental values of the concentration at all positions of the wire mesh sensors. This is due to the fact that the slug of water in the simulation maintains a similar maximum value between the upper downcomer, while the concentration of the experimental slug decreases, as it is weakly dispersed. However, it is important to note that the timescales with which the slug is transported through the inlet nozzle and the upper downcomer are quite comparable and that there is a slight delay on the lower downcomer.

Case E2. In Case E2 (Fig. 7) the rhoratio is set to 2% and the Froude number is Fr=3.0796. The flow rate is set to 15% of the nominal mass flow rate in the cold leg.

The mixing and stratification in the cold leg observed in the experiment is very well described by the simulation. The comparison with the other wire mesh sensor position is that in the range of the measurement error of 3%. The maximum value of the mixing scalar in the experiment in the upper downcomer is 0.35 (CFX 0.28) and in the lower downcomer is 0.126 (CFX 0.131).

Case E3. In Case E3 (Fig. 8) rhoratio is set to 5% and the Froude number is Fr=0.5141. The flow rate is set to 5% of the nominal mass flow rate in the cold leg, which was the lowest flow rate used in the experimental studies.

Again, as in Case E6, mixing and stratification in the cold leg are very well described by the calculation. The maximum value of the mixing scalar in the experiment in the upper downcomer is 0.35 (CFX 0.28) and in the lower downcomer is 0.128 (CFX 0.137). The comparison at the wire mesh sensor positions is in the range of the measurement error.

Case E4. In Case E4 (Fig. 9) the rhoratio is set to 5% and the Froude number is Fr=1.1562. The flow rate is set to 10% of the nominal mass flow rate in the cold leg. The maximum value of the mixing scalar in the experiment in the upper downcomer is 0.16 (CFX 0.25) and in the lower downcomer 0.066 (CFX 0.200). It is important to note that the timescales with which the slug is transported through the inlet nozzle and the upper downcomer are quite comparable and that there is a slight delay on the lower downcomer, which could arise from the poor mixing and stratification in the cold leg in the simulation.

Case E5. In case E5 (Fig. 10) rhoratio is set to 10% and the Froude number is Fr=1.3835. The flow rate is set to 15% of the nominal mass flow rate in the cold leg. The maximum value of the mixing scalar in the experiment at the upper downcomer sensor is 0.14 (CFX 0.23) and at the lower downcomer sensor is 0.067 (CFX 0.200). The mixing and stratification in the cold leg is underpredicted in the simulation, which results in the overprediction of the concentration at all wire mesh sensor positions. The slug of water in the simulation maintains a similar maximum value between the positions of the upper and lower downcomer sensors, while the concentration of the experimental slug is decreased, as it is weakly dispersed. However, it is important to note that the timescales with which the slug is transported through the inlet nozzle and the upper downcomer are quite comparable and that there is only a slight delay on the lower downcomer, which could arise from the poor mixing and stratification in the cold leg.

Case E6. In Case E6 (Fig. 11) the rhoratio is set to 10% and the Froude number is Fr=0.8208. The flow rate is set to 10% of the nominal mass flow rate in the cold leg.

Mixing and stratification in the cold leg is described to be in

Downloaded 02 Jun 2010 to 171.66.16.109. Redistribution subject to ASME license or copyright; see http://www.asme.org/terms/Terms_Use.cfm

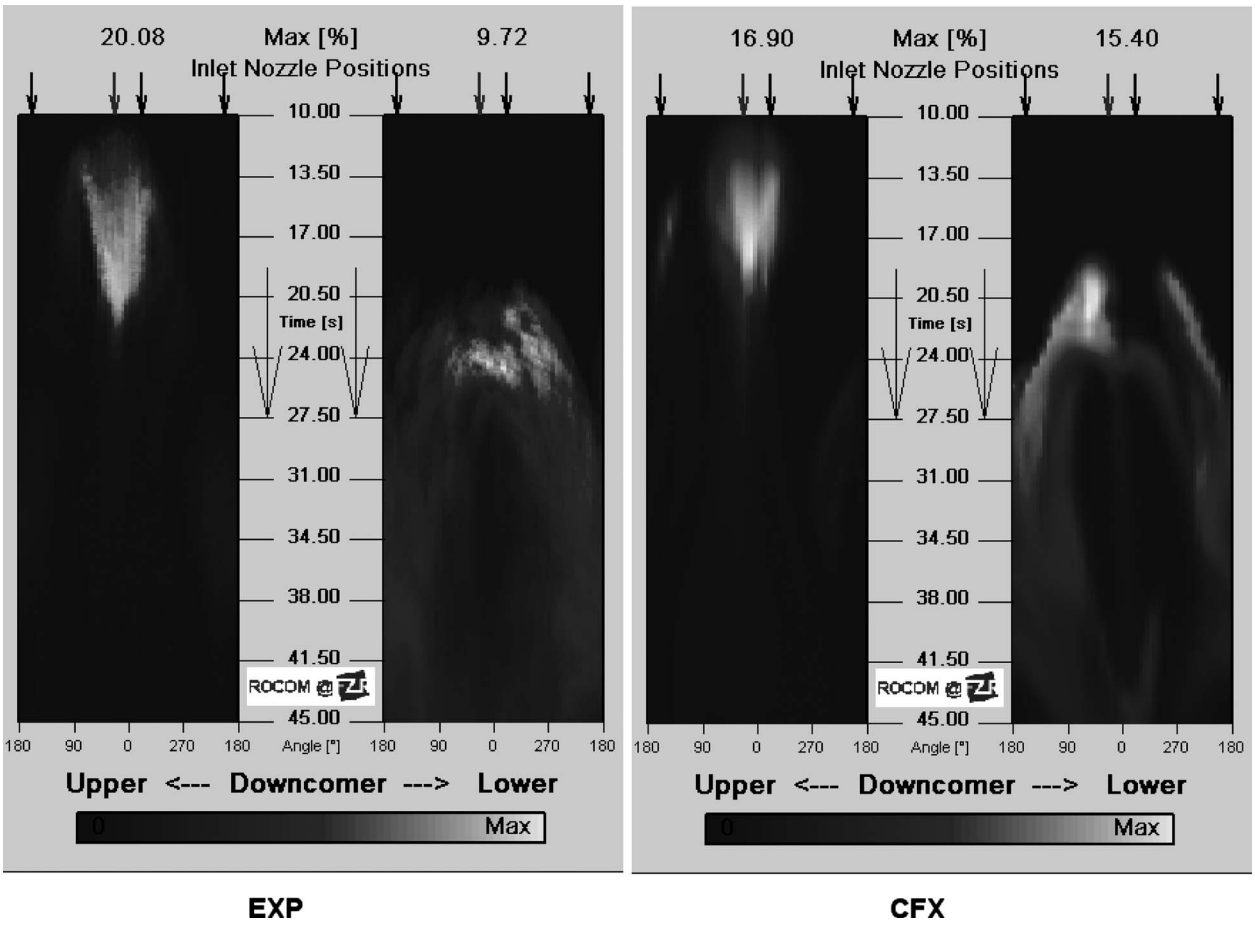


Fig. 11 Upper and lower downcomer—Experiment versus CFX, E5

good agreement between the experiment and simulation. The maximum value of the mixing scalar in the experiment at the upper downcomer is 0.21 (CFX 0.17) and at the lower downcomer is 0.097 (CFX 0.154). The comparison at the wire mesh sensor positions is in the range of the measurement error.

Quantitative Comparison. Figures 12 and 13 show the mixing scalar in the cold leg for the experimental and numerical results for the cases with density differences with E3 as an example for the quantitative comparison. The transient slug behavior is plotted at a local position in the centerline of the sensor in Fig. 12. At the position 0312 the predicted mixing scalar agrees well in both cases with the experimental values. Higher values of the mixing scalar are found due to the stratification. This can be seen in Fig. 13 at 25 s after start of the simulation, which shows the circumferential distribution of the slug at the outer wall of the cold leg sensor. The 0 deg position is at the bottom of the cold leg. The calculations reflect the observed stratification of experiment E3.

Summary

A transition matrix from momentum to buoyancy-driven flow experiments was selected for validation of the CFD software ANSYS CFX. A mesh with 4×10^6 control volumes was used for the calculations. Higher order turbulence models have been developed

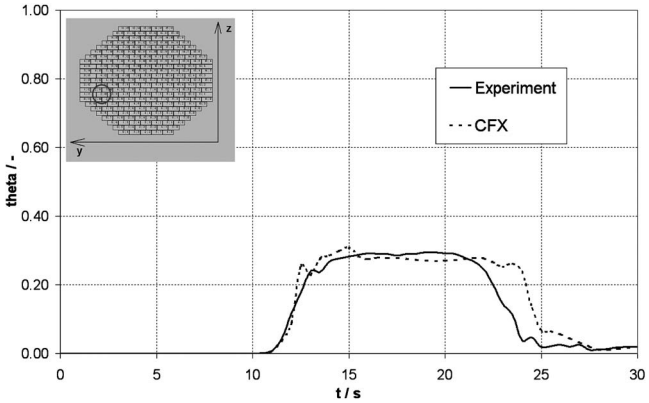


Fig. 12 Time dependent mixing scalar distribution at the cold leg sensor, E3 (local position 0312)

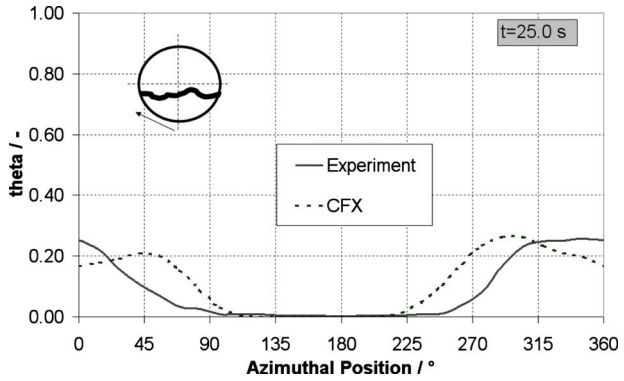


Fig. 13 Mixing scalar distribution in the circumferential positions of the cold leg sensor, 25 s, E3

Downloaded 02 Jun 2010 to 171.66.16.109. Redistribution subject to ASME license or copyright; see http://www.asme.org/terms/Terms_Use.cfm

and implemented into the CFD code, which takes into account anisotropy. Buoyancy generated source and dissipation terms were proposed and introduced into the balance equations for the turbulent kinetic energy.

The results of the experiments and of the numerical calculations show that mixing strongly depends on buoyancy effects: At higher Froude numbers ($Fr > 1.5$) the injected slug propagates in the circumferential direction around the core barrel. With lower Froude numbers ($Fr < 0.85$) buoyancy effects reduce this circumferential propagation at lower mass flow rates and/or higher density differences. The ECC water falls in an almost vertical path and reaches the lower downcomer sensor directly below the inlet nozzle. A flow pattern transition region was observed to be between $0.85 < Fr < 1.5$.

The ANSYS CFX calculations show a good qualitative agreement with the data. At some local positions differences in the predicted and measured concentration fields occur. The obtained experimental and numerical results can be used for further studies of the core behavior using coupled thermohydraulic and neutron-kinetic code systems.

Acknowledgment

This project was partly funded by the German Federal Ministry of Economics and Technology under Contract No. 150 1287.

Nomenclature

σ = electrical conductivity, $S\ m^{-1}$
Θ = mixing scalar
C = the boron concentration, ppm
Fr = Froude number
g = gravity vector, m/s^2
H = height of the downcomer, m
T = temperature, K
t = time, s
v = velocity, m/s
ρ = fluid density, kg/m^3

Indices and Abbreviations

0 = index for the unaffected coolant
1 = index for the disturbed loop
a = index for the ambient water in the downcomer
B = index for Boron
DC = index for the downcomer
in = index for the reactor inlet
t = index for time
x = index for the x coordinate
y = index for the y coordinate
z = index for the z coordinate

References

[1] Grundmann, U., and Rohde, U., 1994, "Investigations on a Boron Dilution Accident for a VVER-440 Type Reactor by the Help of the Code DYN3D," *ANS Topical Meeting on Advances in Reactor Physics*, Knoxville, TN, Apr. 11–15, Vol. 3, pp. 464–471.
[2] Moretti, F., Melideo, D., D'Auria, F., Höhne, T., and Kliem, S., 2007, "CFX Simulations of ROCOM Slug Mixing Experiments," *Proceedings of the 15th International Conference on Nuclear Engineering*, ICONE 15, Nagoya, Japan, Apr. 22–26.
[3] Bieder, U., Fauchet, G., Betin, S., Kolev, N., and Popov, D., 2007, "Simulation of Mixing Effects in a VVER-1000 Reactor," Nucl. Eng. Des. **237**(15–17), pp. 1718–1728.
[4] Prasser, H.-M., Grunwald, G., Höhne, T., Kliem, S., Rohde, U., and Weiss, F.-P., 2003, "Coolant Mixing in a Pressurized Water Reactor: Deboration Transients, Steam-Line Breaks, and Emergency Core Cooling Injection," Nucl. Technol., **143**(1), pp. 37–56.
[5] Höhne, T., 2007, "CFD-Simulations of Thermal Hydraulic Benchmark V1000CT-2 Using ANSYS CFX," *Proceedings of the 15th International Conference on Nuclear Engineering*, ICONE 15, Nagoya, Japan, Apr. 22–26.
[6] Cartland-Glover, G. M., Höhne, T., Kliem, S., Rohde, U., Weiss, F.-P., and Prasser, H.-M., 2007, "Hydrodynamic Phenomena in the Downcomer During Flow Rate Transients in the Primary Circuit of a PWR," Nucl. Eng. Des., **237**(7), pp. 732–748.
[7] 1990, "HDR Safety Program—Thermal Mixing in the Cold Leg and Downcomer of the HDR Test Rig," Report No. PHDR 91-89.
[8] Umminger, K., Kastner, W., Liebert, J., and Mull, T., 1999, "Thermal Hydraulics of PWR's With Respect to Boron Dilution Phenomena: Experimental Results From the Test Facilities PKL and UPTF," Ninth International Topical Meeting on Nuclear Reactor Thermal Hydraulics (NURETH-9), San Francisco, CA, Oct. 3–8.
[9] Hassan, Y. A., and Randorf, J. A., 1997, "Stratification Studies in Nuclear Reactor Components," NURETH-8, Kyoto, Japan, Sept. 30–Oct. 4, 1, p. 449.
[10] Woods, B., 2001, "UM 2×4 Loop Experimental Findings on the Effect of Inertial and Buoyancy Forces on Annular Flow Mixing for Rapid Boron Dilution Transients," Ph.D thesis, University of Maryland, MD.
[11] Höhne, T., Kliem, S., and Bieder, U., 2006, "Modeling of a Buoyancy-Driven Flow Experiment at the ROCOM Test Facility Using the CFD-Codes CFX-5 and TRIO_U," Nucl. Eng. Des. **236**(12), pp. 1309–1325.
[12] Prasser, H.-M., Böttger, A., and Zschau, J., 2001, "A New Electrode-Mesh Tomograph for Gas-Liquid Flows," Flow Meas. Instrum., **9**, pp. 111–119.
[13] Prasser, H.-M., Zschau, J., Peters, D., Pietzsch, G., Taubert, W., and Trepte, M., 2002, "Fast Wire-Mesh Sensors for Gas-Liquid Flows—Visualisation With Up to 10 000 Frames per Second," *International Congress on Advanced Nuclear Power Plants (ICAPP)*, Hollywood FL, Jun. 9–13, Paper No. 1055.
[14] Rohde, U., Kliem, S., Höhne, T., Karlsson, R., Hemström, B., Lillington, J., Toppila, T., Elter, J., and Bezrukov, Y., 2005, "Fluid Mixing and Flow Distribution in the Reactor Circuit—Part 1: Measurement Data Base," Nucl. Eng. Des., **235**, pp. 421–424.
[15] ANSYS CFX.-11 User Manual, 2007, ANSYS-CFX.
[16] Menter, F., 2002, "CFD Best Practice Guidelines for CFD Code Validation for Reactor Safety Applications," ECORA FIKS-CT-2001-00154.
[17] Rohde, U., Höhne, T., Kliem, S., Hemström, B., Scheuerer, M., Toppila, T., Aszodi, A., Boros, I., Farkas, I., Muehlbauer, P., Vyskocil, V., Klepac, J., Remis, J., and Dury, T., 2007, "Fluid Mixing and Flow Distribution in a Primary Circuit of a Nuclear Pressurized Water Reactor—Validation of CFD Codes," Nucl. Eng. Des., **237**(15–17), pp. 1639–1655.

Downloaded 02 Jun 2010 to 171.66.16.109. Redistribution subject to ASME license or copyright; see http://www.asme.org/terms/Terms_Use.cfm

Inert Matrix Fuel Analysis by Means of the TRANSURANUS Code: The Halden IFA-652 In-Pile Test

R. Calabrese
e-mail: rolando.calabrese@bologna.enea.it

F. Vettraino

ENEA,
Innovative Nuclear Systems and Fuel Cycle Closure Division,
via Martiri di Monte Sole, 4,
40129 Bologna, Italy

T. Tverberg
OECD Halden Reactor Project,
P.O. Box 173,
1751 Halden, Norway

Inert matrix fuels (IMFs) are a possible option to reduce separated plutonium stockpiles by burning it in light water reactor (LWR) fleet. A high burning efficiency targeted by preventing new plutonium buildup under irradiation (U-free fuel), a proved high radiation damage, and leaching resistance are fundamental requirements when a once-through fuel cycle strategy is planned. Among other options, both calcia-stabilized zirconia (CSZ) and thoria fulfill these criteria standing as the most promising matrices to host plutonium. While several in-pile tests concerning thoria fuels are found, calcia-stabilized zirconia under-irradiation performance is still to be fully assessed; with this regard the thermal conductivity, markedly lower than the uranium oxide (UOX) and mixed oxide (MOX) cases, plays a fundamental role. For this reason, ENEA has conceived a comparative in-pile testing of three different U-free inert matrix fuel concepts, which have been performed in the OECD Halden HBWR (IFA-652 experiment). The discharge burnup accomplished about 90–97% of the 45 MWd/kg U_{eq} target under typical LWR irradiation conditions. The test rig is a six-rod bundle loaded with IM, IMT, and T innovative fuels. IM and T fuels have, respectively, CSZ and thoria as matrices, the fissile phase being the high enriched uranium (HEU) oxide (UO_2 93% ^{235}U enriched). IMT is a ternary fuel composed by CSZ + thoria matrix and HEU oxide as a fissile phase. Thoria is added in IMT fuel to improve the low IM reactivity feedback coefficients. Pins are instrumented providing fuel centerline temperature, pin inner pressure, and fuel stack elongation measurements. Our purpose is to investigate the key processes of IMF under-irradiation behavior by means of the TRANSURANUS fuel performance code. Thermal conductivity and its degradation with burnup, densification-swelling response, and fission gas release (FGR) are tentatively modeled in the burnup range of IFA-652. In particular, the effects of pellet geometry and fuel microstructures in the IM and IMT cases are pointed out. The consistency of our results is discussed aiming at understanding the in-pile response, as a fundamental step, in the perspective of future deployment of the nuclear fuels we are dealing with. Notwithstanding this ambitious objective, it is clear, however, that these results rely on a limited data set and that, as TRANSURANUS is a semi-empirical code mostly tailored for commercial fuels, the modeling of the IMF is still a work in progress. [DOI: 10.1115/1.2983140]

Introduction

One of the key issues dealing with the public concern on nuclear energy is the plutonium management due to the radiotoxicity and the misuse risk associated with it. To this purpose, worldwide efforts have been devoted to finding efficient solutions to reduce both the radiotoxicity and the amount of plutonium stockpiles [1,2]. One main ENEA recent R&D effort has been focused on the U-free inert matrix fuel concept aimed at burning separated plutonium (both weapon and reactor grade) in LWRs. The prominent feature of these innovative fuels is the pronounced proliferation resistance if compared with commercial MOX. In fact, in the former, while most of the fissile plutonium undergoes fission, no new plutonium is generated under irradiation. Thanks to this achievement, a once-through fuel cycle strategy becomes viable provided a careful choice of the matrix material is made. ENEA has selected calcia-stabilized zirconia and thoria as matrices to be used in three U-free fuel concepts for testing in the OECD Halden HBWR [3–5]. The irradiation test, labeled IFA-652, has been performed in the Halden reactor in the context of the ENEA membership to the HRP. Instrumented pins of IM (CSZ matrix), T (thoria matrix), and IMT (CSZ+thoria matrix) fuels have been irradiated and monitored storing the collected data in a specialized data base environment for the off-line analysis. HEU oxide (93% ^{235}U enriched) is the fissile phase of investigated fuels [6,7].

In this paper, the thermomechanical response of IM (pins 1 and 2) and IMT (pin 6) is studied up to the discharge burnup (about 40 MWd/kg U_{eq}) by using the TRANSURANUS fuel performance code [8]. To this purpose, starting from the TU V1M2J00 standard version, fuel library has been enlarged to include the unirradiated IM and IMT thermophysical properties, and the newly developed under-irradiation modeling was introduced.

IFA-652 Halden Experiment

The IFA-652 test rig is a six-pin fuel bundle, in particular, rods 1 (all hollow pellets) and 2 are loaded with IM fuel, rods 3 and 6 with IMT fuel, and 4 and 5 with T fuel (see Table 1 and Fig. 1) [6,7]. The fuel rods have been fabricated at the IFE-Kjeller (Norway). On the basis that the choice of the fissile material should have a negligible effect on the matrices under-irradiation behavior,

Contributed by International Gas Turbine Institute of ASME for publication in the JOURNAL OF ENGINEERING FOR GAS TURBINES AND POWER. Manuscript received July 25, 2008; final manuscript received August 5, 2008; published online October 2, 2008. Review conducted by Dillip R. Ballal. Paper presented at the 16th International Conference on Nuclear Engineering (ICONE16), Orlando, FL, May 12–15, 2008.

Copyright © 2009 by ASME

Downloaded 02 Jun 2010 to 171.66.16.109. Redistribution subject to ASME license or copyright; see http://www.asme.org/terms/Terms_Use.cfm

Table 1 IFA-652 fuels

Fuel	IM	IMT	T
Density (g cm^{-3})	5.637	6.995	8.180
CSZ (wt %)	81	45	—
Thoria (wt %)	—	39.2	88.3
HEU (wt %)	19	15.8	11.7

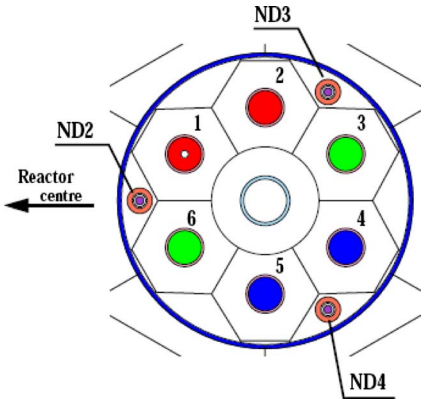


Fig. 1 IFA-652 test rig (cross section)

Table 2 IFA-652 pin design

	Rod 1 (2)	Rod 6
Fuel	IM	IMT
Fuel density (%TD)	89.900	93.155
O/M	2.0	2.0
Thermal shield pellets	UO_2	UO_2
Cladding	Zircaloy 4	Zircaloy 4
Fill gas	He	He
Prepressurization (MPa)	1.0	1.0
Free volume (cm^3)	9.3 (8.4)	8.7
UO_2 pellet length (mm)	10	10
Pin active length (mm)	499.7 (499.7)	499.2
Hollow pellets (mm)	499.7 (97.3)	97.3
Cladding outer diameter (mm)	9.50	9.50
Fuel pellet outer diameter (mm)	8.19	8.19
Fuel pellet inner diameter (mm)	1.80	1.80
Fuel-cladding gap (μm)	170	170
Fraction of dish volume (%)	1	1

Table 3 IFA-652 accumulated burnup (MWd/kg U_{eq})

Rod	1	2	6
Loading 1	5.9	5.8	6.0
Loading 2	24.3	23.4	24.5
Loading 3	41.9	40.5	43.5

for practical reasons, in this experiment the fissile phase is HEU oxide instead of PuO_2. IFA-652 was, however, intended to be a first experiment to be followed by a second one, fully representative with plutonium. The fabrication has been based on dry powders mixing standard route. After pressing at 440 MPa, the green pellets have been sintered at 1700°C (4 h) in a reducing atmosphere (hydrogen) [9,10]. All pins are equipped with fuel temperature thermocouple (TF) and internal pressure transducer (PF). Three pins (2, 4, and 6) house a fuel stack elongation sensor (EF). The rig is also equipped with colinear neutron detectors (NDs) to accurately record the neutron flux along the axial direction and on the midplane section (Fig. 1). The acquisition period is 900 s; data are then stored in the TFDB system [11].

The purpose of this experiment is to investigate the thermal conductivity and its degradation with burnup, the densification-swelling behavior and the FGR of the fuels under study. This paper deals with IM and IMT fuels, in particular, with IFA-652 rods 1, 2, and 6 whose design parameters are resumed in Table 2.

The in-pile test (June 28, 2000–October 22, 2005) succeeded in accomplishing, for analyzed cases, about 90–97% of the 45 MWd/kg U_{eq} target burnup. In Table 3, burnup is detailed in each loading of the IFA-652 experiment. Rods 1, 2, and 6 instrumentation performed well but in the third loading PF1, PF2, and PF6 (inner pressure gauge) and the TF1 and TF6 (fuel centerline temperature thermocouple) showed a partly unreliable response. The TFDB system is the reference source of the IFA-652 experiment data [11]. In Fig. 2 we show the average linear heat rate and the power of the IFA-652 assembly.

IMF Thermophysical Properties

The new TU version embeds the IMF thermophysical characterization of unirradiated sample fuel pellets carried out at the JRC/ITU, Karlsruhe (Germany) [12]. A two-phase microstructure fuel was revealed for both IM and IMT. In the former, the fissile islands (e.g., in the upper right corner in Fig. 3(*a*)) are separated

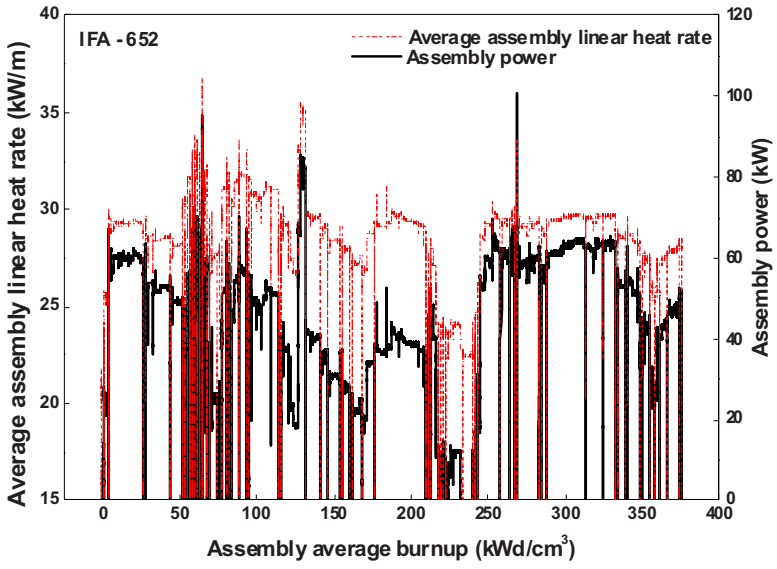


Fig. 2 Average linear heat rate and power of the IFA-652 rig

Downloaded 02 Jun 2010 to 171.66.16.109. Redistribution subject to ASME license or copyright; see http://www.asme.org/terms/Terms_Use.cfm

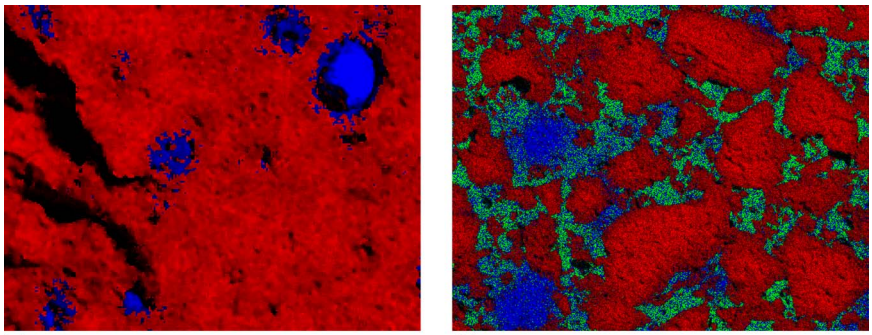


Fig. 3 IMF energy dispersive-X surface mapping

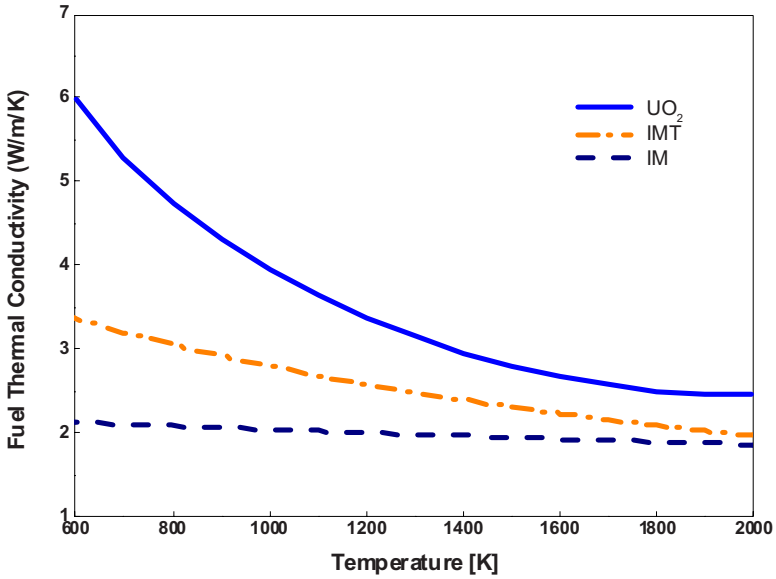


Fig. 4 Fully dense thermal conductivity [8,12]

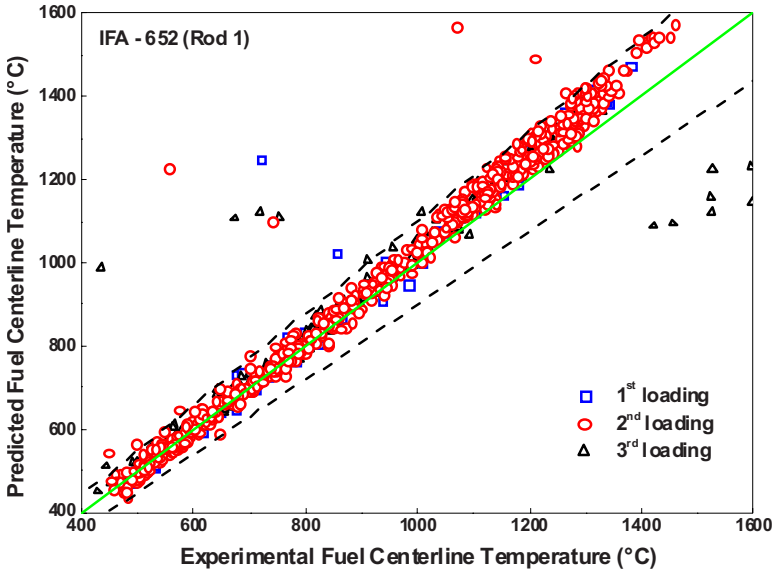


Fig. 5 Fuel centerline temperature—rod 1 (±10% error band)

Downloaded 02 Jun 2010 to 171.66.16.109. Redistribution subject to ASME license or copyright; see http://www.asme.org/terms/Terms_Use.cfm

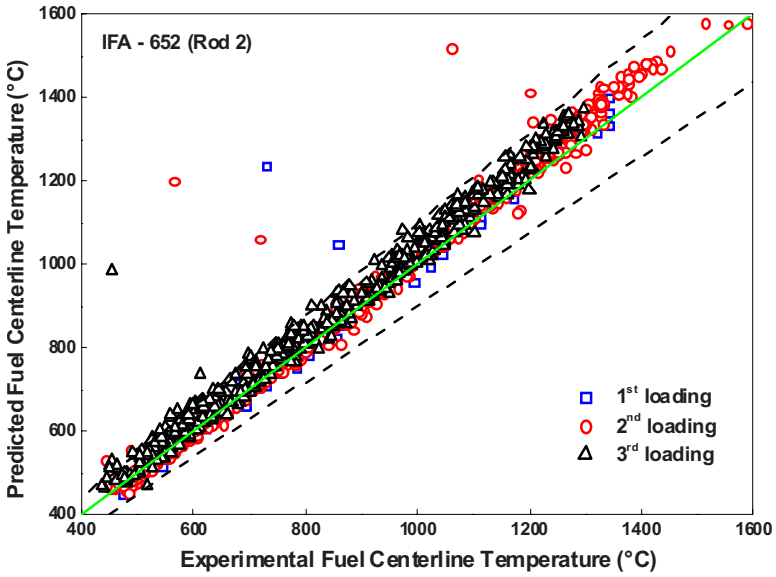


Fig. 6 Fuel centerline temperature—rod 2 (±10% error band)

from the CSZ matrix; in the latter, a "cellular" structure is found with urania dispersed in a single phase together with thoria (light area in Fig. 3(*b*)), being the second phase the CSZ (dark area in Fig. 3(*b*)). The thermal diffusivity, measured by laser-flash method, and the specific heat, by DSC measurement, allowed us to evaluate the IMF thermal conductivity as shown in Fig. 4. In the same figure it is possible to appreciate the comparison with fully dense UO_2 thermal conductivity [8,12,13]. Besides these experimental results, from vendors, further parameters were defined (Young's modulus, yield stress, and emissivity). In this analysis, the IMF thermal conductivities do not degrade with burnup [14,15]. Finally a TU confidential MOX fuel creep correlation has been adopted (implicit treatment).

IMF Complex Behavior

Concerning the fuel complex behavior, we have reviewed and simplified our previous hypotheses [16] aiming at introducing as few as possible changes in the standard TU code version. The modeling has then been lumped in the following topics.

Densification. Assuming that no central hole is formed at these thermal conditions alike in a similar experiment [14,17], it has then been attempted to predict the initial densification by a modified MATPRO-11 resintering model [8]. We assume that a resintering may take place when fuel temperature is above 1600°C (actually lower than the true sintering temperature of the fabrication process). The resintering volume is added to the inner relocation volume of pre-existing cracks or it is accommodated in newly formed circumferential cracks.

Swelling. A 0.5%/at% burnup solid swelling has been assumed.

Fission Gas Release. The diffusion equation is solved by the URGAS algorithm with constant grain boundary saturation limit (1×10^{-4} mol m^{-2}); while pertaining to the thermal diffusion coefficient, the Matzke relationship has been modified by an exponential factor only depending on the local rating (W/g U_{eq}).

TU-standard model has been assumed for the other processes as

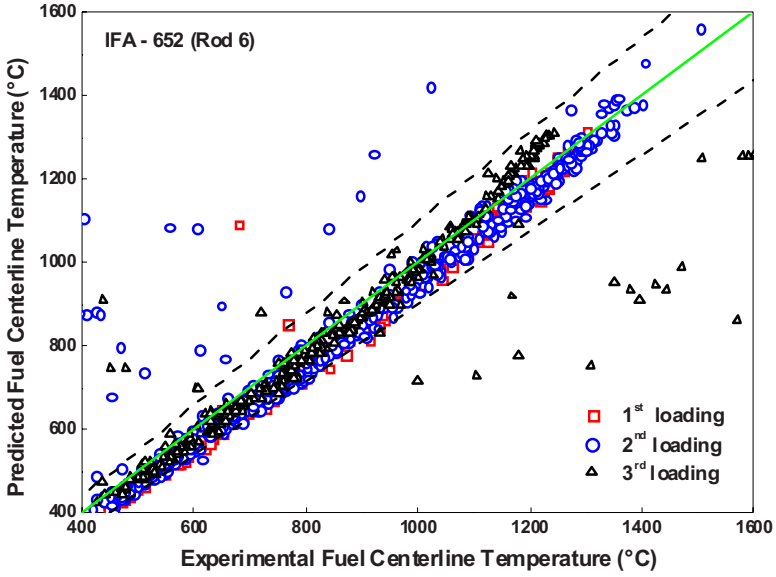


Fig. 7 Fuel centerline temperature—rod 6 (±10% error band)

Downloaded 02 Jun 2010 to 171.66.16.109. Redistribution subject to ASME license or copyright; see http://www.asme.org/terms/Terms_Use.cfm

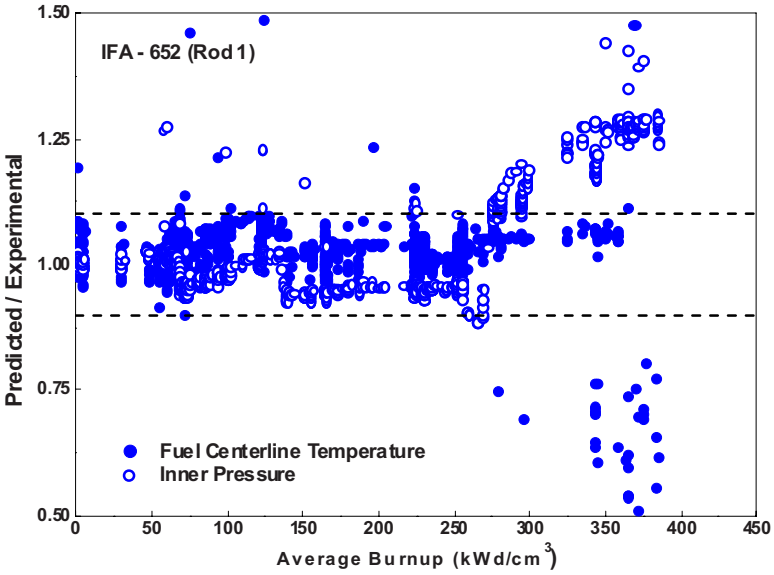


Fig. 8 Ratio of predicted fuel centerline temperature and inner pressure to experimental temperature and inner pressure—rod 1 (±10% error band)

the Ainscough model for grain growth, the URGAP model for the gap conductance, and the FRAPCON-3 model for relocation [8].

Irradiation History and TU Input

A seven-slice axial meshing in the modeling of the single fuel rod (five slices for the fuel active length and two for the shield pellets) has been adopted; for the radial mesh four *coarse* zones are assumed for the fuel region and one for the cladding. The axial meshing is consistent with the fourfold average linear heat rate record as defined in the TFDB. The experimental fuel centerline temperature is compared with the TU code predictions pertaining to the fifth slice.

The average linear heat rate record and the moderator temperature have been imported at each acquisition time (about 10^5 steps) and condensed by the POWER CONDENSE code [18]. The moderator pressure is 3.36 MPa. The shared radial power profile (2D transport code HELIOS calculation) has been assumed not depending on burnup [6].

Results

We grouped the results of calculations as follows:

- unbounded comparison of the fuel centerline temperature and inner pin pressure code predictions with the experimental data (Figs. 5–10)
- analysis of the HSB pin inner pressure (zero power and moderator temperature of 220–222°C) (Figs. 11–13)
- analysis of the HSB fuel stack elongation (rods 2 and 6) (Figs. 14 and 15)
- FGR and HSB gap widths (Figs. 16 and 17).

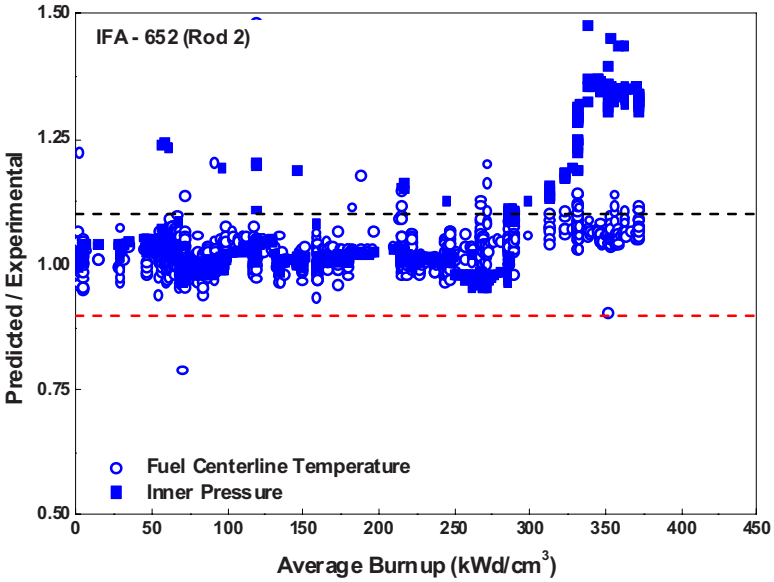


Fig. 9 Ratio of predicted fuel centerline temperature and inner pressure to experimental temperature and inner pressure—rod 2 (±10% error band)

Downloaded 02 Jun 2010 to 171.66.16.109. Redistribution subject to ASME license or copyright; see http://www.asme.org/terms/Terms_Use.cfm

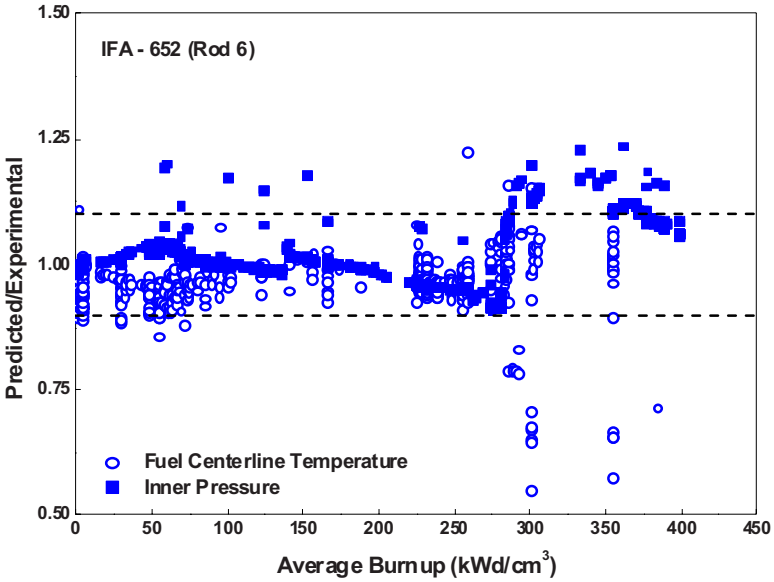


Fig. 10 Ratio of predicted fuel centerline temperature and inner pressure to experimental temperature and inner pressure—rod 6 (±10% error band)

Discussion

The code fuel temperature predictions have a 10% accuracy for all the analyzed pins and the ratio of the theoretical to experimental fuel temperature does not show bias or regular trend until the discharge burnup (Figs. 5–7). Similar statements hold also for the inner pin pressure; moreover, in the concluding part of the irradiation test reported failures of instrumentation are confirmed by the enhanced deviation of ratios from the band of acceptance (Figs. 8–10). Concerning the fuel temperature response (Figs. 5–7), in rods 1 and 2 data are consistently (IM fuel) overestimated, while for rod 6 (IMT fuel) TU code proves an underestimation even if a 13% reduction (with respect to ITU measurement) of the fuel thermal conductivity has been assumed. Relying on these considerations, further investigation to determine the fuel thermal conductivity, especially for IMT fuel, together with a deeper understanding of the contribution to our results of each single TU modeling assumption (e.g., fuel radial power profile) is required; moreover, at this stage, the final deviations we are discussing are of the same order of the experimental uncertainties and further refinement is inconsistent with given data [19]. Nevertheless, in our opinion, an uncertainty analysis of the postprocessing parameters of the raw to experimental data conversion could add useful information to improve the accuracy of the analysis. Regarding the HSB predictions (Figs. 11–15), a high accuracy is found as to the inner pressure of all pins, while the detected EOL failures are confirmed. In the evaluations of the HSB fuel stack elongation (rods 2 and 6), it is noted that accuracy is degrading in the second and third loading when TU fuel stack length evaluations increased consistently with the assumed fuel swelling rate.

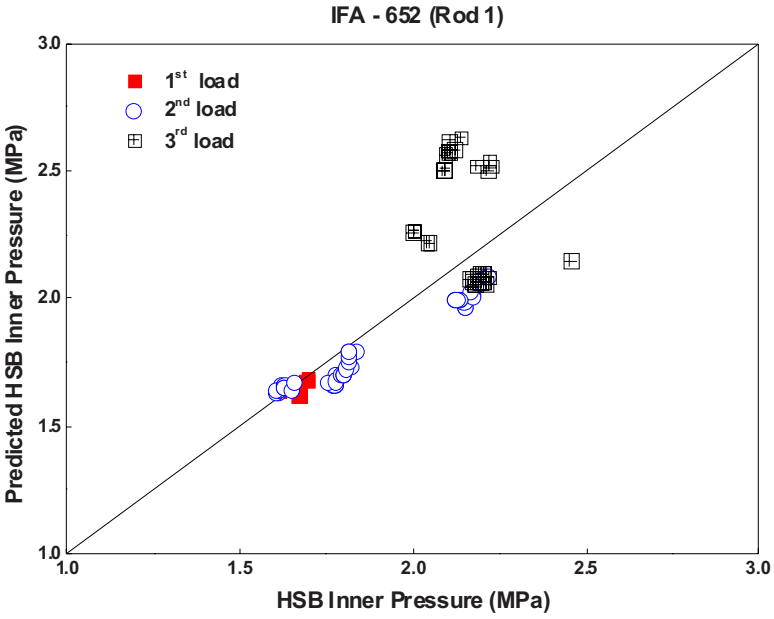


Fig. 11 HSB inner pressure—rod 1

Downloaded 02 Jun 2010 to 171.66.16.109. Redistribution subject to ASME license or copyright; see http://www.asme.org/terms/Terms_Use.cfm

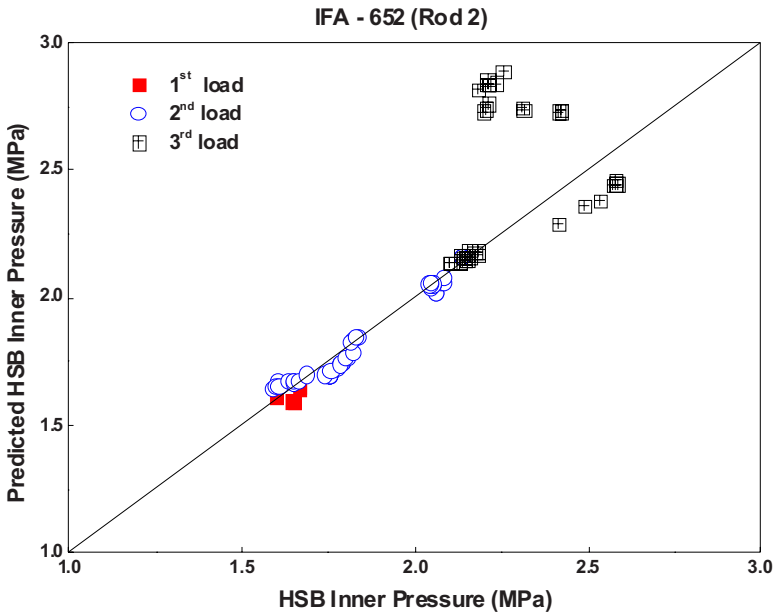


Fig. 12 HSB inner pressure—rod 2

Testing the fuel stack elongation sensor measurements at power (24–25 kW/m at the second slice) we see a sharp shift in the code predictions not followed by the in-pile measurement; we could then argue that stack elongation measurement pertains to the cold pellet shoulders; in this case, it should be expected that pellet swelling is mostly developed in the inner hot region of fuel pellets. A possible "sticking" failure of the fuel stack sensors is not excluded. To ascertain these hypotheses PIE will be fundamental.

Our last results regard predicted FGR and HSB gap width histories (Figs. 16 and 17). FGR takes place for our pins at the peak power ramps with burstlike release; TU code evaluations are in good agreement with the timing of the gas release possibly proving that IMF gas release is mainly a diffusion-driven process.

In our TU modeling the gas diffusion coefficient has been increased questioning the IMF compliance of the experimental Halden Vitanza curve. Rod 1 and 2 FGR predictions are in good agreement suggesting that hollow fuel pin design has a minor impact on fuel temperature with respect to a solid pellet design due to a possible resintering of the inner region of solid pellets (rod 2) that increases the fuel thermal conductivity. The predicted FGR, at the same thermal loading, is significantly higher for IMT than for IM fuel suggesting an important impact of the different microstructures of fuels under study. With this respect, the assumed strong resintering and the fissile "island" macrostructure, as described in the IM fuel, are expected to decrease the FGR. These results, in accordance with literature [20], may prove that IMF FGR figure is degraded with respect to the standard UOX playing the lower thermal conductivity a prominent role (Fig. 4) with a minor effect on the microstructure-related fabrication options (e.g., as-fabricated porosity and thoria content). Finally the

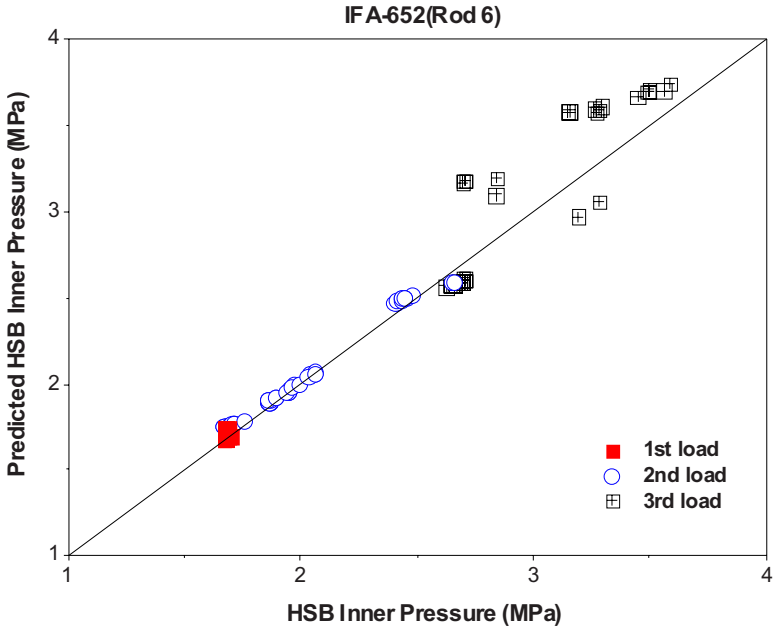


Fig. 13 HSB inner pressure—rod 6

Downloaded 02 Jun 2010 to 171.66.16.109. Redistribution subject to ASME license or copyright; see http://www.asme.org/terms/Terms_Use.cfm

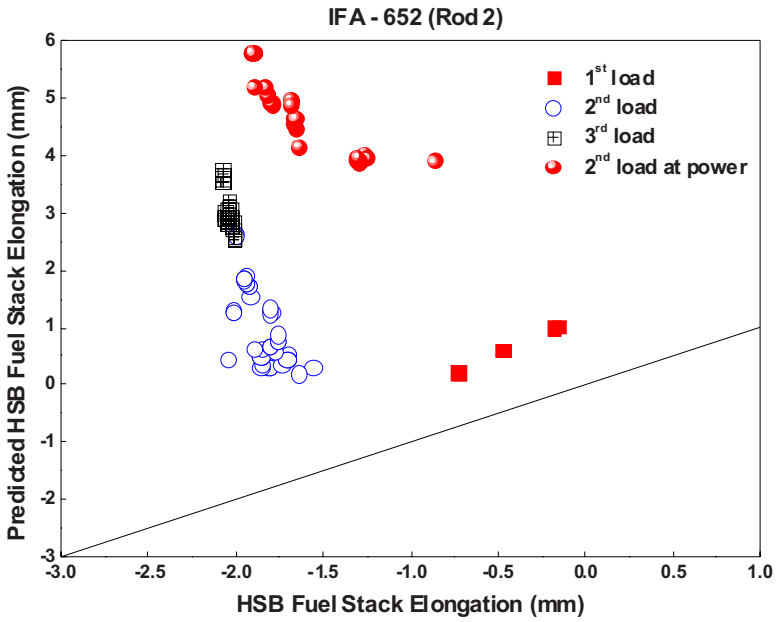


Fig. 14 HSB fuel stack elongation—rod 2

gap width at HSB is foreseen to decrease by about 35 μm during in-reactor residence time causing the gap closure at power in the third loading (not shown).

As final remarks we may confirm that IMF proved to reach a valuable percentage of the target burnup with a limited degradation of under-irradiation performance, in particular, a good dimensional stability and a not degrading fuel thermal conductivity are faced by an enhanced FGR, which could be a limiting factor for the future deployment of IMF under investigation. The thermal conductivity seems standing as a bottleneck in the IMF in-pile performance as it turned out to be difficult to get significant improvement by acting on fabrication parameters [12]. The above statements are certainly not ultimate; in fact, the urgent need of further experimental investigations to let the collected data interpretation be unaffected by the statistics of the specific fuel fabrication process (e.g., densification model) is easily recognized.

From the point of view of the TU code as a tool of investigation, it is important to note that through few changes in the standard code release the fitting of in-pile IFA-652 measurements with an accuracy of the same order of the experimental uncertainties was possible. This empirical approach is a sort of a glance into the key features of the IMF under-irradiation processes without claiming to be a theoretical modeling of fuels we are dealing with. These innovative fuels together with the fuels for the next generation nuclear power systems are expected to be investigated by the so-called multitime scale approach that aims at a deep description of under-irradiation behavior starting from the first-principles analysis at electronic structure scale [21]. These new techniques are very promising but still at an early stage; so far the traditional codes for the nuclear fuel thermomechanical analysis still get

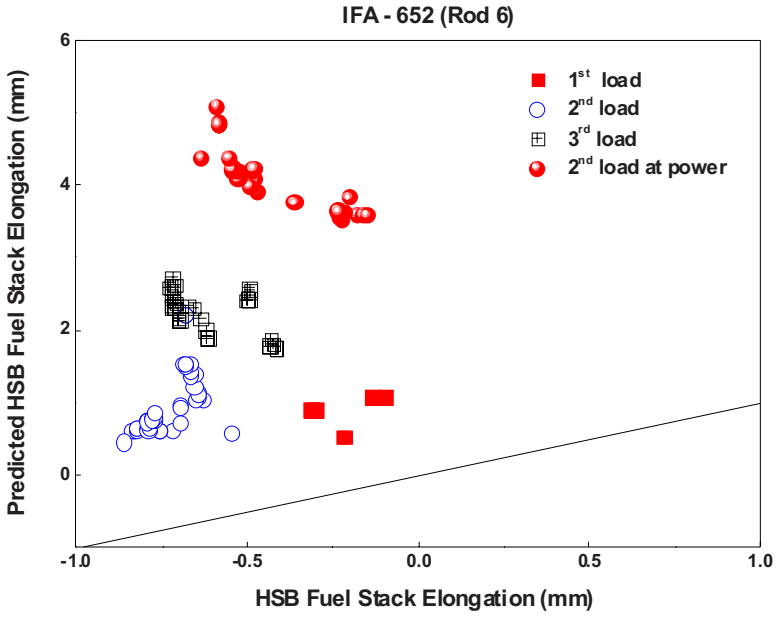


Fig. 15 HSB fuel stack elongation—rod 6

Downloaded 02 Jun 2010 to 171.66.16.109. Redistribution subject to ASME license or copyright; see http://www.asme.org/terms/Terms_Use.cfm

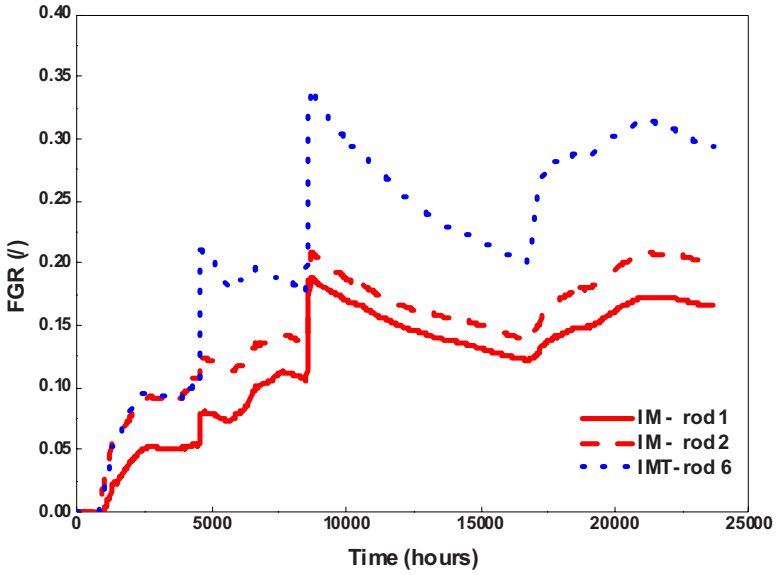


Fig. 16 Predicted FGR

good results without the tremendous amount of computational resources that are coupled with a finely detailed description as in the MTS approach.

Conclusions

In this paper the results of the thermomechanical analysis of the IM (rods 1 and 2) and IMT fuels (rod 6) irradiated in the OECD Halden reactor (IFA-652 experiment) have been described. The calculations have been performed by using a newly developed TU code version, extended to cover the IMF thermophysical properties and the herein proposed under-irradiation modeling. The accuracy of performed calculations is within the experimental uncertainties until the discharge burnup for both fuel temperature at thermocouple and pin inner pressure. Relying on these results we may suggest some preliminary conclusions.

A good IMF dimensional stability is revealed in the IFA-652 fuels even if it is suspected that an intense resintering occurs in the hot region of solid pellets with an unexpected overlapping of hollow and solid pellets in-pile response. If confirmed, a deeper investigation on fabrication process is required. The low accuracy of the fuel stack elongation predictions could support the hypothesis that the fuel swelling takes place in the inner region of pellets. As to the thermal performance, a limited degrading of IMF thermal conductivity with good stability of fuel temperature with burnup was shown.

Regarding the FGR, the TRANSURANUS description by the diffusion model may hold even for the IMF case. In our calculations the TU modeling of the Halden Vitanza curve has been modified (by increasing the thermal diffusion coefficient), so that it is still a debated issue if this commonly accepted reference for UOX FGR could still be applied to our case. As concluding remarks, concerning the higher IMF FGR compared with reference UOX, it seems that fuel suffered from low density. It is expected that the as-fabricated density can be strongly improved by using purified starting material and higher sintering temperatures. The TU evaluation of the HSB gap width is about 20 μm at EOL with closure at power in the third loading; in this case, as the IMF creep cor-

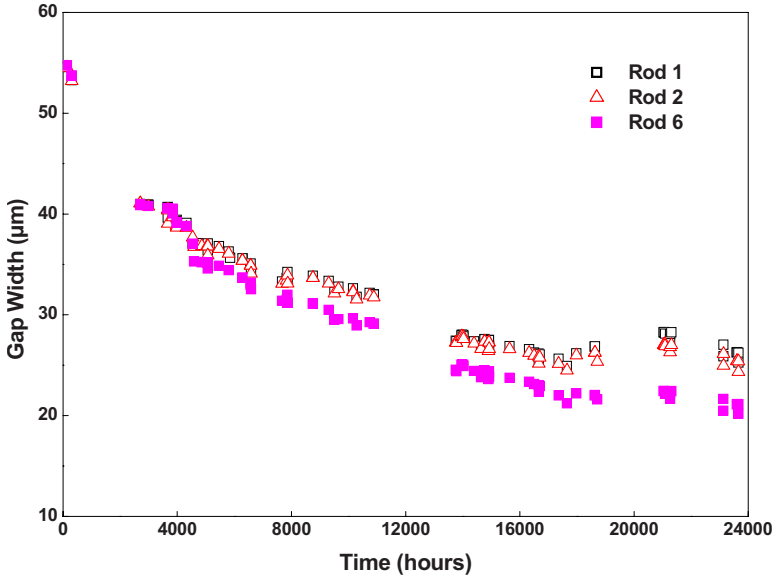


Fig. 17 Predicted HSB gap width (slice 5)

Downloaded 02 Jun 2010 to 171.66.16.109. Redistribution subject to ASME license or copyright; see http://www.asme.org/terms/Terms_Use.cfm

relations are unknown, further considerations could be not realistic at the moment.

The TU code proved to be a fundamental tool in investigating the IFA-652 experimental data by a limited set of key parameters in which the IMF under-irradiation performance could be lumped, but caution is to be taken due to the single-experiment data set investigated and the strictly empirical approach adopted. In the long term, complementary experimental data and MTS approach applications are expected to give an answer to many questions risen regarding the IMF in-pile response. In the near term PIE and deeper investigation of assumed TU input parameters are a viable route to try to fix the milestones of possible future extensive modeling of these innovative fuels.

Nomenclature

CSZ = calcia-stabilized zirconia
DSC = differential scanning calorimetry
EOL = end of life
FGR = fission gas release
HBWR = heavy boiling water reactor
HEU = high enriched uranium
HRP = Halden reactor project
HSB = hot stand-by
IFE = Institutt for Energiteknikk
IMF = inert matrix fuel
ITU = Institute for TransUranium elements
JRC = Joint Research Centre
LWR = light water reactor
MOX = mixed oxide
MTS = multi-time-scale
OECD = Organisation for Economic Co-operation and Development
PIE = postirradiation examination
R&D = Research and Development
TD = theoretical density
TFDB = test fuel data bank
TU = TRANSURANUS code
UOX = uranium oxide

References

[1] Oversby, V. M., McPheeters, C. C., Degueldre, C., and Paratte, J. M., 1997, "Control of Civilian Plutonium Inventories Using Burning in a Non-Fertile Fuel," J. Nucl. Mater., **245**, pp. 17–26.

[2] Ledergerber, G., Degueldre, C., Heimgartner, P., Pouchon, P. M., and Kasemeyer, U., 2001, "Inert Matrix Fuel for the Utilisation of Plutonium," Prog. Nucl. Energy, **38**(3–4), pp. 301–308.

[3] Vettraino, F., Magnani, G., La Torretta, T., Marmo, E., Coelli, S., Luzzi, L., Ossi, P., and Zappa, G., 1999, "Preliminary Fabrication and Characterisation of Inert Matrix and Thoria Fuels for Plutonium Disposition in Light Water Reactors," J. Nucl. Mater., **274**, pp. 23–33.

[4] Lombardi, C., Luzzi, L., Padovani, E., and Vettraino, F., 2001, "Inert Matrix and Thoria Fuels for Plutonium Elimination," Prog. Nucl. Energy, **38**(3–4), pp. 395–398.

[5] Lombardi, C., Mazzola, A., Padovani, E., and Ricotti, M. E., 1999, "Neutronic Analysis of U-free Inert Matrix and Thoria Fuels for Plutonium Disposition in Pressurised Water Reactors," J. Nucl. Mater., **274**, pp. 181–188.

[6] Padovani, E., and Tverberg, T., 2000, "Inert Matrix—Thoria Fuel Irradiation in IFA-652.1," *EP-1652.1, OECD Halden Reactor Project*, Halden, Norway.

[7] Padovani, E., 2000, "Updating Technical Notes for IFA-652.1," *F-Note, OECD Halden Reactor Project*, Halden, Norway.

[8] Lassmann, K., Schubert, A., and van de Laar, J., 2000, "TRANSURANUS Handbook," Version 1 Modification 2 Year 2000, ("V1M2J00"), *European Commission, Joint Research Centre, Institute for Transuranium Elements*, Karlsruhe, Germany.

[9] Oberlander, B. C., Iversen, G., and Espeland, M., 2000, "Qualification of Inert Matrix Fuel (IMF) Pellets and Production of Six IMF Test Rods for the Test Rig IFA-652," IFE/KR/F-2000./090 Institutt For Energiteknikk, Kjeller, Norway.

[10] Vettraino, F., Padovani, E., and Tverberg, T., 2002, "The Inert Matrix&Thoria Fuel Irradiation Testing in Halden," *Proceedings of the Enlarged Halden Programme Group Meeting*, Storefiell, Norway, Sept. 8–13, OECD Halden Reactor Project, Halden, Norway.

[11] Brodal, F., Tverberg, T., and Wiesenack, W., 1998, "Test-Fuel-Data-Bank System User Manual," HWR-549, OECD Halden Reactor Project, Halden, Norway.

[12] Ronchi, C., Ottaviani, J. P., Degueldre, C., and Calabrese, R., 2003, "Thermophysical Properties of Inert Matrix Fuels for Actinide Transmutation," J. Nucl. Mater., **320**, pp. 54–65.

[13] Sheindlin, M., Halton, D., Musella, M., and Ronchi, C., 1998, "Advances in the Use of Laser-Flash Techniques for Thermal Diffusivity Measurement," Rev. Sci. Instrum., **69**(3), pp. 1426–1436.

[14] Kasemeyer, U., Joo, H.-K., and Ledergerber, G., 1999, "Design Study of an Irradiation Experiment With Inert Matrix and Mixed-Oxide Fuel at the Halden Boiling Water Reactor," J. Nucl. Mater., **274**, pp. 160–166.

[15] Hellwig, C., and Kasemeyer, U., 2003, "Inert Matrix Fuel Performance During the First Two Irradiation Cycles in a Test Reactor: Comparison with Modelling Results," J. Nucl. Mater., **319**, pp. 87–94.

[16] Calabrese, R., Vettraino, F., and Tverberg, T., 2007, "TRANSURANUS Modelling of Irradiated Inert Matrix Fuels From Halden IFA-652 Experiment," *Proceedings of the ICAPP 2007*, Nice, France, May 13–18, Paper No. 7293.

[17] Oberlander, B. C., Jenssen, H. K., Hellwig, C., and Nordström, L. A., 2005, "Post Irradiation Examination of Rod 2 of the Inert Matrix Fuel Test IFA-651," *18th Proceedings of the Enlarged Halden Programme Group Meeting on High Burn-Up Fuel Performance, Safety and Reliability*, Lillehammer, Oct. 16–21, OECD HRP, Halden, Norway.

[18] Lassmann, K., Van de Laar, J., and Van Uffelen, P., 2007, "Power Condense: A Program for the Condensation of Power Histories," European Commission, Joint Research Centre, Institute for Transuranium Elements, EUR 22874 EN, Karlsruhe, Germany.

[19] Schubert, A., Győri, C., Elenkov, D., Lassmann, K., and van de Laar, J., 2003, "Analysis of Fuel Centre Temperatures with the TRANSURANUS Code," *Proceedings of the International Conference on Nuclear Fuel for Today and Tomorrow-Experiences and Outlook*, Würzburg, Mar. 16–19, German Nuclear Society KTG, Berlin, Germany.

[20] Hellwig, C., Streit, M., Blair, P., Tverberg, T., Klaassen, F. C., Schram, R. P. C., Vettraino, F., and Yamashita, T., 2006, "Inert Matrix Fuel Behaviour in Test Irradiations," J. Nucl. Mater., **352**, pp. 291–299.

[21] Stan, M., 2005, "Materials Models and Simulations in Support of Nuclear Fuels Development," Report No. LA-UR-05–5652, Los Alamos International Laboratory, Los Alamos, NM.

Downloaded 02 Jun 2010 to 171.66.16.109. Redistribution subject to ASME license or copyright; see http://www.asme.org/terms/Terms_Use.cfm

Development of a Hybrid Turbulent Particle Dispersion Model and Implementation in the Gasflow Code

Zhanjie Xu[1]
Forschungszentrum Karlsruhe,
P.O. Box 3640,
76021 Karlsruhe, Germany
e-mail: zhanjie.xu@iket.fzk.de

John R. Travis
Ingenieurbüro DuBois-Pitzer-Travis,
63071 Offenbach, Germany

Wolfgang Breitung
Forschungszentrum Karlsruhe,
P.O. Box 3640,
76021 Karlsruhe, Germany

Dust mobilization in a vacuum vessel is one of the key issues endangering the security of the International Thermonuclear Experimental Reactor (ITER) in case of loss of vacuum accidents. The turbulent behavior of particles in turbulent flows has to be modeled for successful numerical simulations about particle mobilization. In this study a Lagrangian approach is adopted to formulate the particle transport especially for dust-dilute flows mostly encountered in the vacuum vessel of ITER. Based on the logic frame of the approach and the used computational fluid dynamics (CFD) computer code in the study, a hybrid turbulent particle dispersion model is proposed. The hybrid model features both a deterministic separated flow model and a stochastic separated flow (SSF) model, which are two popular turbulent dispersion models applied in particle simulations, and takes the advantages of the both models. The proposed model is implemented into the particle model of the CFD code successfully and the simulation results are verified against the experimental data. The verifications manifest the validities of the proposed model. In this paper general information about the work of dust mobilization is introduced and the particle turbulent dispersion models are reviewed briefly at first. The hybrid model is then proposed based on the SSF model. An experiment about particle dispersions in an advective wind channel flow with decaying turbulence in the streamwise direction is reviewed in the third section. In the following section about model verification, the decaying turbulence parameters in the channel flow are verified against the experimental data as the first step, and the parameters about the particle dispersions in the verified flow field are then verified against the data. The work is concluded finally.
[DOI: 10.1115/1.2983142]

1 Introduction

The ITER generic site safety report (GSSR) has shown the risk of the coexistence of combustible aerosols such as carbon, beryllium, tungsten, and oxygen even hydrogen in the vacuum vessel when air ingression occurs in case of loss of vacuum accidents (LOVA). The dust mobilization has to be understood before dust explosion simulations in a further step. The present work is primarily concentrated on the particle transport modeling for a computational fluid dynamics (CFD) computer code [1].

It is known that two of the most popular methods applied to formulate particle motions are Eulerian approach and Lagrangian approach [2]. The particles are modeled as a continuous phase in the Eulerian frame and as discrete entities on the Lagrangian approach. The former is suitable for particle-laden flows and the latter for particle-dilute flows. As the most flows expected in the vacuum vessel of ITER in accidents are particle-dilute ones, the Lagrangian approach is chosen in the study.

Basically the fundamental particle transport model has been made for the code in the study based on the Lagrangian approach and been verified [3]. This paper focuses mainly on the topic of turbulent particle dispersion, which is one of the most important aspects of a numerical particle model.

The particle dispersion can be modeled by a parameter of particle diffusivity, or called a particle diffusion coefficient in the light of Eulerian approach. Meanwhile two different ways could be used to model particle dispersions in the frame of Lagrangian approach. One is called deterministic separated flow (DSF) model. Based on this model, the mean fluid velocity is used in the governing equations of particle transport. The particle dispersion is modeled by an additional diffusion coefficient, like in the Eulerian approach. The old particle dispersion model in the code belongs to this category. The other is called stochastic separated flow (SSF) model, where the instantaneous fluid velocity, rather than the mean value, is adopted in the particle transport equations. The turbulent fluctuations of fluid particles result directly in the fluctuations of particle movements, namely, the particle dispersions.

Both the DSF models in the Lagrangian approach and in the Eulerian approach are facing the same problem to formulate the particle diffusivity. That is, both are using only the particle concentration gradient-based information to determine the particle diffusion [4]. Actually the fluid turbulence is also an important contribution to the particle dispersion. Therefore even stronger restrictions exist for the DSF model especially in case of particle-dilute flows, in which particle/particle interactions can be neglected and then the gradient of the particle concentration is hardly able to influence the particle diffusivity.

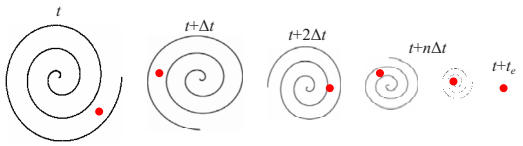
Indeed the code with the old DSF model could not predict successfully the realistic particle diffusivity in an advective flow with a decaying distribution of turbulence in a wind-channel experiment. The situation necessitates developing a new particle dispersion model especially for the code. The proposed model must match the logic frame of the code, in which only the mean fluid velocities are used in the particle transport governing equations. On the other hand, the proposed model must contain the contribution of the fluid turbulence to the particle dispersion, like what

[1]Corresponding author.

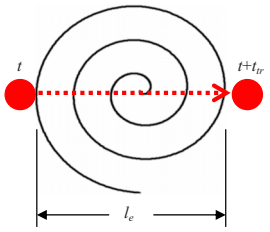
Manuscript received July 28, 2008; final manuscript received July 29, 2008; published online October 2, 2008. Review conducted by Dilip R. Ballal. Paper presented at the 16th International Conference on Nuclear Engineering (ICONE16), Orlando, FL, May 12–15, 2008.

Copyright © 2009 by ASME

Downloaded 02 Jun 2010 to 171.66.16.109. Redistribution subject to ASME license or copyright; see http://www.asme.org/terms/Terms_Use.cfm



(I) Entrapment of particle by eddy



(II) Transit of particle through eddy

Fig. 1 Particle eddy interactions

the the SSF model does. Such a model is in a frame of the DSF method but has a feature of the SSF model. Therefore a so-called "hybrid model" is proposed in this study.

2 Hybrid Particle Dispersion Model

The hybrid model is proposed based on the SSF model. Thus the SSF model is introduced in the first subsection. Then the hybrid model is put forward in the next subsection.

2.1 SSF Model. The particle momentum equation in a Cartesian coordinate system is

$$\frac{du_p}{dt} = \frac{3}{4} C_D \frac{\rho_g}{\rho_p} \frac{(u_g - u_p)|\vec{u}_g - \vec{u}_p|}{d_p} + g \tag{1}$$

where u and ρ are velocity and density, respectively; the subscripts g and p stand for gas and particle, respectively; C_D is the drag coefficient, a function of Reynolds number on particle diameter; $|\vec{u}_g - \vec{u}_p|$ is the drift velocity of particle or relative velocity of particle to fluid; g stands for a body force.

The fluid velocity u_g in Eq. (1) can be decomposed into a mean value $\bar{u}_g$ and a fluctuation, denoted as u_g'. Meanwhile the turbulent flow field is discretized into a host of turbulent eddies with different length scales depending on the local turbulent intensity. A ground hypothesis of the SSF model is that the u_g' is assumed to be constant within an eddy. Each time a particle transits from one eddy to another, the u_g' is renewed by satisfying a Gaussian probability density function (PDF) with a zero mean and a certain deviation. The essential discrimination of different variations of the SSF model relies on how to model the fluctuating velocity of fluid and how often to update it.

Two events could occur in the particle/eddy interaction, as shown in Fig. 1. The particle could be entrapped by the eddy if the inertia of the particle is sufficiently small, a smaller dimension or a lighter mass, or the eddy is sufficiently strong. In this case, the particle moves with the eddy until the eddy dissipates. It implies that the particle movement undergoes the same fluctuation of fluid velocity in the whole lifetime of the eddy. Another thing that could happen is that the particle passes over the eddy if the particle is heavy enough or the met eddy is so small. In this case the updating frequency does not depend on the lifetime of the eddy anymore, but on the particle drift velocity and the dimension of the eddy, namely, the transit time of particle through the eddy.

Based on the standard k-ε turbulence model [1], the length scale of a randomly sampled eddy is given as [5]

$$l_e = C_\mu^{0.5} \frac{k^{1.5}}{\varepsilon} \tag{2}$$

where C_μ is a parameter in the turbulent model, and k and ε are the turbulent kinetic energy and dissipation rate, respectively. Then the lifetime of the eddy is defined as

$$t_e = \frac{l_e}{|u_g'|} \tag{3}$$

where $|u_g'|$ is the absolute value of the fluctuating velocity and u_g' satisfies the Gaussian PDF distribution with a zero mean and a standard deviation of σ, satisfying

$$\sigma = \sqrt{\frac{2}{3}k} \tag{4}$$

On the other hand, the particle transit time is determined as follows. If the body force is not considered, then the momentum equation (1) can be rearranged as

$$\frac{du_p}{dt} = \frac{3 C_D \rho_g |\vec{u}_g - \vec{u}_p|}{4 \rho_p d_p} (u_g - u_p) \tag{5}$$

namely,

$$\frac{du_p}{dt} = \frac{1}{\tau_p}(u_g - u_p) \tag{6}$$

where $\tau_p = 4\rho_p d_p / 3 C_D \rho_g |\vec{u}_g - \vec{u}_p|$ is called the particle relaxation time, characterizing how fast the particle responsds to the variations of the flow field. In case of low particle Reynolds number, τ_p shrinks to $\rho_p d_p^2 / 18 \mu_g$, where μ_g is the molecular dynamics viscosity of fluid or gas.

By integrating Eq. (6), one has

$$u_p = u_g + A_1 \exp\left(-\frac{t}{\tau_p}\right) \tag{7}$$

If an initial condition of $u_p|_{t=0} = u_{p0}$ is assumed, the integration coefficient A_1 can be determined, then Eq. (7) becomes

$$u_p = u_g + (u_{p0} - u_g)\exp\left(-\frac{t}{\tau_p}\right) \tag{8}$$

Owing to $dx_p/dt = u_p$, the equation about particle location x_p can be obtained as

$$\frac{dx_p}{dt} = u_g + (u_{p0} - u_g)\exp\left(-\frac{t}{\tau_p}\right) \tag{9}$$

To integrate Eq. (9) with considering an initial condition of $x_p|_{t=0} = x_{p0}$,

$$x_p = x_{p0} + u_g t + \tau_p (u_{p0} - u_g)\left[1 - \exp\left(-\frac{t}{\tau_p}\right)\right] \tag{10}$$

This equation is used to determine the transit time t_{tr} of a particle through an eddy with a length scale, say, l_e. According to Eq. (10),

$$x_p|_{t=t_{tr}} = x_{p0} + u_g t_{tr} + \tau_p (u_{p0} - u_g)\left[1 - \exp\left(-\frac{t_{tr}}{\tau_p}\right)\right] \tag{11}$$

namely,

$$(x_p|_{t=t_{tr}} - x_{p0}) = u_g t_{tr} + \tau_p (u_{p0} - u_g)\left[1 - \exp\left(-\frac{t_{tr}}{\tau_p}\right)\right] \tag{12}$$

where $(x_p|_{t=t_{tr}} - x_{p0})$ is the absolute travel distance of the particle in the time duration of t_{tr}. $u_g t_{tr}$ is the absolute travel distance of the eddy. Thus the relative travel distance of the particle to the eddy must be $(x_p|_{t=t_{tr}} - x_{p0}) - u_g t_{tr}$. This relative travel distance is required to be the eddy size l_e. Thus, according to Eq. (12), it has to be

Downloaded 02 Jun 2010 to 171.66.16.109. Redistribution subject to ASME license or copyright; see http://www.asme.org/terms/Terms_Use.cfm

$$l_e = \tau_p(u_{p0} - u_g)\left[1 - \exp\left(-\frac{t_{\text{tr}}}{\tau_p}\right)\right] \tag{13}$$

Then,

$$t_{\text{tr}} = -\tau_p \log\left[1 - \frac{l_e}{\tau_p(u_{p0} - u_g)}\right] \tag{14}$$

in a more general form [2]

$$t_{\text{tr}} = -\tau_p \log\left(1 - \frac{l_e}{\tau_p|\vec{u}_p - \vec{u}_g|}\right) \tag{15}$$

Equality (15) is meaningful mathematically only if $l_e < \tau_p|\vec{u}_p - \vec{u}_g|$. Otherwise $t_{\text{tr}} = t_e$.

By considering both the eddy lifetime (3) and the particle transit time (15), the particle/eddy interaction time is defined as

$$t_{\text{int}} = \min(t_e, t_{\text{tr}}) \tag{16}$$

It can be summarized that the fluid velocity fluctuation is kept as constant within every time duration of t_{int} and is renewed with a frequency of $1/t_{\text{int}}$. Moreover the t_{int} is a function of the flow field, turbulence parameters, particle properties, and so on.

2.2 Definition of Hybrid Model. As mentioned in Sec. 1, a DSF model is adopted in the particle model of the current code. The mean fluid velocity is used in the particle governing equations and the particle dispersion is modeled by a turbulent diffusion coefficient of particle [1]. However, in the hybrid model, the use of the mean fluid velocity is retained, but the particle dispersion is modeled based on the particle/eddy interaction mechanism. So this subsection is devoted to describe how the model is initiated and defined.

In the light of the particle/eddy interaction mechanism described in Sec. 2.1, two important assumptions are made for the hybrid model.

(1) The particle diffusion velocity $u_{p\text{diff}}$ is kept as constant when the particle interacts within one eddy. The particle could be entrapped by the eddy or just transit through the eddy.
(2) The particle diffusion velocity $u_{p\text{diff}}$ is updated when the particle comes into a new eddy.

According to the second assumption and Eqs. (3), (15), and (16), the interval time between two sequent updates of $u_{p\text{diff}}$ is determined by the "interaction time" as follows:

$$t_{\text{int}} = \min\left[\frac{l_e}{|u_g'|}, -\tau_p \log\left(1 - \frac{l_e}{\tau_p|\vec{u}_p - \vec{u}_g|}\right)\right] \tag{17}$$

where $l_e = C_\mu^{0.5}(k^{1.5}/\varepsilon)$ and $\tau_p = 4\rho_p d_p / 3C_D\rho_g|\vec{u}_g - \vec{u}_p|$. Equality (17) determines the updating frequency of the particle diffusion velocity $u_{p\text{diff}}$.

The remaining content of this subsection is to define the $u_{p\text{diff}}$. The particle diffusion velocity is defined in view of the physical background of the particle motion to satisfy the following requirements.

(1) The maximum $u_{p\text{diff}}$ cannot exceed the instantaneous fluctuating velocity of fluid particle, u_g', which satisfies the Gaussian PDF distribution with a zero mean and a standard deviation of $\sigma = \sqrt{\frac{2}{3}k}$. In an extreme case, $u_{p\text{diff}} \approx u_g'$ if the particle has the same property as the fluid particle.
(2) If the particle has a smaller mass, $u_{p\text{diff}}$ should be closer to u_g'; if the particle has a bigger inertia, $u_{p\text{diff}}$ should have a bigger deviation to u_g'. This is a straightforward deduction based on the classical Newtonian mechanics.

The first requirement implies that the $u_{p\text{diff}}$ must be a function of u_g'. The second requirement implies that the function of $u_{p\text{diff}}$ has to contain a factor of ratio of certain properties of between the particle and the fluid. The particle fluctuating velocity, or diffusion velocity, caused by the fluid particle fluctuations is most influenced and determined by the particle relaxation time τ_p, which definition can be referred to Sec. 2.1. Accordingly, the fluid relaxation time, called the time scale of fluid particle, is defined as [6]

$$\tau_g = \sqrt{\frac{3}{2}} C_\mu^{0.75} \frac{k}{\varepsilon} \tag{18}$$

where C_μ is a parameter in the standard k-ε turbulence model. It is supposed that the desired property ratio of the particle to the fluid is chosen as τ_p/τ_g.

Based on the above judgment and the two requirements, it is put forward that the $u_{p\text{diff}}$ satisfies the formula

$$u_{p\text{diff}} = \frac{u_g'}{\left[1 + C_\tau\left(\frac{\tau_p}{\tau_g}\right)\right]} \tag{19}$$

where C_τ is a model parameter. It can be determined by numerical tests based on experimental data.

The instantaneous fluctuating velocity of fluid particle, u_g', which satisfies the Gaussian PDF distribution with a zero mean and a deviation of $\sigma = \sqrt{\frac{2}{3}k}$, can be modeled by an inverse error function in numerical practices as follows:

$$u_g' = \pm \sqrt{\frac{2k}{3}}\, \text{erf}^{-1}(\zeta) \tag{20}$$

where ζ is a random number between 0 and 1 and the sign "$\pm$" is also randomly determined. So based on Eqs. (19) and (20), $u_{p\text{diff}}$ is further formulated as

$$u_{p\text{diff}} = \pm \frac{\sqrt{\frac{2k}{3}}}{\left[1 + C_\tau\left(\frac{\tau_p}{\tau_g}\right)\right]} \text{erf}^{-1}(\zeta) \tag{21}$$

According to the logic frame of the code [1], $u_{p\text{diff}}$ is determined by a turbulent diffusion coefficient of particle λ as follows:

$$u_{p\text{diff}} = \pm \sqrt{\frac{4\lambda}{\delta t}}\, \text{erf}^{-1}(\zeta) \tag{22}$$

where δt is the time step in the numerical scheme of the code. By comparing Eqs. (21) and (22), the equivalent λ in the frame of the code can be determined by

$$\lambda = \frac{1}{6} \frac{k\delta t}{\left[1 + C_\tau\left(\frac{\tau_p}{\tau_g}\right)\right]^2} \tag{23}$$

To summarize, the particle diffusion velocity $u_{p\text{diff}}$ depends on the λ expressed in Eq. (23) and is held constant in each particle/eddy interaction time t_{int}. It is updated with a frequency of $1/t_{\text{int}}$.

3 Experiments

Wells and Stock's experimental facility [7,8] is basically a horizontally positioned wind channel with a square cross section. Air flows from the left to the right. At the side of entrance, turbulence is generated by grids installed in the channel. So it is also called grid-generated turbulence. At the downstream, homogeneous isotropy turbulence is expected and its decay is monitored and recorded in experiments. The wind channel and some key parameters are shown in Fig. 2.

Particles are released at the central line of the channel into the uniform advective flow with the grid-generated isotropy streamwise decaying turbulence.

Downloaded 02 Jun 2010 to 171.66.16.109. Redistribution subject to ASME license or copyright; see http://www.asme.org/terms/Terms_Use.cfm

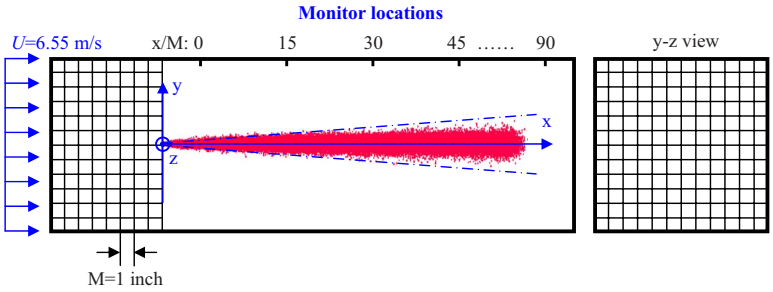


Fig. 2 Wells and Stock's experiment on particle dispersion in grid-generated decaying turbulent advective flow

In Wells and Stock's experiments the distributions along the x-direction of the following parameters are monitored and recorded, and are used to verify the numerical models in the study.

(1) The parameters about the decaying turbulent kinetic energy and dissipation rate: $U^2/u_g'^2$ and ε, where U is the average flow velocity of the advection flow, u_g' is the instantaneous fluctuating velocity of fluid particle, which corresponds to the turbulent kinetic energy, and ε is the turbulence dissipation rate.

(2) The parameters about the particle dispersion: the standard deviation of particle displacements in the y-direction, noted as "mean y^2," and the mean squared particle dispersion velocity in the y-direction, noted as "mean v^2." Both parameters are obtained by statistic calculations on a number of sample particles.

4 Verifications

The numerical flow fields in the wind channel are first verified against the experimental data. The hybrid turbulent particle dispersion model is then verified against the data based on the verified flow fields.

4.1 Verifying Flow Fields With Decaying Turbulence. This is in principle to verify the standard k-ε turbulence model adopted in the code in the study. The wind channel described in Sec. 3 is simulated by the code three dimensionally. The numerical solutions about the turbulence distributions along the central line of the channels are plotted in Figs. 3 and 4, against the experimental data.

In addition analytical solutions in a closed form about the decaying turbulence in the streamwise direction of the uniform advective flow are also deduced as follows:

$$k = \left(-\frac{U}{1-C_{\varepsilon 2}}\right)^{-1/(1-C_{\varepsilon 2})} \left(\frac{\varepsilon_0}{k_0^{C_{\varepsilon 2}}}\right)^{1/(1-C_{\varepsilon 2})} \left[x - \left(\frac{U}{1-C_{\varepsilon 2}}\right)\frac{k_0}{\varepsilon_0}\right]^{1/(1-C_{\varepsilon 2})} \tag{24}$$

$$\varepsilon = \left(-\frac{U}{1-C_{\varepsilon 2}}\right)^{-C_{\varepsilon 2}/(1-C_{\varepsilon 2})} \left(\frac{\varepsilon_0}{k_0^{C_{\varepsilon 2}}}\right)^{1/(1-C_{\varepsilon 2})} \times \left[x - \left(\frac{U}{1-C_{\varepsilon 2}}\right)\frac{k_0}{\varepsilon_0}\right]^{C_{\varepsilon 2}/(1-C_{\varepsilon 2})} \tag{25}$$

where k_0 and ε_0 are the turbulence information at the origin, $C_{\varepsilon 2}$ is a parameter in the turbulence model, and x is the coordinate in the x-direction.

For an isotropy turbulence,

$$k = \tfrac{3}{2}u_g'^2 \tag{26}$$

Thus the value of $U^2u_g'^2$ can be obtained by Eqs. (24) and (26) as follows:

$$\frac{U^2}{u_g'^2} = \frac{3U^2}{2k} \tag{27}$$

Figures 3 and 4 clearly manifest that the advective flow with decaying turbulence is reproduced numerically with consistence to the data and analytical solutions.

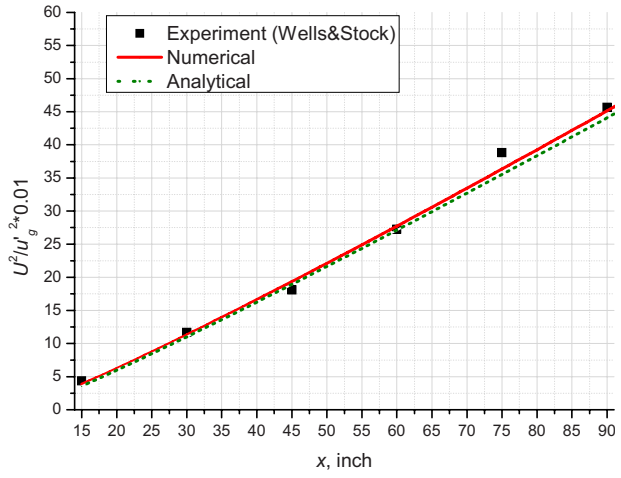


Fig. 3 Verification of the numerical solution against the analytical solution and the experimental data of $U^2/u_g'^2 \times 0.01$

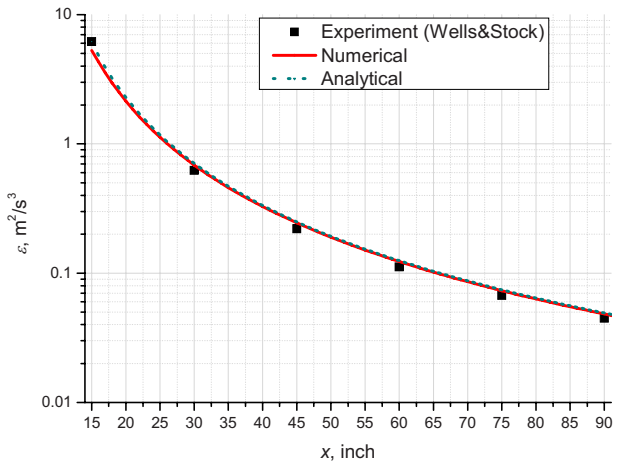


Fig. 4 Verification of the numerical solution against the analytical solution and the experimental data of ε

Downloaded 02 Jun 2010 to 171.66.16.109. Redistribution subject to ASME license or copyright; see http://www.asme.org/terms/Terms_Use.cfm

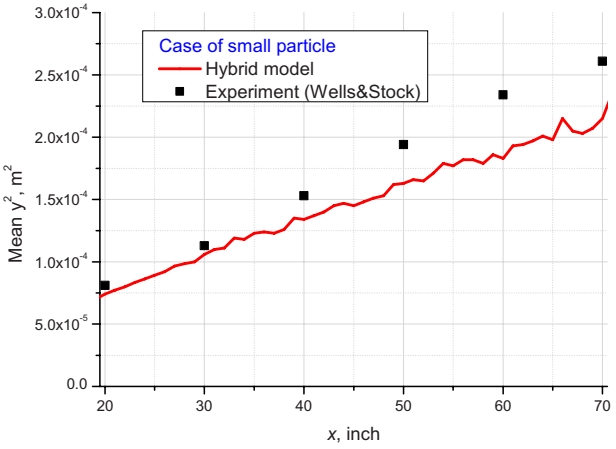


Fig. 5 Comparison of the data and simulation with the hybrid model on particle dispersion distance in the *y*-direction in case of a small particle

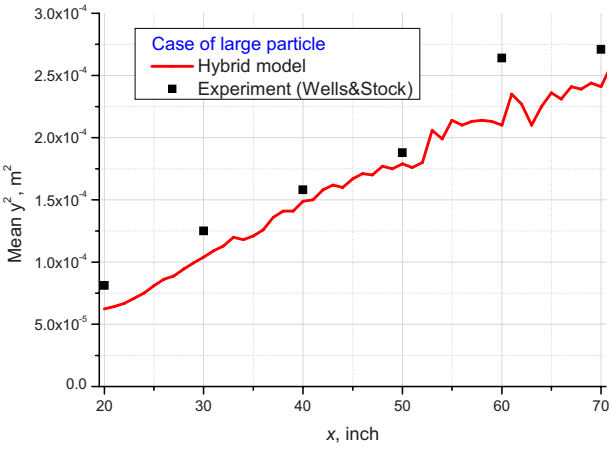


Fig. 7 Comparison of the data and simulation with the hybrid model on particle dispersion distance in the *y*-direction in case of a large particle

4.2 Verifying Hybrid Particle Dispersion Model. To reproduce the experiments numerically, two types of particles are tested. One is denoted as "small particle," with a diameter of 5 μm and density of 2.475×10^3 kg/m^3. The other is denoted as "large particle," with a diameter of 57 μm and density of 2.420 $\times10^3$ kg/m^3. The fluid (air) density is 0.1179 kg/m^3, and the kinematic viscosity 1.617×10^{-5} m^2/s. The gravity is not considered at this stage.

In each simulation, a total of 2×10^5 particles are injected and a physical time of 0.5 s is simulated. Certain initial fluctuating velocities of particles are applied in the case of large particles at the injection point to match the first measurement in the experiments. Moreover, this initial condition is not available in Wells and Stock's paper. However, it is not necessary in the case of small particles in that they can follow the fluctuations of the surrounding fluid field immediately after being released owing to their small inertia. A cell size of 2.54 cm (1 in.) is applied in the statistic calculations.

Figures 5 and 6 show that the numerical predictions are on a little lower side to the data but with an acceptable agreement with the data. The figures also tell that the particle spreading in the *y*-direction is almost linear to the distance from the injection point. It is true at the early phase of the particle cloud spreading, like within the time of 0.5 s in the study, according to the Taylor's theorem [9].

Figures 7 and 8 indicate that the particle dispersion velocity also decreases while the turbulence decays along the *x*-direction. It means that the fluid turbulence information is coupled to the particle turbulent dispersion in a proper way by the proposed hybrid model.

The instantaneous velocity fluctuations (u') of fluid particles, small particles, and large particles are compared in Fig. 9. The figure indicates that the turbulent fluctuations of small particles are much closer to the fluid velocity fluctuations. It means in view of physics that the small particles can follow the instantaneous fluctuations of the surrounding fluid particles more easily owing to their small inertia. However, the fluctuation of large particles is much smaller because of their heavier mass and longer relaxation time. This figure reflects, in a viewpoint, the correctness of the turbulent particle dispersion model.

5 Conclusions

In the work of dust mobilization simulation for ITER, an important turbulent particle dispersion model, called hybrid model, is proposed and implemented into the simulation code [1] successfully. In the new model featuring both a DSF model and a SSF model, the dispersion velocity is determined by a turbulent particle diffusion coefficient, like in a DSF model. However, the

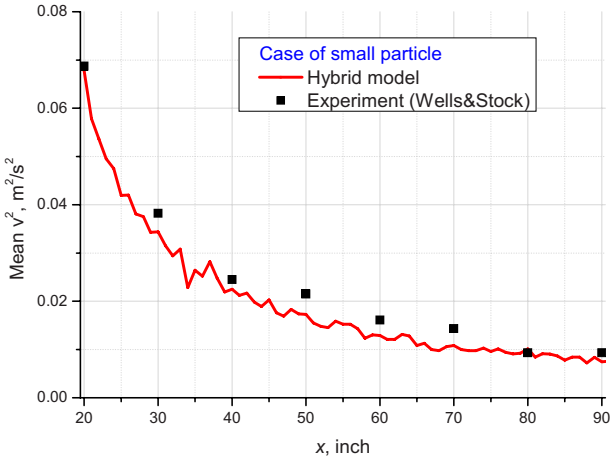


Fig. 6 Comparison of the data and simulation with the hybrid model on particle dispersion velocity in the *y*-direction in case of a small particle

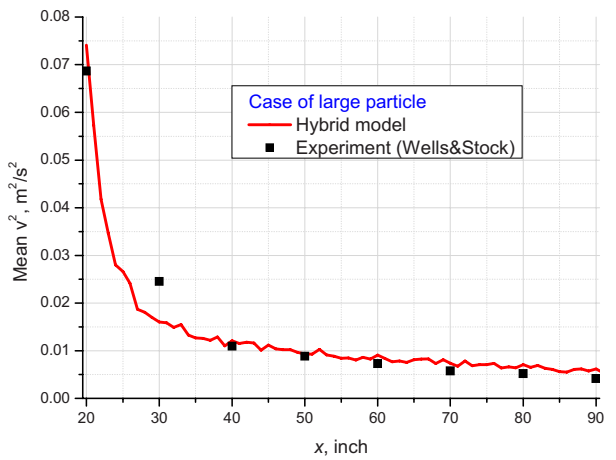


Fig. 8 Comparison of the data and simulation with the hybrid model on particle dispersion velocity in the *y*-direction in case of a large particle

Downloaded 02 Jun 2010 to 171.66.16.109. Redistribution subject to ASME license or copyright; see http://www.asme.org/terms/Terms_Use.cfm

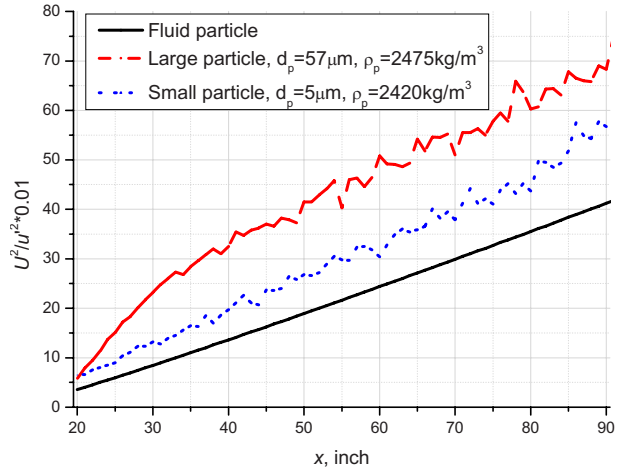


Fig. 9 Comparison of the instantaneous velocity fluctuations of fluid, small particles, and large particles

updating of the particle dispersion velocity is determined by a particle/eddy interaction mechanism, like in a SSF model. The newly developed model is verified against the experimental data in which particles disperse in a uniform advective channel flow with decaying turbulence in streamwise direction. The verifications manifest the validity of the model.

Acknowledgment

This work, supported by the European Communities under the contract of Association between EURATOM and Forschungszentrum Karlsruhe, was carried out within the framework of the European Fusion Development Agreement.

Nomenclature

A_1 = temporary integration coefficient
C_D = drag coefficient
C_τ = particle model parameter
$C_{\varepsilon 2}$ = turbulence model parameter
C_μ = turbulence model parameter
d_p = particle diameter, m
g = gravitational acceleration, m/s^2
k = turbulent kinetic energy, m^2/s^2
k_0 = initial value of k, m^2/s^2
l_e = length scale of turbulent eddy, m
t = physical time, s
t_e = lifetime of turbulent eddy, s
t_{int} = interaction time between particle and eddy, s
t_{tr} = transit time of a particle through an eddy, s
U = average advective flow velocity, m/s
u_g = fluid velocity, m/s
$\bar{u}_g$ = average fluid velocity, m/s
u' = instantaneous velocity fluctuation, m/s
u'_g = instantaneous velocity fluctuation of fluid, m/s
u_p = particle velocity, m/s
u_{p0} = initial value of u_p, m/s
$u_{p\text{diff}}$ = particle diffusion velocity, m/s
x = coordinate in x-direction, m
x_p = particle location in x-direction, m
x_{p0} = initial value of x_p, m
ρ_g = fluid density, kg/m^3
ρ_p = particle density, kg/m^3
ε = turbulent dissipation rate, m^2/s^3
ε_0 = initial value of ε, m^2/s^3
σ = standard deviation of a Gaussian distribution
τ_g = relaxation time of fluid, s
τ_p = relaxation time of particle, s
μ_g = molecular dynamics viscosity, Pa s
ζ = a random number
λ = turbulent diffusion coefficient of particle, m^2/s
δt = time step, s
v = particle dispersion velocity in transverse direction, m/s
y = particle displacement in transverse direction, m

References

[1] Travis, J. R., Spore, J. W., Royl, P., Lam, K. L., Wilson, T. L., Müller, C., Necker, G. A., Nichols, B. D., and Redlinger, R., 1998, "GASFLOW-II: A Three Dimensional Finite-Volume Fluid Dynamics Code for Calculating the Transport, Mixing and Combustion of Flammable Gases and Aerosols in Geometrically Complex Domains, Vol. 1: Theory and Computational Model," Research Center Karlsruhe Report Nos. FZKA-5994 and LA-13357-M.
[2] Hennick, E. A., 1998, "A Comparison of Stochastic Separated Flow Model for Particle Dispersion in Turbulent Flows," Master's thesis, University of Toronto, Toronto, Ontario, Canada.
[3] Xu, Z., Breitung, W., Travis, J. R., and Necker, G., 2007, "Development and Validation of Particle Transport and Diffusion Models for Dust Explosion Simulation in ITER," Annual Meeting on Nuclear Technology, Karlsruhe, Germany, May 22–24.
[4] Lightstone, M. F., 1992, "A Stochastic Model of the Dispersion of Solid Particles in a Turbulent Gaseous Environment," Ph.D. thesis, University of Waterloo, Waterloo. Ontario, Canada.
[5] Gosman, A. D., and Ioannides, E., 1981, J. Energy, **7**, pp. 482–490.
[6] Shirolkar, J. S., Coimbra, C. F. M., and Queiroz McQuay, M., 1996, "Fundamental Aspects of Modeling Turbulent Particle Dispersion in Dilute Flows," Prog. Energy Combust. Sci., **22**, pp. 363–399.
[7] Snyder, W. H., and Lumley, J. L., 1971, "Some Measurements of Particle Velocity Autocorrelation Functions in a Turbulent Flow," J. Fluid Mech., **48**, pp. 41–71.
[8] Wells, M. R., and Stock, D. E., 1983, "The Effects of Crossing Trajectories on the Dispersion of Particles in a Turbulent Flow," J. Fluid Mech., **136**, pp. 31–62.
[9] Taylor, G. I., 1921, "Diffusion by Continuous Movements," *Proceedings of the London Mathematical Society*, London, UK, Series 2, Vol. 20, pp. 196–211.

Downloaded 02 Jun 2010 to 171.66.16.109. Redistribution subject to ASME license or copyright; see http://www.asme.org/terms/Terms_Use.cfm

Preliminary Design Analysis of Hot Gas Ducts for the Nuclear Hydrogen System

Kee-nam Song
e-mail: knsong@kaeri.re.kr

Yong-wan Kim

Korea Atomic Energy Research Institute (KAERI),
P.O. BOX 105, Yuseong-gu,
Daejeon 305-353, Korea

Korea Atomic Energy Research Institute is in the process of carrying out a nuclear hydrogen system by considering the indirect cycle gas cooled reactors that produce heat at temperatures in the order of 950°C. A coaxial double-tube hot gas duct (HGD) is a key component connecting the reactor pressure vessel and the intermediate heat exchanger for the nuclear hydrogen system. Recently, a preliminary design analysis for the primary and secondary hot gas ducts of the nuclear hydrogen system was carried out. These preliminary design activities include a preliminary decision on the geometric dimensions, a preliminary strength evaluation, and an appropriate material selection. In this study, a preliminary strength evaluation for the HGDs of the nuclear hydrogen system has been undertaken. Preliminary strength evaluation results for the HGDs showed that the geometric dimensions of the proposed HGDs would be acceptable for the design requirements.
[DOI: 10.1115/1.2983141]

1 Introduction

A very high temperature gas cooled reactor (VHTR) has been selected as a high energy heat source for a nuclear hydrogen generation. The VHTR can produce hydrogen from heat and water by using a thermochemical process or from heat, water, and natural gas by steam reformer technology or using the high temperature electrolysis of steam. The nuclear hydrogen system being researched at KAERI is planning to produce hydrogen by using nuclear energy and a thermochemical process. Helium gas is tentatively considered as the choice for the coolant of the nuclear hydrogen system since it is an inert gas, with no affinity to a chemical or nuclear activity; therefore the transport of radioactivity in the primary circuit of the nuclear hydrogen system is minimal under a normal operation. Moreover, its gaseous nature avoids problems related to a phase change and water-metal reactions and therefore improves its safety. In this study, a strength evaluation for the HGDs of the nuclear hydrogen system has been undertaken.

2 Nuclear Hydrogen System

The schematic nuclear hydrogen system is shown in Fig. 1. According to Fig. 1, two HGDs and an intermediate heat exchanger (IHX) are needed. One of the HGDs, which is called a primary HGD, is located between the reactor pressure vessel and the IHX. The other HGD, which is called a secondary HGD, is located between the IHX and the SO_3 decomposer. The HGD structure of the nuclear hydrogen system is tentatively considered as a horizontal coaxial double-tube structure as shown in Figs. 2 and 3, which provides a passage for the hot and cold helium gases In this study, a preliminary design evaluation for the primary and secondary HGDs of the nuclear hydrogen system is carried out based on both the tentative design configuration as shown in Table 1 [1] and a preceding research [2] because of its successful operating experience and its simplicities as shown in Figs. 2 and 3. By passing through the nuclear hydrogen system reactor core, the hot helium gas is conveyed via the liner tube of the horizontal HGD to the IHX. After being cooled down, the cold helium gas is returned to the lower section of the reactor pressure vessel via a passage between the coaxial inner tube and the pressure vessel of the primary HGD.

3 Preliminary Design of the Primary HGD

The HGD is a unique component exclusively found in a HTR-module concept [3] where both the nuclear core and the power conversion unit are placed separately into two pressure vessels, which require a connecting duct between them. By passing through the nuclear core in the nuclear hydrogen system, hot helium gas in the order of 950°C is conveyed via the liner tube of the horizontal HGD (primary HGD) to the IHX as shown in Fig. 2. After being cooled down, the cold helium gas in the order of 490°C is returned to the lower section of the reactor pressure vessel via a passage between the coaxial inner tube and the hot gas pressure tube as shown in Fig. 2. In this study, the helium gas pressure in the primary loop is tentatively assumed to be 7.0 MPa as shown in Table 1 [1]. The reactor core is located inside the reactor pressure vessel, while the IHX and helium circulator are in an adjacent vessel, i.e., the IHX vessel. These vessels are also supposed to be connected together by the HGD as shown in Fig. 2, one end is connected to the reactor pressure vessel by a flange and the other end is connected to the IHX by a flange. This structure is composed of a liner tube, an inner tube, a hot gas pressure tube, a thermal-insulating fiber, and a separating taper tube as shown in Fig. 3. The inner tube acts as a supporting structure for the inner and taper tubes. Two sets of bellows are used in its design to compensate for a thermal expansion. The HGD is assumed to be divided into eight sections for an easier installation. Each section is assumed to be connected by a slide joint.

The HGD has the following functions: (1) transporting the hot helium gas from the core to the IHX, (2) transporting the cold helium gas from the IHX to the core, and (3) providing thermal compensations and avoiding large thermal stresses during various operating conditions.

The primary HGD is a Safety Class 3 and Seismic Class 1 component [2]. It consists of flanges, bellows, a liner tube, an inner tube, a separating taper tube, and a thermal-insulating fiber. The design parameters of the primary HGD are listed in Table 2. For the thermal-insulating fiber used in this study the maximum packing pressure is tentatively assumed to be 0.03 MPa.

The primary HGD has to operate at high temperature and medium pressure conditions for several decades. Its performance for a thermal insulation between the hot and cold helium flows, its ability to resist temperature cycles and pressure cycles, and to sustain total structural integrity at high temperature and medium pressure conditions will play an important role for the long-term safe operation of the nuclear hydrogen system. The preliminary geometric dimensions for the primary HGD of the nuclear hydrogen system have been selected by considering the thermal power of the nuclear hydrogen system. The flow velocity (V) of hot helium in the liner tube is assumed to be about 65.4 m/s by considering the design data of a 600 MW_t gas turbine modular reactor [4]. The inner diameter of the primary HGD pressure vessel is obtained on the grounds where the flow velocity (V), the flow rate (ρV), and the dynamic pressure ($1/2\rho V^2$) in the liner tube are the same as those in the annulus between the inner tube and the primary HGD pressure vessel. In this study, we named those ideas as

Contributed by the Nuclear Engineering Division of ASME for publication in the JOURNAL OF ENGINEERING FOR GAS TURBINES AND POWER. Manuscript received July 27, 2008; final manuscript received July 30, 2008; published online October 2, 2008. Review conducted by Dilip R. Ballal.

Copyright © 2009 by ASME

Downloaded 02 Jun 2010 to 171.66.16.109. Redistribution subject to ASME license or copyright; see http://www.asme.org/terms/Terms_Use.cfm

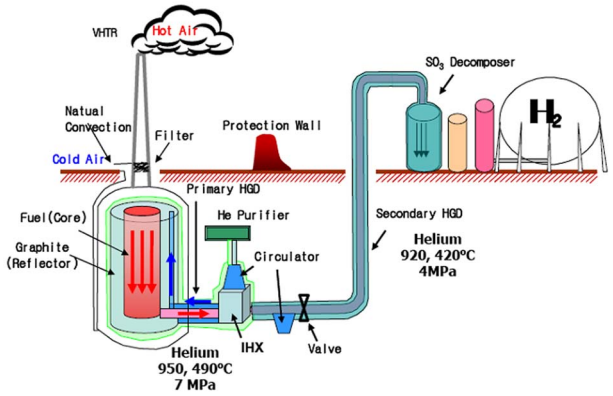


Fig. 1 Nuclear hydrogen system

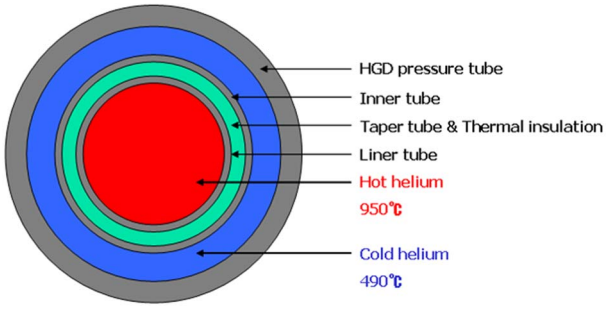


Fig. 3 Cross section of the primary HGD

a constant flow velocity (CFV) model, a constant flow rate (CFR) model, and a constant hydraulic head (CHH) model, respectively. In this case, the primary HGD structure might be insensitive to a flow induced vibration because there are no pressure differences between the hot and cold helium regions.

Structural design and strength evaluation for the primary HGD have been undertaken in the case that the following assumptions are considered. (1) The distance between the axes of the reactor pressure vessel and the IHX is about 8855 mm including the length of the primary HGD made of Alloy 800H, the radius of the reactor and the radius of the IHX made of Mod.9Cr-1Mo. (2) The thermal expansion coefficient of Mod.9Cr-1Mo is $1.25 \times 10^{-5}\ K^{-1}$. (3) The temperature rise of the components of the primary loop boundary under accident conditions is 250°C. (4) The temperature rise of the inner tube made of Alloy 800H under accident conditions is 400°C. (5) The material of the thermal-insulating fiber is Al_2O_3. (6) The flow rate of the helium is 83.73 kg/s. (7) For the used thermal-insulating fiber, the maximum packing pressure is 0.03 MPa and the pressure difference is under 0.2 MPa. Strength evaluation results for the HGD are listed in Table 3.

4 Preliminary Design of the Secondary HGD

The secondary HGD is a connecting duct between the IHX and the SO_3 decomposer as shown in Fig. 1. Hot helium gas in the order of 920°C is conveyed via the liner tube of the horizontal HGD (secondary HGD) to the SO_3 decomposer as shown in Fig. 1. After being cooled down, the cold helium gas in the order of 420°C is returned to the IHX via a passage between the coaxial inner tube and the hot gas pressure tube as shown in Fig. 1. In this study, the helium gas pressure in the secondary loop is tentatively assumed to be 4.0 MPa as shown in Table 1. The structure used to house the secondary HGD of the nuclear hydrogen system is similar to the primary HGD structure as shown in Fig. 4. This structure is composed of a liner tube, an inner tube, a hot gas pressure tube, a thermal-insulating fiber, and a separating taper tube. The inner tube acts as a supporting structure for the inner and taper tubes. Several sets of bellows are used in its design to compensate for a thermal expansion. The secondary HGD is assumed to be divided into several sections for an easier installation. Each section is assumed to be connected by a slide joint. The secondary HGD has the following functions: (1) transporting the hot helium gas from the IHX to the SO_3 decomposer, (2) transporting the cold helium gas from the SO_3 decomposer to the IHX, and (3) providing thermal compensations and avoiding large thermal stresses during various operating conditions.

The secondary HGD is a Safety Class 3 and Seismic Class 1 component. It consists of flanges, bellows, a liner tube, an inner tube, a separating taper tube, and a thermal-insulating fiber. The design parameters of the secondary HGD are listed in Table 4. For the used thermal-insulating fiber in this study the maximum packing pressure is tentatively assumed to be 0.03 MPa.

The secondary HGD has to operate at high temperature and medium pressure conditions for several decades. Its performance for a thermal insulation between the hot and cold helium flows, its ability to resist temperature cycles and pressure cycles, and to sustain total structural integrity at high temperature and medium pressure conditions will play an important role for the long-term safe operation of the nuclear hydrogen system. The preliminary geometric dimensions for the secondary HGD of the nuclear hydrogen system have been tentatively selected by considering the thermal power of the nuclear hydrogen system. The flow velocity (V) of hot helium in the liner tube is assumed to be about 62.9 m/s by considering the design data of a 600 MW_t hydrogen modular reactor. The inner diameter of the secondary HGD

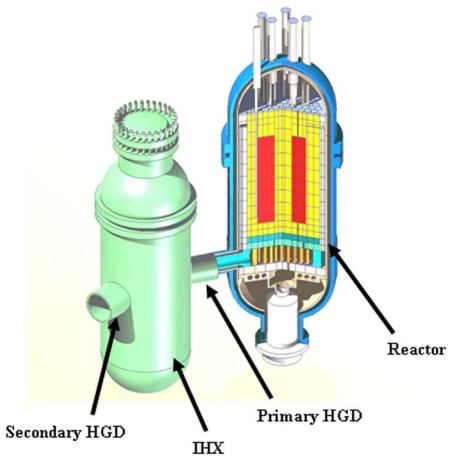


Fig. 2 Position of the primary HGD

Table 1 Tentative design configuration

	Design options
Power (MW_t)	200–250
Fuel type	Prismatic or pebble
Pressure boundary (MPa)	
Primary/secondary loop	~7.0/4.0
Inlet/outlet temperature (°C)	
Primary loop	~490/950
Secondary loop	~420/920

Downloaded 02 Jun 2010 to 171.66.16.109. Redistribution subject to ASME license or copyright; see http://www.asme.org/terms/Terms_Use.cfm

Table 2 Design parameters of the primary HGD for the CFV, CFR, and CHH models

	Outer diameter (mm)			Thickness (mm)			Design temperature (°C)
	CFV	CFR	CHH	CFV	CFR	CHH	
Liner tube	786	786	786	7	7	7	950
Inner tube	1046	1046	1046	10	10	10	550
Annulus	1211	1300	1252	82.5	127	103	
HGD pressure tube	1571	1670	1622	60	65	65	490

pressure vessel is obtained on the grounds where the flow rate (ρV) and the dynamic pressure ($1/2\rho V^2$) in the liner tube are the same as those in the annulus between the inner tube and the secondary HGD pressure vessel. In this case, the secondary HGD structure might be insensitive to a flow induced vibration because there are no pressure differences between the hot and cold helium regions.

Structural design and strength evaluation for the secondary HGD have been undertaken in the case that the following assumptions are considered: (1) The distance between the axes of the IHX vessel and the SO_3 decomposer is tentatively considered as about 100 m for the sake of safety of hydrogen explosion and overall efficiency. (2) The thermal expansion coefficient of Mod.9Cr-1Mo, the temperature rise of the components of the primary loop boundary under accident conditions, and the temperature rise of the inner tube made of Alloy 800H under accident conditions are the same as those of the primary HGD. (3) The material of the thermal-insulating fiber is Al_2O_3. (4) The flow rate of the helium is 77.05 kg/s. (5) For the thermal-insulating fiber used, the maximum packing pressure is 0.03 MPa and the pressure difference is under 0.2 MPa. Strength evaluation results for the HGD are listed in Table 5.

Table 3 Strength evaluation results of the primary HGD for the CFV, CFR, CHH, and HB models (MPa)

		Results			
	Design limit	CFV	CFR	CHH	HB
Liner tube	14	11.0	11.0	11.0	11.0
Inner tube	165	10.3	10.3	10.3	10.3
HGD pressure tube	72	70.6	70.0	67.4	70.9

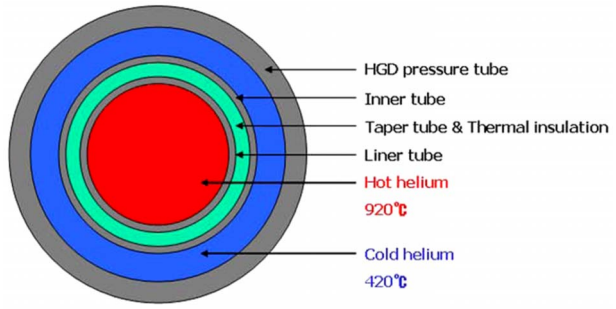


Fig. 4 Cross section of the secondary HGD

5 Conclusions

Indirect cycle gas cooled reactors that produce heat at temperatures in the order of 950°C are being considered in the nuclear hydrogen system at KAERI. Preliminary strength evaluation results for the primary and secondary HGDs of the nuclear hydrogen system showed that the preliminary decision on the geometric dimensions would be acceptable for the design requirements.

Acknowledgment

This project has been carried out under the nuclear R & D program by Ministry of Education, Science and Technology in Republic of Korea.

Nomenclature

V = flow velocity of hot helium in the liner tube
ρ = density of helium
ρV = flow rate of hot helium in the liner tube
$\frac{1}{2}\rho V^2$ = dynamic pressure in the liner tube

Table 4 Design parameters of the secondary HGD for the CFV, CFR, and CHH models

	Outer diameter (mm)			Thickness (mm)			Design temperature (°C)
	CFV	CFR	CHH	CFV	CFR	CHH	
Liner tube	1001	1001	1001	8	8	8	920
Inner tube	1261	1261	1261	10	10	10	480
Annulus	1468	1600	1527	103.5	169.5	133	
HGD pressure tube	1798	1934	1857	120	120	120	420

Table 5 Strength evaluation results of the secondary HGD for the CFV, CFR, CHH, and HB models (MPa)

		Results			
	Design limit	CFV	CFR	CHH	HB
Liner tube	14	12.3	12.3	12.3	12.3
Inner tube	165	12.4	12.4	12.4	12.4
HGD pressure tube	72	65.2	68.1	67.9	67.7

Downloaded 02 Jun 2010 to 171.66.16.109. Redistribution subject to ASME license or copyright; see http://www.asme.org/terms/Terms_Use.cfm

References

[1] Chang, J. H., Kim, Y. W., Lee, K. Y., Lee, Y. W., Lee, W. J., Noh, J. M., Kim, M. W., Lim, H. S., Shin, Y. J., Bae, K. K., and Jung, K. D., 2007, "A Study of a Nuclear Hydrogen Production Demonstration Plant," Nuclear Engineering and Technology, **39**(2), pp. 111–122.

[2] Huang, Z. Y., Zhang, Z. M., Yao, M. S., and He, S. Y., 2002, "Design and Experiment of Hot Gas Duct for the HTR-10," Nucl. Eng. Des., **218**, pp. 137–145.

[3] Lohnert, G. H., 1990, "Technical Design Features and Essential Safety-Related Properties of the HTR-Module," Nucl. Eng. Des., **121**, pp. 259–275.

[4] Song, K. N., and Kim, Y.-W., 2008, "Preliminary Design Analysis of Hot Gas Ducts for the Nuclear Hydrogen System," *Proceedings of the 16th International Conference on Nuclear Engineering*, Orlando, FL, May 11-15, Paper No. ICONE16-48145.

Downloaded 02 Jun 2010 to 171.66.16.109. Redistribution subject to ASME license or copyright; see http://www.asme.org/terms/Terms_Use.cfm